DURABILITY OF PRECAST PRESTRESSED CONCRETE PILES IN MARINE ENVIRONMENTS

A Dissertation
Presented to
The Academic Faculty

by

R. Brett Holland

In Partial Fulfillment
of the Requirements for the Degree
Doctor of Philosophy in the
School of Civil & Environmental Engineering

Georgia Institute of Technology

August 2012

DURABILITY OF PRECAST PRESTRESSED CONCRETE PILES IN MARINE ENVIRONMENTS

Approved by:

Dr. Lawrence Kahn, Co-Advisor
School of Civil & Environmental Engineering
Georgia Institute of Technology

Dr. Kimberly Kurtis, Co-Advisor
School of Civil & Environmental Engineering
Georgia Institute of Technology

Dr. Preet Singh
School of Materials Science & Engineering
Georgia Institute of Technology

Dr. Reginald DesRoches
School of Civil & Environmental Engineering
Georgia Institute of Technology

Dr. Jason Weiss
School of Civil Engineering
Purdue University

Date Approved: June 20, 2012

ACKNOWLEDGEMENTS

I would first like to express my tremendous gratitude to my advisors, Dr. Lawrence F. Kahn and Dr. Kimberly E. Kurtis. I am truly appreciative of the opportunity you both gave me with this research and the encouragement to explore wherever the results led us. I cannot fully express my sincere thanks to Dr. Kahn for always having an open door policy and spending many afternoons in his office discussing research, classes, and life in general.

I would also like to thank my thesis committee members Dr. Preet Singh, Dr. Reginald DesRoches, and Dr. Jason Weiss for reading this dissertation and providing valuable feedback that led to a more complete investigation and report.

The bulk of this research project was funded by the Georgia Department of Transportation (GDOT) under research project number 07-70. I am also grateful for the financial assistance provided by the Georgia Tech Presidential Fellowship, the Georgia Chapter of ACI, and the ARCS foundation.

This work would not have been possible without the generosity of Bob Sylvia of TXI Riverside, Daniel Green of National Cement, Wayne Wilson of Holcim, Ralph Hodgins and Ron Thomas of Sika, and Greg Moormann of SAS Stressteel who donated the materials necessary to complete this research. I would like to thank the following people at the Georgia Department of Transportation who took the time to discuss the project, offer suggestions, and provide open access to many of their resources: Myron Banks, Jeff Carroll, Mike Clements, Slade Cole, Andy Doyle, Mike Garner, Supriya

Kamatkar, Paul Liles, Mandi Reinshagen, Brian Scarbrough, Kevin Schwartz, and Lisa Sikes.

I want to thank Jeremy Mitchell for all of his help through my time at the structures lab and all of the time we spent talking about life while stepping away from work for a few minutes. Mike Anderson and J.J. Martino provided invaluable support with all of the IT related issues that arose through my time at Georgia Tech. I want to thank the numerous undergraduate research assistants who worked with me over the years and without whom this work would not have been completed: Fred Aguayo, Samuel Gil, Robert Heusel, Abdul Kabbara, Kristin Kendrick, Mark Kim, Luke Li, Mitchell McKay, Mackenzie Prestera, Daniel Schuetz, Armin Vosough, and Michael Wong.

I would also like to acknowledge many colleagues and friends who have offered the support and encouragement that allowed me to survive this experience. First, all of my coworkers in the Kahn and Kurtis groups at Georgia Tech over the years: Kennan Crane, Jonathan Hurff, Robert Moser, Jennifer Dunbeck, Katherine Snedeker, Victor Garas, Eric Davidson, Amal Jayapalan, Jun Chen, Nathan Mayercsik, Andrea Mezencevova, and Boyeon Lee. Thanks also to my fellow grad students and friends who were always willing to lend an ear and a hand: Jared Eubanks, Ben Deaton, Jong-Han Lee, Tim Wright, Curtis O'Malley, Andrew Bechtel, Josh Gresham, Cliff Bishop, Falak Shah, and Nick Reynolds.

Most importantly, I want thank my parents, Hank and Phyllis Holland, my grandmother, Charlsie Woody, my brother, Lee Holland, and my sisters, Sheree and Samantha Holland for their continued unending love, support, and encouragement.

TABLE OF CONTENTS

CHAPTER	Page #
ACKNOWLEDGEMENTS	ii
LIST OF TABLES	x
LIST OF FIGURES	xiv
LIST OF SYMBOLS	xxiv
SUMMARY	xxvii
CHAPTER 1: INTRODUCTION	1
1.1 Purpose and Objectives	1
1.2 Need for Research	2
1.3 Scope	4
1.4 Organization of Dissertation	6
CHAPTER 2: BACKGROUND INFORMATION	8
2.1 Deterioration Mechanisms of Concrete Piles in Marine Environments	8
2.2 Chlorides in Concrete	9
2.2.1 Sources of Chlorides	10
2.2.2 Transport Mechanisms	11
2.2.2.1 Chloride Diffusion	11
2.2.2.2 Chloride Binding	12
2.2.2.3 Chloride Permeation	13
2.2.2.4 Chloride Absorption	13
2.2.3 Chloride Induced Corrosion	14
2.2.4 Test Methods for Chloride Durability	15
2.2.4.1 AASHTO T259: Salt Ponding Test	15
2.2.4.2 Bulk Diffusion Test	16
2.2.4.3 Rapid Chloride Permeability Test	17
2.2.4.4 Electrical Migration Techniques	18
2.2.4.5 Resistivity Techniques	19
2.2.4.6 Summary	20
2.2.5 Effects of Mix Design on Chloride Durability	21

2.2.5.1 Water-to-Cementitious Materials Ratio 21
2.2.5.2 Age at Exposure 22
2.2.5.3 Supplementary Cementitious Materials 24
2.3 Carbonation of Concrete 28
2.3.1 Carbonation Modeling 30
2.3.2 Environmental Conditions 31
2.3.3 Concrete Mix Design Effects on Carbonation 32
2.4 Sulfate Attack 34
2.4.1 Degradation Mechanisms 34
2.4.2 Test Methods for Sulfate Attack Durability 36
2.4.2.1 ASTM C 1012 Expansion Tests 36
2.4.2.2 Compression Strength Degradation Testing 37
2.4.3 Effect of Binder Composition 37
2.4.3.1 Fly Ash 38
2.4.3.2 Slag 40
2.4.3.3 Silica Fume 41
2.4.3.4 Metakaolin 42
2.4.3.5 Ternary Blends 43
2.4.3.6 SCM's Summary 44
2.5 Biological Attack 45
2.6 Self-healing of Cracked Concrete 46
2.6.1 Crack Healing Mechanism 48
2.6.2 Permissible Crack Widths 48
2.6.3 Chloride Ingress into Cracked Concrete 49
2.6.4 Self-healing of Cracks 52
2.7 Summary 57
CHAPTER 3: FORENSIC INVESTIGATION OF I-95 AT TURTLE RIVER BRIDGE 58
3.1 Introduction 58
3.1.1 Bridge Description 59
3.1.2 Inspection Report Data for Original Substructure 64

3.2 Corrosion of Prestressing Steel 64
3.2.1 Visual Assessment of Damage 66
3.2.2 Half-cell Corrosion Potentials 70
3.2.3 Chloride Profiles 72
3.2.3.1 Test Methodology 74
3.2.3.2 Results, Chloride Concentrations 76
3.2.3.3 Chloride Ingress Modeling 82
3.2.4 Conclusions, Corrosion of Prestressing Steel 84
3.3 Sulfate Attack 85
3.3.1 Visual Assessment of Damage 86
3.3.2 Hardness Measurements 88
3.3.3 Compressive Strength Testing 91
3.3.4 X-Ray Diffraction 95
3.3.4.1 XRD Results from Atmospheric Region 97
3.3.4.2 XRD Results from Splash Zone 99
3.3.4.3 XRD Results from High Tide Region 103
3.3.4.4 XRD Results from Low Tide 106
3.3.4.5 XRD Results from Submerged Region 110
3.3.5 Thermo-Gravimetric Analysis 113
3.3.6 Conclusions, Sulfate Attack 118
3.4 Biodeterioration 119
3.4.1 Visual Inspection of Damage 119
3.4.2 Microscopy Characterization 122
3.5 Conclusions 124
3.5.1 Summary of Results 124
3.5.2 Future Research Topics and Recommendations 125
CHAPTER 4: MIX DESIGN DEVELOPMENT AND MECHANICAL PROPERTIES 127
4.1 Development of Concrete Mix Designs 127
4.1.1 Concrete Mix Design 127
4.1.2 Raw Material Properties 133

4.1.2.1 Cement 133
4.1.2.2 SCM's 135
4.1.2.3 Fine Aggregate 138
4.1.2.4 Coarse Aggregate 138
4.1.3 Air Contents 139
4.2 Mechanical Property Characterization 140
4.2.1 Compressive Strength 140
4.2.2 Elastic Modulus 142
CHAPTER 5: CHLORIDE INGRESS RESISTANCE OF HIGH PERFORMANCE CONCRETE 144
5.1 Introduction 144
5.2 Experimental Program 145
5.3 Results and Discussion 146
5.3.1 Rapid Chloride Permeability 146
5.3.2 Bulk Diffusion 148
5.4 Service Life Modeling 153
5.4.1 Diffusion Coefficient Estimation 154
5.4.1.1 Life 365 155
5.4.1.2 Concrete Works 156
5.4.1.3 Diffusion Coefficient Estimation from RCPT Results 158
5.4.1.4 Comparison with Experimental Results 159
5.4.2 Corrosion Initiation Period Estimation 163
5.5 Conclusions and Recommendations 167
CHAPTER 6: SULFATE RESISTANCE OF HIGH PERFORMANCE CONCRETE 169
6.1 Introduction 169
6.2 Experimental Program 171
6.3 Results and Discussion 173
6.3.1 ASTM C 1012 Expansion Testing 174
6.3.2 Compressive Strength Testing 177
6.3.3 Quantitative X-Ray Diffraction 188

6.3.4 Discussion of Results 191
6.3.4.1 Comparison of QXRD and Compressive Strength Data 191
6.3.4.2 Comparison of QXRD and Expansion Data 194
6.3.4.3 Comparison of Expansion and Compressive Strength Data 196
6.4 Conclusions and Recommendations 198
CHAPTER 7: CARBONATION RESISTANCE OF HIGH PERFORMANCE CONCRETE 200
7.1 Introduction 200
7.2 Experimental Program 202
7.3 Results and Discussion 203
7.3.1 Carbonation Results 203
7.3.2 Modeling 212
7.3.2.1 Carbonation Constant Estimation 212
7.3.2.2 Service Life Estimation 216
7.4 Conclusions and Recommendations 219
CHAPTER 8: SELF-HEALING OF HIGH PERFORMANCE CONCRETE 220
8.1 Introduction 220
8.2 Experimental Program 222
8.2.1 Concrete Mix Designs 222
8.2.2 Sample Preparation 223
8.2.3 Crack Healing Measurements 225
8.2.4 Chloride Diffusion Measurements 225
8.3 Results and Discussion 227
8.3.1 Crack Measurements 227
8.3.2 Chloride Ingress 232
8.3.2.1 Chloride Profiles 233
8.3.2.2 Chloride Transport Modeling 236
8.3.2.3 Crack Width Influence on Chloride Ingress 244
8.3.2.4 Diffusion Coefficient of Self-Healed Specimens 245

8.3.3 Service Life Modeling 247
8.4 Conclusions and Recommendations 249
CHAPTER 9: DISCUSSION OF DURABILITY TESTING RESULTS 252
9.1 Introduction 252
9.2 Summary of Results 252
9.2.1 Mechanical Properties 252
9.2.2 Chloride Ingress Resistance 253
9.2.3 Sulfate Attack Resistance 255
9.2.4 Carbonation Resistance 260
9.2.5 Self-Healing of Cracked Concrete 261
9.3 Comparison of Durability Characteristics 263
9.3.1 Uncracked Concrete Piles with Non-Corrosion Resistant Prestressing Strands 264
9.3.2 Concrete Piles with Corrosion Resistant Prestressing Strands 266
9.4 Recommendations 266
CHAPTER 10: CONCLUSIONS AND RECOMMENDATIONS 268
10.1 Conclusions 268
10.2 Recommendations 271
10.2.1 General Recommendations 271
10.2.2 Final Design Recommendations 273
10.2.3 Future Research 274
APPENDIX A: GEORGIA COASTAL BRIDGE INSPECTIONS 276
APPENDIX B: INTERVIEW SUMMARIES 305
APPENDIX C: CHLORIDE INGRESS RESULTS 315
APPENDIX D: CARBONATION TESTING RESULTS 321
APPENDIX E: SULFATE ATTACK RESULTS 329
APPENDIX F: SELF-HEALING INVESTIGATION RESULTS 364
APPENDIX G: HPMC USAGE CONDITIONS 377
REFERENCES 384

LIST OF TABLES

Table		Page #
Table 2.1:	Chloride ion penetrability based on charge passed	17
Table 2.2:	Summary of chloride resistance test procedures	20
Table 2.3:	Exposure classes as specified by ACI 201	36
Table 2.4:	Maximum expansion percentages specified by ACI 201	36
Table 2.5:	Recommended replacement percentages of SCM's	44
Table 2.6:	Permissible crack widths for exposure conditions	49
Table 3.1:	Comparison of Life 365 estimates to experimental data	83
Table 3.2:	Chemical symbols with correlated composition for XRD profiles	97
Table 3.3:	XRD results summary for 2 ft above high tide	99
Table 3.4:	XRD results summary for high tide	103
Table 3.5:	XRD results summary for 5 ft below high tide	106
Table 3.6:	XRD results summary for 12 ft below high tide	110
Table 4.1:	ACI durability criteria mix design (T2)	129
Table 4.2:	Current HPC mix design (T3-F15)	130
Table 4.3:	Base experimental mix design	130
Table 4.4:	Binder compositions for experimental mix designs	132
Table 4.5:	Oxide analysis and Bogue compositions of cement samples	133
Table 4.6:	Particle size distributions and Blaine Fineness values	134
Table 4.7:	Oxide analysis for SCM samples	136
Table 4.8:	Particle size analysis of SCM samples	137
Table 4.9:	Air contents of mix designs	140
Table 4.10:	Compressive strength and standard deviations at 3, 28, and 56 days	141
Table 4.11:	Elastic modulus and standard deviation at 56 days	143
Table 5.1:	Profile grinding increments	146
Table 5.2:	Chloride ion penetrability based on charge passed	147
Table 5.3:	Experimental diffusion coefficients	149
Table 5.4:	Experimental and estimated apparent diffusion coefficients	160

Table 5.5:	Percent difference of estimates to experimental apparent diffusion Coefficient	161
Table 5.6:	Estimated corrosion initiation times	165
Table 6.1:	Exposure classes as specified by ACI 201	170
Table 6.2:	Binder compositions	172
Table 6.3:	Maximum expansion percentages specified by ACI 201	172
Table 6.4:	Sulfate compressive strength degradation testing proposed limits	185
Table 6.5:	Exposure class ratings for mix designs based upon sulfate exposure strength degradation criterion	188
Table 6.6:	Initial calcium hydroxide content, % change in 90 to 180 day QXRD data, and 180 day relative strengths for investigated mix designs	192
Table 6.7:	Oxide contents of binder compositions	193
Table 6.8:	Summary of sulfate testing results	198
Table 7.1:	Experimental carbonation constants	208
Table 7.2:	Oxide contents of binder compositions	211
Table 7.3:	Experimental and estimated carbonation constants	214
Table 7.4:	Required cover distances for intended service life goals	218
Table 8.1:	Self-healing mix design binder compositions	223
Table 8.2:	Profile grinding increments	226
Table 8.3:	Flexural crack specimens mean initial crack width and depth	229
Table 8.4:	Tensile crack specimens initial crack width and standard deviation	229
Table 8.5:	Mean chloride content at depth of reinforcement (76.2 mm)	236
Table 8.6:	Traditional approach to Fick’s second law regression analysis results	237
Table 8.7:	Modified approach to Fick’s second law regression analysis results	238
Table 8.8:	Ratio of cracked diffusion coefficient to control diffusion coefficient for flexural and tensile cracked specimens	246
Table 8.9:	Estimated corrosion initiation times for control and cracked samples	249
Table 9.1:	Compressive strength elastic modulus data for mix designs	253
Table 9.2:	Exposure classes as specified by ACI 201	256
Table 9.3:	Maximum expansion percentages specified by ACI 201	256
Table 9.4:	ASTM C 1012 expansion test results and exposure ratings	257
Table 9.5:	Strength degradation testing limits for exposure classes	258

Table 9.6: Suggested exposure class rating for mix designs 260
Table 9.7: Required cover distances for carbonation induced corrosion protection 261
Table 9.8: Recommended mix designs for 75 and 100 year service life using non-corrosion resistant prestressing strands 265
Table A.1: Bridge ID numbers and names for locations inspected 277
Table A.2: pH, chloride, and sulfate contents of water samples 301
Table A.3: Water salinity based on dissolved salt (NaCl) concentration 302
Table C.1: Rapid chloride permeability charge passed and initial current measurements for all mix designs 315
Table C.2: T2 bulk diffusion results 316
Table C.3: T3-F15 bulk diffusion results 316
Table C.4: F25 bulk diffusion results 317
Table C.5: F25-MK5 bulk diffusion results 317
Table C.6: F25-MK10 bulk diffusion results 318
Table C.7: F25-SF10 bulk diffusion results 318
Table C.8: S35-MK5 bulk diffusion results 319
Table C.9: S50-MK5 bulk diffusion results 319
Table C.10: S35-SF5 bulk diffusion results 320
Table C.11: S50-SF5 bulk diffusion results 320
Table D.1: Mean carbonation depth as indicated by phenolphthalein indicator 321
Table D.2: Standard devation of carbonation depth 322
Table D.3: Experimentally determinate carbonation constants and R^2 values 328
Table E.1: ASTM C 1012 expansion readings from initial to 15 weeks 329
Table E.2: ASTM C 1012 expansion readings from 4 months to 11 months 330
Table E.3: ASTM C 1012 expansion readings from 12 months to 18 months 330
Table E.4: Compressive strength gain of mortar cubes for ASTM C 1012 criterion 331
Table E.5: Initial strength of paste cube samples at beginning of exposure 332
Table E.6: 28 days strength of control and sulfate exposure specimens 333
Table E.7: 90 days strength of control and sulfate exposure specimens 333
Table E.8: 180 days strength of control and sulfate exposure specimens 334
Table E.9: C_2S and C_3S contents of mix designs after sulfate exposure 360
Table E.10: C_3A and C_4AF contents of mix designs after sulfate exposure 360

Table E.11: Portlandite and quartz contents of mix designs after sulfate exposure 361
Table E.12: Calcite and ettringite contents of mix designs after sulfate exposure 361
Table E.13: Monocarbonate and gypsum contents of mix designs after sulfate exposure 362
Table E.14: Periclase and mullite contents of mix designs after sulfate exposure 362
Table E.15: Kuzelite contents of mix designs after sulfate exposure 363
Table F.1: Type II control sample titration data 369
Table F.2: Type II tension sample titration data 370
Table F.3: Type II flexure sample titration data 370
Table F.4: T3-F15 control sample titration data 371
Table F.5: T3-F15 tension sample titration data 371
Table F.6: T3-F15 flexure sample titration data 372
Table F.7: F25 control sample titration data 372
Table F.8: F25 tension sample titration data 373
Table F.9: F25 flexure sample titration data 373
Table F.10: S35-MK5 control sample titration data 374
Table F.11: S35-MK5 tension sample titration data 374
Table F.12: S35-MK5 flexure sample titration data 375
Table F.13: S50-MK5 control sample titration data 375
Table F.14: S50-MK5 tension sample titration data 376
Table F.15: S50-MK5 flexure sample titration data 376
Table G.1: Maximum inland distance and elevation of sites requiring use of HPMC 380

LIST OF FIGURES

Figure		Page #
Figure 1.1:	Deterioration of bridge substructures in Georgia's coastal counties	3
Figure 1.2:	Scope of experimental program	5
Figure 2.1:	Typical degradation mechanisms in coastal concrete piling	9
Figure 2.2:	Service life model for corrosion induced damage	10
Figure 2.3:	Typical chloride migration cell	19
Figure 2.4:	Effect of water-to-cement ratio on diffusion coefficient of plain Portland cement concrete	22
Figure 2.5:	Effect of age of exposure on diffusion coefficient in plain Portland cement concrete	23
Figure 2.6:	Comparison of time dependent diffusion coefficients with estimator	24
Figure 2.7:	Effect of silica fume content on diffusion coefficient	26
Figure 2.8:	Effect of SCM's on diffusion coefficient	27
Figure 2.9:	$Ca(OH)_2$ concentration as an indicator of carbonation depth measured using thermogravimetric analysis	29
Figure 2.10:	Effect of relative humidity on carbonation rate	31
Figure 2.11:	Effect of water-to-cement ratio on carbonation depth	32
Figure 2.12:	Effect of binder composition on carbonation depth	33
Figure 2.13:	Expansion results for cements replaced with fly ash	39
Figure 2.14:	Expansion of slag cements exposed to sulfate solution	40
Figure 2.15:	Compressive strength loss of silica fume mortars in sodium sulfate	41
Figure 2.16:	Compressive strength loss of silica fume mortars in magnesium sulfate	42
Figure 2.17:	10% silica fume mortars exposed to 5% sodium sulfate and 5% magnesium sulfate	42
Figure 2.18:	Compressive strength reduction of metakaolin cements	43
Figure 2.19:	Effect of fly ash and silica fume on cements exposed sodium sulfate	44
Figure 2.20:	Two types of corrosion processes in the region of cracks	47
Figure 2.21:	Chloride profiles for cracked concrete after 30 days exposure	52
Figure 2.22:	Water flow versus duration for different crack widths	54
Figure 2.23:	Effect of self-healing on RCPT samples	56

Figure 3.1:	Typical degradation mechanisms in coastal concrete piling	59
Figure 3.2:	Location of I-95 at Turtle River Bridge	60
Figure 3.3:	Overall view of bridge before and after upgrade	61
Figure 3.4:	View of bridge substructure before and after upgrade	62
Figure 3.5:	Piles from Turtle River Bridge	63
Figure 3.6:	Pile after removal of biological growth	63
Figure 3.7:	Corrosion induced longitudinal cracking of piles	67
Figure 3.8:	Corrosion induced delamination, loss of steel section, and staining	67
Figure 3.9:	Cracking and delamination pattern on the cross-section in splash and tidal zones	68
Figure 3.10:	Corrosion of prestressing steel in extracted core	68
Figure 3.11:	Phenolpthalein indicator solution on sawn surface of pile	70
Figure 3.12:	Half-cell potential measurement set-up	71
Figure 3.13:	Half-cell potential map of the four faces of a Turtle River Bridge pile	72
Figure 3.14:	Filtration of chloride sample and titration of sample	76
Figure 3.15:	Locations of chloride concentration sampling	77
Figure 3.16:	Total chloride content of concrete columns at various depths	78
Figure 3.17	Free chloride content of concrete columns at various depths	79
Figure 3.18:	Comparison of total to free chloride concentration	80
Figure 3.19:	Total and free chloride profiles at measured depths	81
Figure 3.20:	Cracking along corner of pile and marine growth in crack	87
Figure 3.21:	Whitish discoloration near surface in submerged region	88
Figure 3.22:	Rebound hammer calibration	89
Figure 3.23:	Rebound hammer results	90
Figure 3.24:	Vicker’s hardness measurements	91
Figure 3.25:	Compressive strength core locations	92
Figure 3.26:	Compressive strength core locations and surface and interior samples	93
Figure 3.27:	Compressive strength of undamaged interior concrete	94
Figure 3.28:	Compressive strength of surface versus interior concrete	95
Figure 3.29:	XRD sample	96
Figure 3.30:	XRD profile for atmospheric region at 0-12.7 mm increment	98

Figure 3.31: XRD profile for atmospheric region at 12.7-38.1 mm increment 98
Figure 3.32: XRD profile for splash zone at 0-12.7 mm increment 100
Figure 3.33: XRD profile for splash zone at 12.7-38.1 mm increment 101
Figure 3.34: XRD profile for splash zone at 38.1-63.5 mm increment 101
Figure 3.35: XRD profile for splash zone at 63.5-88.9 mm increment 102
Figure 3.36: XRD profile for splash zone at 88.9-114.3 mm increment 102
Figure 3.37: XRD profile for high tide region at 0-12.7 mm increment 104
Figure 3.38: XRD profile for high tide region at 12.7-38.1 mm increment 104
Figure 3.39: XRD profile for high tide region at 38.1-63.5 mm increment 105
Figure 3.40: XRD profile for high tide region at 63.5-88.9 mm increment 105
Figure 3.41: XRD profile for high tide region at 88.9-114.3 mm increment 106
Figure 3.42: XRD profile for low tide at 0-12.7 mm increment 107
Figure 3.43: XRD profile for low tide at 12.7-38.1 mm increment 108
Figure 3.44: XRD profile for low tide at 38.1-63.5 mm increment 108
Figure 3.45: XRD profile for low tide at 63.5-88.9 mm increment 109
Figure 3.46: XRD profile for low tide at 88.9-114.3 mm increment 109
Figure 3.47: XRD profile for submerged region at 0-12.7 mm increment 111
Figure 3.48: XRD profile for submerged region at 12.7-38.1 mm increment 111
Figure 3.49: XRD profile for submerged region at 38.1-63.5 mm increment 112
Figure 3.50: XRD profile for submerged region at 63.5-88.9 mm increment 112
Figure 3.51: XRD profile for submerged region at 88.9-114.3 mm increment 113
Figure 3.52: TGA for 2.74 m above high tide 115
Figure 3.53: TGA for 0.6 m above high tide 115
Figure 3.54: TGA for high tide region 116
Figure 3.55: TGA for 1.52 m below high tide 117
Figure 3.56: TGA for 3.66 m below high tide 118
Figure 3.57: Surface damage to concrete piling 120
Figure 3.58: Boreholes in limestone aggregate of cores 120
Figure 3.59: Spicules of *Cliona caribbea* 121
Figure 3.60: *Cliona caribbea* boring sponge 122
Figure 3.61: Silicate rod-like structures inside of boreholes through aggregate 123

Figure 3.62:	EDS spectrum of rod-like structures	123
Figure 4.1:	ACI 211.4R-08 Mixture design procedure	128
Figure 4.2:	Particle size distributions for cement samples	135
Figure 4.3:	Particle size distributions for SCM samples	137
Figure 4.4:	Gradation curve of natural sand	138
Figure 4.5:	F25 air void sample scanner image and binarized image	139
Figure 4.6:	Compressive strength and standard deviations at 3, 28, and 56 days	141
Figure 4.7:	Elastic modulus vs. compressive strength and estimator equations	143
Figure 5.1:	Rapid chloride permeability set-up	147
Figure 5.2:	RCPT results	148
Figure 5.3:	Chloride profile for T2	150
Figure 5.4:	Chloride profiles for T3-F15, F25, F25-MK5, and F25-MK10	151
Figure 5.5:	Chloride profiles for F25-SF5, F25-SF10, S35-MK5, and S50-MK5	152
Figure 5.6:	Chloride profiles for S35-SF5 and S50-SF5	153
Figure 5.7:	Service life model for corrosion induced damage	154
Figure 5.8:	Experimental and estimated diffusion coefficients	160
Figure 5.9:	Estimated chloride profiles after various exposure periods	163
Figure 5.10:	Corrosion initiation time for experimental results	165
Figure 5.11:	Estimated corrosion initiation times without maturity correction	166
Figure 6.1:	ASTM C 1012 expansion results for cement mixes	175
Figure 6.2:	ASTM C 1012 expansion results for binder compositions containing fly ash	176
Figure 6.3:	ASTM C 1012 expansion results for binder compositions containing slag	176
Figure 6.4:	T5 180-day control and sulfate exposure specimens	178
Figure 6.5:	T3 180-day control and sulfate exposure specimens	178
Figure 6.6:	Strength gain curves for control and sulfate exposure samples from T2 and T3	179
Figure 6.7:	Strength gain curves for control and sulfate exposure samples from T5, T3-F15, F25, and F25-MK5	180
Figure 6.8:	Strength gain curves for control and sulfate exposure samples from F25-MK10, F25-SF5, F25-SF10, and S35-MK5	181

Figure 6.9:	Strength gain curves for control and sulfate exposure samples from S50-MK5, S35-SF5, and S50-SF5	182
Figure 6.10:	Relative strength of sulfate exposure samples compared to strength of control samples at start of test	184
Figure 6.11:	Relative strength curves for cement specimens	186
Figure 6.12:	Relative strength curves for fly ash binder compositions	186
Figure 6.13:	Relative strength curves for slag binder compositions	187
Figure 6.14:	Calcium hydroxide content of total crystalline phases of control and sulfate exposure samples as determined by QXRD	189
Figure 6.15:	Ettringite content of total crystalline phases of control and sulfate exposure samples as determined by QXRD	190
Figure 6.16:	Gypsum content of total crystalline phases of control and sulfate exposure samples as determined by QXRD	191
Figure 6.17:	CaO content versus strength degradation and CaO versus SiO_2 content of mixture designs	193
Figure 6.18:	Expansion versus ettringite content at 180 days, calcium hydroxide content of control sample at 180 days, gypsum content at 180 days of sulfate exposure, and combined gypsum and ettringite content at 180 days of sulfate exposure	195
Figure 6.19:	Relationship between CaO content and 12-month sulfate exposure ASTM C 1012 expansion	196
Figure 7.1:	T2 carbonation samples	203
Figure 7.2:	Carbonation curves for T2, T3-F15, and F25	204
Figure 7.3:	Carbonation curves for F25-MK5, F25-MK10, F25-SF5, and F25-SF10	205
Figure 7.4:	Carbonation curves for S35-MK5, S50-MK5, S35-SF5, and S50-SF5	206
Figure 7.5:	Carbonation constants for mixture designs containing SCM's	209
Figure 7.6:	Carbonation constant compared to SiO_2, Al_2O_3, and CaO content	211
Figure 7.7:	Experimental and estimated carbonation constants	215
Figure 7.8:	Predicted carbonation front location versus time for fly ash mixtures	217
Figure 7.9:	Predicted carbonation front location versus time for slag mixtures	217
Figure 7.10:	Predicted carbonation front location versus time for T2, F25-SF5, and S50-SF5	218
Figure 8.1:	Absorption ratio contour plot for 0.15 mm surface crack width opening specimen after 1 hour of ponding, crack length versus maximum sorption depth after 1 hour of water exposure	221

Figure 8.2:	Cracking methods, dimensions, and crack opening measurement locations for tensile crack and flexure crack specimens	224
Figure 8.3:	Mean crack width after exposure to initial mean crack width ratio of flexure crack specimens over exposure time	231
Figure 8.4:	Mean crack width after exposure to initial mean crack width ratio of tensile crack specimens over exposure time	231
Figure 8.5:	S35-MK5 F1 sample with crack filling, F25 F1 sample with less crack filling after 120 days of exposure	232
Figure 8.6:	Type II chloride profiles for control, tension, and flexure cracks	234
Figure 8.7:	T3-F15 chloride profiles for control, tension, and flexure cracks	234
Figure 8.8:	F25 chloride profiles for control, tension, and flexure cracks	234
Figure 8.9:	S35-MK5 chloride profiles for control, tension, and flexure cracks	235
Figure 8.10:	S50-MK5 chloride profiles for control, tension, and flexure cracks	235
Figure 8.11:	Regression analysis results for control samples	239
Figure 8.12:	Regression analysis results from Type II flexure crack specimens	241
Figure 8.13:	Regression analysis results from T3-F15 flexure crack specimens	241
Figure 8.14:	Regression analysis results from F25 flexure crack specimens	241
Figure 8.15:	Regression analysis results from S35-MK5 flexure crack specimens	242
Figure 8.16:	Regression analysis results from S50-MK5 flexure crack specimens	242
Figure 8.17:	Regression analysis results from Type II tension crack specimens	242
Figure 8.18:	Regression analysis results from T3-F15 tension crack specimens	243
Figure 8.19:	Regression analysis results from F25 tension crack specimens	243
Figure 8.20:	Regression analysis results from S35-MK5 tension crack specimens	243
Figure 8.21:	Regression analysis results from S50-MK5 tension crack specimens	244
Figure 8.22:	Crack width versus background chloride content of cracked sections	245
Figure 8.23:	Apparent diffusion coefficient ratio of cracked to uncracked samples versus mean initial crack width	247
Figure 9.1:	Estimated corrosion initiation times for mixture designs	254
Figure 9.2:	Relative strength of specimens compared to initial control specimens after sulfate exposure	259
Figure A.1:	Bridges inspected along Georgia’s coastal counties	278
Figure A.2:	Substructure of Harriett’s Bluff Road at Deep Creek Bridge	279

Figure A.3:	Corrosion damage of cast-in-place barrier of Harriett's Bluff Road at Deep Creek Bridge	280
Figure A.4:	Overall view of Houlihan Bridge	280
Figure A.5:	Surface abrasion of concrete substructure of Houlihan Bridge	281
Figure A.6:	Surface abrasion of concrete substructure of Houlihan Bridge	282
Figure A.7:	Pile-bent substructure of US 17 at Back River Bridge	283
Figure A.8:	Vertical cracking at corner of concrete piles on US 17 at Back River Bridge	284
Figure A.9:	Corrosion damaged piling with FRP jacket retrofit on US 17 at Back River Bridge	284
Figure A.10:	Overall view of US 80 at Lazeratto Creek Bridge	285
Figure A.11:	Grout repair of transverse crack in precast prestressed concrete pile on US 80 at Lazeratto Creek Bridge	286
Figure A.12:	Honeycombind and exposed corroding reinforcement in pile cap on US 80 at Lazeratto Creek Bridge	286
Figure A.13:	Underside of Island Expressway at Wilmington River Bridge	287
Figure A.14:	Deterioration of limestone aggregates present at concrete surface on Island Expressway at Wilmington River Bridge	288
Figure A.15:	Severe damage to concrete piling on Island Expressway at Wilmington River Bridge	288
Figure A.16:	Oatland Island Research Bridge	289
Figure A.17:	Pile-bent substructure of Oatland Island Research Bridge	290
Figure A.18:	Long Bridge Road at Ebenezer Creek Bridge	291
Figure A.19:	Grout repair of transverse cracking likely caused by overdriving on Long Bridge Road at Ebenezer Creek Bridge	291
Figure A.20:	Surface abrasion of concrete below high-water mark on Long Bridge Road at Ebenezer Creek Bridge	292
Figure A.21:	Updated I-95 at Turtle River Bridge	293
Figure A.22:	Transfer beam with original piles left in-place on I-95 at Turtle River Bridge	294
Figure A.23:	Torras Causeway at Little River Bridge and adjacent fishing pier	295
Figure A.24:	Pile-bent on Torras Causeway at Little River Bridge approach span	296
Figure A.25:	Corrosion damage in original Torras Causeway at Little River Bridge substructure	296
Figure A.26:	Ocean Highway at Riceboro Creek Bridge	297

Figure A.27:	Deterioration of precast prestressed concrete piles in substructure of Ocean Highway at Riceboro Creek Bridge	298
Figure A.28:	Overall view of Ocean Highway at Champney's River Bridge	299
Figure A.29:	Remaining piles on bank adjacent to Ocean Highway at Champney's River Bridge	299
Figure A.30:	Typical surface abrasion of concrete on Ocean Highway at Champney's River Bridge	300
Figure D.1:	T2 carbonation samples	322
Figure D.2:	T3-F15 carbonation samples	323
Figure D.3:	F25 carbonation samples	323
Figure D.4:	F25-MK5 carbonation samples	324
Figure D.5:	F25-MK10 carbonation samples	324
Figure D.6:	F25-SF5 carbonation samples	325
Figure D.7:	F25-SF10 carbonation samples	325
Figure D.8:	S35-MK5 carbonation samples	326
Figure D.9:	S50-MK5 carbonation samples	326
Figure D.10:	S35-MK5 carbonation samples	327
Figure D.11:	S50-MK5 carbonation samples	327
Figure E.1:	Control and 180-day sulfate exposure specimens for T2, T3, and T5	335
Figure E.2:	Control and 180-day sulfate exposure specimens for T3-F15, F25, and F25-MK5	336
Figure E.3:	Control and 180-day sulfate exposure specimens for F25-MK10, F25-SF5, and F25-SF10	337
Figure E.4:	Control and 180-day sulfate exposure specimens for S35-MK5, S50-MK5, and S35-SF5	338
Figure E.5:	Control and 180-day sulfate exposure specimen for S50-SF5	339
Figure E.6:	T2 180-day Control XRD Pattern	339
Figure E.7:	T3 180-day Control XRD Pattern	340
Figure E.8:	T5 180-day Control XRD Pattern	340
Figure E.9:	T3-F15 180-day Control XRD Pattern	341
Figure E.10:	F25 180-day Control XRD Pattern	341
Figure E.11:	F25-MK5 180-day Control XRD Pattern	342
Figure E.12:	F25-MK10 180-day Control XRD Pattern	342

Figure E.13: F25-SF5 180-day Control XRD Pattern 343
Figure E.14: F25-SF10 180-day Control XRD Pattern 343
Figure E.15: S35-MK5 180-day Control XRD Pattern 344
Figure E.16: S50-MK5 180-day Control XRD Pattern 344
Figure E.17: S35-SF5 180-day Control XRD Pattern 345
Figure E.18: S50-SF5 180-day Control XRD Pattern 345
Figure E.19: T2 90-day Sulfate Exposure XRD Pattern 346
Figure E.20: T3 90-day Sulfate Exposure XRD Pattern 346
Figure E.21: T5 90-day Sulfate Exposure XRD Pattern 347
Figure E.22: T3-F15 90-day Sulfate Exposure XRD Pattern 347
Figure E.23: F25 90-day Sulfate Exposure XRD Pattern 348
Figure E.24: F25-MK5 90-day Sulfate Exposure XRD Pattern 348
Figure E.25: F25-MK10 90-day Sulfate Exposure XRD Pattern 349
Figure E.26: F25-SF5 90-day Sulfate Exposure XRD Pattern 349
Figure E.27: F25-SF10 90-day Sulfate Exposure XRD Pattern 350
Figure E.28: S35-MK5 90-day Sulfate Exposure XRD Pattern 350
Figure E.29: S50-MK5 90-day Sulfate Exposure XRD Pattern 351
Figure E.30: S35-SF5 90-day Sulfate Exposure XRD Pattern 351
Figure E.31: S50-SF5 90-day Sulfate Exposure XRD Pattern 352
Figure E.32: T2 180-day Sulfate Exposure XRD Pattern 353
Figure E.33: T3 180-day Sulfate Exposure XRD Pattern 353
Figure E.34: T5 180-day Sulfate Exposure XRD Pattern 354
Figure E.35: T3-F15 180-day Sulfate Exposure XRD Pattern 354
Figure E.36: F25 180-day Sulfate Exposure XRD Pattern 355
Figure E.37: F25-MK5 180-day Sulfate Exposure XRD Pattern 355
Figure E.38: F25-MK10 180-day Sulfate Exposure XRD Pattern 356
Figure E.39: F25-SF5 180-day Sulfate Exposure XRD Pattern 356
Figure E.40: F25-SF10 180-day Sulfate Exposure XRD Pattern 357
Figure E.41: S35-MK5 180-day Sulfate Exposure XRD Pattern 357
Figure E.42: S50-MK5 180-day Sulfate Exposure XRD Pattern 358
Figure E.43: S35-SF5 180-day Sulfate Exposure XRD Pattern 358

Figure E.44:	S50-SF5 180-day Sulfate Exposure XRD Pattern	359
Figure F.1:	Post-tensioning of specimens	364
Figure F.2:	Crack width measurement marks ever ½ in. on flexure specimen	364
Figure F.3:	Graduate students taking crack width measurements before sealing and exposure	365
Figure F.4:	Graduate student sealing the sides of specimens with aluminum tape	365
Figure F.5:	Sealed specimens with aluminum tape and epoxy with exposure container attached	366
Figure F.6:	Exposure surface inside of ponding container with simulated seawater solution	366
Figure F.7:	Microscopy image of Type II flexure crack	367
Figure F.8:	Microscopy image of Type II tension crack	367
Figure F.9:	Microscopy image of T3-F15 flexure crack	367
Figure F.10:	Microscopy image of T3-F15 tension crack	367
Figure F.11:	Microscopy image of F25 flexure crack	368
Figure F.12:	Microscopy image of F25 tension crack	368
Figure F.13:	Microscopy image of S35-MK5 flexure crack	368
Figure F.14:	Microscopy image of S35-MK5 tension crack	368
Figure F.15:	Microscopy image of S50-MK5 flexure crack	369
Figure F.16:	Microscopy image of S50-MK5 tension crack	369
Figure G.1:	Chloride concentration versus distance inland	378
Figure G.2:	Chloride concentration versus site elevation	379
Figure G.3:	Sulfate concentration versus distance inland	379
Figure G.4:	Sulfate concentration versus site elevation	379
Figure G.5:	Map of chloride sampling sites	381
Figure G.6:	Map of sulfate sampling sites	382
Figure G.7:	Proposed HPMC use map for submerged piles	383

LIST OF SYMBOLS

A	Cross-sectional area of specimen
ACI	American Concrete Institute
AASHTO	American Association of State Highway and Transportation Officials
ASR	Alkali silica reaction
ASTM	American Society for Testing and Materials
C_i	Concentration of species I, mol/cm^3
C_o	Initial chloride concentration of the cementitious mixture prior to submersion in the exposure solution, % mass
C_s	Chloride concentration at interface between exposure liquid and test specimen, % mass
CH	Calcium hydroxide content, %
CSE	Copper / copper sulfate reference electrode
C-S-H	Calcium-silicate-hydrate content, %
CTL	Chloride threshold limit
C(x,t)	Chloride concentration at depth, x, and time, t, % mass
CO_2	Carbon dioxide content of air at concrete surface, %
d	Depth of carbonation front
D	Diffusion coefficient, m^2/s
D_a	Apparent chloride diffusion coefficient, m^2/s
D_{avg}	Average diffusion coefficient, m^2/s
$D_{e,CO2}$	Diffusivity of CO_2 in carbonated concrete, mm^2/yr
D_{eff}	Effective chloride diffusion coefficient, m^2/s
D_{ref}	Diffusion coefficient at reference age, m^2/s
D_{SF}	Diffusion coefficient of silica fume containing concrete, m^2/s
D_{ult}	Diffusion coefficient after complete hydration, m^2/s
D_{28}	Diffusion coefficient of Portland cement concrete at 28-days, m^2/s
D(t)	Diffusion coefficient at time t
DRUW	Dry rodded unit weight
EDS	Energy dispersive x-ray analysis

ESEM	Environmental scanning electron microscopy
F	Faraday's Constant, 95,500 Coulombs/mol
f_c'	Compressive strength, MPa
FA	Fly ash content, % mass
FHWA	Federal Highway Administration
FRP	Fiber reinforced polymer
GDOT	Georgia Department of Transportation
HPC	High performance concrete
HPMC	High performance marine concrete
HRWRA	High range water reducing admixture
HSC	High strength concrete
ICP	Inductively coupled plasma atomic emission spectroscopy
K	Carbonation constant, $mm/yr^{0.5}$
L	length of specimen, mm
m	Diffusion decay index
M	Mass of titration sample, g
MK	Metakaolin
MSA	Maximum size aggregate
n	Curve fitting factor
N	Normality of silver nitrate solution
NCHRP	National Cooperative Highway Research Program
QXRD	Quantitative x-ray diffraction
R	Universal gas constant, 8.315 J/mol-K
RCPT	Rapid chloride permeability test
SG	Ground-granulated blast-furnace slag content, % mass
SCC	Self-consolidating concrete
SCP	Standard Concrete Products
SCM's	Supplementary cementitious materials
SF	Silica fume content, % mass
SSD	Saturated surface dry moisture condition
SSE	Sum of squares due to error

t_{eff}	Effective age of concrete
t_{ref}	Reference age of concrete
T	average temperature, K
TGA	Thermo-gravimetric analysis
USGS	United States Geological Survey
V	Volume of titrant used at equivalence point
W	Mean initial crack width at exposure surface, μm
w/c	Water-to-cement ratio by weight
w/cm	Water-to-cementitious materials ratio by weight
XRD	X-ray diffraction
Z	Charge of species i
$\delta C/\delta t$	Concentration gradient

SUMMARY

The purpose of the research was to (1) characterize the durability requirements and field performance of prestressed concrete piles in marine environment, and (2) develop potential high performance marine concretes (HPMC) that would be capable of 100+ year service lives in brackish and seawater environments.

The characterization of pile durability was accomplished through a forensic investigation of bridge piles from a decommissioned bridge, interviews of Georgia Department of Transportation engineers and inspectors, and site inspections of bridges showing substructure deterioration. The results suggested that potential HPMC's must be able to provide adequate resistance to chloride ingress, carbonation, and sulfate attack.

Nine potential HPMC mixture designs were developed utilizing Class F fly ash, slag, metakaolin, and silica fume in binary and ternary mixes. Extensive testing was performed to quantify chloride ingress, carbonation, sulfate attack, and the influence of cracks and self-healing on chloride ingress.

Chloride ingress tests found that ternary mixture designs provided superior resistance compared to binary mixture designs; including of 5 to 10% silica fume to a Type II Portland cement plus Class F fly ash mix increased the service life approximately 25%. Bulk diffusion tests and service life modeling considering only chloride ingress showed that ternary mixture designs with Type II cement, slag and metakaolin provided service lives over 100 years before corrosion initiation would occur.

Sulfate attack resistance was characterized using both expansion and strength degradation test methods. Compressive strength degradation testing demonstrated that

mixture designs with a high initial CaO content, determined through oxide analysis of the cement and SCMs, performed well, presumably due to the formation of calcium hydroxide (CH) which served as a buffer to the decalcification of calcium-silicate-hydrate (C-S-H) in the formation of gypsum. However, high CaO contents led to poor performance on expansion testing due to the availability of large amounts of calcium hydroxide to react with sulfate ions to form expansive ettringite. Slag mixture designs containing metakaolin performed well with both test methods. Slag mixture designs containing metakaolin performed well on both criteria, and they had moderate CaO contents (44 to 50%) and utilized sulfate resistant ASTM C 150 (2009) Type II cements with low C_3A contents.

Carbonation resistance was determined by exposing concrete prisms to a high CO_2 environment and by measuring the depth to the carbonation front. The results were used to perform service life modeling of times to carbonation induced corrosion initiation and to determine necessary cover dimension. Carbonation performance of ternary mixture designs showed that they were capable of providing service lives in excess of 200 years using a 5 mm (0.2 in.) cover. Mixture designs with 5% to 10% silica fume and 25% fly ash performed the best, resulting in a service life over 95% longer than 25% fly ash alone.

The investigation into the influence of self-healing on chloride ingress into cracked sections demonstrated that prestressed concrete piles in marine environments can undergo self-healing of tension and flexure induced cracks where the crack widths were less than 186 μm (0.007 in.). Service life modeling considering initiation of reinforcement corrosion was performed, and the model demonstrated that the presence of cracks decreases the service life of a structure by over 40% compared to uncracked concrete whether self-healing occurs or not. Mixture designs containing slag and Type II cement or cement-only show the greatest propensity for self-healing to occur according to

crack width measurements and chloride ingress resistance measurements. If cracks cannot be prevented, corrosion resistant reinforcing steel should be used to achieve a 100+ year life span.

The results of the durability assessments for chloride ingress, carbonation, and sulfate attack led to the development of mixture design capable of achieving 75 and 100 year service lives for prestressed concrete piles. The research concluded that uncracked prestressed concrete piles made with non-corrosion resistant steel required protection from sulfate attack, carbonation, and chloride ingress to achieve 75 to 100 year service lives. For cracked sections, corrosion resistant prestressing steel should be used with concrete resistant to sulfate attack; such mixes include Type II cement, at least 25% cementitious content of Class F fly ash or slag, and 5% or more silica fume or metakaolin.

CHAPTER 1

INTRODUCTION

1.1 Purpose and Objectives

The purpose of this research was to develop and evaluate concrete mixture designs to prolong service lives of precast prestressed concrete piles in aggressive marine environments. The research was focused on increasing the resistance of high performance concrete (HPC) mixture designs to the various deterioration mechanisms present in coastal exposures. HPC differs from high strength concrete (HSC), in that high performance concrete encompasses any concrete meeting particular performance requirements (strength, durability, workability), where as HSC is purely based upon a strength requirement. In particular, the research focused on five primary objectives:

1. Determine and quantify environmental conditions in marine environments in Georgia, as well as design details and construction practices, which may limit service life of reinforced concrete elements
2. Establish properties of current HPC mixture designs in use as a basis for comparison with proposed designs
3. Investigate the resistance of new high performance marine concrete (HPMC) mixture designs to chloride ingress, sulfate attack, and carbonation resistance,
4. Investigate the potential for the self-healing of cracks in HPMC and the effect on chloride ingress in cracked sections under prestressing forces

5. Provide recommendations and draft design standards for HPMC mixture designs for concrete piling

1.2 Need for Research

Nearly 53% of the United States population lives in coastal counties and the growth rate of the population in coastal regions is increasing (Crossett, et. al., 2004). The increase in population has led to an increased demand for infrastructure in coastal counties. Additionally, there is an increase in the relative frequency of natural hazard occurrences, including hurricanes and flooding, that leads to an increased likelihood of infrastructure interacting with water or seawater during its service life (UNEP, 2005).

Over 13% of the 595,000 bridges in the United States are classified as structurally deficient according to the Federal Highway Administration (FHWA). Studies have indicated that 15% of the structural deficiencies reported are the results of corrosion. An estimated $4 billion is spent annually to maintain and replace corroded bridge structures (Koch, et. al., 2008). The indirect costs of corrosion are estimated to be an additional $50 to $200 billion annually, due to increased traffic, bridge closures, and affected businesses. The FHWA is proposing to require all new construction be designed for a 75 to 100 year lifespan; however, current design methods and construction practices are proving unable to meet this requirement (Koch, et. al., 2008).

The deterioration of concrete structures in marine environments has become an area of concern after several Georgia Department of Transportation structures in coastal environments have shown extensive deterioration after only 30 years of service. Figure

1.1 presents the substructure status of concrete bridge substructures over bodies of water in Georgia, where it was found that 29.3% of the bridges showed damage to the substructure. The concrete bridges can experience damage due to multiple deterioration mechanisms, including chemical, physical, and biological attack. This deterioration leads to reductions in mechanical properties, serviceability, and aesthetics of the structure.

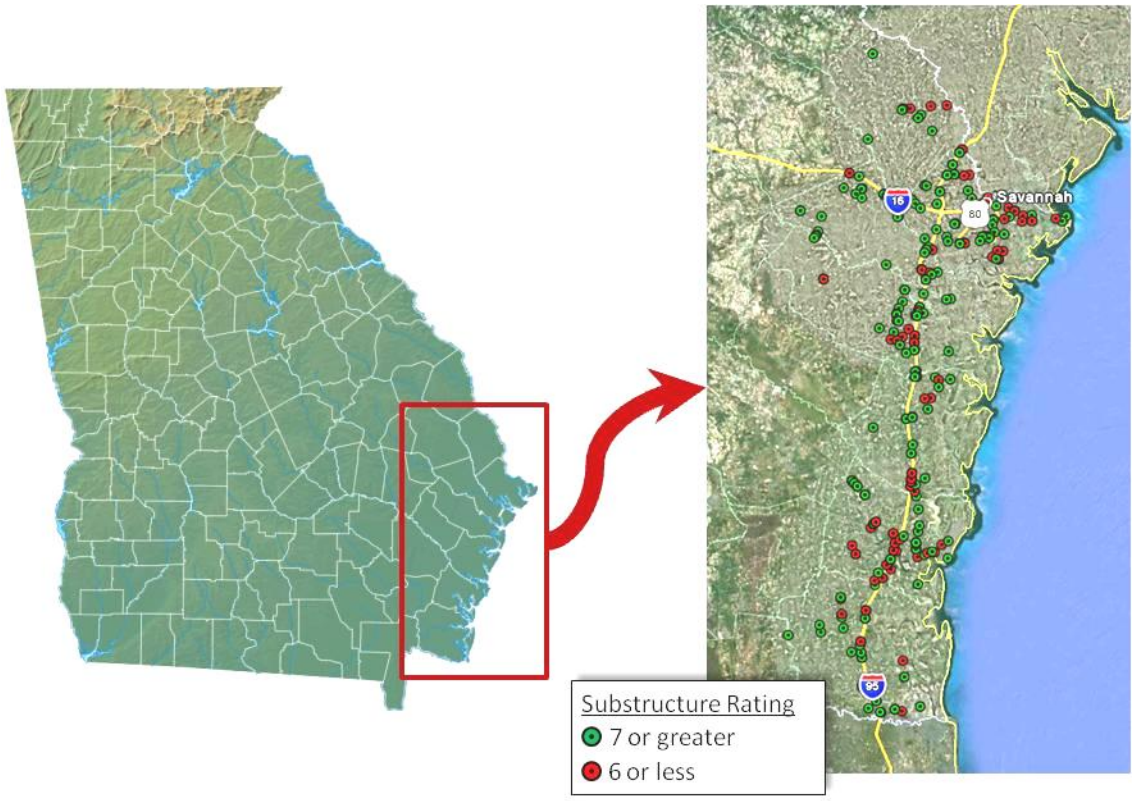

Figure 1.1: Deterioration of bridge substructures in Georgia's coastal counties

In order to develop and construct durable bridge structures capable of providing a 100+ year lifespan, it is critical to fully understand the degradation mechanisms present in Georgia's marine environment. After the durability concerns are identified, mixture

designs must be developed and tested for their performance when subjected to a marine environment and life cycle modeling performed to ensure a 100+ year lifespan.

1.3 Scope

This scope of the experimental program is presented in the flowchart in Figure 1.2, which was developed to complete the objectives presented in section 1.1. Two phases of work were conducted to accomplish the objectives through sets of experiments aimed to characterize and develop HPMC capable of a 100+ year lifespan. First a series of tasks was conducted to characterize the durability concerns for prestressed precast concrete piles exposed to marine environments. This objective was completed by performing a thorough literature review (Chapter 2), reviewing bridge inspection reports and visiting bridge sites (Appendix A), and performing a forensic investigation of piles from a decommissioned bridge substructure (Chapter 3).

Based upon the findings, a second series of experiments was performed to develop and evaluate the durability characteristics of mixture designs exposed to a marine environment. The research investigated the use of binary and ternary blend cements utilizing supplementary cementitious materials (SCM's) to accomplish adequate chloride, sulfate, and carbonation resistance. Coatings, corrosion inhibitors, and other admixture mitigation techniques were not considered. Ten potential HPMC mixture designs were cast, in addition to two control mixture designs representing the current GDOT high performance concrete mixture design and a Portland cement concrete without SCM's.

Mechanical property testing was performed on the mixture designs for compressive strength gain behavior and elastic modulus for suitability with current strength requirements and estimator equations. Durability testing was performed for carbonation using an accelerated test method and existing modeling techniques utilized

for predicting corrosion initiation due to decreased pH. Chloride ingress resistance was characterized on samples using accelerated and long-term exposure techniques and the results used for predicting usable service lives of structures.

The results of the durability assessment were used to develop life cycle estimates using existing modeling techniques. For life cycle modeling, only single species ingress due to diffusion was considered. Additionally, for research conducted on self-healing of cracks, only autogenous healing due to continued hydration of cementitious phases and calcium carbonate formation were investigated. The use of encapsulated materials and biological self-healing was not included in this investigation. Biological attack was not considered in the development of HPMC mixture designs.

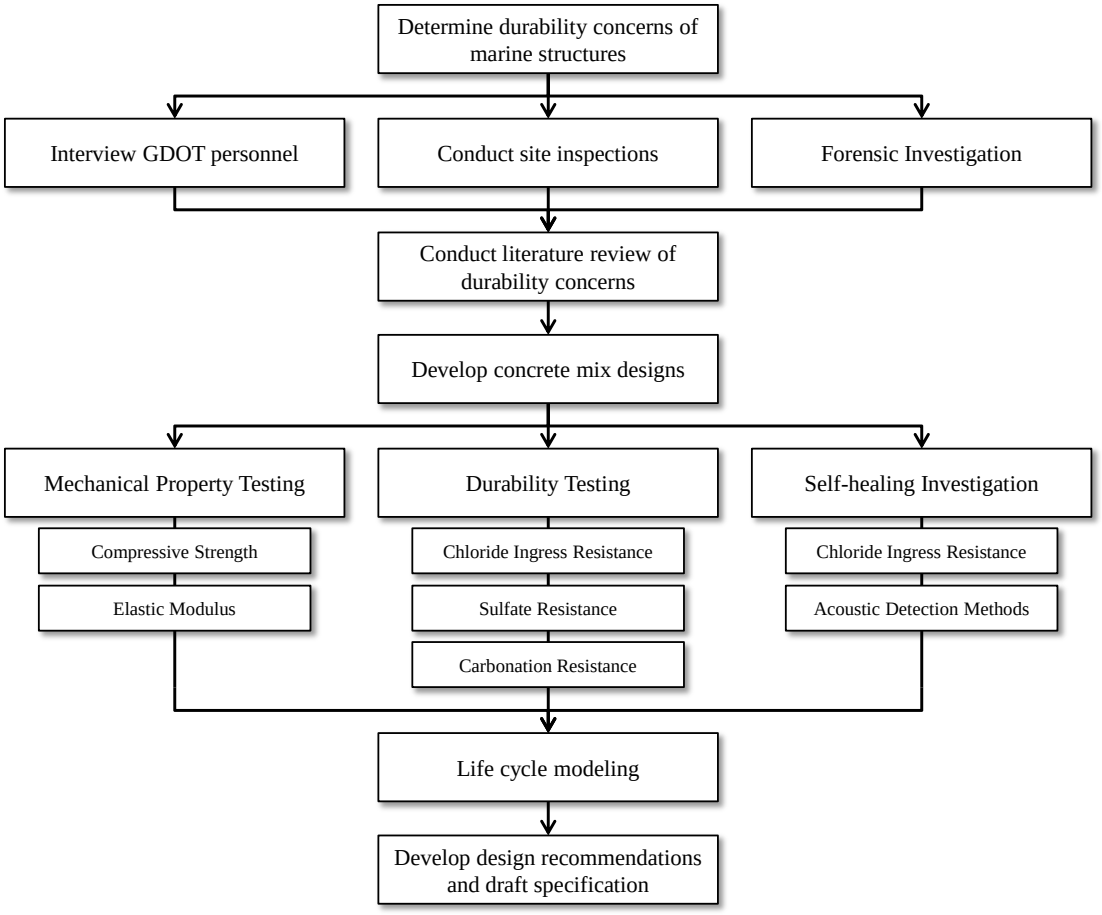

Figure 1.2: Scope of experimental program

1.4 Organization of Dissertation

- Chapter 2 presents the results of a literature review into the degradation mechanisms of chloride induced corrosion, carbonation, sulfate attack and biological attack which are present in marine structures, as well as the influence of cracks and self-healing on durability. Areas where additional research is necessary are identified.
- Chapter 3 presents the results of a forensic investigation into the degradation mechanisms present in the decommissioned piles from the I-95 at Turtle River Bridge.
- Chapter 4 introduces the development of potential HPMC mixture designs, the mixing procedure and raw material properties, and mechanical properties of each mixture design, including compressive strength gain and elastic modulus.
- Chapter 5 presents the results of chloride ingress resistance testing of potential HPMC mixture designs utilizing accelerated and long-term ponding procedures and service life modeling based upon the experimental findings.
- Chapter 6 presents the findings of studies into the sulfate resistance of potential HPMC mixture designs utilizing expansion and strength degradation measurements and investigates changes to composition of each mixture design when subjected to a sulfate rich environment.
- Chapter 7 presents the results of carbonation resistance testing of the potential HPMC mixture designs and service life modeling based upon the experimental findings utilizing existing techniques.

- Chapter 8 presents the findings of a study into the self-healing capability of binary and ternary blend cements and the influence of self-healing on chloride ingress. Optical crack width measurements were performed to characterize crack filling and closing during a ponding period. Chloride profiles were determined and the results used for service life predictions.
- Chapter 9 investigates the suitability of potential mixture designs for marine environments based upon the results of the durability testing and a performance specification approach is suggested for future mixture design development and testing.
- Chapter 10 provides a summary of the research performed and its primary conclusions. Recommendations for the implementation of HPMC for the production of durable prestressed concrete piles and areas requiring future research are given.
- Appendices include the results of coastal bridge inspections, GDOT personnel interviews, additional results not presented in the body of the dissertation, proposed HPMC usage conditions, and a list of references for all chapters.

CHAPTER 2

BACKGROUND INFORMATION

2.1 Deterioration Mechanisms of Concrete Piles in Marine Environments

Concrete structures exposed to marine environments are subjected to multiple deterioration mechanisms. The reinforcing steel, aggregate, and paste all have the potential for degradation under the environmental conditions present. Figure 2.1 shows the typical degradation mechanisms that occur in marine environments.

Prestressed concrete piling in coastal exposures is subjected to biological, physical, and chemical attack. From the forensic investigation (Chapter 3), the durability concerns identified included chloride ingress and chloride induced corrosion (Section 2.2), carbonation of concrete and carbonation induced corrosion (Section 2.3), sulfate attack of concrete (Section 2.4), biological attack of concrete (Section 2.5), and the self-healing of cracked concrete (Section 2.6). Reinforcement corrosion is amplified in Chapter 2 of Volume 2 of this report.

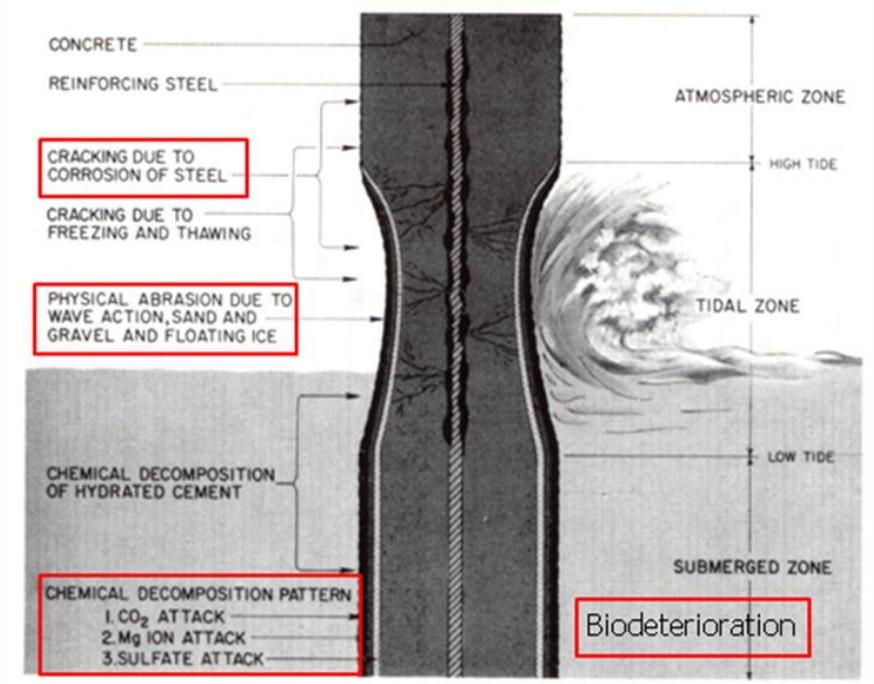

Figure 2.1: Typical degradation mechanisms in coastal concrete piling (Mehta, 1991)

2.2 Chlorides in Concrete

The ingress of chlorides into reinforced concrete is an important concern for the durability of prestressed concrete piles. The rate of ingress and concentration of chlorides at the steel reinforcement depth can dictate the usable service lives of structures by inducing damage by the corrosion of prestressing steel (ACI 222, 2001). Figure 2.2 demonstrates life cycle model for estimating the service life of a structure, where the initiation period is the length of time for chlorides to ingress to the reinforcement and initiate corrosion, and the propagation period is the length of time after initiation before the structure must be replaced.

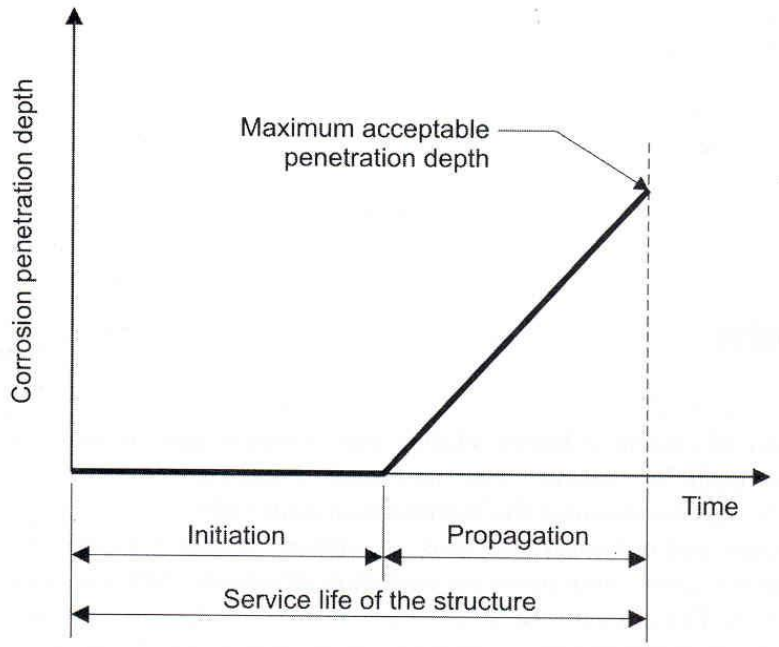

Figure 2.2: Service life model for corrosion induced damage (Bertolini, et al., 2004)

2.2.1 Sources of Chlorides

Chlorides can be introduced into concrete from either internal or external sources. Internal sources of chlorides could include the use of sea water for mixing water, dredged aggregate, aggregate washed with sea water, and chloride containing admixtures (Bertolini, et al., 2004). External chlorides typically occur from environmental factors. Typical external sources are from the ingress of seawater in marine environments, and from the use of deicing salts containing chlorides in colder climates (Bertolini, et al., 2004). Additionally, concrete may be exposed to chlorides if used in industrial applications where chemicals may contain chlorides, like dry-cleaning facilities, paper mills, and aquariums (Bertolini, et al., 2004).

2.2.2 Transport Mechanisms

External chlorides ingress into concrete occurs through several transport mechanisms. Three primary forms of transport occur in concrete: diffusion, permeation, and absorption (Stanish, et al, 1997). Additionally, the binding of chlorides can affect these transport mechanisms (Bertolini, et al., 2004). For life cycle modeling, typically only diffusion-based transport is considered (Rodriguez, 2001). Additionally, the models to be used do not account for the presence of other ions on the ingress of chlorides.

2.2.2.1 Chloride Diffusion

The primary form of ingress through the bulk of the concrete is through diffusion, often modeled to Fick's second law (Bertolini, et al., 2004). Diffusion occurs due to the presence of a concentration gradient, where ions flow from areas of high concentration to low concentration (Stanish, et al., 1997). Fick's second law is given in Eq. 2.1 for non-steady state conditions.

$$\frac{\partial C}{\partial t} = D_{eff} \frac{\partial^2 C}{\partial x^2} \qquad \text{(Eq. 2.1)}$$

Solving this equation using the boundary conditions that the surface concentration is constant, initial background concentration is zero, and that infinite points are zero yields Eq. 2.2. This solution to Fick's second law is often used to model the ingress of chlorides into concrete, and neglects other transport mechanisms present (Rodriguez, 2001). The diffusion coefficient is a material property, and can be determined using several methods (Section 2.2.4). The water to cement ratio, cement chemistry, and age of

the structure have large effects on the diffusion coefficient, and are discussed in Section 2.2.5 (Suryavanshi, et al., 2002).

$$C(x,t) = C_s - (C_s - C_o) * \text{erf}\left(\frac{x}{\sqrt{4*D_a*t}}\right) \quad \text{(Eq. 2.2)}$$

Where,

$C(x,t)$	=	chloride concentration, measured at depth x and exposure time t, mass %
C_s	=	projected chloride concentration at the interface between the exposure liquid and test specimen that is determined by the regression analysis, mass %
C_o	=	initial chloride-ion concentration of the cementitious mixture prior to submersion in the exposure solution, mass %
x	=	depth below the exposed surface, m
D_a	=	apparent chloride diffusion coefficient, m^2/s
t	=	the exposure time, s
erf	=	$\frac{2}{\sqrt{\pi}} * \int_0^z \exp(-u^2)\, du$

This interpretation of diffusion data is not representative of the exact behavior occurring due to the chlorides ingressing through a non-homogeneous solution, the effects of the capillary pore structure (which is prevalent in near-surface concrete) and absorption (section 2.2.2.4), and the effects of chloride binding (section 2.2.2.2).

2.2.2.2 Chloride Binding

Within the concrete, chlorides exist in a free or uncombined form and in bound forms, where they may combine with existing hydration products or unhydrated cementitious and supplementary cementitious material phases. The bound chlorides do not contribute to corrosion initiation in concrete (Mohammed and Hamada, 2003). In the bound form, the most common product formed is Friedel's salt [$Ca_2Al(OH)_6Cl{\cdot}2H_2O$].

The extent of chloride binding that can occur in a mix depends upon the cementitious materials contained in the mix (Mohammed and Hamada, 2003).

2.2.2.3 Chloride Permeation

Permeation occurs due to the presence of a pressure gradient. If an applied hydraulic head exists on one face of the concrete and chlorides are present, they may permeate into the concrete under the pressure gradient. This mechanism requires a large pressure head to cause the flow of chlorides to the depth of reinforcement (Stanish, et al., 1997), which may be present in concrete piping or pressurized containment vessels. The pressure head present on marine bridge structures is rarely large enough to cause any significant chloride transport through permeation.

2.2.2.4 Chloride Absorption

As a concrete surface is exposed to the environment, it will undergo wetting and drying cycles. When water, potentially containing chlorides, encounters a dry surface, it will be drawn into the pore structure through absorption, which is a capillary suction due to surface tension in the capillaries. Absorption is a physical process driven by moisture gradients, and for wetting and drying cycles the depth of drying is small in high quality concretes. Therefore, absorption is not able to bring chlorides to the depth of reinforcement for a good quality concrete (Stanish, et al., 1997). Absorption differs from adsorption, which is the adhesion of ions to a surface, and is not a significant cause of chloride ingress in concrete.

2.2.3 Chloride-Induced Corrosion

Concrete's highly alkaline environment (pH >11) allows for the formation of a thin oxide layer on the surface of reinforcing steel. The thin passive film protects the steel from corrosion in alkaline environments. If the passive layer is destroyed, active corrosion will initiate. The passive film can be broken down by decreasing the pH to less than approximately 10 of the surrounding environment, localized attack of the passive film by aggressive ions, or a concurrence of both (Bertolini, et al., 2004). The initiation of general corrosion resulting from a decreased pH is addressed in section 2.3.

Chlorides from the surrounding marine environment are able to ingress into the concrete over time through various transport mechanisms. The protective oxide film that forms on the surface of the steel in the alkaline concrete environment is broken down locally by the presence of a sufficient local chloride concentration, and pitting corrosion can result. Pitting is a localized form of corrosion which initiates when chlorides attack defect sites in the passive film. Two reactions that occur in breaking down the passive film due to chloride ion presence are given below in Eq. 2.3 and Eq. 2.4 (Bertolini, et al., 2004).

$$Fe^{3+} + 6Cl^{-} \rightarrow FeCl_6^{-3} \quad \text{(Eq. 2.3)}$$

$$FeCl_6^{-3} + 2OH^{-} \rightarrow Fe(OH)_2 + 6Cl^{-} \quad \text{(Eq. 2.4)}$$

The reactions do not consume the chlorides, and they lower the pH at the pitting site by depleting the OH^- ions in the formation of the relatively less soluble iron oxides. In concrete, the surrounding regions remain alkaline, and hydroxide ions are available in the pore solution which causes the surrounding regions to act as cathodes for the

corrosion reactions. As the pit grows, it gains a net positive charge from the hydrogen and metal ions which attract more chlorides into the pit, causing an autocatalytic reaction. At the surface, a porous cap can form from the corrosion products that further allows the pit to grow.

The corrosion of the prestressing steels leads to a loss of steel section. Additionally, the corrosion of steel leads to the formation of iron oxides which are less dense than the original steel and occupy up to 6.5 times more volume depending upon the oxide formed. The formation of oxides causes tensile forces in the surrounding concrete which can lead to cracking and delamination of the cover concrete as well as rust staining on the surface of the piles. The cracking and delamination leads to reduced strength of the structural element, as well as greatly lowering the resistance of the concrete to further ingress of chlorides and other deleterious substances and leads to accelerated corrosion.

2.2.4 Test Methods for Chloride Durability

Several methods exist for the determination of chloride transport properties in concrete. This section introduces the most common methods and investigates the advantages and drawbacks of each.

2.2.4.1 AASHTO T259: Salt Ponding Test

The AASHTO T259 (1980) test is a long-term test that measures the penetration of chloride into concrete. The experimental set-up consists of three slabs at least 76.2 mm (3 in.) thick and a having a surface are of 3,000 mm^2 (46.5 in^2). The slabs are moist cured for 14 days, then stored in at 50% relative humidity for 28 days. All sides of the

specimen are sealed except for the top and bottom face; then the specimen has a 3% NaCl solution ponded on the top surface for 90 days. After the exposure period, the chloride concentrations of 0.5 in. thick sections are determined.

The AASHTO T259 test provides a crude one-dimensional chloride ingress profile; however, the profile attained is the result of multiple transport phenomenon, including sorption, wicking, and diffusion (Stanish, et al., 1997). These transport mechanisms may be present in structures, but the impact of wicking and sorption are amplified in this test method due to its relatively short duration where diffusion may not be the primary transport mechanism (Stanish, et al., 1997).

2.2.4.2 Bulk Diffusion Test

The bulk diffusion test (ASTM C 1556, 2004) was developed to overcome some of the deficiencies of the salt ponding test for measuring diffusion. Specimens are fully saturated with limewater and sealed on all but one surface at the time of exposure. This helps to prevent initial sorption effects and wicking action during the test (Stanish, et al.,1997). The specimens are exposed to a 2.8 M NaCl solution for a minimum of 35 days.

Profile grinding is performed on the sample after the exposure period. The total chloride concentration of each increment is determined in accordance with ASTM C 1152 (2004). A regression analysis of the results to Fick's Second Law (Eq. 2.2) allows for the determination of an apparent diffusion coefficient. The bulk diffusion test yields a better estimate of the diffusion behavior of a concrete mix; however, the exposure period must be extended to 90 days or more for HPC (ASTM C 1556, 2004).

2.2.4.3 Rapid Chloride Permeability Test

The ASTM C 1202 (2007) Rapid Chloride Permeability Test (RCPT) is an electrical migration test. The test is performed on a 50.8 mm (2 in.) thick piece of a 101.6 mm (4 in.) diameter cylinder. The specimen is fully saturated, and subjected to a 60 V DC voltage for 6 hours with one face exposed to a 3% NaCl solution and the other to a 0.3 M NaOH solution. The total charge passed is monitored and used to rate the concrete according to the criterion in Table 2.1. GDOT currently uses the RCPT test as a durability requirement for HPC mixture designs with a maximum charge passed of 2,000 coulombs (GDOT, 2004).

Table 2.1: Chloride ion penetrability based on charge passed (ASTM C 1202, 2007)

Charge Passed (coulombs)	**Chloride Ion Penetrability**
> 4,000	High
2,000-4,000	Moderate
1,000-2,000	Low
100-1,000	Very Low
<100	Negligible

The RCPT measures both permeability and ionic movement. Additionally, the movement of all ions present are measured, not just chloride ions, and can affect the test result (Stanish, et al.,1997). Andrade (1993), Zhang and Gjorv (1991), Roy (1989), and Geiker, et al. (1990) have criticized that high voltage applied leads to an increase in temperature, which increases the charge passed. Additionally, the inclusion of conductive materials like steel fibers and calcium nitrate inhibitors will cause a higher charge to be measured (Stanish, et al.,1997).

The RCPT provides a short-term rating of the permeability of concrete, but the precision of the results can have a coefficient of variation on a single test up to 12.3% (Mobasher and Mitchell, 1988). Despite the drawbacks and limitations, attempts have been made to correlate RCPT results to apparent diffusion coefficients by Thomas and Jones (1996) and Berke and Hicks (1992).

2.2.4.4 Electrical Migration Techniques

The movement of chloride ions can be accelerated through the use of an electrical field. The intensity of this field is often lower than that used by the RCPT to decrease heating of the sample. The movement of ions in a solution subjected to an electrical field is governed by the Nernst-Planck equation (Andrade, 1993) and a simplified version can be used to determine the diffusion coefficient.

Electrical migration tests are typically performed in a two-chamber cell with the concrete sample dividing the two cells, as shown in Figure 2.3. The size of the specimen, applied voltage, and initial concentration of chlorides present in the cathode chamber vary from the multiple versions of this test that have been developed by Streicher and Alexander (1995), Zhang and Gjorv (1991), Andrade and Sanjuan (1994), McGrath and Hooten (1996) and many others.

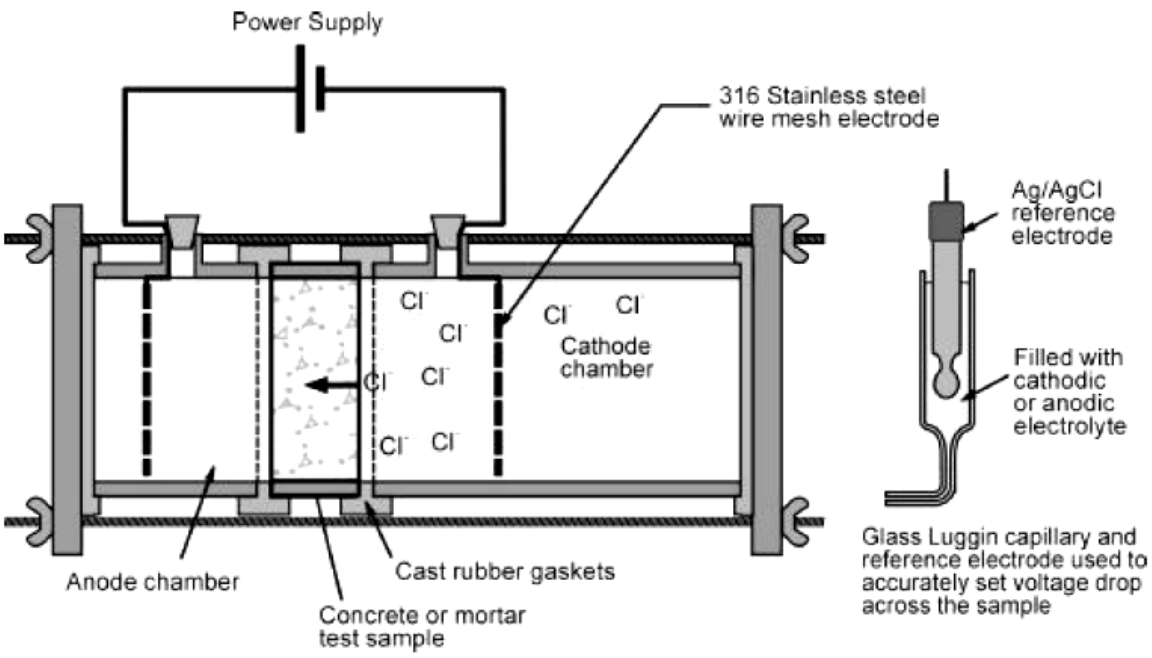

Figure 2.3: Typical chloride migration cell (Stanish, et al., 1997)

The interpretation of the electrical migration tests is different from the RCPT test in that the downstream chloride content in the anode chamber is measured periodically. This ensures that only the movement of chloride ions is considered in determination of the diffusion coefficient. Electrical migration techniques have the same drawback as the RCPT test in that conductive materials will affect the results.

2.2.4.5 Resistivity Techniques

Resistivity measurements are another method for assessing the chloride penetration resistance of concrete. Two methods of resistivity testing are to apply a voltage to a specimen and measuring the current, or the Wenner array probe technique with applies a current and measures the potential.

Resistivity techniques can be rapidly performed and avoid heating of the concrete due to the use of lower voltages (Streicher and Alexander, 1995). However, the conductivity of the pore solution has a large effect on the measured resistance and methods of accounting for it or standardizing the pore solution during testing are difficult (Stanish, et al.,1997). Resistivity techniques, like the RCPT and electrical migration tests, are sensitive to the use of conductive materials in the concrete mixture design, such as silica fume and certain fibers.

2.2.4.6 Summary

Table 2.2 provides a summary of the test methods described in the previous sections. Each test has strengths and weaknesses in its ability to determine the chloride resistance properties of concrete. For long term tests, the bulk diffusion test appears to be the best technique for accurate determination of diffusion coefficients. For short term, the RCPT and Wenner array probe are the only techniques that have standard versions of the procedure.

Table 2.2: Summary of chloride resistance test procedures

Test Method		**Chloride Ion Movement**	**At a Constant Temperature**	**Affected by Conductors in Concrete**	**Approximate Duration**
Long Term	Salt Ponding	Yes	Yes	No	90 days
	Bulk Diffusion	Yes	Yes	No	40-120 days
Short Term	RCPT	No	No	Yes	6 hours
	Electrical Migration	Varies	Yes	Yes	Varies
	Resistivity	Varies	Yes	Yes	1-30 minutes

2.2.5 Effects of Mixture design on Chloride Durability

Alterations to concrete mixture design can drastically affect the chloride ingress properties. The primary parameters with large effects on the diffusion coefficient of concrete are the water to cementitious materials ratio, age at exposure, and the addition of supplementary cementitious materials (SCMs).

2.2.5.1 Water-to-cementitious materials ratio

Polder (1995), Luping and Nilsson (1992), Luping (1995), Bamforth (1993), Collepardi (1972), Diab (1988), Dhir (1990), and Johnson (1996) each investigated the effect of varying water-to-cement ratios on the diffusion coefficient of concrete. The results of these investigations are shown in Figure 2.4. The data show that the diffusion coefficient increases with the water-to-cement ratio. The large spread of values on the graph for the same water-to-cement ratio is due to differences in the mixture designs, including aggregate type and content, type of cement used, and maturity before exposure.

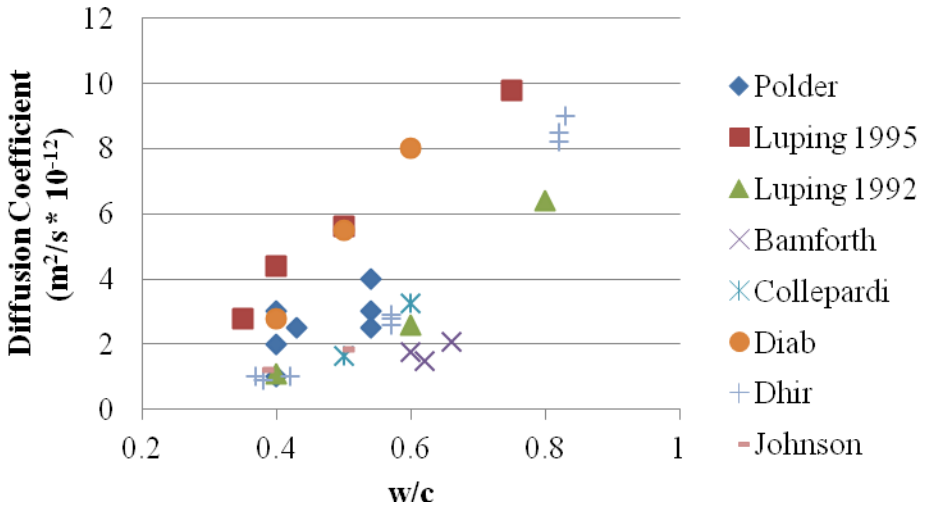

Figure 2.4: Effect of water-to-cement ratio on diffusion coefficient in plain Portland cement concrete (1 m^2/s = 1,550 in^2/s)

2.2.5.2 Age at exposure

The effect of age of exposure on the diffusion coefficient was investigated by Polder (1995), Luping and Nilsson (1992), Kanaya (1998), Pedersen and Arntsen (1998), and Mangat and Molloy (1994), and the results of their studies are shown in Figure 2.5. The data suggest that the diffusion coefficient decreases as the chloride exposure is initiated at later concrete ages. Stanish and Thomas (2003) developed Eq. 2.5 to predict the diffusion coefficient of concrete at any age given that it is known through testing for at least one age. The coefficient, m, for mixture designs can be determined experimentally using the procedure developed by Stanish and Thomas (2003) using bulk diffusion tests.

$$D_{avg} = D_{ref}\left(\frac{t_{ref}}{t_{eff}}\right)^{m} \quad \text{(Eq. 2.5)}$$

Where,

D_{avg}	=	average diffusion coefficient at t_{eff}
D_{ref}	=	diffusion coefficient at reference age
t_{ref}	=	reference age of concrete
t_{eff}	=	effective age of concrete
m	=	coefficient based upon mix parameters
	=	0.32 for Portland cement, 0.66 for 25% fly ash replacement

Figure 2.6 shows Stanish's estimator equation plotted with the experimental results for diffusion coefficients of plain Portland cement concrete mixes. The data suggest the estimator equation provides an accurate estimate of how the diffusion coefficient varies with time. The decreased diffusion coefficient with time suggests that longer curing periods would lead to decreased rates of chloride ingress.

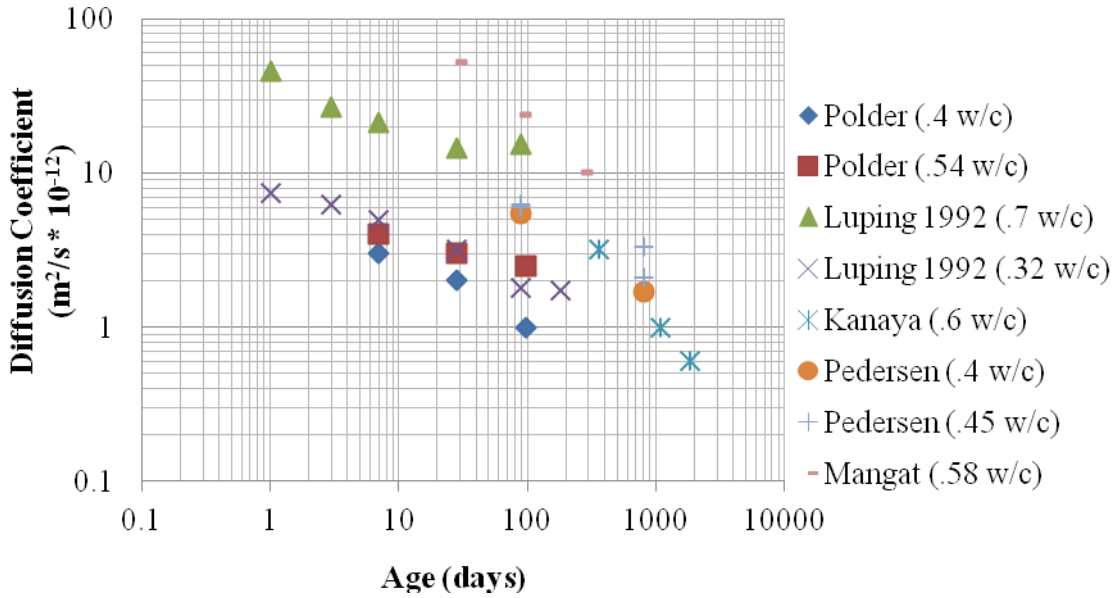

Figure 2.5: Effect of age of exposure on diffusion coefficient in plain Portland cement concrete (1 m^2/s = 1,550 in^2/s)

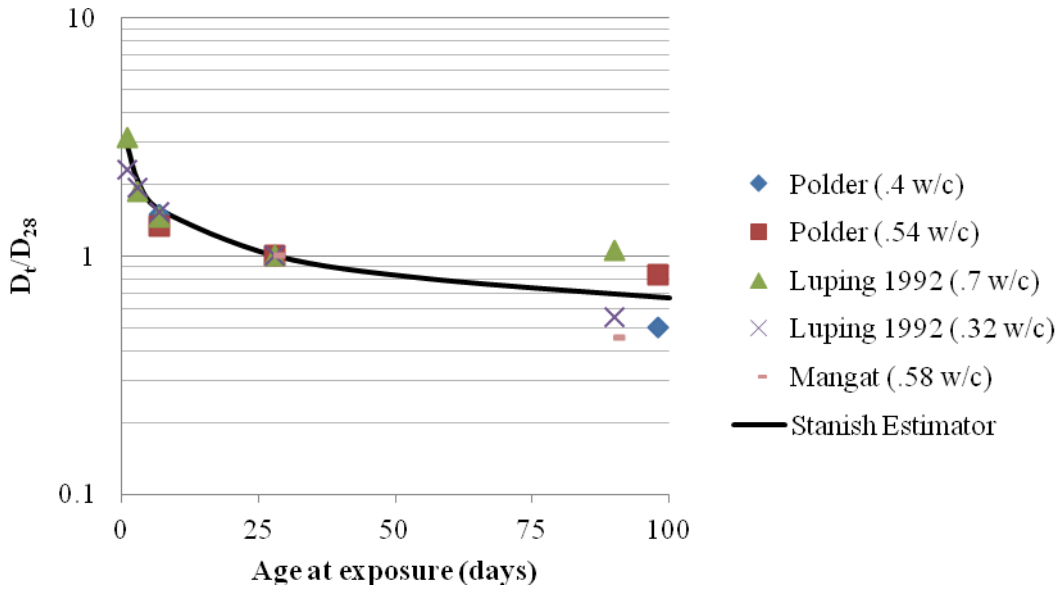

Figure 2.6: Comparison of time dependent diffusion coefficients with estimator equation

2.2.5.3 Supplementary Cementitious Materials

The effect of using SCMs on the diffusion coefficient has been widely studied. The four primary types of SCMs utilized are slag, fly ash, silica fume, and metakaolin. Basheer, et al. (2002), Bleszynski, et al. (2002), Luo, et al. (2003), Mangat and Molloy (1994), Saleem, et al. (2010), Thomas and Bamforth (1999), Thomas, et al. (2008), and Thomas, et al. (1999) investigated the use of slag replacement of cement on the chloride resistance of concrete. It was found that replacement levels over 50% resulted in large reductions in the diffusion coefficient. Thomas, et al. (2008) found that the best performance occurred with a combination of a low w/cm (water-to-cementitious materials ratio) and replacement levels above 40%. It was found that for high w/cm (>0.5) in slag replacement mixture designs that salt scaling of samples exposed to wetting and drying cycles was an issue. It was found by Thomas, et al. (2008) that slag causes a

larger decrease in the apparent diffusion coefficient over time than a plain Portland cement concrete.

Fly ash has been shown to drastically improve chloride ingress resistance by Basheer, et al. (2002), Mangat and Molloy (1994), Papadakis (2000), Thomas and Bamforth (1999), Thomas and Matthews (2004), and Thomas, et al. (1999). Thomas and Matthews (2004) found that like slag, fly ash causes a larger decrease in the apparent diffusion coefficient over time than a plain Portland cement concrete. Papadakis (2000) investigated the effect of using a Class F fly ash (low CaO) versus a Class C fly ash (high CaO) and found that both have similar effects, but that a low CaO content leads to a marginally lower diffusion coefficient.

Silica fume has been shown capable of decreasing the diffusion coefficient by orders of magnitude by Bentz (2000), Bleszynski, et al. (2002), Mangat and Molloy (1994), Papadakis (2000), Saleem, et al. (2010), Smith (2001), and Thomas, et al. (1999). Figure 2.7 shows the results of studies performed by Bentz (2000), where the decrease in diffusion coefficient is plotted for various replacement levels of silica fume. This result is in contradiction to the findings of Basheer, et al. (2002), who found that silica fume resulted in an approximately 30% decrease in the diffusion coefficient from a plain Portland cement concrete.

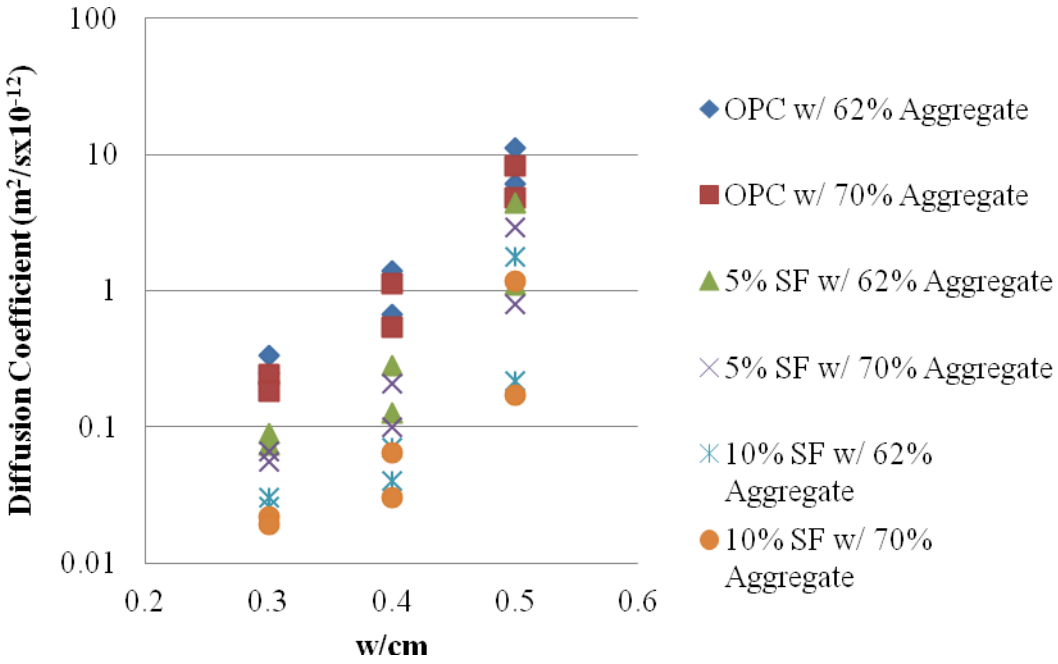

Figure 2.7: Effect of silica fume content on diffusion coefficient (1 m^2/s = 1,550 in^2/s)

The replacement of cement with metakaolin has been shown to dramatically lower the diffusion coefficient of concrete by Basheer, et al. (2002), Batis, et al. (2005), Gruber, et al. (2001), and Saleem, et al. (2010). Many of the studies compared equivalent replacement levels of silica fume and metakaolin and the results varied on which provided the largest improvement for the same replacement level. Batis, et al. (2005) found that metakaolin replacement levels over 20% will begin to increase the diffusion coefficient, and that the optimum replacement levels are between 8-12%, which was in agreement with the findings of Gruber, et al. (2001).

Saleem, et al. (2010) investigated the use of ternary blends of slag, silica fume, and metakaolin with Portland cement with 20% replacement levels of each. The results showed that ternary blends containing metakaolin and silica fume provided the largest decrease in the diffusion coefficient from control samples.

Thomas, et al. (1999) investigated the use silica fume and fly ash ternary blend cements and found that the ternary blends provided superior chloride ingress resistance to binary blends. The fly ash provided a long-term decrease in the diffusion coefficient, while silica fume increased early age resistance.

Basheer, et al. (2002) investigated the use of ternary blends containing fly ash or slag with metakaolin or silica fume. The results of the investigation are shown in Figure 2.8. The results showed that the use of ternary blends resulted in lower diffusion coefficients than binary blends.

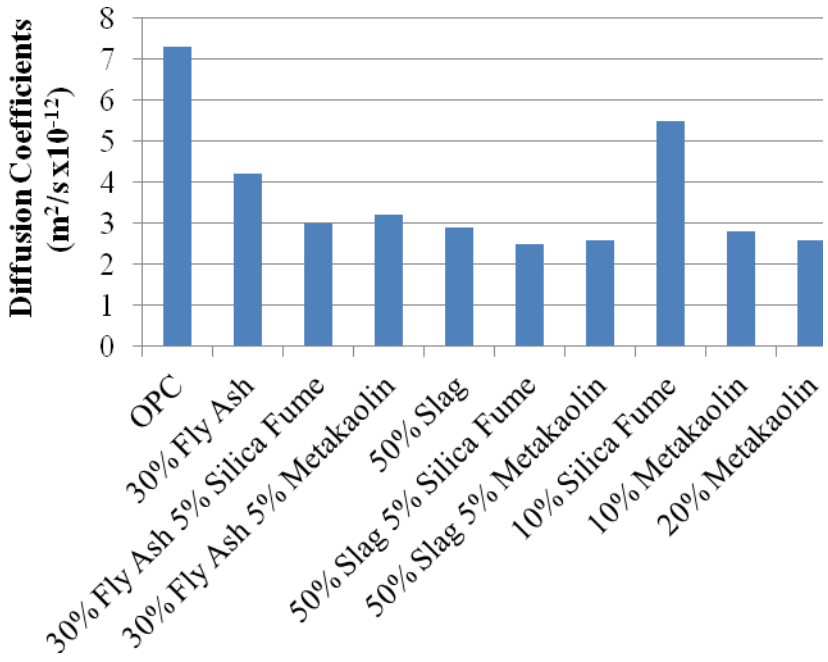

Figure 2.8: Effect of SCMs on diffusion coefficient (Basheer, et al., 2002)
(1 m^2/s = 1,550 in^2/s)

2.3 Carbonation of Concrete

Carbonation of concrete can occur due the diffusion of carbon dioxide from the atmosphere through the pores of concrete. Carbonation of concrete leads to the depletion of calcium hydroxide, which causes the decrease in pH, and can lead to a loss of calcium silicate hydrate (C-S-H), which is the primary strength giving component of hydrated cement paste (Neville, 1997). Carbonation of concrete can cause strength loss of the concrete and initiate corrosion of reinforcing steel due to the decreased pH (Papadakis, et al, 1991). Additionally, carbonation shrinkage can occur and alter the surface properties and cause cracking near the exposed surface of a structural element (Mindess, et al., 2003).

Eqs. 2.6 to 2.8 show the reactions that occur in the pore solution to cause the decrease in pH (Bohni, 2005). Water has been included as both a reactant and product due to the intermediate step in each reaction where carbonic acid is formed when carbon dioxide and water are together.

$$2NaOH+H_2O+CO_2 \rightarrow Na_2CO_3 + 2H_2O \quad \text{(Eq. 2.6)}$$

$$2KOH+H_2O+CO_2 \rightarrow K_2CO_3 + 2H_2O \quad \text{(Eq. 2.7)}$$

$$Ca(OH)_2+H_2O+CO_2 \rightarrow CaCO_3 + 2H_2O \quad \text{(Eq. 2.8)}$$

The sodium and potassium carbonates formed have a high solubility and remain in solution, but the calcium carbonate has a low solubility and precipitates out of the solution, often filling the pore structure and causing a denser microstructure. The consumption of alkali hydroxyls and dissolution of solid $Ca(OH)_2$ leads to a reduction in

the pH to approximately 8 to 9 (Broomfield, 2007). Once the pH drops to this range at the depth of reinforcing, carbonation induced corrosion will occur as the passive film on the surface of the steel becomes unstable (Broomfield, 2007). Figure 2.9 illustrates a typical distribution of pH with carbonation depth.

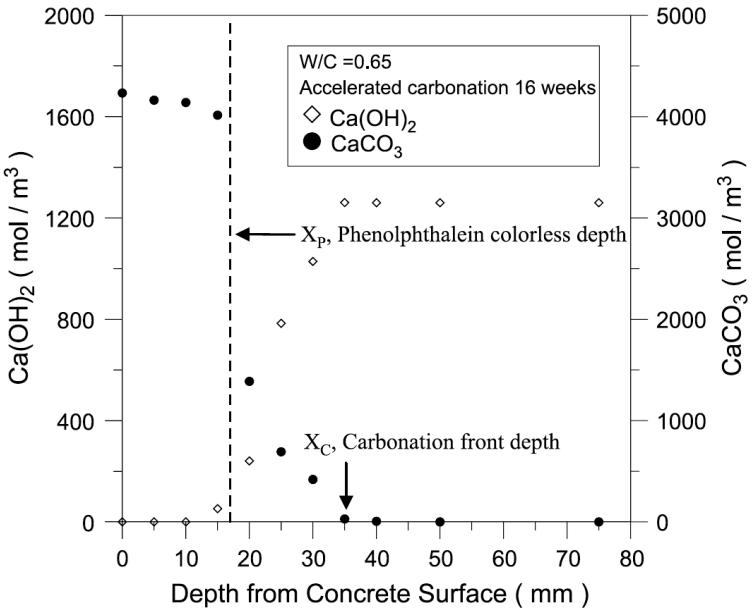

Figure 2.9: $Ca(OH)_2$ concentration as an indicator of carbonation depth measured using thermogravimetric analysis (Chang and Chen, 2006) (1 mm = 0.04 in.)

With an understanding of the rate of corrosion and how carbonation occurs over time (Section 2.3.1), the time to onset of corrosion can be estimated. The rate of carbonation is greatly affected by environmental factors such as humidity, temperature, CO_2 concentration (Section 2.3.2), and concrete properties (Section 2.3.3).

2.3.1 Carbonation Modeling

Carbonation has been shown to be a diffusion based phenomenon by Papadakis, et al. (1991). A simple model for carbonation is that the depth of ingress is proportional to the n^{th} root of time, as given in Eq. 2.9 (Bertolini, et al., 2004).

$$d = Kt^{1/n} \quad \text{(Eq. 2.9)}$$

Where,

d	=	depth of carbonation
K	=	carbonation constant
t	=	time
n	=	curve fitting factor

Research by Papadakis, et al. (1991) and Papadakis (2000) formed a more sophisticated model that gives a mathematical and physical meaning to the constant, K. A generic form of the Papadakis (2000) model is given in Eq. 2.10.

$$x_c = \sqrt{\frac{2\ D_{e,CO_2}\left(\frac{CO_2}{100}\right)t}{0.33CH + 0.214CSH}} \quad \text{(Eq. 2.10)}$$

Where,

x_c	=	depth of carbonation
$D_{e,CO2}$	=	diffusivity of CO_2 in carbonated concrete, m^2/s
CO_2	=	carbon dioxide content of ambient air at concrete surface
t	=	time, s
CH	=	estimated calcium hydroxide content
CSH	=	estimated calcium-silicate-hydrate content

2.3.2 Environmental Conditions

The effect of humidity on carbonation rate is shown in Figure 2.10. The maximum carbonation rate has been shown by Papadakis, et al. (1991) and Bertolini, et al. (2004) to occur at approximately 55-65% relative humidity. At high levels of relative humidity, the void space present in the hydrated cement paste (HCP) is largely filled with water, limiting the transport of carbon dioxide into the concrete. Additionally, at low levels of relative humidity, insufficient water is available in the pores to solubilize CO_2 and $Ca(OH)_2$ which are required for carbonation to occur.

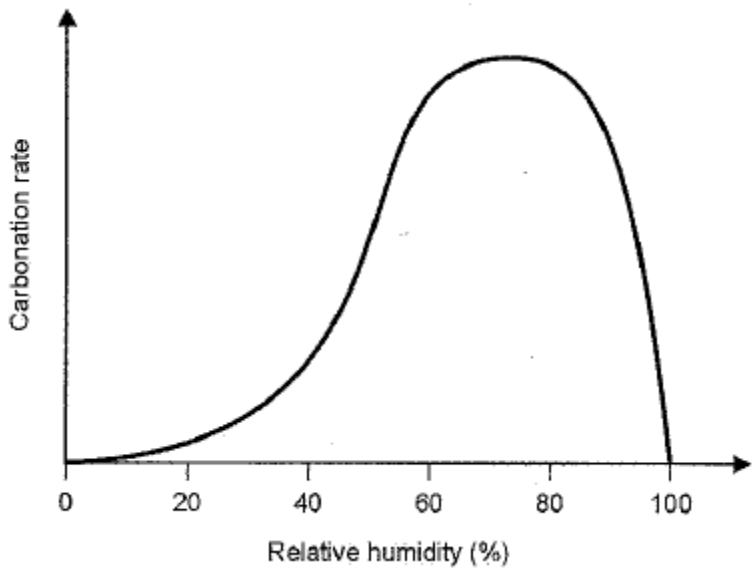

Figure 2.10: Effect of relative humidity on carbonation rate (Bertolini, et al., 2004)

An increase in temperature will cause the carbonation rate to increase (Bertolini, et al., 2004). The CO_2 concentration can have a large impact on carbonation rates. Atmospheric CO_2 levels vary from 0.03% in rural areas, up to 0.3% in industrial and urban areas, and up to 3% in areas such as highway tunnels or power plants (ACI 222,

2001). The concentration of dissolved carbon dioxide in seawater can be up to 15% and reacts with the water to form carbonic acid (Bertolini, et al., 2004).

2.3.3 Concrete Mixture design Effects on Carbonation

The permeability of concrete has a large influence on the rate of carbonation. Decreasing the water-to-cement ratio (w/c) can vary the permeability by orders of magnitude (Papadakis, et al., 1991). Figure 2.11 shows the effect of water-to-cement ratio on depth of carbonation. Research by Bertolini, et al. (2004) and Sulapha, et al. (2003) showed that increased wet curing lengths led to reductions in the rate and depth of carbonation, as shown in Figure 2.12.

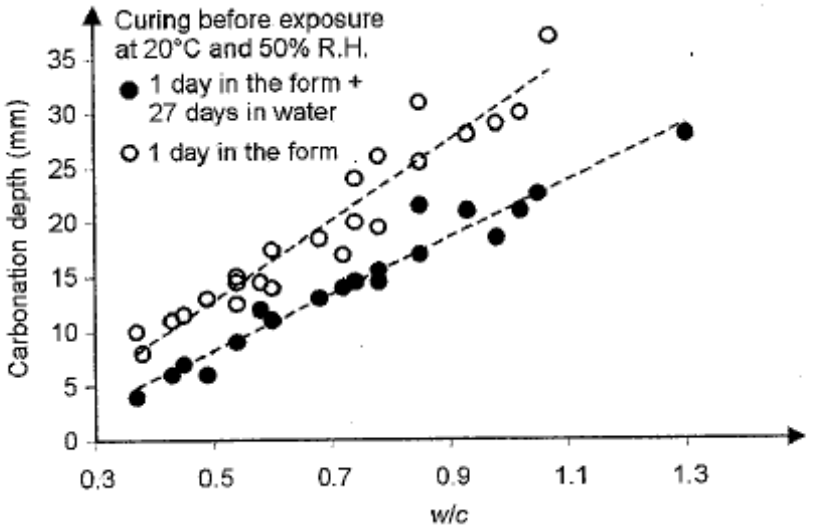

Figure 2.11: Effect of water-to-cement ratio on carbonation depth (Bertolini, et al., 2004) (1mm = 0.04 in.)

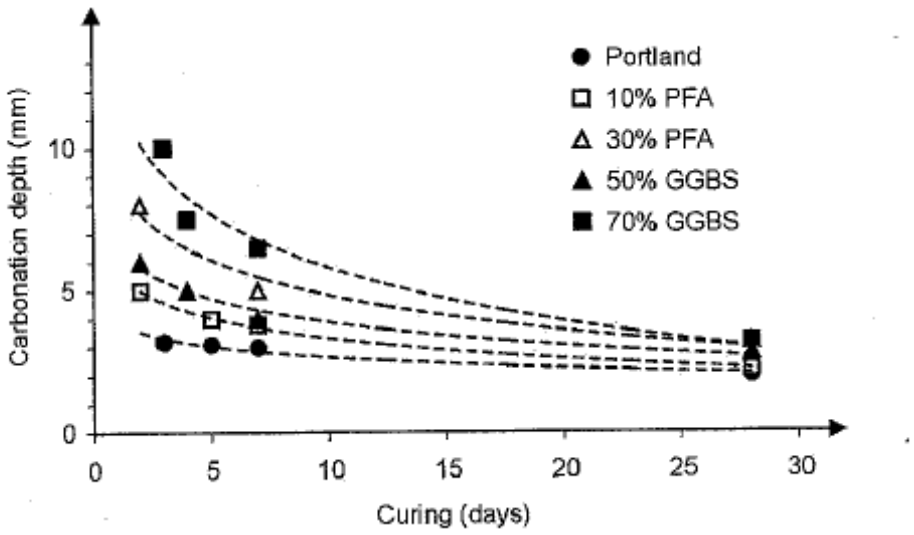

Figure 2.12: Effect of binder composition on carbonation depth (Bertolini, et al., 2004) (1 mm = 0.04 in.)

Also, the binder composition has a large influence on the carbonation resistance. The use of SCMs may decrease the initial pH of the concrete through consumption of calcium hydroxide (CH), but also decreases the permeability by refinement of the pore structure and the creation of secondary calcium silicate hydrate (C-S-H) (Bertolini, et al., 2004). Research by Atis (2003), Maslehuddin, et al. (1996), Papadakis (2000), Sideris, et al. (2006), and Sulapha, et al. (2003) on concretes utilizing fly ash replacement for cement showed that the carbonation depth increased with increasing the replacement levels. Additionally, Papadakis (2000) demonstrated that the CaO content of fly ash had a negligible effect on the carbonation rate. Slag replacement of cement was shown to increase the carbonation depth by Maslehuddin, et al. (1996) and Sulapha, et al. (2003).

The replacement of cement with silica fume was shown to increase the carbonation depth (as defined by the color change of a phenolphthalein solution) at all ages by Papadakis (2000) and Sulapha, et al. (2003). The results of Maslehuddin, et al. (1996) contradict this finding, and showed that a 10% replacement with silica fume led to

a decrease in carbonation rate compared to a plain Portland cement concrete. Sulapha, et al. (2003) found that 10% silica fume replacement performed better than fly ash replacement (20-50%) and slag replacement (65%). Additionally, Sulapha, et al. (2003) found that a ternary blend of 10% silica fume and 55% slag replacement performed better than a 55% slag only mixture.

The research performed on carbonation has shown that the addition of slag or fly ash leads to an increase in carbonation depth. However, Sideris, et al. (2006) found that the carbonation rate was lower at later ages for mixture designs containing SCMs. This suggests that the decreased pH initially due to CH consumption in the formation of secondary C-S-H may be offset in the long-term by the decreased rate of ingress due to the formation of a more dense matrix with smaller pores in the presence of SCMs.

The research by Sulapha, et al. (2003) on ternary blended cement suggests that ternary blends may offer lower rates of carbonation than binary mixture designs. No research on the carbonation resistance of mixture designs containing metakaolin cements was found.

2.4 Sulfate Attack

2.4.1 Degradation Mechanisms

Concrete piling in seawater and brackish water can be exposed to high concentrations of sulfates. The primary forms of sulfates present are $NaSO_4$, $MgSO_4$, and $CaSO_4$ (Skalny, et al., 2002). Damage to the concrete due various reactions between the ingressing sulfate ions and hydration products and anhydrous cement phases in the

cement paste is termed “sulfate attack”. Two primary mechanisms are associated with sulfate attack. First, sulfate ions can react with monosulfo- aluminate or available tricalcium aluminate (C_3A) to form ettringite. The formation of ettringite can be expansive and lead to cracking and spalling. In addition, sulfate ions may react with available calcium hydroxide to form gypsum. If there is no Portlandite present, then the calcium comes from the decomposition of the calcium silicate hydrate phase (C-S-H). The loss of calcium from the C-S-H leads to a reduction in strength (Skalny, et al., 2002).

In the case of magnesium sulfate attack, additional reaction mechanisms are possible. Magnesium sulfate reacts with Portlandite to form brucite, in addition to gypsum. Simultaneously, C-S-H is decomposed and converted to an amorphous hydrous silica or magnesium silicate hydrate phase. The decomposition of C-S-H is significantly faster with exposure to magnesium sulfate compared to sodium sulfate (Skalny, et al., 2002).

The concentration of sulfates has a large effect on the extent and rate of sulfate attack. ACI 201 (2010) provides guidelines for four exposure classes and requirements to protect against each level of exposure. Table 2.3 shows the requirements proposed by ACI 201 for a given sulfate exposure in water. The recommended cement type is based upon an ASTM C 150 (2009) cement designation. Alternatively, the ASTM C 1157 (2011) performance based specification for cements can be used. For the S3 exposure class, ASTM C 1012 (2009) expansion tests must be performed to classify a blended cement or the use of SCMs sufficient for this exposure condition. ACI 201 (2010) does not provide design guidelines based upon the source of sulfates or the cation present, but only on the concentration of sulfate ions.

Table 2.3: Exposure Classes as specified by ACI 201 (2010)

Exposure Class		Cement Type	Exposure (ppm)	w/cm
S0	Not Applicable	No Restriction	$SO_4 < 150$	None
S1	Moderate	Type II	$150 \leq SO_4 < 1,500$	w/cm < 0.5
S2	Severe	Type V	$1,500 \leq SO_4 < 10,000$	w/cm < 0.45
S3	Very Severe	Type V + Pozzolan or Slag	$SO_4 > 10,000$	w/cm < 0.40

2.4.2 Test Methods for Sulfate Attack Durability

2.4.2.1 ASTM C 1012 Expansion Tests

The ASTM C 1012 (2009) test is performed on 25.4 mm x 25.4 mm x 285.8 mm (1 in. x 1 in. x 11.25 in.) mortar bars exposed to a 5% Na_2SO_4 solution. Samples are moist cured until the time of exposure, which begins once a minimum strength of 19.65 MPa (2,850 psi) is achieved. The expansion of the bars is measured periodically, typically for 12-18 months. The results are compared with the expansion limits given by ACI 201 (2010) in Table 2.4, which correspond to the equivalent binder compositions recommended for the exposure classes outlined in Table 2.3.

Table 2.4: Maximum expansion percentages specified by ACI 201 (2010)

Exposure Class	Expansion Percent		
	6 Months	12 Months	18 Months
S1	0.10%	-	-
S2	0.50%	0.10%	-
S3	-	-	0.10%

The test measures expansion due to ettringite formation, but does not account for strength loss. Additionally, the age at exposure can cause a large variation in the initial expansion. This effect is amplified when comparing Portland cement with SCM containing mixtures since the strength gain behavior is altered, and therefore so is the age when the strength criterion is met (Thomas, et al., 1999).

2.4.2.2 Compression Strength Degradation Testing

Mehta (1975), Mehta and Gjorv (1974), Kurtis, et al. (2001), Brown (1981), and Lee, et al. (2005) performed compressive strength testing of paste cubes exposed to sulfate solutions. The tests performed by Mehta (1975), Kurtis, et al. (2001), and Brown (1981) utilized a pH controlled test in a 4% Na_2SO_4 solution that was circulated. Lee, et al. (2005) tested the strength degradation of samples exposed to a 5% Na_2SO_4 solution and a 5% $MgSO_4$ solution. The exact details of each test methodology utilized varied; however, the results measured were directly comparable to a material property. Research is necessary to determine if there is a correlation between the strength loss and expansion of samples.

2.4.3 Effect of Binder Composition

Alterations to the binder composition has been shown to improve sulfate resistance of concretes. It has been shown that decreasing the C_3A content will increase sulfate resistance (Mindess, 2003). Additionally, lowering the water-to-cementitious materials ratio will lead to a more resistance mixture (Kurtis, et al., 200) by slowing the rate of sulfate ingress.

For severe exposures including seawater, it has been shown (Mindess, et al., 2003) that the use of a sulfate resistant cement (ASTM C 150 (2009) Type II or V) alone is not sufficient to prevent damage. In a severe environment, a low C_3A content helps to eliminate damage due to ettringite formation and a low water-to-cement ratio helps decrease the rate of ingress, but the CH and potentially C-S-H are vulnerable to attack (Mindess, et al., 2003). Additionally, Kurtis, et al. (2000) showed that a low C_3S content helps improve sulfate durability.

The use of SCMs as a partial replacement of cement has been shown to produce large improvements in the resistance of binder compositions to sulfate attack. There are two primary causes for the improvement of sulfate resistance by the use of SCMs. First, the "dilution effect" occurs since the addition of SCMs generally reduces the amount of C_3A present in the binder, which leads to less susceptibility to ettringite formation (Sideris, 2006). Second, the "pozzolanic effect" occurs when pozzolanic SCMs react with calcium hydroxide (CH) and water to produce secondary calcium-silicate-hydrate (C-S-H). The formation of secondary C-S-H increases the density of the hydrated cement paste by filling capillary pores, which improves the strength and transport properties (Sideris, 2006). The "pozzolanic effect" occurs slowly and the improvement in durability properties will only occur after adequate time has passed for the materials to react (Odler, 1997).

2.4.3.1 Fly ash

The use of fly ash replacement has been shown to have positive or negative effects on the sulfate resistance, depending on the CaO content. Research by Tikalsky

and Carrasquillo (1992) showed that fly ash with high CaO contents increased the risk of sulfate attack compared to a plain ASTM C 150 (2009) Type II cement. Additionally, it was found that the replacement of cement with a low CaO fly ash increased the sulfate resistance. The research of Bonakdar and Mobasher (2010) found that the use of high CaO content fly ash lead to improved sulfate resistance over Portland cement, but that low CaO content fly ashes led to superior resistance.

The research of Mangat and El-Khatib (1995) demonstrated similar findings, and that replacement levels of 22% to 33% with a low CaO fly ash led to dramatic improvement in sulfate resistance, as shown in Figure 2.13. It was found that an 11% replacement level had deleterious effects to the sulfate resistance. Monteiro and Kurtis (2003) demonstrated similarly that replacement levels between 25% and 45% with a low CaO fly ash led to improved sulfate resistance.

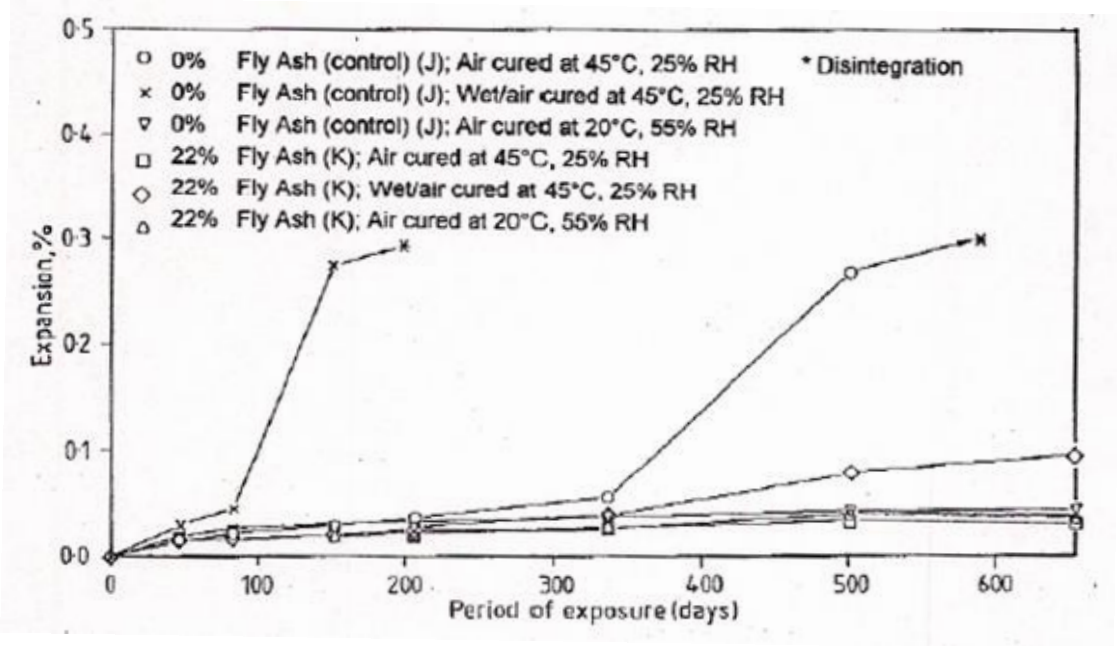

Figure 2.13: Expansion results for cements replaced with fly ash (Mangat and Khatib, 1995)

2.4.3.2 Slag

Research by Mangat and Khatib (1995), Hooten and Emery (1990), and Rozeire, et al. (2009) that slag replacement levels above 40% led to dramatic improvement in the sulfate resistance of binders. The results of Hooten and Emery (1990), shown in Figure 2.14, demonstrated that with increasing replacement the resistance to sulfates increased. The results showed that any replacement level above 40% resulted in samples meeting the 18 month expansion limit given by ACI 201 (2010).

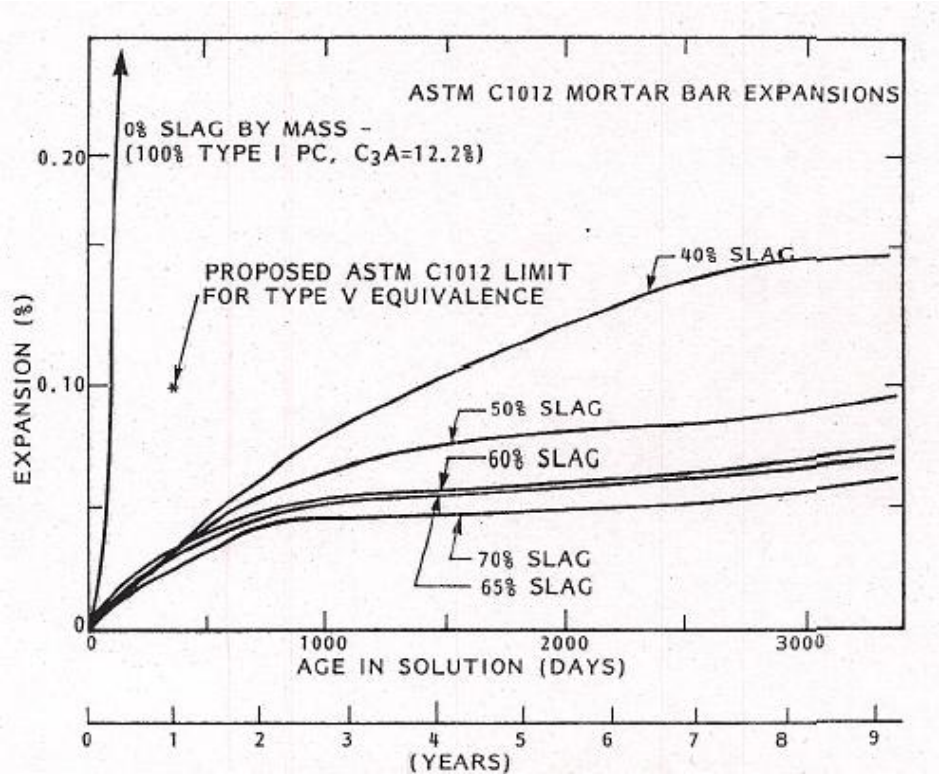

Figure 2.14: Expansion of slag cements exposed to sulfate solution (Hooten and Emery, 1990)

2.4.3.3 Silica Fume

The expansion of silica fume blended cements was studied by Torii and Mitsunori (1994) and Akoz, et al. (1995) and found that replacement levels between 5% and 10% led to increased sulfate resistance. Torii and Mitsunori (1994) found that replacement levels above 10% led to decreasing sulfate resistance.

The strength degradation behavior of silica fume blended cements was studied by Lee, et al. (2005), Al-Amoudi (2002), and Bonen (1993). It was found that silica fume replacement levels of 5% to 10% lead to increased resistance to strength loss to samples exposed Na_2SO_4 over Portland cement, as shown in Figure 2.15. However, silica fume showed increased strength loss compared to Portland cement when exposed to $MgSO_4$, as shown in Figure 2.16. Figure 2.17 shows samples after 180 days of exposure. The increased damage observed is attributed to the easier attack of C-S-H due to the decreased CH content of silica fume containing blended cements.

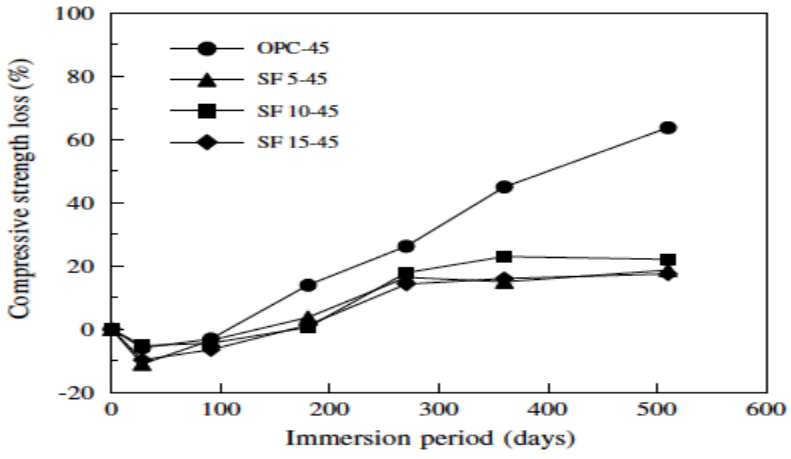

Figure 2.15: Compressive strength loss of silica fume mortars in sodium sulfate (Lee, et al., 2005)

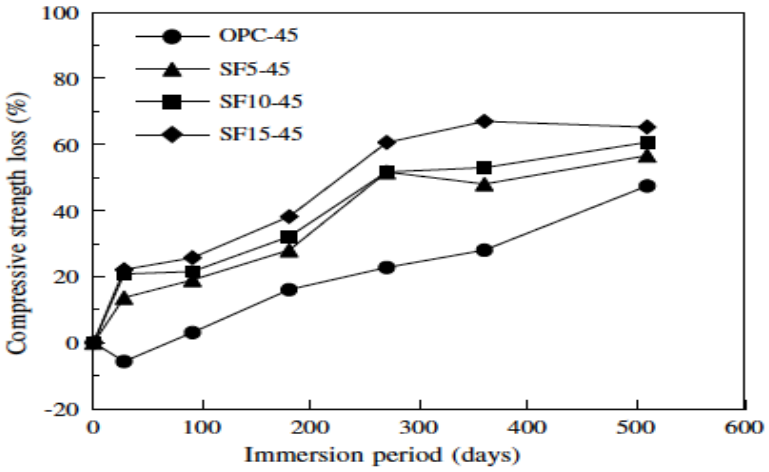

Figure 2.16: Compressive strength loss of silica fume mortars in magnesium sulfate (Lee, et al., 2005)

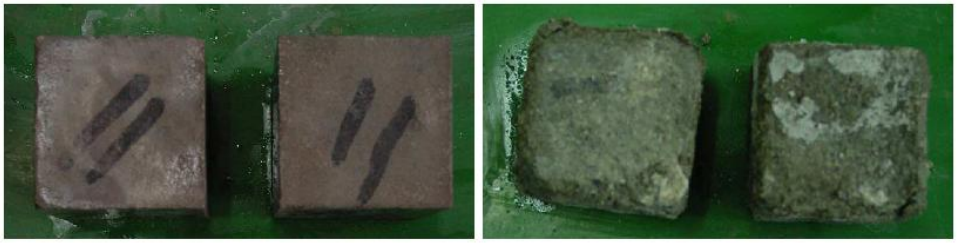

Figure 2.17: 10% silica fume mortars exposed to 5% sodium sulfate (left) and 5% magnesium sulfate (right) (Lee, et al., 2005)

2.4.3.4 Metakaolin

The expansion of blended cements containing metakaolin was investigated by Courard, et al. (2003) and Khatib and Wild (1998) and found that replacement levels above 10% led to improvement of the sulfate resistance. However, a replacement level of 5% led to lowered resistance.

The compressive strength degradation of metakaolin blended cements was studied by Khatib and Wild (1998) and Guneyisi, et al. (2010) and found that replacement levels above 10% led to increased resistance to strength loss in a Na_2SO_4 solution compared to

Portland cement. The results of Guneyisi, et al. (2010) are shown in Figure 2.18, where increasing metakaolin content led to increasing sulfate resistance.

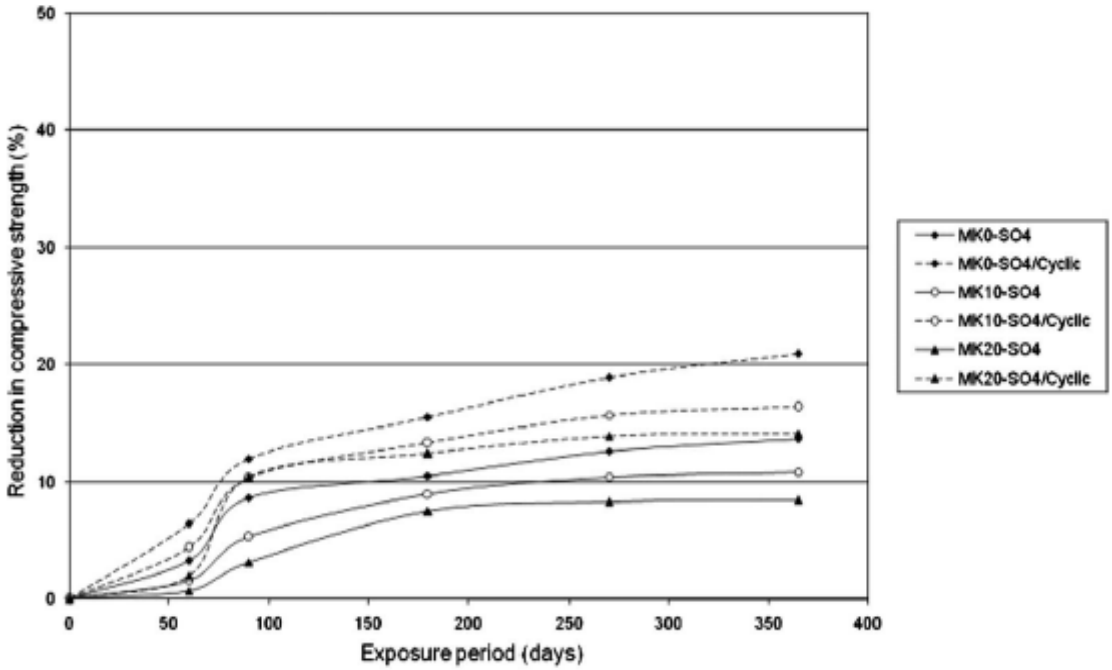

Figure 2.18: Compression strength reduction of metakaolin cements (Guneyisi, et al., 2010)

2.4.3.5 Ternary Blends

Thomas, et al. (1999) investigated the use of ternary blended cements containing fly ash and silica fume. The study compared the ternary mix to binary mixture designs containing low and high CaO content fly ashes. The expansion results are shown in Figure 2.19, which show that the addition of 3% silica fume to a sulfate susceptible mix (high CaO content fly ash) led to dramatic improvement of sulfate resistance.

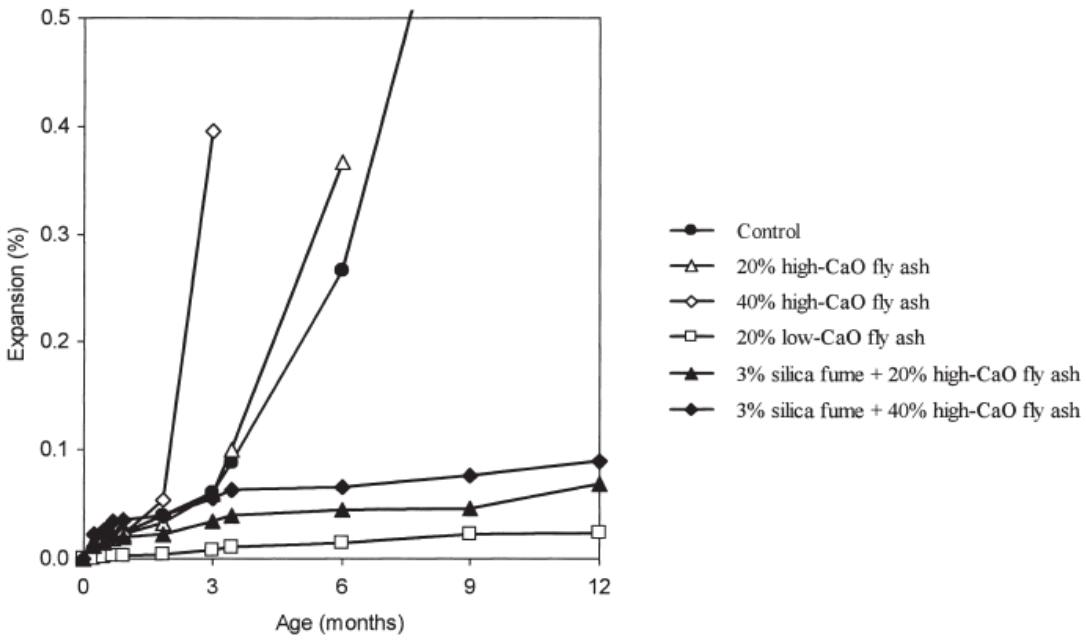

Figure 2.19: Effect of fly ash and silica fume on cements exposed to sodium sulfate (Thomas, et al., 1999)

2.4.3.6 SCMs Summary

Previous research has shown that the replacement levels given in Table 2.5 of SCMs will lead to improved sulfate resistance from a plain Portland cement. The research by Thomas, et al. (1999) suggests that the combination of SCMs in ternary mixture designs may lead to further improvement of sulfate resistance and needs to be investigated.

Table 5: Recommended replacement percentages of SCMs

Material	Class F - Fly Ash	Slag	Metakaolin	Silica Fume
% Replacement	25-35	50-80	5-20	5-10

2.5 Biological Attack

The biological attack on marine structures occurs due to several different organisms and damage mechanisms. Barnacles, mollusks, and sea urchins are known to secrete acids which can deteriorate the concrete and lead to the presence of boreholes (Mehta, 1991). Additionally, Lea (1971) reports mollusks that produce ammonium carbonate, which causes significant damage to concrete. Bacterial degradation of concrete marine structures has been reported due to the presence of anaerobic bacteria, *Thiobacilli*, that produce sulfuric acid which is highly corrosive to concrete and reinforcing steel (Mehta, 1991). Additionally, from the results in Chapter 5 and Scott, et al., (1988), it was identified that the boring sponge, *Cliona*, will attack limestone aggregate in marine structures.

Biological attack may be a concern in prestressed concrete piles, specifically the effect of the boring sponge, *Cliona*. There have been reports of *Cliona* sponges at Gardiner's Island, New York (Nicol and Reisman, 1976), along the coast of Virginia (Hopkins, 1962), Corpus Christi, Texas (Miller, et al., 2010), and off the coast of Jamaica (Scott, et al., 1988).

A reported case of boring sponge attack was reported in Jamaica due to *Cliona lampa* (Scott, et al., 1988). The sponges burrowed through the limestone aggregate of concrete masonry blocks. The damage was primarily at the corners, and irregular shaped bore holes occurred in the aggregate. The sponges use etching secretions to penetrate calcium carbonate and form the boreholes (Nicol and Reisman, 1976). The genus *Cliona* sponges leave silicate spicules near the surface of their borings. The length of the spicules varies by species but is typically between 200 μm to 400 μm (Zea and Weil, 2003). Studies on

the erosion rate of the sponge show that the rate may exceed 1 mm (0.04 in.) per year of ingress in solid limestone (Neumann, 1966). Further research is needed on biological attack of concrete piles including a foundation of knowledge on the species causing attack, the rate and effects of their ingress, as well as methods of preventing and mitigating damage to existing piles need to assessed.

2.6 Self-healing of Cracked Concrete

The cracking of concrete can have a large influence on the transport and durability behavior of structures. Cracks increase the penetrability of concrete, reduce concrete strength, decrease aesthetics of structures, and may indicate deterioration of the structure (Rodriguez, 2001). As discussed in Chapter 5, piles in marine environments are primarily susceptible to reflective tensile cracking due to driving and to flexure cracking during handling and placement.

Corrosion in cracked concrete starts either in the crack zone or in the area adjacent to the crack. Figure 2.20 from Rodriguez (2001) demonstrates the two following corrosion mechanisms that can be observed:

- The anodic and cathodic reactions take place in the crack. The anodic and cathodic areas are small and located close to each other and cause microcell corrosion where the oxygen required is provided by the crack.
- The reinforcement in the crack zone is anodic, and the passive steel surface adjacent to the crack acts as the cathode, forming a macro corrosion cell. The

steel surface involved in the cathode reaction is typically larger, causing a higher corrosion rate.

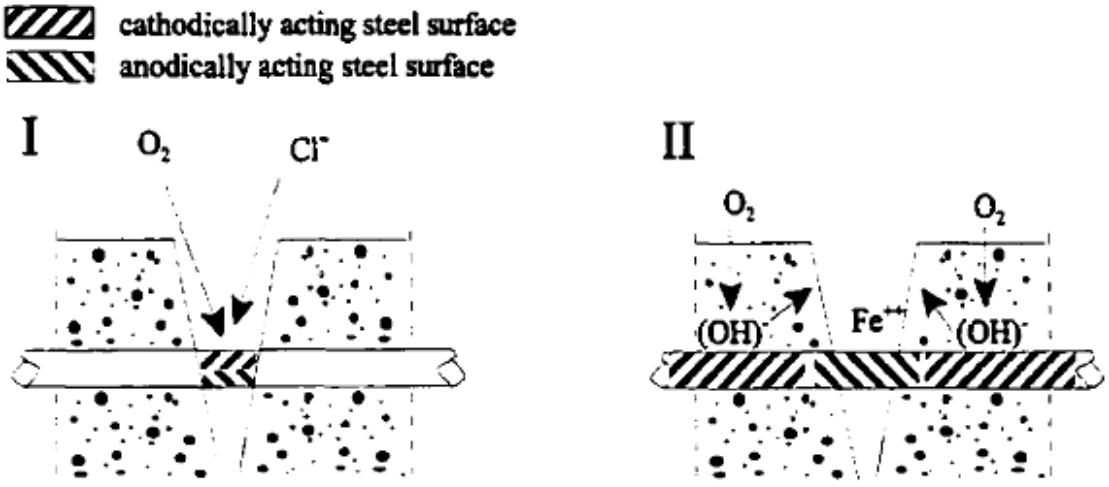

Figure 2.20: Two types of corrosion processes in the region of cracks (Rodriguez, 2001)

It has been reported by many authors that corrosion in cracked concrete typically occurs as a direct result of cracking and the initiation time is reduced compared to uncracked concrete in similar conditions (Suzuki, et al., 1989; Suzuki, et al., 1990; Borgard, et al., 1991; Bentur, et al., 1997; Thursesson, et al., 1997) and the rate of corrosion is typically higher in cracked concrete due to increased availability of oxygen and water (Otsuki, et al., 2000). Additionally, it has been shown that increasing crack width decreased the initiation time for corrosion (Suzuki, et al., 1990). The influence of crack size is presented in section 2.6.3.

2.6.1 Crack Healing Mechanisms

It has been shown that cracks in concrete can self-heal and reduce the penetrability of chlorides into the section (Jacobsen, et al., 1998). Autogenous healing of cracked concrete can occur due to the cementitious material's capability to heal and fill cracks in fractured concrete by (1) the formation of calcium carbonate or calcium hydroxide (Neville, 1997), (2) sedimentation of particles (Edvardsen, 1999), and (3) continuing hydration and swelling of the cement matrix (Neville, 1997). Additionally, research has been shown that microbial self-healing (Van Tittelboom, et al., 2010; Biswas, et al., 2010; Jonkers, et al., 2010; De Muynck, et al., 2008; Patil, et al., 2008; Bang, et al., 2001) and encapsulated aided self-healing (Yang, 2009) can occur.

Previous research by Lauer and Slate (1955) and Heide (2005) has shown that the following environmental conditions must be present for self-healing to occur: the presence of water, stability of the crack, and that the liquid may not lead to a leaching or dissolution reaction. Prestressed concrete piles in marine environments provide each of these environmental conditions necessary for self-healing to occur.

2.6.2 Permissible Crack Widths

Of course, the effects of cracking on concrete depend on the crack width and depth. Many existing specifications set recommended values for the maximum chloride content, minimum cover thickness, and maximum tolerable crack width. Crack widths are often limited based upon the exposure environment, and Table 2.6 gives the recommended values by ACI 224 (1998).

Table 2.6: Permissible crack widths for exposure conditions (ACI 224, 1990)

	Tolerable Crack Width	
Exposure Condition	**in.**	**mm**
Dry air, protective membrane	0.016	0.41
Humidity, moist air, soil	0.012	0.30
De-icing chemicals	0.007	0.18
Seawater and seawater spray; wetting and drying	0.006	0.15
Water-retaining structures	0.004	0.10

The recommended values do not form a design guideline that ensures adequate protection for any desired service life. Edvardsen (1999) made recommendations for permissible crack widths ranging from 0.1 to 0.25 mm (0.004 to 0.01 in.) where the results showed that cracks could be expected to almost completely self-heal and have similar flow rates under a pressure head to virgin concrete.

2.6.3 Chloride Ingress into Cracked Concrete

The influence of flexure cracking on chloride ingress has been widely studied. Mangat and Gurusamy (1987) chloride diffusion into cracked steel fiber reinforced concrete. Crack widths of between 0.069 mm (0.0027 in.) and 1.08 mm (.0425 in.) were produced and samples were subjected to cyclic wetting and drying to represent splash and tidal zone marine exposure. The results showed that the chloride concentration near the cracks increased as the crack width increased. The chloride concentration increase was most pronounced for crack widths 0.51 mm (0.02 in.) and wider.

Raharinaivo, et al. (1986) performed a similar study investigating the influence of crack width on chloride diffusivity in samples submerged in a salt solution. The results showed that the diffusion coefficient of cracked concrete being one or two orders of

magnitude larger than uncracked concrete, and wider cracks resulted in higher diffusion coefficients. Their results contradicted Mangat and Gurusamy (1987) in that even small cracks (approximately 0.1 mm (0.004 in.)) were found to be significant. Rodriguez (2001) asserts that the noticed differences are most likely due to differences in the concrete types utilized.

Francois and Maso (1988) performed a long-term study on concrete beams loaded in three-point bending, that were exposed to a salt-fog while loaded. Crack widths between 0.05 to 0.5 mm (0.002 to 0.02 in.) were studied. The authors found that chlorides quickly penetrated in the tension zone and was triggered by damage at the paste-aggregate interface. It was found that chlorides penetrated through the crack and diffused through the walls of the crack into the surrounding concrete. As part of the same study, Francois and Arliguie (1999) reported that the apparent chloride diffusion coefficient was related to the tensile stress in the reinforcing bar, and could be used as a guideline for evaluation of chloride ingress into concrete subjected to a tensile stress. Konin, et al. (1998) investigated chloride ingress with microcracking due to flexural loads and also found a linear relationship between the chloride apparent diffusion coefficient and the applied tensile stress in the rebar for tensile stresses between 0 to 220.6 MPa (0 to 32 ksi), which agreed with the findings of Francois and Arliguie (1999).

Chloride diffusivity of concrete cracked in flexure was also studied by Gowripalan, et al. (2000). Concrete prisms were cracked in flexure and stressed with bolts to maintain a crack width of 0.3 mm (0.0118 in.) and were ponded in a salt solution for 300 days. Their results found that the apparent chloride diffusion coefficient is larger in the tensile than in the compression zone. This finding was consistent with the findings

of Francois and Maso (1988). The authors proposed that the crack width-to-cover ratio should be used as a performance parameter instead of the crack width alone, since the crack width at the surface is not the same as the crack width at the steel with flexure induced cracks.

Edvardsen (1995) investigated the relationship between crack width and water permeability, since chloride ions are transported with water. The results of the study showed that the flow of water through cracks is proportional to the cube of the crack width. Additionally, it was found that crack healing significantly reduced the flow of water through the sample. This suggests that self-healing would also limit the flow of chlorides into the section through a crack.

Sahmaran (2007) investigated the chloride diffusivity of cracked concrete with varying crack widths. Specimens were precracked to various widths and subjected to ponding of a salt water solution. The chloride profiles for various crack widths were determined and are shown in Figure 2.21. The relationship between the crack width and diffusion coefficient was found to be a power relation. Additionally, for cracks less than 0.13 mm (0.005 in.) the effect of crack widths on the effective diffusion coefficient was found to be marginal. Cracks with a width less than 0.05 mm (0.002 in.) experienced significant self-healing which further reduced the effective diffusion coefficient.

The research findings on cracked concrete behavior identified that self-healing is a viable mechanism for limiting the ingress of chloride ions into a cracked concrete section.

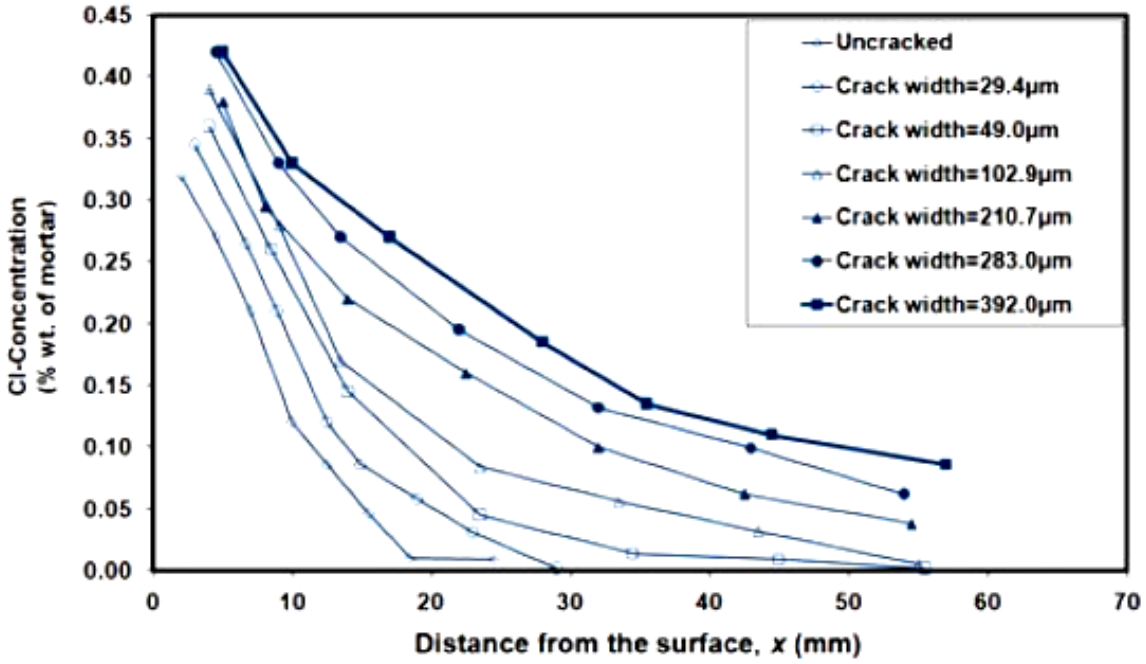

Figure 2.21: Chloride profiles for cracked concrete after 30 days exposure (Sahmaran, 2007) (1 mm = 0.04 in.)

2.6.4 Self-healing of Cracks

The research findings on cracked concrete behavior identified that self-healing is a viable mechanism for limiting the ingress of chloride ions into a cracked concrete section. Lauer and Slate (1955) performed studies by cracking prism specimens in flexure and holding together with a rubber band and exposing to water then retesting the strength gain across the crack due to self-healing. The investigation revealed that samples experienced larger strength recovery when having a high w/cm and when initial cracking was performed at early ages. Additionally, it was noted that fly ash was detrimental to the healing process and it was hypothesized that this was due to the smaller amount of CH present, which normally serves as nucleation sites for calcium carbonate which is the primary component of self healing observed.

Research by Ismail, et al. (2008) investigated the ingress of chlorides into cracked sections using an expansive ring to generate controlled crack sizes. It was found that young specimens exhibited greater self-healing and lower effective diffusion coefficients then specimens with the same crack size at later ages, which shows a similar trend to the strength recovery findings of Lauer and Slate (1955).

Jacobsen, et al. (1996) also investigated the chloride resistance of self-healed concrete. Tests were performed by inducing freeze thaw damage into specimens, then allowing them to heal. After healing, electrical migration tests were performed to quantify the effect of self-healing on chloride ingress. It was found that specimens where the cracks (crack width < 0.012 mm (0.0004 in.)) were not allowed to heal had ingress rates an order of magnitude higher than virgin concrete. Self-healed cracks exhibited an ingress rate of approximate 25% of the unhealed cracks, but never returned to the rates observed in virgin concrete, which was also found by Parks, et al. (2010).

Edvardsen (1999) studied the influence of self-healing on water permeability of cracked samples. The research showed that smaller crack widths led to lower flow rates and quicker sealing of cracks, as is shown in Figure 2.22. It was concluded from the study that the primary form of self-healing is the precipitation of calcium carbonate, and that mixture design plays a secondary role in self-healing.

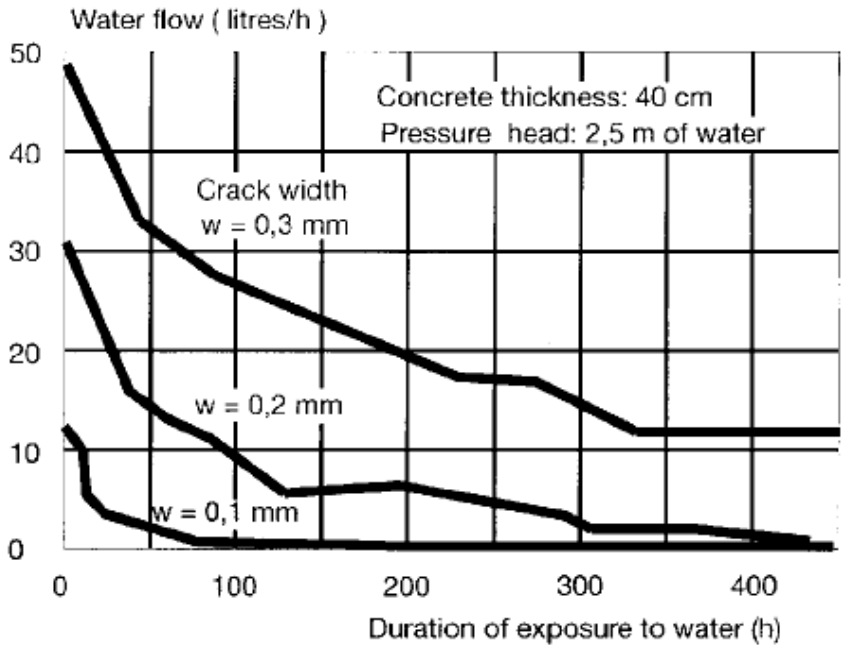

Figure 2.22: Water flow versus duration for different crack widths (Edvardsen, 1996) (1 mm = 0.04 in.)

Rodriguez (2001) investigated the diffusion of chlorides into cracked concrete sections. Experiments were performed by creating through specimen cracks, sealing of all sides except the top surface, and exposing to a salt water solution. Profile grinding was performed to diagnose 2-D diffusion around crack sites. Results showed that 25% slag replacement specimens were better at resisting chloride ingress in cracked sections than Portland cement only specimens. The author noted that more research is need in the area of flexure cracks with a V-shape.

Heide (2005) investigated the influence of self-healing on strength recovery through the use of artificial flexure cracks. It was found that lower degrees of hydration led to increased self-healing capabilities, which is in agreement with the findings of Lauer and Slate (1955). The author found that mixture designs containing slag performed

well on the recovery strength compared to plain Portland cement concrete. The author recognized the need for more research on the influence of slag contents on self-healing, as well as the influence of other SCMs.

Termkhajonkit, et al. (2009) investigated the effect of self-healing of shrinkage cracks on chloride ingress. Electrical migration tests were performed on specimens subjected to drying and autogenous shrinkage cracking after 28 and 91 days of moist curing. It was found that 25% replacement of cement with low CaO fly ash had significantly lower apparent diffusion coefficients than plain Portland cement samples. The authors identified the need for investigation on the effect of fly ash on the self-healing of larger cracks that are formed at early ages.

Sahmaran, et al. (2008) studied the behavior of high volume fly ash self-consolidating concrete (SCC) subjected to microcracking from compressive loading. Cylinder samples were loaded to 70% and 90% of the max compression stress then soaked in water for up to 30 days then the rapid chloride permeability and compressive strength was measured for samples containing 0, 35, and 55% cement replacement with a low CaO fly ash. The results of the study are shown in Figure 2.23. It was found that fly ash samples recovered significantly more of the chloride resistance after 15 and 30 days of healing than plain Portland cement concrete samples. It was proposed that the cause of this was that the high volume replacement with fly ash led to unhydrated fly ash being available along the crack surface for self-healing and the formation of secondary C-S-H across the crack.

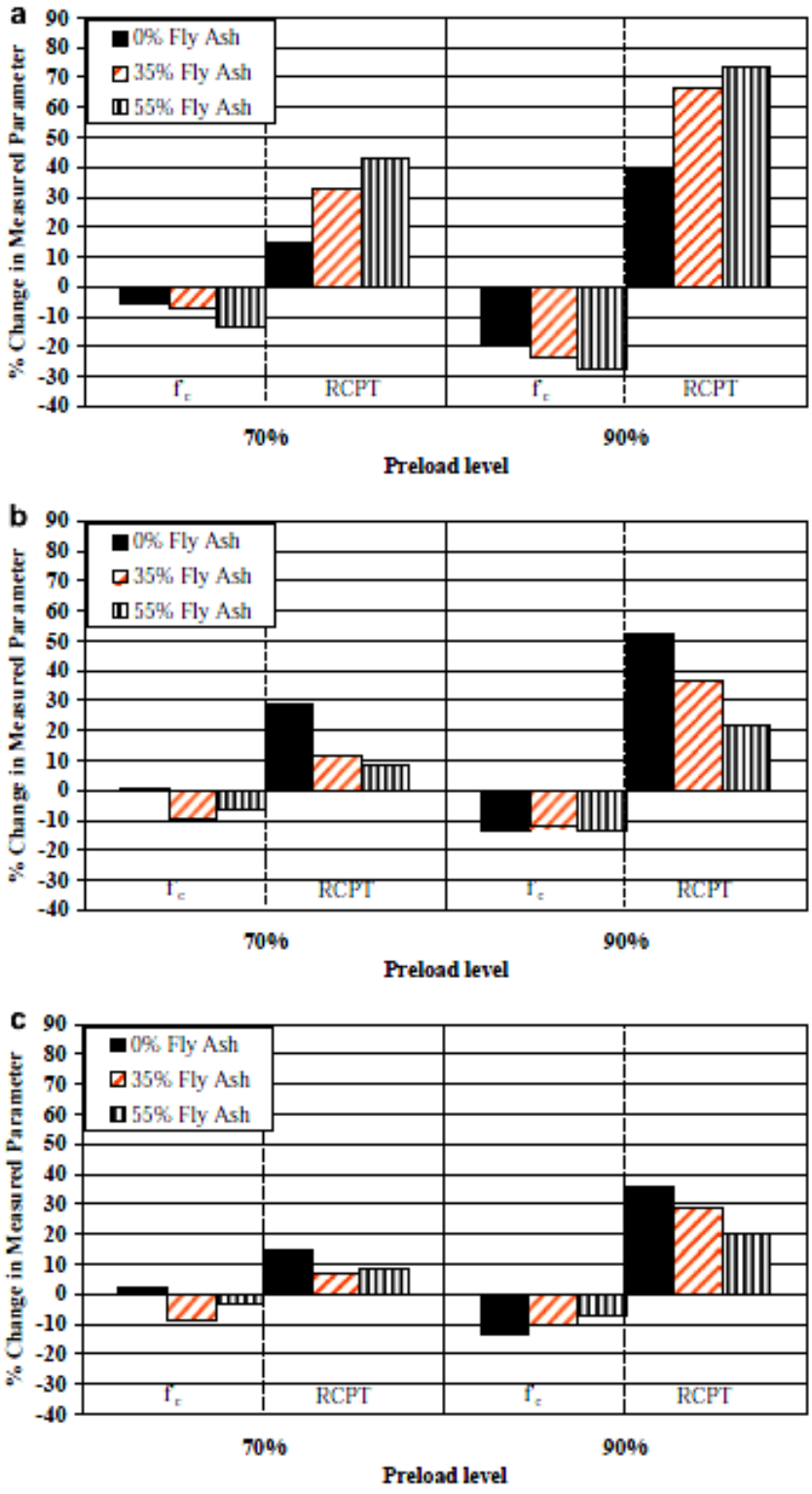

Figure 2.23: Effect of self-healing on RCPT samples before (a) no healing, (b) 15 days of healing, and (c) 30 days of healing (Sahmaran, et al., 2008)

2.7 Summary

The literature review of chloride induced corrosion, carbonation, sulfate attack, biological attack, and cracked concrete behavior of structures exposed to marine environments established the current foundation of knowledge available and the areas where research is needed. Research was identified as being needed on the following topics:

- The chloride ingress behavior of ternary blend cements containing metakaolin or silica fume
- The carbonation behavior of low water-to-cementitious material ratios
- Determination of the influence of silica fume replacement of cement on carbonation behavior
- The behavior of ternary blend cements exposed to carbonation
- Carbonation performance of blended cements containing metakaolin
- The sulfate resistance of ternary blend cements containing metakaolin and low CaO fly ash
- The influence of slag and fly ash on the self-healing and chloride ingress of cracked concrete sections
- The self-healing behavior of V-shaped cracks subjected to chloride ingress
- Determination of the self-healing behavior of ternary blend cements subjected to chloride ingress

CHAPTER 3

FORENSIC INVESTIGATION OF I-95 AT TURTLE RIVER BRIDGE

3.1 Introduction

The objective of this research was to characterize the degradation mechanisms present in prestressed concrete piles exposed to marine environments in Georgia. With an in-depth understanding of relevant degradation phenomena, novel methods to increase the durability of coastal bridges can be developed with the goal of increasing bridge service lives to 100+ years. To better identify the pile deterioration mechanisms, piles from the I-95 at Turtle River Bridge in Brunswick, Georgia were investigated.

The deterioration of prestressed concrete piles in marine environments is a growing expense for the Georgia Department of Transportation (GDOT). Bridges are having to be replaced after less than 40 years in service, which is significantly less than the 75 to 100 year service life desired by the Federal Highway Administration (FHWA). For example, the substructure of the I-95 at Turtle River Bridge was replaced after only 32 years in service.

The exposure of structural concrete to the harsh Georgia coastal environment can cause several forms of degradation. The forms of attack vary with the exposure zone on the piling, as shown in Figure 3.1. Corrosion of the prestressing steel typically occurs in the tidal and splash zones, while carbonation and sulfate attack may occur in the submerged regions of the piles (Mehta, 1991). The piles recovered from the Turtle River

Bridge upgrade were investigated for these damage mechanisms, in addition to inspection for any other potential degradation hazards. Section 3.2 investigates damage caused by corrosion of the prestressing steel. Section 3.3 examines the degradation of the piles due to sulfate attack. Section 3.4 investigates the biological attack that occurred on the concrete piles. Section 3.5 presents the conclusions and recommendations drawn from this study and suggest future research in certain areas.

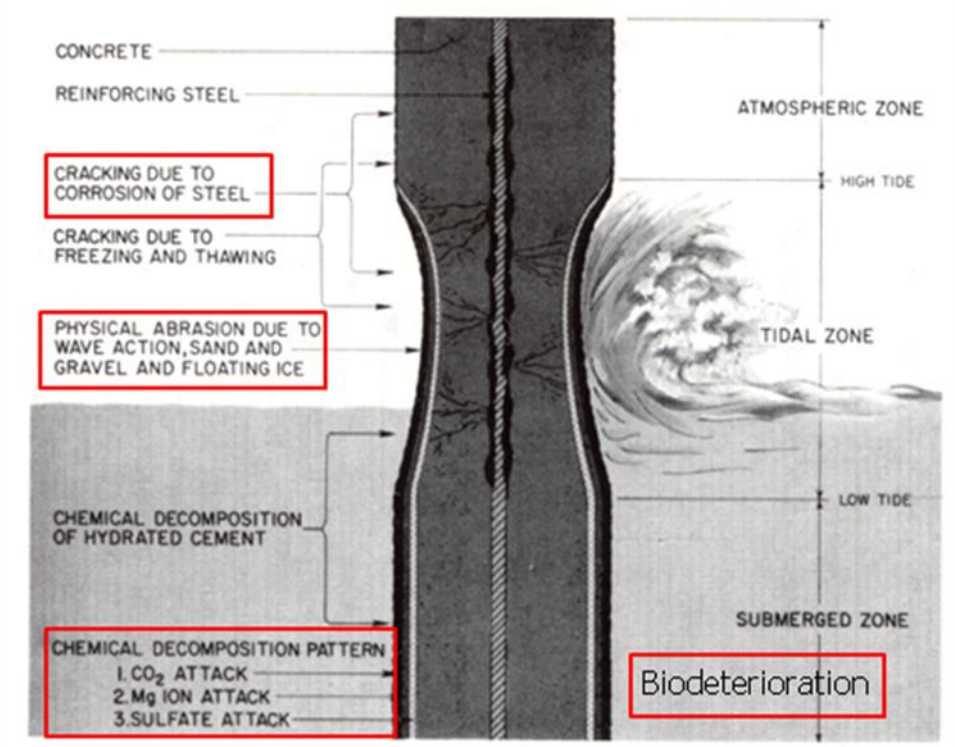

Figure 3.1: Typical degradation mechanisms in coastal concrete piling (Mehta, 1991)

3.1.1 Bridge Description

The I-95 at Turtle River Bridge (Structure ID: 127-0052-1) is located approximately 16 km (10 miles) from the Atlantic coast, near Brunswick, GA, in Glynn County, as shown in Figures 3.2 and 3.3. The original bridge was constructed in 1977,

and upgraded in 2009 by replacing the heavily damaged substructure. The damage observed by inspection teams is presented in section 3.1.2. Figure 3.3 shows the original and upgraded Turtle River Bridge. The bridge has 43 spans and has a total length of 1.06 km (3,488 ft). The bridge has a concrete road deck. The bridge has three primary spans, which are approximately 61 m (200 ft) in length and are supported by steel I-girders. The remaining 40 spans are supported by prestressed concrete girders. The girders rested on elastomeric bearing pads on pier caps. The substructure consisted of 0.76 m x 0.76 m (30 in. x 30 in.) hollow prestressed concrete piles, which supported the pier caps.

The piles were constructed with 14 mm (9/16") diameter prestressing strands and a 0.50 water-to-cement (w/c) ratio concrete using ASTM C 150 Type I cement. Natural sand was used for the fine aggregate, and a 25.4 mm (1 in.) maximum size aggregate (MSA) limestone coarse aggregate.

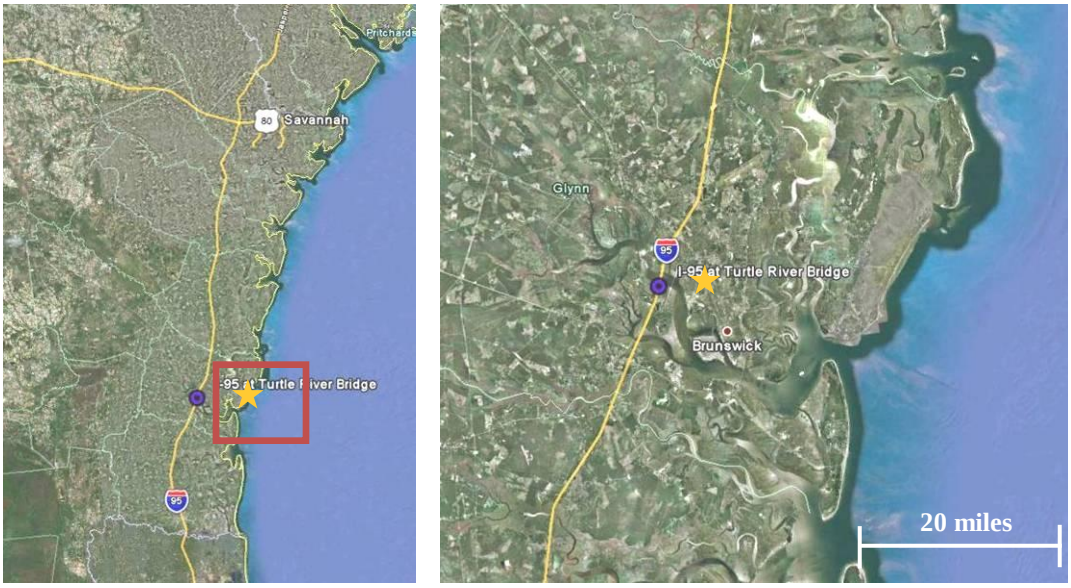

Figure 3.2: Location of I-95 at Turtle River Bridge

(a) (b)

Figure 3.3: Overall view of bridge (a) before and (b) after upgrade

The substructure on the bridge was replaced using large transfer beams and drilled caissons into the subgrade. Figure 3.4 shows the original and upgraded substructure. The piles used for the forensic investigation were removed during construction so that the new caissons could be built. Only existing piles that interfered with the new substructure were removed. In Figure 3.4 (b), the old piling can be seen in place under the new bridge structure.

(a)

(b)

(c)

Figure 3.4: View of bridge substructure (a) before, (b) transfer girder after upgrade, and (c) drilled caisson support after upgrade

Four piles were delivered to the Georgia Tech in February, 2010. Figure 3.5 shows the piles upon delivery. Three of the piles contained the splash, tidal, and submerged regions, and the fourth was a fully submerged section. Figure 3.6 shows a pile after cleaning the biological growth off of the surface. The splash, tidal, and submerged zones are labeled.

Figure 3.5: Piles from Turtle River Bridge

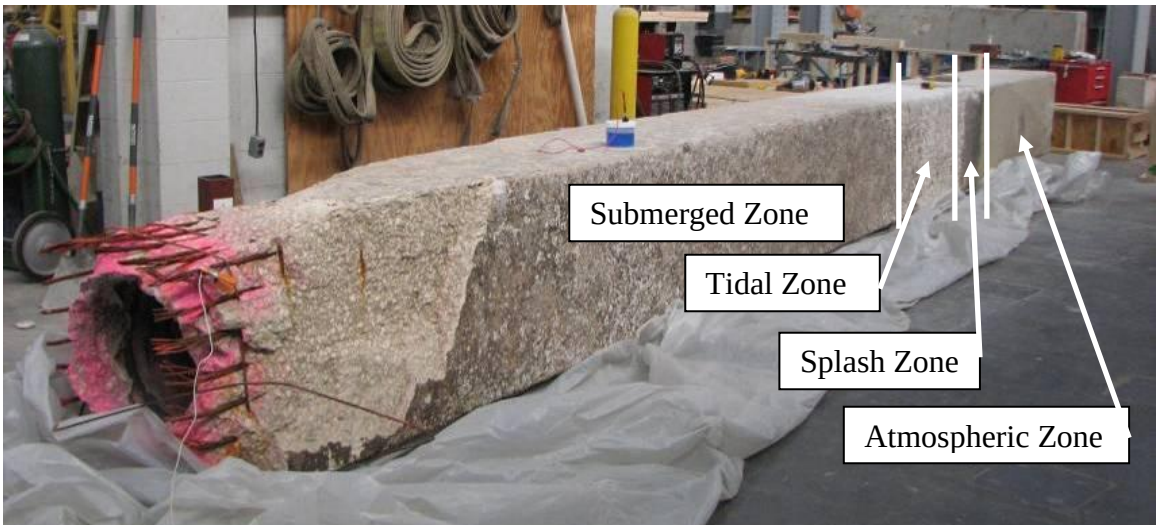

Figure 3.6: Pile after removal of biological growth

3.1.2 Inspection Report Data for Original Substructure

Access to the most recent inspection reports for the Turtle River Bridge was provided by GDOT. The most recent inspection of the substructure before replacement was performed in 2005, along with notes from previous inspections. The bridge inventory listing and bridge inspection reports are given in Appendix A.

In the splash and tidal zones of piles, visual inspection of the piles showed heavy marine growth, moderate scaling and abrasion, vertical cracking, spalling, exposed prestressing steel, rust staining, and delaminations. The reported vertical cracks varied in width from hairline to 6.4 mm (1/4 in.). For the submerged region of the piles, it was noted that the concrete piles were "soft" and that the concrete could be easily chiseled off. Also, several piles had vertical cracks in the corners that ran from the mudline up 1.83 m to 3.66 m (6 ft to 12 ft), with a width varying from hairline to 0.8 mm (0.030 in.) in width. Additionally, according to the report, multiple piles had been encased in a fiberglass sheath with epoxy as a rehabilitation method.

The inspection reports suggest visual signs of degradation consistent with chloride-induced corrosion of the reinforcement plus chemical attack and potential biological attack of the concrete. The forensic investigation of the recovered piles characterized the deterioration mechanisms present that caused the observed damage.

3.2 Corrosion of Prestressing Steel

Concrete's highly alkaline environment allows for the formation of a thin oxide layer on the surface of reinforcing steel. The thin passive film protects the steel from

corrosion in alkaline environments. If the passive layer is destroyed, active corrosion can occur. The passive film can be broken down by decreasing the pH of the surrounding environment, local attack from aggressive ions, or a concurrence of both (Bertolini, et al., 2004).

Chlorides from the surrounding marine environment are able to ingress into the concrete over time through various transport mechanisms. The protective oxide film that forms on the surface of the steel in the alkaline concrete environment is broken down locally by the presence of a sufficient local chloride concentration, and pitting corrosion can result. Pitting is a localized form of corrosion which initiates when chlorides attack defect sites in the passive film. Two reactions that occur in breaking down the passive film are given below in Eq. 3.1 and Eq. 3.2 (Bertolini, et al., 2004).

$$Fe^{3+} + 6Cl^- \rightarrow FeCl_6^{-3} \quad \text{(Eq. 3.1)}$$

$$FeCl_6^{-3} + 2OH^- \rightarrow Fe(OH)_2 + 6Cl^- \quad \text{(Eq. 3.2)}$$

The reactions do not consume the chlorides, and lower the pH at the pitting site by depleting the OH^- ions in the formation of the iron oxides. In concrete, the surrounding regions remain alkaline, and hydroxide ions are available in the pore solution which causes the surrounding regions to act as cathodes for the corrosion reactions. As the pit grows, it gains a net positive charge from the hydrogen and metal ions which attract more chlorides into the pit, causing an autocatalytic reaction. At the surface, a porous cap can form from the corrosion products that further allows the pit to grow.

The corrosion of the prestressing steels leads to a loss of steel section. Additionally, the corrosion of steel leads to the formation of iron oxides which are less dense than the original steel and occupy more volume. The formation of oxides causes tensile forces in the surrounding concrete and can lead to cracking and delamination of the cover concrete, as well as rust staining on the surface of the piles.

The causes and extent of damage produced by chloride-induced corrosion were investigated by performing a visual assessment of the damage (section 3.2.1), mapping the corrosion potentials (section 3.2.2), and determining the chloride profiles (section 3.2.3). The chloride profiles were used for service life modeling.

3.2.1 Visual Assessment of Damage

A visual inspection of the splash and tidal zones of the piles showed vertical cracks along the corners of the piles as shown in Figure 3.7. The average crack widths were approximately 0.25 mm (0.01 in.), but were as large as 1.27 mm (0.05 in.). Additionally, delamination of the cover concrete had occurred over the corner strand on one pile. The exposed surface showed extensive corrosion damage to the strand and staining of the surrounding concrete (Figure 3.8). The delamination occurred normal to the surface of the concrete through the corner strand location as illustrated in Figure 3.9.

(a) (b)

Figure 3.7: (a,b) Corrosion induced longitudinal cracking of piles

(a) (b)

Figure 3.8: (a,b) Corrosion induced delamination, loss of steel section, and staining of piles

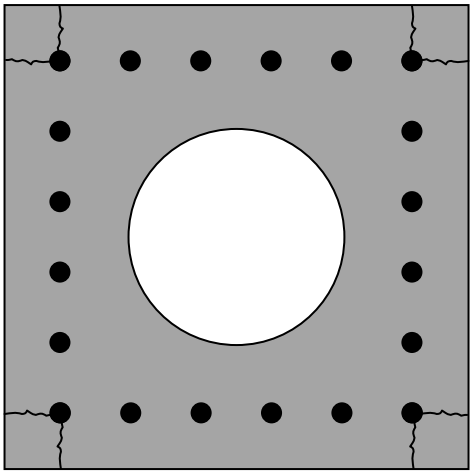

Figure 3.9: Cracking and delamination pattern on the cross-section in splash and tidal zone

Inspection of corroded strands indicated the presence of pits and preferential locations in the crevices between the braided wires of the strand. Figure 3.10 shows a core through a corroded strand and a magnified image of the corrosion products around the strand.

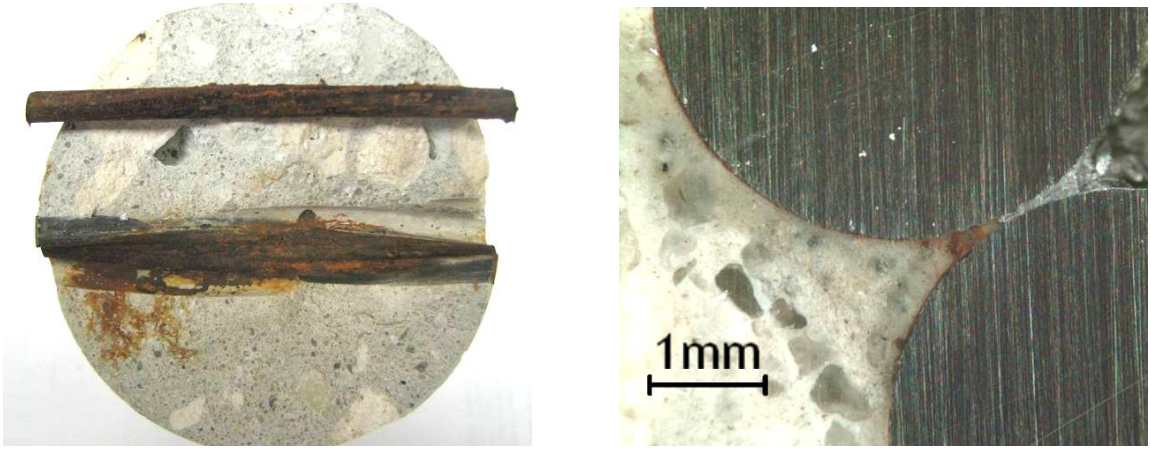

(a) (b)

Figure 3.10: Corrosion of prestressing steel in extracted core

The pH of the concrete cover was studied by using a phenolphthalein indicator solution on freshly cut surfaces of the piles. The indicator solution turns pink if the pH is above approximately 9.2, representing uncarbonated concrete. The carbonation front can be seen in Figure 3.11. The carbonation front was found to be approximately 25.4 mm (1 in.) beneath the exposed surface of the piling, both in the submerged and tidal regions. This limited depth suggests that it is unlikely that corrosion of the reinforcement was caused by carbonation, but that a combination of decreased pH and ingress of chlorides caused pitting corrosion to occur.

Although carbonation of the concrete did not cause general corrosion of the reinforcement, it may have contributed to degradation of the cover concrete. Carbonation of concrete leads to the depletion of calcium hydroxide, which causes the decrease in pH, and can lead to a loss of calcium silicate hydrate (C-S-H), which is the primary strength giving component of hydrated cement paste (Neville, 1997). Additionally, ettringite is unstable at a pH below 11 (Neville, 1997).

(a) (b)

Figure 3.11: (a) Phenolpthalein indicator solution on sawn surface of pile, and (b) measurement of carbonation front

3.2.2 Half-cell Corrosion Potentials

The half-cell potential of the imbedded steel strands was used to identify regions where corrosion was occurring in accordance with ASTM C 879 (2009). The measurements were performed by measuring the half-cell potential of a strand versus a $Cu/CuSO_4$ electrode (CSE) using a voltmeter and by measuring the potential at 0.3 m (1 ft) intervals along the length of the pile. An electrical contact solution consisting of liquid dish detergent mixed with water was used to wet the surface for readings. Figure 3.12 shows the experimental set-up used.

Figure 3.12: Half-cell potential measurement set-up

Figure 3.13 shows the half-cell corrosion potentials from all four sides of a pile. According to ACI Committee 222 (2001), a half-cell potential greater than 350 mV indicates a 90% or greater probability of corrosion occurring. A half-cell potential less than 200 mV indicates a 10% or less probability of corrosion occurring. The results suggest that from 0.6 m (2 ft) above high tide and below that there is a strong probability that corrosion is occurring. The rate of corrosion cannot be determined using this method. Therefore, a half-cell potential in excess of 350 mV does not indicate that corrosion is occurring at a highly deleterious rate. The corrosion rate is heavily influenced by environmental factors, including adequate presence of moisture and oxygen. If insufficient oxygen is present, then the corrosion rate can be orders of magnitude smaller.

The lack of oxygen in the submerged zones of piles explains why no corrosion induced damage was seen, even though the half-cell potential suggests that corrosion is

occurring. The tidal and splash zones of piles have adequate access to moisture and oxygen due to the wetting and drying cycles present. This leads to a significantly faster corrosion rate, which could be the reason for the large amount of damage found.

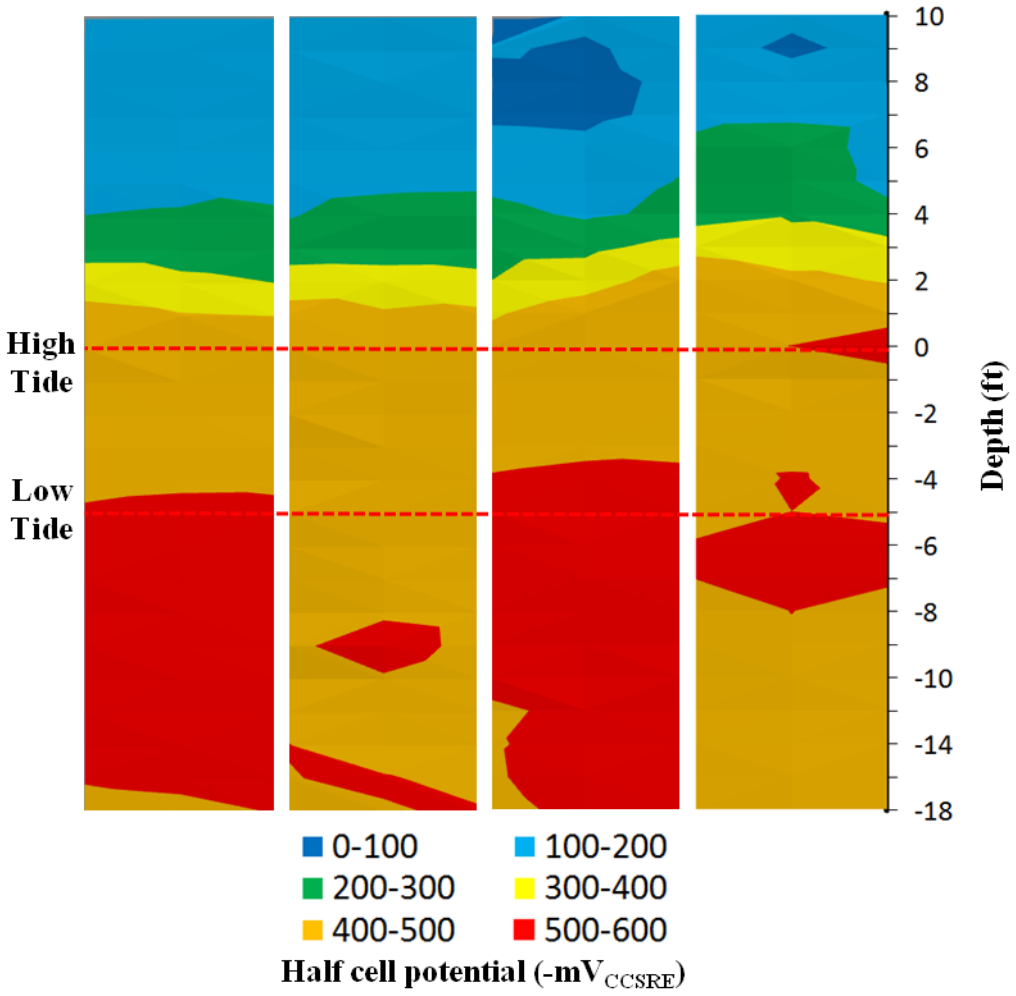

Figure 3.13: Half-cell potential map of the four faces of a Turtle River Bridge pile (1 ft = 0.3 m)

3.2.3 Chloride Profiles

The concentration of chloride ions near the reinforcement surface is critical in causing the onset of pitting corrosion and in furthering the corrosion reactions; therefore,

it is important to understand the migration of chloride ions through the concrete and to understand the interactions between those ions and the cementitious system. Chlorides ingress into the concrete piles from the surrounding brackish water. Their movement through the concrete is often modeled with Fick's second law of diffusion. However, other transport mechanisms, like capillary action, can affect the transport of chlorides through the cement paste. The apparent diffusion coefficient of a concrete mix exposed to chlorides can be determined experimentally and used for service life estimation in a given environment (Bertolini, et al., 2004).

Within the concrete, chlorides exist in a free or uncombined form and in bound forms, where they may combine with existing hydration products or unhydrated cementitious phases. In the bound form, the most common product formed is Friedel's salt [$Ca_2Al(OH)_6Cl \cdot 2H_2O$]. When the concentration of chlorides reaches a threshold value at the surface of the reinforcing steel, corrosion will initiate when the passive film is broken down. There is considerable debate as to how to define the chloride threshold limit (CTL) and what the value should be (Mohammed and Hamada, 2003). The threshold values are typically reported as the total or free chlorides as a percent mass of concrete (or cement) or by the ratio of the concentration of chloride ions to the concentration of hydroxyl ions ($[Cl^-]/[OH^-]$).

In practice, the total chloride content is used more frequently for threshold values, even though it is generally believed that the free chlorides are responsible for the initiation of corrosion (Mohammed and Hamada, 2003). The CTL is typically assumed to be between 0.4% to 1% mass of binder, or approximately 0.05% to 0.2% by mass of concrete, for total chloride content (Bertolini, et al., 2004). However, reported values for

the CTL have varied from 0.04% to 8.34% by mass of binder based upon total chloride content (Angst, et al., 2009). The CTL is difficult to define since the reported values vary with cement composition, water to cement ratio, exposure temperature, internal pH, and type of steel used (Angst, et al., 2009).

3.2.3.1 Test Methodology

The total chloride concentration was measured using the ASTM C 1152 (2004) procedure, which was performed by taking 76.2 mm (3 in.) diameter cores through the depth of the cross-section, drilling at 12.7 mm (1/2 in.) increments using a 9.5 mm (3/8 in.) masonry bit, and collecting the powder. The concrete powder was ground using a mortar and pestle and sieved until a minimum of 30 g passed through the 850 μm sieve for each depth increment. The acid soluble chloride testing was performed by measuring 10 g of the powder into a beaker and adding 75 ml of reagent water. Next, 25 ml of dilute (1:1) nitric acid was added to the beaker. The sample was stirred until any lumps were broken up. Next, the sample was rapidly heated to a boil for 10 seconds, then removed from heat. The sample was then filtered using a Buchner funnel and filtration flask with suction through a Grade 41 coarse-textured filter paper. The sample was then allowed to cool to 25 °C. The sample was titrated with Silver nitrate solution (0.1 N) to determine the acid soluble chloride content.

The free chloride concentration was measured using the ASTM C 1218 (1999) procedure, which was performed by taking 76.2 mm (3 in.) diameter cores through the depth of the cross-section, drilling at 12.7 mm (1/2 in.) increments using a 9.5 mm (3/8 in.) masonry bit, and collecting the powder. The concrete powder was ground using a

mortar and pestle and sieved until 30 g passed through the 850 μm sieve for each depth increment. The water soluble chloride testing was performed by measuring 10 g of the powder into a beaker and adding 50 ml of reagent water. Next, the sample was covered and brought to a rapid boil for 5 minutes. The sample was allowed to sit for 24 hours. Next, the sample was filtered using a Buchner funnel and filtration flask with suction through a Grade 40 Class G filter paper. After filtering, 3 ml of (1:1) nitric acid and 3 ml of hydrogen peroxide (30% solution) were added to the sample, which was then covered and allowed to stand for 1 minute. The sample was then brought to a boil for 10 seconds while still covered, then removed from heat. The sample was then allowed to cool to 25 °C. The sample was titrated to determine the water soluble chloride content.

Titrations were performed using the Metrohm 798 MPT Titrino. A silver/silver chloride standard electrode was used. Silver nitrate solution (0.1 N) was added in 0.1 ml aliquots to the sample until an equivalence point was achieved. Figure 3.14 shows the filtration and titration methods. The chloride content was then determined using Eq. 3.3 to compute the percent chlorides by mass of sample.

$$Cl, \% = 3.545 * V * N/M \qquad \text{(Eq. 3.3)}$$

Where,

V = milliliters of $AgNO_3$ solution used for titration at equivalence point
N = exact normality of $AgNO_3$ solution
M = mass of sample, g

(a) (b)

Figure 3.14: (a) Filtration of chloride sample, and (b) titration of sample

3.2.3.2 Results, Chloride Concentrations

Total and free chloride concentrations were determined at various heights along the pile, as shown in Figure 3.15. The locations were chosen to coincide with the atmospheric, splash, high and low tide, and submerged regions of the pile. The notation used for identifying samples was that a positive value indicated a depth below high tide, and a negative value was above high tide. Cores were taken in the center of the pile to avoid the effect of 2-D transport from another surface of the pile.

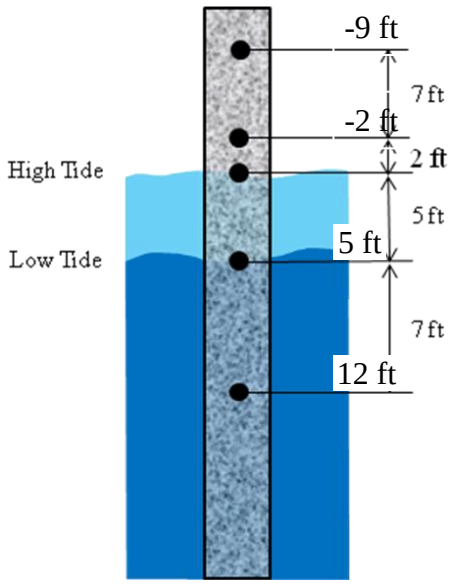

Figure 3.15: Locations of chloride concentration sampling (1ft = 0.3 m)

Figure 3.16 shows the total chloride concentrations from each sampling location with respect to depth into the cross-section. The results suggest that the concentration of total chlorides at the level of the reinforcement is significantly higher than the CTL values given in the literature. The concentrations were in agreement with the half-cell corrosion potentials, which suggested that active corrosion was occuring due to depassivation and destruction of the passive film on the surface of the steel. The chloride profiles for high tide, 1.52 m (5 ft), and 3.66 m (12 ft) elevations were very similar. However, the concentration at the surface varied widely between the elevations and may be due to the presence of wetting and drying cycles in the tidal zone compared to the fully saturated condition in the submerged region. The 0.6 m (2 ft) above high tide profile had a greatly reduced chloride content compared to submerged regions. Additionally, was observed from the 2.74 m (9 ft) above high tide data that the background chloride content in the mix was 0.01% by mass of concrete. The low

background content suggested that the mix did not use seawater for mixing, dredged fine aggregate, or large quantities of chloride containing admixtures.

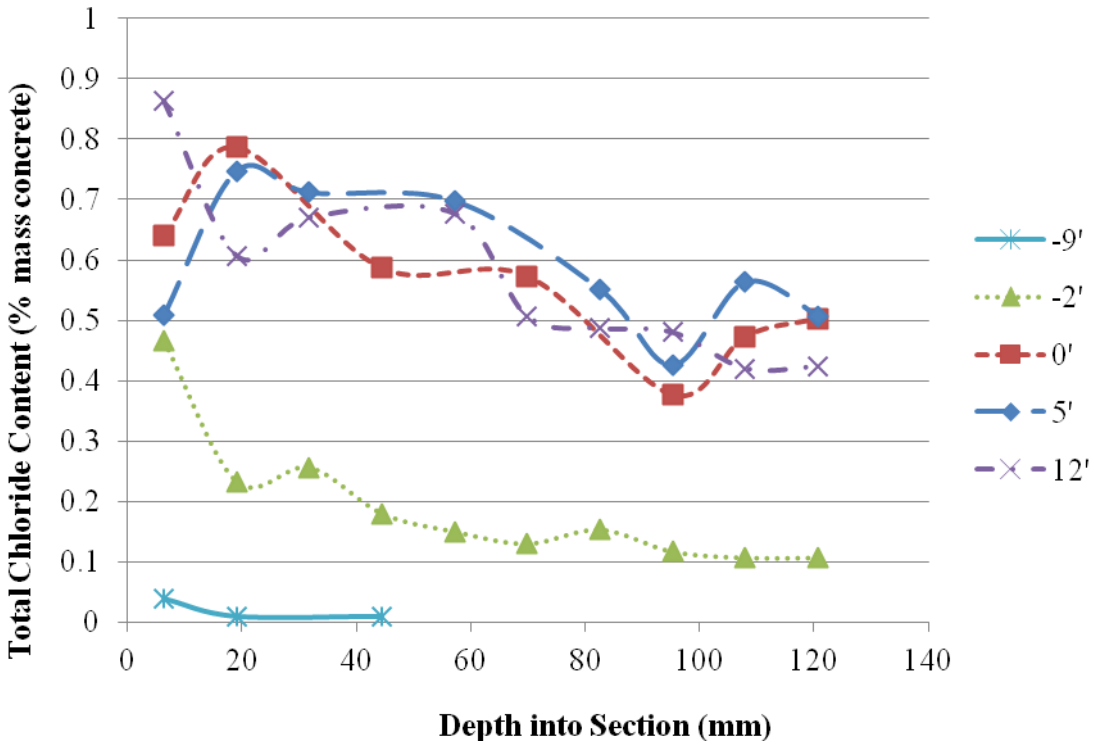

Figure 3.16: Total chloride content of concrete columns at various depths

Figure 3.17 shows the free chloride concentration profile at the selected locations along the length of the pile. The results suggest that the concentration of free chlorides at the level of the reinforcement is significantly higher than the CTL values given in the literature. The free chloride profiles follow a similar trend to the total chloride profile at each depth. The profile for 9 ft above high tide shows that all chlorides present over ½ in. into the section were bound.

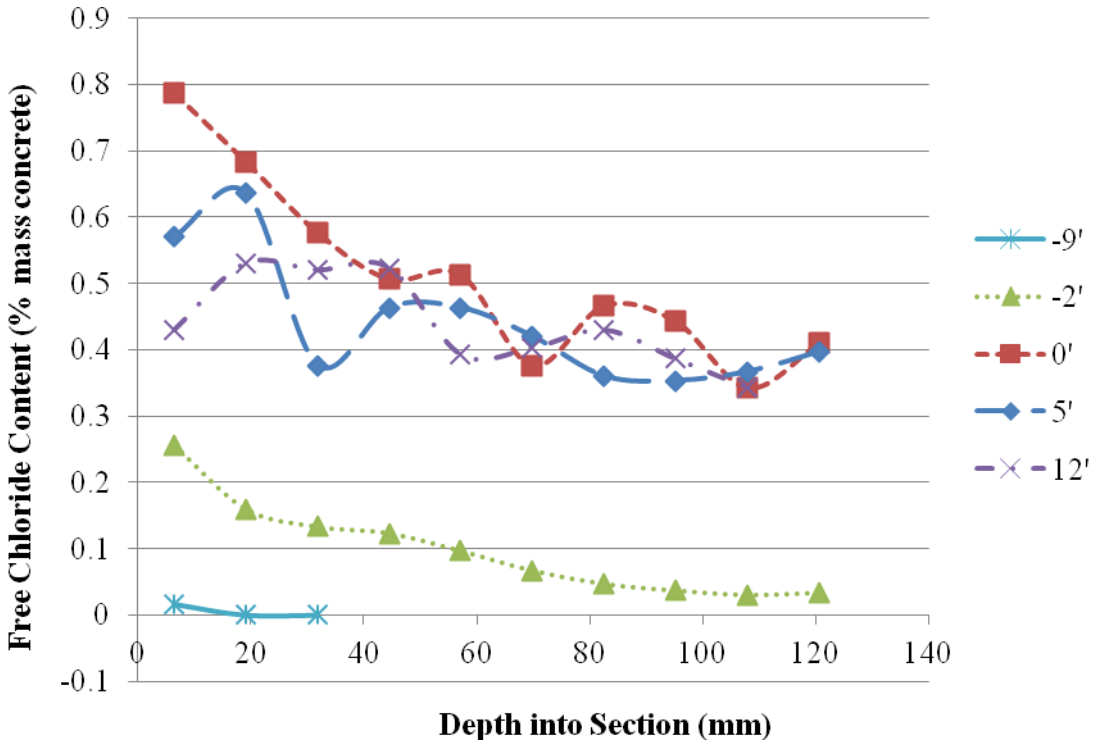

Figure 3.17: Free chloride content of concrete columns at various depths

A comparison of the total to free chloride content measured at each increment from the piles is given in Figure 3.18. From a simple linear regression between the total and free chloride concentrations, it was found that 18.6% of the total chloride content is bound. There is a large scattering of data, but the percent bound chlorides is consistent with the value of 18.7% found by Mohammed and Hamada (2003) from field exposure measurements.

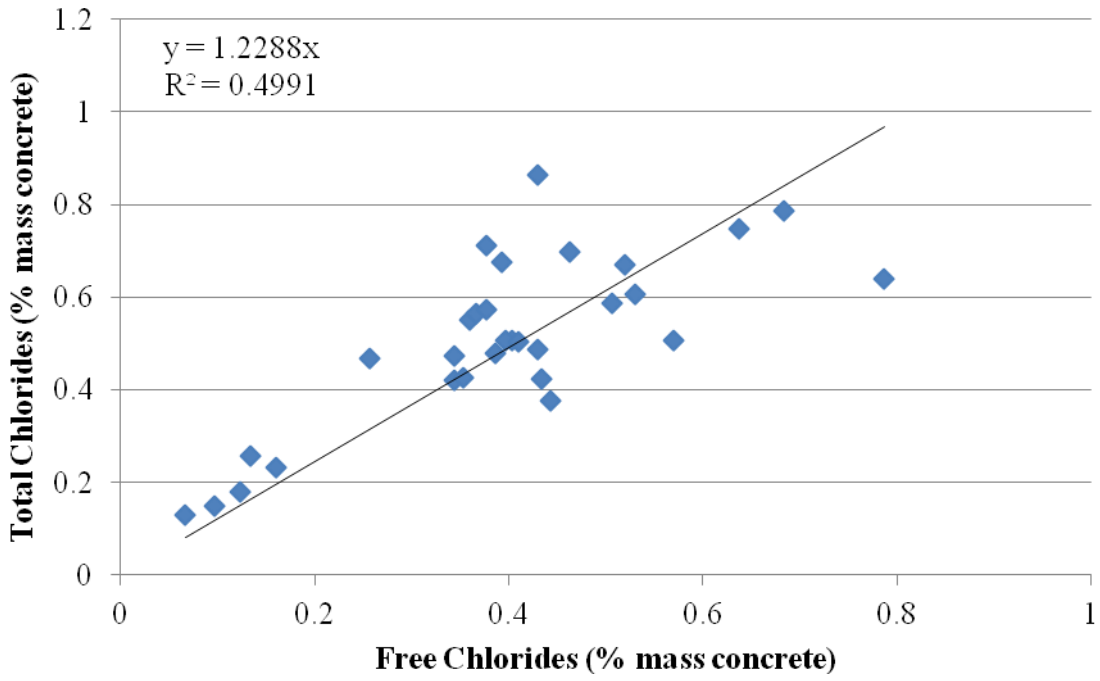

Figure 3.18: Comparison of total to free chloride concentrations

Figures 3.19 shows the free and total chloride concentrations at 12 ft, 5 ft, high tide, and -2 ft. The free chloride content follows a similar profile to the total chlorides, but the value is reduced due to binding of chlorides. The concentrations near the surface were highly variable between acid and water samples for the same depth, and could be due to variable surface conditions of cores due to biological attack and coring induced damage.

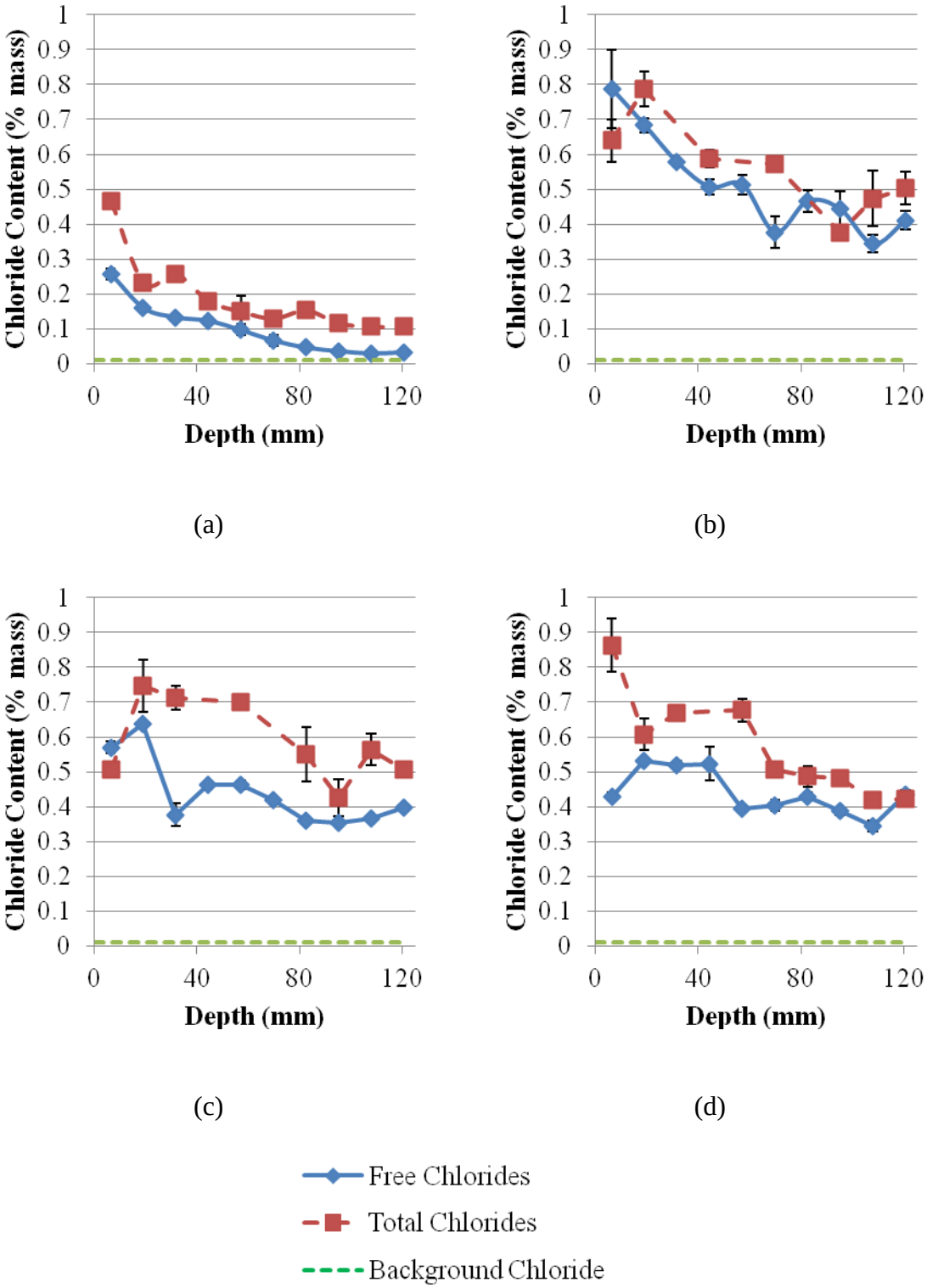

Figure 3.19: Chloride profiles at (a) 0.6 m (2 ft) above high tide, (b) high tide, (c) 1.52 m (5 ft) below high tide, and (d) 3.66 m (12 ft) below high tide (25.4 mm = 1 in.)

3.2.3.3 Chloride Ingress Modeling

The ingress of chlorides into a structure is often treated as a diffusion-based transport phenomenon (Bertolini, et al., 2004). Fick's second law can be used with experimental data to determine the diffusion coefficient that characterizes the diffusion-based transport properties of a concrete mix. Additionally, if the diffusion coefficient and environmental parameters are known, the time necessary for the CTL to be reached can be determined and used for service life modeling.

The chloride profiles were used to determine the apparent chloride diffusion coefficient by performing a non-linear regression analysis, using the method of least squares to fit to the equation given by Eq. 3.4 (ASTM C 1152, 2004).

$$C(x,t) = C_s - (C_s - C_o) * \text{erf}\left(\frac{x}{\sqrt{4 * D_a * t}}\right) \qquad \text{(Eq. 3.4)}$$

Where,

C(x,t)	=	chloride concentration, measured at depth x and exposure time t, mass %
C_s	=	projected chloride concentration at the interface between the exposure liquid and test specimen that is determined by the regression analysis, mass %
C_o	=	initial chloride-ion concentration of the cementitious mixture prior to submersion in the exposure solution, mass %
x	=	depth below the exposed surface, m
D_a	=	apparent chloride diffusion coefficient, m^2/s
t	=	the exposure time, s
erf	=	$\frac{2}{\sqrt{\pi}} * \int_0^z \exp(-u^2)\, du$

An approximation developed by Winitzki (2006) for the error function was used to perform the regression analysis. The approximation, given in Eq. 3.5, results in a maximum relative error of less than 1.3%.

$$\operatorname{erf}(x) \approx \left[1 - \exp\left(-x^2\left(\frac{\frac{4}{\pi}+0.147x^2}{1+0.147x^2}\right)\right)\right]^{\frac{1}{2}} \quad \text{(Eq. 3.5)}$$

Life 365 Service Life Prediction Model (Ehlen, 2009) was used to estimate the diffusion coefficient and expected service life of the structure. The primary parameters necessary for using Life 365 are the structure location, exposure type, concrete cover distance to reinforcing steel, and mixture design details, including w/cm, percent replacement of cement with supplementary cementitious materials, and use of corrosion inhibitors. The results of the nonlinear regression diffusion coefficient results compared to the Life 365 estimates are shown in Table 3.1.The Life 365 estimates were based upon a marine tidal zone exposure in Savannah, Georgia for a 0.50 w/c mixture design using only Portland cement. The experimentally determined data were compared to the Life 365 data for the estimated time to corrosion initiation based upon a CTL of 0.05% by mass of concrete, which is the default value use by Life 365 (Ehlen, etal., 2009).

Table 3.1: Comparison of Life 365 estimates to experimental data (1 m = 3.3 ft)

	Experimental	**Life 365**	**% Difference**
Diffusion Coefficient ($m^2/s * 10^{-11}$)	1.65	1.38	16.36
Surface chloride concentration (% mass concrete)	0.797	0.800	0.44
Time to corrosion inititiation (years)	3.1	3.7	19.35

Overall, Life 365 gave reasonable predictions of diffusion coefficient, surface chloride concentration and time to corrosion (Table 3.1). Life 365 underestimated the

diffusion coefficient that was observed from curve fitting. However, the diffusion coefficient observed could be influenced by other damage mechanisms that were occurring in the piles. The observed biological attack, sulfate attack, and potential cracking from construction practices could all lead to an increased permeability and diffusion coefficient. The discrepancy between diffusion coefficients is responsible for the variation in time to corrosion initiation. Life 365 and the experimental data were in agreement on the surface concentration for this exposure zone. The time to corrosion initiation was significantly less than the 75+ year lifespan desired by GDOT. After corrosion initiates, the time until repair or replacement is required varies heavily on the corrosion rate, which can vary by orders of magnitude. The Life 365 program assumes a 6 year propagation time in their service life calculations (Ehlen, et al., 2009). However, frequently the failure of a structure due to chloride-induced corrosion is assumed to occur at corrosion initiation for service life modeling (Bertolini, et al., 2004).

3.2.4 Conclusions, Corrosion of Prestressing Steel

The piles from the Turtle River Bridge showed extensive damage from chloride-induced corrosion. The corrosion half-cell potentials indicated that the prestressing strands were undergoing active corrosion from the tidal zone to mudline. The chloride profiles indicated that the concentration of chlorides at the reinforcement, 0.35% to 0.45% by mass of concrete, was significantly higher than the 0.05% necessary to initiate pitting corrosion. The large amount of concrete cracking and spalling and of steel corrosion damages were limited to the tidal and splash zones on the piles, due to the limited availability of oxygen in the fully submerged regions of the piles.

The diffusion coefficient for chloride transport in the concrete showed that the concentration of chlorides at the level of the steel would exceed the threshold value after only 3.1 years of service in the marine environment. This suggests that the concrete mix used is not adequate for long-term exposure to this environment. The service life analysis program Life 365 was able to predict the diffusion coefficient to within 16% of the measured value. The measured was higher, likely due to contributions of additional forms of degradation to increased permeability in the concrete piles.

3.3 Sulfate Attack

Concrete piling in seawater and brackish water can be exposed to high concentrations of sulfates. In addition to sulfates present in the water, it is being investigated if additional sulfates may be produced by bacteria on the surface of the piles. The primary forms of sulfates present are $NaSO_4$ and $MgSO_4$ (Skalny, et al., 2002). Damage to the concrete due various reactions between the ingressing sulfate ions and hydration products and anhydrous cement phases in the cement paste is termed "sulfate attack". Two primary mechanisms are associated with sulfate attack. First, sulfate ions can react with monosulfoaluminate or available tricalcium aluminate to form ettringite. The formation of ettringite can be expansive and lead to cracking and spalling. The calcium consumed in this reaction comes from the dissolution of available Portlandite. In addition, sulfate ions may react with available calcium hydroxide to form gypsum. If there is no Portlandite present, then the calcium comes from the decomposition of the

calcium silicate hydrate phase (C-S-H). The loss of calcium from the C-S-H leads to a reduction in strength (Skalny, et al., 2002).

In the case of magnesium sulfate attack, additional reaction mechanisms are possible. Magnesium sulfate reacts with Portlandite to form brucite, in addition to gypsum. Simultaneously, C-S-H is decomposed and converted to an amorphous hydrous silica or magnesium silicate hydrate phase. The decomposition of C-S-H is significantly faster with exposure to magnesium sulfate compared to sodium sulfate (Skalny, et al., 2002).

Visible signs of sulfate-induced damage include a whitish appearance of the cement paste in damaged areas, as well as cracking (due to expansion), softening of the paste, delaminations, and spalling, with , with the damage typically starting at corners and edges. In addition, loss of strength, modulus and can be measured (Neville, 1997). The sulfate attack damage to the bridge piles was characterized by performing a visual inspection of the piles, hardness measurements, and TGA (thermo-gravimetric analysis) and XRD (x-ray diffraction) analysis.

3.3.1 Visual Assessment of Damage

A visual assessment of the submerged region was performed. Cracks were found near the corners of the piles that extended from the mudline up to low tide. The width of these crack varied widely, with a maximum of 1.27 mm (0.05 in.), but most were approximately 0.64 mm (0.025 in.) in width. Spalling and abrasion was also apparent at the surface. Additionally, marine life had grown along the cracks that growth may have

led to increased deterioration. Figure 3.20 shows the measurement of a crack, along with marine growth inside of a crack.

(a) (b)

Figure 3.20: (a) Cracking along corner of pile, and (b) marine growth in crack

A core taken through the cross-section revealed a visible whitish discoloration of the cement paste near the surface in the submerged region of the pile as shown in Figure 3.21. The depth of the color change was consistent with the cracking location along the corners of the piles.

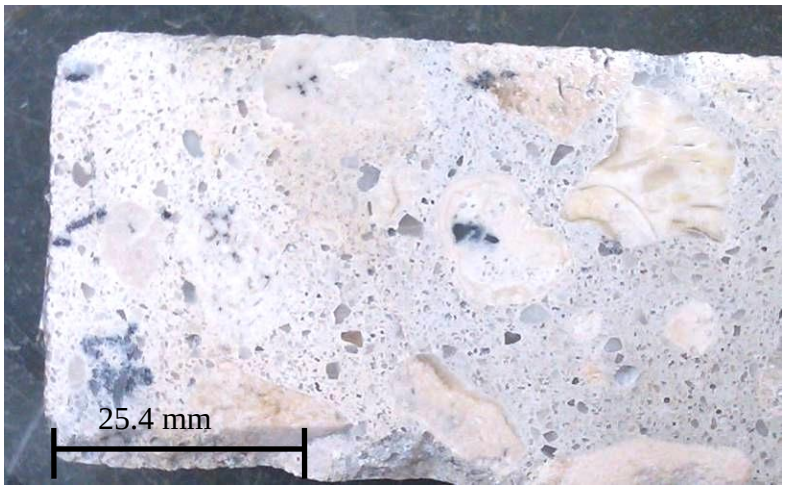

Figure 3.21: Whitish discoloration near surface in submerged region (1 in. = 25.4 mm)

3.3.2 Hardness Measurements

To determine if a variation existed between the different exposure regions, the hardness of the concrete was measured using two different methods - rebound hammer to measure coarser variations in hardness along the length of the piles and Vickers hardness to measure finer variations in hardness through the depth of the pile. . Rebound hammer testing was performed at 0.3 m (1 ft) increments along the length of the pile in accordance with ASTM C 805 (2008). A minimum of 10 readings were taken at each location on a smooth surface. Any reading outside the average by more than 6 units was discarded. The calibration from rebound number to strength (or hardness) is provided by the manufacturer for each orientation of testing. The calibration is affected by moisture condition of the concrete, depth of carbonation, and other environmental factors that make the relationship highly variable. However, the rebound hammer number was correlated to a strength for interpreting results to correct for the orientation of the hammer

during testing, which affects the rebound number. The calibration from rebound number to strength (or hardness) was provided by the manufacturer (Figure 3.22).

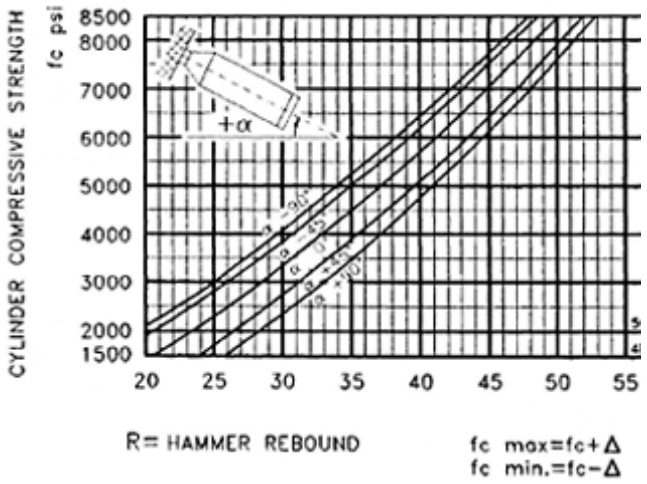

Figure 3.22: Rebound hammer calibration (1,000 psi = 6.9 MPa)

The results from the rebound hammer testing performed on two piles have been converted into compressive strengths, as previously described, and are shown in Figure 3.23. A negative depth represents above high tide; a positive depth is below high tide. The results suggest a large change in surface hardness, and potentially strength, that occurs in between the splash and low tide region of the piles. The results show an average reduction in strength of approximately 50% from the region of the pile exposed to the atmosphere to the submerged concrete. The reduction in strength occured rapidly near the high tide region of the piles, and continued to decrease at a gradual rate with increasing depth.

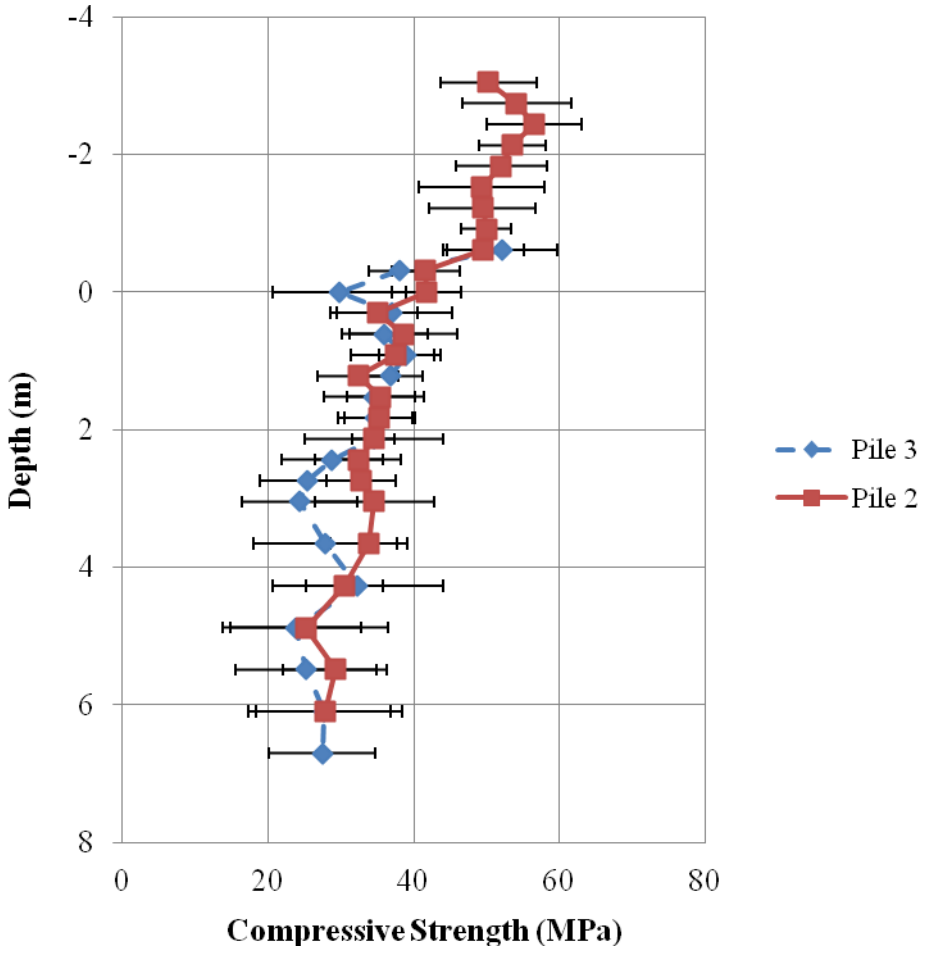

Figure 3.23: Rebound hammer results (1,000 psi = 6.9 MPa)

Vicker's indentation measurements were performed on polished slices of cores to determine the variation in micro-hardness of the cement paste with depth into the section. Vicker's indentations were performed in accordance with ASTM C 1327 (2008) using 1 kg mass applied for 15 seconds. A minimum of 5 indentations were made at 6.35 mm (¼ in.) increments into the section on sections polished with 1 micron alumina.

The indentations were measured using a Leica TCS NT confocal microscope. Measurements were made to the nearest micrometer across both diagonals, then the average used for calculating the hardness number. Figure 3.24 shows the results of the

measurements for 0.6 m (2 ft) above high tide and 3.66 m (12 ft) below in the submerged region. The outer 50.8 mm (2 in.) of the submerged region had a reduced hardness compared to the 0.6 m (2 ft) above high tide sample. The depth at which the hardness significantly increased coincided with the location of the whitish color change on the samples.

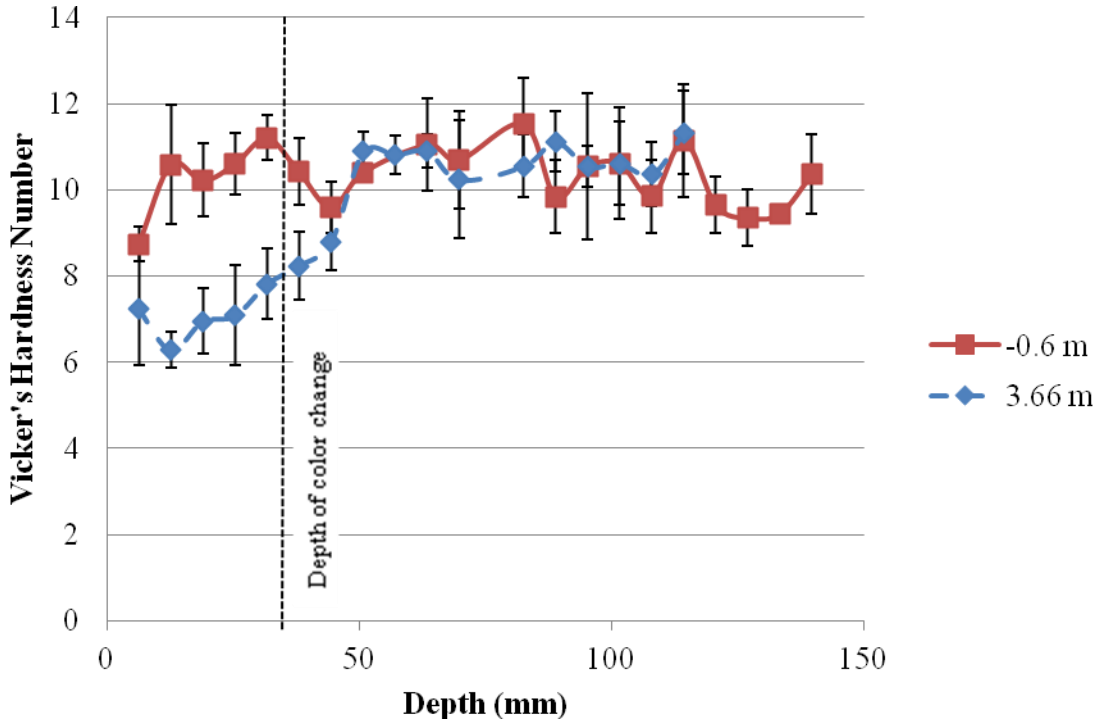

Figure 3.24: Vicker's hardness measurements

3.3.3 Compressive Strength Testing

The compressive strength of the piles was determined in accordance with ACI 214.4R-10 (ACI Committee 214, 2010) and ASTM C 39 (2005). Two sets of tests were performed. First, three 76.2 mm (3 in.) diameter cores were obtained away from the surface of the pile, as shown in Figure 3.25. Three sets of cores were taken along the

length of the pile in the atmospheric, tidal, and submerged zones for comparison of the undamaged concrete along the length of the piles. The specimens were cut to a 152.4 mm (6 in.) length using a wet cut concrete saw.

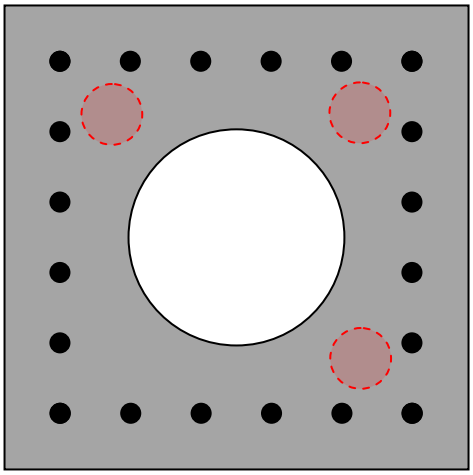

Figure 3.25: Compressive strength core locations

Also, cores were taken through the section to determine if there was a variation between concrete near the surface and the interior undamaged concrete. Cores were taken at -2.74 m (-9 ft), high tide, 1.52 m (5 ft), and 3.66 m (12 ft) depth. Four 76.2 mm (3 in.) diameter cores were taken through the section and cut to 76.2 mm (3 in.) lengths, one at the surface and a section near the center of the pile at each location tested. The location and diagram of the stub specimens are shown in Figure 3.26.

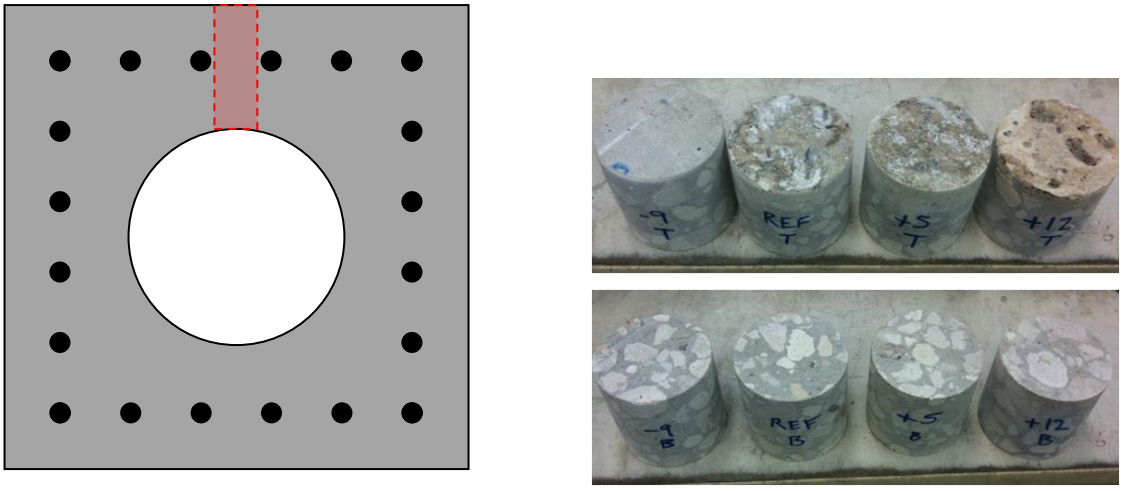

(a) (b)

Figure 3.26: (a) Compressive strength core locations, and (b) surface (top) and interior samples (bottom)

The results of the compressive strength testing of undamaged interior concrete along the length of the piles are given in Figure 3.27. The average compressive strength from all three locations was 40.82 MPa (5.92 ksi), which is above the design strength of 34.47 (5 ksi). ANOVA testing, using an alpha of 0.1, showed that the concrete from all three locations at the interior of the pile was statistically equivalent. Since the undamaged interior concrete was shown to be the same in the submerged, tidal, and atmospheric zones of the pile, the data suggested that the variation in rebound hammer results was due to a softening of the surface, and not a variation in undamaged concrete properties.

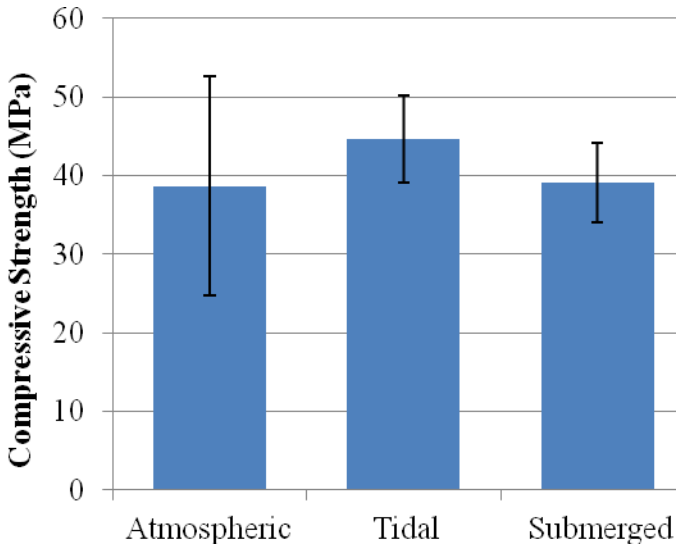

Figure 3.27: Compressive strength of undamaged interior concrete
(1,000 psi = 6.895 MPa)

The results of the stub compression tests comparing the surface to interior concrete are shown in Figure 3.28. The compressive strengths of the interior samples at all depths were determined to be statistically equivalent using ANOVA testing with alpha equal to 0.1. ANOVA analysis between the surface and interior concrete at each depth showed that only the -2.74 m (-9 ft) and high tide sections were statistically equivalent. The 1.52 m (5 ft) and 3.66 m (12 ft) samples both had statistical evidence to show the average compressive strengths were not the same. At 1.52 m (5 ft) depth, the surface compressive strength was 80% of the interior concrete's strength. In the submerged region, the surface compressive strength was 55% of the interior concrete's strength. The strengths measured were consistent with the strengths determined from the impact hammer measurements.

The large reduction in compressive strength may be explained by a loss of C-S-H from sulfate attack or other forms of degradation, including carbonation. All of the surface samples from 3.66 m (12 ft) below high tide failed due to a crushing near the

surface and a single large crack through the remainder of the sample. The paste portion in the crushed region was a powdery consistency after failure.

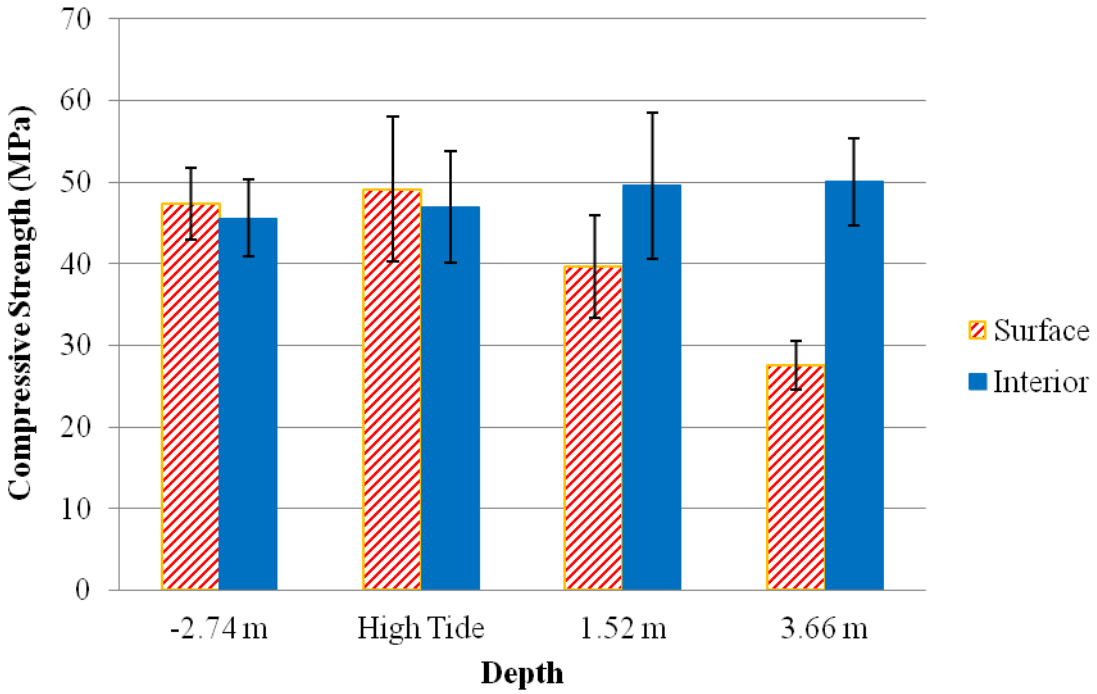

Figure 3.28: Compressive strength of surface versus interior concrete (1,000 psi = 6.895 MPa)

3.3.4 X-Ray Diffraction

Powder X-ray diffraction (XRD) was performed on ground concrete samples to identify variances in the composition at various heights and depths into the cross section. Samples were taken at -2.74 m (-9 ft.), -0.6 m (-2 ft), high tide, 1.52 m (5 ft), and 3.66 m (12 ft) corresponding to the atmospheric, splash, high tide, low tide, and submerged regions of the piles. Powder was obtained by taking a 76.2 mm (3 in.) diameter core through the section and then drilling at controlled increments using a 9.5 mm (3/8 in.) masonry bit. Powder was collected from the surface in a 12.7 mm (½ in.) increment, then

at 25.4 mm (1 in.) increments into the cross-section. The powder samples were then ground with mortar and pestle and sieved through an 850 μm (No. 20) sieve. Figure 3.29 shows a prepared XRD sample.

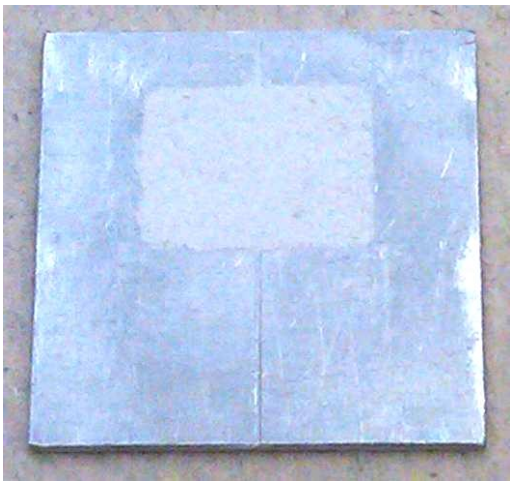

Figure 3.29: XRD sample

XRD analysis was performed using a Philip's X'Pert XRD system. The scan was performed over a 2θ range of 5˚ to 75˚ using a scan rate of 0.05˚ per second under Cu K-α radiation. Table 3.2 gives the notation used in labeling the peaks on the XRD profiles for each sample. In multiple incidences, peak locations for two or more phases overlapped. If other unique peaks for each phase were identified, then the shared peak was labeled for both phases.

The calcium carbonate and calcium manganese carbonate phases represented the coarse aggregate in the concrete, as well as carbonated cement and calcium hydroxide. The quartz phase represented the fine aggregate used. The calcium hydroxide, ettringite, and gypsum phases occurred in the hydrated cement paste fraction of the sample.

Calcium silicate hydrate, the predominant product of Portland cement hydration, is largely amorphous, producing a broad peak around 30^{o} on the 2θ scale.

Table 3.2: Chemical Symbols with Correlated Composition for XRD Profiles

Symbol	Composition
CH	Calcium Hydroxide
Ca	Calcium Carbonate (Calcite)
Ca(Mg)	Calcium Manganese Carbonate
Q	Quartz
E	Ettringite
G	Gypsum

3.3.4.1 XRD Results from Atmospheric Region

The results at 2.74 m (9 ft) above high tide is given in Figures 3.30 and 3.31 for the 0 to 12.7 mm (0 to 0.5 in.) and 12.7 mm to 38.1 mm (0.5 to 1.5 in.) increments, respectively. The results from these samples serve as a reference for samples located in the exposure zones of the piles. The 2.74 m (9 ft) above high tide samples showed the same compositions at both depth increments. Quartz, calcium carbonate, and calcium magnesium carbonate were all present due to the coarse and fine aggregate. The peaks from the aggregate are more intense than the paste phases due to their increased volume fraction. Calcium hydroxide was detected, but no residual ettringite from hydration or gypsum. Additionally, the amorphous rise is present from a 2θ of approximately 20˚ to 75˚ and indicates the presence of non-crystalline phases like calcium silicate hydrate.

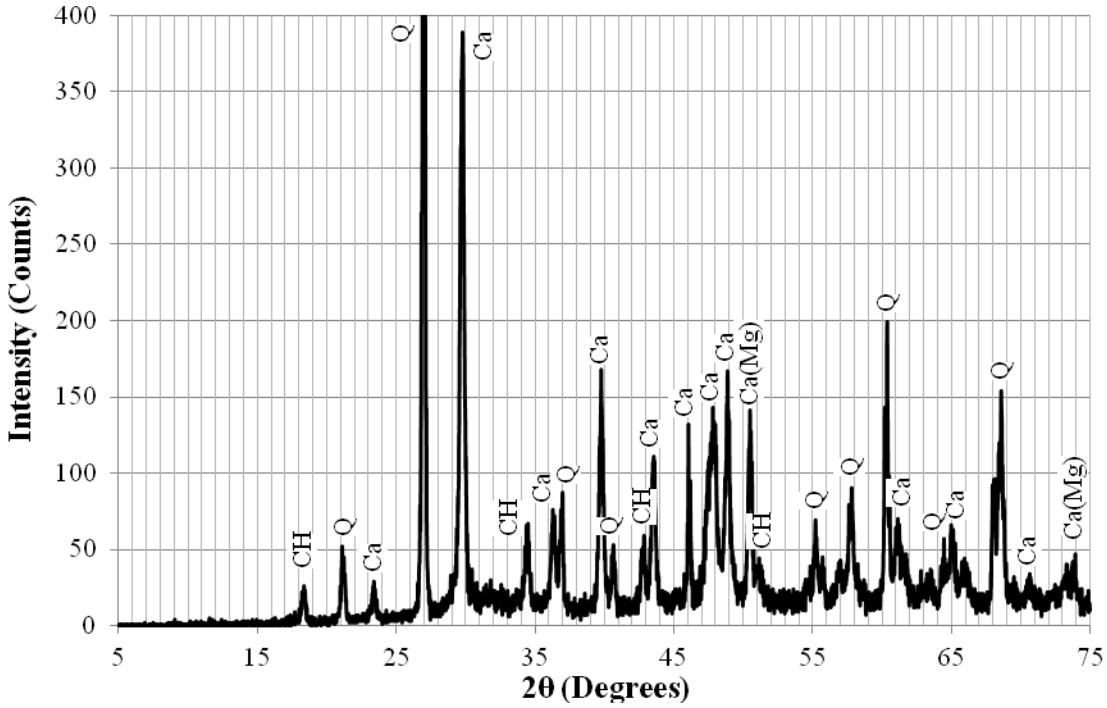

Figure 3.30: XRD profile for atmospheric region at 0 -12.7 mm increment into section

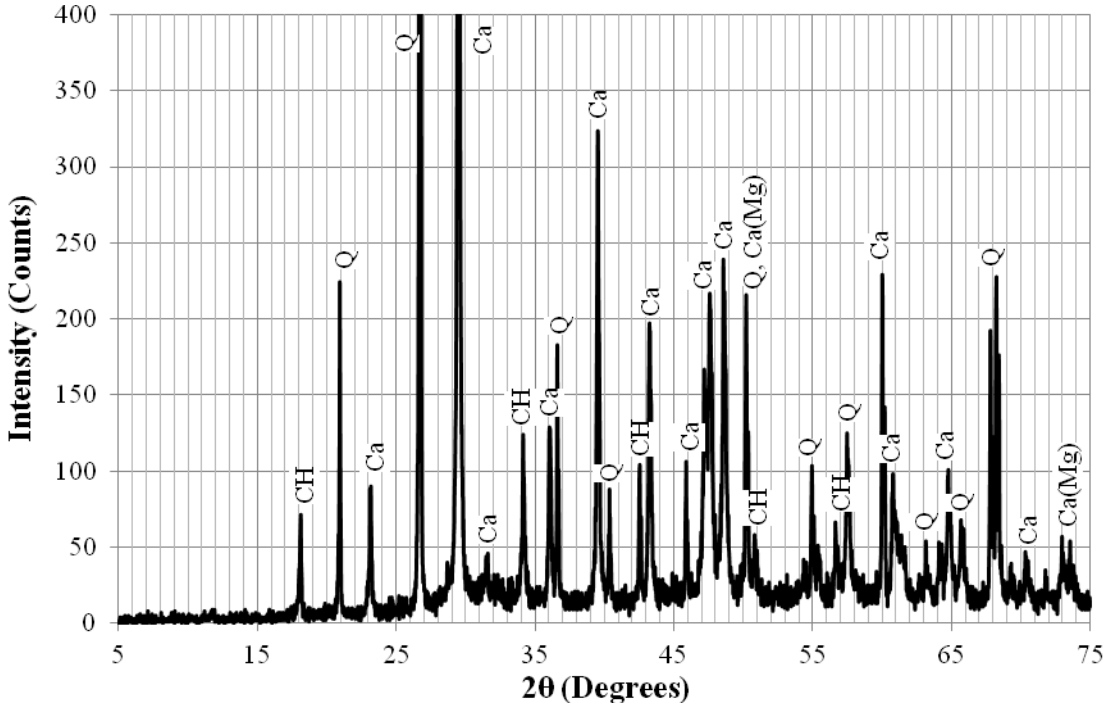

Figure 3.31: XRD profile for atmospheric region at 12.7 – 38.1 mm increment into section

3.3.4.2 XRD Results from Splash Zone

Samples from 0.6 m (2 ft) above high tide were taken to characterize the splash zone of the piles. Table 3.3 provides a summary of the results from all increments tested, where a check-mark represents the phase was present and an x-mark if not found in the increment. Calcium carbonate, calcium manganese carbonate, and quartz were detected in all samples.

Table 3.3: XRD results summary for splash zone (1 in. = 25.4 mm)

Increment (mm)	0-12.7	12.7-38.1	38.1-63.5	63.5-88.9	88.9-114.3
Calcium Hydroxide	✓				
Ettringite	×				
Gypsum	✓	✓	✓	×	×
Calcite	✓				
Calcium Manganese Carbonate	✓				
Quartz	✓				

The XRD profiles for the 0-12.7 mm, 12.7-38.1 mm, 38.1-63.5 mm, 63.5-88.9 mm, and 88.9-114.3 mm (0-0.5 in., 0.5-1.5 in., 1.5-2.5 in., 2.5-3.5 in., and 3.5-4.5 in.) increments are given in Figures 3.32, 3.33, 3.34, 3.35, and 3.36, respectively. The results show the presence of gypsum near the surface, but it was not detected deeper than 63.5 mm (2.5 in.) into the section, and no ettringite was detected. The presence of gypsum may result from prolonged exposure to brackish water, which contains large amounts of sodium sulfate and magnesium sulfate. The sulfate concentration was measured to be 1527 mg/L at the Turtle River Bridge during high tide. Calcium hydroxide was present at all depths sampled, suggesting that an alkaline pH was maintained. The XRD profiles deeper than 63.5 mm (2.5 in.) into the section are identical to the atmospheric region

samples from 2.74 m (9 ft) above high tide, which suggest that no significant changes to the microstructure have occurred in those increments.

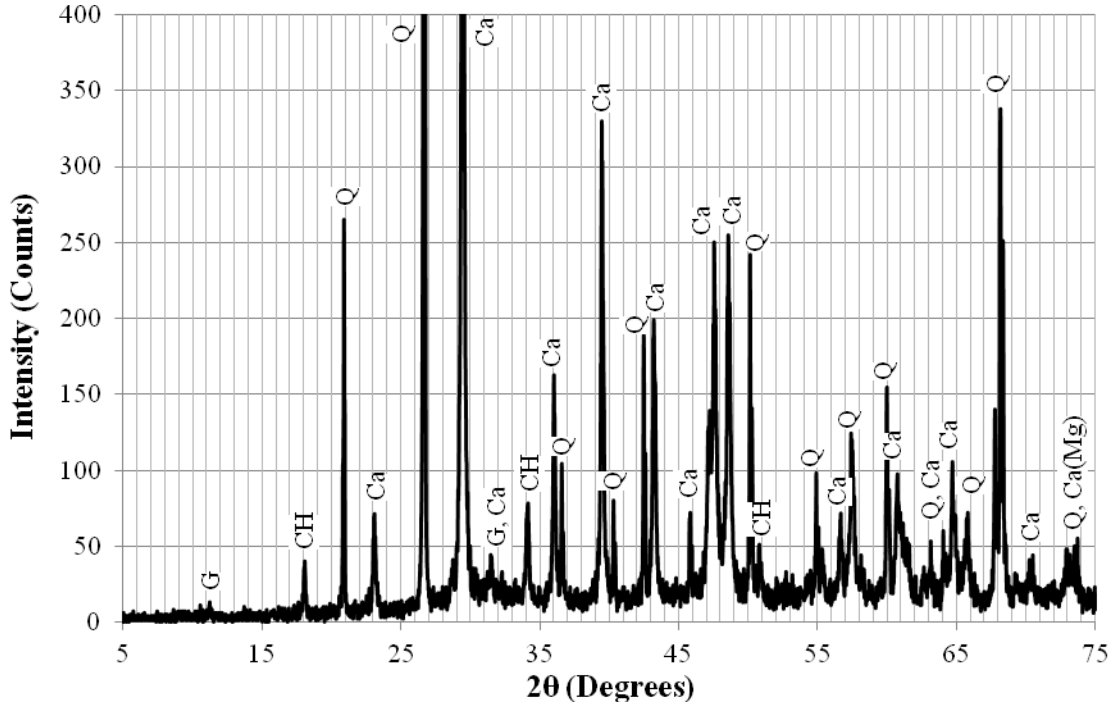

Figure 3.32: XRD profile for splash zone at 0-12.7 mm increment into section

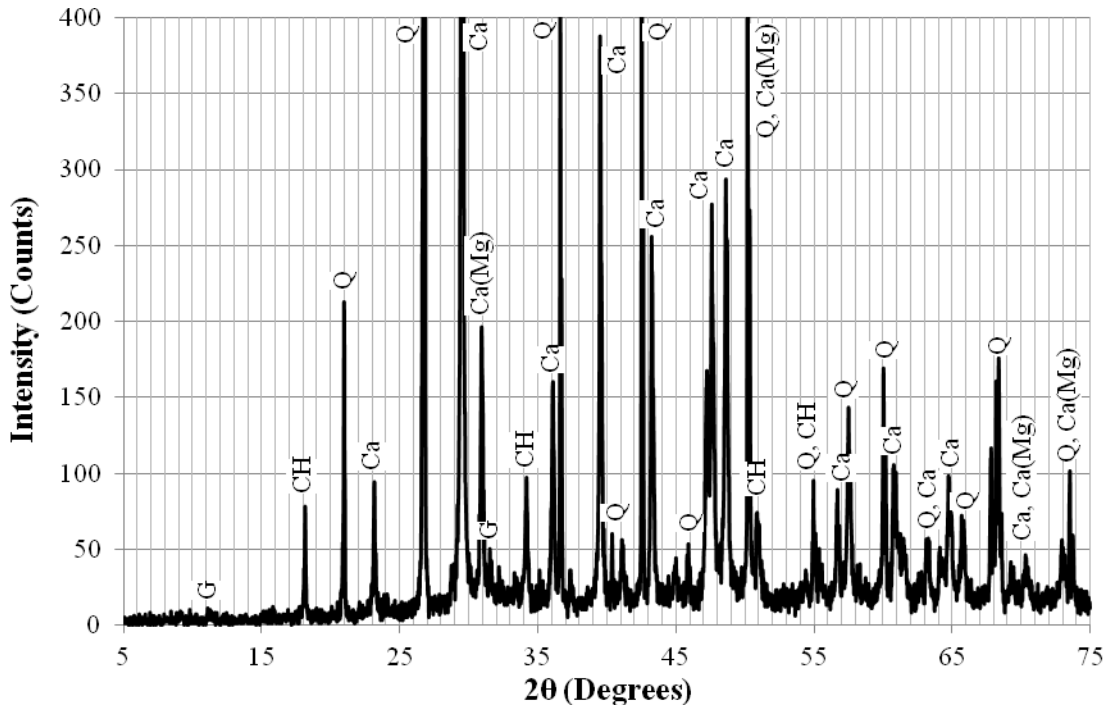

Figure 3.33: XRD profile for splash zone at 12.7-38.1 mm increment into section

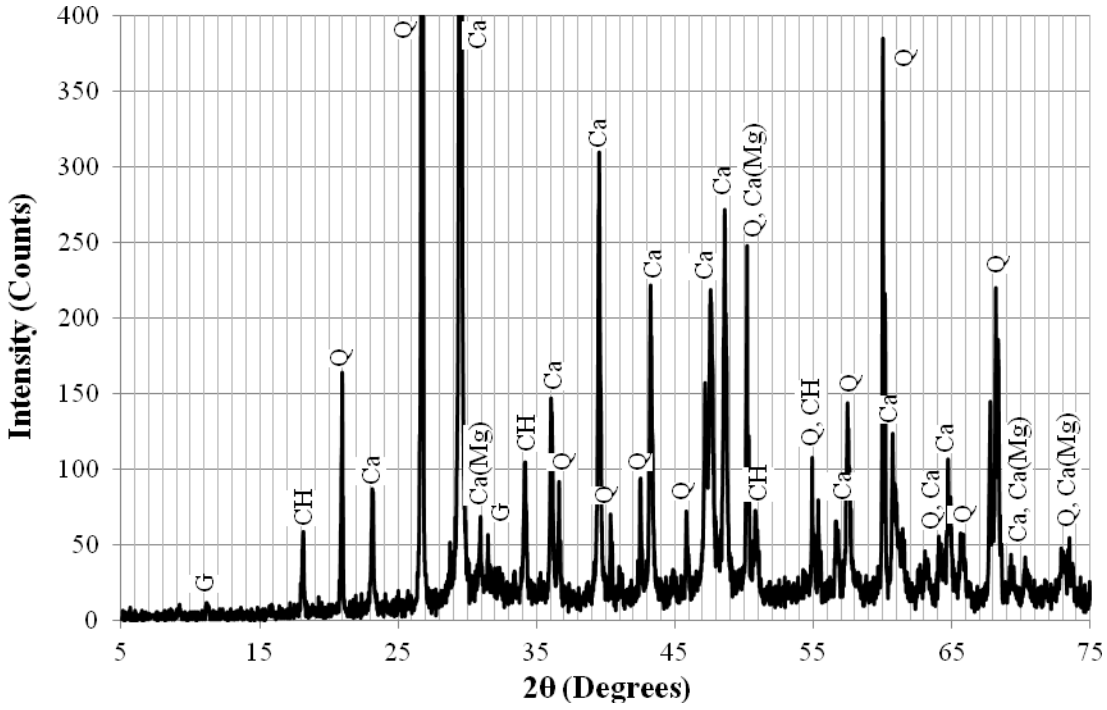

Figure 3.34: XRD profile for splash zone at 38.1-63.5 mm increment into section

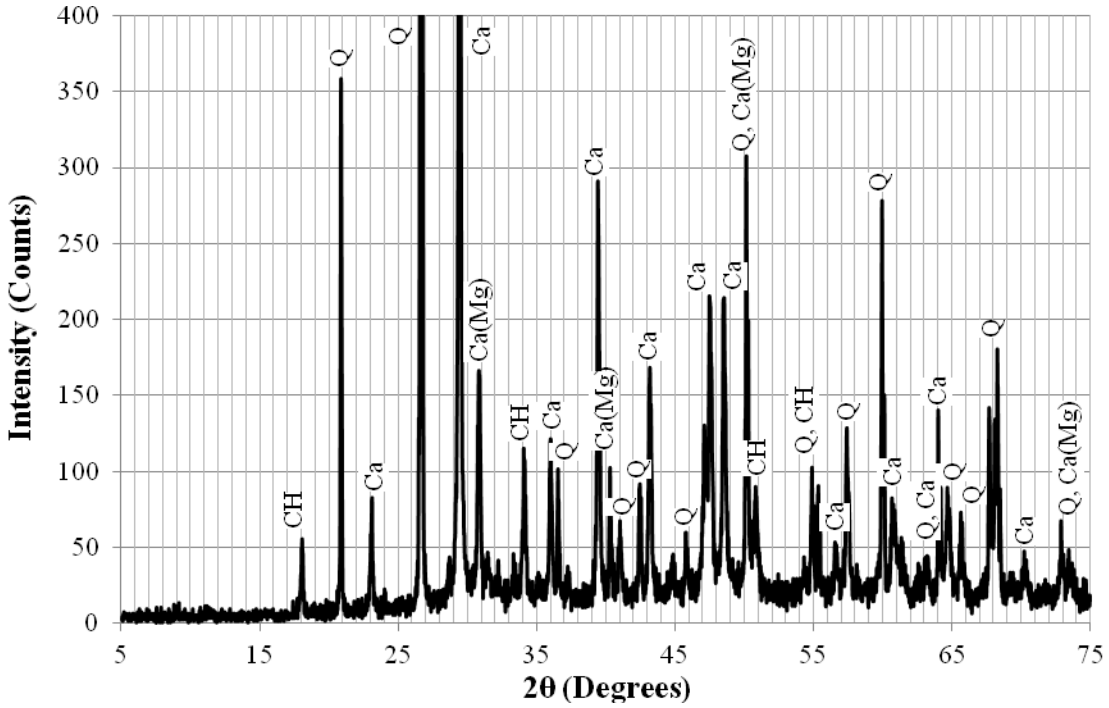

Figure 3.35: XRD profile for splash zone at 63.5-88.9 mm increment into section

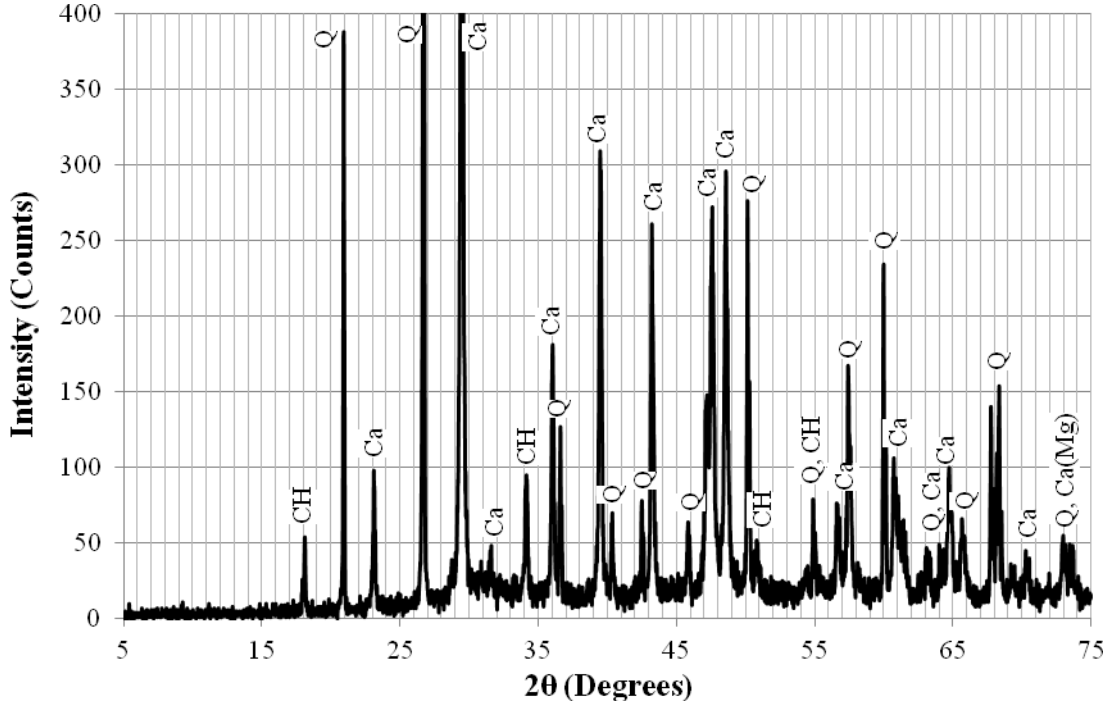

Figure 3.36: XRD profile for splash zone at 88.9-114.3 mm increment into section

3.3.4.3 XRD Results from High Tide Region

Table 3.4 provides a summary of the results from all increments tested at the high tide region of the pile.

Table 3.4: XRD results summary for high tide (1 in. = 25.4 mm)

Increment (mm)	0-12.7	12.7-38.1	38.1-63.5	63.5-88.9	88.9-114.3
Calcium Hydroxide	✓				
Ettringite	✓	✓	×	✓	×
Gypsum	✓				
Calcite	✓				
Calcium Manganese Carbonate	✓				
Quartz	✓				

The XRD profiles for the 0-12.7 mm, 12.7-38.1 mm, 38.1-63.5 mm, 63.5-88.9 mm, and 88.9-114.3 mm (0-0.5 in., 0.5-1.5 in., 1.5-2.5 in., 2.5-3.5 in., and 3.5-4.5 in.) increments can be found in Figures 3.37, 3.38, 3.39, 3.40, and 3.41, respectively. The results show a small presence of ettringite in the surface to 88.9 mm (3.5 in.) depth increments, and gypsum throughout the depth. Calcium hydroxide was present at all depths, but the intensity near the surface is greatly reduced from the other increments. These results suggest changes in the microstructure from the reference samples that are consistent with sulfate attack. The presence of ettringite at depths nearer to the surface and gypsum throughout the section depth suggest that sulfate ions were able to penetrate through much of the depth of the pile at the high tide location.

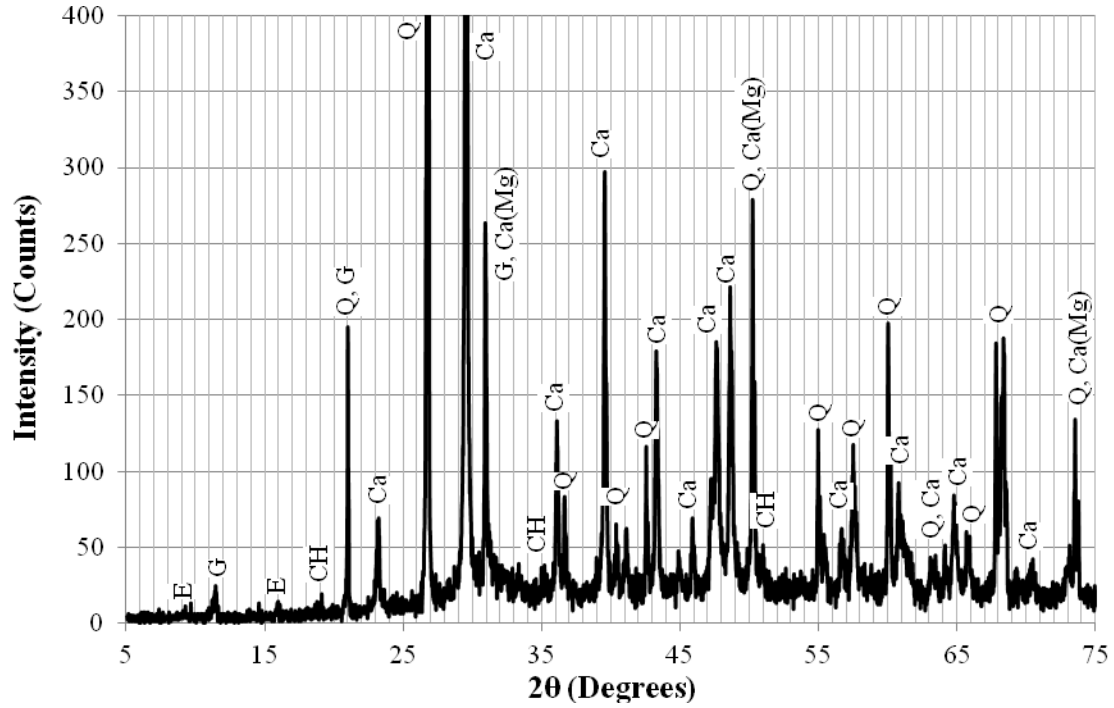

Figure 3.37: XRD profile for high tide region at 0-12.7 mm increment into section

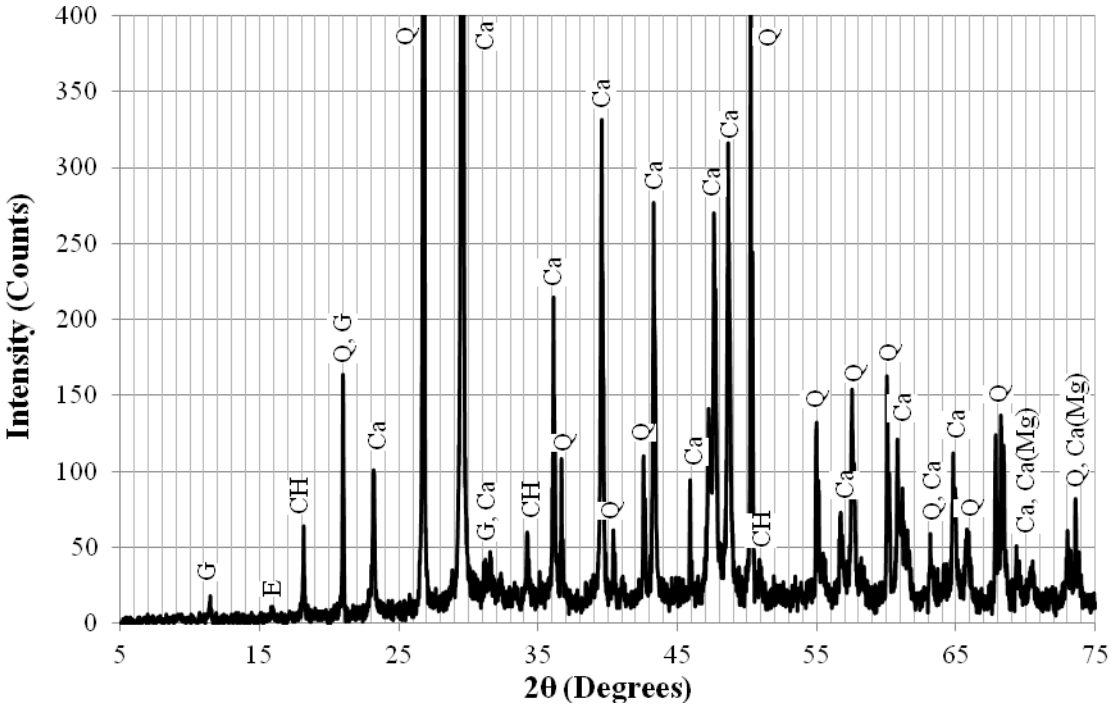

Figure 3.38: XRD profile for high tide region at 12.7-38.1 mm increment into section

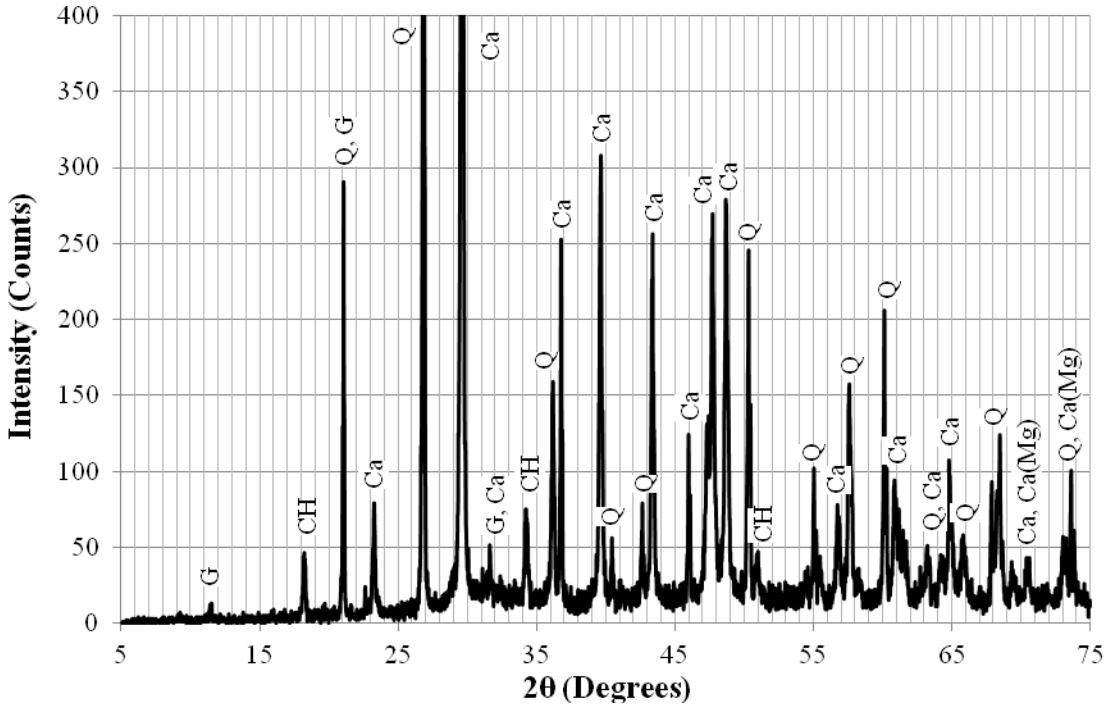

Figure 3.39: XRD profile for high tide region at 38.1-63.5 mm increment into section

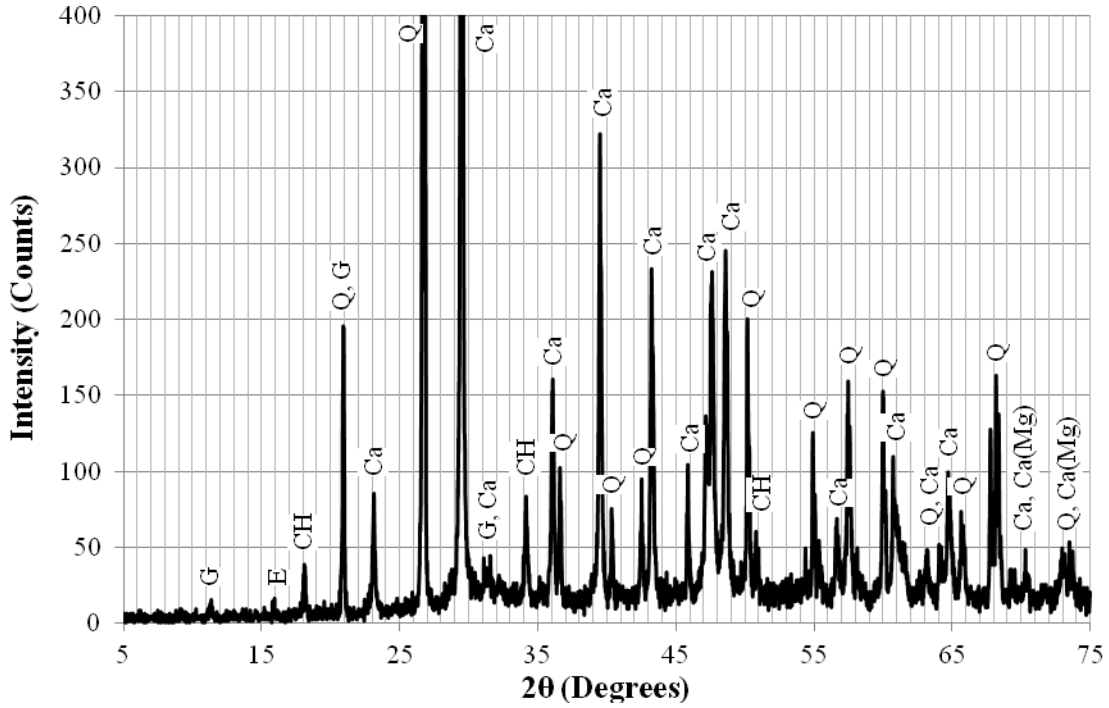

Figure 3.40: XRD profile for high tide region at 63.5-88.9 mm increment into section

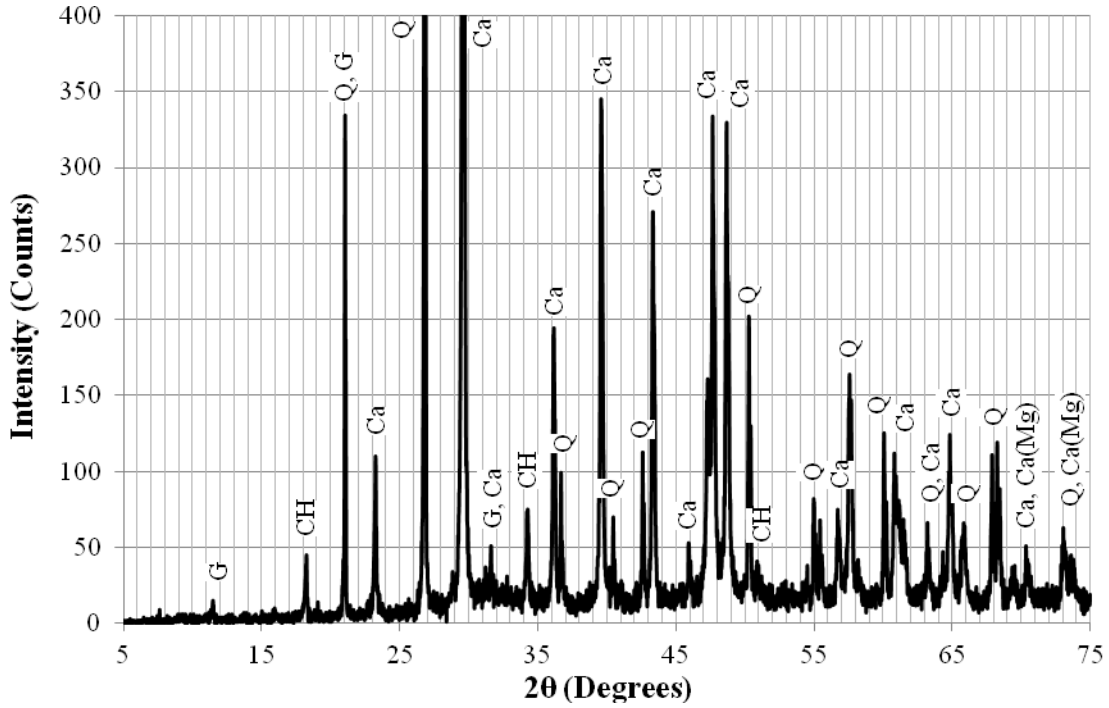

Figure 3.41: XRD profile for high tide region at 88.9-114.3 mm increment into section

3.3.4.4 XRD Results from Low Tide

Samples from 1.52 m (5 ft) below high tide were taken to characterize the low tide region of the piles. Table 3.5 provides a summary of the results from all increments tested.

Table 3.5: XRD results summary for low tide (1 in. = 25.4 mm)

Increment (mm)	0-12.7	12.7-38.1	38.1-63.5	63.5-88.9	88.9-114.3
Calcium Hydroxide	×	×	✓	✓	✓
Ettringite	✓	×	×	×	×
Gypsum	✓				
Calcite	✓				
Calcium Manganese Carbonate	✓				
Quartz	✓				

The XRD profiles for the 0-12.7 mm, 12.7-38.1 mm, 38.1-63.5 mm, 63.5-88.9 mm, and 88.9-114.3 mm (0-0.5 in., 0.5-1.5 in., 1.5-2.5 in., 2.5-3.5 in., and 3.5-4.5 in.) increments can be found in Figures 3.42, 3.43, 3.44, 3.45, and 3.46, respectively. The results show a small presence of ettringite at the surface, and gypsum throughout the depth. Calcium hydroxide was not detected in the outer 38.1 mm (1.5 in.) of the section, but was present in depth increments farther into the section. These results, like the others presented previously, suggest changes in the microstructure compared to the reference samples that are consistent with sulfate attack and carbonation.

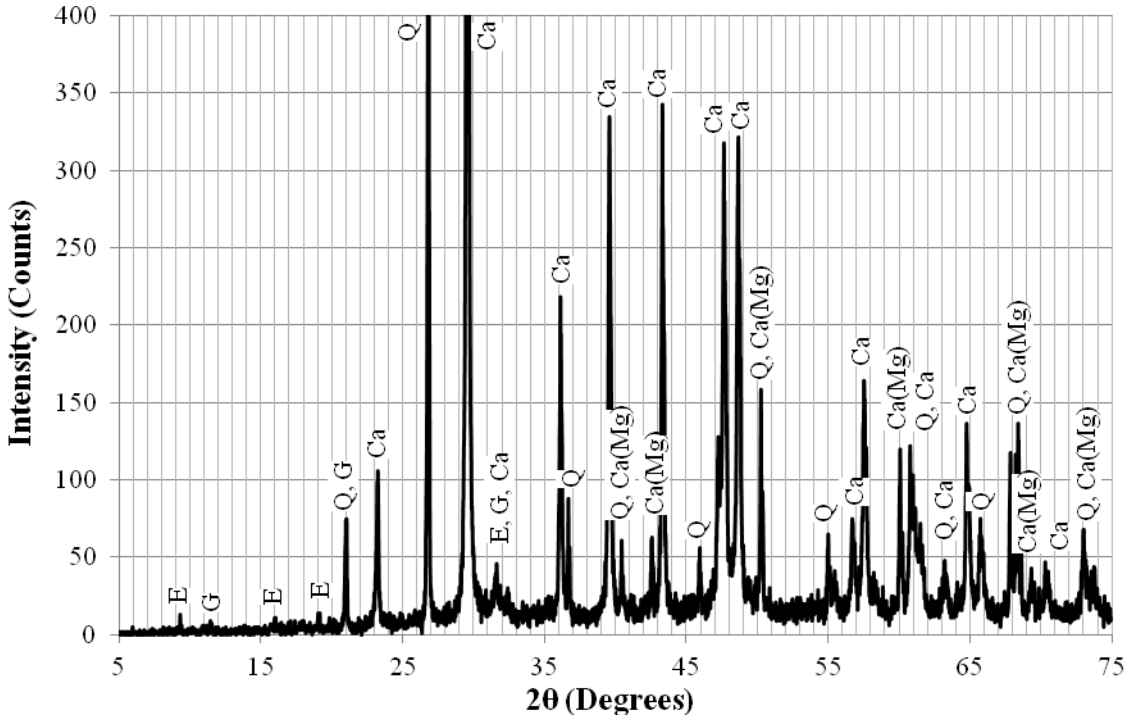

Figure 3.42: XRD profile for low tide at 0-12.7 mm increment into section

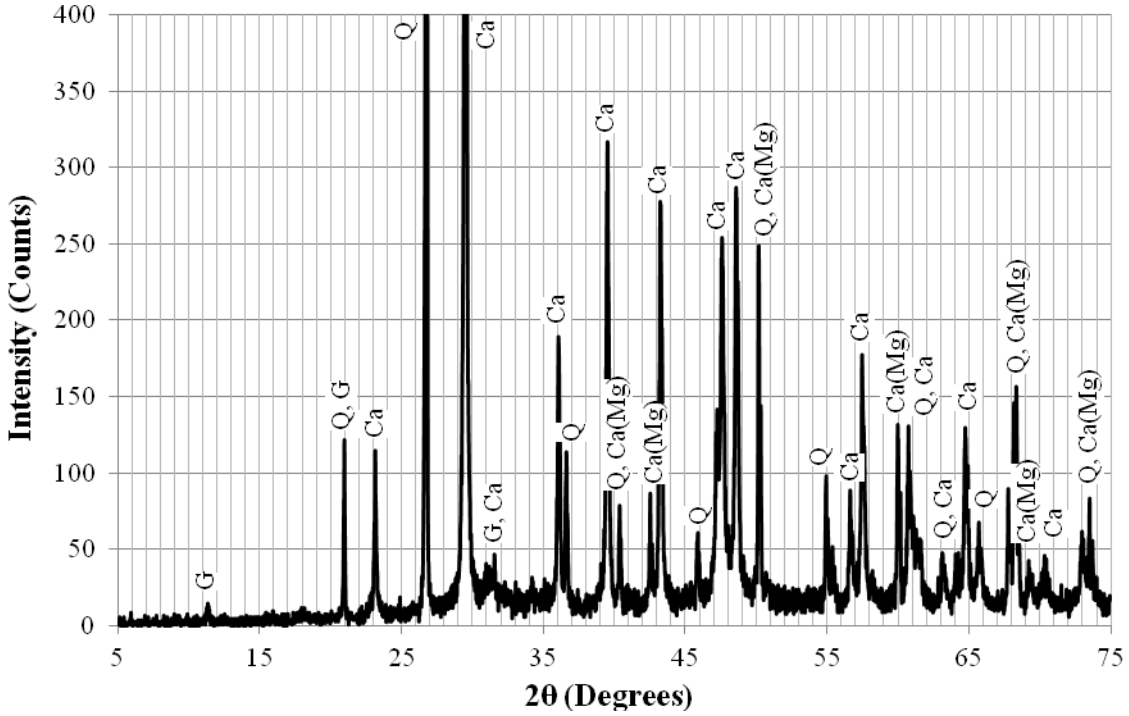

Figure 3.43: XRD profile for low tide at 12.7-38.1 mm increment into section

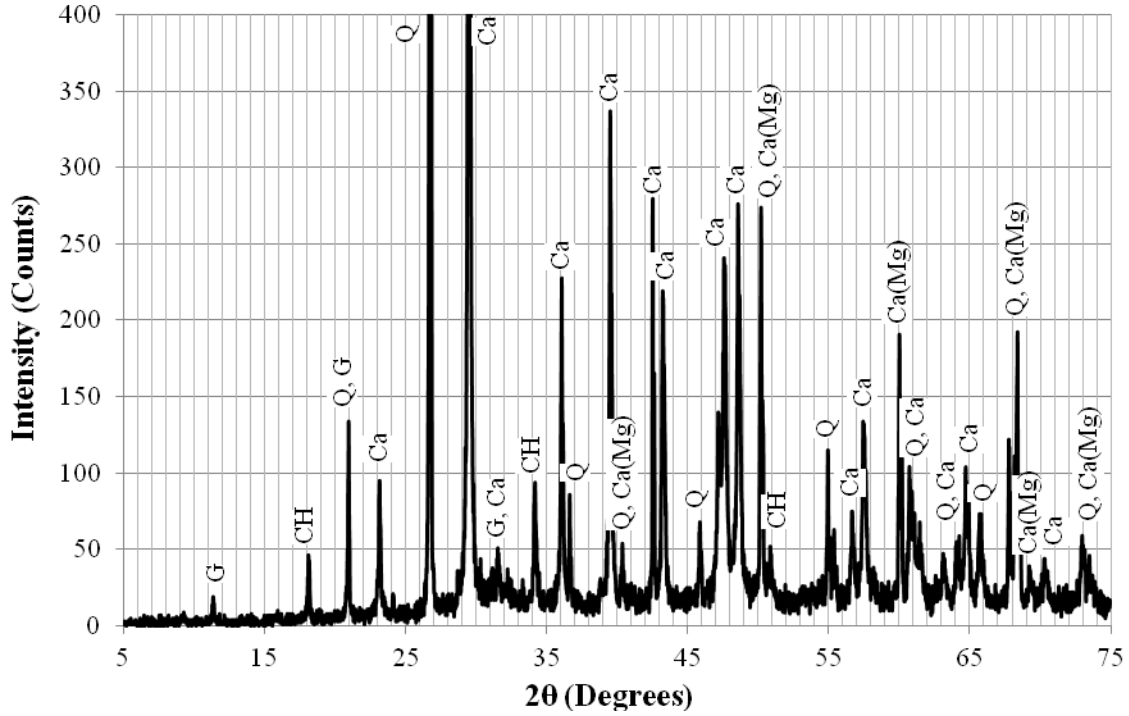

Figure 3.44: XRD profile for low tide 38.1-63.5 mm increment into section

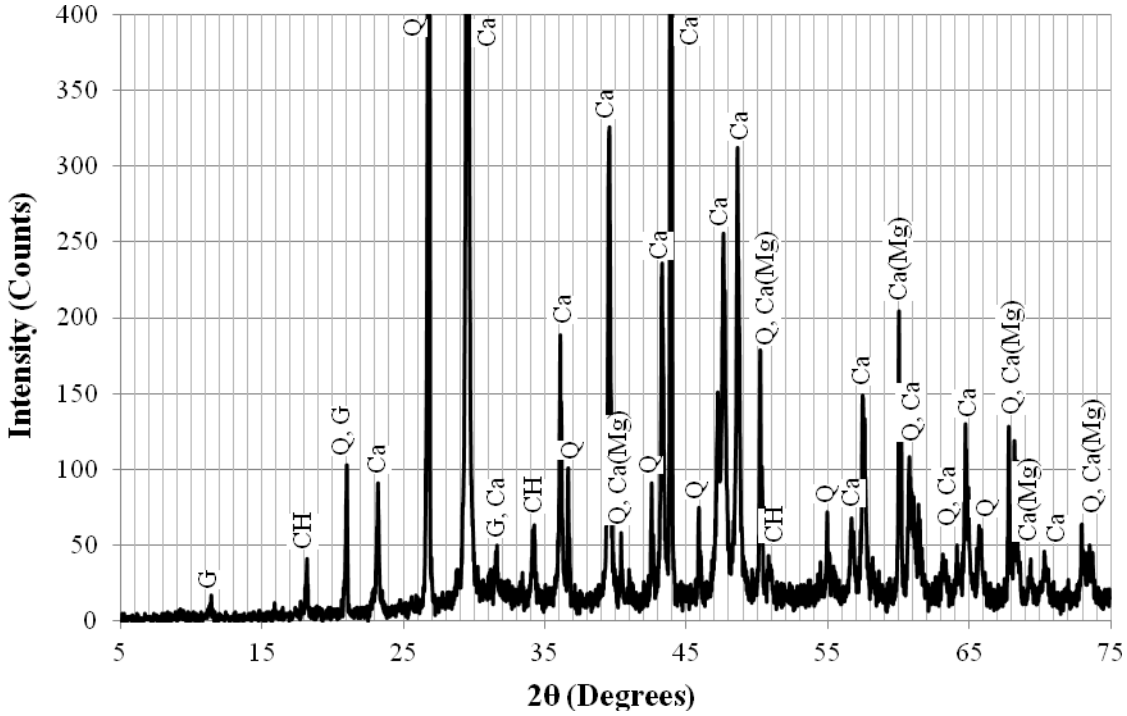

Figure 3.45: XRD profile for low tide at 63.5-88.9 mm increment into section

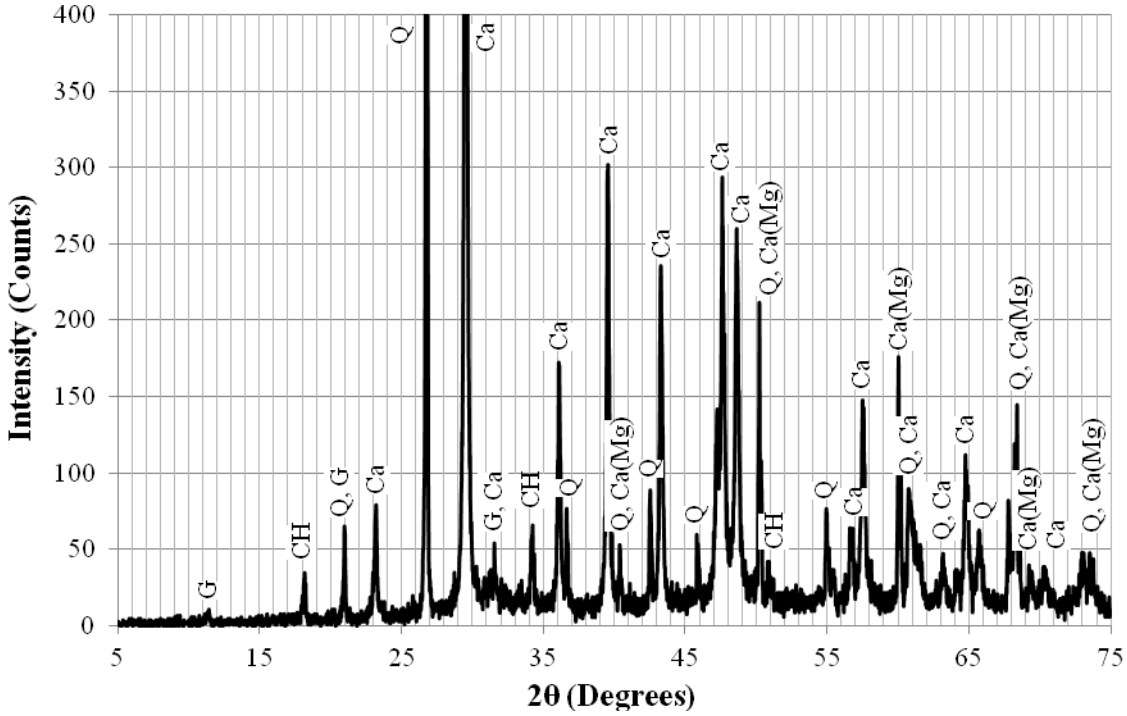

Figure 3.46: XRD profile for low tide at 88.9-114.3 mm increment into section

3.3.4.5 XRD Results from Submerged Region

Samples from 3.66 m (12 ft) below high tide were taken to characterize the submerged region of the piles. Table 3.6 provides a summary of the results from all increments tested.

Table 3.6: XRD results summary for the submerged region (1 in. = 25.4 mm)

Increment (mm)	0-12.7	12.7-38.1	38.1-63.5	63.5-88.9	88.9-114.3
Calcium Hydroxide	×	×	✓	✓	✓
Ettringite	✓	✓	×	×	×
Gypsum	✓				
Calcite	✓				
Calcium Manganese Carbonate	✓				
Quartz	✓				

The XRD profiles for the 0-12.7 mm, 12.7-38.1 mm, 38.1-63.5 mm, 63.5-88.9 mm, and 88.9-114.3 mm (0-0.5 in., 0.5-1.5 in., 1.5-2.5 in., 2.5-3.5 in., and 3.5-4.5 in.) increments can be found in Figures 3.47, 3.48, 3.49, 3.50, and 3.51, respectively. The results show a presence of ettringite near the surface, and gypsum throughout the depth. Calcium hydroxide was not detected in the outer 38.1 mm (1.5 in.) of the section, but was present at deeper depths into the section. These results suggest changes in the microstructure compared to the reference samples that are consistent with sulfate attack. The lack of calcium hydroxide near the surface also suggests carbonation and/or leaching.

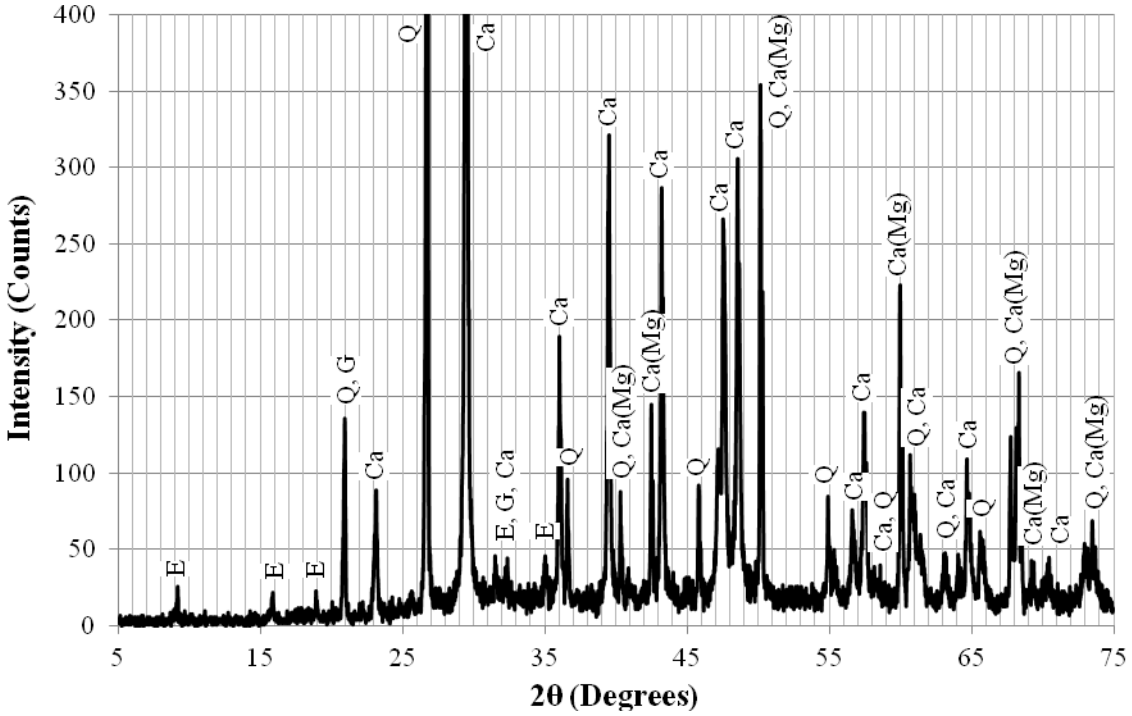

Figure 3.47: XRD profile for submerged region at 0-12.7 mm increment into section

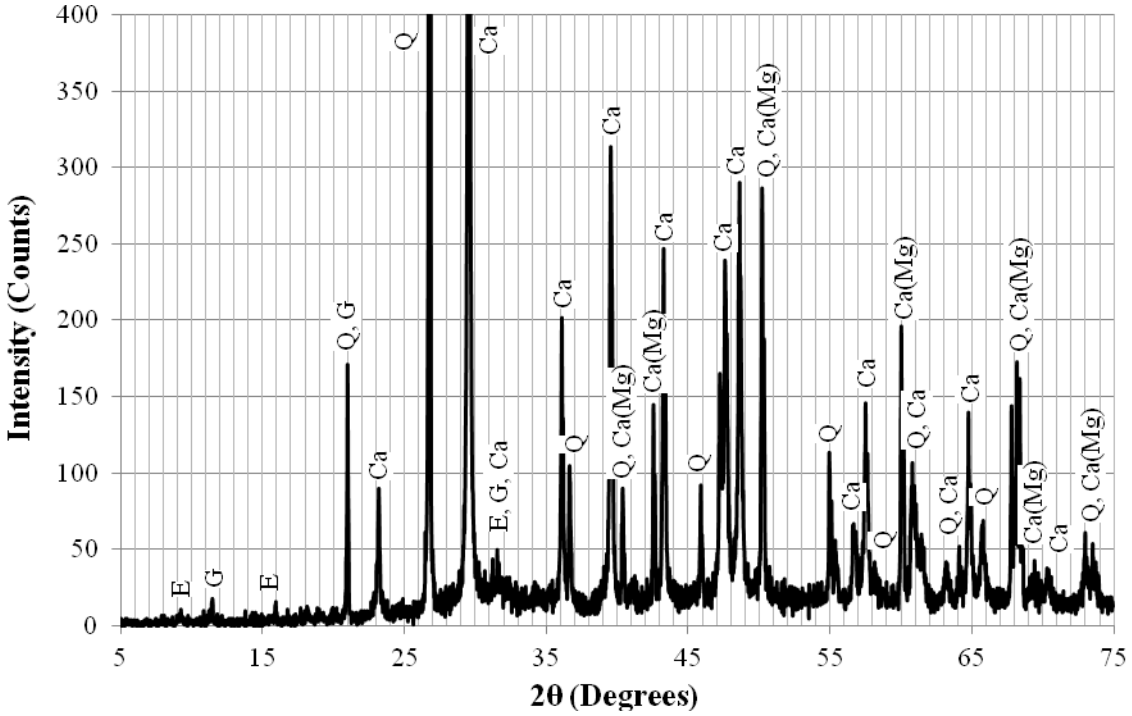

Figure 3.48: XRD profile for submerged region at 12.7-38.1 mm increment into section

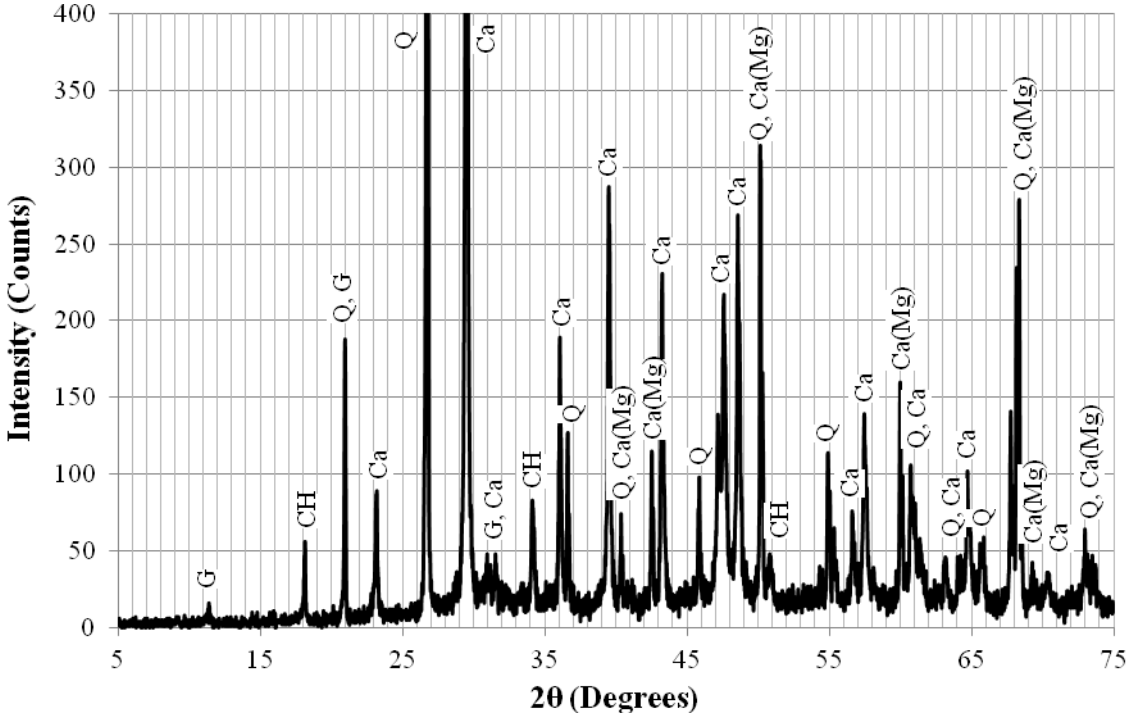

Figure 3.49: XRD profile for submerged region at 38.1-63.5 mm increment into section

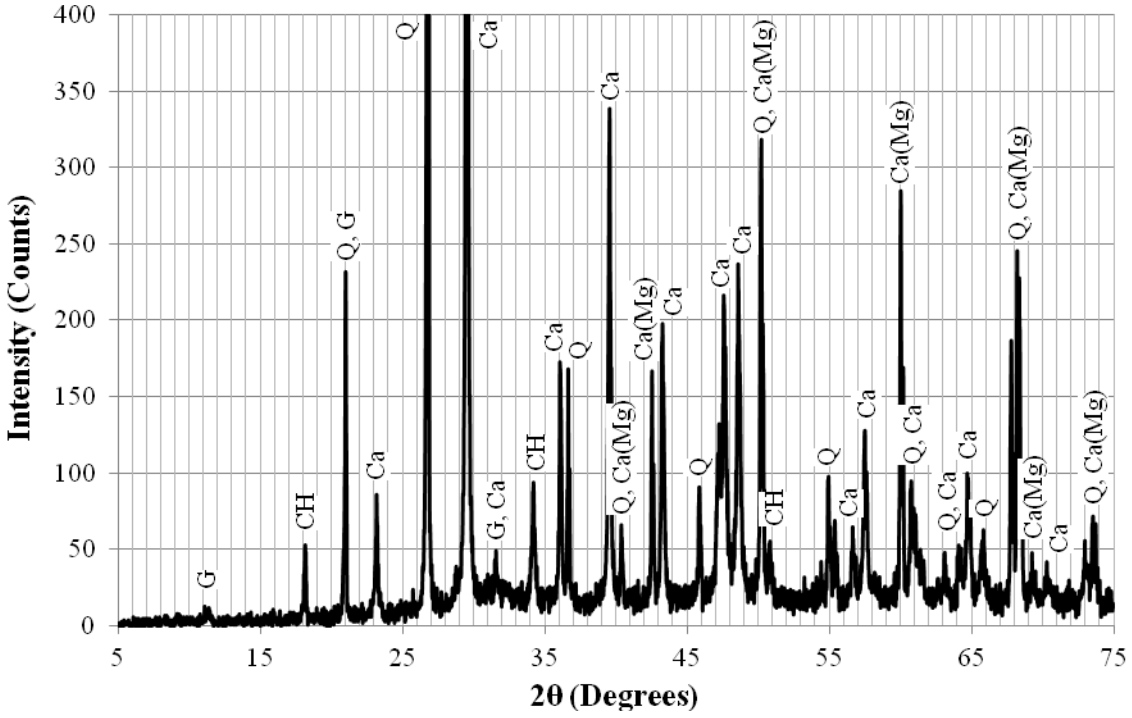

Figure 3.50: XRD profile for submerged region at 63.5-88.9 mm increment into section

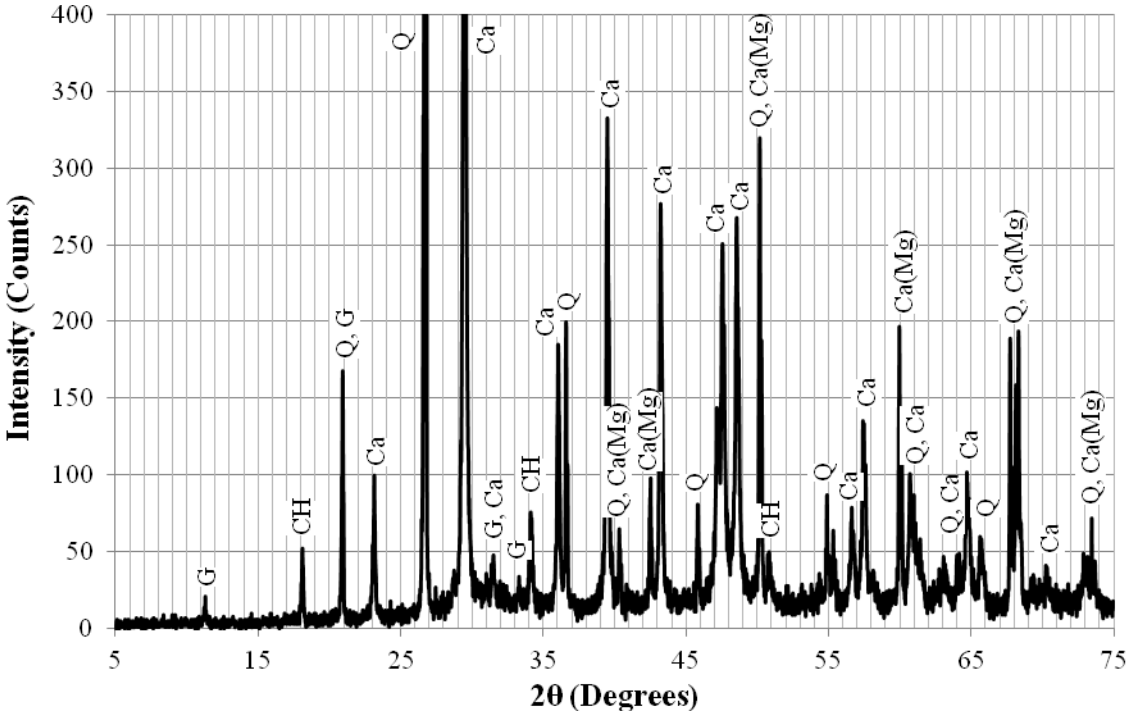

Figure 3.51: XRD profile for submerged region at 88.9-114.3 mm increment into section

3.3.5 Thermo-Gravimetric Analysis

Thermo-gravimetric analysis (TGA) was performed on ground concrete samples to identify variations in the composition at various heights and depths into the cross section. Samples were taken at –2.74 m, 0.6 m, high tide, 1.52 m, and 3.66 m (9 ft. -2 ft, high tide, 5 ft, and 12 ft). Powder was obtained by taking a 76.2 mm (3 in.) diameter core through the section and then drilling at controlled increments using a 9.5 mm (3/8 in.) masonry bit. Powder was collected from the surface 12.7 mm (½ in.) increment, then in 25.4 mm (1 in.) increments into the cross-section. The powder samples were then ground with mortar and pestle and sieved through an 850 μm (No. 20) sieve.

The analysis was performed using a Seiko TG/DTA in accordance with ASTM E 1131 (2008). Approximately 30 mg of sample powder were placed in platinum pans and

brought to 100˚C and held for one hour to remove any remaining free water from the sample. After the initial hold period, the sample was heated at a rate of 10˚C per minute up to a maximum temperature of 950˚C, while continually measuring the mass of the sample.

TGA analysis allows for determination of phases present based upon mass loss over their degradation temperatures. Ettringite decomposes at temperatures less than 115˚C and is not easily determined using TGA due to degradation temperature coinciding with the evaporation of free water. C-S-H undergoes dehydration between 100˚C to 200˚C, and a decomposition and change in structure between 200˚C and 400˚C. Portlandite ($Ca(OH)_2$) undergoes dehydroxylation between 425˚C and 600˚C. Above 750˚C, calcium carbonate degrades. However, because the coarse aggregate used was primarily calcium carbonate, the mass loss in this temperature range does not represent only a degradation of calcium carbonate in the cement paste.

Figures 3.52 and 3.53 show the TGA mass loss curves for the 2.74 m (9 ft) and 0.6 m (2 ft) above high tide samples. Both curves show a consistent mass loss in the regions due to alteration of C-S-H and decomposition of Portlandite. The mass loss due to alteration of C-S-H is a gradual change over the thermal range. The decomposition of Portlandite occurs over a small temperature range near 425˚C. A consistent mass loss of 1% occurred in all of the samples at these depths due to the loss of Portlandite. The presence of Portlandite in all of the depths tested is consistent with the XRD results.

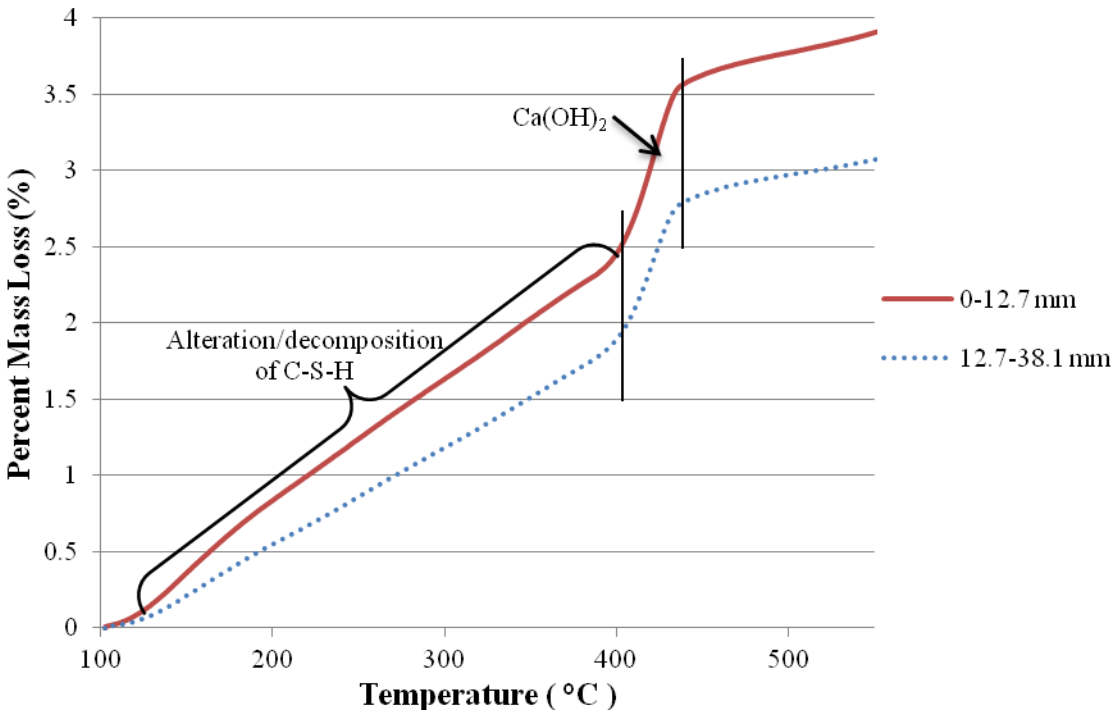

Figure 3.52: TGA for 2.74 m (9 ft) above high tide

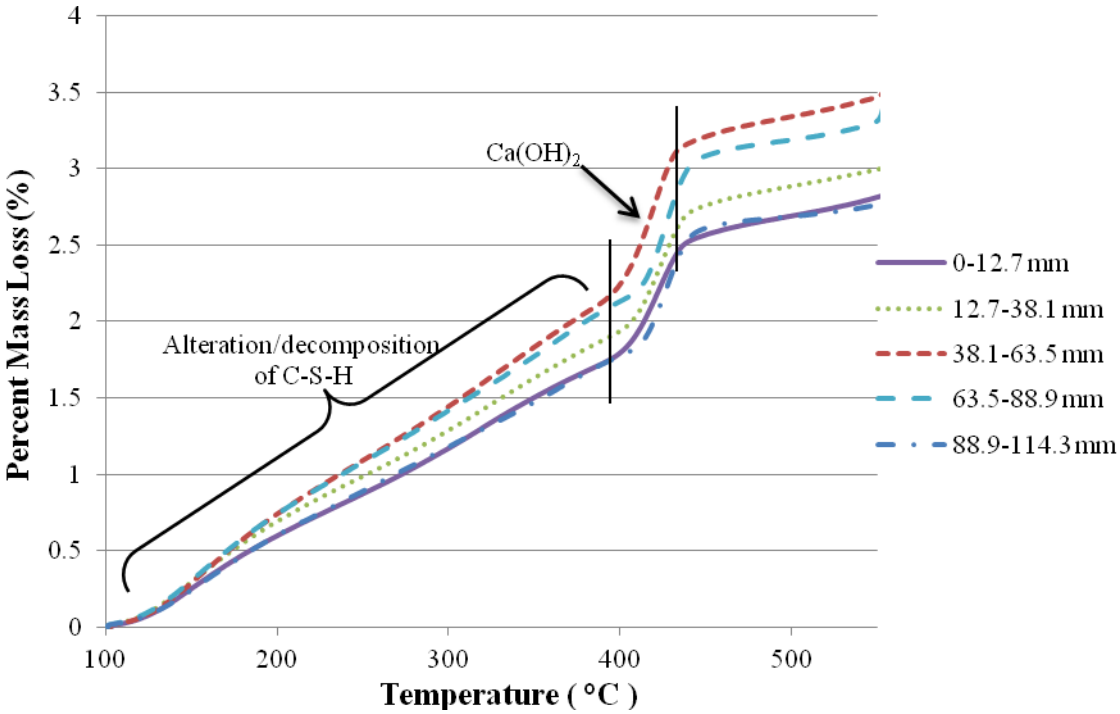

Figure 3.53: TGA for 0.6 m (2 ft) above high tide

The results of TGA on the high tide region are shown in Figure 3.54. The samples from 12.7 mm (0.5 in.) and farther into the section are consistent with the 2.74 m and 0.6 m (9 ft and 2 ft) above high tide samples. There is a consistent mass loss due to degradation of Portlandite present. The surface interval sample does not show an appreciable mass loss due to Portlandite degradation. This is not in complete agreement with XRD results, which suggested a small amount of Portlandite was present compared to the other increments tested at the depth. The TGA data may be more accurate due to the test giving quantitative characterization of phases present and being more sensitive to small amounts of phases present.

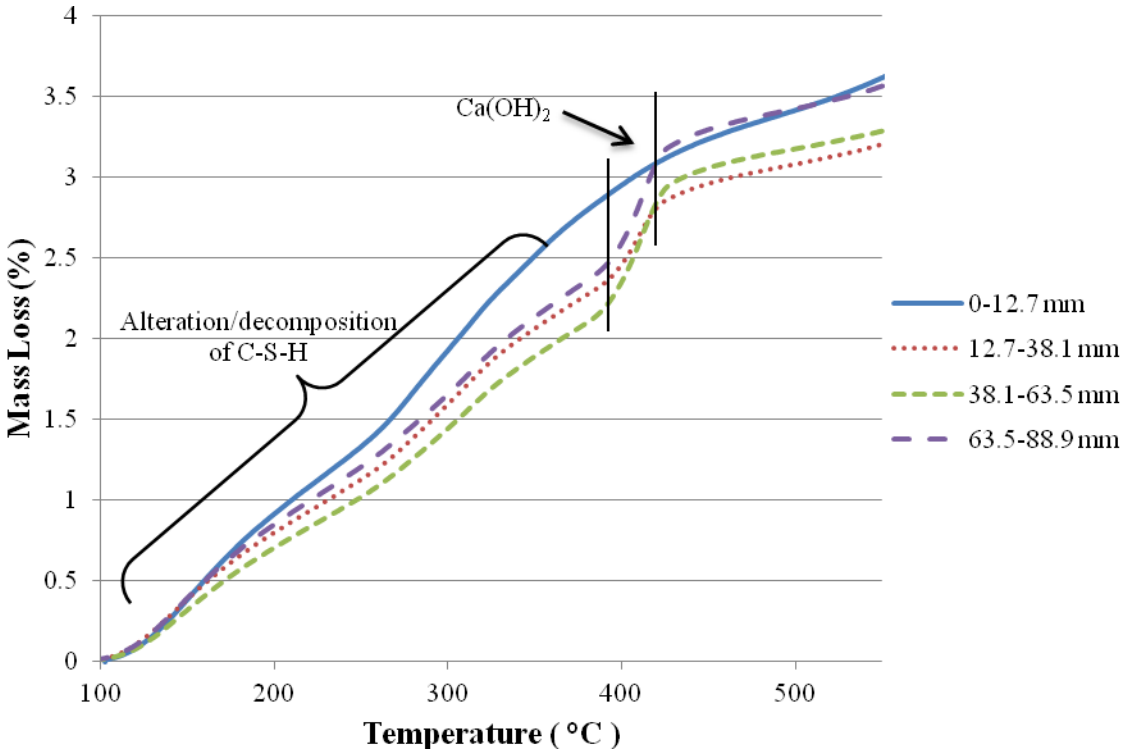

Figure 3.54: TGA for high tide region

The TGA results for 1.52 m and 3.66 m (5 ft and 12 ft) below high tide are shown in Figure 3.55 and 3.56, respectively. The surface interval on both data sets showed a decreased rate of mass loss between 100˚C and 400˚C than samples farther into the cross-section and at unsubmerged depths. This suggests that C-S-H was lost on the surface of the piles, most likely due to sulfate attack and carbonation. Additionally, the outer 38.1 mm (1.5 in.) of both samples showed an absence of Portlandite. This is consistent with XRD results for these depths. Additionally, the mass loss during the degradation of Portlandite decreased from the loss observed in 2.74 m (9 ft) above high tide samples, suggesting a decreased amount present. These results are consistent with the damage patterns that would occur with sulfate attack.

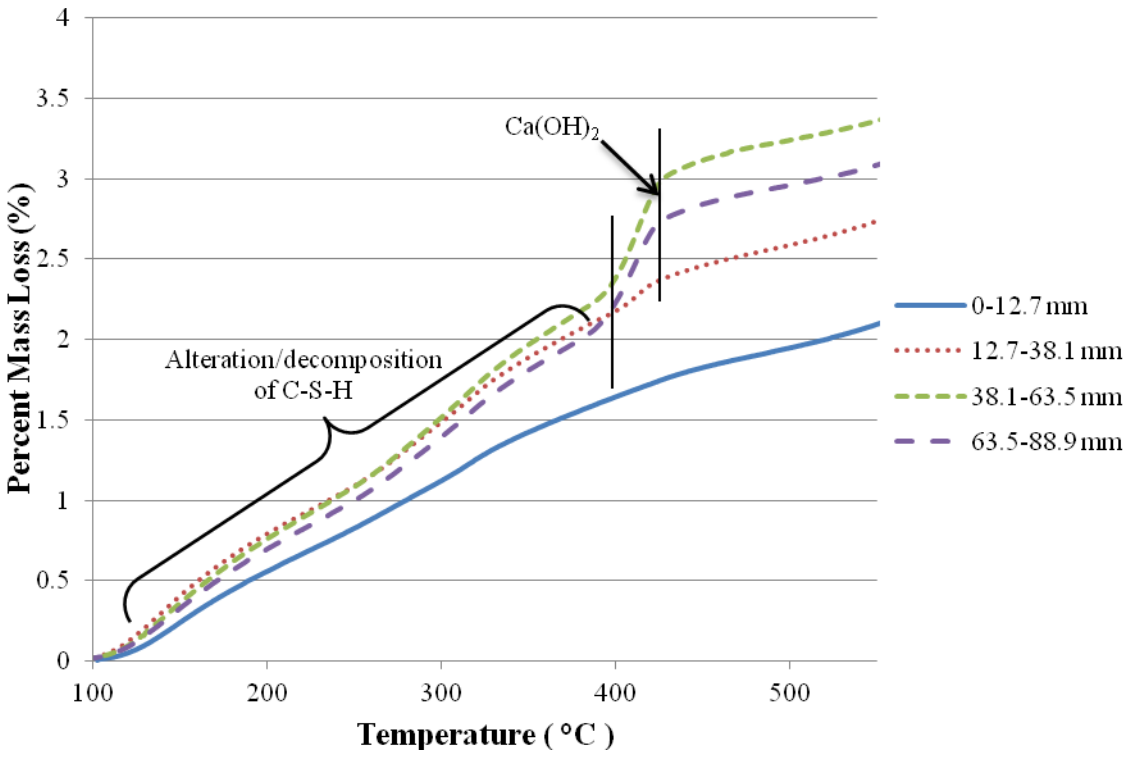

Figure 3.55: TGA for 1.52 m (5 ft) below high tide

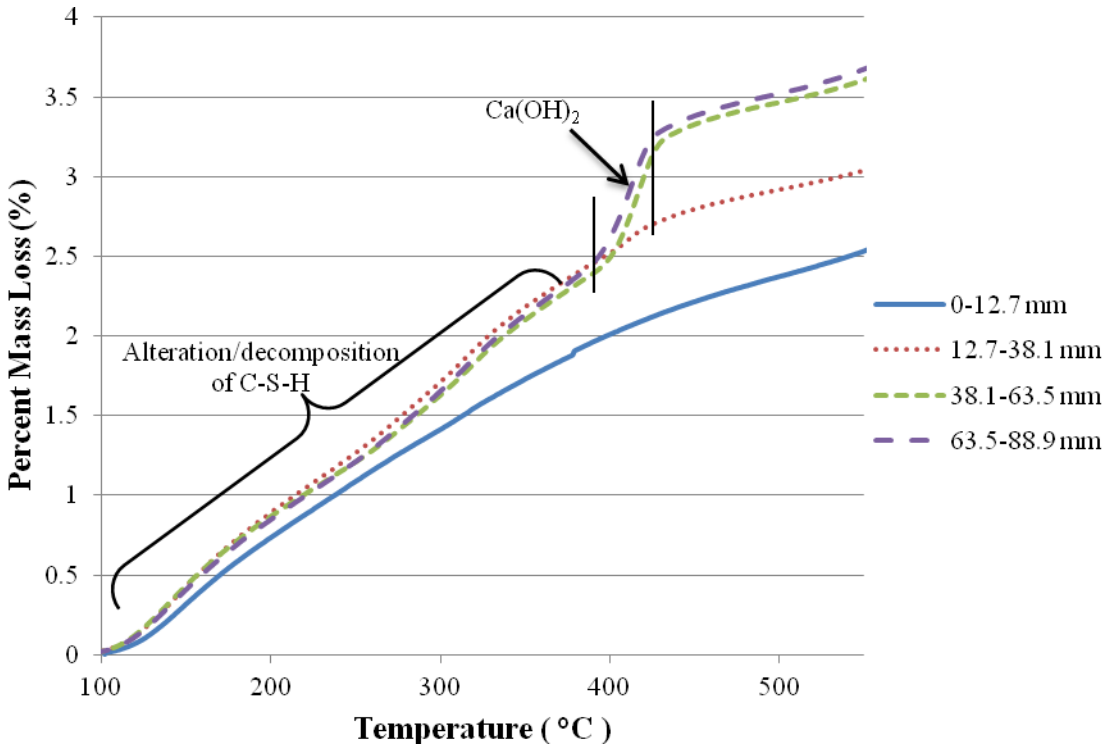

Figure 3.56: TGA for 3.66 m (12 ft) below high tide

3.3.6 Conclusions, Sulfate Attack

The piles from the I-95 at Turtle River Bridge exhibited several characteristics of sulfate attack. The submerged regions of the piles showed an absence of calcium hydroxide near the surface, and the presence of gypsum and ettringite. This result is consistent with sulfate attack, which would lead to a decrease in calcium hydroxide near the surface, and the presence of ettringite and gypsum. Additionally, TGA suggested a decrease in C-S-H near the surface that is also consistent with carbonation and which would cause decreased compressive strength. Testing of cores for compressive strength showed a decrease of 45% near the surface of the pile in the submerged regions. The use of a ASTM C 150 (2009) Type I cement, an ordinary rather than sulfate-resisting cement,

and a w/c of 0.50 could have allowed the sulfates from the surrounding water to ingress into the section over time and cause the extensive damage found.

3.4 Biodeterioration

There have been few reported cases of biological attack on coastal concrete structures. Here, a visual inspection and microscopic analysis techniques were used to characterize the biological attack on the piles.

3.4.1 Visual Inspection of Damage

A visual inspection was performed on the submerged region of the piles. No significant deterioration was visible until after cleaning the marine growth off of the surface of the piles. After removal of biological growth, large amounts of surface damage were visible. The damage, as seen in Figure 3.57, consisted of large pits on the surface of the piles. The damage was more pronounced along the corners of the piles, where the presence of boreholes and spalling were present. The pits occurred where coarse aggregate had been present on or near the surface of the piles.

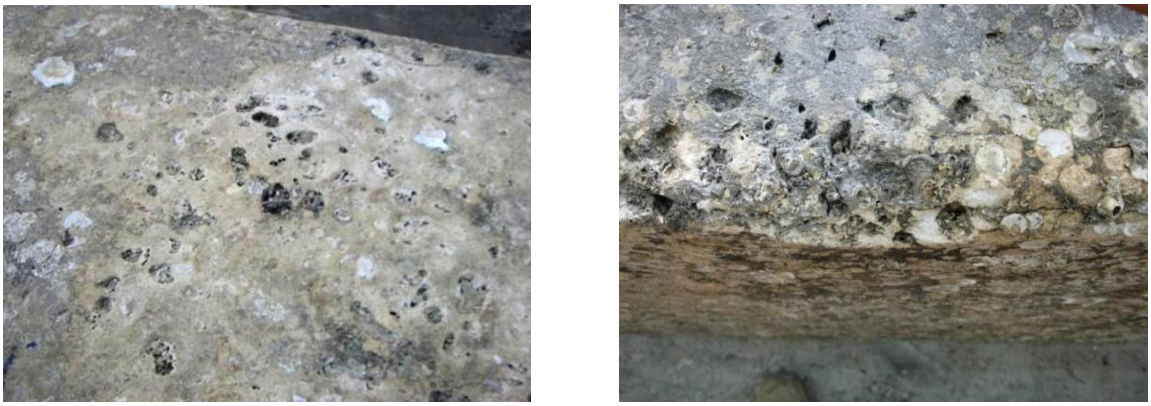

(a) (b)

Figure 3.57: Surface damage to concrete piling

Cores taken in the submerged region showed extensive damage to aggregate within 25.4 mm (1.0 in.) of the surface of the piles, as shown in Figure 3.58. Boreholes were present in aggregate near the surface in over 70% of cores taken. Damage was observed at over 25.4 mm (1 in.) depth into the section.

(a) (b)

Figure 3.58: Boreholes in limestone aggregate of cores

The damage pattern observed visually was consistent with reported descriptions of Cliona borings on limestone and coral. A reported case of boring sponge attack was reported in Jamaica due to *Cliona lampa* (Scott, et al., 1988). The sponges burrowed through the limestone aggregate of concrete masonry blocks. The damage was primarily at the corners, and irregular shaped bore holes occurred in the aggregate. The sponges use etching secretions to penetrate calcium carbonate and form the boreholes (Nicol and Reisman, 1976). The genus *Cliona* sponges leave silicate spicules near the surface of their borings. The length of the spicules varies by species but is typically between 200 μm to 400 μm (Zea and Weil, 2003). Figure 3.59 shows spicules from *Cliona caribbaea*.

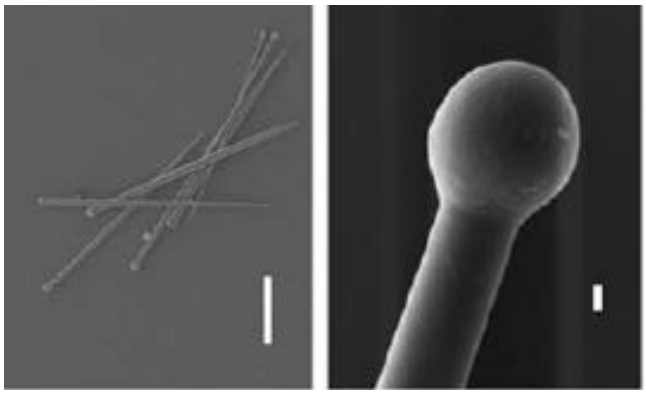

Figure 3.59: Spicules of *Cliona caribbea* (Zea and Weil, 2003)

There have been reports of *Cliona* sponges at Gardiner's Island, New York (Nicol and Reisman, 1976), along the coast of Virginia (Hopkins, 1962), Corpus Christi, Texas (Miller, et al., 2010), and off the coast of Jamaica (Scott, et al., 1988). Studies on the erosion rate of the sponge show that the rate may exceed 1 mm (0.04 in.) per year of ingress in solid limestone (Neumann, 1966). The rate of biological degradation of the limestone aggregate in these piles, > 25.4 mm (1 in.) in 35 years, is consistent with the

rate of attack measured by Neumann (1966) for *Cliona* on solid limestone. The boring sponge is shown in Figure 3.60 on a coral reef.

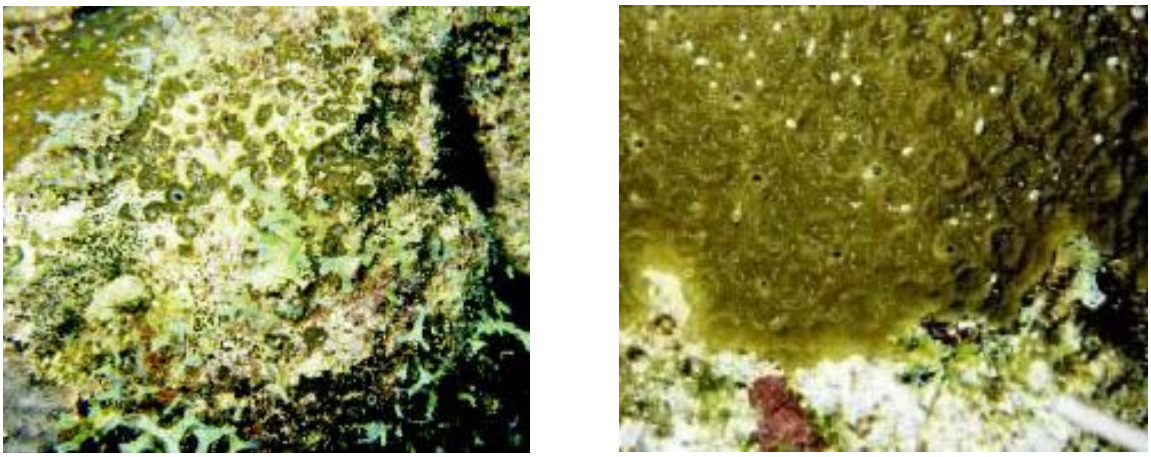

(a) (b)

Figure 3.60: *Cliona caribbaea* boring sponge (Zea, 2003)

3.4.2 Microscopy Characterization

Further investigation of the boreholes using environmental scanning electron microscopy at (ESEM) revealed the presence of rod-like structures. Energy dispersive x-ray analysis (EDS) of the rod-like structures revealed them to be highly silicate in composition. The rod-like structures inside of a borehole in the aggregate are shown in Figure 3.61, and the corresponding EDS spectrum is shown in Figure 3.62.

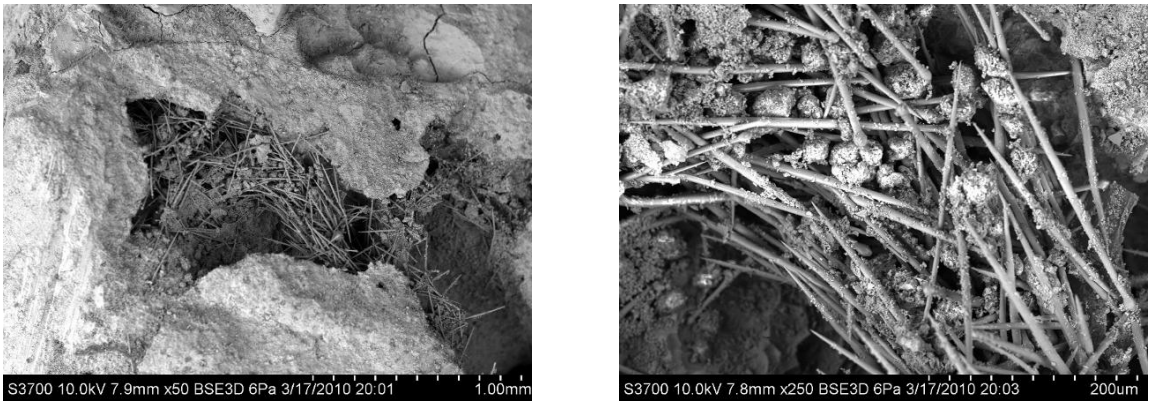

(a) (b)

Figure 3.61: (a,b) Silicate rod-like structures inside of boreholes through aggregate (Courtesy of Robert Moser)

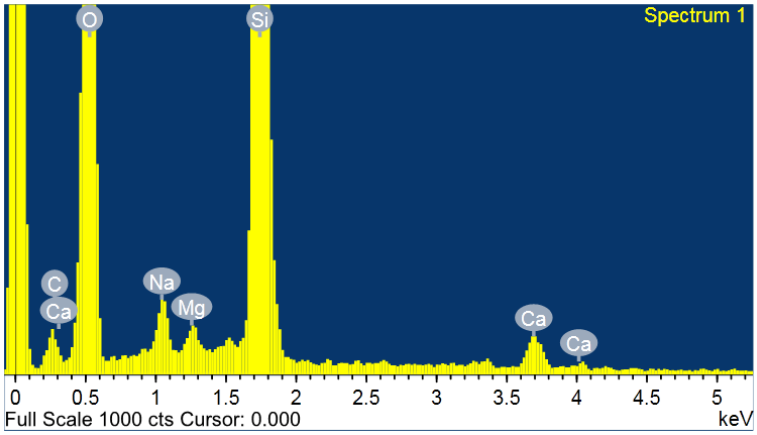

Figure 3.62: EDS spectrum of rod-like structures (Courtesy of Robert Moser)

Characterization of the limestone aggregate by EDS showed that the aggregate was composed primarily of calcium carbonate, although some aggregates were calcium magnesium carbonate, as expected. The types of calcite present were in agreement with XRD results. The composition of the aggregate suggests it is a Pleistocene limestone that is commonly found in southern Florida and the Bahamas.

Morphological and chemical comparison suggests that the rod-like structures resemble the siliceous spicules of *Cliona* boring sponges. The bioerosion patterns were similar to those reported by Scott (1988) in submerged concrete structures in Jamaica subjected to bioerosion from *Cliona caribbaea*. The patterns suggest that boring sponges are the most likely source of this form of damage to the piles. Further research is needed to better understand how the boring sponge damages the aggregate and to develop mitigation techniques for preventing damage in new construction.

3.5 Conclusions

3.5.1 Summary of Results

The forensic investigation of the I-95 at Turtle River Bridge piles revealed extensive damage from multiple deterioration mechanisms. Chloride-induced corrosion of the prestressing strands in the splash and tidal zones of the piling had induced cracking and delamination of the cover concrete as well as a loss of steel cross-section. The level of ingress of chloride ions suggested that the concrete was inadequate to provide 100+ year service life in the marine environment. Additionally, severe deterioration of the concrete due to sulfate attack and carbonation occurred in the submerged regions of the piles. A loss of over 40% of the compressive strength near the surface of the piles occurred due to loss C-S-H and the formation of ettringite and gypsum. Also, in the submerged regions of the piles, extensive damage to the coarse aggregate had occurred. This damage was likely caused by the presence of *Cliona* boring sponges. The piles exhibited extensive damage that led to the discovery of unexpected threats to bridge

substructures in marine environments, and the study emphasized the need for adequate protection from known environmental hazards.

3.5.2 Future Research Topics and Recommendations

The forensic investigation of the damage to the piles from the I-95 at Turtle River Bridge indicated a need for research in several areas as follows: (1) the development of high performance, normal strength concretes capable of withstanding sulfate attack, carbonation and chloride ingress to ensure service lives exceeding 100+ years while also meeting strength and design criteria necessary for precast concrete applications; (2) the development and implementation of corrosion -resistant metallurgies possessing the mechanical properties necessary for use as prestressing strand; and (3) the biological attack on piles needs to be investigated, and a foundation of knowledge on the species causing attack, the rate and effects of their ingress, as well as methods of preventing and mitigating damage to existing piles need to assessed.

The forensic investigation also demonstrated a need for changes in the construction materials used. First, eliminate the use of calcium carbonate-based (Limestone) aggregate to prevent a large source of nutrients for the biological life that attacked the surface of the piles. The use of limestone powder in cement has not yet been examined, but may also provide a source of nutrients for the biological life. Second, use an ASTM C 150 (2009) Type II or ASTM C 1157 (2004) Class MS cement in place of an ASTM C 150 (2009) Type I or III cement to mitigate the risk of sulfate attack on future concrete structures as recommended by ACI Committee 201 (2008). An ASTM C 150 (2009) Type III Cement can be used in conjunction with supplementary cementitious

materials or admixtures if the expansion for the ASTM C 1012 (2009) test meets the limits given by ACI Committee 201 (2008). Future research to be performed will develop draft design recommendations and concrete specifications to mitigate damage from the marine environment and allow for longer service lives.

CHAPTER 4

MIXTURE DESIGN DEVELOPMENT AND MECHANICAL PROPERTIES

4.1 Development of Concrete Mixture designs

High performance marine concrete (HPMC) mixture designs were developed with the goal of providing a 100+ year service life in Georgia's marine environment. This was performed by using the results of the forensic report (Chapter 3), coast trip report (Appendix A), and GDOT personnel interviews (Appendix B) to determine the durability characteristics and requirements that must be met to achieve this goal.

4.1.1 Concrete Mixture design

The mixture designs investigated were developed to resist carbonation, sulfate attack, and to mitigate chloride induced corrosion of reinforcement as the primary durability concerns. Additionally, from the GDOT personnel interviews it was recognized that the presence of cracking should be considered for its effect on the above degradation mechanisms. The mixture designs developed and tested represent the current concretes being used by the Georgia Department of Transportation (GDOT), a mixture design meeting the minimum ACI 201.2R-10 (2010) durability requirements, and new mixture designs which may be capable of meeting the durability requirements for a 100+ year life-span in an aggressive marine environment.

Mixture designs were proportioned using the ACI 211.4R-08 (2008) procedure. The ACI 211.4R-08 (2008) process for developing mixture designs in presented in Figure 4.1. The ACI 211.4R-08 (2008) was used in place of the ACI 211.1-91 (1991) document due to the required strength, f_{cr}', of 42.7 MPa (6,200 psi) exceeding the values given for

proportioning when following the recommendations Table 5.3.2.2 in ACI 318R-11 (2011) for a design strength of 34.5 MPa (5,000 psi), which is the minimum strength requirements for precast prestressed concrete piles in Georgia at 56 days (GDOT, 2004).

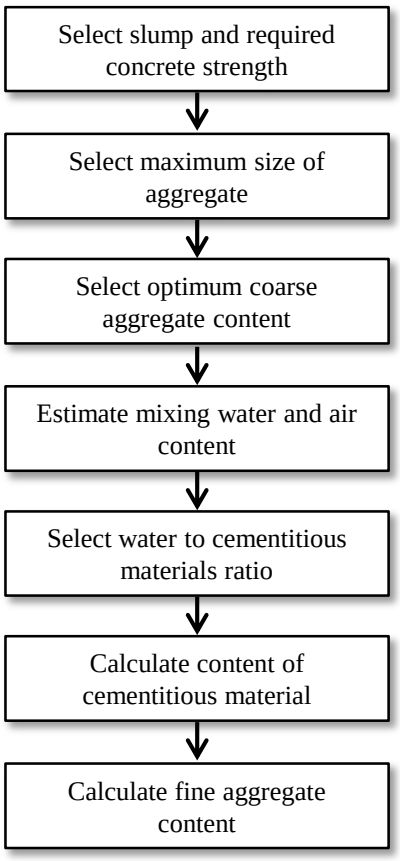

Figure 4.1: ACI 211.4R-08 (2008) Mixture design procedure

Mixture designs are labeled with the notation of SCM – replacement level was used, unless a cement type other than an ASTM C 150 (2009) Type II cement was used, where the type of cement was denoted by T3 or T5 for a Type III or V cement before listing the SCM's present. SCM's were abbreviated with the following notation: fly ash (F), slag (S), silica fume (SF), and metakaolin (MK).

The T2 mixture design meets the minimum ACI 201.2R-10 (2010) durability requirements for Georgia's marine environment was developed by selecting a 50.8-101.6

mm (2-4 in.) slump. Next, a 19 mm (3/4 in.) maximum-size coarse aggregate (MSA) was selected based upon the 42.7 MPa (6,200 psi) design strength and locally available aggregate gradations. Next, a coarse aggregate content of 0.72 was selected. A water content of 181 kg/m^3 (305 lb/yd^3) was obtained based upon the MSA and desired slump. The water-to-cement ratio of 0.40 was selected based upon the durability requirements for a seawater exposure which meets the corrosion protection of reinforcement category C2. An ASTM C 150 (2009) Type II cement was selected to meet sulfate exposure requirements for an S1 exposure. Georgia's marine environment requires an S1 or S2 protection level depending upon the distance inland, as discussed in Appendix H. The final mixture design for T2 is given in Table 4.1.

Table 4.1: ACI durability criterion mixture design (T2)

Material	**Weight (kg/m^3)**	**Weight (lb/yd^3)**
Water	181	305
Type I/II cement	452	763
Natural Sand	650	1096
#67 Stone	1130	1905

Table 4.2 gives the mixture design for a typical GDOT high performance concrete (T3-F15) currently being used for piles in the state of Georgia, which contains both an air entraining admixture and a super plasticizer. This mixture design was provided by GDOT.

Table 4.2: Current HPC mixture design (T3-F15)

Material	Weight (kg/m^3)	Weight (lb/yd^3)
Water	182	307
Type I/II cement	468	789
Type F Fly Ash	83	140
Natural Sand	595	1003
#67 Stone	952	1606

For all potential HPMC mixture designs a high range water reducing admixture (HRWRA) was utilized, therefore an initial slump of 25.4-50.8 mm (1-2 in.) was selected before the addition of the HRWRA. Next, a 19 mm (3/4 in.) MSA was selected since the required strength was below 62 MPa (9,000 psi), and is a readily available size in Georgia. Next, a coarse aggregate content of 0.72 was selected based upon the MSA. A water content of 169 kg/m^3 (285 lb/yd^3) was selected based upon the MSA and desired slump. Lastly, a w/cm of 0.30 was selected based upon previous findings in the literature for durability requirements. From the literature review (Chapter 2) it was found that decreasing the water-to-cementitious materials ratio and the addition of supplementary cementitious materials (SCM's) increased the durability of concrete by creating a denser microstructure. Table 4.3 shows the base mixture design investigated for potential HPMC.

Table 4.3: Base experimental mixture design

Material	Weight (kg/m^3)	Weight (lb/yd^3)
Water	169	285
Binder	563	950
Natural Sand	514	866
#67 Stone	1130	1905

This research will investigate the use of binary and ternary blended cements containing slag, Class F fly ash, silica fume, and metakaolin with an ASTM C 150 (2009) Type II moderate sulfate resistance cement. The binder compositions investigated are given in Table 4.4. The dosages of air-entraining and high-range water reducers were determined during mixing to attain desired workability of a slump of between 2 and 7 in. and air content values of between 3.5 to 6.5%. Five of the mixture designs were investigated for the effect of self-healing capabilities on the ingress of chlorides. These mixture designs are designated with a check mark by their binder compositions.

Table 4.4: Binder compositions for experimental mix designs

Mix ID	Cement (%)	Cement Type	Fly Ash (%)	Slag (%)	Silica Fume (%)	Metakaolin (%)	w/cm	Self-Healing
T2	100	II	0	0	0	0	0.4	-
T3-F15	85	III	15	0	0	0	0.33	✓
TypeII	100	II	0	0	0	0	0.3	✓
F25	75	II	25	0	0	0	0.3	✓
F25-SF5	70	II	25	0	5	0	0.3	-
F25-MK5	70	II	25	0	0	5	0.3	-
F25-SF10	65	II	25	0	10	0	0.3	-
F25-MK10	65	II	25	0	0	10	0.3	-
S35-MK5	60	II	0	35	0	5	0.3	✓
S50-MK5	45	II	0	50	0	5	0.3	✓
S35-SF5	60	II	0	35	5	0	0.3	-
S50-SF5	45	II	0	50	5	0	0.3	-

4.1.2 Raw Material Properties

4.1.2.1 Cement

Oxide analysis and particle size distributions for each cement utilized in the project were measured. An ASTM C 150 (2009) Type II cement and Type III cement were provided by National Cement out of the Lawrenceville, Georgia terminal. An ASTM C 150 (2009) Type V cement was acquired from TXI's Riverside, California plant. Table 4.5 presents the results of the oxide analysis on the cement samples and the Bogue potential compositions.

Table 4.5: Oxide analysis and Bogue compositions of cement samples

Sample		Type II OPC	Type III OPC	Type V OPC
SiO_2	%	20.51	20.80	20.81
Al_2O_3	%	4.65	4.96	4.30
Fe_2O_3	%	3.35	3.30	4.14
CaO	%	62.60	63.74	63.52
MgO	%	2.81	1.06	1.40
SO_3	%	2.99	3.46	2.55
LOI	%	1.85	1.50	2.08
Na_2O	%	0.07	0.11	0.22
K_2O	%	0.75	0.53	0.44
TiO_2	%	0.28	0.26	0.20
P_2O_5	%	0.04	0.14	0.15
MnO	%	0.05	0.03	0.12
SrO	%	< 0.01	< 0.01	< 0.01
C_3S	%	54	54	58
C_2S	%	18	19	16
C_3A	%	6.7	7.6	4.4
C_4AF	%	10	10	13
Gypsum	%	6.4	7.5	5.5

Each of the cements met their respective ASTM C 150 (2009) limits for each component of the Bogue composition. The C_3A content of the Type III cement was

extremely low, in the range of what is expected from a Type I/II. The C_3A content of the Type V mix was 4.4%, which is slightly lower than the limit of 5%.

The particle size distribution of each cement and the Blaine fineness is given in Table 4.6. The particle size distribution was determined using a wet dispersion particle size analysis. The particle size was measured using a laser diffractometer with the particles in suspension in isopropyl alcohol. The Type III cement had the smallest median particle size and highest fineness, as expected. The gradation curves are shown in Figure 4.2. The gradations for the Type II and Type V cements were similar, with an average particle size of 14.2 and 13.83 μm, respectively.

Table 4.6: Particle size distributions and Blaine Finess Values (1μm = 39.4 microinches)

	Type II %	**Type III %**	**Type V %**
<1μm	1.83	2.55	2.15
<1.5 μm	3.29	4.40	4.14
<2 μm	4.62	5.99	6.03
<3 μm	7.29	9.27	9.89
<4 μm	10.36	13.21	14.06
<6 μm	18.12	23.15	22.79
<8 μm	26.77	34.01	30.97
<12 μm	42.19	52.99	44.46
<16 μm	56.09	67.70	56.24
<24 μm	77.62	85.04	74.96
<32 μm	88.69	91.81	86.18
<48 μm	95.88	96.14	95.04
<64 μm	97.68	97.47	97.58
<96 μm	98.71	98.45	98.94
<128 μm	99.06	98.86	99.30
<192 μm	99.38	99.26	99.55
median μm	14.20	11.31	13.83
Blaine Value (m^2/kg)	433.90	630.10	429.60

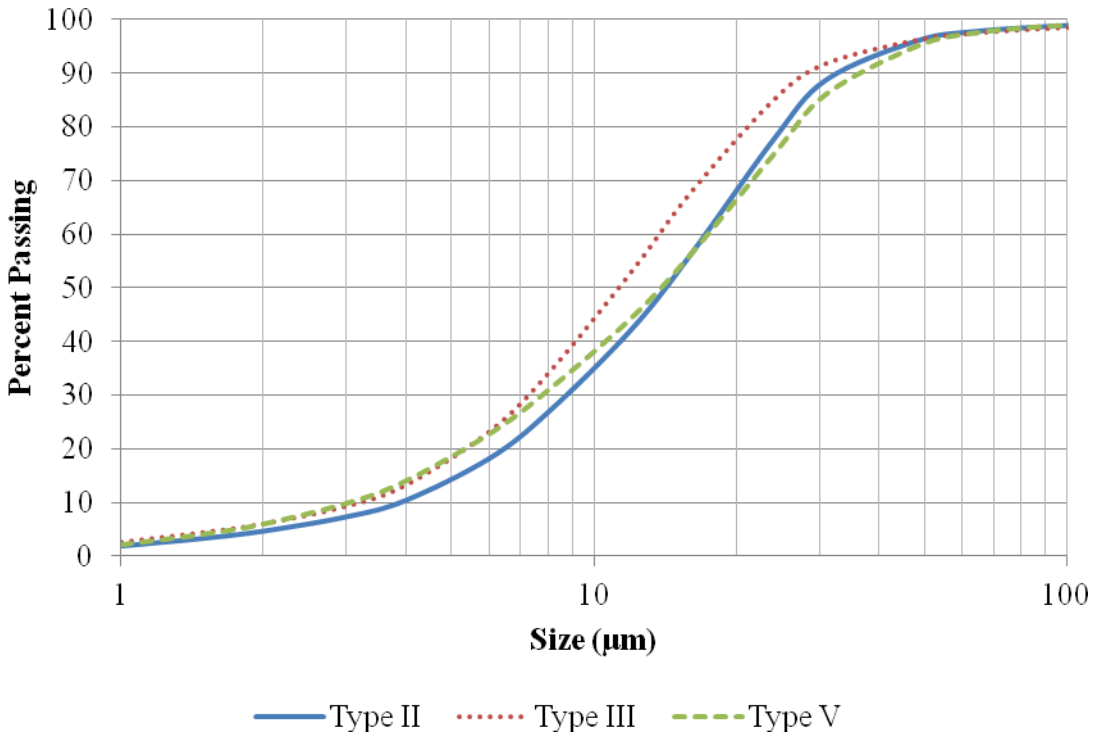

Figure 4.2: Particle size distributions for cement samples

4.1.2.2 SCM's

Oxide analysis and particle size distributions were performed on all four SCM's utilized for mixture designs. Table 4.7 shows the results of the oxide analysis. The silica fume was composed of over 94% SiO_2. The slag was composed primarily of four phases: SiO_2, Al_2O_3, CaO, and MgO. The fly ash was composed primarily of SiO_2 and Al_2O_3 as was the metakaolin.

Table 4.7: Oxide analysis for SCM samples

Sample		Silica Fume	Slag	Fly Ash	Metakaolin
SiO_2	%	94.43	38.95	55.95	51.28
Al_2O_3	%	0.37	8.04	29.39	44.27
Fe_2O_3	%	0.09	0.41	4.91	0.40
CaO	%	0.59	37.23	1.05	0.08
MgO	%	0.37	12.10	0.86	0.17
SO_3	%	0.16	1.83	0.29	0.13
LOI	%	3.00	-0.24	2.69	0.96
Na_2O	%	0.08	0.28	0.29	0.41
K_2O	%	0.68	0.42	2.16	0.11
TiO_2	%	0.01	0.29	1.72	1.85
P_2O_5	%	0.12	0.01	0.48	0.29
MnO	%	0.03	0.38	0.02	0.01
SrO	%	< 0.01	0.05	0.13	0.01

The particle size distribution of each SCM is given in Table 4.8. The gradation curves are shown in Figure 4.3. From the gradations, the average particle size of metakaolin was smaller than any other component. The silica fume had the largest particle size due to being a densified powder.

Table 4.8: Particle size analysis of SCM samples (1 µm = 39.4 microinches)

	Silica Fume %	**Metakaolin %**	**Slag %**	**Fly Ash %**
<1µm	0.00	3.62	2.46	0.91
<1.5 µm	0.02	9.96	5.51	1.65
<2 µm	0.12	17.73	8.40	2.30
<3 µm	0.40	32.12	13.98	3.47
<4 µm	0.79	42.86	19.69	4.71
<6 µm	1.71	57.31	31.42	7.84
<8 µm	2.77	66.84	42.65	12.01
<12 µm	5.21	77.89	61.80	21.95
<16 µm	8.24	83.36	76.18	32.03
<24 µm	15.51	87.96	90.58	47.36
<32 µm	23.12	89.87	95.44	57.66
<48 µm	38.35	91.91	98.44	72.08
<64 µm	50.68	93.35	99.34	81.83
<96 µm	64.65	95.64	99.87	92.11
<128 µm	73.34	97.25	99.99	96.16
<192 µm	87.09	98.74	100.00	98.47
median µm	62.93	4.87	9.43	25.80

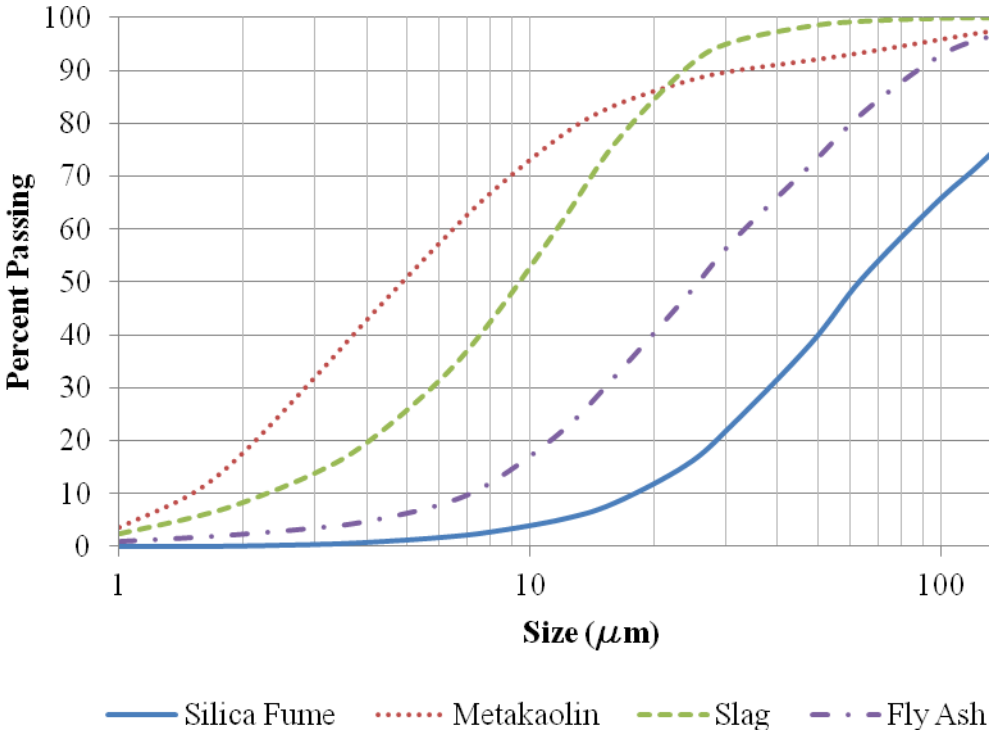

Figure 4.3: Particle size distributions for SCM samples

4.1.2.3 Fine Aggregate

A natural sand from Sand-Rock Transit in Atlanta, Georgia was used as the fine aggregate in the casting and development of mixture designs. The gradation curve for the sand is shown in Figure 4.4. The fineness modulus was found to be 2.69. The absorption capacity was found to be 1.01% with a specific gravity of 2.597 when at the saturated surface dry (SSD) condition.

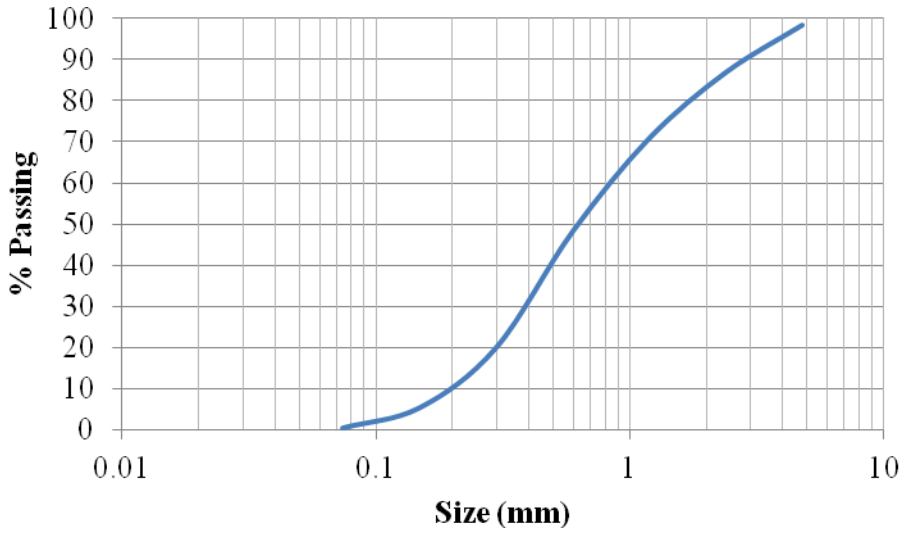

Figure 4.4: Gradation curve of natural sand (1 in. = 25.4 mm)

4.1.2.4 Coarse Aggregate

A crushed granite coarse aggregate from Vulcan's Lithonia, Georgia quarry was used in the casting and development of mixture designs. The aggregate had an absorption capacity of 0.40% and a specific gravity of 2.745 when at SSD moisture condition. The dry rodded unit weight (DRUW) was found to be 1,570 kg/m^3 (97.8 pcf).

4.1.3 Air Contents

GDOT currently requires an air content in HPC mixture designs of between 3.5 to 6.5%. The air content of each mixture design was determined by image analysis of polished sections of cut 102 mm x 203 mm (4 in. x 8 in.) concrete cylinders. Samples were cut with a wet saw and the surface polished by successively finer silicon carbide polishing papers with grit sizes of 60, 120, 250,320, 400, and 600. The time on each polishing paper was doubled from the previous as finer grits were used. After polishing, the sampling area was darkened and a calcium carbonate powder was wiped across the surface, filling the voids present. Samples were scanned at 1200 DPI using ImageJ. After scanning the images were binarized, causing the solid section to become black and the air voids white. Figure 4.5 (a) shows the scanned image, and Figure 4.5 (b) the binarized image for an F25 mixture design sample. The area fraction of the voids was obtained by summing the total area of white pixels (air voids) and dividing by the total dimension of the image.

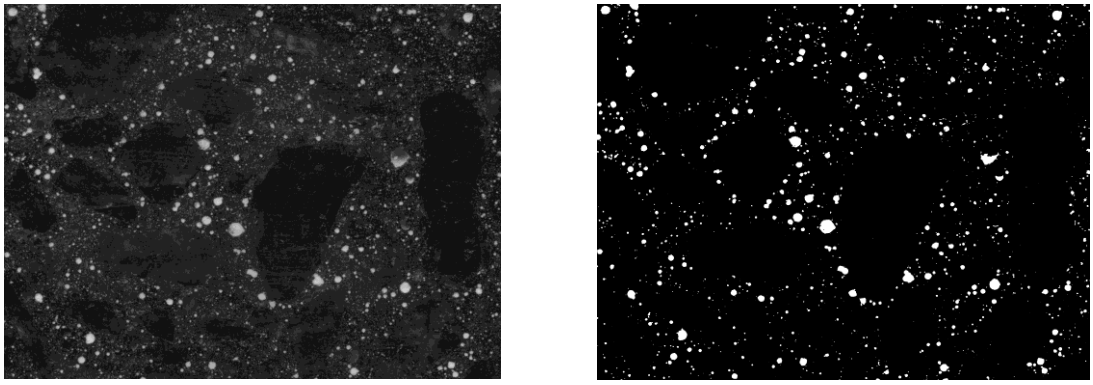

(a) (b)

Figure 4.5: F25 air void sample (a) scanner image and (b) binarized image

The air contents of each mixture design are given in Table 4.9. The current HPC mixture design used by Georgia (T3-F15) had an air content of 5.3%. The experimental mixture designs were dosed with the manufacturer recommended 29.6 mL (1 oz.) per

45.4 kg (100 lbs) of cementitious materials for Sika AEA-14 air entrainer. Only mixture designs F25 and S35-SF5 met the required air contents currently used by the state of Georgia. For the other mixture designs, further refinement of the air entrainer dosage is required if air contents in that range are desired for use with high performance marine concretes.

Table 4.9: Air contents of mixture designs

	Air Content (% Volume)
Type II	2.1
T3-F15	5.3
F25	4.8
F25-MK5	3.2
F25-MK10	2.3
F25-SF5	2.9
F25-SF10	2.8
S35-MK5	2.5
S50-MK5	2.8
S35-SF5	4.9
S50-SF5	3.0

4.2 Mechanical Property Characterization

4.2.1 Compressive Strength

The compressive strength of each mixture design was investigated. The compressive strength was measured in accordance with ASTM C 39 (2005) on 102 mm x 203 mm (4 in. x 8 in.) cylinders. Three cylinders from each mixture design were tested at 3, 28, and 56 days of age to determine the strength characteristics of each mix for precast use. Figure 4.6 shows the strength gain curves. All mixture designs had a compressive strength above 31 MPa (4,500 psi) at 3 days of age. Table 4.10 presents the compressive strengths and standard deviations at 3, 28, and 56 days.

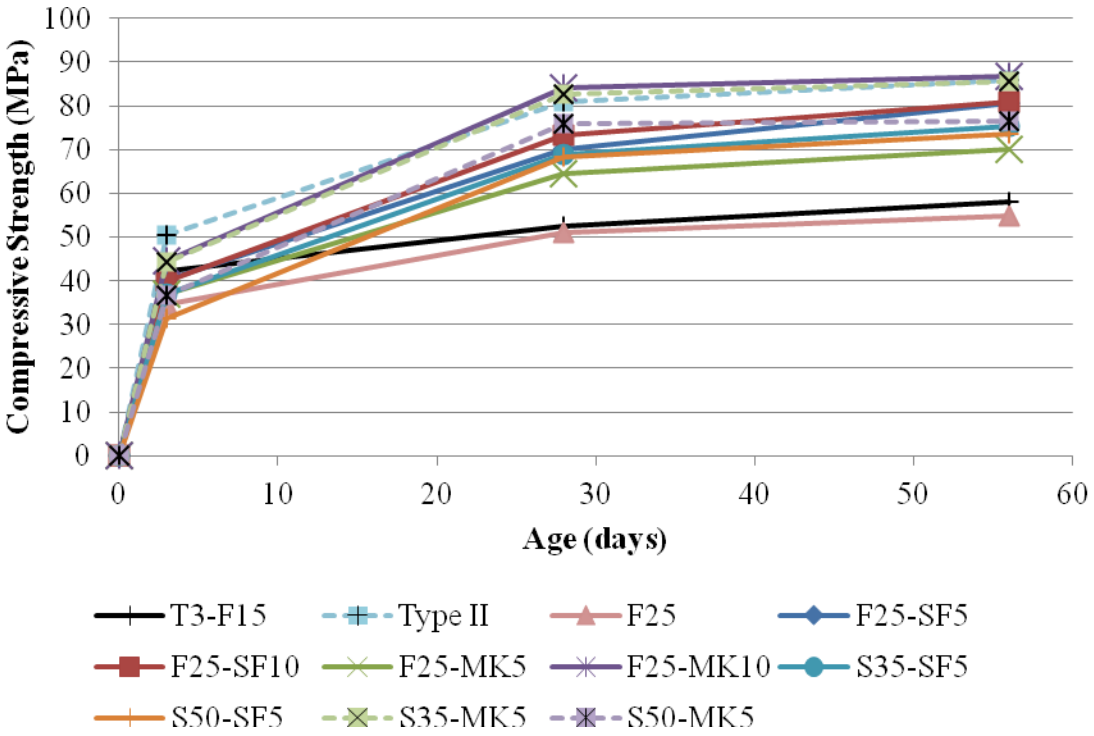

Figure 4.6: Compressive strength gain curves (1 ksi = 6.895 MPa)

Table 4.10: Compressive strength and standard deviations at 3, 28, and 56 days (1 ksi = 6.895 MPa)

	Compressive Strength (MPa)					
	3 -days		28-days		56-days	
Mixture Design	**Avg.**	**Std. Dev.**	**Avg.**	**Std. Dev.**	**Avg.**	**Std. Dev.**
Type II	50.5	0.8	81.0	3.6	86.0	3.3
T3-F15	42.3	1.1	52.6	2.7	58.1	0.5
F25	34.7	0.4	51.1	0.8	55.0	2.0
F25-MK5	36.9	1.6	64.5	1.7	69.9	1.5
F25-MK10	44.7	1.8	84.0	1.5	86.7	0.9
F25-SF5	40.2	0.7	70.1	2.1	80.7	0.6
F25-SF10	40.0	0.6	73.2	2.6	80.9	1.8
S35-MK5	44.3	1.4	82.8	1.9	85.5	2.5
S50-MK5	36.6	0.5	76.0	1.6	76.4	3.1
S35-SF5	37.1	1.2	68.9	1.6	75.2	2.7
S50-SF5	31.3	0.1	68.4	0.8	73.6	0.6

GDOT currently requires a compressive strength of 27.6 MPa (4,000 psi) for release of prestressing and a 34.5 MPa (5,000 psi) 56-day strength for mixture designs (GDOT, 2004). The longer a mix takes to develop the release strength, the longer it takes to produce each pile and increases the costs to the precast plant. All mixture designs met the release strength within three days and satisfied the 56-day requirement as well.

For precast applications, high early strength is desirable for a quick turnaround from casting to release. The current mixture design used by GDOT (T3-F15) had a 3-day strength of 42.1 MPa (6,100 psi), and two of the proposed high-performance marine concrete (HPMC) mixture designs exceeded this at 3-days, F25-MK10 and S35-MK5. Although the other mixture designs met the strength requirements, further refinement and analysis of early age strength gain and the effect of curing regimes may be needed to develop the release strength more rapidly.

4.2.2 Elastic Modulus

The elastic modulus of each mixture design was investigated in accordance with ASTM C 469 (2002). Figure 4.6 present the elastic modulus results for tests performed on three 152.4 mm x 304.8 mm (6 in. x 12 in.) cylinders at 56 days of age. The AASHTO (2007), ACI 363 (1997), and Rizkalla (NCHRP, 2007) estimation equations are also plotted in Figure 4.7. The ACI 363 (1997) estimator equation, which was developed for high-strength concrete, is in best agreement with the measured elastic moduli. Table 4.11 gives the measured elastic modulus and standard deviation for each mixture design at 56 days.

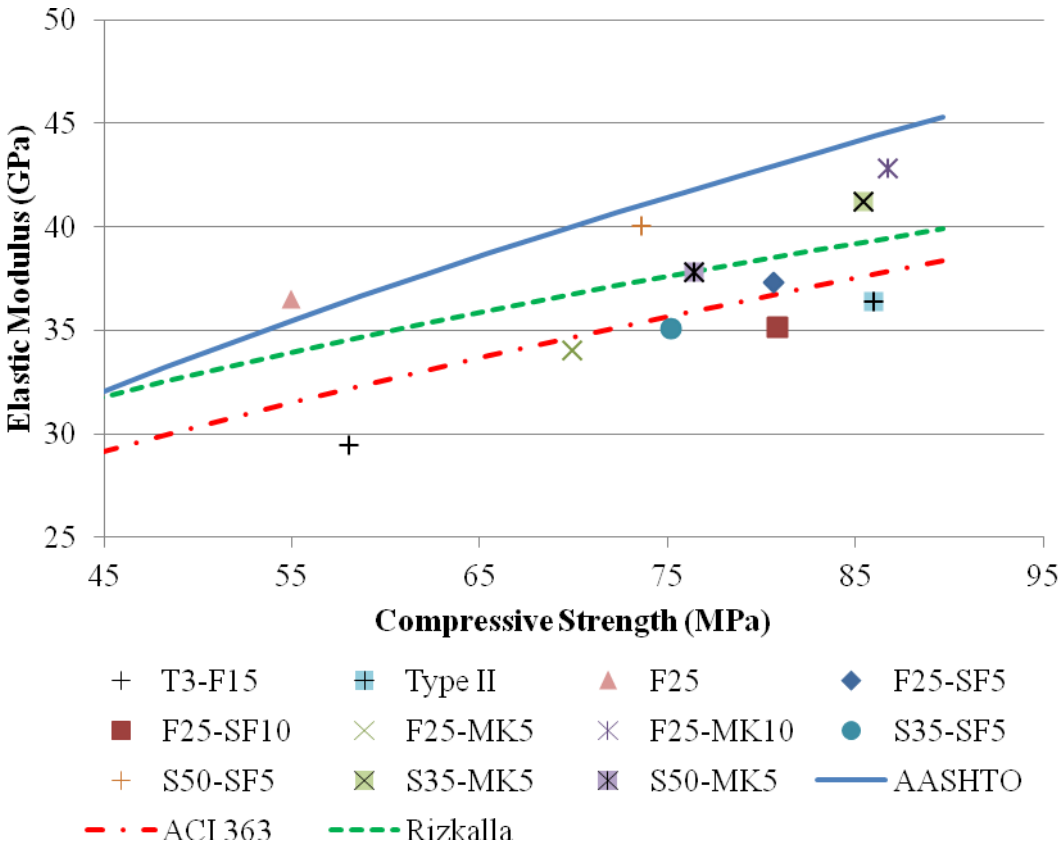

Figure 4.7: Elastic modulus vs. compressive strength and estimator equations (1 ksi = 6.895 MPa)

Table 4.11: Elastic modulus and standard deviation at 56-days (1,000 ksi = 6.895 GPa)

	Elastic Modulus (GPa)	
Mix Design	**Average**	**Std. Dev.**
Type II	36.4	0.5
T3-F15	29.5	2.1
F25	36.5	2.6
F25-MK5	34.1	1.8
F25-MK10	42.8	2.7
F25-SF5	37.3	1.3
F25-SF10	35.1	1.1
S35-MK5	41.2	2.3
S50-MK5	37.8	2.6
S35-SF5	35.1	0.6
S50-SF5	40.1	1.8

CHAPTER 5

CHLORIDE INGRESS RESISTANCE OF HIGH PERFORMANCE CONCRETE

5.1 Introduction

Chlorides from the surrounding marine environment are able to ingress into concrete over time through various transport mechanisms, as discussed in Chapter 2. The protective oxide film that forms on the surface of the steel in the alkaline concrete environment is compromised locally by the presence of a sufficient chloride concentration, and pitting corrosion can result. Pitting is a localized form of corrosion which initiates at defect sites in the passive film.

The corrosion of the prestressing steels leads to a loss of steel section. Additionally, the corrosion of steel leads to the formation of iron oxides which are less dense than the original steel and which occupy more volume. The formation of oxides causes tensile forces in the surrounding concrete and can lead to cracking and delamination of the cover concrete, as well as to rust staining on the surface of the piles. Damage to the cover can increase the rate of chloride ingress, promoting corrosion, and potentially leading to other forms of degradation of the concrete.

The cover concrete serves as a barrier to the ingress of chloride ions to the depth of the reinforcing steel. The rate of ingress is dependent upon the cover concrete's transport properties. The primary objective of this study was to develop and test the adequacy of potential HPMC mixture designs to provide a 100+ year service life in a

marine environment by protecting the embedded prestressing strand and mild reinforcement from chloride-induced corrosion.

5.2 Experimental Program

Twelve mixture designs were developed to determine the adequacy of current T3-F15 mix and potential HPMC mixture designs for providing adequate protection to chloride ingress. These mixture designs were presented in Chapter 4.

A series of experiments were performed to determine the resistance of each mixture design to chloride ingress. The chloride transport properties of each concrete mixture design were evaluated using a rapid migration test and a long-term ponding test. The chloride ingress resistance of each mixture design was determined using ASTM C 1202 (2007) Rapid Chloride Permeability Test (RCPT) at 56 days of age on two 50.8 mm (2 in.) thick slices of 101.6 mm (4 in.) diameter concrete cylinders.

The bulk diffusion test (ASTM C 1556, 2004) was run on each mixture design. Two 101.6 mm x 203.2 mm (4 in. x 8 in.) cylinders were cast and fog room cured for 28 days. Next, specimens were cut and the initial chloride content determined. Specimens were sealed on all but one surface using Sikadur 32 epoxy and then fully saturated in a lime-saturated water bath. After the saturation period, samples were placed in a sodium chloride solution (165 g/L) for 180 days. Profile grinding was performed on the sample after an exposure period of 180 days. The total chloride concentration of each increment was determined in accordance with ASTM C 1152 (2004). Table 5.1 shows the grinding increments utilized. A regression analysis of the results to Fick's Second Law (Eq. 2.2) was performed for the determination of an apparent diffusion coefficient.

The results of the bulk diffusion testing were used to perform service life modeling of each mixture design. Life 365 (Ehlen, 2009) and Concrete Works (Concrete Durability Center, 2007) were used to perform service life estimates for each mixture design.

Table 5.1: Profile grinding increments

Increment	Depth, mm (in.)	
1	0-1	(0-0.039)
2	1-2	(0.039-0.079)
3	2-3	(0.079-0.118)
4	3-4	(0.118-0.157)
5	4-5	(0.157-0.197)
6	5-6	(0.197-0.236)
7	6-8	(0.236-0.315)
8	8-10	(0.315-0.394)

5.3 Results and Discussion

5.3.1 Rapid Chloride Permeability

The rapid chloride permeability test set-up is shown in Figure 5.1. ASTM C 1202 (2007) suggests using the rating system shown in Table 5.2 when comparing mixture designs. GDOT currently requires mixture designs for marine exposure to pass a 2,000 coulomb limit (GDOT, 2004). This limit corresponds to a rating of Low or better using Table 5.2.

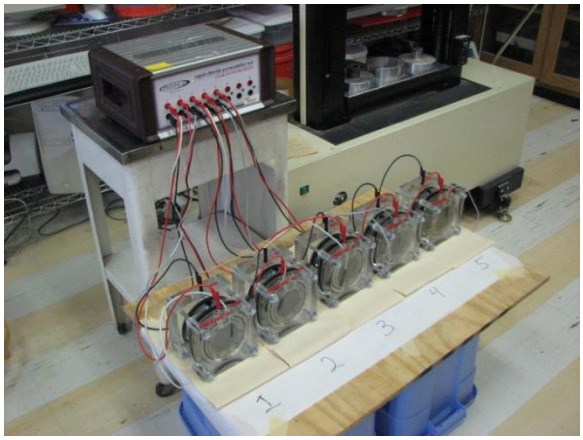

Figure 5.1: Rapid chloride permeability set-up

Table 5.2: Chloride ion penetrability based on charge passed (ASTM C 1202, 2007)

Charge Passed (coulombs)	Chloride Ion Penetrability
> 4,000	High
2,000-4,000	Moderate
1,000-2,000	Low
100-1,000	Very Low
<100	Negligible

Figure 5.2 shows the results of the RCPT testing. All mixture designs met the current GDOT limit. All ternary blended cement mixture designs had less than 700 coulombs passed, which is considerably lower than the 1,500 coulombs measured on the current T3-F15. This suggests that the ternary blend cements provide significant improvement in chloride resistance to the mixture designs currently in use.

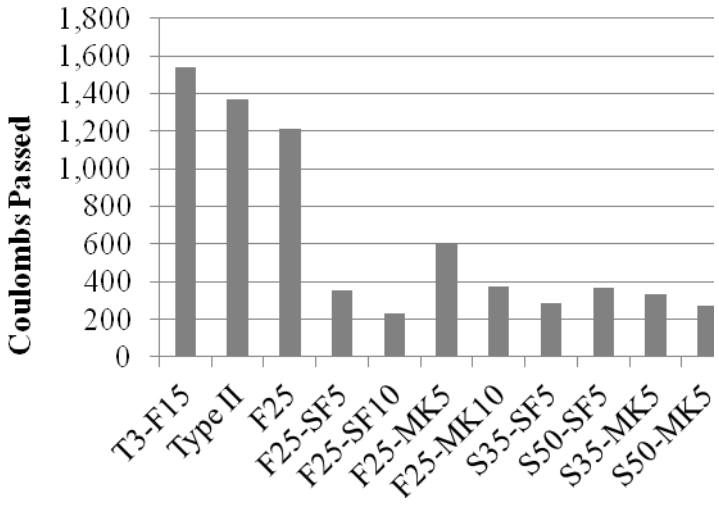

Figure 5.2: RCPT results

5.3.2 Bulk Diffusion

The bulk diffusion chloride profiles of each mixture design were measured. Next, a regression analysis was performed fitting the results to Fick's second law of diffusion, for which the solution is given in Eq. 5.1. Previous research has shown that diffusion is the primary transport mechanism responsible for the ingress of chlorides into the samples over long ponding periods.

$$C(x,t) = C_s - (C_s - C_o) * \text{erf}\left(\frac{x}{\sqrt{4 * D_a * t}}\right) \quad \text{(Eq. 5.1)}$$

Where,

C(x,t)	=	chloride concentration, measured at depth x and exposure time t, mass %
C_s	=	projected chloride concentration at the interface between the exposure liquid and test specimen that is determined by the regression analysis, mass %
C_o	=	initial chloride-ion concentration of the cementitious mixture prior to submersion in the exposure solution, mass %
x	=	depth below the exposed surface, m
D_a	=	apparent chloride diffusion coefficient, m^2/s
t	=	the exposure time, s
erf	=	$\frac{2}{\sqrt{\pi}} * \int_0^z \exp(-u^2)\, du$

The apparent chloride diffusion coefficients determined from bulk diffusion testing are given in Table 5.3. The results varied by over an order of magnitude. Mixture designs with lower water-to-cementitious materials ratio had lower diffusion coefficients. Additionally, ternary mixture designs had lower diffusion coefficients than binary mixture designs.

Table 5.3: Experimental Diffusion Coefficients (1 m^2/s = 1,550 in^2/s)

Mix	**D_a (m^2/s)**
T2	1.74E-11
T3-F15	2.67E-12
F25	2.63E-12
F25-MK5	2.07E-12
F25-MK10	2.66E-12
F25-SF5	2.06E-12
F25-SF10	2.08E-12
S35-MK5	1.23E-12
S50-MK5	1.31E-12
S35-SF5	1.91E-12
S50-SF5	2.18E-12

The chloride profiles for all of the mixture designs are given in Figures 5.3 through 5.6. The solid line with diamond markers are the experimental data points, and the dashed line is the result of the regression to Fick's second law. Additional increments were performed on mixture designs T2 and F25 to capture the tail due to deeper penetration of chlorides into the samples.

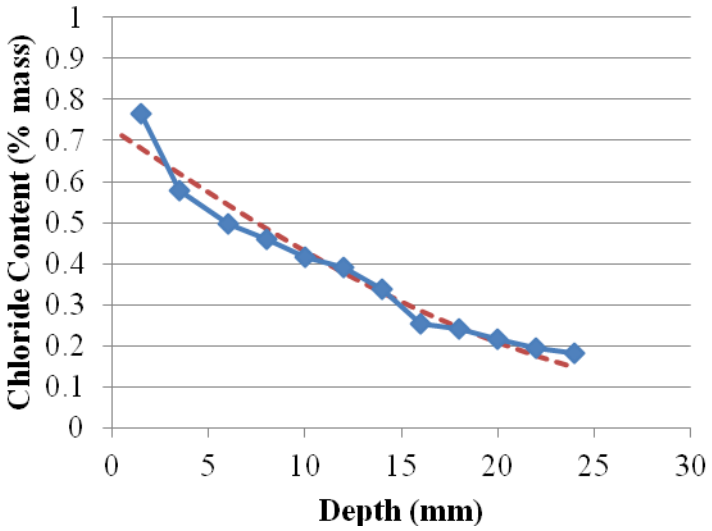

Figure 5.3: Chloride profile for T2 (1 in. = 25.4 mm)

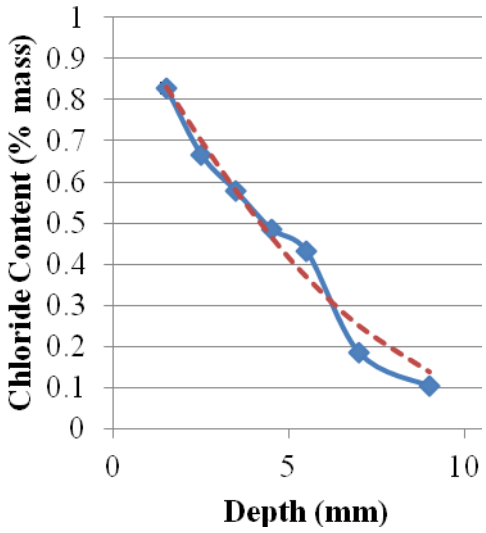

(a)

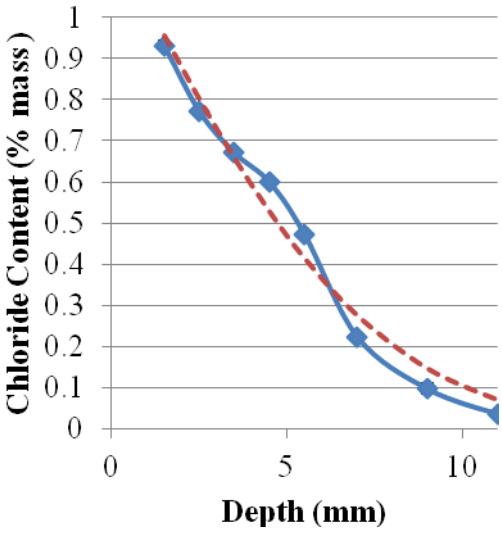

(b)

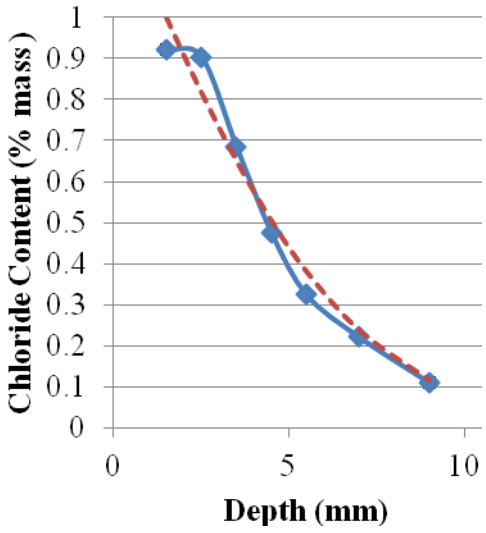

(c)

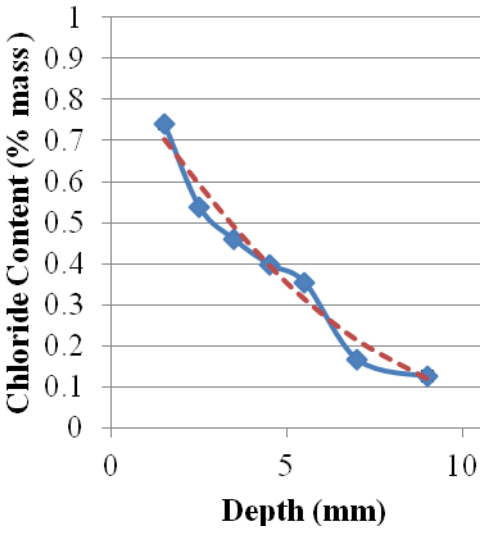

(d)

Figure 5.4: Chloride profiles for (a) T3-F15, (b) F25, (c) F25-MK5, and (d) F25-MK10 (1 in. = 25.4 mm)

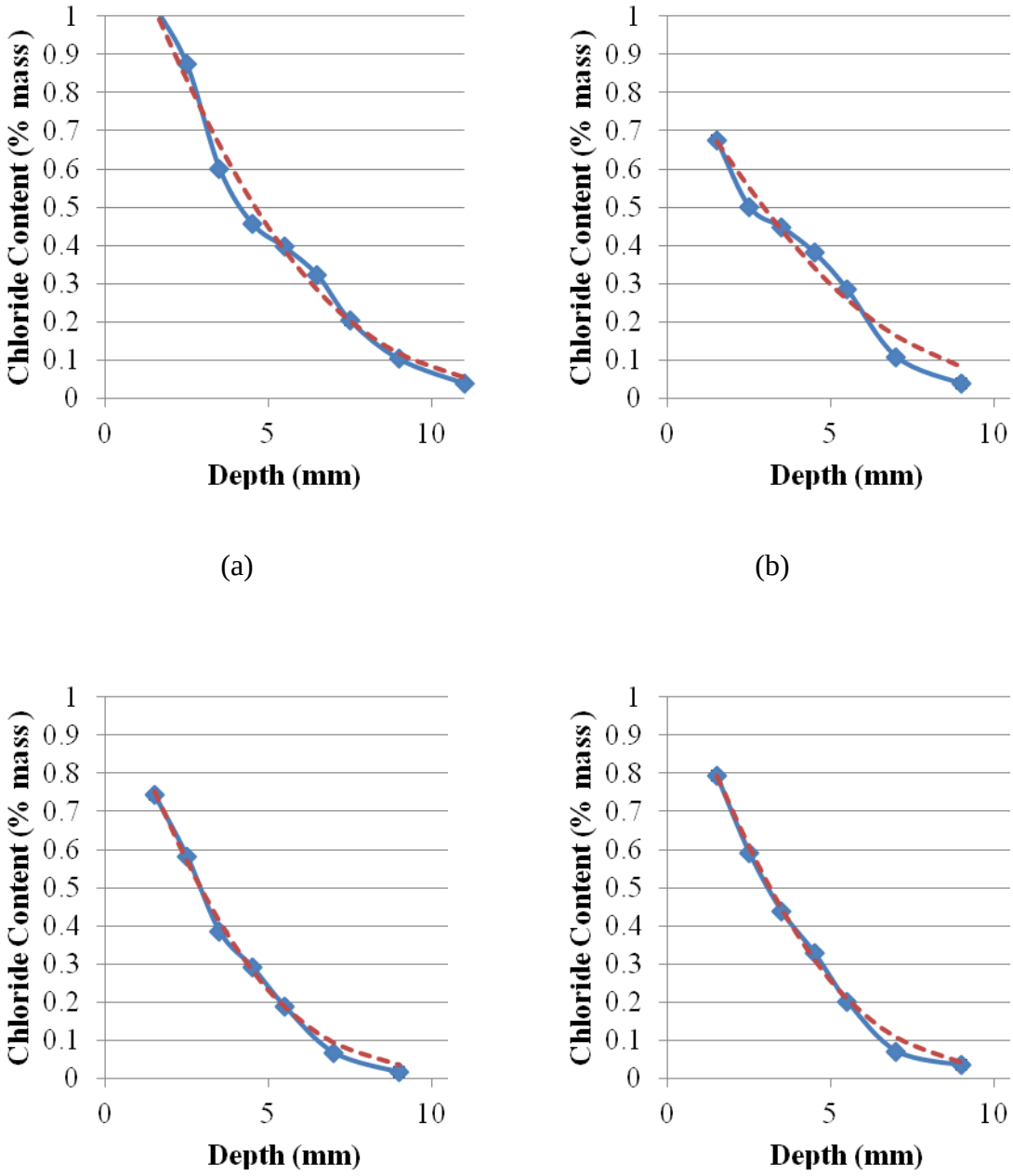

Figure 5.5: Chloride profiles for (a) F25-SF5, (b) F25-SF10, (c) S35-MK5, and (d) S50-MK5 (1 in. = 25.4 mm)

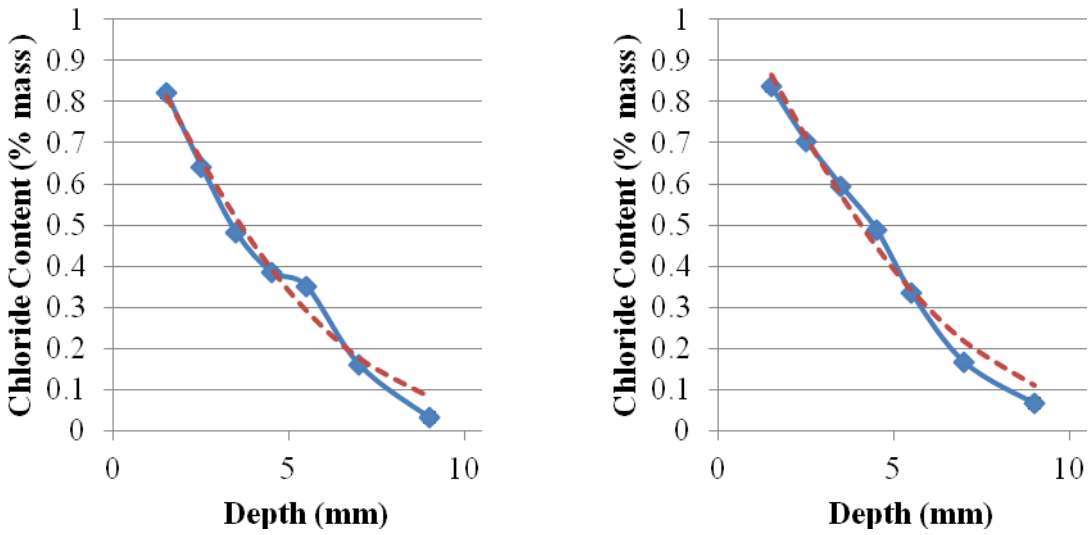

(a) (b)

Figure 5.6: Chloride profiles for (a) S35-SF5 and (b) S50-MK5 (1 in. = 25.4 mm)

5.4 Service Life Modeling

The results of the bulk diffusion tests were used to perform service life modeling to determine the estimated corrosion initiation time. Figure 5.7 shows a basic corrosion service life model which consists of two phases: corrosion initiation time and propagation period. The initiation period is the time it takes for the chloride threshold limit (CTL) to be exceeded at the level of steel. Since diffusion is the primary transport mechanism, the time period for exceedance can be estimated. The propagation period reported in the literature varies significantly and depends upon several parameters including the rate of corrosion and what is concluded to be the end of service life state of damage (Bertolini, et al., 2004).

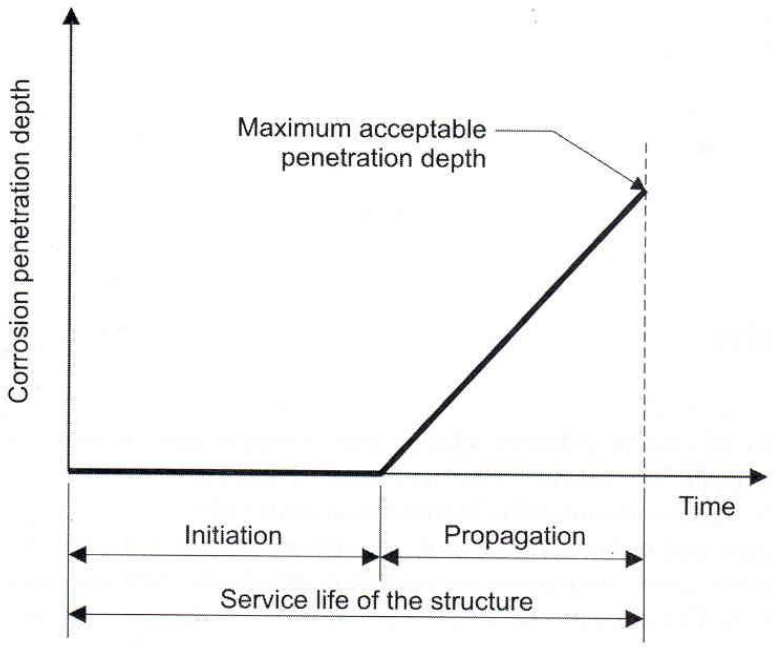

Figure 5.7: Service life model for corrosion induced damage (Bertolini, et al., 2004)

5.4.1 Diffusion Coefficient Estimation

The diffusion coefficient of concrete varies depending on several parameters associated with the mixture design, including: w/cm, SCM's, and concrete maturity. The diffusion coefficient of concrete is not constant over the service life of the structure, but rather continues to decrease due to continued hydration and maturation of the hydrated cement paste (Stanish and Thomas, 2003).

When experimentally measuring diffusion coefficients or estimating them for service life modeling, not only pure diffusion is reflected by the measured values. Often experimental or estimated values are referred to as apparent or effective diffusion coefficients since they are also influenced by other transport mechanisms and represent the diffusion coefficient at a single point in time (Stanish and Thomas, 2003). Life 365 (Ehlen, 2009) and Concrete Works (Concrete Durability Center, 2007) provide estimates for the apparent diffusion coefficient at various ages through the use of a reference

diffusion coefficient (often 28 days) and then account for the decrease over time through the use of a decay index.

5.4.1.1 Life 365

Life 365 (Ehlen, 2009) provides a method for estimating the diffusion coefficient of mixture designs for preliminary estimates of their service life. The basis for the estimation is that the chloride diffusion coefficient is a function of time and mixture design parameters. Eq. 5.2 shows the relationship assumed to account for time-dependent changes in the diffusion coefficient.

$$D(t) = D_{ref}\left(\frac{t_{ref}}{t}\right)^{m} \quad \text{(Eq. 5.2)}$$

Where,

D(t)	=	diffusion coefficient at time t (days), m^2/s
D_{ref}	=	diffusion coefficient at time t_{ref} (28 days for Life 365), m^2/s
m	=	diffusion decay index (0.2 for Portland cement)

For estimation a base diffusion coefficient at t_{ref} = 28 days, D_{28}, is estimated first for a straight Portland cement mixture design, then adjustment factors made based upon the addition of SCM's. Eq. 5.3 gives the equation for estimating the D_{28} of a Portland cement mixture based upon the w/cm.

$$D_{28} = 1 \times 10^{(-12.06+2.40*w/cm)} \quad \text{(Eq. 5.3)}$$

Where,

D_{28}	=	diffusion coefficient of Portland cement, m^2/s
w/cm	=	water-to-cementitious materials ratio

The addition of SCM's to concrete mixture designs are accounted for based upon the type of SCM utilized. Silica fume is known to react quickly and affect early age behavior by decreasing the diffusion coefficient. Life 365 accounts for this through the

application of a reduction factor to the D_{PC}, which is calculated using Eq. 5.3. The method for applying the reduction factor is given in Eq. 5.4 for silica fume. Silica fume is not assumed to have an effect on the diffusion decay index, m, which accounts for long-term time-dependent reductions of the diffusion coefficient. Life 365 does not have an adjustment factor currently for the influence of metakaolin on diffusion behavior of mixture designs.

$$D_{SF} = D_{PC} * e^{-0.165*SF} \quad \text{(Eq. 5.4)}$$

Where,

D_{SF} = diffusion coefficient silica fume containing concrete, m^2/s
SF = silica fume content, % (valid up to 15%)

The addition of fly ash and slag are assumed to not have an effect on the early-age diffusion coefficient, D_{28}. Both have been shown to decrease the apparent diffusion coefficient over long-term exposures. Life 365 accounts for this through modifying the diffusion decay index, m, as shown in Eq. 5.5.

$$m = 0.2 + 0.4(FA/50 + SG/70) \quad \text{(Eq. 5.5)}$$

Where,

m = diffusion decay index
FA = fly ash content, % (valid up to 50%)
SG = slag content, % (valid up to 70%)

5.4.1.2 Concrete Works

Concrete Works (Concrete Durability Center, 2007) utilizes a different method for estimating the diffusion coefficient of mixture designs for preliminary estimates of their service life. The basis for the estimation is similar to Life 365, in that the chloride diffusion coefficient is a function of time and mixture design parameters. Eq. 5.6 shows

the relationship assumed to account for time-dependent changes in the diffusion coefficient.

$$D(t) = D_{28}\left(\frac{28}{t}\right)^{m} + D_{ult}\left(1 - \left(\frac{28}{t}\right)^{m}\right) \quad \text{(Eq. 5.6)}$$

Where,

$D(t)$ = diffusion coefficient at time t (days), m^2/s
D_{28} = diffusion coefficient at 28 days, m^2/s
m = diffusion decay index (0.2 for Portland cement)
D_{ult} = diffusion coefficient after complete hydration, m^2/s
= $D_{28} * \left(\frac{28}{36500}\right)^{m}$

For estimation a base diffusion coefficient ,D_{28}, is estimated first for a straight Portland cement mixture design, then adjustment factors made based upon the addition of SCM's. Eq. 5.7 gives the equation for estimating the D_{28} of a Portland cement mixture based upon the w/cm.

$$D_{28} = 2.17 * 10^{-12} * e^{\frac{w/cm}{0.279}} \quad \text{(Eq. 5.7)}$$

Where,

D_{28} = diffusion coefficient of Portland cement, m^2/s
w/cm = water-to-cementitious materials ratio

The addition of SCM's to concrete mixture designs are accounted for based upon the type of SCM utilized. Concrete Works accounts for the effect of silica fume through the application of a reduction factor to the D_{PC}, which is calculated using Eq. 5.8. Silica fume is not assumed to have an effect on the diffusion decay index, m, which accounts for long-term time-dependent reductions of the diffusion coefficient. Life 365 does not have an adjustment factor currently for the influence of metakaolin on diffusion behavior of mixture designs.

$$D_{SF} = D_{PC}\left(0.206 + 0.794 * e^{\frac{-SF}{2.51}}\right) \quad \text{(Eq. 5.8)}$$

Where,

D_{SF} = diffusion coefficient silica fume containing concrete, m^2/s
SF = silica fume content, % (valid up to 15%)

The addition of fly ash and slag are assumed to not have an effect on the early-age diffusion coefficient, D_{28}. Concrete Works accounts for the use of fly ash and slag through modifying the diffusion decay index, m, as shown in Eq. 5.9.

$$m = 0.26 + 0.4(FA/50 + SG/70) \quad \text{(Eq. 5.9)}$$

Where,

m = diffusion decay index
FA = fly ash content, % (valid up to 50%)
SG = slag content, % (valid up to 70%)

5.4.1.3 Diffusion Coefficient Estimation from RCPT Results

A method for calculating the apparent diffusion coefficient from the total charge passed in the ASTM C 1202 (2007) test was developed by Barde, et al. (2009). This approach uses an empirical solution to the Nernst-Einstein equation to relate the charge passed during the RCPT to an apparent diffusivity, and does not account for the influence of the pore solution chemistry. Eq. 5.10 shows the relationship developed.

$$D = \frac{R*T*L*(0.75)}{Z^2*F^2*C_i*V*A*t} \quad \text{(Eq. 5.10)}$$

Where,

D	=	diffusion coefficient, m^2/s
R	=	universal gas constant, 8.314 J/mol-K
T	=	average temperature, K
L	=	length of specimen, typically 50 mm
Z	=	charge of species I, Coulombs
F	=	Faraday's Constant, 96500 Coulombs/mol
C_i	=	concentration of species I, mol/cm^3
V	=	voltage, typically 60 V
A	=	cross-sectional area of specimen, typically 7865 mm^2
t	=	test duration, typically 21600 seconds

5.4.1.4 Comparison with Experimental Results

Using the outlined procedures utilized by Life 365 and Concrete Works for estimating the diffusion coefficient, Table 5.4 shows the measured and estimated values for the apparent diffusion coefficient. Table 5.4 also contains the diffusion coefficient determined using the Barde, et al. (2009) empirical approach using the Nernst-Einstein relationship from RCPT data. Figure 5.8 shows the estimated and measured diffusion coefficients for each mixture design. No estimates were made for mixture designs containing metakaolin, since neither program currently has that capability. Table 5.5 shows the percent difference associated with each estimate method compared to the experimental results, calculated using Eq. 5.11.

$$\%\ Difference = \left|\frac{Experimental - Estimate}{Experimental}\right| * 100 \quad \text{(Eq. 5.11)}$$

Table 5.4: Experimental and estimated reference diffusion coefficients
(1 m^2/s = 1,550 in^2/s)

	D_a (m^2/s)			
Mix	**Experimental**	**Nernst-Einstein**	**Life 365**	**Concrete Works**
T2	1.74E-11	3.69E-11	1.32E-11	1.48E-11
T3-F15	2.67E-12	6.94E-12	7.15E-12	8.95E-12
F25	2.63E-12	5.47E-12	5.22E-12	6.82E-12
F25-MK5	2.07E-12	2.73E-12	-	-
F25-MK10	2.66E-12	1.68E-12	-	-
F25-SF5	2.06E-12	1.59E-12	2.29E-12	2.14E-12
F25-SF10	2.08E-12	1.04E-12	1.00E-12	1.50E-12
S35-MK5	1.23E-12	1.50E-12	-	-
S50-MK5	1.31E-12	1.23E-12	-	-
S35-SF5	1.91E-12	1.30E-12	2.29E-12	2.14E-12
S50-SF5	2.18E-12	1.64E-12	1.95E-12	1.80E-12

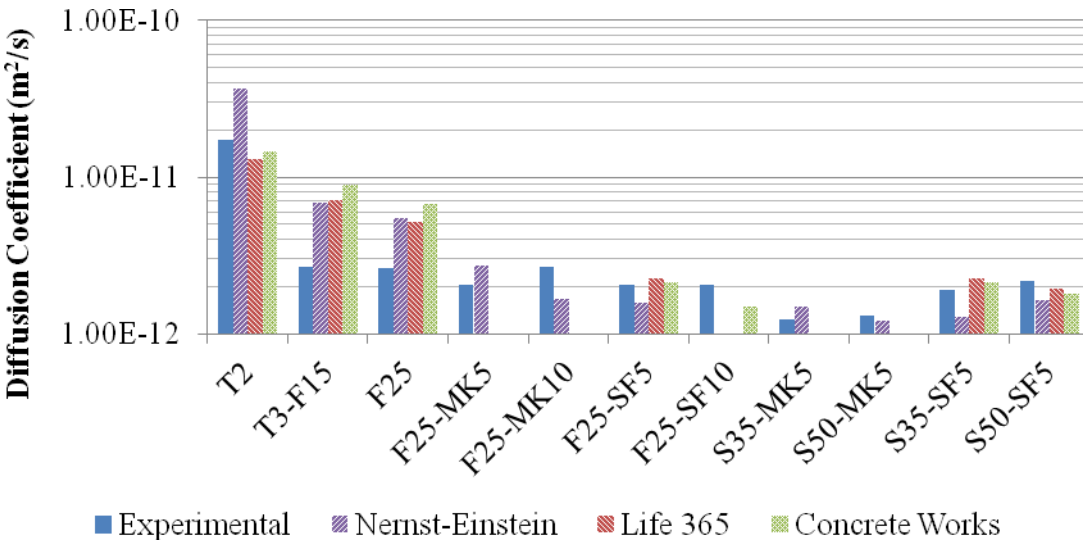

Figure 5.8: Experimental and estimated diffusion coefficients (1 m^2/s = 1,550 in^2/s)

Table 5.5: Percent difference of estimates to experimental apparent diffusion coefficient

	% Difference		
Mix	**Nernst-Einstein**	**Life 365**	**Concrete Works**
T2	112	25	15
T3-F15	160	168	236
F25	108	99	160
F25-MK5	32	-	-
F25-MK10	37	-	-
F25-SF5	22	11	4
F25-SF10	50	52	27
S35-MK5	22	-	-
S50-MK5	6	-	-
S35-SF5	32	20	12
S50-SF5	24	10	17

Life 365 estimated all diffusion coefficients to within an order of magnitude except for T3-F15, which is less than the range of experimental values between mixture designs. Also, Life 365 appears to over-estimate the influence of silica fume contents above 5%. This may be due to the difficulty in properly dispersing high silica fume contents when mixing. Concrete Works estimated the diffusion coefficient of high silica fume content mixture designs more accurately than Life 365. Both Life 365 and Concrete Works over estimate the diffusion coefficient of T3-F15 and F25 by over 99%. This over-estimation would lead to an extremely conservative estimate of usable service life. For ternary mixture designs, Concrete Works estimated the diffusion coefficient to within 27%, and Life 365 to within 20% except for F25-SF10 where it underestimated by 52%.

The Barde, et al. (2009) empirical solution to the Nernst-Einstein approach using the RCPT test data over-estimates the diffusion coefficient for cement only and binary mixture designs. The empirical approach to the Nernst-Einstein approach provided estimates for the diffusion coefficient of metakaolin mixture designs to within 37%. For ternary mixture designs the method under-estimated the diffusion coefficient by up to

50%. The discrepancy in the estimated and measured values is likely due to discrepancies with the pore solution chemistry assumed in the approach and that of the actual samples. Additionally, the degree of saturation of samples could have a large impact since bulk diffusion samples were moist cured for 28 days, while RCPT samples were vacuum saturated at 56 days of age.

The apparent diffusion coefficient can be used to determine the chloride profile at various ages for different mixture designs and can account for the continued maturation of the concrete using the diffusion decay index, m. Figure 5.9 shows the estimated chloride profiles for both T3-F15 and S50-MK5 at various ages when exposed to ingress from a single face using the Life 365 maturity approach presented in Section 5.4.1.2. The D_{28} value of S50-MK5 was approximately 50% of the T3-F15 and had an m value of 0.48 compared to 0.32, respectively. It was observed that after each exposure period the depth of penetration for S50-MK5 was significantly lower than for the previous period. The relationship between diffusion coefficient and depth of ingress at each age was not a linear function.

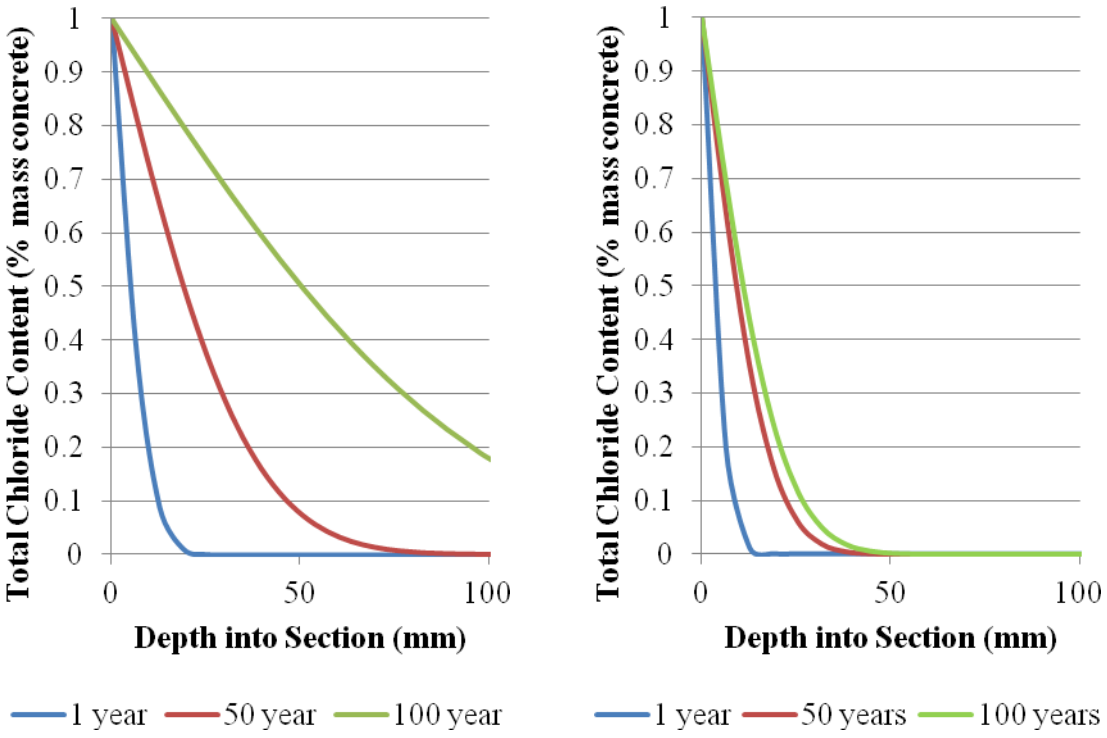

(a) (b)

Figure 5.9: Estimated chloride profiles after various exposure periods for (a) T3-F15 and (b) S50-MK5 (1 in. = 25.4 mm)

5.4.2 Corrosion Initiation Period Estimation

The corrosion initiation period was calculated using Life 365's internal solver and the estimated diffusion decay indexes. The program is able to account for two-dimensional flow of chlorides for the square pile geometry using the two-dimensional Crank-Nicolson approach (Ehlen, et al., 2009). For estimation, a 76.2 mm (3 in.) cover distance was used on an 457 mm (18 in.) square pile. A chloride threshold limit (CTL) of 0.05% by weight of concrete was used to estimate the corrosion initiation time with service life models.

The results of the analysis for predicted service life for the experimentally determined apparent diffusion coefficients and estimated diffusion coefficients are shown in Figure 5.10 and values presented in Table 5.6. The maturity factors estimated by Life

365 were used with the experimentally determined diffusion coefficient to estimate the usable service life.

For the experimentally determined values, the mixture design T2, which would be obtained by following the minimum requirements of ACI 201.2R-10 (2010) would initiate corrosion after only 7 years. T3-F15 would initiate corrosion after approximately 55 years. All ternary mixture designs would provide a minimum initiation time of 73 years. S50-MK5 and F25-SF5 provided the longest initiation times for slag and fly ash mixture designs, respectively.

The Life 365 estimates were over 50% lower for T3-F15 and F25, which are both mixture designs that contain only fly ash. The estimated values for ternary blends including slag and silica fume were within 17 years (~16%). The estimate for 10% silica fume was over 100% higher than the experimental value, which matches the noted difference in estimated diffusion coefficient in section 5.4.1. Concrete Works provided similar estimates for T2, T3-F15, and F25. Due to a limitation in the program, service life estimates were not available for mixture designs where the usable service life exceeded 100 years. Figure 5.10 shows a 100 year life span for Concrete Works estimates that showed a mixture design capable of exceeding the 100 year limitation.

Using the diffusion coefficient determined from the Nernst-Einstein relationship with the maturation factors of Life 365, service life estimates were determined. For cement only and binary mixture designs, the estimates were the most accurate to the bulk diffusion estimated service life over prediction methods. However, for ternary mixture designs the estimates drastically overestimated the usable service life.

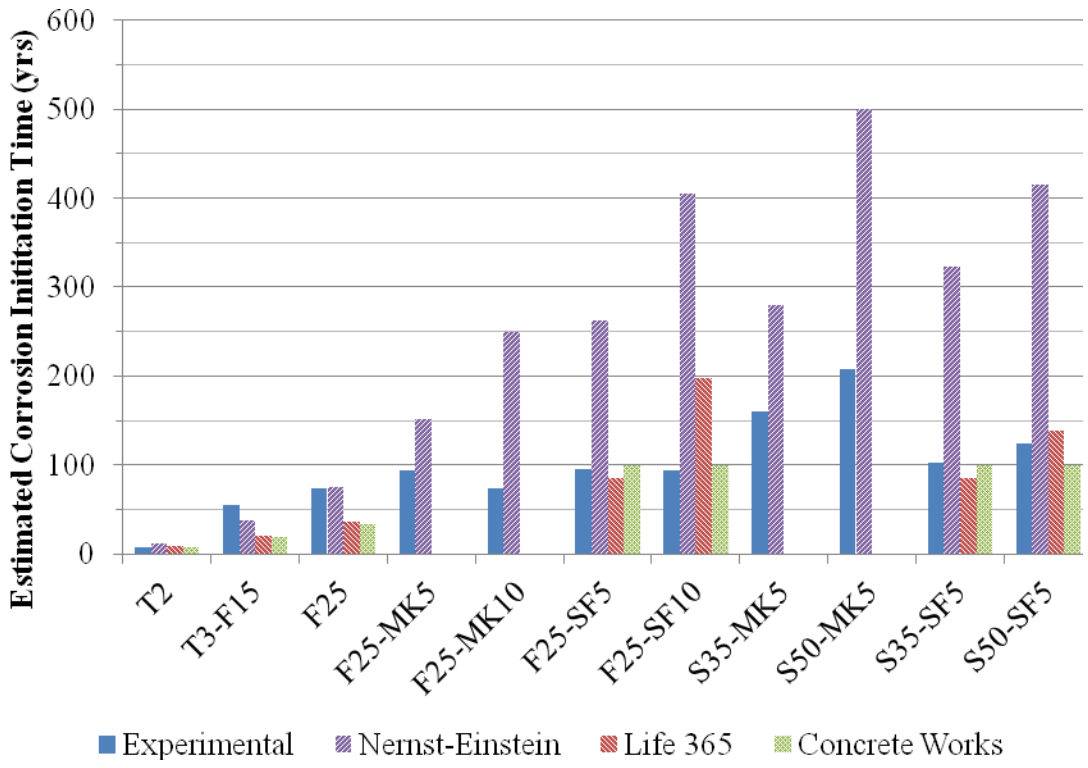

Figure 5.10: Corrosion initiation time for experimental results

Table 5.6: Corrosion initiation times

	Expected Initiation Time (years)			
Mix	**Experimental**	**Nernst-Einstein**	**Life 365**	**Concrete Works**
T2	7	12	9	8
T3-F15	55	38	20	20
F25	74	75	36	34
F25-MK5	94	152	-	-
F25-MK10	73	250	-	-
F25-SF5	95	262	85	>100
F25-SF10	94	405	198	>100
S35-MK5	160	280	-	-
S50-MK5	207	500	-	-
S35-SF5	103	323	85	>100
S50-SF5	124	416	139	>100

A highly conservative estimate of corrosion initiation time is to use the 180 day measured diffusion coefficient for each mixture design, and to not account for continued maturation of the concrete that leads to a long-term decrease in the apparent diffusion coefficient. It is known that the actual values should be longer than the estimated values using this method. Figure 5.11 shows the results of estimated corrosion initiation time not accounting for time-dependent decreases in the diffusion coefficient.

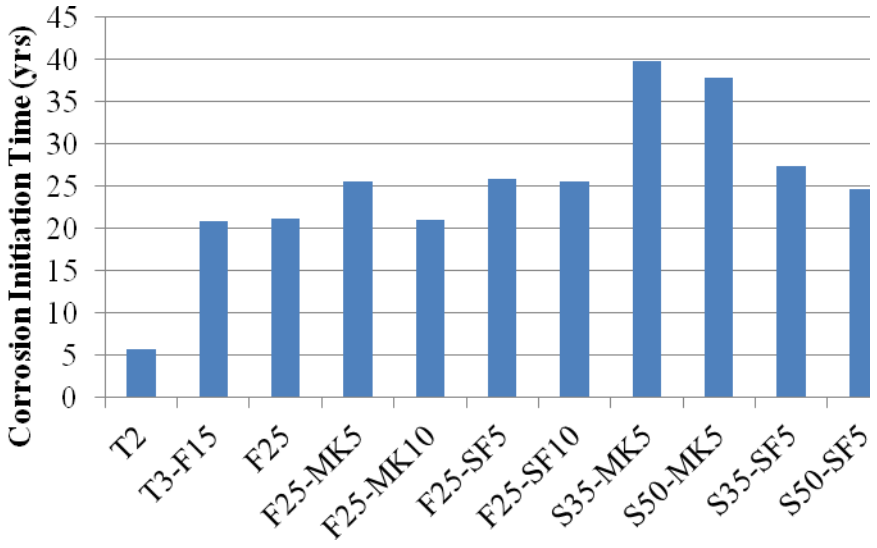

Figure 5.11: Estimated corrosion initiation times without maturity correction

Using this method, the initiation times decreased significantly as was expected. The maximum initiation times were provided by S35-MK5 and S50-MK5, with values of 39.8 and 37.8 years, respectively. The F25-SF5 mixture design provided the longest service life of any fly ash mixture design.

5.5 Conclusions and Recommendations

The study into the chloride ingress resistance of binary and ternary mixture designs found that ternary mixture designs provide superior resistance compared to binary mixture designs. Decreasing the w/cm was found to improve resistance. The RCPT demonstrated the decrease in penetrability of mixture designs and agreed with the results of the bulk diffusion testing. The service life modeling showed that mixture designs capable of an estimated 70 year or longer service life had a charge of less than 1000 coulombs passed during the RCPT. Bulk diffusion tests and service life modeling showed that ternary mixture designs with slag and metakaolin provide the longest service lives. Additionally, estimates from Life 365 and Concrete Works for the diffusion coefficient and estimated service life varied widely from observed behavior. The estimation of diffusion coefficients from the charge passed during ASTM C 1202 (2007) testing was accurate for cement only and binary mixture designs, but highly unconservative for ternary mixture designs where it over-estimated the time to corrosion by a minimum of 61%.

This study has led to the following recommendations for design, quality assurance testing, and future research:

- Use S50-MK5 or F25-SF5 to maximize usable service lives of structures with respect to corrosion initiation depending upon whether a slag or fly-ash mix is preferred.
- Use of a 1000 Coulomb limit for HPMC mixture designs.
- Life 365 can be used to estimate corrosion initiation times, given that the diffusion coefficient is determined experimentally.
- The empirical approach developed by Barde, et al. (2009) to the Nernst-Einstein relationship should not be used to calculate diffusion coefficients for ternary mixture designs due to under-estimating the apparent diffusion coefficient.

Further research is needed to account for the pore solution chemistry of mix designs in the empirical solution.

- Development of estimation techniques for mixture designs utilizing metakaolin are needed.
- Future work on estimation of service lives with the Concrete Works program is needed with a consideration period that can be extended to beyond 100 years.

CHAPTER 6

SULFATE RESISTANCE OF HIGH PERFORMANCE CONCRETE

6.1 Introduction

One objective of this study was to develop and test potential HPMC binder compositions for their resistance to sulfate attack. Concrete piling in seawater and brackish water can be exposed to high concentrations of sulfates. The primary forms of sulfates present in environments surrounding concrete structures are $NaSO_4$, $MgSO_4$, and $CaSO_4$ (Skalny, et al., 2002). Damage to the concrete due various reactions between the ingressing sulfate ions and hydration products and anhydrous cement phases in the cement paste is termed "sulfate attack". Two primary mechanisms are associated with sulfate attack. First, sulfate ions can react with monosulfo-aluminate or available tricalcium-aluminate (C_3A) to form ettringite, as shown in Eq. 6.1. The formation of ettringite can be expansive and can lead to cracking and spalling.

$$2SO_4^{2-} + Ca_4Al_2(OH)_{12} \cdot SO_4 \cdot 6H_2O + 2Ca^{2+} \rightarrow Ca_6Al_2(OH)_{12}(SO_4)_3 \cdot 26H_2O \quad \text{(Eq. 6.1)}$$

In addition, sulfate ions may react with available calcium hydroxide (CH) to form gypsum, as shown in Eq. 6.2. If there is no CH present, then the calcium comes from the decomposition of the calcium silicate hydrate phase (C-S-H). The loss of calcium from the C-S-H leads to a reduction in strength (Skalny, et al., 2002).

$$SO_4^{2-} + Ca^{2+} + 2H_2O \rightarrow CaSO_4 \cdot 2H_2O \quad \text{(Eq. 6.2)}$$

The concentration of sulfates has a large effect on the extent and rate of sulfate attack. ACI 201 (2010) provides guidelines for four exposure classes and requirements to protect against each level of exposure. Table 6.1 shows the requirements proposed by ACI 201 for a given sulfate exposure in water. The recommended cement type is based upon an ASTM C 150 (2009) cement designation. Alternatively, the ASTM C 1157 (2011) performance based specification for cements can be used and requires testing following the ASTM C 1012 (2009) procedure with expansion limits. For Georgia's brackish water and marine exposures, sulfate levels fall into the S1 to S2 categories based upon the results of the environmental condition survey presented in Appendix H.

Table 6.1: Exposure Classes as specified by ACI 201 (2010)

Exposure Class		**Cement Type***	**Exposure**		**Max w/cm**
			% by mass	**ppm**	
S0	Not Applicable	No Restriction	$SO_4 < 0.10$	$SO_4 < 150$	None
S1	Moderate	Type II	$0.10 \leq SO_4 < 0.20$	$150 \leq SO_4 < 1{,}500$	0.5
S2	Severe	Type V	$0.20 \leq SO_4 < 2.0$	$1{,}500 \leq SO_4 < 10{,}000$	0.45
S3	Very Severe	Type V + Pozzolan or Slag	$SO_4 > 2.0$	$SO_4 > 10{,}000$	0.4

*Alternatively, any blend of Portland cement of any type meeting ASTM C150 or C1157 with fly ash or natural pozzolan meeting ASTM C618, silica fume meeting ASTM C1240, or slag meeting ASTM C989 that meets the expansion requirements given in Table 6.3 when tested in accordance with ASTM C1012 may be used.

The ACI 201 (2010) approach does not provide design guidelines based upon the source of sulfates or the cation present, but only on the concentration of sulfate ions. Also, the ASTM C 1580 (2009) method suggested by ACI 201 (2010) for determining the sulfate content does not account for the solubility limits of the sulfate salts present and may under- or overestimate the actual concentration present in practice. The ACI 201 (2010) approach for sulfate durability does not correlate the expected service life to

the measured expansion at various ages and therefore meeting the requirements for a given exposure class does not guarantee adequate resistance to provide a 100+ year lifespan. The use of ASTM C 1012 (2009) expansion tests only accounts for one of the two deleterious reactions associated with sulfate attack and may not provide a full characterization to a mixture designs performance in a sulfate-laden environment. In order to accurately characterize the sulfate resistance properties of a mixture design, both the expansion and strength degradation reactions must be accounted for to assure satisfactory performance.

6.2 Experimental Program

The expansion and compressive strength behavior of thirteen binder compositions subjected to sulfate exposure were evaluated. The binder compositions evaluated are given in Table 6.2. ASTM C 150 (2009) Type II, III, and V cements were used for comparison with binary and ternary compositions containing SCM's; each mixture was designed to increase sulfate resistance based upon previous research findings (Chapter 2). SCM's are given as a percent of total binder composition.

Table 6.2: Binder compositions

	Cement		SCM's (%)			
Mix ID	**%**	**Type**	**Fly Ash**	**Slag**	**Silica Fume**	**Metakaolin**
T2	100	Type II	0	0	0	0
T3	100	Type III	0	0	0	0
T5	100	Type V	0	0	0	0
T3-F15	85	Type III	15	0	0	0
F25	75	Type II	25	0	0	0
F25-SF5	70	Type II	25	0	5	0
F25-SF10	65	Type II	25	0	10	0
F25-MK5	70	Type II	25	0	0	5
F25-MK10	65	Type II	25	0	0	10
S35-MK5	60	Type II	0	35	0	5
S50-MK5	45	Type II	0	50	0	5
S35-SF5	60	Type II	0	35	5	0
S50-SF5	45	Type II	0	50	5	0

The sulfate resistance of each mixture design was investigated using two accelerated test methods. Accelerated expansion tests were performed in accordance with ASTM C 1012 (2009) on mortar samples with the binder compositions given in Table 6.2 and compared against the expansion limits provided by ACI 201 (2010) for different exposure classes, as given in Table 6.3. Expansion tests were performed for 18 months.

Table 6.3: Maximum expansion percentages specified by ACI 201 (2010)

Exposure Class	**Expansion (%)**		
	6 Months	12 Months	18 Months
S1	0.10%	-	-
S2	0.50%	0.10%	-
S3	-	-	0.10%

Compressive strength testing was performed on paste cube samples by the method used by Mehta (1975). Paste cube samples (12.7 mm, 0.5 in) were cast simultaneously

with ASTM C 1012 (2009) samples using a 0.5 w/cm and cured in the molds for 24 hours, then moist cured for 7 days at 50˚C. After the curing period, samples were placed into a 4% Na_2SO_4 solution where the pH was maintained at 7.2 by autotitration with sulfuric acid. By maintaining a constant pH, the effects of leaching of calcium hydroxide were minimized and better replicated field conditions. Through the use of sulfuric acid, Brown (1981) showed that the sulfate concentration remains constant. For each mix, the compressive strength of control and exposed samples were tested at the time of exposure, as well as, 28, 90, and 180 days after exposure. Eight samples with sulfate exposure and eight control samples were tested at each age at a load rate of 272 kg/min (600 lb/min). Quantitative x-ray diffraction (QXRD) was run on 90 and 180 day samples to determine compositional changes.

The compressive strength test accounts for the deterioration of CH and C-S-H to form gypsum, which is more commonly reported in field studies of sulfate damage. The ASTM C 1012 (2009) test only accounts for the effects of ettringite formation in its expansion evaluation. Cracking caused by ettringite or gypsum formation and ettringite expansion, as well as C-S-H deterioration adversely affects the measured compressive strength, and, therefore, both primary reactions are accounted for in the compressive strength test methodology.

6.3 Results and Discussion

The results of the expansion testing and compressive strength testing with sulfate exposure are presented in sections 6.3.1 and 6.3.2, respectively. The results of QXRD analysis is presented in section 6.3.3. Section 6.3.4 presents detailed discussion and comparison of the experimental results.

6.3.1 ASTM C 1012 Expansion Testing

Figure 6.1 shows the expansion results for the ASTM C 150 (2009) Type II, III, and V cements (T2, T3, and T5, respectively) and a dashed line gives the expansion limits, as presented in Table 6.3, for exposure classes S2 and S3. According to ACI 201 (2010) Georgia's marine environments fall into exposure category S2, which has a 6 month and 12 month limit of 0.05% and 0.1% expansion, respectively. Testing was continued to 18 months for comparison with the S3 18 month limit of 0.1% expansion to determine the adequacy of mixture designs for more severe environments.

Only T3 failed the 12-month limit, which was expected since both T2 and T5 binders contain low C_3A contents (<5%) and are ASTM C 150 (2011) sulfate resistant cements. This suggests that an ASTM C 150 (2011) Type III cement alone is not capable of providing adequate sulfate resistance in Georgia's marine environment, but a Type II or V cement may be able to provide adequate resistance for an expansion based criterion. T2 and T5 failed the 18 month limit at 14 and 13 months, respectively. The 18 month limit suggests that cements alone – even sulfate resistant cements – are not for an S3 exposure environment, which is not required but preferable for construction in Georgia. All three cements examined, however, should perform well in an S1 environment, as they each passed the 6 month 0.1% expansion limit.

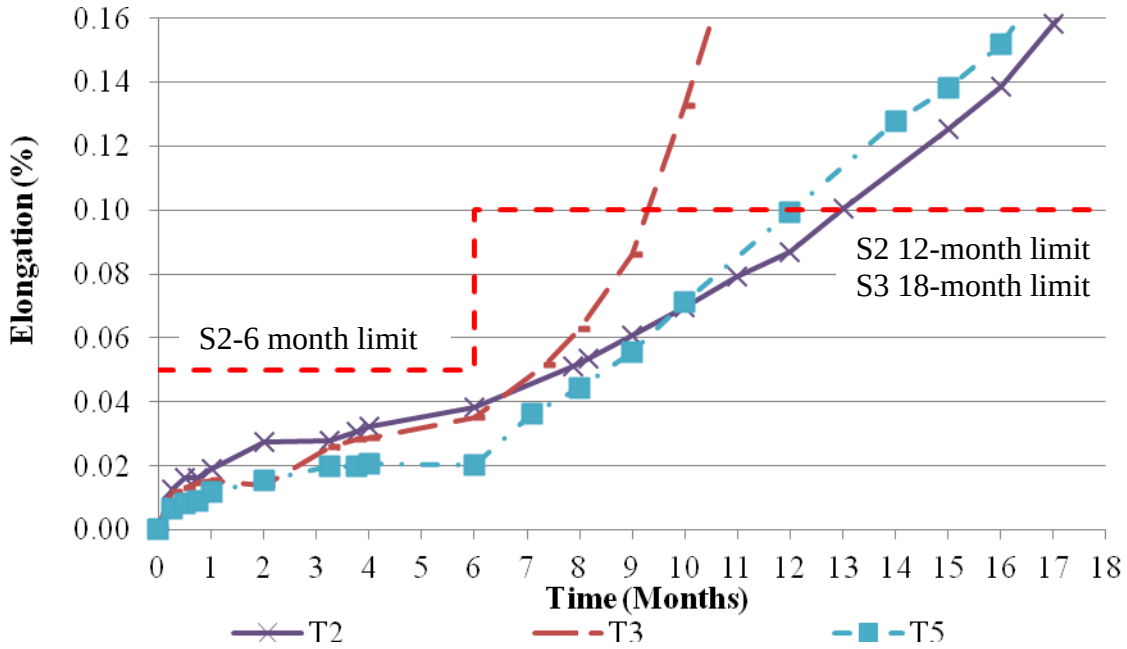

Figure 6.1: ASTM C 1012 expansion results for cement mixes

Figure 6.2 and 6.3 show the expansion results for binder compositions containing fly ash and slag, respectively, with the dashed red line representing the expansion limits. All of the blended cement mixture designs (T3-F15, F25, F25-MK5, F25-MK10, F25-SF5, F25-SF10, S35-MK5, S50-MK5, S35-SF5, and S50-SF5) met the severe exposure (S2) expansion limits, which suggests that these mixture designs possess adequate resistance to sulfate attack for the marine environments in Georgia according to ACI 201. F25-MK5 failed the 18 month expansion limit, suggesting it provides lower sulfate resistance than the other ternary mixture designs, but is still suitable for an S1 or S2 exposure environment.

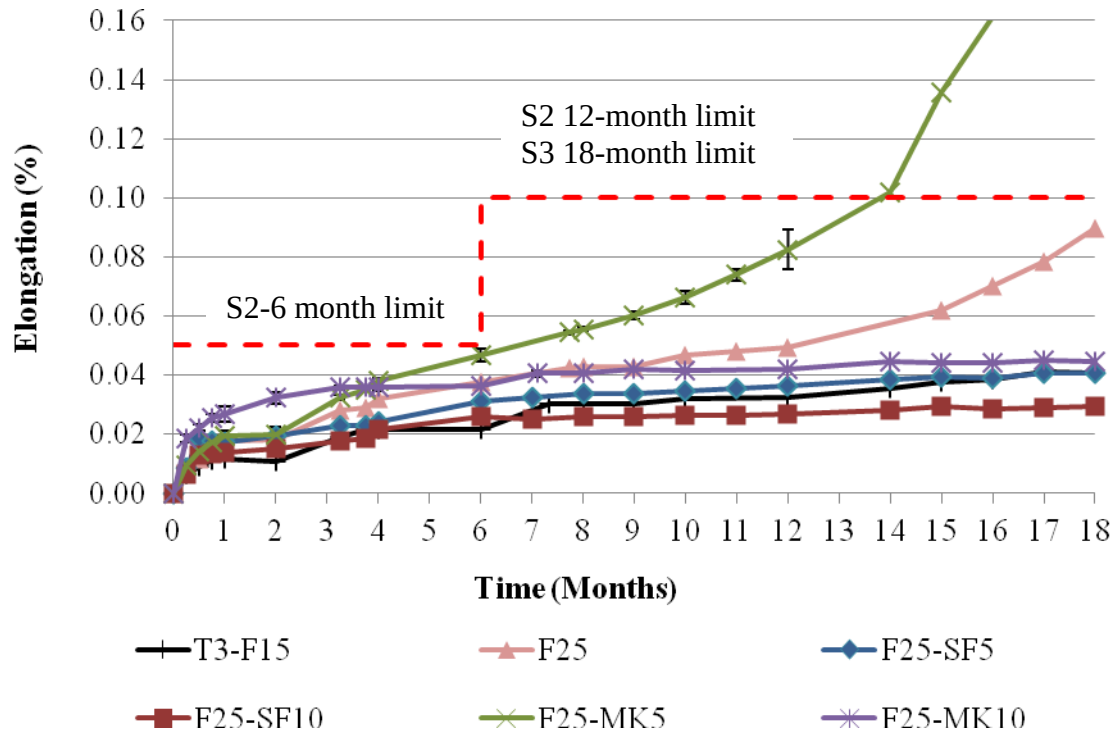

Figure 6.2: ASTM C 1012 expansion results for binder compositions containing fly ash

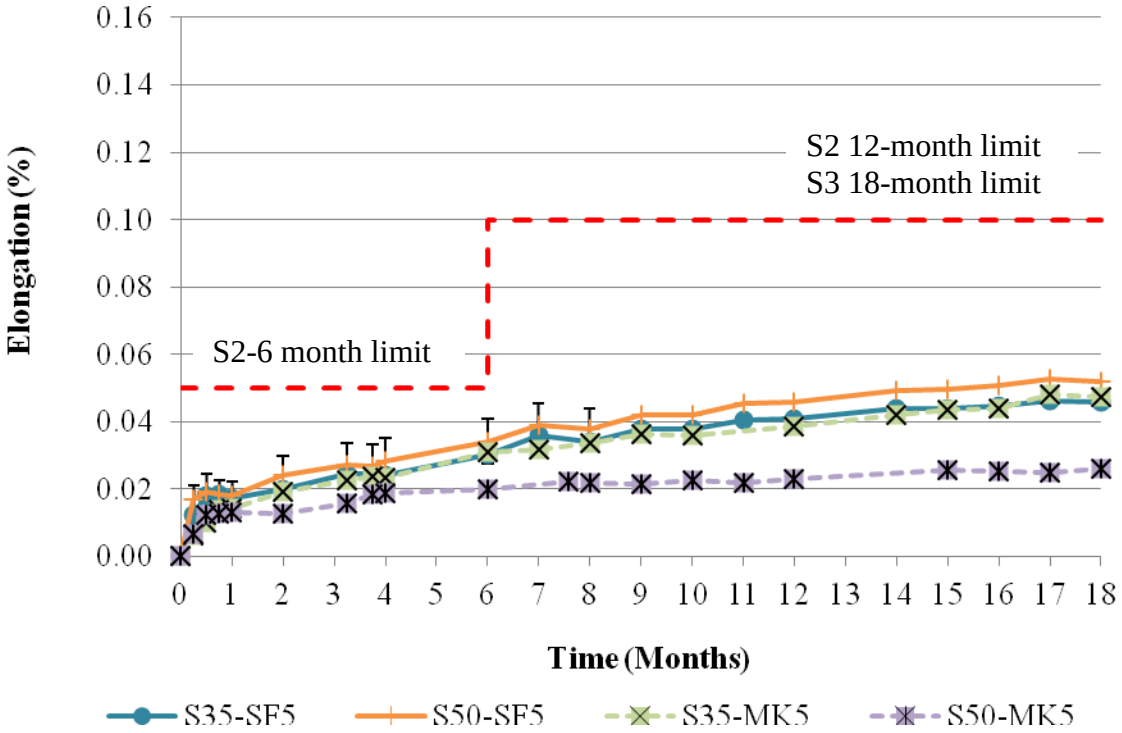

Figure 6.3: ASTM C 1012 expansion results for binder compositions containing slag

The results of expansion testing have shown that any of the investigated binder compositions provide adequate sulfate resistance for an S1 environment. All binder compositions except for T3 demonstrated satisfactory sulfate resistance for S2 exposure classes and are suitable for use in Georgia according to ACI 201 (2010). All mixture designs except cement only (T2, T3, and T5) and F25-MK5 passed the 18 month S3 exposure condition. This suggests that any of these mixture designs are capable of providing excellent sulfate resistance using the expansion failure criterion for an S1, S2, or S3 exposure environment. Mixture design F25 demonstrated an increasing rate of expansion leading up to the 18 month reading, and may not be as sulfate resistant as the other passing mixture designs.

6.3.2 Compressive Strength Testing

The compressive strength testing was performed for 180 days of exposure to samples in a sodium sulfate solution. After the exposure period, varying degrees of visible damage were observed. Figure 6.4 shows a T5 control and sulfate exposure sample after 180 days. The sulfate exposure sample had cracking along the edges of the cube, but no spalling of corners or surfaces. In contrast, Figure 6.5 shows a T3 control and sulfate exposure sample. The sulfate exposure sample had extensive cracking and spalling of corners and edges.

Figure 6.4: T5 180-day control (left) and sulfate (right) exposure 0.5 in. paste cube specimens

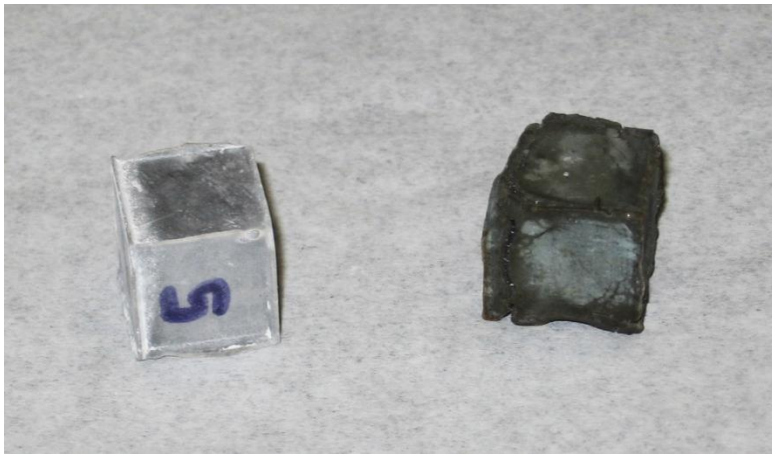

Figure 6.5: T3 180-day control (left) and sulfate (right) exposure 0.5 in. paste cube specimens

The results of the compression strength testing of each mixture design are shown in Figures 6.6 to 6.9. The solid blue line represents the strength behavior of samples exposed to sulfate exposure, and the dashed red line with square markers shows the strength of control samples. The T2 (Figure 6.6-a) and T5 (Figure 6.7-a) sulfate exposure samples were stronger than the control samples at all ages of exposure, but both the control and sulfate exposure samples demonstrated similar strength gain behavior. The

strength gain may be attributed to the T2 and T5 mixture designs having no SCM's, and therefore more CH present to serve as a buffer to the decalcification of the C-S-H (Eq. 6.1). All binder compositions besides T2 and T5 demonstrated lower strength in sulfate exposed samples after 180 days than control specimens. Data points give the ± one-standard deviation range.

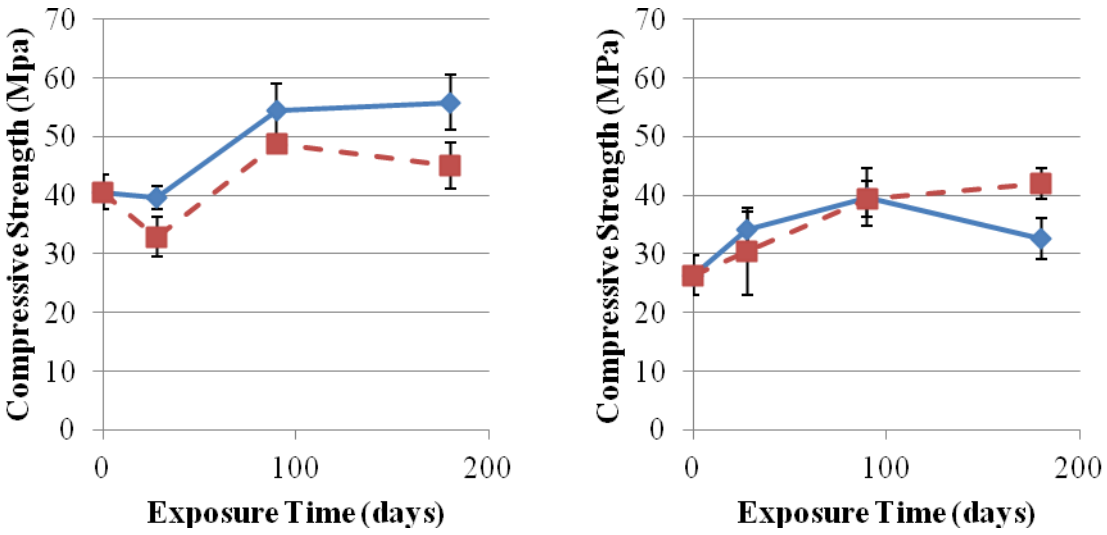

(a) (b)

Figure 6.6: Strength gain curves for control (red dashed line) and sulfate exposure (blue solid line) samples for (a) T2 and (b) T3 (1,000 psi = 6.89 MPa)

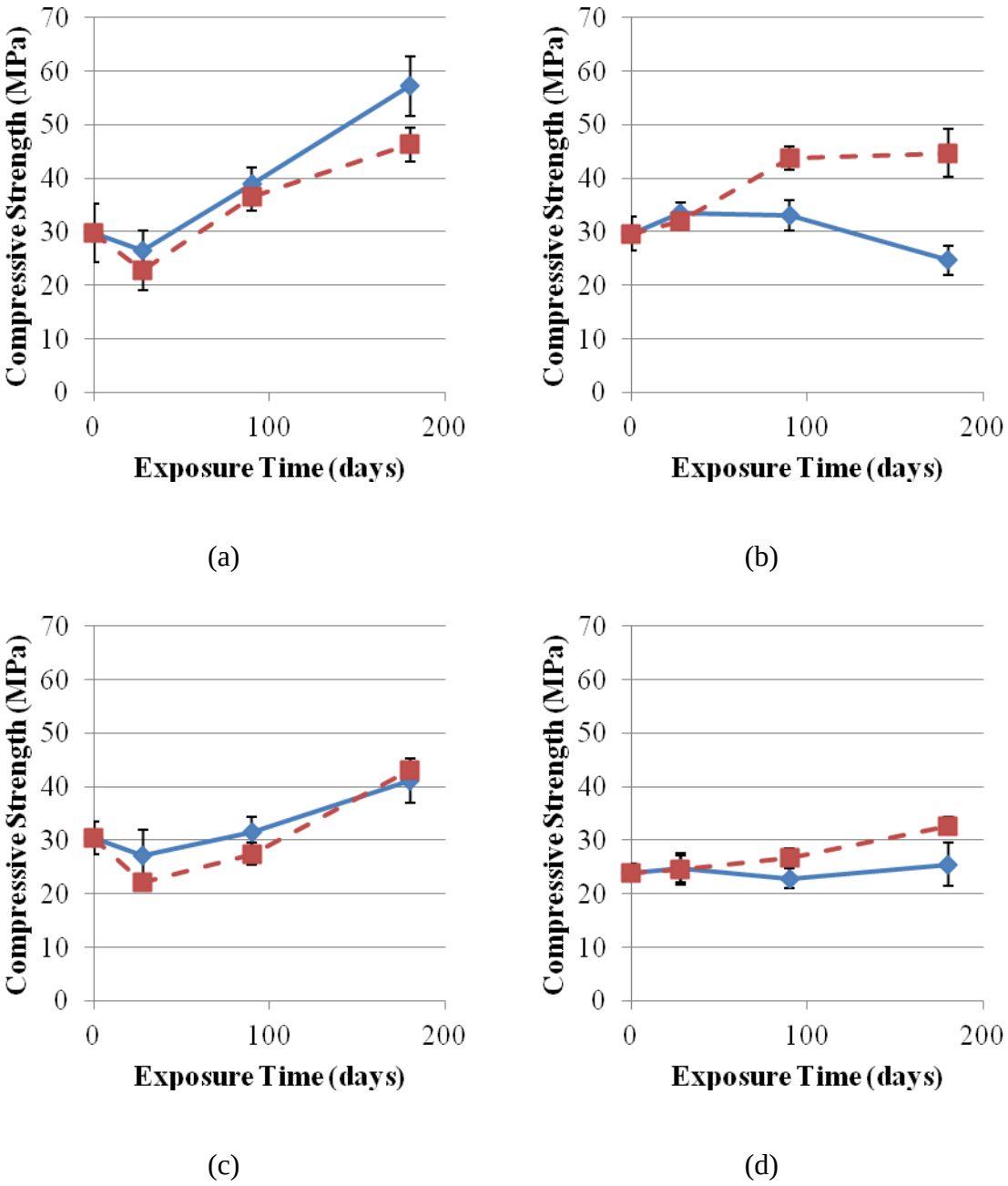

Figure 6.7: Strength gain curves for control (red dashed line) and sulfate exposure (blue solid line) samples for (a) T5, (b) T3-F15, (c) F25, and (d) F25-MK5 (1,000 psi = 6.89 MPa)

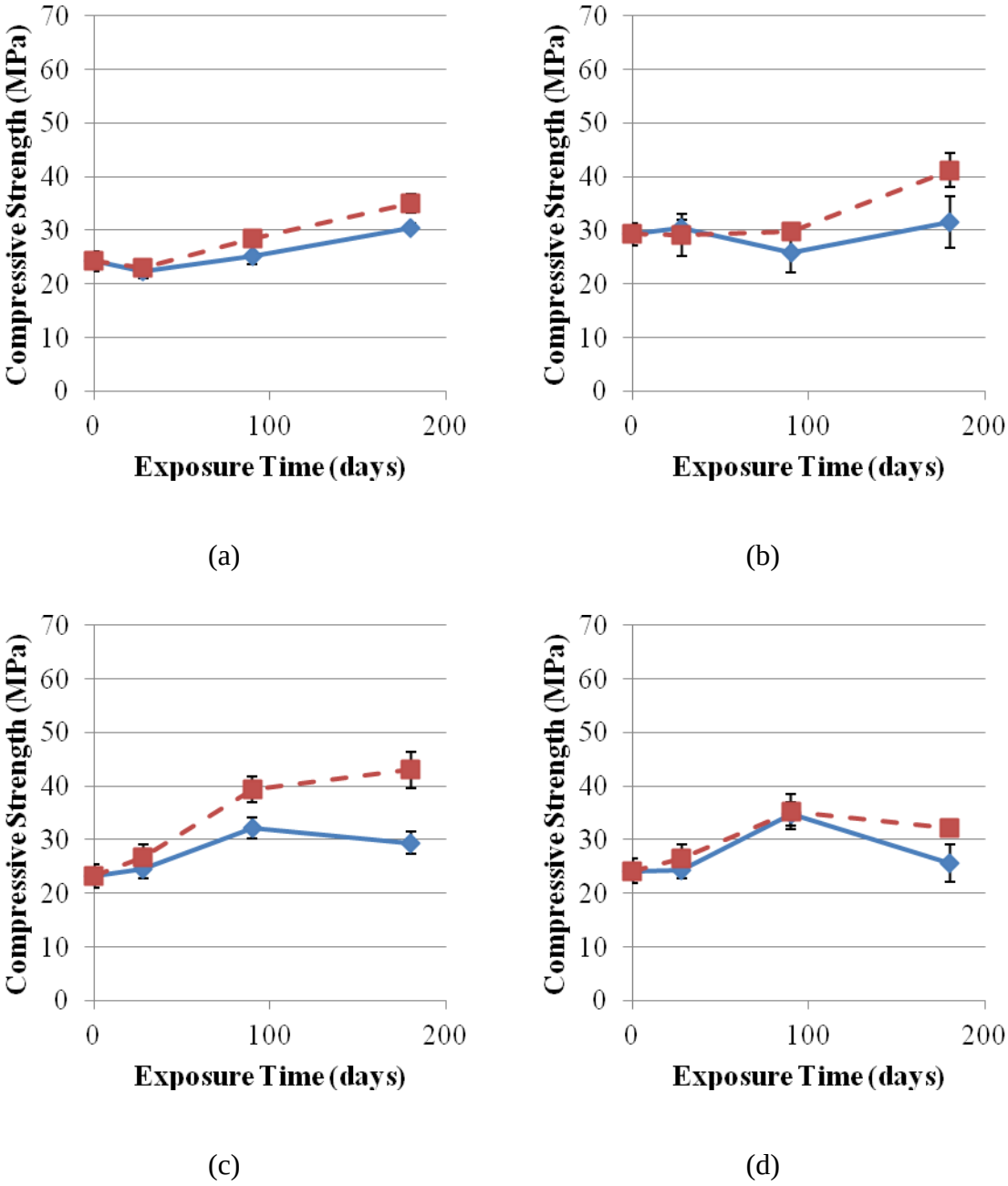

Figure 6.8: Strength gain curves for control (red dashed line) and sulfate exposure (blue solid line) samples for (a) F25-MK10, (b) F25-SF5, (c) F25-SF10, and (d) S35-MK5 (1,000 psi = 6.89 MPa)

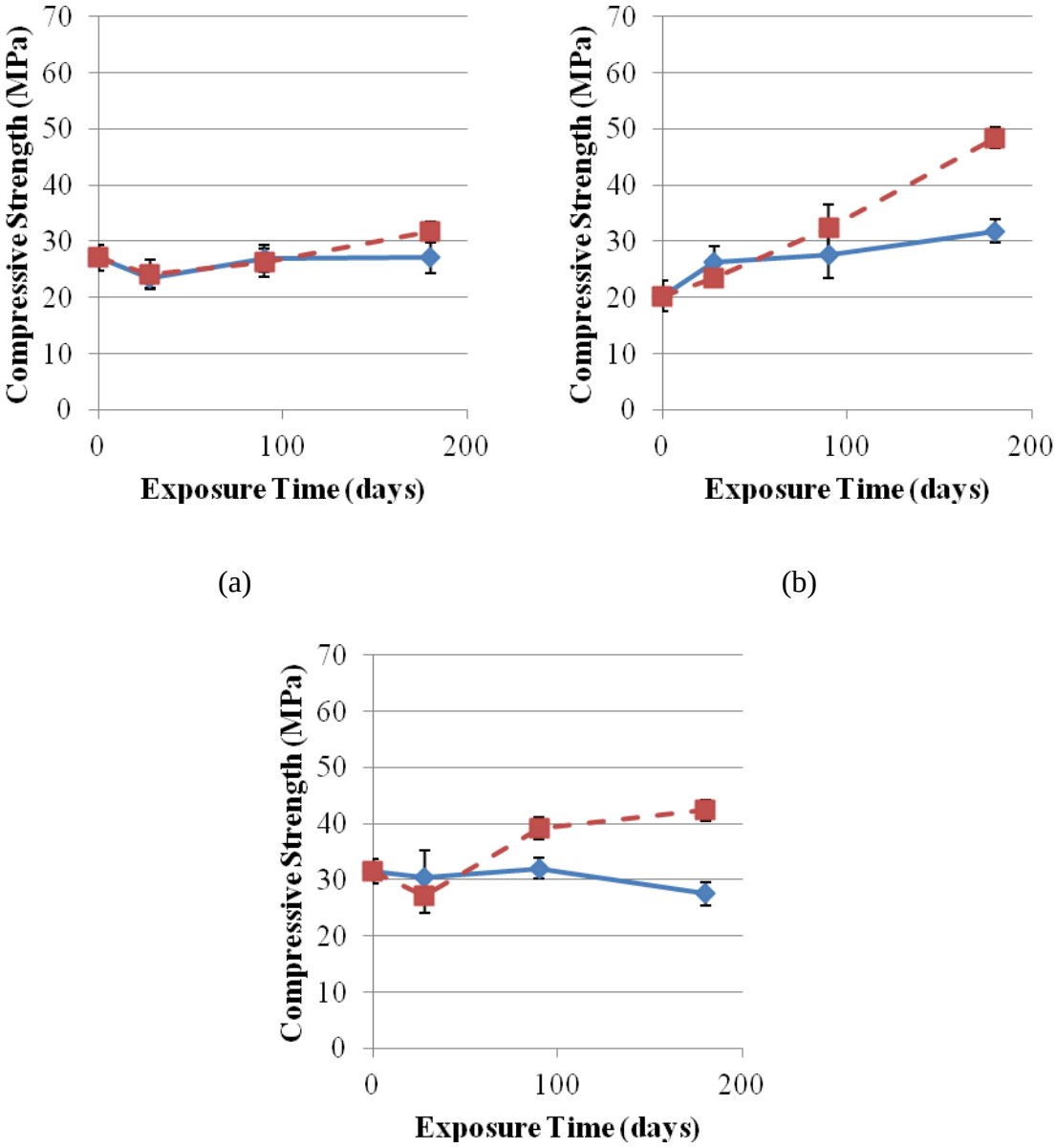

Figure 6.9: Strength gain curves for control (red dashed line) and sulfate exposure (blue solid line) samples for (a) S50-MK5, (b) S35-SF5, and (c) S50-SF5 (1,000 psi = 6.89 MPa)

The relative strength of each mixture design compared to the control sample at the same age was calculated using Eq. 6.3 and plotted in Figures 6.10 for 28, 90, and 180 days of exposure. The relative strength was determined using sulfate and control samples

of the same age, which differs from the Mehta (1975) test method where all strengths were relative to the initial strength at the beginning of exposure.

$$Relative\ Strength = \frac{Sulfate\ Exposure\ Strength}{Control\ Sample\ Strength} \times 100 \qquad \text{(Eq. 6.3)}$$

Hypothesis testing was performed with an α of 0.05 for statistical equivalency of sulfate exposure specimens and control specimens. After 28 days of exposure, no sulfate exposure samples showed statistically significant lower strengths than the control specimens. However, T2 sulfate exposure specimens showed a statistically significant higher strength than the control specimens. The increasing strength of the ASTM C 150 (2011) Type II cement samples result matches the findings of Kurtis, et al. (2001).

After the 90 day exposure period, the T3-F15, F25-SF10, and S50-SF5 mixture designs showed statistically significant decreases in strength. T3-F15 showed the largest decrease in strength, with a 22% decrease in strength compared to the control specimens. No mixture designs demonstrated statistically significant higher strengths in sulfate exposure specimens than control specimens.

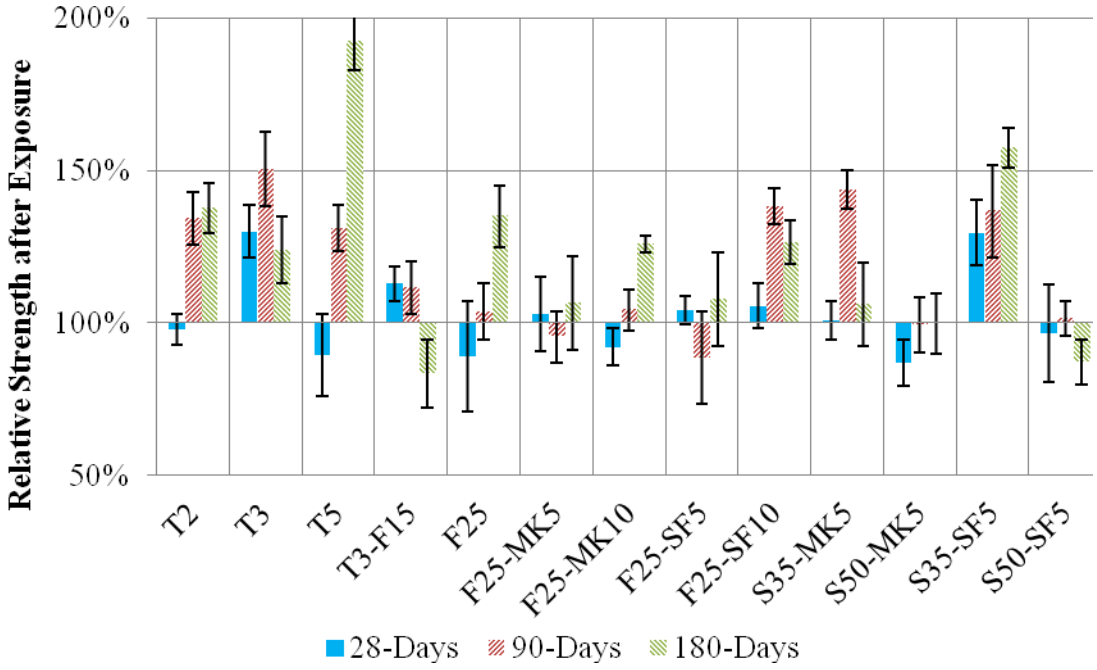

Figure 6.10: Relative strength of sulfate exposure samples compared to the strength of control samples at start of test (7-days of age)

After the 180 day exposure period, the T3, T3-F15, F25-SF10, S35-SF5, and S50-SF5 mixture designs showed statistically significant decreases in strength. T3-F15 showed the largest decrease in strength, with a 42% decrease in strength compared to the control specimens. T2 and T5 demonstrated statistically significant higher strengths in sulfate exposure specimens than control specimens.

Figures 6.11 through 6.13 show the relative strength of samples at each age versus exposure time for binder compositions containing only cement (Figure 6.13), fly ash mixes (Figure 6.14), and slag mixes (Figure 6.15). The limits given in Table 6.4 were used to evaluate the performance of binder compositions, where f_{c180} is the average 180-day compressive strength of sulfate exposure samples, σ_{180} is the standard deviation of the 180-day compressive strength sulfate exposure samples, and f_{ci} is the control compressive strength at the start of the test. The limits were proposed based upon the work of Kurtis (2001) and Cohen and Mather (1991) where it was identified that limits

on the compressive strength degradation must be based upon strength loss, since cements will continue hydrating in the sulfate solution and may experience pore filling due to reaction with ingressing sulfates. Since both effects can result in strength gain, an increase in strength does not necessarily relate to improved sulfate resistance. Two criterion were chosen and place varying levels of restriction upon the strength degradation behavior. First, for a severe sulfate exposure, S2, the 180-day compressive strength plus one standard deviation of sulfate exposure specimens must be higher than the initial strength. This limit accounts for the inherent variability with paste cube testing and any mixture design demonstrating strength loss to below its initial strength will fail. For a very severe exposure, S3, the limit is that the 180-day compressive strength plus one standard deviation of sulfate exposure specimens must be higher than the 90-day sulfate expose specimens compressive strength. This enforces that a mix cannot exhibit a strength loss even after prolonged sulfate exposure. Additionally, this limit will minimize the influence of continued hydration through using strengths determined after 90 days of exposure.

Table 6.4: Sulfate compressive strength degradation testing proposed limits

Exposure Class	**Strength Limit**
S1	-
S2	$f_{c180}+\sigma_{180} > f_{ci}$
S3	$f_{c180}+\sigma_{180} > f_{c90}$

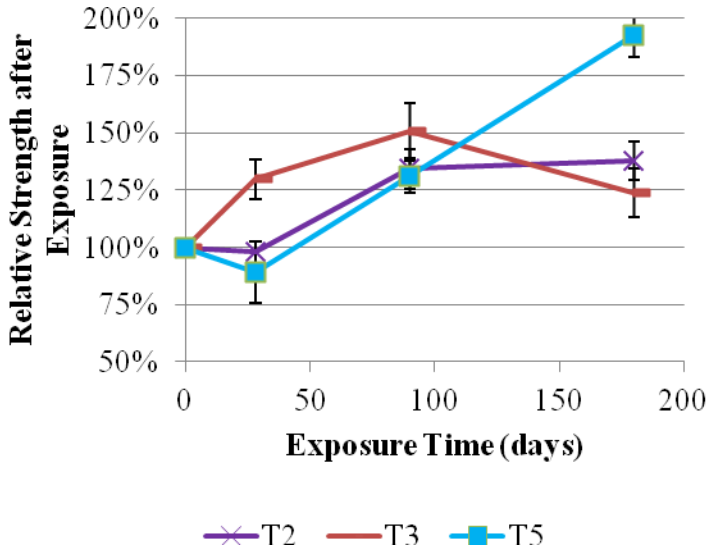

Figure 6.11: Relative strength curves for cement specimens

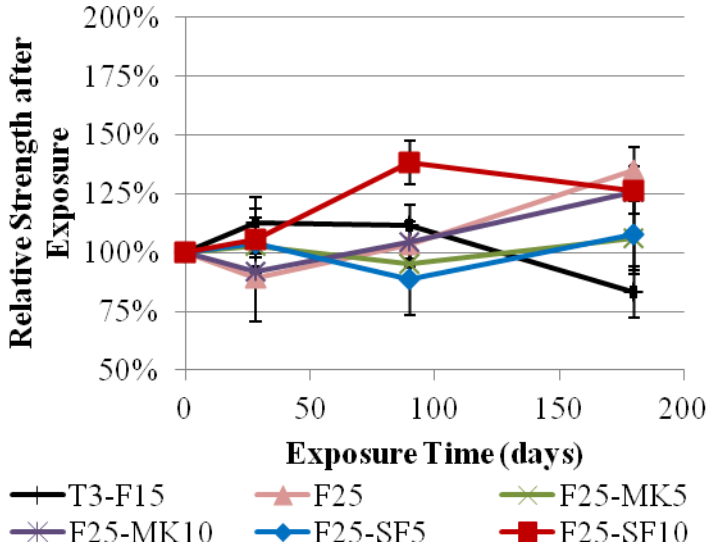

Figure 6.12: Relative strength curves for fly ash binder compositions

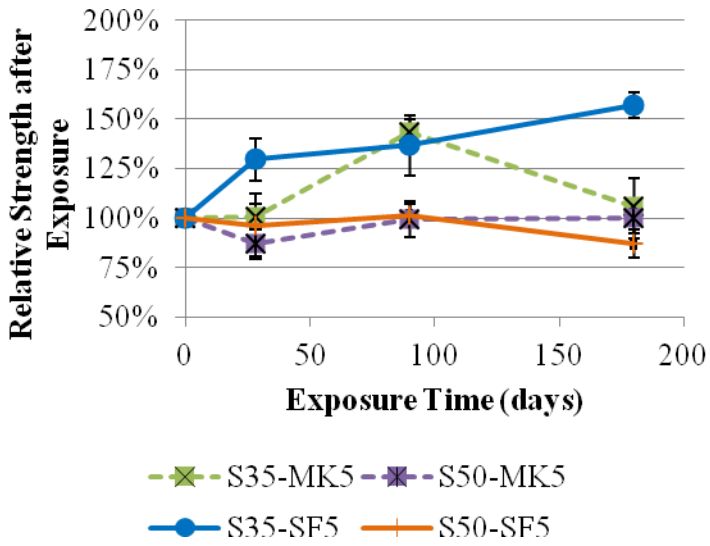

Figure 6.13: Relative strength curves for slag binder compositions

For cement only specimens, both T2 and T5 never exhibited strength loss. T3 showed increasing strength loss at 90 and 180 days. All fly ash mixture designs showed a decreasing trend in strengths after the 28 days of exposure. T3-F15 showed the largest decrease in strength. For slag specimens, mixes containing slag and silica fume performed worse than metakaolin mixture designs. Table 6.5 presents the exposure class rating for each mixture design based upon compressive strength degradation criterion. T3-F15 and S50-SF5 failed the severe exposure limits, suggesting they are only suitable for a S1 sulfate exposure class. T3, F25-SF10, and S35-MK5 failed the S3 exposure limit, suggesting they are suitable for S1 or S2 exposure classes. The sulfate resistance cement only compositions (T2, T5) and F25, F25-MK5, F25-MK10, F25-SF5, S50-MK5, and S35-SF5 passed the S2 and S3 limits, and are suitable for any sulfate exposure using the strength degradation criterion.

Table 6.5: Exposure class ratings for mixture designs based upon sulfate exposure strength degradation criterion

Mix	Strength Degradation Rating
T2	S3
T3	S2
T5	S3
GDOT-HPC	S1
F25	S3
F25-MK5	S3
F25-MK10	S3
F25-SF5	S3
F25-SF10	S2
S35-MK5	S2
S50-MK5	S3
S35-SF5	S3
S50-SF5	S1

6.3.3 Quantitative X-Ray Diffraction

Quantitative x-ray diffraction results were obtained on 180 day control and 90 and 180 day sulfate exposure specimens from compressive strength testing to determine the compositional characteristics that led to high sulfate attack resistance. Samples were obtained by crushing and grinding of the entire strength testing paste cubes. The results are presented as a percentage of the crystalline phases found, and do not represent a total percentage of all phases present in the sample since amorphous phases, like C-S-H, are not included. Lower amounts of crystalline phases are expected in mixture designs containing SCM's due to the depletion of CH and formation of secondary C-S-H and must be considered in the interpretation of QXRD results. The diffraction patterns and full list of phases located are presented in Appendix F.

The calcium hydroxide (CH) content for control and sulfate exposure specimens is shown in Figure 6.14. The QXRD results show that all pastes initially had CH present

in control samples. Mixture designs containing only cement (T2, T3, and T5) had the most present, as was expected due to lack of pozzolanic reaction. Control samples from mixture designs containing SCM's had lower CH contents due to the consumption of CH in the formation of secondary C-S-H. Control samples from ternary blends with fly ash had lower CH contents than ternary slag mixture designs. The CH contents of control samples with equivalent metakaolin and silica fume replacement levels showed similar CH contents.

Sulfate exposure specimens showed a decrease in CH from control samples, as well as continued loss of CH with continued sulfate exposure. Plain cement specimens maintained higher levels of CH with exposure than binary and ternary mixture designs. Sulfate exposure specimens from ternary blends with fly ash showed the lowest levels of CH remaining. Additionally, specimens containing silica fume showed greater loss of CH than equivalent metakaolin mixture designs.

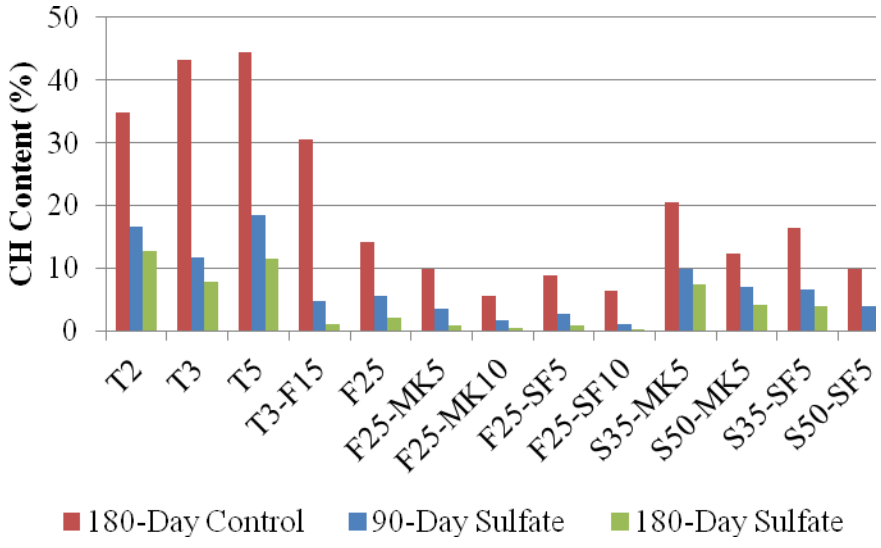

Figure 6.14: Calcium hydroxide content of total crystalline phases of control and sulfate exposure samples as determined by QXRD

The ettringite contents for each mixture design are shown in Figure 6.15. All mixture designs had ettringite present in control samples, which is expected due to the hydration of cement. All samples showed increases in ettringite content with sulfate exposure. Binary and ternary mixture designs showed greater increases in ettringite than cement only mixture designs. The ettringite content between 90 and 180 days of exposure decreased in mixture designs T3-F15 and all silica fume containing mixture designs (F25-SF5, F25-SF10, S35-SF5, and S50-SF5), which were also the mixture designs showing the greatest strength loss.

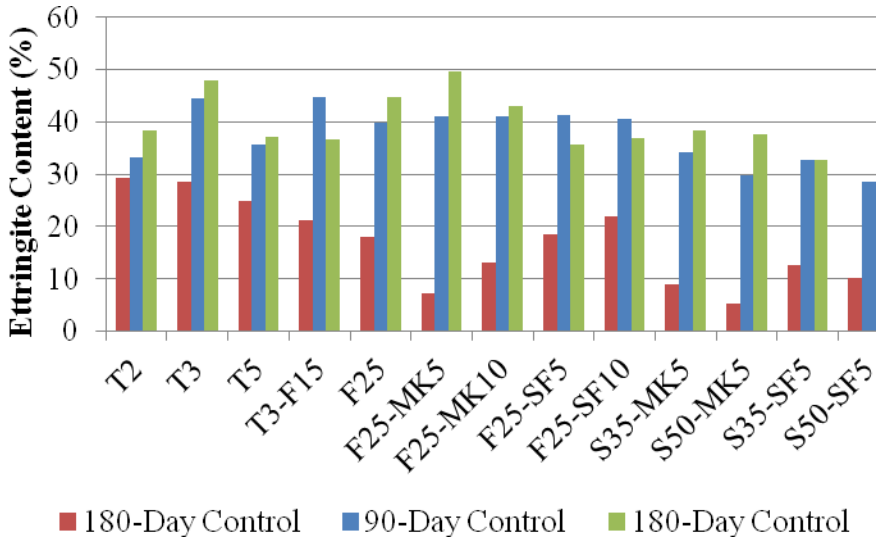

Figure 6.15: Ettringite content of total crystalline phases of control and sulfate exposure samples as determined by QXRD

The gypsum content of the control and sulfate exposure specimens are shown in Figure 6.16. Gypsum was not found in the control samples for any mixture design. All mixture designs showed gypsum formation with sulfate exposure. Mixture designs T5, T3-F15, and ternary blends with silica fume showed the greatest increase in gypsum content between 90 and 180 days of sulfate exposure, and all of those mixture designs except for T5 also showed significant strength degradation.

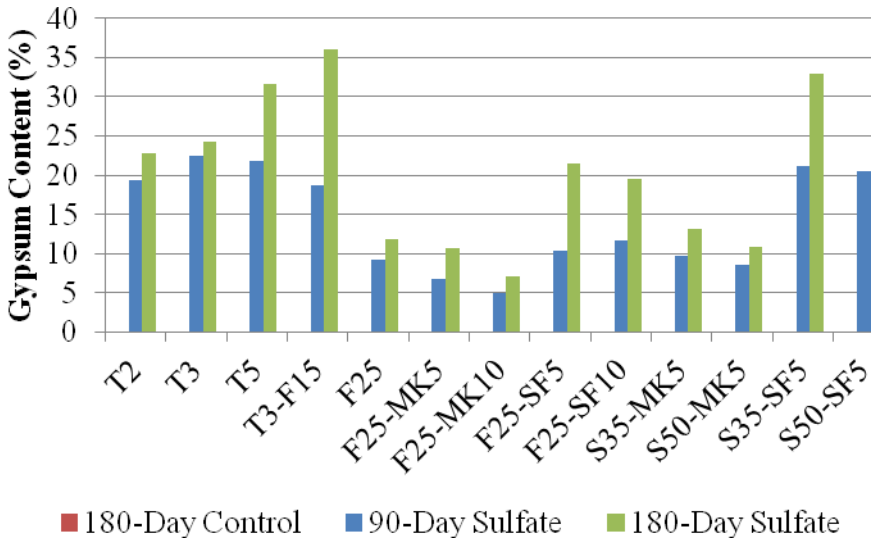

Figure 6.16: Gypsum content of total crystalline phases of control and sulfate exposure samples as determined by QXRD

6.3.4 Discussion of Results

6.3.4.1 Comparison of QXRD and Compressive Strength Data

A comparison of the QXRD data to the sulfate compression data showed that the change in calcium hydroxide content and gypsum content with sulfate exposure is strongly related to the compressive strength degradation as shown in Table 6.6. The data show that mixture designs with low initial CH contents exhibit greater relative strength loss with exposure. Additionally, it was observed that increasing gypsum content led to strength degradation in sulfate exposure samples. No correlation was observed between ettringite content and strength loss.

Table 6.6: Initial calcium hydroxide content, % change in 90 to 180 day QXRD data, and 180 day relative strengths for investigated mixture designs

		% Change from 90 to 180-day Sulfate Samples			180-Day Relative Strength (%)
Mixture design	**Control CH**	**CH**	**Ettringite**	**Gypsum**	
T2	34.9	-23.1	15.5	18.0	124.0
T3	43.2	-33.1	7.6	8.6	77.7
T5	44.4	-38.0	3.9	44.4	123.8
T3-F15	30.5	-76.2	-17.9	93.5	55.2
F25	14.1	-62.2	12.1	30.2	95.4
F25-MK5	9.8	-75.2	20.6	56.3	78.0
F25-MK10	5.5	-72.3	4.7	40.1	87.4
F25-SF5	8.9	-69.3	-13.9	108.9	76.5
F25-SF10	6.3	-74.2	-9.2	67.7	68.3
S35-MK5	20.5	-24.5	11.6	35.2	79.7
S50-MK5	12.3	-40.7	26.6	26.9	85.2
S35-SF5	16.5	-41.8	0.1	55.7	65.7
S50-SF5	9.9	-29.6	-4.9	60.4	65.0

The overall oxide content (i.e. cement plus SCM oxides) of each mixture design were calculated (Table 6.7) and compared with the strength loss results to understand the cause of certain mixture designs demonstrating lower calcium hydroxide contents and more susceptibility to gypsum formation. The results demonstrated a relationship between the SiO_2 and CaO contents and strength loss. It was found that for increasing binder CaO contents, the relative paste strength increased, as is shown in Figure 6.17 (a). The CaO content relates to the CH content of mixture designs via hydration of the calcium silicate phases in clinker. Therefore, a mixture design with a high CaO content will be expected to have a higher CH content. Due to its greater solubility, the CH content will be consumed before decalcification of the C-S-H occurs and therefore higher CH pastes are believed to offer better resistance to strength degradation.

It is worth noting that due to replacement of more calcium-rich cement with more silicon-rich SCMs, the CaO content and SiO_2 content of pastes are inversely related,

shown in Figure 6.17 (b). For example, mixture designs with silica fume had lower CaO contents than equivalent metakaolin mixture designs. Generally, lower CaO mixes, including the silica fume ternary blends, exhibited greater strength loss compared to control samples.

Table 6.7: Oxide contents of binder compositions

	Oxide Content (%)			
Mixture design	**SiO_2**	**Al_2O_3**	**Fe_2O_3**	**CaO**
T2	20.51	4.65	3.35	62.60
T3	20.80	4.96	3.30	63.74
T5	20.81	4.30	4.14	63.52
T3-F15	26.07	8.62	3.54	54.34
F25	29.37	10.84	3.74	47.21
F25-MK5	30.91	12.82	3.59	44.09
F25-MK10	32.45	14.80	3.45	40.96
F25-SF5	33.07	10.62	3.58	44.11
F25-SF10	36.76	10.41	3.41	41.01
S35-MK5	28.50	7.82	2.17	50.59
S50-MK5	31.27	8.33	1.73	46.79
S35-SF5	30.66	5.62	2.16	50.62
S50-SF5	33.43	6.13	1.72	46.81

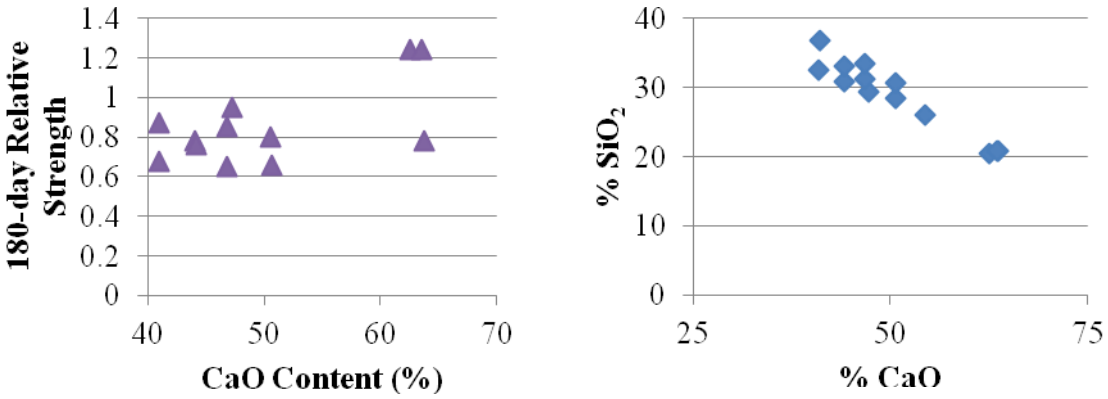

(a) (b)

Figure 6.17: (a) CaO content versus strength degradation and (b) CaO versus SiO_2 content of mixture designs

Mixture designs T2 and T5 showed an increase in strength with decreasing CH content over time. However, this can be explained by the chemical processes that lead to the strength degradation. The formation of gypsum can lead to a "pore blocking" effect, where gypsum forms in existing voids in the near-surface region, effectively increasing density and decreasing the penetrability of the sample locally due to gypsum's low solubility. Also, in the formation of gypsum, CH is preferentially attacked. However, if the CH has been consumed then the primary strength giving phase C-S-H is attacked (Skalny, et al., 2002). Therefore, mixture designs with large initial CH contents provide a larger buffer to the attack of the C-S-H than mixture designs containing SCM's which deplete the CH content in the formation of secondary C-S-H.

6.3.4.2 Comparison of QXRD and Expansion Data

The QXRD data was utilized to explain the observed expansion behavior of each mixture design. The 180 day sulfate exposure paste cubes were compared with 12 month expansion. The data suggest that mixture designs which had large ettringite contents in sulfate exposure specimens experienced greater expansion as shown in Figure 6.18 (a). Similarly, mixture designs with large calcium hydroxide contents present in sulfate exposure samples experienced more expansion as shown in Figure 6.18 (b). The calcium hydroxide content depletion is related to expansion behavior since it is consumed in the formation of both gypsum and ettringite. The ettringite formation during sulfate attack can be expansive in nature and explains why increasing ettringite content is associated with increased expansion from the QXRD results. The gypsum content did not suggest a relationship with measured expansion, but the total gypsum and ettringite content did correlate with expansion, as is shown in Figure 6.18 (c) and (d), respectively.

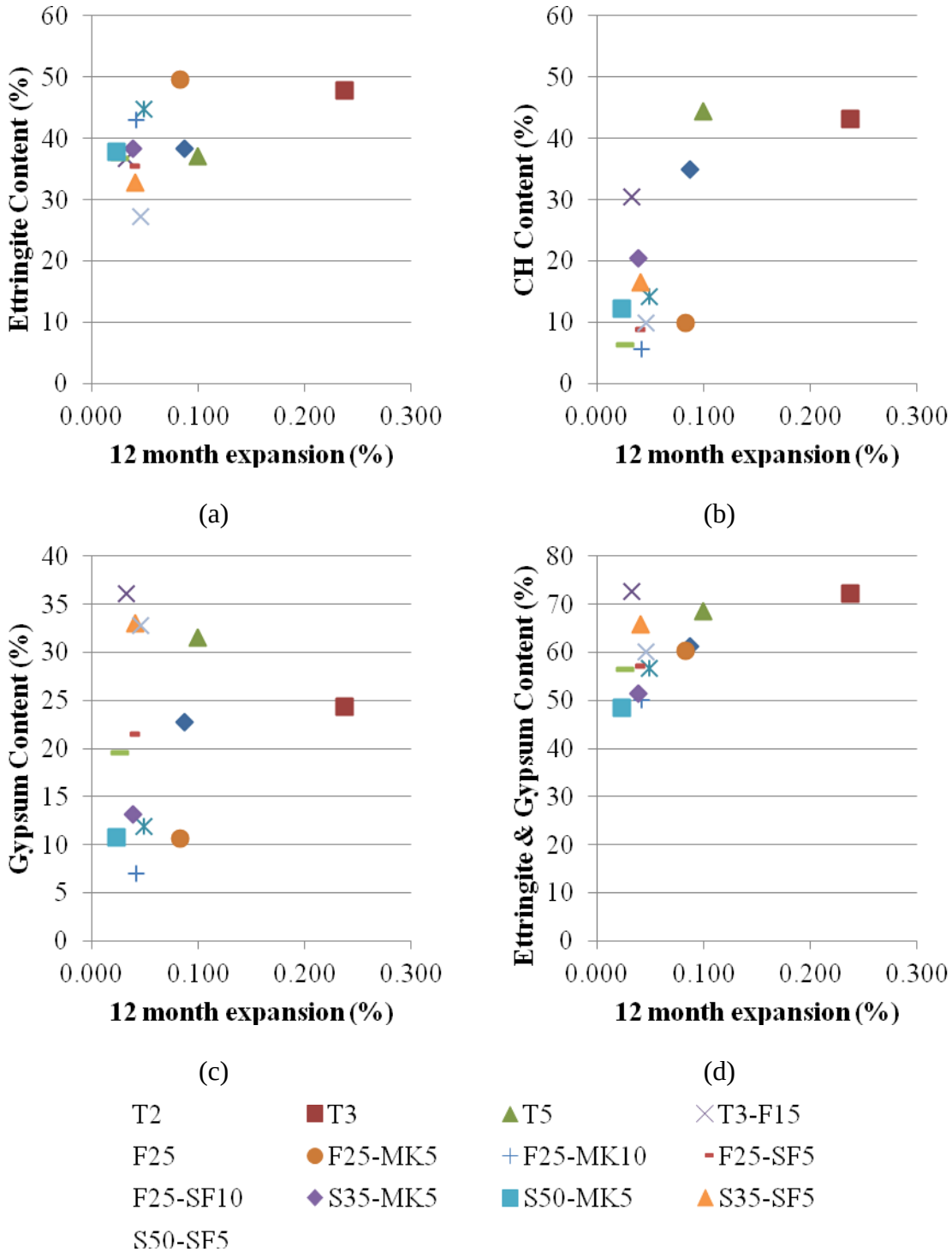

Figure 6.18: Expansion versus (a) ettringite content at 180 days, (b) calcium hydroxide content of control sample at 180 days, (c) gypsum content at 180 days of sulfate exposure, and (d) combined gypsum and ettringite content at 180 days of sulfate exposure

The oxide contents of each binder composition (Table 6.7) were compared with the expansion measurements to determine the compositional trends of mixture designs with good or poor performance on expansion testing. The data suggests that the expansion behavior is related to the initial binder CaO content, as is shown in Figure 6.19. It was found that for increasing CaO contents, the expansion increased. The CaO content relates to the CH content of pastes, therefore, a mixture design with a high CaO content will have a higher CH content paste. The CH is consumed in the formation of ettringite, which is leads to expansion.

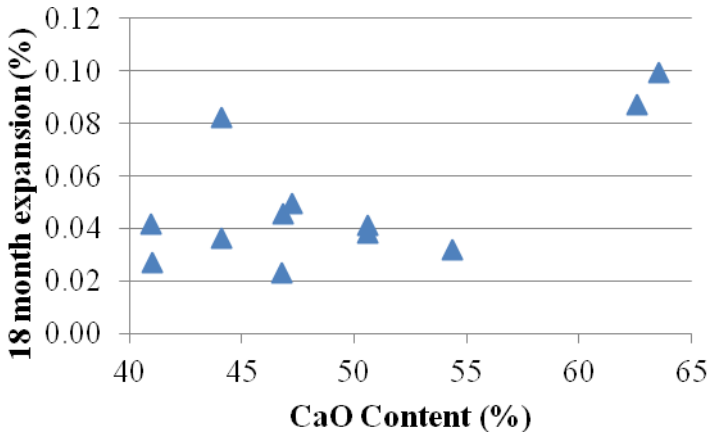

Figure 6.19: Relationship between CaO content and 12-month sulfate exposure ASTM C 1012 expansion

6.3.4.3 Comparison of Expansion and Compressive Strength Data

The performance of binder compositions exposed to sulfate solutions varied widely depending upon whether the ASTM C 1012 (2009) expansion behavior or compressive strength was being measured. For example, using the expansion criterion mixture designs with low CaO contents, such as mixture designs containing silica fume, showed very good behavior and were suitable for the very severe, S3, exposure conditions. However, when using the strength degradation testing limits, low CaO

contents were detrimental and led to mixture designs with high silica fume contents performing poorly.

The variance in performance demonstrates that neither test alone is adequate for determining sulfate performance. The results suggest that both the ASTM C 1012 (2009) and compressive strength testing should be used to test for sulfate attack resistance until a more comprehensive test method is developed that is capable of accounting for both degradation mechanisms.

Table 6.8 provides a summary of the strength and expansion test results, as well as an overall rating for sulfate resistance considering both of these criteria. Boxes highlighted in red represent a mixture design suitable for exposure class S1, yellow for exposure class S2, and green for exposure class S3. When results from strength and expansion testing do not agree, the lower exposure class is assumed to govern predicted sulfate resistance. For example, while T2 and T5 performed the best on the strength testing, both however failed the 18 month limit for expansion testing and are as a result rated for S2 environments. T3 performed poorly on both tests, which is to be expected since it was not designed for sulfate resistance. Slag mixture designs containing metakaolin performed well with both test methods. Mixture designs containing silica fume performed poorer at strength testing than their equivalent metakaolin mixes with the same replacement levels. Mixture designs that performed well on both criteria had moderate CaO contents (44 to 50%) and utilized sulfate resistant ASTM C 150 (2011) Type II cements with low C_3A contents.

The testing performed to characterize the adequacy of mixture designs for sulfate exposure only evaluated the effect of composition by using a high w/cm of 0.485 and 0.5 for expansion and compressive strength testing, respectively. Transport properties of mixture designs also can help in sulfate resistance by limiting the rate of ingress of sulfates. From the carbonation (Chapter 7) and chloride ingress resistance (Chapter 5) it has been shown that the use of SCM's with a low w/cm greatly decreases the

penetrability of concrete. Therefore, the use of a high sulfate resistance binder composition containing SCM's and a low w/cm is recommended. Additionally, based upon the findings of Chapter 8 for the influence of cracks on chloride ingress, research is needed to understand the influence of increased permeability on sulfate attack due to the presence of cracks.

Table 6.8: Summary of sulfate testing results

Mix	Strength Degradation Rating	ASTM C 1012 Rating	Overall Exposure Rating
T2	S3	S2	S2
T3	S2	S1	S1
T5	S3	S2	S2
T3-F15	S1	S3	S1
F25	S3	S3	S3
F25-MK5	S3	S2	S2
F25-MK10	S3	S3	S3
F25-SF5	S3	S3	S3
F25-SF10	S2	S3	S2
S35-MK5	S2	S3	S2
S50-MK5	S3	S3	S3
S35-SF5	S3	S3	S3
S50-SF5	S1	S3	S1

6.4 Conclusions and Recommendations

The results of this sulfate resistance study demonstrated that the measured performance varied widely depending upon the measured property. The following conclusions and recommendations were supported by the results of this study:

- F25-MK10, F25-SF5, S50-MK5 or S35-SF5 are recommended for use in very severe sulfate rich environments.

- Testing procedures that account for expansion and strength degradation must be used in developing HPMC. Testing for only one of the two degradation mechanisms will not guarantee adequate sulfate resistance for 100+ year service lives.
- Expansion testing showed that cement only samples exhibited significantly higher expansion than SCM containing compositions. Large expansions may be of concern in a prestressed concrete structure where the expansion may cause an increase in the precompression force in the member, and in doing so increase the stress in the prestressing steel.
- Mixture designs containing silica fume are more susceptible to compressive strength degradation in sulfate rich environments than equivalent replacement levels of metakaolin due to lower CaO contents that cause quicker decalcification of the C-S-H due to lower CH contents.
- A high CaO content in binder compositions leads to good performance on strength loss criterion due to the formation of calcium hydroxide, which serves as a buffer to C-S-H decalcification and strength loss.
- The ettringite content and expansion behavior of mixture designs is correlated, and mixture designs susceptible to the formation of large amounts of ettringite will fail expansion criterion.
- Research is needed to correlate the measured expansion or compressive strength in an accelerated test method to field performance and service life modeling.
- Research is needed on the influence of cracks on sulfate attack and ingress, since it has been shown by Moser (2011) that sulfates can play an active role in the depassivation of the oxide film on steel reinforcement and lead to active corrosion in an environment with sulfates and chlorides present.

CHAPTER 7

CARBONATION RESISTANCE OF HIGH PERFORMANCE CONCRETE

7.1 Introduction

The objectives of this portion of the study were to test the carbonation resistance of potential HPMC's and to perform service life modeling of each mix to determine the predicted corrosion initiation period. Carbonation of concrete can occur due the diffusion of carbon dioxide from the atmosphere and water through the pores of concrete. Carbonation of concrete leads to the depletion of calcium hydroxide, which causes a decrease in pH, and can lead to decomposition of hydration products. Loss of calcium silicate hydrate (C-S-H), which is the primary strength giving component of hydrated cement paste (Neville, 1997), is particularly of concern. Carbonation of concrete can cause strength loss of the concrete and initiate corrosion of reinforcing steel due to the decreased pH (Papadakis, et al., 1991). Therefore, maintaining high pH levels helps assure protection of embedded reinforcing steel.

Many HPC's utilize a lower water-to-binder ratio along with supplementary cementitious materials (SCM's) to improve overall strength and durability. While previous research (Papadakis, et al. 1991) has established that decreasing the water-to-cementitious materials ratio (w/cm) will increase the resistance of concrete to carbonation, the influence of SCMs on carbonation resistance has been less certain. Previous research on the use of binary mixture designs has shown that the use of SCMs may decrease the initial pH of the concrete through consumption of calcium hydroxide (CH), but their use also decreases the permeability by refinement of the pore structure

and the creation of secondary calcium silicate hydrate (C-S-H) (Bertolini, et al., 2004). Research by Atis (2003), Maslehuddin, et al. (1996), Papadakis (2000), Sideris, et al. (2006), and Sulapha, et al. (2003) on concretes utilizing fly ash replacement for cement showed that the carbonation depth (as defined by the color change of a phenolphthalein solution) increased with increasing the replacement levels. Slag replacement of cement was shown to increase the carbonation depth by Maslehuddin, et al. (1996) and Sulapha, et al. (2003) for replacement levels of 70% and 30 to 65%, respectively. The replacement of cement with silica fume was shown to increase the carbonation depth at all ages by Papadakis (2000) and Sulapha, et al. (2003). The results of Maslehuddin, et al. (1996) contradict this finding, and showed that a 10% replacement with silica fume led to a decrease in carbonation rate compared to a plain Portland cement concrete. Sulapha, et al. (2003) found that 10% silica fume replacement performed better than fly ash replacement (20-50%) and slag replacement (65%). Sideris, et al. (2006) found that the carbonation rate was lower at later ages for mixture designs containing SCMs. This suggests that the decreased pH initially due to CH consumption in the formation of secondary C-S-H may be offset in the long-term by the decreased rate of ingress due to the formation of a more dense matrix with smaller pores in the presence of SCMs.

Significantly less work has been performed on the carbonation resistance of ternary mixture designs. Sulapha, et al. (2003) found that a ternary blend of 10% silica fume and 55% slag replacement performed better than a 55% slag only mixture. Li and Zhang (2011) studied the influence of ternary mixture designs containing slag and fly ash (33% total replacement) and binary mixture designs with the same replacement level. The results of Li and Zhang (2011) demonstrated that the addition of slag to a fly ash

mixture design drastically improves carbonation resistance. A study by Jia, et al., (2012) also investigated the use of slag and fly ash ternary mixture designs and found that increasing replacement levels, regardless of proportions, led to decreased carbonation resistance for mixture designs with a w/cm of 0.37 or higher, but that the effect decreased with decreasing w/cm suggesting that transport may have an influence. Research by Sulapha, et al. (2003) on ternary blended cement suggests that ternary blends utilizing slag and silica fume may offer lower rates of carbonation than binary mixture designs.

Based upon the previous research into the carbonation resistance of binary mixture designs, it is evident that more research is needed into the carbonation resistance of binary and ternary mixture designs using low w/cm, since it appears that transport may begin to control instead of composition with a more refined microstructure. Additionally, the influence of ternary mixture designs other than the combination of slag, fly ash, and cement are needed. The objective of this study was to investigate the carbonation resistance of low w/cm binary and ternary mixture designs containing combinations of fly ash, slag, metakaolin, and silica fume.

7.2 Experimental Program

The carbonation resistance properties of the mixture designs presented in Chapter 4 were characterized by using an accelerated exposure test based upon the procedure used by Papadakis, et al. (1991). The test was performed on concrete prisms exposed to a 20% carbon dioxide environment, at 55% relative humidity and 40˚ C in a Nuaire US Autoflow NU-4850 Incubator. Samples were moist cured for 28 days in a fog room, conditioned at 55% relative humidity and 40˚C for 7 days, and then placed into the carbonation chamber. After various exposure periods, a phenolphthalein indicator solution (1% phenolphthalein, 20% water, 79% ethanol w/v), similar to that used by

Sulapha (2003) and and Atis (2002), was applied to the cut surfaces; and the distance to the carbonation front, as defined by color change at pH of 9.2, was measured.

The results were compared with estimator equations developed by Papadakis (2000). Additionally, modeling of the carbonation depth versus time was performed to aid in service life prediction calculations for corrosion initiation.

7.3 Results and Discussion

7.3.1 Carbonation Results

The carbonation depth was measured at various ages, and the depth of carbonation versus time for each mixture design is shown in Figures 7.1 through 7.3. After 28 days of exposure, T2 had carbonated over 19 mm (0.75 in.). Figure 7.1 shows the T2 carbonation samples sprayed with phenolphthalein after 1, 3, 7, 14, and 28 days of exposure. For samples with a lower w/cm the exposure period was extended to 1 year.

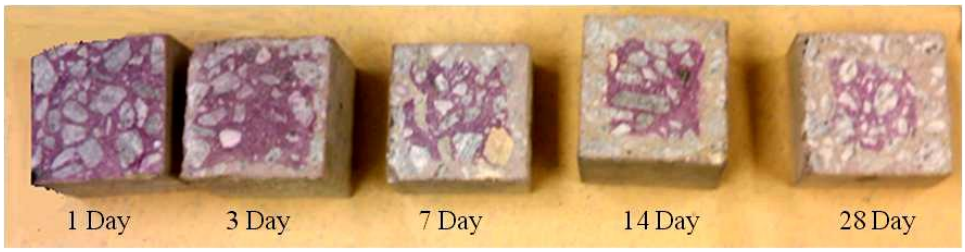

Figure 7.1: T2 carbonation samples (76.2 x 76.2 mm samples (3 in. x 3 in.)

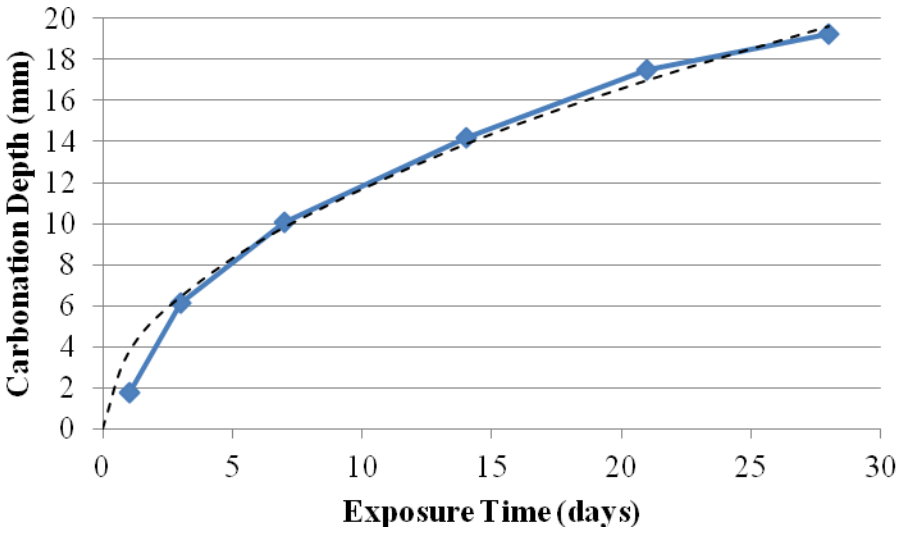

(a)

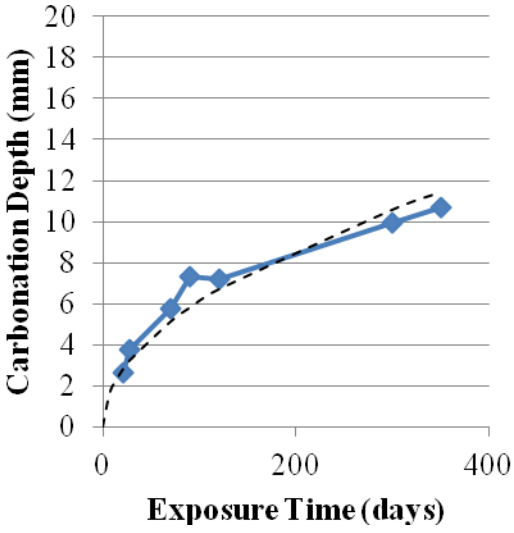

(b)

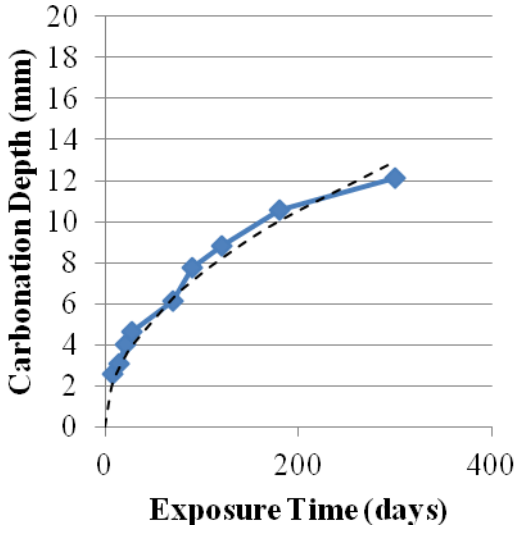

(c)

Figure 7.2: Carbonation curves for (a) T2, (b) T3-F15, and (c) F25 (1 in. = 25.4 mm)

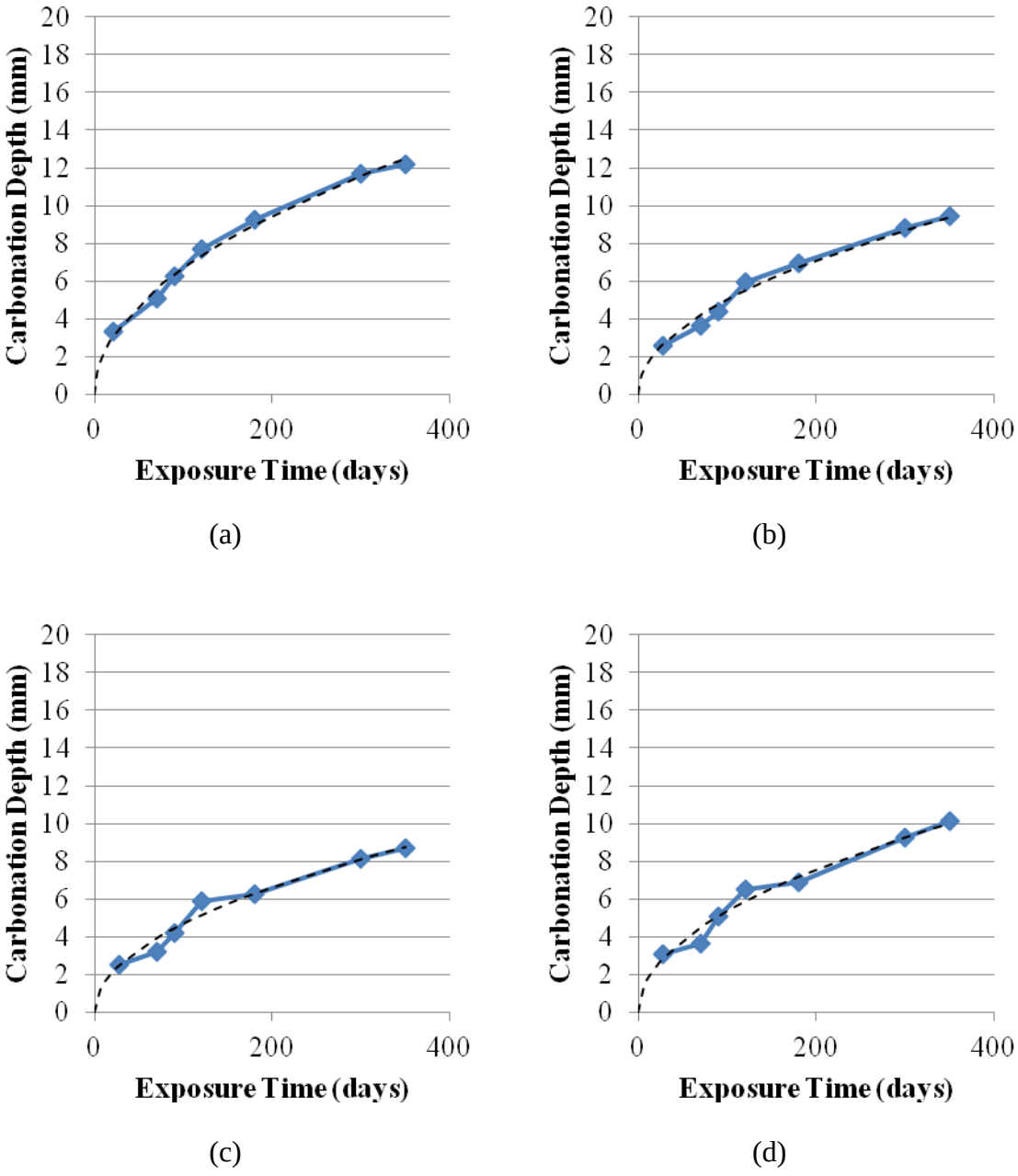

Figure 7.3: Carbonation curves for (a) F25-MK5, (b) F25-MK10, (c) F25-SF5, (d) F25-SF10 (1 in. = 25.4 mm)

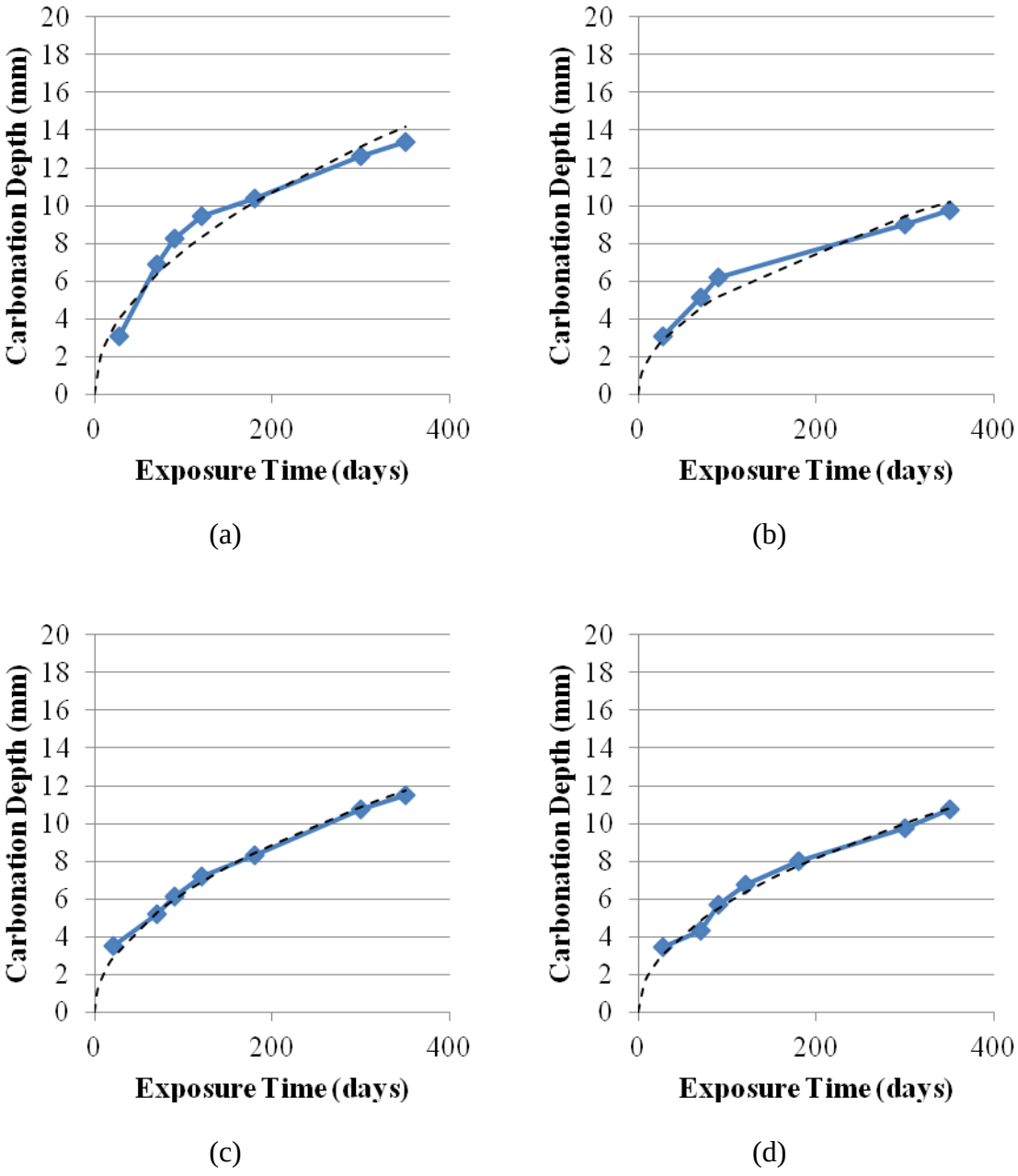

Figure 7.4: Carbonation curves for (a) S35-MK5, (b) S50-MK5, (c) S35-SF5, (d) S50-SF5 (1 in. = 25.4 mm)

Carbonation has been shown to be a diffusion-based phenomenon by Papadakis, et al. (1991). A simple model for carbonation is that the depth of ingress is proportional to the n^{th} root of time, as given in Eq. 7.1 (Bertolini, et al., 2004). Typically, n is assumed to be 2, resulting in the depth of ingress being proportional to the square root of time. Figures 7.2 to 7.4 also show the regression curve (dashed line) which fit Eq. 7.1 to the experimental data. Table 7.1 gives the measured carbonation constants from the regression analysis.

$$d = Kt^{1/n} \qquad \text{(Eq. 7.1)}$$

Where,

d = depth of carbonation, mm
K = carbonation constant, $mm/yr^{0.5}$
t = time, years
n = curve fitting factor, assumed to be 2

The regression analysis with R^2 values of 0.92 or higher showed that there was good agreement between the experimental data and Eq. 7.1 for the depth of carbonation being proportional to the square root of the exposure time.

The carbonation testing showed that mixture designs with higher water-to-cementitious materials ratios (w/cm) had significantly higher rates of carbonation. Mixture design T2, which had a 0.4 w/cm had a carbonation rate an order of magnitude higher than specimens with a 0.33 (T3-F15) or 0.3 w/cm (all other mixture designs) and is in agreement with the behavior observed by Papadakis, et al. (1991).

Table 7.1: Experimental carbonation constants (1 in. = 25.4 mm)

Mix	Slope Parameter ($mm/yr^{0.5}$)
T2	70.8
T3-F15	11.7
F25	14.3
F25-MK5	12.8
F25-MK10	9.6
F25-SF5	8.9
F25-SF10	10.2
S35-MK5	14.5
S50-MK5	10.4
S35-SF5	12.0
S50-SF5	11.1

The influence of SCM's on the carbonation rate varied widely based upon the type and replacement levels utilized. Figure 7.5 shows the carbonation constant (K) of mixture designs containing SCM's. The results suggest that increasing the fly ash content from 15% to 25% leads to an increase in the carbonation constant, even with a decreased w/cm. This is in agreement with the results of Papadakis (2000) which found that increasing fly ash content led to increased carbonation constants. The results suggest that the use of a ternary blend utilizing metakaolin or silica fume with fly ash leads to a decreased carbonation rate compared to a binary mixture design containing only cement and fly ash. Additionally, it was found that increasing contents of metakaolin from 5% to 10% led to a decrease in the carbonation constant. However, increasing silica fume contents led to an increase in the carbonation constant, but a 10% replacement level of silica fume had a lower carbonation constant that a binary blend with no silica fume or metakaolin.

The results of ternary blends containing slag showed a trend of decreasing carbonation constant with increasing slag content. Sulapha, et al. (2003) found that for a 65% replacement level with slag that the carbonation coefficient could decrease

compared to a cement-only sample and that the carbonation constant was related to the fineness of the slag used.

The results suggest that ternary blends containing fly ash and silica fume offer the lowest rate of carbonation from accelerated testing. Additionally, overall silica fume addition provides lower carbonation rates than equivalent replacement levels with metakaolin.

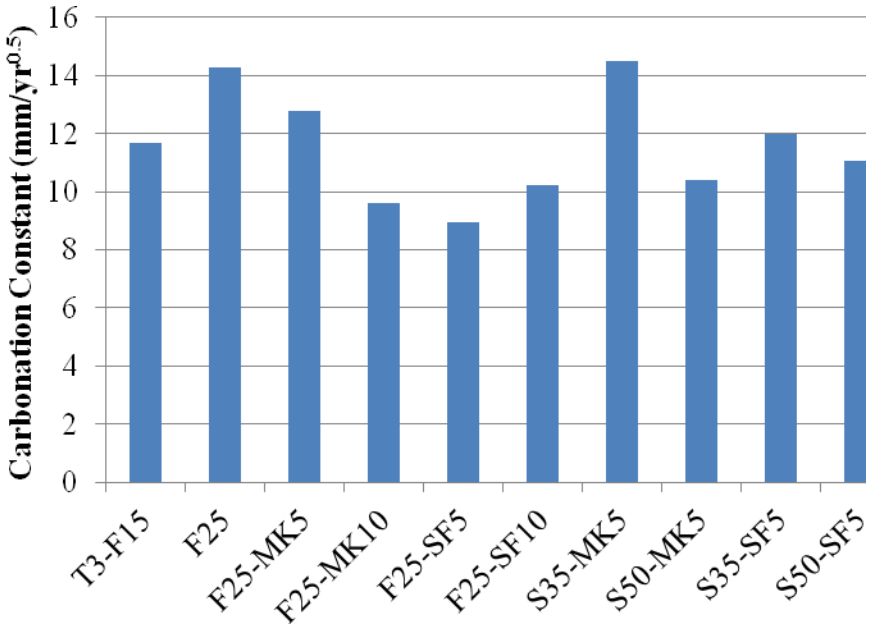

Figure 7.5: Carbonation constants for mixture designs containing SCM's
(1 in. = 25.4 mm)

The composition of each mixture design was investigated to determine the chemical characteristics that caused the observed trends. Table 7.2 shows the total oxide contents of each binder composition. A comparison of the oxide content to the measured carbonation coefficient shows that an apparent relationship exists between the SiO_2, Al_2O_3, and CaO contents and carbonation resistance as shown in Figure 7.6. It was found that an increasing SiO_2 and Al_2O_3 contents led to a decrease in the carbonation constant, and that increasing the CaO content of the mix led to decreased carbonation resistance.

The relationship between the CaO content and carbonation constant is in disagreement with the current theory that an increase in CaO content increases the calcium hydroxide content of the mixture design. An increase in calcium hydroxide means more CO_2 must penetrate to carbonate the concrete, thus leading to increased resistance. Previous authors that had suggested that relationship (Sulapha, et al., 2003; Papadakis, 2000; Papadakis, et al., 1991) were investigating concretes cast with w/cm of 0.5 or higher primarily, where transport properties may not have controlled. Sulapha, et al. (2003) investigated the pore structure size of mixture designs and found that keeping the binder composition and quantity the same, but decreasing the w/c led to a decrease in carbonation constant and the maximum size pores, suggesting that transport may be extremely important in the carbonation resistance of concrete. As part of the study, the pore structure of binary and ternary mixture designs with a 0.5 w/cm were investigated and it was found that fly ash and silica fume mixture designs offered the best refinement of the pore structure, and slightly higher carbonation constants than cement only samples.

The relationship between SiO_2 and Al_2O_3 content and carbonation constant does not appear to be a direct result of the composition, either. The results suggest that this relationship is transport based, since ternary mixture designs containing fly ash metakaolin or silica fume had the highest silica and alumina contents, and would be expected to have the most refined microstructure, which agrees with the findings of Sulapha , et al. (2003). Additionally, this result suggests that at low w/cm transport properties may control the carbonation resistance more than composition.

Table 7.2: Oxide contents of binder compositions

	SiO_2	Al_2O_3	Fe_2O_3	CaO
T2	20.51	4.65	3.35	62.60
T3-F15	26.07	8.62	3.54	54.34
F25	29.37	10.84	3.74	47.21
F25-MK5	30.91	12.82	3.59	44.09
F25-MK10	32.45	14.80	3.45	40.96
F25-SF5	33.07	10.62	3.58	44.11
F25-SF10	36.76	10.41	3.41	41.01
S35-MK5	28.50	7.82	2.17	50.59
S50-MK5	31.27	8.33	1.73	46.79
S35-SF5	30.66	5.62	2.16	50.62
S50-SF5	33.43	6.13	1.72	46.81

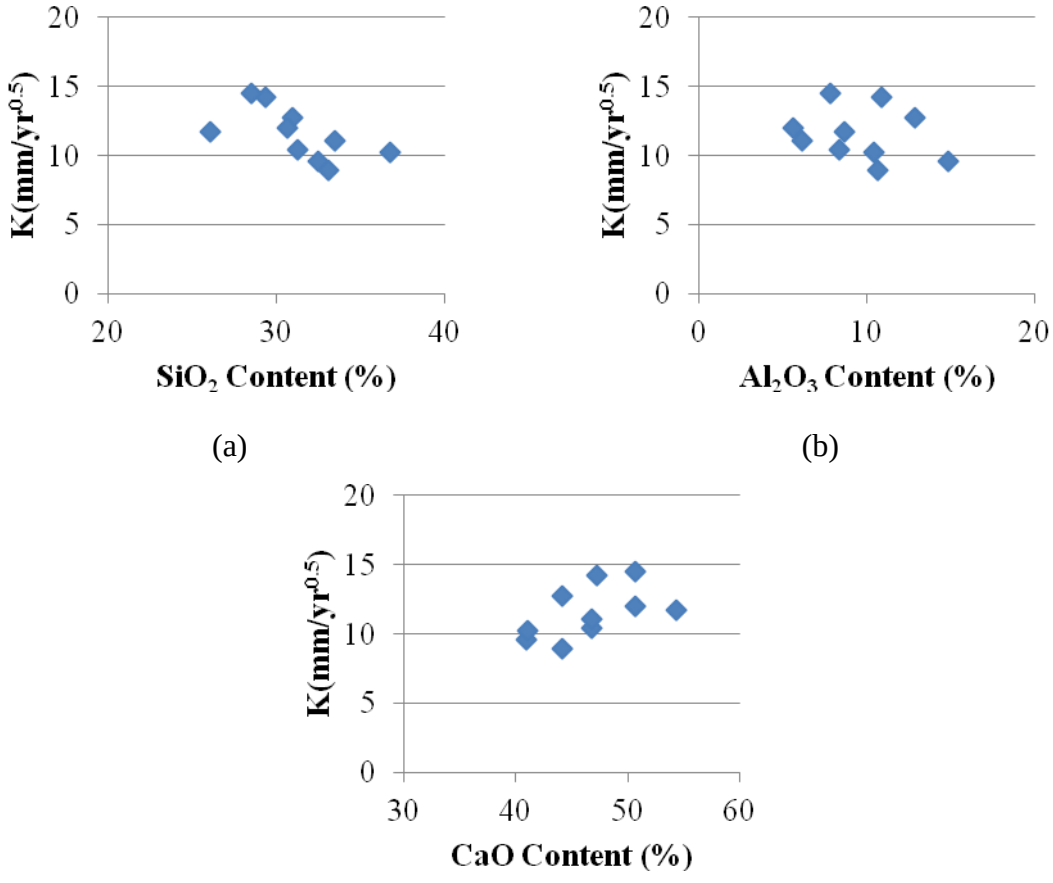

Figure 7.6: Carbonation constant compared to the (a) SiO_2 content, (b) Al_2O_3 content, and (c) CaO content (1 in. = 25.4 mm)

7.3.2 Modeling

7.3.2.1 Carbonation Constant Estimation

The ability to estimate and model the ingress of the carbonation front in concrete is necessary for accurate service life estimates. Sulapha, et al. (2003) studied the carbonation resistance of concretes produced using plain Portland cement concrete, and binary and ternary blends containing slag and silica fume. The results of the Sulapha, et al. (2003) study suggested that the carbonation constant, K, is related to the compressive strength of the concrete by Eq. 7.2 for a 6.5% CO_2 accelerated test environment.

$$K = -0.6 * f_c' + 54.27 \qquad \text{(Eq. 7.2)}$$

Where,

K = carbonation constant, $mm/yr^{0.5}$

f_c' = compressive strength at time of exposure, MPa

Papadakis, et al. (1991) and Papadakis (2000) presented a sophisticated model that gave a mathematical and physical meaning to the constant, K. A generic form of the Papadakis (2000) model is given in Eq. 7.3. The model provides a method for estimating the carbonation depth of mixture designs containing cement and fly ash or silica fume. Additionally, the method establishes a technique for accounting for the carbon dioxide level and relative humidity.

$$d = \sqrt{\frac{2\,D_{e,CO_2}\left(\frac{CO_2}{100}\right)t}{0.33CH + 0.214CSH}} \qquad \text{(Eq. 7.3)}$$

Where,

d	=	depth of carbonation, mm
$D_{e,CO2}$	=	diffusivity of CO_2 in carbonated concrete, mm^2/yr
CO_2	=	carbon dioxide content of ambient air at concrete surface, %
t	=	time, yr
CH	=	estimated calcium hydroxide content, %
CSH	=	estimated calcium-silicate-hydrate content, %

The relationship can be simplified into the same form as presented in Eq. 7.1, where the depth of carbonation is proportional to square root of time by a constant that accounts for the exposure conditions and mixture design properties. Eq. 7.4 provides the relationship between the carbonation constant, K, and the calculation method presented by Papadakis (2000). This relationship was used to calculate the experimental carbonation constant for ambient carbon dioxide levels and the estimation method used to predict the carbonation constant for mixture designs F25 and T3-F15.

$$K = \sqrt{\frac{2\,D_{e,CO_2}\left(\frac{CO_2}{100}\right)}{0.33CH + 0.214CSH}} \qquad \text{(Eq. 7.4)}$$

Where,

K	=	carbonation constant, $mm/yr^{0.5}$
$D_{e,CO2}$	=	diffusivity of CO_2 in carbonated concrete, mm^2/yr
CO_2	=	carbon dioxide content of ambient air at concrete surface, %
CH	=	estimated calcium hydroxide content, %
CSH	=	estimated calcium-silicate-hydrate content, %

Table 7.3 shows the measured and estimated values for the carbonation constant using the Sulapha, et al. (2003) and Papadakis (2000) methods for a 0.04% CO_2 environment. Only plain Portland cement concretes and binary mixture designs with fly

ash were able to be predicted with current estimation techniques provided by Papadakis (2000). However, estimates were made for fly ash and silica fume ternary mixture designs based upon the Papadakis (2000) approach, but not using the explicitly intended method. Figure 7.7 shows the estimated and measured values for carbonation constants of all tested mixture designs.

Table 7.3: Experimental and estimated carbonation constants (1 in. = 25.4 mm)

Mix	**Experimental K ($mm/yr^{0.5}$)**	**Sulapha Estimated K Eq. 7.2 ($mm/yr^{0.5}$)**	**Papadakis Estimated K Eq. 7.4 ($mm/yr^{0.5}$)**
T2	2.24	2.30	1.27
T3-F15	0.37	1.78	0.66
F25	0.45	1.85	0.48
F25-MK5	0.40	1.22	-
F25-MK10	0.30	0.30	-
F25-SF5	0.28	0.96	0.56*
F25-SF10	0.32	0.81	0.81*
S35-MK5	0.46	0.36	-
S50-MK5	0.33	0.67	-
S35-SF5	0.38	1.01	-
S50-SF5	0.35	1.04	-

*Estimates made based upon Papadakis (2000) approach, but not as explicitly intended by original author

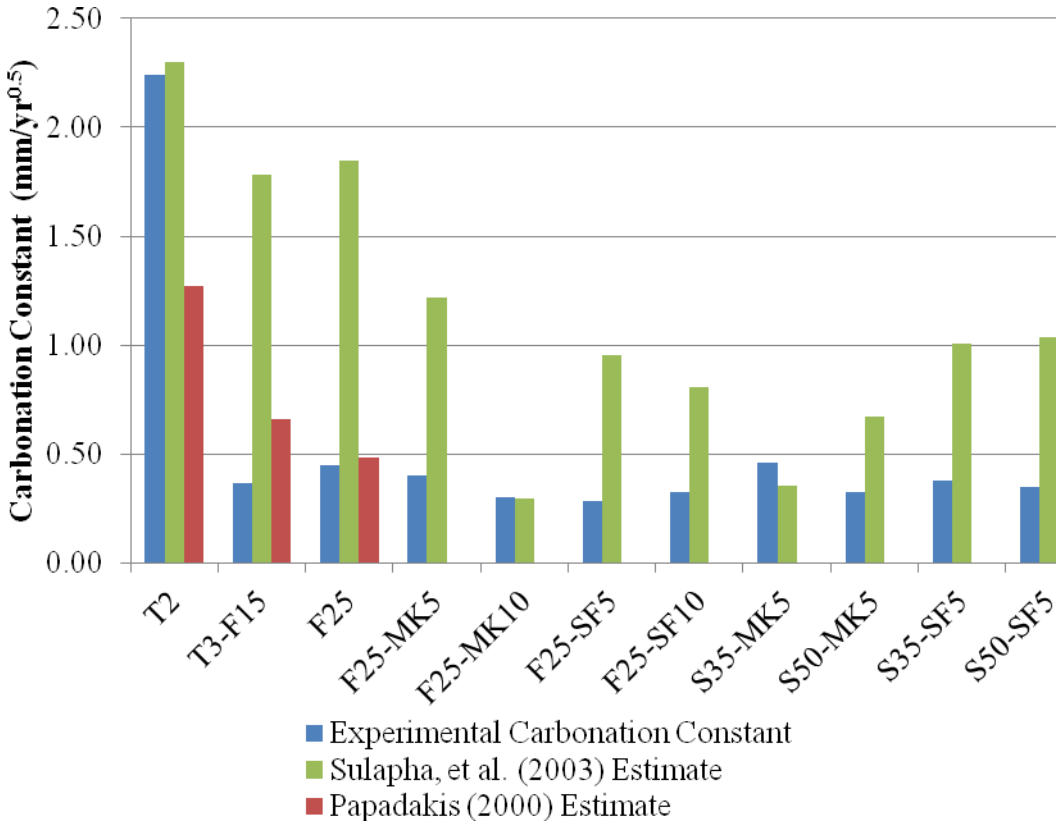

Figure 7.7: Experimental and estimated carbonation constants (1 in. = 25.4 mm)

The Papadakis (2000) estimation technique underestimated the carbonation constant for mixture design T2 by 42%, which led to an over-estimate for the predicted service life. The Papadakis (2000) technique overestimated the carbonation constant for fly ash mixture designs, which led to a shorter predicted service life. The Sulapha, et al. (2003) estimate procedure overestimated all carbonation constants except for mixture design S35-MK5, where it was 22% lower than the experimental value. The results suggest that the Sulapha, et al. (2003) procedure would provide a more conservative estimate for the carbonation constant utilizing readily available material properties.

7.3.2.2 Service Life Estimation

The results of for the carbonation constant given in Table 7.3 were used to estimate the carbonation front with time for an ambient exposure. Figures 7.8 and 7.9 show the estimated carbonation front versus time for fly ash and slag mixture designs, respectively. Based upon one-dimensional ingress, none of the fly ash or slag mixture designs would have the carbonation front reach the level of steel with a 76.2 mm (3 in.) cover in a 200 year service life. F25-SF5 and S50-SF5 provided the lowest ingress for fly ash and slag mixture designs respectively, with fly ash mixture designs containing silica fume performing the best. Figure 7.10 shows the predicted carbonation front locations for T2 and the best performing fly ash and slag ternary mixture designs. It can be observed that all mixture designs provided adequate protection for carbonation, but ternary mixture designs with lower water-to-cementitious materials ratios and fly ash performed better than the other mixture designs.

Table 7.4 shows the necessary cover distances to provide a service life of 100, 500, and 1,000 years. The estimated cover distances and service life are only for carbonation resistance. If in an environment containing chlorides then other factors must be considered for design, as discussed in Chapter 9. All mixture designs provided an estimated service life in excess of 1,000 years using the current 76.2 mm (3 in.) cover depth for reinforcement in precast prestressed piles, suggesting that using a low w/cm mixture design containing SCM's will provide adequate resistance to carbonation for a typical exposure environment for prestressed precast concrete piles. All mixture designs tested are capable of providing a 100 year lifespan with a 25.4 mm (1 in.) cover distance. For ternary mixture designs, theoretically only a 5 mm (0.2 in.) cover is necessary for a 100 year service life, and a 15 mm (0.6 in.) cover could provide a 1,000 year service life. If the cover distance is decreased with the same dimension pile, the flexural resistance would increase and it may be possible to decrease the number of strands used.

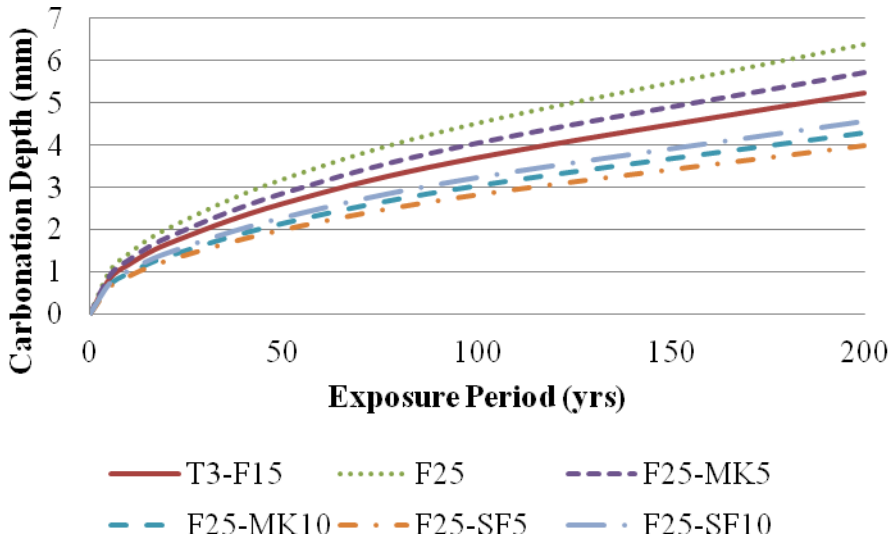

Figure 7.8: Predicted carbonation front location versus time for fly ash mixture designs (1 in. = 25.4 mm)

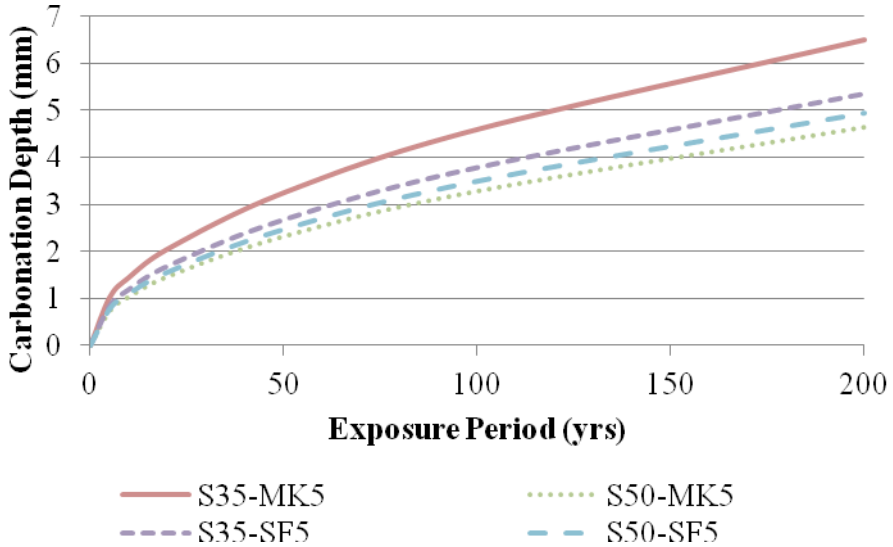

Figure 7.9: Predicted carbonation front location versus time for slag mixture designs (1 in. = 25.4 mm)

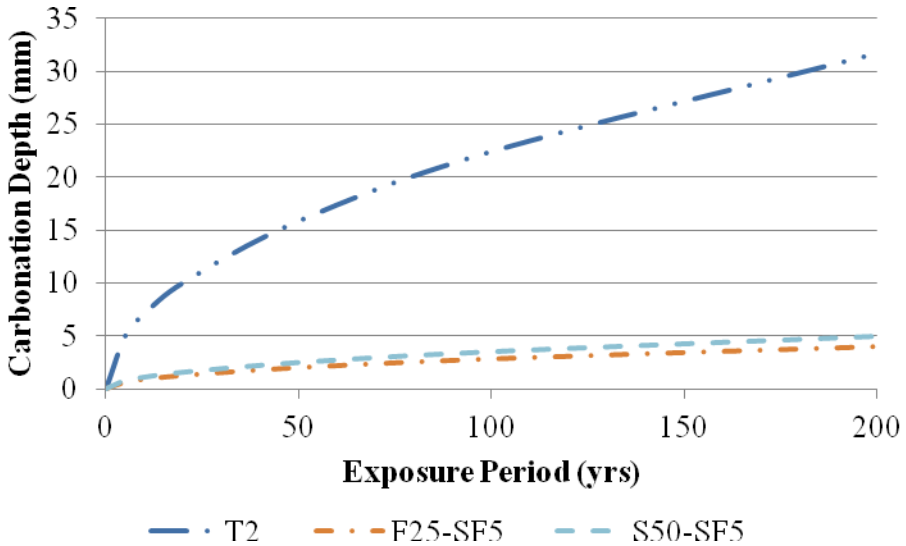

Figure 7.10: Predicted carbonation front location versus time for T2, F25-SF5 and S50-SF5 (1 in. = 25.4 mm)

Table 7.4: Required cover distances for intended service life goals (1 in. = 25.4 mm)

	Required Cover Distance (mm)		
Mixture design	**100 yrs**	**500 yrs**	**1,000 yrs**
T2	22.4	50.1	70.8
T3-F15	3.7	8.3	11.7
F25	4.5	10.1	14.3
F25-MK5	4.0	9.0	12.8
F25-MK10	3.0	6.8	9.6
F25-SF5	2.8	6.3	8.9
F25-SF10	3.2	7.2	10.2
S35-MK5	4.6	10.3	14.5
S50-MK5	3.3	7.3	10.4
S35-SF5	3.8	8.5	12.0
S50-SF5	3.5	7.8	11.1

7.4 Conclusions and Recommendations

The study into carbonation performance of potential HPMC mixture designs showed that ternary mixture designs are capable of providing service lives in excess of 200 years using a 5 mm (0.2 in.) cover. The results showed that the Papadakis (2000) estimation technique both overestimated and underestimated carbonation constants which could lead to an unconservative estimate of usable service life before corrosion initiation. The Sulapha, et al. (2003) procedure provided conservative estimates of the carbonation constants. The results showed that the carbonation rate decreased significantly with lowering of the w/cm ratio and that transport properties control carbonation resistance at low w/cm. Additionally, for mixture designs containing SCM's, ternary mixture designs with silica fume and fly ash perform the best.

The results of this study led to the following recommendations:

- The necessary cover distance for carbonation resistance can be decreased to 5 mm (0.2 in.). However, if other durability concerns exist then a different cover requirement may be necessary for providing the target service life.
- Use 0.3 w/cm mixture designs with fly ash and silica fume to ensure service lives in excess of 100 years.
- Future research is needed to develop service life models which account for 2-D ingress of the carbonation front.
- An estimation technique for accurately estimating the carbonation constant is needed for ternary mixture designs.
- Future research is needed into the behavior of cracked concrete subjected to carbonation and its influence on service life.

CHAPTER 8

SELF-HEALING OF HIGH PERFORMANCE CONCRETE

8.1 Introduction

The cracks in concrete can have a large influence on the transport and durability behavior of structures. Cracks increase the penetrability of concrete, reduce concrete strength, decrease aesthetics of structures, and may indicate deterioration of the structure (Rodriguez, 2001). Piles in marine environments are primarily susceptible to reflective tensile cracking due to driving and to flexure cracking during handling and placement as discussed in Appendix B.

It has been reported by many authors that corrosion in cracked concrete typically occurs as a direct result increased rate of transport of aggressive agents at or near the site of cracking and that the corrosion initiation time is reduced compared to uncracked concrete in similar conditions (Suzuki, et al., 1989; Suzuki, et al., 1990; Borgard, et al., 1991; Bentur, et al., 1997; Thursesson, et al., 1997). Research by Pease, et al. (2009) demonstrated that the cracks led to the sorption of water into the section surrounding the crack, and that the depth of ingress was a function of crack length, as shown in Figure 8.1. This suggests that deep cracks with wider surface widths will allow for deeper penetration of water and harmful ions into the section surrounding the crack. Further, the rate of corrosion is typically higher in cracked concrete due to increased availability of oxygen and water (Otsuki, et al., 2000).

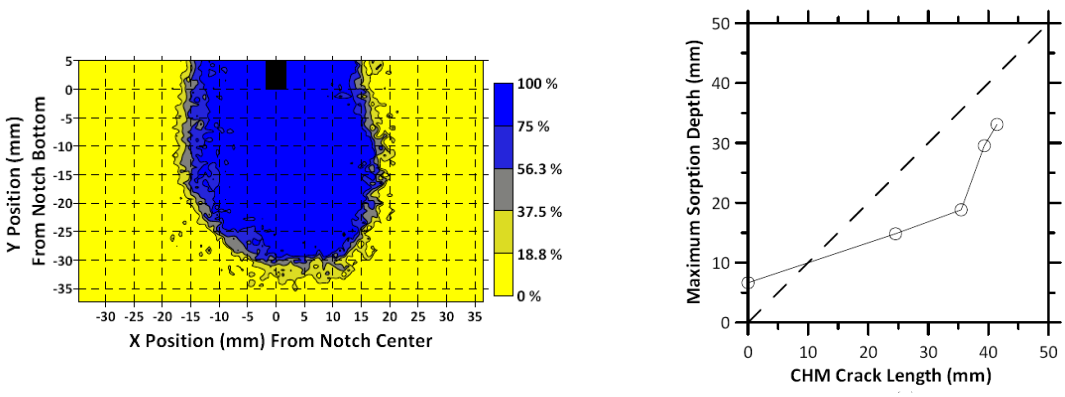

(a) (b)

Figure 8.1: (a) Absorption ratio contour plot for 0.15 mm (0.006 in.) surface crack width opening specimen after 1 hour of ponding (b) Crack length versus maximum sorption depth after 1 hour of water exposure (Pease, et al., 2009) (1 in. = 25.4 mm)

It has been shown that microcracks, or cracks less than 250 μm (0.0098 in.) wide, in concrete can self-heal and reduce the penetrability of chlorides into the section (Jacobsen, et al., 1998). Self-healing of cracked concrete has been shown to occur due to the cementitious material's capability to fill cracks in fractured concrete by (1) the formation of calcium carbonate or calcium hydroxide (Neville, 1997), (2) sedimentation of particles (Edvardsen, 1999), and (3) continuing hydration and swelling of the cement matrix (Neville, 1997). Previous research by Lauer and Slate (1955) and Heide (2005) has shown that the following conditions must be present for self-healing to occur: the presence of water, stability of the crack, and that the liquid may not lead to a leaching or dissolution reaction. Prestressed concrete piles in marine environments provide each of these environmental conditions necessary for self-healing to occur.

The purpose of this study was to test the self-healing capabilities of high performance concrete (HPC) mixture designs utilizing supplementary cementitious materials (SCM's) and the influence of self-healing on chloride ingress through flexural

and tension induced cracks. HPC mixture designs were evaluated for their chloride ingress resistance in cracked and uncracked concrete, and service life modeling was performed to characterize the influence of the self-healing of cracks formed in concrete structures during construction which were then subjected to long-term chloride exposure.

The HPC mixture designs typically used for coastal exposures utilize fly ash or slag to refine the microstructure of the concrete and increase the resistance to chloride ingress. Previous research by Rodriguez (2001) and Heide (2005) have shown that mixture designs containing slag showed higher degrees of self-healing than Portland cement only mixture designs when using chloride transport or strength recovery measurements. Termkhajonkit, et al. (2009) and Sahmaran, et al. (2008) studied the influence of fly ash on self-healing of shrinkage cracks and microcracking in samples subjected to electrical chloride migration tests; they found that fly ash mixture designs showed higher resistance to chloride ingress than cement only mixture designs. No research on the influence of silica fume or metakaolin on the self-healing of concrete was found.

8.2 Experimental Program

8.2.1 Concrete Mixture designs

Five mixture designs were developed to determine the influence of binder composition on the self-healing of cracks. The mixture designs were low water-to-cementitious materials ratio (w/cm) mixture designs that represent a current HPC (T3-

F15) with a 0.33 w/cm, and four other mixture designs developed using ACI 211.4R-08 (2008) with a 0.30 w/cm. Table 8.1 gives the binder compositions of each mixture design investigated. The total cementitious content of T3-F15 was 551 kg/m^3 (929 lb/yd^3), and the other mixture designs had a total cementitious materials content of 563 kg/m^3 (950 lb/yd^3) and were mixed using a natural sand and crushed granite coarse aggregate. Detailed information on the composition, particle size distribution, and aggregate properties is given in Chapter 4. Six prism specimens (127 x 127 x 457 mm (5 x 5 x 18 in.)) were cast from each mixture design: two control samples (C1,C2), two tensile crack samples (T1,T2) and two flexure crack samples (F1,F2).

Table 8.1: Self-healing mixture design binder compositions

Mix ID	Cement (%)	Cement Type	Fly Ash (%)	Slag (%)	Metakaolin (%)	w/cm
Type II	100	II	0	0	0	0.3
T3-F15	80	III	15	0	0	0.33
F25	75	II	25	0	0	0.3
S35-MK5	60	II	0	35	5	0.3
S50-MK5	45	II	0	50	5	0.3

8.2.2 Sample Preparation

The specimens were moist cured and then pre-cracked with a through-specimen tensile crack or with a flexural crack at 14 days of age. The crack orientations were chosen to represent the possible cracking patterns observed in piles due to reflective tension cracking and flexural cracking during handling. Through-section tensile cracks were created using knife edge bearings and flexural cracks were created using a three point bending test, as shown in Figure 8.2. Figure 8.2 also gives the dimensions of the test specimens and shows the surface where the crack width measurements were made for

each sample, denoted with a W. For flexure specimens, the exposure surface was the tension face of the sample.

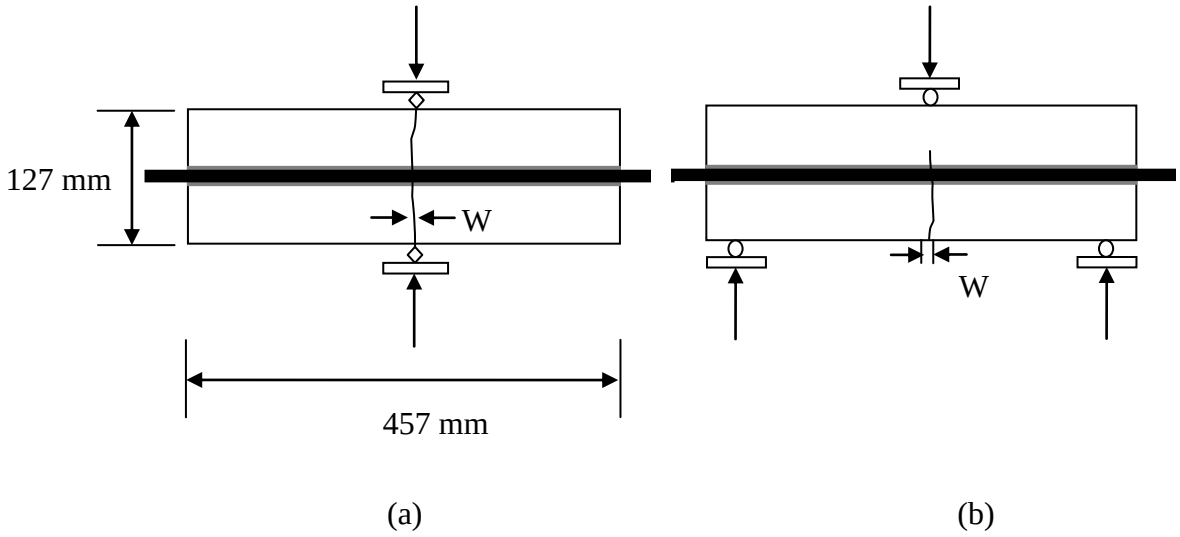

Figure 8.2: Cracking methods, dimensions, and crack opening measurement location for (a) tensile crack and (b) flexure crack specimens (1 in. = 25.4 mm)

After cracking the specimens, 6.2 MPa (900 psi) uniform compressive prestressing was applied to the specimens using internal unbonded post-tensioning bars to simulate the current level of prestressing used in the state of Georgia. This post-tensioning controlled the crack widths, which are discussed in section 8.2.3. The post-tensioning stress was maintained by tensioning the bars daily for a week, then weekly for the remainder of the ponding period to account for losses due to creep, shrinkage, and relaxation. Samples were ponded with a simulated seawater solution containing chlorides (165g/L NaCl) after precracking for a period of 120 days to simulate a marine exposure where chlorides would be available to ingress into the section and initiate corrosion.

8.2.3 Crack Healing Measurements

The crack widths were measured immediately after cracking and post-tensioning using an Elcometer 900 crack microscope with a 50x magnification and 25.4 μm (0.001 in.) tolerance rotating scale. The readings were continued weekly until the end of the 120 day ponding period. The exposure face of flexure samples was the tension face during cracking, where the maximum crack widths would be observed. The depth of the flexure cracks was determined along the sides of the sample where a wedge shape was formed. For tension samples, the exposure face was the face of the sample not subjected to the knife edge bearings. Readings were taken along the exposure face of each sample at 12.7 mm (0.5 in.) increments, for a total of 9 crack width measurements being used to calculate the mean and standard deviation.

8.2.4 Chloride Diffusion Measurements

Profile grinding was performed on the sample after an exposure period of 120 days by milling off increments along the crack opening using a 12.7 mm (½ in.) diameter masonry bit in a milling machine. The milling started on the exposure face and was performed across the length of the crack. This milling pattern was continued at each depth increment into the section following the crack. The total chloride concentration of each increment was determined in accordance with ASTM C 1152 (2004). Table 8.2 shows the grinding increments utilized for uncracked and cracked specimens. Larger increments were utilized on cracked specimens to account for deeper penetration of chlorides due to the presence of the crack.

Table 8.2: Profile grinding increments

	Depth, mm (in.)			
Increment	**Uncracked**		**Cracked**	
1	0-1	(0-0.039)	0-2	(0-0.079)
2	1-2	(0.039-0.079)	2-4	(0.079-0.157)
3	2-3	(0.079-0.118)	4-6	(0.157-0.236)
4	3-4	(0.118-0.157)	6-8	(0.236-0.315)
5	4-5	(0.157-0.197)	8-10	(0.315-0.394)
6	5-6	(0.197-0.236)	10-12	(0.394-0.472)
7	6-8	(0.236-0.315)	12-14	(0.472-0.551)
8	8-10	(0.315-0.394)	14-16	(0.551-0.630)

A regression analysis of the chloride concentration results were compared to Fick's Second Law of an infinite half-plane subjected to a constant surface concentration (Eq. 8.1). The comparison determined an apparent diffusion coefficient. The results of the chloride profile determination were used to perform service life modeling of each mixture design using Life 365 and the experimentally determined diffusion coefficients (Ehlen, 2009).

$$C(x,t) = C_s - (C_s - C_o) * \text{erf}\left(\frac{x}{\sqrt{4 * D_a * t}}\right) \quad \text{(Eq. 8.1)}$$

Where,

C(x,t)	=	chloride concentration, measured at depth x and exposure time t, mass %
C_s	=	projected chloride concentration at the interface between the exposure liquid and test specimen that is determined by the regression analysis, mass %
C_o	=	initial chloride-ion concentration of the cementitious mixture prior to submersion in the exposure solution, mass %
x	=	depth below the exposed surface, m
D_a	=	apparent chloride diffusion coefficient, m^2/s
t	=	the exposure time, s
erf	=	$\frac{2}{\sqrt{\pi}} * \int_0^z \exp(-u^2)\, du$

8.3 Results and Discussion

The crack width measurement results are presented in section 8.3.1. Section 8.3.2 gives the chloride ingress measurements and section 8.3.3 discusses service life modeling efforts for cracked concrete sections.

8.3.1 Crack Measurements

The crack widths visible on the surfaces of both tension and flexural crack specimens were measured immediately after cracking and the application of the post-tensioning load. Tables 8.3 and 8.4 present the measured crack widths and standard deviations for flexural and tension crack samples immediately after cracking and post-tensioning, respectively. Table 8.3 also gives the measured crack depths for flexure samples measured to the nearest 12.7 mm (0.5 in.). Tension samples exhibited through cracks and flexural cracks demonstrated a wedge shaped with the crack opening on the

tension face being the widest. Flexural cracks were not full depth except for sample F1 of mixture design Type II.

The measured crack widths along the exposure surface for flexural cracks were 121 micrometers (0.0048 in.) or smaller, with an average of 64.7 micrometers (0.0025 in.). The flexural crack depths ranged from 101 to 127 mm (0.004 to 0.005 in.), with a mean depth of 106 mm (0.0042 in.). The crack width opening was measured along the length of the crack on the exposure face to account for the large variability observed and capture a mean width. The measured crack widths for tensile crack specimens ranged from between 76 to 186 micrometers (0.003 to 0.0073 in.), with an average crack width of 127.1 micrometers (0.005 in.). All of the measured crack widths were below the reported threshold of 250 micrometers (0.0098 in.) that previous research had shown to be the upper limit on crack widths where self-healing could be expected (Edvardsen, 1999).

The variation in crack widths along the exposure surface observed between mixture designs for each type of specimen was expected due to using cracking specimens under load, instead of using artificial cracks, an approach utilized in some other studies where cracks were preformed into the sample using a spacer (Heidi, 2005). The formation of real cracks was preferred for this study over artificially created cracks, since it would give information on the expected cracks widths that could occur in precast prestressed concrete piles. Additionally, the surface of the crack would not be a smooth interface, but would be a roughened surface with both paste and aggregate exposed. An artificial crack with have a smooth surface with only the paste content exposed for self-healing to occur.

Table 8.3: Flexural crack specimens mean initial crack width and depth (1 in. = 25.4 mm)

		Crack Width (μm)		Crack Depth (mm)
Mix	**Specimen**	**Average**	**Std. Dev.**	
Type II	F1	80.4	37.0	127.0
	F2	96.2	65.1	114.3
	Average	88.3	-	120.7
T3-F15	F1	34.9	13.1	101.6
	F2	28.6	9.0	114.3
	Average	31.8	-	108.0
F25	F1	33.3	20.3	101.6
	F2	31.8	18.0	101.6
	Average	32.5	-	101.6
S35-MK5	F1	64.9	25.8	101.6
	F2	82.6	22.5	101.6
	Average	73.7	-	101.6
S50-MK5	F1	121.4	56.5	101.6
	F2	73.0	9.0	101.6
	Average	97.2	-	101.6

Table 8.4: Tensile crack specimens initial crack width and standard deviation (1 in. = 25.4 mm)

		Crack Width (μm)	
Mix	**Specimen**	**Average**	**Std. Dev.**
Type II	T1	186.3	110.0
	T2	121.4	64.5
	Average	153.8	-
T3-F15	T1	139.7	85.9
	T2	152.4	147.0
	Average	146.1	-
F25	T1	120.7	110.1
	T2	116.1	58.4
	Average	118.4	-
S35-MK5	T1	76.2	40.7
	T2	94.5	78.6
	Average	85.4	-
S50-MK5	T1	104.8	31.7
	T2	158.8	144.2
	Average	131.8	-

The crack widths were monitored throughout the ponding process on the surface of the specimens. Figure 8.3 shows the mean crack width after exposure to mean initial crack width ratio for flexural specimens of each mixture design. Figure 8.4 shows the mean crack width after exposure to mean initial crack width ratio for tensile specimens of each mixture design. The cracks on all specimens began to have visible formation of products in the crack over time; however, the crack width was still apparent and measured. Therefore, the crack width readings do not account for the filling of the crack, but only the closing of it (e.g., change in mouth width). Figure 8.5 shows a crack that has filled in and one where product formation was not visible across the crack. The filling of the crack is likely due to the formation of calcium carbonate and calcium hydroxide in the crack. The crack width measurements captured the swelling and hydration of the crack surfaces, but not the filling of the crack itself.

The flexural and tensile crack width readings showed an initial closing of the crack during the period of 0 to 7 days, likely due to the swelling of the matrix due to saturation. After the initial closing, each mixture design demonstrated continuing closing of the crack until an asymptotic value was approached, at approximately 50 days. Additionally, samples from S35-MK5 demonstrated a faster closing to the asymptotic value, by 35 days, of the crack than other mixture designs.

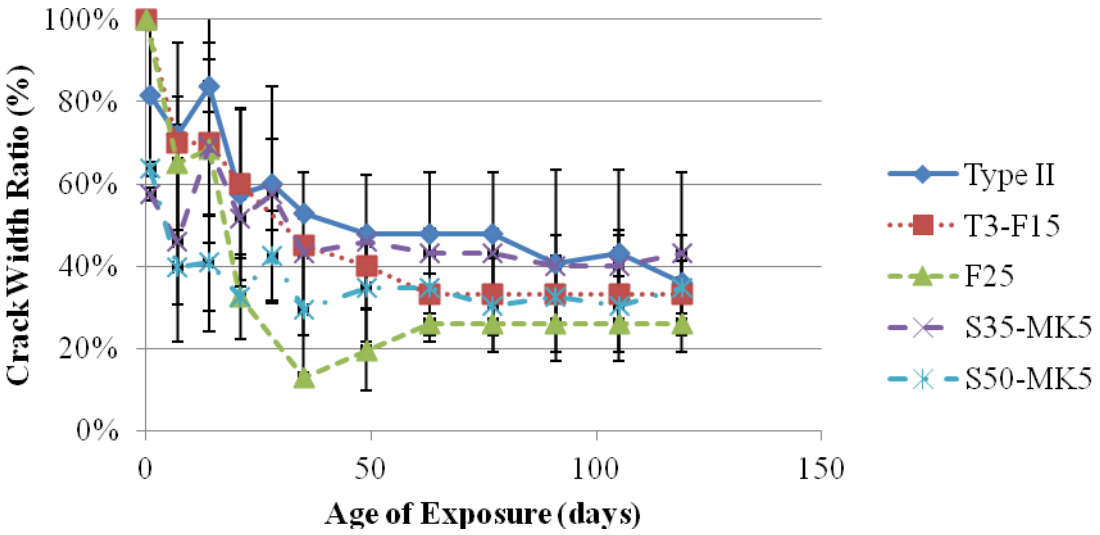

Figure 8.3: Mean crack width after exposure to initial mean crack width ratio of flexure crack specimens over exposure time

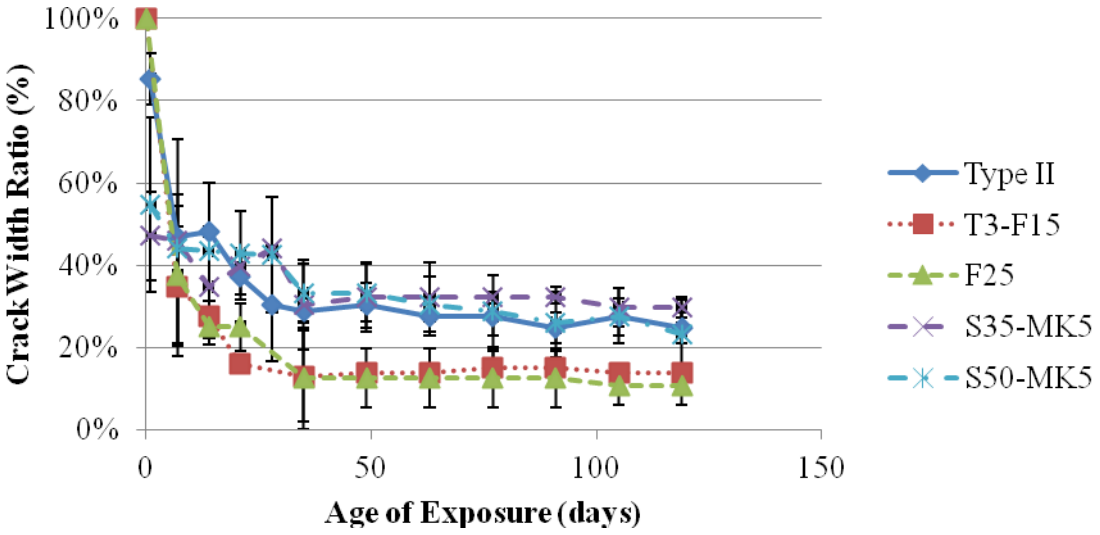

Figure 8.4: Mean crack width after exposure to initial mean crack width ratio of tensile crack specimens over exposure time

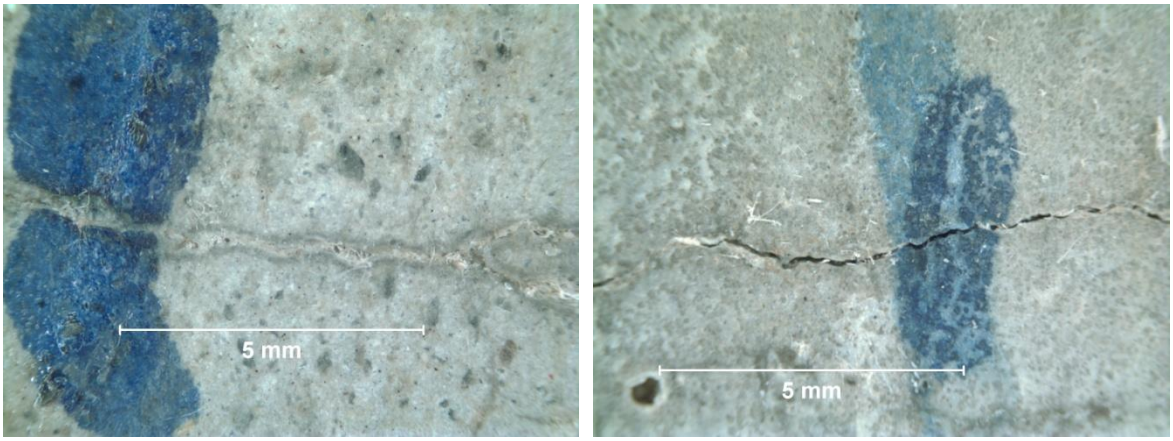

(a) (b)

Figure 8.5: (a) S35-MK5 F1 sample with crack filling, (b) F25 F1 sample with less crack filling after 120 days of exposure

8.3.2 Chloride Ingress

The chloride ingress resistance of cracked concrete was characterized by performing ponding with simulated seawater solution on cracked and control samples. Profile grinding and titrations were performed to determine chloride profiles, which had analysis run to determine experimental apparent diffusion coefficients. The determined apparent diffusion coefficients were then used for service life modeling efforts using a 0.05% by mass of concrete chloride threshold limit (CTL) at which corrosion would initiate.

The results of titrations to determine acid-soluble chloride content in the samples ground from the cracked and uncracked regions in the concretes are given in section 8.3.2.1. Section 8.3.2.2 discusses the modeling of chloride ingress in cracked sections and the appropriateness of traditional models for uncracked concrete being applied to cracked concrete. Section 8.3.3 presents the results of service life modeling for uncracked and cracked concrete in marine environments.

8.3.2.1 Chloride Profiles

The chloride profiles of control, tension, and flexure cracked specimens were determined using profile grinding and acid soluble chloride content determination in accordance with ASTM C 1152 (2004). Two titrations were run at each depth increment, and represent the average chloride content of a 9.5 mm (3/8 in.) wide section at that depth. The 2-D ingress from the crack surface and exposure surface was not accounted for, since only the influence of the crack on chloride ingress to the level of the steel was of interest. The chloride profiles for each type of specimen are presented in Figures 8.6 through 8.10 by mixture design using the increments presented in Table 8.2. The control samples chloride profiles are shown with a solid line, the tension samples a dashed line, and the flexure samples by a dash-dot line.

All cracked samples demonstrated higher concentrations of chlorides deeper into the section than control samples. Additionally, titrations on ground samples from 76.2 mm (3 in.) into the section demonstrated that flexure and tension cracked samples did not approach a zero concentration with further distance into the section . Generally, the profiles for tension samples showed the greater concentrations of chlorides than flexure specimens. This suggests that the chloride profile is a function of the mean crack width on the exposure surface as was determined in section 8.3.1, since tension cracks had larger crack opening widths than the flexure crack specimens initially.

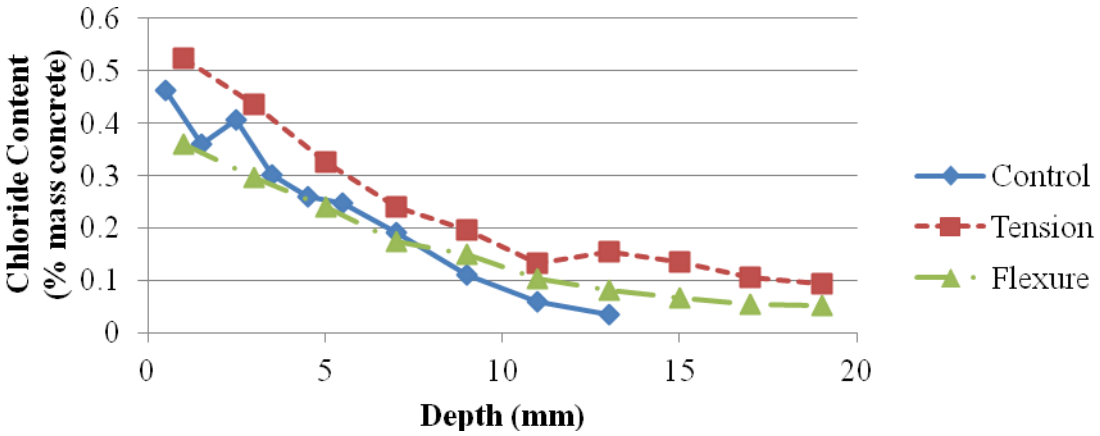

Figure 8.6: Type II chloride profiles for control, tension, and flexure crack specimens

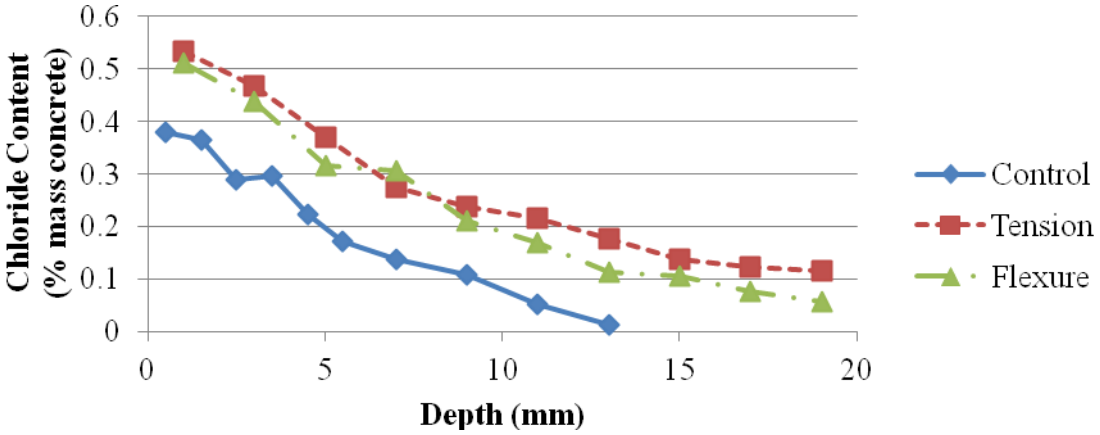

Figure 8.7: T3-F15 chloride profiles for control, tension, and flexure crack specimens

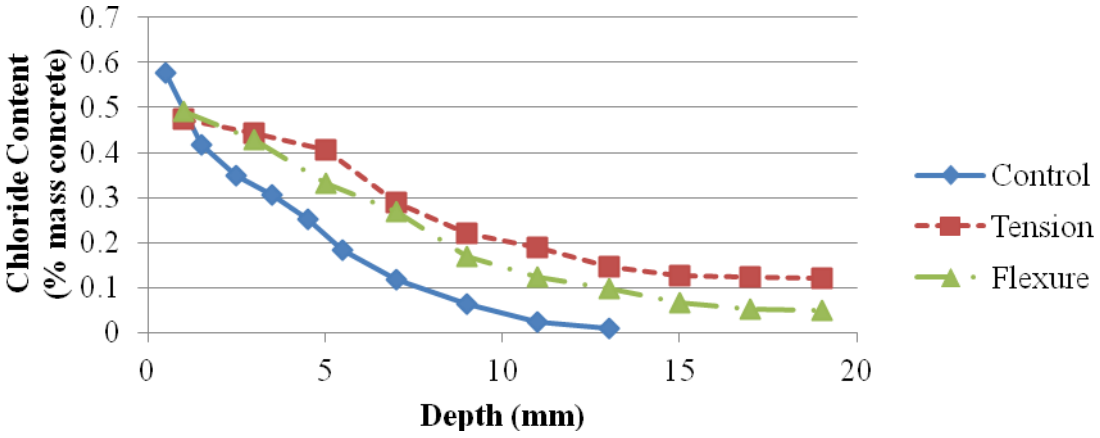

Figure 8.8: F25 chloride profiles for control, tension, and flexure crack specimens

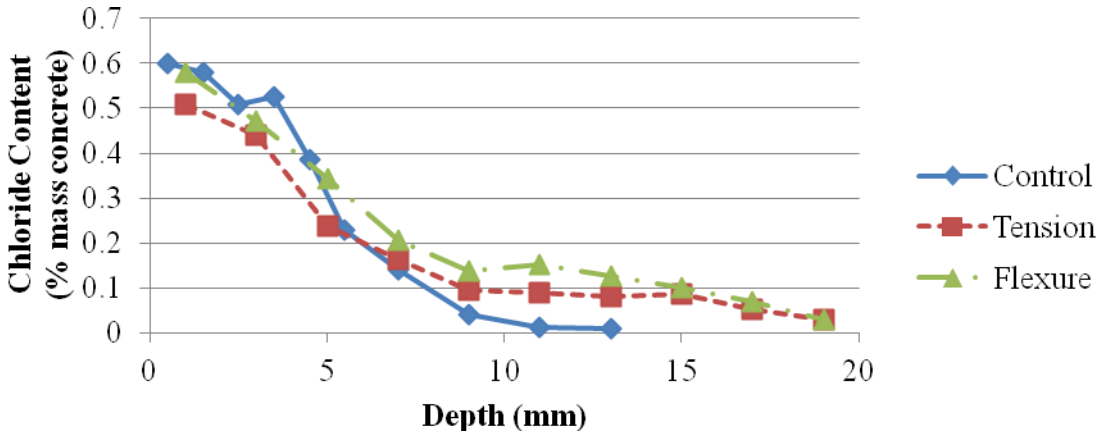

Figure 8.9: S35-MK5 chloride profiles for control, tension, and flexure crack specimens

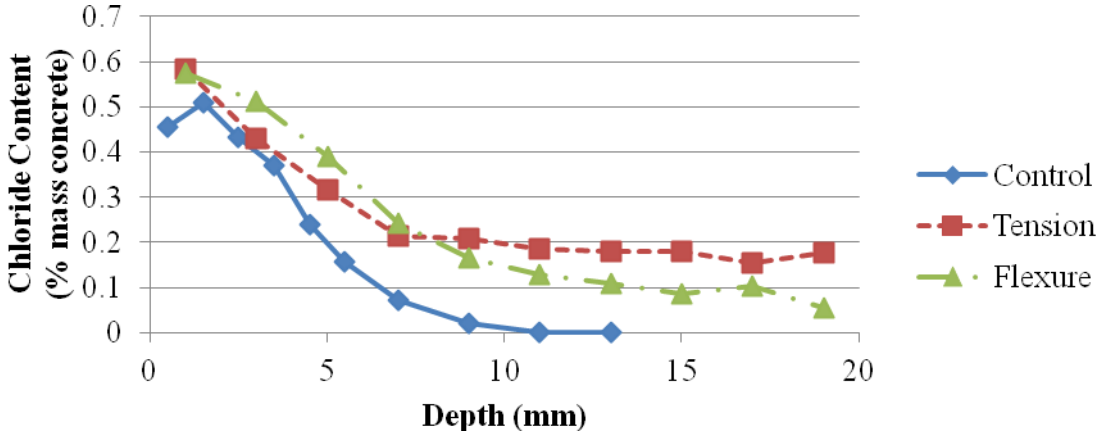

Figure 8.10: S50-MK5 chloride profiles for control, tension, and flexure crack specimens

In addition to the profiles of the outer most 19 mm (0.75 in.), the chloride content at 76.2 mm (3 in.) into the section was determined (Table 8.5), which is the cover depth of the reinforcement with the current GDOT pile design. The chloride content at the depth of reinforcing in flexure specimens was lower than in tension crack specimens. This may be due to the narrower width of the crack as well as the influence of the crack shape. The flexure cracks were not full depth and had a wedge shape. Therefore, the

width of flexure cracks at the depth of reinforcing may likely be smaller than the width measured at the surface.

Table 8.5: Mean chloride content at depth of reinforcement (76.2 mm, 3 in.)

	Chloride Content (% mass concrete)			
	Flexure		Tension	
Mixture design	**Avg.**	**Std. Dev.**	**Avg.**	**Std. Dev.**
Type II	0.012	0.0025	0.051	0.0035
T3-F15	0.011	0.0037	0.057	0.0394
F25	0.007	0.0000	0.036	0.0030
S35-MK5	0.000	0.0000	0.030	0.0083
S50-MK5	0.007	0.0100	0.064	0.0610

8.3.2.2 Chloride Transport Modeling

The results of the chloride profile determination in both control and cracked samples were used to determine the apparent diffusion coefficient. The results were fit to Fick's second law utilizing two different approaches. First, the traditional approach presented by Eq. 8.1 was utilized where C_o, the initial background content, was taken as the chloride content of the concrete prior to exposure (C_o = 0 %). Table 8.6 presents the apparent diffusion coefficients and the sum of squares due to error (SSE) statistic that measures the goodness of fit for using the standard Fick's second law approach. An SSE value below 0.005 represents a good fit between the regression and the experimental data. Using this method, all of the chloride profiles would approach a 0% concentration at large depths into the section. However, the chloride profiles for cracked specimens demonstrated an asymptotic behavior farther into the section towards a non-zero background content.

A modified approach was utilized in the regression analysis to Fick's second law by leaving the C_o value as a parameter to be determined through the regression instead of being the constant chloride background content of the concrete mixture design. The C_o value calculated using this method represents the background content of the area immediately surrounding the crack (6.4 mm either side of crack) that was ground using the 12.8 mm diameter masonry bit. The modified approach was utilized in regression analysis of cracked specimens only, and accounts for the sorption that Pease, et al. (2009) found to occur along the crack face. The results of the modified approach regression analysis are shown in Table 8.7. The modified approach showed lower SSE values, indicating a better fit with the data. On average, the SSE value with the modified approach was 48% lower than the standard method of applying Fick's second law.

Table 8.6: Traditional approach to Fick's second law regression analysis results (1 in. = 25.4 mm)

	Diffusion Coefficient (m^2/s)			**SSE**		
Mixture design	**Control**	**Flexure Crack**	**Tension Crack**	**Control**	**Flexure Crack**	**Tension Crack**
Type II	2.99E-12	5.85E-12	7.30E-12	0.0055	0.0014	0.0116
T3-F15	2.43E-12	5.99E-12	8.81E-12	0.0022	0.0029	0.0083
F25	1.67E-12	4.25E-12	7.87E-12	0.0007	0.0017	0.0081
S35-MK5	1.43E-12	4.25E-12	2.55E-12	0.0014	0.0112	0.0149
S50-MK5	1.04E-12	3.82E-12	1.56E-11	0.0041	0.0109	0.0217

Table 8.7: Modified approach to Fick's second law regression analysis results (1 in. = 25.4 mm)

	Diffusion Coefficient (m^2/s)		**C_o (% mass concrete)**		**SSE**	
Mixture design	**Flexure Crack**	**Tension Crack**	**Flexure Crack**	**Tension Crack**	**Flexure Crack**	**Tension Crack**
Type II	4.24E-12	2.66E-12	0.024	0.086	0.0007	0.0038
T3-F15	5.20E-12	4.60E-12	0.017	0.076	0.0025	0.0026
F25	3.53E-12	4.55E-12	0.020	0.063	0.0010	0.0043
S35-MK5	2.65E-12	1.12E-12	0.041	0.050	0.0091	0.0028
S50-MK5	2.17E-12	1.47E-12	0.055	0.148	0.0053	0.0104

Figure 8.11 shows the regression analysis results (solid line) and experimental data (diamond markers) for control samples from each mixture design. The regression demonstrated good agreement with the experimental data.

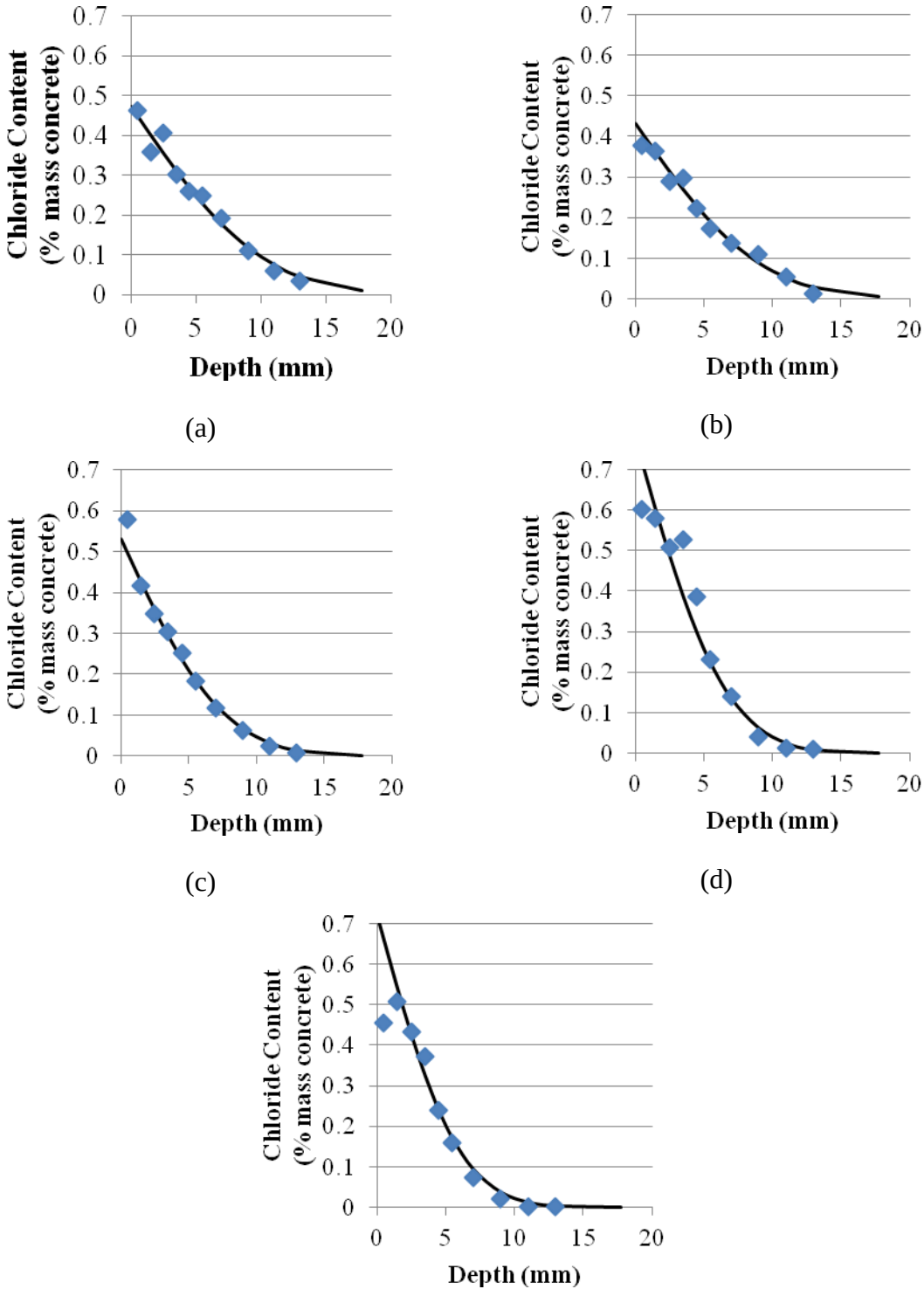

Figure 8.11: Regression analysis results for control samples from mixture design (a) Type II, (b) T3-F15, (c) F25, (d) S35-MK5, and (e) S50-MK5 (1 in. = 25.4 mm)

Figures 8.12 through 8.16 show the regression analysis results (solid line) and experimental data (diamond markers) for flexure crack samples from each mixture design and Figures 8.17 through 8.21 show the regression analysis results (solid line) and experimental data (diamond markers) for tension crack samples with the experimental measurements at the depths provided in Table 8.2. For flexure crack specimens, both techniques provided similar estimates. The modified procedure better matches the behavior of the experimental data farther into the section than the standard approach using Fick's second law. The tail of the chloride profile is the primary area of interest, since its behavior will dictate when adequate concentration of chlorides reach the level of the steel to induce corrosion.

The modified approach provided a much better fit to the tension crack samples than the traditional model. The standard approach with Fick's second law led to underestimating the chloride ingress near the surface and deep into the section. The underestimation of the chloride ingress deep into the section was due to the presence of the background content due to the initial ingress of chlorides into the section through the crack. The use of a model that under-estimates the chloride content in the section will lead to over-estimating the usable service life. More discussion on service life evaluation is given in section 8.3.2.3.

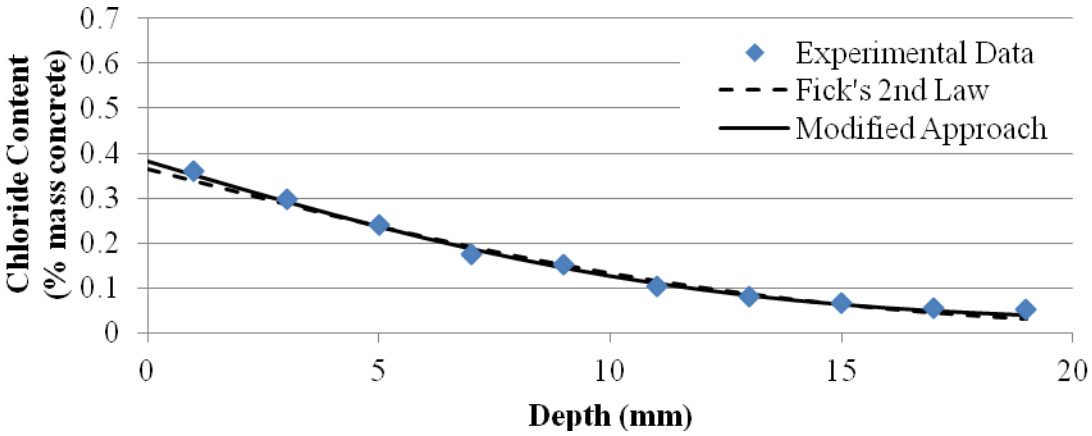

Figure 8.12: Regression analysis results for Type II flexure crack specimens

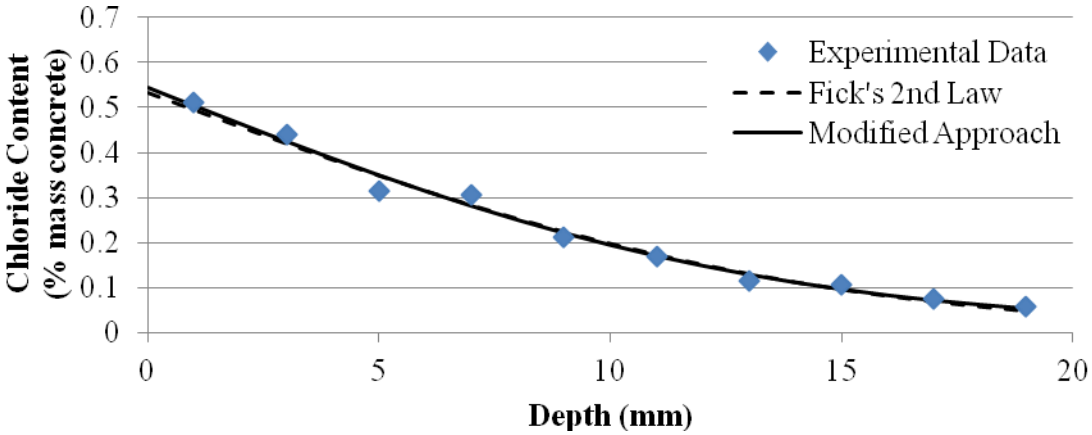

Figure 8.13: Regression analysis results for T3-F15 flexure crack specimens

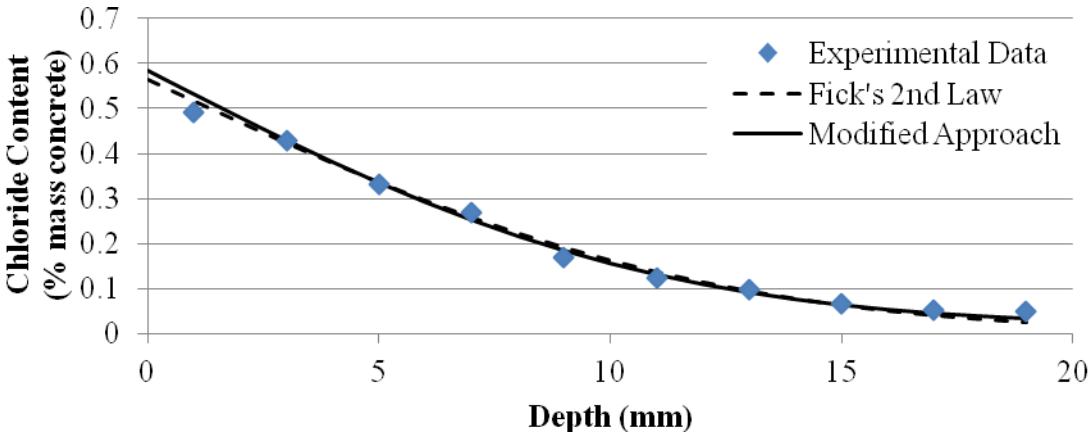

Figure 8.14: Regression analysis results for F25 flexure crack specimens

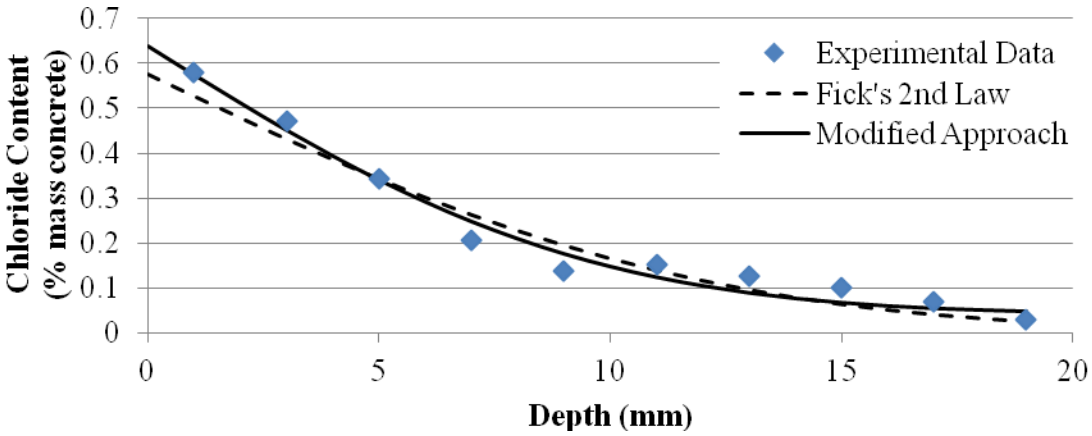

Figure 8.15: Regression analysis results for S35-MK5 flexure crack specimens

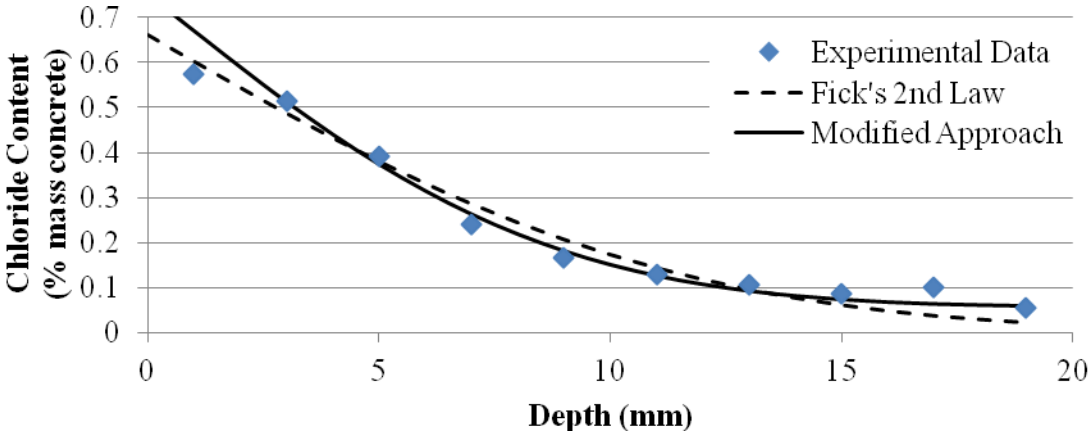

Figure 8.16: Regression analysis results for S50-MK5 flexure crack specimens

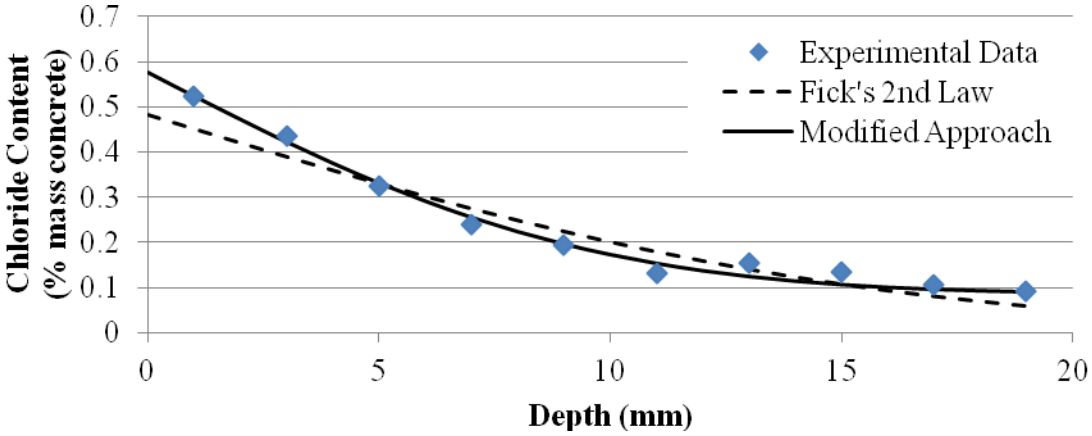

Figure 8.17: Regression analysis results for Type II tension crack specimens

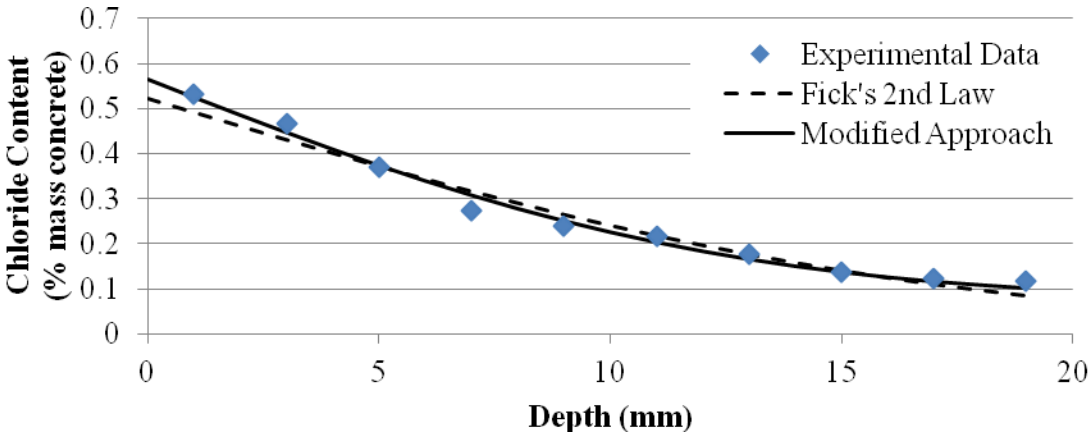

Figure 8.18: Regression analysis results for T3-F15 tension crack specimens

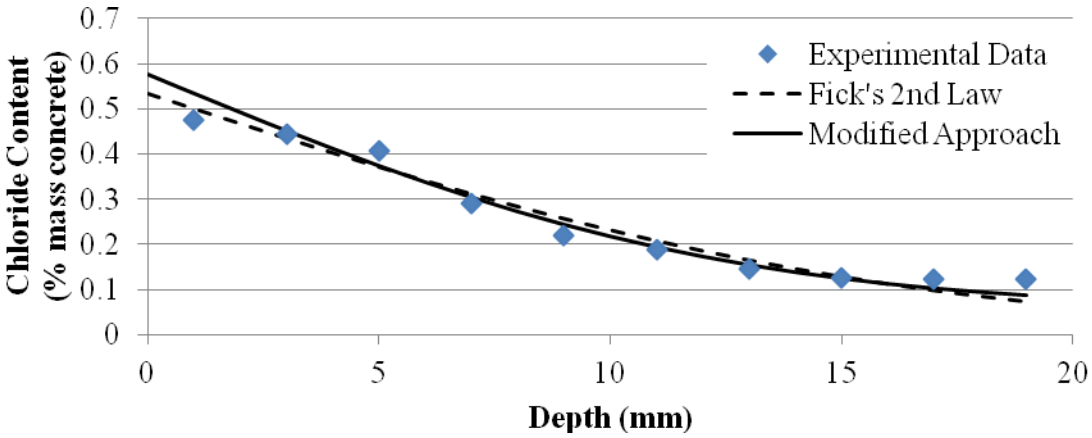

Figure 8.19: Regression analysis results for F25 flexure tension specimens

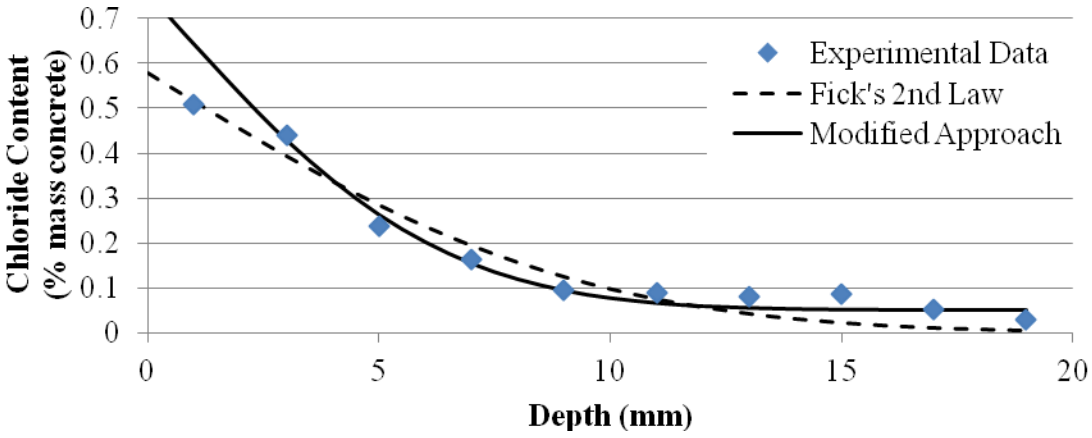

Figure 8.20: Regression analysis results for S35-MK5 tension crack specimens

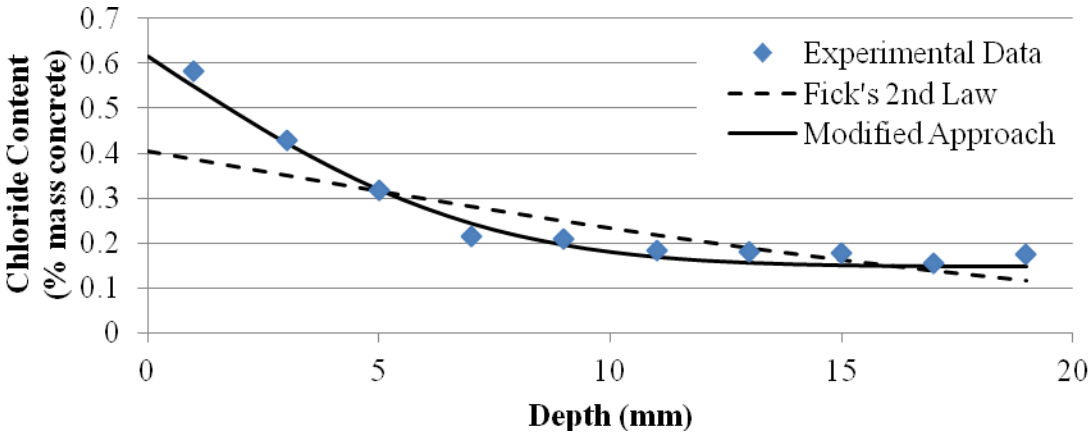

Figure 8.21: Regression analysis results for S50-MK5 tension crack specimens

8.3.2.3 Crack Width Influence on Chloride Ingress

A comparison of the background content (C_o) determined using the modified approach and the mean initial crack width for each specimen across the exposure face showed a linear relationship. This suggests that this observed background content ingresses upon initial exposure. Figure 8.22 shows the experimental data, as well as a linear regression demonstrating the observed trend between crack width and C_o. The strong correlation between crack size and background content suggests that the background content for a cracked section could be estimated using Eq. 8.2.

$$C_o = 0.0005 * W \qquad \text{(Eq. 8.2)}$$

Where,

C_o = initial background content due to presence of crack, % mass concrete

W = mean initial crack width at exposure surface, μm

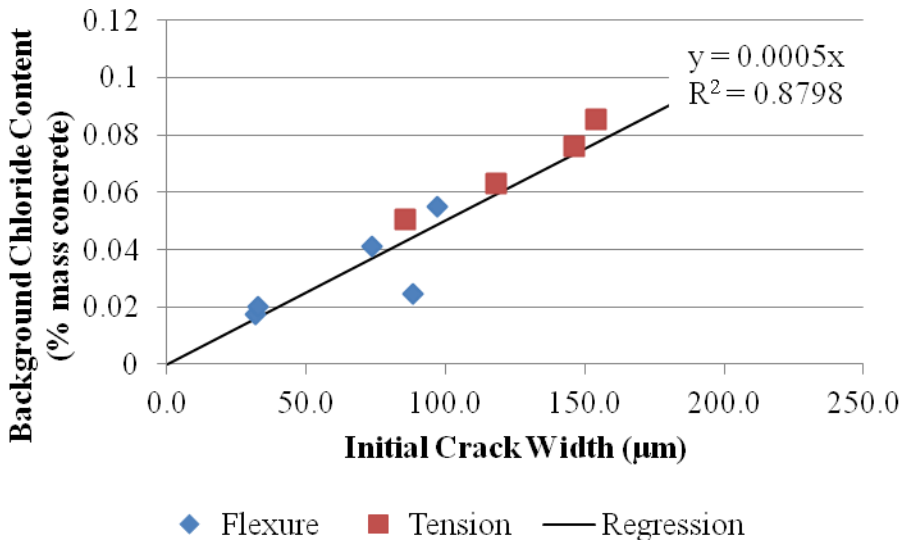

Figure 8.22: Crack width versus background chloride content of cracked sections (0.001 in. = 25.4 µm)

8.3.2.4 Diffusion Coefficient of Self-Healed Specimens

The apparent diffusion coefficients determined using the modified technique for cracked specimens was compared with the measured diffusion coefficient from control samples. The ratio between the cracked and control sample diffusion coefficients are presented in Table 8.8. Tension cracks from all mixture designs demonstrated lower diffusion coefficients than flexure samples of the same mixture designs. This suggests that crack width alone does not determine the apparent diffusion coefficient in a cracked section, since the flexure cracks had smaller widths. More research is needed to understand this relationship, but the geometry of the crack may play a role.

Table 8.8: Ratio of cracked diffusion coefficient to control diffusion coefficient for flexural and tensile cracked specimens

	$D_{a,\,cracked} / D_{a,\,uncracked}$	
Mixture design	**Flexure**	**Tension**
Type II	1.42	0.89
T3-F15	2.14	1.89
F25	2.12	2.73
S35-MK5	1.86	0.73
S50-MK5	2.10	1.42

A comparison of the diffusion coefficient ratio and crack widths showed there was not a correlation between them (Figure 8.23). The apparent diffusion coefficient ratio did vary by mixture design and showed that certain mixture designs show a lower ratio, with the ratio approaching 1.0. This suggests that these mixture designs demonstrate the largest propensity for self-healing to occur, due to the recovery of diffusion behavior approaching that of uncracked concrete. The Type II and S35-MK5 mixture designs showed the lowest ratios for flexural and tensile cracks, respectively. The fly ash mixture designs (T3-F15 and F25) showed the highest ratios. This suggests that mixture designs containing cement only or slag, among those examined here, show the greatest potential for self-healing in a chloride-laden environment.

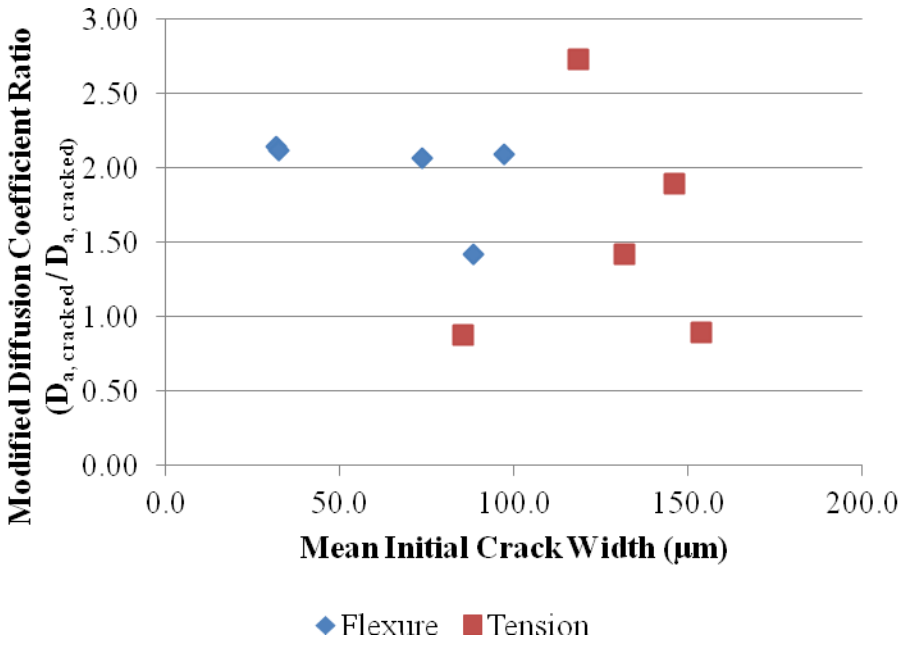

Figure 8.23: Apparent diffusion coefficient ratio of cracked to uncracked samples versus mean initial crack width (0.001 in. = 25.4 μm)

It is important to note that even though the diffusion coefficient across the crack may recover a significant amount of its resistance to chloride ingress, before that can occur a large background content of chlorides had penetrated the section as part of the water required for self-healing to occur. Further research is needed to better understand the role of initial chloride penetration and rate of self-healing on long-term performance of reinforced concrete.

8.3.3 Service Life Modeling

The results of section 8.3.2.2 were used to perform service life modeling of tension and flexure crack specimens. Service life modeling was performed using Life 365 (Ehlen, 2009). The service life modeling assumed a 76.2 mm (3 in.) cover depth and a constant diffusion coefficient with respect to time. A 0.05% by mass of concrete

chloride threshold limit (CTL) was used to determine the time at which the concentration of chlorides at the depth of the reinforcement was sufficient to initiate corrosion. Two service lives were predicted for cracked specimens utilizing the standard approach with Fick's second law, as well as with the modified approach presented in 8.3.2.2 where background content from the regression analysis was input as the background content of the mixture design.

Table 8.9 shows the predicted initiation times for control, flexural, and tensile crack specimens using both diffusion coefficients determined using the standard and modified regression analyses. The estimated initiation times for control samples are smaller than the estimated times presented in Chapter 5 (Figure 5.11) due to not accounting for the decay of the diffusion coefficient over time. Additionally, the self-healing samples were exposed at a younger age (14 vs. 28 days) and had a shorter exposure period, which would lead to finding a higher apparent diffusion coefficient since the concrete was not the same maturity.

The results show that the presence of a crack, regardless of the size or self-healing, decreases the initiation time by at least 40%. Additionally, the modified approach with Fick's second law always predicted a shorter initiation time than the standard approach. This suggests that not considering the initial ingress of chlorides will lead to an over-estimate of the usable service life. The results show that for flexure cracks, which had smaller crack widths, the standard and modified approaches with Fick's second law yielded similar initiation times if the background content was not above the CTL. For tension samples using the modified approach, the background content present in all of the tension crack samples was above the CTL of 0.05% by mass

of concrete, meaning that corrosion would initiate immediately upon exposure. The standard approach would estimate that the structure could withstand 3 or more years before initiation and shows that it is important to account for the initial ingress of chlorides in the model.

Table 8.9: Estimated corrosion initiation times for control and cracked samples

	Estimated Corrosion Initiation Time (yrs)				
		Flexure		Tension	
Mixture design	Control	Standard	Modified	Standard	Modified
Type II	10.2	6.6	6.6	5.7	0.0
T3-F15	11.8	6.5	6.2	5.1	0.0
F25	15.4	8.1	7.8	5.4	0.0
S35-MK5	18.7	8.1	7.0	11.4	0.0
S50-MK5	22.1	8.7	0.0	3.6	0.0

8.4 Conclusions and Recommendations

The results of this study demonstrated that prestressed concrete piles in marine environments can undergo self-healing of tension and flexure induced cracks where the crack widths were less than 186 μm (0.0073 in.). Chlorides present in the seawater ingress into the crack and result in a background content. The background content present was shown to be proportional to the crack size. Analysis of the data suggest that current Fick's second law modeling techniques do not capture the true behavior of chloride ingress in cracked concrete, but a modification to the model allows for better agreement with experimental data and can account for the initial background content due to the presence of the crack.

Service life modeling considering initiation of reinforcement corrosion was performed, and the model demonstrated that the presence of cracks decreases the service life of a structure by over 40%. Additionally, service life estimates reiterated the importance of using a model in good agreement with observed behavior or else over-estimation of usable service life will occur.

The results of this study led to the following recommendations for the self-healing of cracked concrete in seawater:

- Prevent the cracking of piles during construction and placement if at all possible to maximize the usable service life.
- If unable to guarantee the construction of uncracked concrete, corrosion resistant reinforcing steel must be used to achieve a 100+ year life span.
- Utilize the modified approach to Fick's second law which considers cracking by use of an increased C_o (initial background content due to the presence of a crack) when evaluating and modeling the service life of cracked concrete.
- Mixture designs capable of self-healing exhibit a recovery of some of the chloride ingress properties, but the initial ingress of chlorides with the seawater to self-heal the crack drastically diminishes the usable service life. Therefore, self-healing of cracks with widths of 30 μm (0.001 in.) or larger cannot be counted on to provide service lives similar to uncracked concrete.
- Mixture designs containing slag or cement-only show the greatest propensity for self-healing to occur according to crack width measurements and chloride ingress resistance measurements.

The following areas were determined to need further research based upon the findings of this study:

- Research is needed to understand the relationship between the type of crack and the recovery of the diffusion coefficient for mixture designs capable of self-healing.
- Determination of the influence of crack sizes smaller than 30 μm (0.001 in.) on chloride ingress for mixture designs capable of self-healing and the determination of the maximum permissible crack size for reinforced concrete structures in a marine environment.
- Research into the time dependency of the diffusion coefficient for cracked concrete in marine exposures to determine if similar maturation behavior is observed to uncracked concrete.

CHAPTER 9

DISCUSSION OF DURABILITY TESTING RESULTS

9.1 Introduction

The durability test results presented in Chapters 5 through 8 investigated the resistance to chloride ingress, sulfate attack, and carbonation as well as the self-healing capabilities of nine potential high performance marine concretes (HPMC) under consideration for coastal bridge elements. The objectives of this chapter are to analyze the suitability of each mixture design for providing a 100+ year service life in a marine environment and to provide recommendations for HPMC mixture designs capable of providing a 100+ year service life.

Section 9.2 summarizes the results of the individual durability studies and explains the key findings. Section 9.3 synthesizes the results of the durability studies for the determination of mixture designs suitable for marine environments in Georgia. Based upon this analysis, section 9.4 provides the final recommendations for HPMC mixture designs.

9.2 Summary of Results

9.2.1 Mechanical Properties

The compressive strength gain behavior of the concrete mixture designs was evaluated in Chapter 4, along with the elastic modulus at 56 days. Table 9.1 shows the

mean compressive strength at 3, 28, and 56 days as well as the mean elastic modulus at 56 days and the ACI 363 (1997) elastic modulus estimate for each mixture design.

GDOT currently requires a compressive strength of 27.6 MPa (4,000 psi) for release of prestressing and 34.5 MPa (5,000 psi) compressive strength at 56-days for mixture designs (GDOT, 2004). All mixture designs met the release strength within three days and satisfied the 56-day requirement as well. The ACI 363 (1997) elastic modulus estimation technique is suggested for use with the HPMC mixture designs evaluated.

Table 9.1: Compressive strength and elastic modulus data for mixture designs (1 ksi = 6.89 MPa)

	Compressive Strength (MPa)			**Elastic Modulus (GPa)**	
	3-Day	**28-Day**	**56-Day**	**Experimental**	**ACI 363**
T3-F15	42.3	52.6	58.1	29.5	32.2
F25	34.7	51.1	55.0	36.5	31.5
F25-MK5	36.9	64.5	69.9	34.1	34.7
F25-MK10	44.7	84.0	86.7	42.8	37.8
F25-SF5	40.2	70.1	80.7	37.3	36.7
F25-SF10	40.0	73.2	80.9	35.1	36.8
S35-MK5	44.3	82.8	85.4	41.2	37.6
S50-MK5	36.6	76.0	76.4	37.8	35.9
S35-SF5	37.1	68.9	75.2	35.1	35.7
S50-SF5	31.3	68.4	73.6	40.1	35.4

9.2.2 Chloride Ingress Resistance

The chloride ingress resistance of the proposed HPMC mixture designs was evaluated in Chapter 5. The results of the bulk diffusion testing were used to perform service life modeling of each mixture design. The corrosion initiation period was calculated using Life 365's internal solver and the estimated diffusion decay indexes. The program is able to account for two-dimensional flow of chlorides for the square pile

geometry using the two-dimensional Crank-Nicolson approach (Ehlen, et al., 2009). The program does not account for the influence of chloride binding. For estimation, a 76.2 mm (3 in.) cover distance was used on an 457 mm (18 in.) square pile. A chloride threshold limit (CTL) of 0.05% by weight of concrete was used to estimate the corrosion initiation time with service life models.

The results of the service life modeling are shown in Figure 9.1. The mixture design T2, which would be obtained by following the minimum requirements of ACI 201.2R-08 (2008) would initiate corrosion after only 7 years. T3-F15, the current HPC mixture design, would initiate corrosion after approximately 55 years. All ternary mixture designs would provide a minimum initiation time of 73 years. S50-MK5 and F25-SF5 provided the longest initiation times, 207 and 95 years, for mixture designs containing slag and fly ash, respectively. However, it should be noted that these service life predictions do not consider cracking, and it is known that reflective cracking is a concern for driven elements (e.g., piles). Therefore, if cracking may occur then the recommendations from section 9.2.5 must be followed.

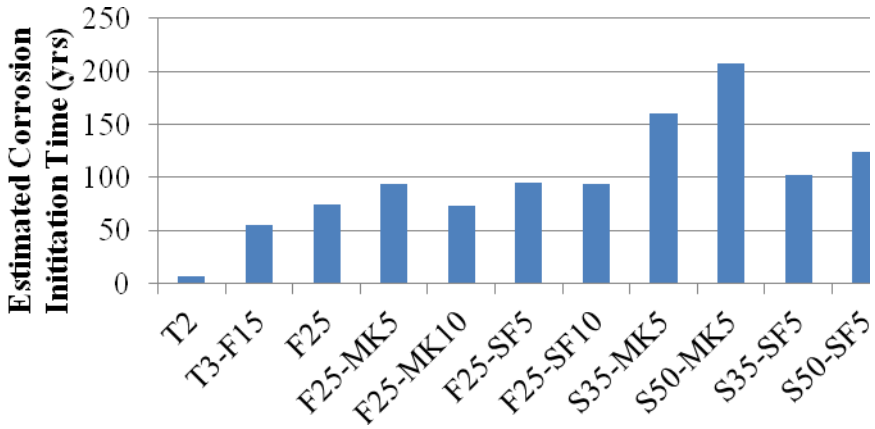

Figure 9.1: Estimated corrosion initiation times for mixture designs

9.2.3 Sulfate Attack Resistance

The expansion and compressive strength behavior of several binder compositions subjected to sulfate exposure were evaluated for expansion and strength degradation behavior. The binder compositions evaluated are presented in Chapter 6 (Table 6.2). ASTM C 150 (2009) moderately sulfate resistant Type II, highly resistant Type V, and high early strength (less sulfate resistant) Type III cements were used for comparison in the evaluation of binary and ternary compositions containing SCM's; each mixture was designed to increase sulfate resistance based upon previous research findings (Chapter 2).

The sulfate resistance of each mixture design was investigated using two accelerated test methods – expansion and change in strength. The use of ASTM C 1012 (2009) expansion tests only accounts for one of the two deleterious reactions associated with sulfate attack and may not provide a full characterization to a mixture designs performance in a sulfate-laden environment. In order to accurately characterize the sulfate resistance properties of a mixture design, both the expansion and strength degradation reactions must be accounted for to assure satisfactory performance. The details of each experiment are presented in Chapter 6.

Table 9.2 shows the requirements proposed by ACI 201 (2010) for a given sulfate exposure in water. The recommended cement type is based upon an ASTM C 150 (2009) cement designation. Alternatively, the ASTM C 1157 (2011) performance based specification for cements can be used and requires testing following the ASTM C 1012 (2009) procedure with the expansion limits given in Table 9.3. For Georgia's brackish water and marine exposures, sulfate levels fall into the S1 to S2 categories based upon the results of the environmental condition survey presented in Appendix H.

Table 9.2: Exposure Classes as specified by ACI 201 (2010)

Exposure Class		Cement Type	Exposure		Max w/cm
			% by mass	ppm	
S0	Not Applicable	No Restriction	$SO_4 < 0.10$	$SO_4 < 150$	None
S1	Moderate	Type II	$0.10 \leq SO_4 < 0.20$	$150 \leq SO_4 < 1{,}500$	0.5
S2	Severe	Type V	$0.20 \leq SO_4 < 2.0$	$1{,}500 \leq SO_4 < 10{,}000$	0.45
S3	Very Severe	Type V + Pozzolan or Slag	$SO_4 > 2.0$	$SO_4 > 10{,}000$	0.4

Table 9.3: Maximum expansion percentages specified by ACI 201 (2010)

Exposure Class	Expansion (%)		
	6 Months	12 Months	18 Months
S1	0.10%	-	-
S2	0.50%	0.10%	-
S3	-	-	0.10%

Expansion tests were run for 18 months to test the viability of each mixture design for all exposure classes. The expansion results of each mixture design at 6, 12, and 18 months, as well as the corresponding maximum permissible exposure rating are shown in Table 9.4. The results of expansion testing demonstrated that any of the investigated binder compositions provide adequate sulfate resistance for an S1 environment. All binder compositions except for T3 demonstrated satisfactory sulfate resistance for S2 exposure classes and are suitable for use in Georgia according to ACI 201 (2010). All mixture designs except cement only (T2, T3, and T5) and F25-MK5 passed the 18 month S3 exposure criteria. These results suggest that any of these mixture designs are capable of providing the required sulfate resistance using the expansion failure criterion for an S1, S2, or S3 exposure environment. Mixture design F25 demonstrated an increasing rate of

expansion leading up to the 18 month reading, and may not be as sulfate resistant as the other passing mixture designs.

Table 9.4: ASTM C 1012 expansion test results and exposure ratings

Mixture design	6-Month Expansion	12-Month Expansion	18-Month Expansion	ACI 201 Exposure Rating
T2	0.038	0.087	0.177	S2
T3	0.035	0.237	0.907	S1
T5	0.020	0.099	0.201	S2
T3-F15	0.021	0.032	0.041	S3
F25	0.038	0.050	0.090	S3
F25-MK5	0.047	0.083	0.218	S2
F25-MK10	0.036	0.042	0.045	S3
F25-SF5	0.031	0.036	0.041	S3
F25-SF10	0.026	0.027	0.028	S3
S35-MK5	0.031	0.039	0.047	S3
S50-MK5	0.020	0.023	0.026	S3
S35-SF5	0.030	0.041	0.046	S3
S50-SF5	0.034	0.046	0.052	S3

Strength degradation testing was performed for 180 days, with compression breaks made at 28, 90, and 180 days of exposure. The results (Appendix E) were compared with the strength limits given in Table 9.5 for the exposure classes presented in Table 9.2. For a severe sulfate exposure, S2, it is proposed that the 180-day compressive strength plus one standard deviation must be higher than the initial strength found before exposure. The initial strength, f_{ci}, is determined by cube tests at an age of 7 days. For a very severe exposure, S3, it is proposed that the limit is that the 180-day compressive strength plus one standard deviation must be higher than the 90-day sulfate expose specimen's compressive strength.

Table 9.5: Strength degradation testing limits for exposure classes

Exposure Class	Strength Limit
S1	-
S2	$f_{c180}+\sigma_{180} > f_{ci}$
S3	$f_{c180}+\sigma_{180} > f_{c90}$

Figure 9.2 shows the results of the compressive strength degradation testing for each mixture design. The relative strength is the compressive strength after exposure divided by f_{ci}. For cement only specimens, both T2 and T5 never exhibited strength loss. T3 showed increasing strength loss at 90 and 180 days. T3-F15 showed the largest decrease in strength. For slag specimens, mixes containing slag and silica fume lost more strength than comparable metakaolin mixture designs. Table 9.6 presents the exposure class rating for each mixture design based upon compressive strength degradation criterion proposed here. T3-F15 and S50-SF5 failed the severe exposure limits, suggesting they are suitable for a S1 sulfate exposure class environment. T3, F25-SF10, and S35-MK5 failed the S3 exposure limit, suggesting they are suitable for S1 or S2 exposure class environments. The sulfate resistance cement only compositions (T2, T5) and F25, F25-MK5, F25-MK10, F25-SF5, S50-MK5, and S35-SF5 passed the S2 and S3 limits, and are suitable for any sulfate exposure using the strength degradation criterion.

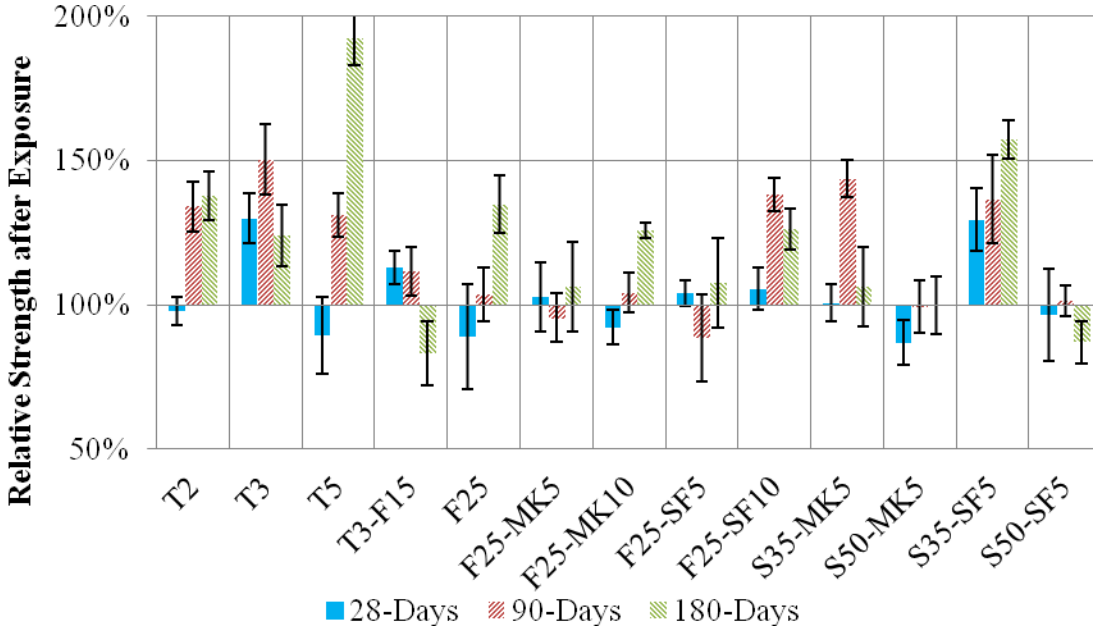

Figure 9.2: Relative strength of specimens compared to initial control specimens after sulfate exposure

Table 9.6 provides a summary of the strength and expansion test results. Boxes highlighted in red represent a mixture design suitable for exposure class S1, yellow for exposure class S2, and green for exposure class S3. The exposure class rating for sulfate resistance was determined by using the lowest rating from expansion and compressive strength degradation test results. T2 and T5 performed the best on the sulfate strength testing; however, failed the 18 month limit for expansion testing. T3 performed poorly on both tests, which is to be expected since it was not designed for sulfate resistance but instead was included for comparison, as a less resistant composition. Based upon the findings of the studies, all mixture designs except T3, T3-F15, and S50-MK5 are suitable for Georgia's coastal environment of an exposure class, S2. The F25, F25-MK10, F25-SF5, S50-MK5, and S35-SF5 mixture designs provided adequate performance for the very severe sulfate exposure, S3, and are recommended for use in potential HPMC.

Table 9.6: Suggested exposure class rating for mixture designs

Mix	Strength Degradation Rating	ASTM C 1012 Rating	Overall Exposure Rating
T2	S3	S2	S2
T3	S2	S1	S1
T5	S3	S2	S2
T3-F15	S1	S3	S1
F25	S3	S3	S3
F25-MK5	S3	S2	S2
F25-MK10	S3	S3	S3
F25-SF5	S3	S3	S3
F25-SF10	S2	S3	S2
S35-MK5	S2	S3	S2
S50-MK5	S3	S3	S3
S35-SF5	S3	S3	S3
S50-SF5	S1	S3	S1

9.2.4 Carbonation Resistance

The carbonation resistance properties of the mixture designs presented in Chapter 4 were characterized by using an accelerated exposure test based upon the procedure used by Papadakis, et al. (1991). Samples were placed into a high CO_2 (20%) environment at 55% relative humidity and 40^{o} C and tested periodically for one year. A regression analysis was performed on the carbonation front measurements to estimate the carbonation constant of each mixture design. Service life modeling was performed using the experimentally determined carbonation to estimate the required cover distance for each mixture design to provide a 100 year service life in a 0.04% CO_2 exposure.

Table 9.7 presents the cover distances necessary to prevent carbonation induced corrosion for a service life of 100, 500, and 1,000 years. Carbonation induced corrosion is expected when the pH at the level of reinforcement is reduced to below 10. All mixture designs provided an estimated service life in excess of 1,000 years using the

current 76.2 mm (3 in.) cover depth for reinforcement in precast prestressed piles, suggesting that using a low w/cm mixture design containing SCM's will provide adequate resistance to carbonation for a typical marine exposure environment for prestressed precast concrete piles. All mixture designs tested are capable of providing a 100 year lifespan with a 25.4 mm (1 in.) cover distance. For ternary mixture designs, theoretically only a 5 mm (0.2 in.) cover is necessary for a 100 year service life, and a 15 mm (0.61 in.) cover could provide a 1,000 year service life. If the cover distance is decreased with the same dimension pile, the flexural resistance would increase, and it may be possible to decrease the number of strands required.

Table 9.7: Required cover distances for carbonation induced corrosion protection (1 in. = 25.4 mm)

	Required Cover Distance (mm)		
Mixture design	**100 yrs**	**500 yrs**	**1,000 yrs**
T2	22.39	50.06	70.80
T3-F15	3.70	8.27	11.69
F25	4.51	10.09	14.27
F25-MK5	4.04	9.02	12.76
F25-MK10	3.04	6.79	9.61
F25-SF5	2.82	6.31	8.93
F25-SF10	3.24	7.24	10.24
S35-MK5	4.59	10.26	14.51
S50-MK5	3.28	7.34	10.38
S35-SF5	3.79	8.48	11.99
S50-SF5	3.50	7.82	11.06

9.2.5 Self-Healing of Cracked Concrete

An investigation was performed to determine the influence of cracks on the ingress of chlorides into precast prestressed concrete piles, since piles in marine environments are susceptible to reflective tensile cracking due to driving and to flexure

cracking during handling and placement as discussed in Appendix B. Six prism specimens (127 mm x 127 mm x 457 mm (5 in. x 5 in. x 18 in.)) were cast from each of the 5 mixture designs presented in Chapter 4. Samples were cracked to simulate tensile and flexure cracks. After cracking the specimens, 6.2 MPa (900 psi) uniform compressive prestressing was applied to the specimens using internal unbonded post-tensioning bars to simulate the current level of prestressing used in the state of Georgia. The mean induced crack widths ranged from 31.8 to 97.2 μm (.0013 in. to 0.0038 in.) for flexure-induced cracks and 85.4 to 153.8 μm (.0034 in. to .0061 in.) for splitting tension-induced cracks. The crack measurements when measured immediately after cracking and post-tensioning along the exposure face of the sample.

The samples were ponded with a 165 g/L simulated seawater solution for 120 days; then profile grinding was performed to determine chloride ingress into the section through the crack. The chloride profiles were used for the determination of apparent diffusion coefficients and background contents used for service life modeling using Life 365 and a CTL of 0.05% by mass of concrete.

The chloride profiles suggested that an initial concentration of water with chlorides penetrates the crack upon exposure. In a non-self-healing concrete, the crack would serve as another exposure face and allow for the same concentration of chlorides as the surrounding environment to penetrate quickly and initiate corrosion. In a self-healing concrete, the initial concentration of water with chloride initiates self-healing. In self-healing specimens, it was found that the initial concentration that penetrates the section is proportional to the crack width. For crack widths above 100 μm (0.004 in.), it was found that the initial concentration at the depth of the reinforcement (76 mm, 3 in.)

was sufficient to initiate corrosion using a CTL of 0.05%., meaning that the service life was effectively 0 years when a 100 μm (0.004 in.) or wider crack was present and extended to the level of the reinforcement. The results of the service life modeling demonstrated that the presence of a crack, regardless of the size or self-healing, decreases the initiation time by at least 40%. For example, a small (50 μm (0.002 in.) wide crack) with mixture designs with a high propensity for self healing (S35-MK or Type II) results in a 40% reduction in service life. For a mixture design with a lower propensity for self-healing (T3-F15, F25) the service life would be over 50% shorter.

The results of the study suggest that the cracking of piles during construction and placement must be prevented if at all possible to maximize the usable service life. If unable to guarantee the construction of uncracked concrete, corrosion resistant reinforcing steel must be used to ensure a 100+ year life span.

9.3 Comparison of Durability Characteristics

The findings of the studies presented in section 9.2 provide valuable insight into the durability characteristics of each mixture design when subjected to individual degradation phenomenon. However, as discussed in Chapter 3, the marine environment of Georgia requires an HPMC to be resistant to chloride ingress, carbonation, and sulfate attack to maximize the usable service life.

Based upon the findings of the self healing investigation (Chapter 8), two potential sets of durability requirements exist for the following exposures: (1) Uncracked concrete piles with non-corrosion resistant prestressing strands, (2) Uncracked or cracked

concrete piles with corrosion resistant prestressing strands. As previously described, the presence of a 100 μm (0.004 in.) or wider surface-breaking crack, extending through the cover to the reinforcement, in concrete exposed to seawater would initiate corrosion well short of the desired 75 year service life and is not considered as part of the analysis.

9.3.1 Uncracked Concrete Piles with Non-Corrosion Resistant Prestressing Strands

HPMC mixture designs for precast prestressed concrete piles using non-corrosion resistant metallurgies in marine environments are susceptible to damage due to chloride induced corrosion, carbonation induced corrosion, and sulfate attack. Two catagories of mixture designs are suggested that are capable of providing 75 and 100 year service lives.

The chloride ingress resistance testing demonstrated that all ternary mixture designs were capable of providing a 75 year service life, except F25-MK10, when using a 76.2 mm (3 in.) concrete cover. No binary or cement-only mixture designs were capable of a 75 year service life for chloride induced corrosion resistance, and only ternary mixture designs containing slag were capable of providing a 100 year service life for chloride induced corrosion resistance.

Carbonation induced corrosion resistance testing demonstrated that the investigated mixture designs were all capable of a 100 year life span when using a 76.2 mm (3 in.) cover. Results suggested that a cover distance of 5 mm (0.2 in.) would provide adequate resistance to carbonation for ternary mixture designs. However, the chloride induced corrosion resistance controls for cover distance, and a 76.2 mm (3 in.) cover or larger must be maintained.

Sulfate attack resistance testing suggested that the mixture designs meeting the S2 requirements (T2, F25-MK5, F25-MK10, F25-SF5, F25-SF10, S35-MK5, S50-MK5, and S35-SF5) are satisfactory for use in Georgia's marine exposure and are suggested for a 75 year service life capability. To ensure a 100 year service life mixture designs meeting the S3 requirements (F25-MK10, F25-SF5, S50-MK5 or S35-SF5) are recommended for sulfate resistance.

Based upon the criterion outlined above for chloride ingress, carbonation, and sulfate attack resistance, Table 9.8 presents the recommended mixture designs for a 75 and 100 year service life using a check mark for adequate resistance for uncracked piles with non-corrosion resistant prestressing steel. For a 75 year service life, mixture designs F25-MK5, F25-SF5, F25-SF10, S35-MK5, S50-MK5, and S35-SF5 are recommended. For a 100 year service life, mixture designs S50-MK5 and S35-SF5 are recommended.

Table 9.8: Recommended mixture designs for 75 and 100 year service life using non-corrosion resistant prestressing strands

Mixture design	**75 year Capability**	**100 year Capability**
T2		
T3-F15		
F25		
F25-MK5	✓	
F25-MK10		
F25-SF5	✓	
F25-SF10	✓	
S35-MK5	✓	
S50-MK5	✓	✓
S35-SF5	✓	✓
S50-SF5		

9.3.2 Concrete Piles with Corrosion Resistant Prestressing Strands

HPMC mixture designs for precast prestressed concrete piles using corrosion resistant metallurgies in marine environments are susceptible to damage due to sulfate attack only. Two catagories of mixture designs are suggested that are capable of providing 75 and 100 year service lives. Sulfate attack resistance testing suggested that the mixture designs meeting the S2 requirements (T2, F25-MK5, F25-MK10, F25-SF5, F25-SF10, S35-MK5, S50-MK5, and S35-SF5) are satisfactory for use in Georgia's marine exposure and are suggested for a 75 year service life capability. To ensure a 100 year service life mixture designs meeting the S3 requirements (F25-MK10, F25-SF5, S50-MK5 or S35-SF5) are recommended.

9.4 Recommendations

The results of this investigation into improving the durability of precast prestressed concrete piles in marine exposures has led to the following groups of recommendations for design based upon the exposure conditions.

The following recommendations are made for concrete piles constructed using non-corrosion resistant prestressing strands:

- Prevent the cracking of piles during construction and placement if at all possible to maximize the usable service life. If unable to guarantee the construction of uncracked concrete, corrosion resistant reinforcing steel must be used to achieve a 100+ year life span.

- Use a 76.2 mm (3 in.) cover distance with a recommended mixture design for the desired service life of 75 or 100 years to ensure desired durability characteristics.
- For a minimum service life of 75 years, use one of the following mixture designs: F25-MK5, F25-SF5, F25-SF10, S35-MK5, S50-MK5, or S35-SF5.
- For a minimum service life of 100 years, use one of the following mixture designs: S50-MK5 and S35-SF5

The following recommendations are made for concrete piles constructed using corrosion resistant prestressing strands, such as high strength 2205 stainless steel strands, where only sulfate resistance need be considered.

- For a minimum service life of 75 years, use one of the following mixture designs: T2, F25-MK5, F25-MK10, F25-SF5, F25-SF10, S35-MK5, S50-MK5, and S35-SF5
- For a minimum service life of 100 years, use one of the following mixture designs: F25-MK10, F25-SF5, S50-MK5 or S35-SF5

CHAPTER 10

CONCLUSIONS AND RECOMMENDATIONS

10.1 Conclusions

The results of the study on concrete materials for piles in a marine environment established that a new mixture termed HPMC is needed to provide adequate resistance to chloride ingress, carbonation, and sulfate attack in order to provide a 100+ year lifespan. The development and testing of potential HPMC mixture designs found that through the use of ternary mixture designs it is possible to provide durability characteristics that allow for a service life in excess of the 100 year goal.

The study into the chloride ingress resistance of binary and ternary mixture designs found that ternary mixture designs provide superior resistance compared to binary mixture designs; including of 5 to 10% silica fume to a Type II Portland cement plus Class F fly ash mix increases the service life approximately 25%. The RCPT demonstrated the decrease in chloride penetrability of mixture designs and agreed with the results of the bulk diffusion testing. The service life modeling showed that mixture designs capable of an estimated 70 year or longer service life had a charge of less than 1000 coulombs passed during the RCPT. Bulk diffusion tests and service life modeling showed that ternary mixture designs with slag and metakaolin provide the longest service lives. Additionally, estimates from Life 365 ® and Concrete Works ® for the diffusion coefficient and estimated service life varied widely from observed behavior. The estimation of diffusion coefficients from the charge passed during ASTM C 1202 (2007) testing was accurate for cement-only and binary mixture designs, but highly unconservative for ternary mixture designs where it over-estimated the time to corrosion by more than 60%.

Testing for resistance to sulfate attack demonstrated that the performance characteristic measured during sulfate exposure had significant effect on the apparent resistance of mixture designs. Compressive strength degradation testing demonstrated that mixture designs with a high initial CaO content, determined through oxide analysis of the cement and SCMs, performed well, presumably due to the formation of calcium hydroxide (CH) which served as a buffer to the decalcification of calcium-silicate-hydrate (C-S-H) in the formation of gypsum. However, high CaO contents led to poor performance on expansion testing due to the availability of large amounts of calcium hydroxide to react with sulfate ions to form expansive ettringite. Slag mixture designs containing metakaolin performed well with both test methods. Mixture designs containing silica fume performed poorer at strength testing than their equivalent metakaolin mixes with the same replacement levels. Mixture designs that performed well on both criteria had moderate CaO contents (44 to 50%) and utilized sulfate resistant ASTM C 150 (2009) Type II cements with low C_3A contents.

The study into carbonation performance of potential HPMC mixture designs showed that ternary mixture designs are capable of providing service lives in excess of 200 years using a 5 mm (0.2 in.) cover. The results showed that the Papadakis (2000) estimation technique resulted in carbonation constants which could lead to an anticipated service life greater than actual. The Sulapha, et al. (2003) procedure provided conservative estimates of the carbonation constants. Test results showed that the carbonation rate decreased significantly with lowering of the w/cm ratio and that transport properties control carbonation resistance at low w/cm. Additionally, for mixture designs containing SCM's, ternary mixture designs with 5% to 10% silica fume and 25% fly ash performed the best, resulting in an service life over 95% longer than 25% fly ash alone.

The investigation into the influence of self-healing on chloride ingress into cracked sections demonstrated that prestressed concrete piles in marine environments can

undergo self-healing and filling of tension and flexure induced cracks where the crack widths were less than 186 μm (0.0073 in.) at the beginning of exposure. Chlorides present in the seawater ingress into the crack and result in an increased background content. The chloride background content present was shown to be proportional to the crack size. Analysis of the data suggested that current Fick's second law modeling techniques do not capture the true behavior of chloride ingress in cracked concrete, but a modification to the model allows for better agreement with experimental data and can account for the initial background content due to the presence of the crack. Service life modeling considering initiation of reinforcement corrosion was performed, and the model demonstrated that the presence of cracks decreases the service life of a structure by over 40% compared to uncracked concrete. Mixture designs containing slag or cement-only show the greatest propensity for self-healing to occur according to crack width measurements and chloride ingress resistance measurements. The results of the self-healing study suggest that the cracking of piles during construction and placement should be prevented if at all possible to maximize the usable service life. If unable to guarantee the construction of uncracked concrete, corrosion resistant reinforcing steel should be used to achieve a 100+ year life span.

The results of the durability assessments for chloride ingress, carbonation, and sulfate attack led to the development of mixture design suggestions for 75 and 100 year service lives for prestressed concrete piles. The recommended mixture designs are presented in section 10.2.2. It was determined that uncracked sections with non-corrosion resistant steel required protection from sulfate attack, carbonation, and chloride

ingress. For cracked sections, corrosion resistant prestressing steel must be used and the concrete mixture design must provide adequate resistance to sulfate attack.

10.2 Recommendations

The results of the durability assessment and development of HPMC mixture designs has led to a series of general recommendations (Section 10.2.1) for individual durability concerns, and final recommendations for HPMC mixture designs depending upon the target service life and reinforcement utilized (Section 10.2.2). Additionally, the results of the studies led to the suggestions in Section 10.2.3 of future research areas where more work is needed to develop better understandings of durability concerns and methods of estimating mixture design performance and service life modeling.

10.2.1 General Recommendations

The following mixture design recommendations are made for resistance to chloride ingress:

- Use S50-MK5 or F25-SF5 to maximize usable service lives of structures with respect to reinforcement corrosion initiation depending upon whether a slag or fly-ash mix is preferred.
- Use of a 1000 Coulomb limit for ASTM C 1202 rapid chloride permeability test.
- Life 365 can be used to estimate corrosion initiation times, given that the diffusion coefficient is determined experimentally.
- The Barde, et al. (2009) empirical approach to the Nernst-Einstein relationship should not be used to calculate diffusion coefficients for ternary mixture designs due to under-estimating the apparent diffusion coefficient.

The following mixture design recommendations are made for resistance to sulfate attack:

- Use a sulfate resistant cement, Type II or V, or a combination of cement and SCMs identified below to meet limits on strength degradation and expansion in sulfate environments.
- F25-MK10, F25-SF5, S50-MK5 or S35-SF5 are recommended for use in very severe sulfate rich environments (e.g, S3); for less severe S2 conditions, T2, F25-MK5, F25-MK10, F25-SF5, F25-SF10, S35-MK5, S50-MK5, and S35-SF5 should perform satisfactorily.
- Testing procedures that account for both the expansion and strength degradation behavior of mixture designs should be used in developing HPMC. Satisfactory performance for only one of the two degradation mechanisms does not guarantee adequate sulfate resistance for 100+ year service lives.
- HPMC mixture designs should be a binary or ternary mixture design with low expansion behavior. Expansion testing showed that cement only samples exhibited significantly higher expansion than compositions containing SCM's. Large expansions may be of concern in a prestressed concrete structure where the expansion may cause an increase in the precompression force in the member and an increase the tensile stress in the prestressing steel.

The following mixture design recommendation is made for resistance to carbonation: Use a w/cm not greater than 0.33 mixture designs with SCM's to ensure service lives in excess of 100 years.

The results of the self-healing study led to the following recommendations for the design and construction practices with cracked concrete in seawater:

- Utilize the modified approach to Fick's second law which considers cracking by use of an increased C_o (background content due to initial chloride ingress into crack) when evaluating and modeling the service life of cracked concrete.
- Mixture designs capable of self-healing exhibit a recovery of some of the chloride ingress properties, but the initial ingress of chlorides with the seawater to self-heal the crack diminishes the usable service life. Therefore, self-healing of cracks with widths of 30 μm (0.001 in.) or larger cannot be counted on to provide service lives similar to uncracked concrete.

10.2.2 Final Design Recommendations

Design and construction practice recommendations were developed based upon the findings of the individual durability studies. Recommendations were made for the case of uncracked concrete using non-corrosion resistant prestressing strands where sulfate attack, carbonation resistance, and chloride ingress resistance needed to be considered. Additionally, for cracked concrete, corrosion resistant reinforcement must be used, and only sulfate attack is considered in the development of HPMC mixture designs.

The following recommendations are made for concrete piles constructed using non-corrosion resistant metallurgies for prestressing strands and non-prestressed reinformement:

- Prevent the cracking of piles during construction and placement if at all possible to maximize the usable service life. If unable to guarantee the construction of

uncracked concrete, corrosion resistant reinforcing steel must be used to achieve a 100+ year life span.

- Use a 76 mm (3 in.) cover distance with a recommended mixture design for the desired service life of 75 or 100 years to ensure desired durability characteristics.
- For a minimum service life of 75 years, use one of the following mixture designs: F25-MK5, F25-SF5, F25-SF10, S35-MK5, S50-MK5, or S35-SF5.
- For a minimum service life of 100 years, use one of the following mixture designs: S50-MK5 and S35-SF5

The following recommendations are made for cracked concrete piles which must be constructed with corrosion resistant metallurgies for prestressing strands and non-prestressed reinforcement:

- For a minimum service life of 75 years, use one of the following mixture designs: T2, F25-MK5, F25-MK10, F25-SF5, F25-SF10, S35-MK5, S50-MK5, and S35-SF5
- For a minimum service life of 100 years, use one of the following mixture designs: F25-MK10, F25-SF5, S50-MK5 or S35-SF5

10.2.3 Future Research

The results of this study have led to the following recommendations of areas for future research and investigation:

- Development of estimation techniques for mixture designs utilizing metakaolin.
- Future work on estimation of service lives with the Concrete Works program with a consideration period that can be extended to beyond 100 years,

- Correlation of the measured expansion or compressive strength in an accelerated test method to field performance and service life modeling of sulfate resistance,
- Research on the influence of cracks on sulfate attack and ingress, since it has been shown by Moser (2011) that sulfates can play an active role in the depassivation of the oxide film on steel reinforcement and can lead to active corrosion in an environment with sulfates and chlorides present,
- Development of a testing procedure for sulfate attack that is able to consider expansion and strength degradation behavior with a single test,
- Development of service life models which account for 2-D ingress of the carbonation front, similar to the two-dimensional Crank-Nicolson approach currently used in chloride ingress modeling,
- Estimation technique for accurately determining the carbonation constant for ternary mixture designs,
- Determination of the effect of cracks on concrete carbonation ,
- Determination of the relationship between the type of crack and the recovery of the diffusion coefficient for mixture designs capable of self-healing,
- Determination of the influence of crack sizes smaller than 30 μm (0.001 in.) on chloride ingress for mixture designs capable of self-healing and the determination of the maximum permissible crack size for reinforced concrete structures in a marine environment,
- Determination of the relationship between concrete maturation and the diffusion coefficient for cracked and uncracked concrete,
- Development of service life models capable of considering multiple durability issues.

APPENDIX A

GEORGIA COASTAL BRIDGE INSPECTIONS

Prepared by Robert D. Moser and R. Brett Holland

A.1 Overview

Bridges of interest in the coastal counties with reported damage to the concrete piling were inspected from May 2nd through the 4th, 2010. Additionally, interviews were performed with Georgia Department of Transportation (GDOT) personnel at the Savannah and Brunswick offices and with Standard Concrete Products (SCP) engineers in Savannah and summaries are presented in Appendix B.

A.2 Bridge Inspections

Eleven bridge sites shown in Figure A.1 were inspected during the trip. Table A.1 gives the bridge numbers and names. The sites were selected based on the extent and types of damage noted in inspection reports provided by the GDOT Bridge Maintenance Office, varying proximities to the coast, and distribution throughout the coastal counties of Georgia. All bridges spanned rivers or inlets with fresh or brackish waters. At each site, photos were taken of any visible damage, and water samples collected for pH, sulfate content, and chloride content testing.

Table A.1: Bridge ID Numbers and Names for Locations Inspected

Bridge Name	Bridge Number
Harriet's Bluff Road at Deep Creek Bridge	039-0049
Houlihan Bridge	051-0054
US 17 at Back River Bridge	051-0059
US 80 at Lazeratto Creek Bridge	051-0066
Island Expressway at Wilmington River Bridge	051-0132
Oatland Island Research Bridge	051-5013
Long Bridge Road at Ebenezer Creek Bridge	103-0030
I-95 at Turtle River Bridge	127-0052
Torras Causeway at Little River Bridge	127-0063
Ocean Highway at Riceboro Creek Bridge	179-0005
Ocean Highway at Champney's River Bridge	191-0005

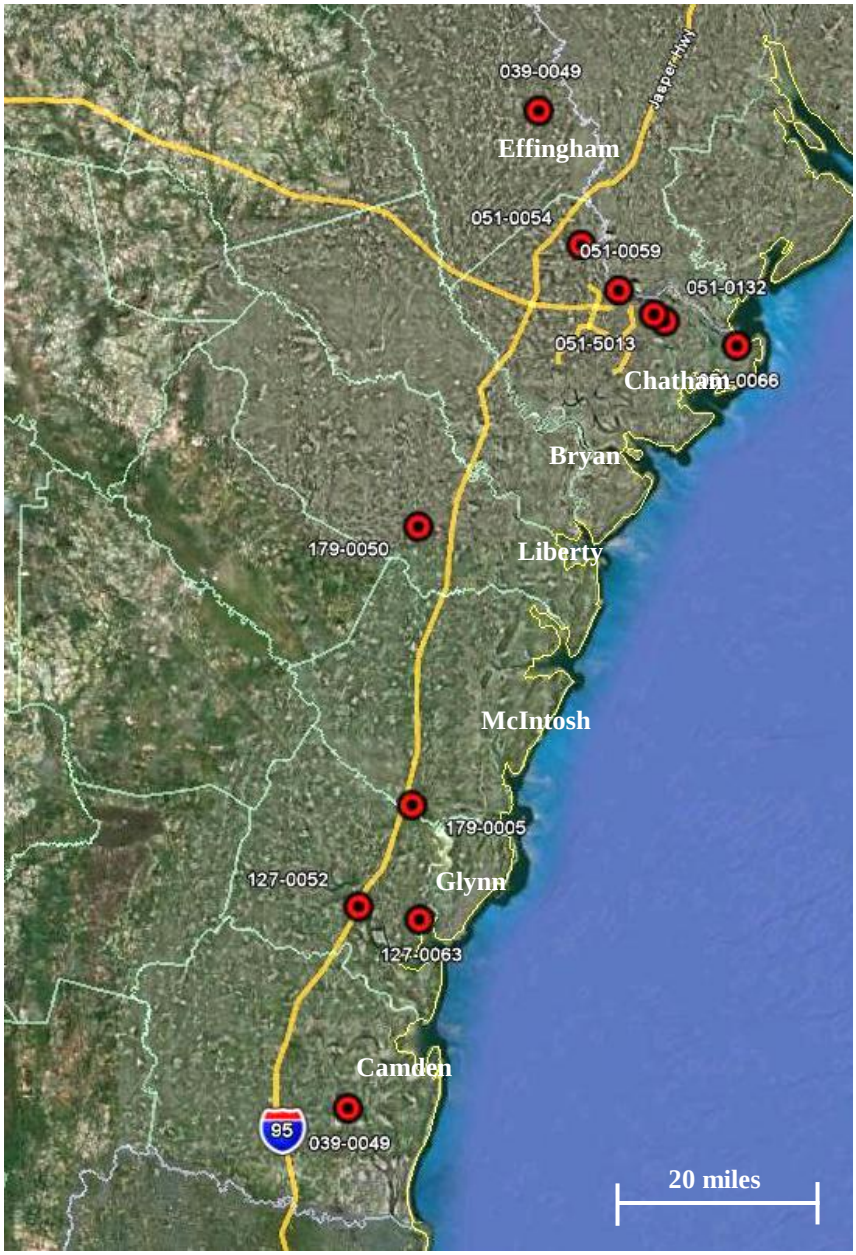

Figure A.1: Bridges inspected along Georgia's coastal counties.
Red dots indicate bridge locations (1 mile = 1.6 km)

A.2.1 Harriett's Bluff Road at Deep Creek Bridge (Bridge No. 039-0049)

Located approximately 12.9 km (8 miles) from the coast in Camden county, the Harriett's Bluff Road Bridge spanning Deep Creek exhibited significant corrosion-related deterioration, primarily in its superstructure. The bridge was constructed in 1964 with a

reinforced concrete superstructure and precast concrete pile-bent substructure system. The substructure looked to be in fairly good condition, with minimal surface abrasion and heavy marine growth and oyster scale in the tidal region (Figure A.2). However, given that the inspection coincided with high tide, a detailed assessment of the substructure could not be made.

Figure A.2: Substructure of Harriett's Bluff Road at Deep Creek Bridge (Bridge No. 039-0049)

The superstructure of the bridge exhibited the most significant deterioration. Cracking and spalling of concrete, especially in the cast-in-place concrete railing/barrier system, was widespread throughout the superstructure. Typical corrosion damage observed in the barrier is shown in Figure A.3 below.

Figure A.3: Corrosion damage in cast-in-place Barrier of Harriett's Bluff Road at Deep Creek Bridge (Bridge No. 039-0049)

A.2.2 Houlihan Bridge (Bridge No. 051-0054)

Constructed in 1953, the Houlihan Bridge is located approximately 27.4 km (17 miles) from the coast near Port Wentwork in Chatham county. The bridge consists of a reinforced concrete beam superstructure, a precast concrete pile-bent substructure, and a central movable steel truss span. An overall view of the bridge is shown in Figure A.4.

Figure A.4: Overall view of Houlihan Bridge (Bridge No. 051-0054)

Similar to what had been recorded in GDOT bridge inspection reports, the most significant deterioration observed on the Houlihan Bridge was found in the submerged and tidal zone of the concrete substructure. Significant surface abrasion was ubiquitous, with fully exposed aggregates from the top of the splash zone down. In some cases, abrasion was so aggressive that hourglassing of the piles could be seen even at a distance. Some typical photos of surface abrasion are shown in Figures A.5 and A.6. In Figure A.5, it should be noted that abrasion occurred on both the precast piling and the cast-in-place support for the movable bridge span in the background. Given the bridge's location fairly far inland, little oyster shell was present on the piles.

Figure A.5: Surface abrasion of concrete substructure on Houlihan Bridge (Bridge No. 051-0054)

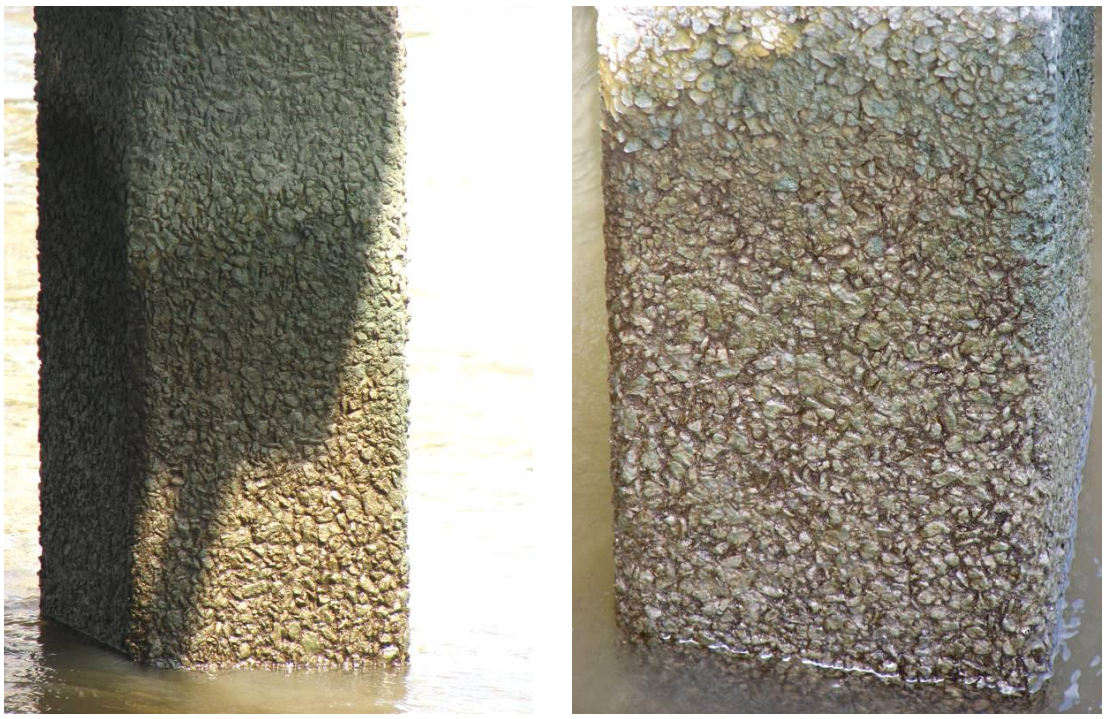

Figure A.6: Surface abrasion of concrete substructure on Houlihan Bridge (Bridge No. 051-0054)

A.2.3 US 17 at Back River Bridge (Bridge No. 051-0059)

The Back River Bridge is located at the Georgia – South Carolina border just east from the Talmadge Bridge, approximately 19.3 (12 miles) from the coast in Chatham county. The bridge was constructed in 1954 with a reinforced concrete beam superstructure and a precast pile-bent substructure with a total length of approximately 0.8 km (0.5 miles). The precast pile substructure, which is shown in Figure A.7, is extensive and has been severly damaged by corrosion.

Figure A.7: Pile-bent substructure of US 17 at Back River Bridge (Bridge No. 051-0059)

Almost all piles have vertical cracks at the corners, extending from the waterline up to 0.61 m to 0.91 m (2 to 3 ft) above high tide with rust staining present. Many of the cracks appear to be much larger than hairline in width, although measurements were limited due to the marsh surrounding the bridge. Typical damage observed in the piles is shown in Figure A.8. The substructure had recently undergone a retrofit of the piles conducted by an external contractor. This retrofit consisted of fiber-reinforced polymeric (FRP) jackets being compression fitted onto the most significantly damaged piles in order to provide confinement of the cracked concrete and to limit any subsequent corrosion damage. A typical jacketed pile is shown in Figure A.9.

Figure A.8: Vertical cracking at corner of concrete pile on US 17 at Back River Bridge (Bridge No. 051-0059)

Figure A.9: Corrosion damaged piling with FRP jacket retrofit on US 17 at Back River Bridge (Bridge No. 051-0059)

A.2.4 US 80 at Lazeratto Creek Bridge (Bridge No. 051-0066)

Located adjacent to the coast at the mouth of the Savannah River in Chatham county, the US 80 Bridge spanning Lazeratto Creek was constructed in 1960 with a precast concrete and steel girder superstructure and a precast pile-bent substructure. The overall bridge structure is shown in Figure A.10 below, with only the central steel spans of the bridge over water.

Figure A.10: Overall view of US 80 at Lazeratto Creek Bridge (Bridge No. 051-0066)

Due to the marsh adjacent to the bridge and our inspection occuring at high tide, limited access to the substructure in the spans over water was available for photos. In the dry marsh approach spans, a detailed inspection of the precast piles could be made. Grout repairs of what looked to be traverse cracks likely caused during driving were observed in some piles (see Figure A.11). Poor construction in the cast-in-place pile caps was also evident with honeycombing and exposed reinforcement in some cases (see Figure A.12).

Figure A.11: Grout repair of traversve crack in precast concrete pile on US 80 at Lazeratto Creek Bridge (Bridge No. 051-0066)

Figure A.12: Honeycombing and exposed corroding reinforcement in pile cap on US 80 at Lazeratto Creek Bridge (Bridge No. 051-0066)

A.2.5 Island Expressway at Wilmington River Bridge (Bridge No. 051-0132)

Located approximately 12.9 km (8 miles) inland in Chatham County, the Island Expressway Bridge spanning the Wilmington River was constructed in 1963 using a precast concrete girder superstructure and precast pile-bent substructure. A steel

moveable span is located in the center of the bridge. An overall view of the bridge as seen from the underside is shown in Figure A.13. The adjacent bridge shown on the right of Figure A.13 carrying westbound traffic appears to be much newer and constructed with piers rather than pile bents. No record of the reconstruction of the westbound lanes was found in the inspection reports.

Figure A.13: Underside of Island Expressway at Wilmington River Bridge (Bridge No. 051-0132)

At low tide a detailed inspection of the submerged regions of the piling was performed. Limestone aggregates showed deterioration and abrasion on all piles (see Figure A.14). The limestone aggregate were exposed on the surface of the piles due to pop-outs and and showed severe abrasion. Large longitudinal cracks at the corners with rust staining were present in most piles. Severe cases of cracking and spalling, as well as "hour-glassing" in the tidal region, are shown in Figure A.15.

Figure A.14: Deterioration of limestone aggregates present at concrete surface on Island Expressway at Wilmington River Bridge (Bridge No. 051-0132)

Figure A.15: Severe damage to concrete piling on Island Expressway at Wilmington River Bridge (Bridge No. 051-0132)

A.2.6 Oatland Island Research Bridge (Bridge No. 051-5013)

The Oatland Island Research Bridge was constructed in 1987 using precast concrete girders and a precast concrete pile bent substructure. An overall view of the bridge is shown in Figure A.16. The bridge was constructructed using a variety of corrosion mitigation methods. The following methods were used in each bent: epoxy coated strands, calcium nitrite corrosion inhibitors, and high performance concrete with SCMs. While access to the substructure for photos was limited due to the surrounding marsh and oyster shell growth on the piling, all of the piles looked to be in excellent condition with no apparent cracking and very limited surface abrasion (Figure A.17).

Figure A.16: Oatland Island Research Bridge (Bridge No. 051-5013)

Figure A.17: Pile-bent substructure of Oatland Island Research Bridge
(Bridge No. 051-5013)

A.2.7 Long Bridge Road at Ebenezer Creek Bridge (Bridge No. 103-0030)

Located approximately 48.3 km (30 miles) inland in Effingham county, the Long Bridge Road Bridge spanning Ebenezer creek was constructued in 1968 with a reinforced concrete superstructure and precast concrete pile-bent substructure. An overall view of the bridge is shown in Figure A.18.

Figure A.18: Long Bridge Road at Ebenezer Creek Bridge (Bridge No. 103-0030)

Bridge 103-0030 was selected for inspection primarily due to the mention of driving cracks in the piles recorded in its inspection report. Tranverse cracks which had been repaired with grout were observed on two piles but were not present throughout the bridge. A typical repair is shown in Figure A.19.

Figure A.19: Grout repair of tranverse cracking likely caused by overdriving on Long Bridge Road at Ebenezer Creek Bridge (Bridge No. 103-0030)

The most predominant deterioration observed on the bridge was degradation of the paste fraction of the concrete piling in regions from the high-water mark down. Above the high-water mark, the concrete was in good condition. Below the high-water mark, the paste was extremely friable and could be scratched easily. This condition was observed on all piles. A typical case of surface abrasion is shown in Figure A.20.

Figure A.20: Surface abrasion of concrete below high-water mark on Long Bridge Road at Ebenezer Creek Bridge (Bridge No. 103-0030)

A.2.8 I-95 at Turtle River Bridge (Bridge No. 127-0052)

The Turtle River Bridge is located approximately 16.1 km (10 miles) from the coast near Brunswick, GA in Glynn County. The bridge was recently upgraded but was inspected because it was the site where piles were pulled and shipped to the Georgia Tech Structural Engineering and Materials Laboratory for further forensic investigation in

February, 2010. The piles that used for the forensic investigation showed the following deterioration mechanisms: abrasion and “hour glassing” in the splash zone, longitudinal cracking and spalling in the tidal and submerged regions, rust staining along the corners of the piles, softening of the concrete in the submerged region, and biological attack on the limestone aggregate.

Due to the expense of pulling all the piles, only those which needed to be removed were, with the rest of the piles from the original bridge left in place underneath the new structure. The new structure consists of precast concrete girders and drilled shafts supporting large transfer beams which span to substructure of the old bridge. An overall view of the new Turtle River Bridge is shown in Figure A.21. Figure A.22 shows the substructure of the new bridge with the original piles integrated into the large transfer beam. The bridge was inspected near high-tide and limited access for photos was available under the bridge.

Figure A.21: Updated I-95 at Turtle River Bridge (Bridge No. 127-0052)

Figure A.22: Transfer beam with original piles left in-place on I-95 at Turtle River Bridge (Bridge No. 127-0052)

A.2.9 Torras Causeway at Little River Bridge (Bridge No. 127-0063)

The Torras Causeway Bridge was constructed as part of a series of bridges in 1986 close to the coast near Brunswick, GA in Glynn county. The bridge was built to replace an older corrosion damaged bridge using precast concrete girder superstructure and a precast concrete pile-bent substructure with larger piers in the center spans over the intercoastal waterway. An overall view of the structure is shown in Figure A.23, taken from the adjacent fishing pier which is actually the remains of the original Torras Causeway Bridge constructed in the 1950s.

Figure A.23: Torras Causeway at Little River Bridge (Bridge No. 127-0063) on right and adjacent fishing pier on left

With the heavy oyster shell growth present in the tidal zone of the piles, it was difficult to see any surface abrasion or damage from a distance. No longitudinal cracking or rust staining could be seen on any of the piles. A typical pile-bent at the waterline is shown in Figure A.24. Access to the original bridge was also available from the adjacent dry marsh. The piles under the original bridge showed significant deterioration with large longitudinal cracks, rust staining, and spalling of concrete. On many of the piles, concrete repair jackets were present. A typical pile form the older structure is shown in Figure A.25.

Figure A.24: Pile-bent on Torras Causeway at Little River Bridge (Bridge No. 127-0063) approach span

Figure A.25: Corrosion damage in original Torras Causeway at Little River Bridge substructure (Bridge No. 127-0063)

A.2.10 Ocean Highway at Riceboro Creek Bridge (Bridge No. 179-0005)

Located 32.2 km (20 miles) inland over Riceboro Creek in Liberty County, bridge 179-005 was constructed with a reinforced concrete superstructure and precast concrete pile-bent substructure in 1957. An overall view of the bridge is shown in Figure A.26. All piles showed significant deterioration with surface abrasion of the paste fraction below the high-water mark, longitudinal cracks at the corners, and rust staining from corrosion present on most piles (see Figure A.27).

Figure A.26: Ocean Highway at Riceboro Creek Bridge (Bridge No. 179-0005)

Figure A.27: Deterioration of precast concrete piles in substructure of Ocean Highway at Riceboro Creek Bridge (Bridge No. 179-0005)

A.2.11 Ocean Highway at Champney's River Bridge (Bridge No. 191-0005)

The Ocean Highway Bridge is located approximately 16.1 km (10 miles) inland spanning Champney's River in McIntosh county. The bridge was constructed in 1981 with a precast concrete girder superstructure and precast concrete pile-bent substructure. An overall view of the structure is shown in Figure A.28. Hollow square piles, 0.91 m x 0.91 m (36 in. x36 in.), were used in the substructure. Leftover piles from the bridge were piles on the bank forming a seawall at an adjacent boat ramp. Close-up examination of these piles revealed the concrete was manufactured using limestone coarse aggregates (see Figure A.29).

Figure A.28: Overall view of Ocean Highway at Champney's River Bridge (Bridge No. 191-0005)

Figure A.29: Remaining piles on bank adjacent to Ocean Highway at Champney's River Bridge (Bridge No. 191-0005)

A fishing pier attached to the side of the bridge was used to take photos of the substructure. The bridge was inspected at high tide and photos of regions of the piles well below the high water mark could not be taken. Surface abrasion, particularly at the site of

limestone aggregates, was present on all of the piles. No significant cracking or rust staining was observed on any of the piles. The typical condition of the piles is illustrated in Figure A.30.

Figure A.30: Typical surface abrasion of concrete on Ocean Highway at Champney's River Bridge (Bridge No. 191-0005)

A.3 Water Sample Testing

Water samples were collected at eight of the bridge sites visited. Access to collect samples at the other sites was not possible. The samples were tested for chloride content, sulfate content, and pH. Chloride contents were obtained by diluting 1 mL (0.034 oz) of the sample with 50 mL (1.69 oz) of deionized water and titrating using the Metrohm 798 MPT Titrino. A silver / silver chloride standard electrode was used. 0.1 N silver nitrate is added in 0.1 ml steps to the sample until an equivalence point is achieved.

The sulfate content was determined by performing inductively coupled plasma atomic emission spectroscopy (ICP) on a Perkin Elmer Optima 7300 DV Optical Emission Spectrometer. The pH was measured using a Thermo Scientific Orion 3-Star Plus pH Portable Meter. The results of the tests performed on the water samples are given in Table A.2.

Table A.2: pH, Chloride, and Sulfate Contents of Water Samples

Bridge Name	**Bridge ID**	**pH**	**% NaCl (g/g)**	**Tide**	**$[SO_4^{2-}]$ (mg/L)**
Harriet's Bluff Road at Deep Creek Bridge	039-0049	7.41	2.77	High	2070.75
Houlihan Bridge	051-0054	7.04	0.05	Low	52.91
Island Expressway at Wilmington River Bridge	051-0132	7.32	1.38	Low	1058.58
Long Bridge Road at Ebenezer Creek Bridge	103-0030	5.88	0.00	Low	13.65
I-95 at Turtle River Bridge	127-0052	7.47	1.99	High	1527.54
Torras Causeway at Little River Bridge	127-0063	7.41	2.34	Mid	1746.22
Ocean Highway at Riceboro Creek Bridge	179-0005	7.25	0.38	Low	219.95
Ocean Highway at Champney's River Bridge	191-0005	7.18	0.00	High	22.65

The salt content of water is used to differentiate between fresh, brackish, and saline (sea) water. Table A.3 shows the general ranges of NaCl concentrations as given by the USGS (2010). From Table A.3, it can be seen that all of the bridges except for the 051-0054, 103-0030, and 191-0005 are in brackish water. The three bridges considered to be in fresh water were located further inland than the rest investigated and no signs of corrosion induced damage were noticed.

Table A.3: Water Salinity Based on Dissolved Salt (NaCl) Concentration

Fresh water	Brackish water	Ocean Water
<0.1 %	0.1-3.5 %	3.5 %

The pH of water is highly variable. According to the USGS (2010), seawater has a pH of between 8 and 9. However, the average field pH is 4.7 for coastal Georgia (USGS, 2010). The values of pH observed at the inspected bridge sites fell between the two reported values. Only bridge 103-0030 was located in acidic water. The damage observed on the bridge was consistent with the signs of acid attack, including the observations of exposed course aggregate on the surface due to the loss of paste, and severe softening of the paste content. The other bridge locations had a near neutral pH, typically measuring in the range of 7.1 to 7.4.

The sulfate contents varied significantly among the water samples. Seawater has an average sulfate content of 2,700 mg/L (Bertolini, et al., 2004), and a study by Murata, et al. (1997) suggests that the sulfate content in brackish water is typically in excess of 1,000 mg/L. The measured values of sulfate concentrations at the bridge sites varied by two orders of magnitude. The wide spread of observed concentrations could be due to both varying distance from the coast, as well as the tide when measured (USGS, 2010). ACI 201.2 (2010) provides design requirements based upon the sulfate content in water, and requires preventative measures to protect against damage to the concrete by sulfate attack for a concentration above 150 mg/L. Additional measures are required for concentrations exceeding 1500 mg/L, which would apply to three of the bridges visited. ACI 201.2 (2010) states that for concentrations less than 150 mg/L no special requirements are necessary for sulfate resistance. For concentrations between 150 and

1,500 mg/L the w/c should be no greater than 0.50 and an ASTM C 150 Type II or ASTM C 1174 Class MS cement should be used. For concentrations between 1,500 and 10,000 mg/L the w/c should be no greater than 0.45 and an ASTM C 150 Type V or ASTM C 1174 Class HS cement should be used.

X-ray diffraction was performed on piles from the Turtle River Bridge (127-0052) to examine if sulfate attack was the cause of the softening of the surface concrete. The concentration of sulfates in the water appears to be sufficient to cause significant sulfate attack, but other local sources of sulfates, particularly biological sources, may contribute to the degradation as well.

The concentrations of sulfates and chlorides in the water can vary widely with variations in rainfall and seasonal effects. Regional data will be investigated further to determine the extent of this variation, and how the data collected compares with historical data.

A.4 Summary

The inspections of bridges along the coast suggest that the causes of damage observed during the forensic investigation of piling from the Turtle River Bridge is representative of other bridges located along the coast. The types of damage observed were cracking and staining due to corrosion, abrasion and "hour-glassing" in splash and tidal zones, loss of limestone aggregates, and severe biological growth in tidal zones. The interviews of GDOT field personnel and SCP employees suggest that driving

practices for piles have improved over the last several decades; however, when damage is noticed during driving, there is no standard method of repair or rejection criterion.

The current HPC mix design requirements being used by GDOT lead to a significantly more durable concrete than the concrete mixes used in the past. However, GDOT limits the replacement of cement with SCM's to lower levels than currently being employed by Florida, therefore, the benefits of higher replacement levels need to be evaluated. Additionally, GDOT does not require the use of an ASTM C 150 Type II or ASTM C 1174 Class MS cement in coastal concrete piling, but there is evidence that sulfate attack may occur in this environment if preventative measures are not taken.

APPENDIX B

INTERVIEW SUMMARIES

B.1 GDOT Preconstruction and Maintenance Division Interviews

Interviews were performed with staff from the GDOT preconstruction and maintenance divisions to establish observed damage, current design methods and criterion, and research areas of interest. Interviews were later conducted with GDOT field office employees in District 5, Savannah and Brunswick. Mr. Richard Potts of Standard Concrete Products, Savannah, was also interviewed because that company supplies may prestressed concrete piles to GDOT.

B.2 Paul Liles and Mike Clements

Messrs. Paul Liles and Mike Clements were interviewed on January 25th, 2010 at the Georgia Department of Transportation's One Georgia Center location. Topics discussed in the meeting were the goals that the Georgia Department of Transportation (GDOT) hopes to achieve from this project, observed trends of corrosion induced damage in coastal Georgia bridges, GDOT experience with mitigation techniques, and current design practices.

It was established the desired goals of the project for GDOT are as follows: (1) the development and implementation of corrosion resistant stainless steel strands for prestressed concrete piles in the substructure of coastal bridges; (2) development of service life and damage estimation capabilities based on salinity maps for concrete mix

designs; and (3) provide design recommendations to achieve service lives in excess of 100 years.

Corrosion induced damage has been observed primarily in simple pile bent bridges in coastal and marsh regions. The damage is localized primarily in the piles, not in the pile or pier caps. This may partially be due to the fact that most of the bridges have the pile caps directly below the girders and elevated from the water. GDOT prefers to use prestressed concrete piles over steel H-piles and sheet piling in aggressive environments. The damage on the concrete piles is mostly found in the splash zone, extending approximately .46 m (18 in.) to either side of the mean water level in most cases. There is also concern that piles may be damaged during driving which may lead to cracking. No testing has been done to verify this, but driving guidelines are given in the GDOT specifications to prevent this damage. The state currently does not have requirements for the jetting of piles for placement except in special soil conditions.

GDOT is currently employing the following design practices to provide corrosion resistance in prestressed concrete piling: (1) Use of high performance concretes that contain supplementary cementitious materials, a low water to cementitious material ratio, and are limited to a maximum of 2000 coulombs charge passed on the rapid chloride permeability test; (2) a minimum cover distance of 50.8 mm (2 in.) is required for increased durability, and no piling less than 0.3 m (12 in.) in width is used; and (3) the superstructures of bridges are built a minimum of 0.3 to 0.61 m (1 to 2 ft) above the 50 year storm water level. Additional information on the standard pile sections is available through AASHTO and the GDOT website. Currently no service life modeling efforts are used in the design of prestressed concrete piles.

GDOT has attempted to implement several other methods for providing corrosion resistance, but have discontinued the use for various reasons. A bridge in Chatham country was constructed using corrosion inhibitors, epoxy coated rebar, and supplementary cementitious materials on individual piles. A report was written in the 1980's on this project, but no monitoring after construction was completed. Cathodic protection was implemented on the Sidney Lanier Bridge in Brunswick, Georgia. The system proved to have large maintenance issues and GDOT no longer will use electrochemical methods of protection for future projects. Epoxy coated rebar was briefly used in concrete piles, but discontinued after poor performance was observed by the Florida DOT.

B.3 Mike Clements and Andy Doyle

Messrs. Mike Clements and Andy Doyle were interviewed on February 1st, 2010 at the Georgia Department of Transportation's Confederate Avenue office. Topics discussed included inspection techniques used, typical damage to concrete piles observed, and repair techniques for damaged piles.

GDOT performs inspections of prestressed concrete piles using a dive team of inspectors. The submerged regions of piles are inspected by visually scanning the surface of each face of the pile along the length while also running hands along surface for damage. A small hammer is used to tap at the surface if damage is suspected. If cracks are observed, the size is noted and attempt to open them is made. The atmospheric and splash zones of the piles are visually inspected for damage and a hammer is used similarly to in the submerged section of the piles.

Typical types of damage that have been observed are as follows: (1) degradation and softening of concrete starting at 0.3 to 0.61 m (1 to 2 ft) below the water line and extending to the mudline; (2) longitudinal cracks along the corners of the piles extending from mudline to low tide region of pile; and (3) color change and spalling of concrete along corners of piles in submerged region.

If damage is observed, GDOT does not have standard methods of repair. The repair methods employed vary by district, and are only performed in response to damage. Currently no preventative repair is performed on concrete piles.

B.4 Myron Banks and Jeff Carroll

Messrs. Myron Banks and Jeff Carroll were interviewed on February 8th, 2010 at the GDOT Materials and Research Branch facility. Topics discussed included GDOT mix design specifications for prestressed concrete piles, reported damage patterns to concrete piles, and areas of research needed.

GDOT has two mix design specifications for prestressed concrete piles. Any piling in an aggressive environment has been required to follow the high performance concrete (HPC) specifications for the last 2 to 3 years. The HPC guidelines require a maximum of 2,000 coulombs passes on the rapid chloride permeability test, a maximum water to cementitious materials ratio of 0.35, and a 28 day strength of at least 34.5 MPa (5,000 psi). Fly ash can be used as a cement replacement up to 15%, without any restrictions on whether Type C or F is used. If alkali silica reaction (ASR) is a concern, then Type F is used with a CaO limit of 5%. Silica fume is allowed as a replacement up to 10%. Mix designs meeting these criterion often contain air entraining admixtures and

super-plasticizers. For other regions, a Class AAA concrete can be used. The specification for this mix has been in place and unchanged for over 25 years. The mix has a minimum cement requirement of 400 kg/m^3 (675 lb/yd^3), a maximum water to cementitious materials ratio of 0.44, an air content of 2.5 to 6%, and a minimum strength of 34.5 MPa (5,000 psi) at 28 days of age.

The prestressed concrete piles are typically placed at between 7 to 14 days of age. Standard designs utilize a 76 mm (3 in.) cover distance for strands. No life cycling modeling is currently employed, but is an area of interest. GDOT has not attempted to implement mitigation methods that are available or in use in other states. South Carolina requires the use of a calcium nitrite corrosion inhibitor in their mix designs. GDOT does allow for the use of fibers and slag, but neither are being utilized.

The following types of damage have been reported or observed: (1) transverse cracking with a spacing of 0.91 m to 1.52 m (3 ft to 5 ft), possibly due to over-driving or reflective cracking; (2) spalling of corners of the piles down to the level of the corner strand in the splash zone; (3) surface wear from wave action; and (4) delamination of cover concrete due to corrosion.

Areas of interest for research are the as follows: (1) development of lower permeability concrete mix designs; (2) the effect of micro-cracking during driving practices on the durability of prestressed concrete piles; and (3) feasibility self-healing concrete for improved durability characteristics.

B.5 GDOT Savannah

Messrs. Mike Garner and Slade Cole were interviewed on May 3, 2010 in the Savannah GDOT District 5 office. The damage patterns in piles were discussed, as well as the repair techniques employed. Until recently, overdriving of piles was not considered or heavily monitored. Contractors would continue to attempt to drive the piles without regard to a "refusal" limit, which is approximately 10 blows per 12.7 mm (½ in.). Overdriving in the coastal region now is typically only a concern when a hard layer of soil or lime rock layer is reached, but the refusal limits are monitored.

The reflective cracking of piles is still an area of concern for GDOT. It most commonly occurs when a soft layer of soil is hit immediately following a hard layer, or when the contractor is not following standard practice (bad pads or oversized hammer). Reflective cracking is identified by "dusting" of the piles where a small amount of powdery material is lost from the cracked region. The cracks are typically very small, and hard to find (hairline) due to prestressing effects. If a reflective crack occurs in the Savannah region, the procedure for repair varies, depending on the location in the pile. If the crack location is below the mud line, then no repair is made; however, if the crack will be located above the mud line, then it is patched with epoxy. The 0.46 m (18 in.) square piling is the most common to have reflective cracking occur. The hypothesized reasoning for this is that the 0.46 m (18 in.) design has a lower precompression stress than the other sizes and therefore is more susceptible to developing tensile forces during driving.

Once piles begin showing major signs of deterioration, there are two primary methods of repair that are used. The first method is to encase the piling in concrete, by

either placing a corrugated steel tube around it and filling with concrete, or by using a plastic jacket and pumping concrete into it. The second method of repair is to epoxy jacket the piles, which is expensive to perform. This technique was employed on the Back River Bridge discussed in Section B.3. These are not long-term solutions to bridge deterioration, but simply methods to add a short amount of time before the bridge will require replacement.

For future research, construction is about to begin on a project which will have over 1000 piles driven, and the GDOT is willing to help in attempting to determine the effects on driving on permeability due to microcracking. Additionally, for future trips it may be possible to use a boat to closer inspect a few bridges of interest.

B.6 Standard Concrete Products

Messrs. Richard Potts and Alan Pritchard of Standard Concrete Products – Savannah were interviewed on May 3, 2010 at the plant. Concrete mix designs were discussed and their variability between requirements of different states. In Georgia, any piling going into "aggressive" coastal environments is required to be cast using a high performance concrete. The HPC mix specifications require a rapid chloride permeability of less than 2000 Coulombs, which is the upper limit for the rating of "Low Chloride Ion Penetrability" according to ASTM C 1202. Fly ash can be used as up to 15% cement replacement and silica fume for up to 10%. Additionally, once cast, the concrete must age at least 18 hours or until the release strength is met, which is between 24.1 to 27.6 MPa (3,500-4,000 psi) depending on the pile size. The piles must meet 34.5 MPa (5,000 psi) design strength requirements before placement and must also be at least 5 days of age.

The mix design that SCP uses contains 15% Class F fly ash replacement, no silica fume, and a high paste content of approximately 534 kg/m^3 (900 lb/yd^3) of cementitious material. Their mix design has an ultimate strength of 55.2 to 69.0 MPa (8,000 to 10,000 psi). Silica fume is avoided in their mix designs due to its higher cost and an increased susceptibility to shrinkage cracking. All of their mix designs specify a granite coarse aggregate and a natural sand fine aggregate. The piles are typically delivered and placed at 7-14 days of age.

The normal strength standard mix that is produced for piling in regions other than the "aggressive" environment is a 445 kg/m^3 (750 lb/yd^3) cement content mix with no supplementary cementitious materials and no requirement on the rapid chloride permeability.

The mix designs for other states vary considerably with those for Georgia. The mix design for Florida employs 18% fly ash replacement and a variable design strength which is typically 41.4 to 55.2 MPa (6,000 to 8,000 psi). Florida also allows for the use of ultra-fine fly ash. South Carolina utilizes a calcium nitrite corrosion inhibitor in several of their mixes. Alan Pritchard agreed to email the mix designs and state specifications that are used for these states.

The concrete piles that were forensically investigated from the I-95 at Turtle River Bridge were most likely produced at Gates Precast in Jacksonville, Florida. The mix designs at the time of construction were typically a 0.5 w/c with no SCM addition. Richard Potts will contact the former plant manager there and attempt to find out more specific information.

It was reiterated that overdriving of piles in Georgia was previously not heavily controlled or monitored. Also, Mr. Potts said that the 0.46 m (18in.) piling is understressed compared to the other size designs in Georgia with an effective P/A of approximately 4.8 MPa (700 psi) after losses compared to most having 5.5 to 6.2 MPa (800-900 psi), and he believed that such understressing is the cause of increased amount of reflective cracks noticed when using 0.46 m (18 in.) piling.

The use of epoxy coated or stainless steel prestressing strand to increase the corrosion resistance of piles was also discussed. Richard stated that SCP had used epoxy coated strand briefly. Temperature control problems (which influence the properties of the epoxy) were found to be a concern in addition to the sand grit embedded in the epoxy to increase bond. The sand grit causes excessive wear on the beds and grips. SCP expressed interest in the use of stainless steel strand for the construction of "highly" corrosion resistant piling, although they were concerned that the high cost to produce the piles (~40% of cost is steel currently) would limit the economic feasibility of their use in bridge construction.

B.7 GDOT Brunswick

Messrs. Lisa Sikes and Brian Scarbrough were interviewed on May 4, 2010 in the GDOT Brunswick office. Damage and construction practices of piling were discussed. It was reiterated again that the 0.46 m (18 in.) piling is problematic with reflective cracking. In contrast to the Savannah office, the Brunswick office personnel will reject piling if "dusting" is seen during driving. The commonplace practice of overdriving in older construction was again discussed. When asked about a few of the bridges of interest, it

was noted that there were paper mills present in close proximity and that run-off from them may be partially responsible for some damage seen on the piles. Brian Scarbrough agreed to email pictures of damaged piling on another bridge that was not visited over the South Brunswick River on I-95.

The I-95 at Turtle River piles that were delivered to the Georgia Tech Structures Laboratory were battered piles located on the edge of the bents. The remainder of the piling is still in place, although no longer in a load carrying capacity. Photos are shown in Chapter 3.

APPENDIX C

CHLORIDE INGRESS RESULTS

The data from the rapid chloride permeability testing is presented in section C.1. The titration data for bulk diffusion testing is given in section C.2 for each mix design. The 0.5 mm (0.02 in.) increment was not used in regression analysis performed to determine diffusion coefficients with measured data.

C.1 Rapid Chloride Permeability

Table C.1: Rapid chloride permeability charge passed and initial current measurements for all mix designs, tests at 56 days

	Charge Passed (Coulombs)			Initial Current (Amps)		
Mix Design	**#1**	**#2**	**Average**	**#1**	**#2**	**Average**
T2	9,071	7,313	8,192	265.4	217.9	241.7
Type II	1,460	1,284	1,372	52.1	58.6	55.4
T3-F15	1,623	1,459	1,541	64.6	60.6	62.6
F25	1,220	1,207	1,214	57.1	56.3	56.7
F25-MK5	624	590	607	26.7	25.0	25.9
F25-MK10	371	375	373	16.1	16.0	16.1
F25-SF5	371	337	354	16.2	14.2	15.2
F25-SF10	222	239	231	9.3	10.0	9.7
S35-MK5	330	335	333	15.2	15.4	15.3
S50-MK5	289	257	273	12.6	11.7	12.2
S35-SF5	285	292	289	13.1	13.3	13.2
S50-SF5	358	372	365	15.1	15.5	15.3

C.2 Bulk Diffusion Raw Data

Tables C.2 though C.11 provide the raw titration data from the bulk diffusion tests where the depth in mm (1 in. = 25.4 mm) is to the midsection of the interval. Samples were sealed at 28 days and exposed for 180 days prior to grinding.

Table C.2: T2 bulk diffusion results

	Chloride Content (% mass concrete)		
Depth (mm)	**Sample 1**	**Sample 2**	**Average**
0.5	0.93	0.91	0.92
1.5	0.77	0.76	0.77
3.5	0.59	0.57	0.58
6	0.50	0.50	0.50
8	0.45	0.47	0.46
10	0.42	0.42	0.42
12	0.39	0.39	0.39
14	0.34	0.33	0.34
16	0.26	0.25	0.26
18	0.24	0.24	0.24
20	0.22	0.22	0.22
22	0.20	0.19	0.20
24	0.18	0.18	0.18

Table C.3: T3-F15 bulk diffusion results

	Chloride Content (% mass concrete)		
Depth (mm)	**Sample 1**	**Sample 2**	**Average**
0.5	1.19	1.17	1.18
1.5	0.83	0.83	0.83
2.5	0.66	0.67	0.67
3.5	0.57	0.58	0.58
4.5	0.49	0.48	0.49
5.5	0.43	0.43	0.43
7	0.18	0.19	0.18
9	0.12	0.09	0.10

Table C.4: F25 bulk diffusion results

	Chloride Content (% mass concrete)		
Depth (mm)	**Sample 1**	**Sample 2**	**Average**
0.5	0.91	0.89	0.90
1.5	0.94	0.93	0.93
2.5	0.77	0.77	0.77
3.5	0.67	0.67	0.67
4.5	0.60	0.60	0.60
5.5	0.47	0.47	0.47
7	0.23	0.21	0.22
9	0.10	0.10	0.10
11	0.04	0.04	0.04

Table C.5: F25-MK5 bulk diffusion results

	Chloride Content (% mass concrete)		
Depth (mm)	**Sample 1**	**Sample 2**	**Average**
0.5	1.31	1.31	1.31
1.5	0.98	0.86	0.92
2.5	0.87	0.93	0.90
3.5	0.73	0.64	0.69
4.5	0.53	0.42	0.48
5.5	0.28	0.37	0.33
7	0.21	0.23	0.22
9	0.10	0.13	0.11

Table C.6: F25-MK10 bulk diffusion results

	Chloride Content (% mass concrete)		
Depth (mm)	**Sample 1**	**Sample 2**	**Average**
0.5	0.85	0.87	0.86
1.5	0.73	0.75	0.74
2.5	0.54	0.54	0.54
3.5	0.45	0.46	0.46
4.5	0.39	0.41	0.40
5.5	0.35	0.36	0.35
7	0.16	0.18	0.17
9	0.12	0.13	0.13

Table C.7: F25-SF10 bulk diffusion results

	Chloride Content (% mass concrete)		
Depth (mm)	**Sample 1**	**Sample 2**	**Average**
0.5	1.02	1.04	1.03
1.5	1.02	1.03	1.03
2.5	0.86	0.88	0.87
3.5	0.58	0.62	0.60
4.5	0.44	0.47	0.46
5.5	0.39	0.40	0.40
6.5	0.32	0.33	0.32
7.5	0.20	0.20	0.20

Table C.8: S35-MK5 bulk diffusion results

	Chloride Content (% mass concrete)		
Depth (mm)	**Sample 1**	**Sample 2**	**Average**
0.5	0.87	0.85	0.86
1.5	0.69	0.67	0.68
2.5	0.51	0.50	0.50
3.5	0.44	0.45	0.45
4.5	0.38	0.38	0.38
5.5	0.28	0.29	0.28
7	0.09	0.12	0.11
9	0.04	0.03	0.04

Table C.9: S50-MK5 bulk diffusion results

	Chloride Content (% mass concrete)		
Depth (mm)	**Sample 1**	**Sample 2**	**Average**
0.5	0.85	0.84	0.84
1.5	0.74	0.75	0.74
2.5	0.58	0.58	0.58
3.5	0.37	0.39	0.38
4.5	0.28	0.30	0.29
5.5	0.19	0.18	0.19
7	0.06	0.07	0.07
9	0.00	0.03	0.02

Table C.10: S35-SF5 bulk diffusion results

	Chloride Content (% mass concrete)		
Depth (mm)	**Sample 1**	**Sample 2**	**Average**
0.5	0.82	0.84	0.83
1.5	0.79	0.79	0.79
2.5	0.59	0.59	0.59
3.5	0.44	0.44	0.44
4.5	0.32	0.33	0.33
5.5	0.19	0.21	0.20
7	0.07	0.07	0.07
9	0.02	0.05	0.03

Table C.11: S50-SF5 bulk diffusion results

	Chloride Content (% mass concrete)		
Depth (mm)	**Sample 1**	**Sample 2**	**Average**
0.5	1.02	0.99	1.00
1.5	0.79	0.85	0.82
2.5	0.64	0.65	0.64
3.5	0.49	0.47	0.48
4.5	0.39	0.38	0.39
5.5	0.35	0.35	0.35
7	0.15	0.17	0.16
9	0.04	0.02	0.03

APPENDIX D

CARBONATION TESTING RESULTS

D.1 Carbonation Depth Measurements

D.1.1 Carbonation Depth Data

The carbonation depth on samples was measured relative to exposure at 28 days, after a 21 day moist curing, and 7 day conditioning period.

Table D.1: Mean carbonation depth as indicated by phenolphthalein indicator solution (1 in. = 25.4 mm)

Exposure Time (days)	**3**	**7**	**14**	**21**	**28**	**70**	**90**	**120**	**180**	**300**	**350**
Mix Design	**Carbonation Depth (mm)**										
T2	6.1	10.2	14.2	17.5	19.3	-	-	-	-	-	-
T3-F15	-	-	-	2.5	3.8	5.8	7.4	7.1	-	9.9	10.7
F25	-	2.5	3.0	4.1	4.6	6.1	7.9	8.9	10.4	12.2	13.2
F25-MK5	-	-	-	3.3	-	5.1	6.4	7.6	9.4	11.7	12.2
F25-MK10	-	-	-	-	2.5	3.6	4.3	5.8	6.9	8.9	9.4
F25-SF5	-	-	-	-	2.5	3.3	4.3	5.8	6.4	8.1	8.6
F25-SF10	-	-	-	-	3.0	3.6	5.1	6.6	6.9	9.1	10.2
S35-MK5	-	-	-	-	3.0	6.9	8.1	9.4	10.4	12.7	13.5
S50-MK5	-	-	-	-	3.0	5.1	6.1	-	-	8.9	9.7
S35-SF5	-	-	-	3.6	-	5.3	6.1	7.1	8.4	10.7	11.4
S50-SF5	-	-	-	-	3.6	4.3	5.8	6.9	8.1	9.7	10.7

Table D.2: Standard deviation of carbonation depth as indicated by phenolphthalein indicator solution (1 in. = 25.4 mm)

Exposure Time (days)	**3**	**7**	**14**	**21**	**28**	**70**	**90**	**120**	**180**	**300**	**350**
Mix Design	**Carbonation Depth (mm)**										
T2	0.5	0.5	0.8	1.3	0.5	-	-	-	-	-	-
T3-F15	-	-	-	0.3	0.5	0.3	0.5	0.3	-	0.5	0.5
F25	-	0.3	0.3	0.3	0.3	0.3	0.8	0.8	0.3	0.5	0.5
F25-MK5	-	-	-	0.3	-	0.3	0.3	0.5	0.3	0.5	0.3
F25-MK10	-	-	-	-	0.3	0.3	0.3	0.5	0.5	0.5	0.5
F25-SF5	-	-	-	-	0.3	0.5	0.5	0.3	0.3	0.3	0.3
F25-SF10	-	-	-	-	0.3	0.3	0.3	0.5	0.5	0.5	0.5
S35-MK5	-	-	-	-	0.5	0.3	0.5	0.5	0.5	0.3	0.8
S50-MK5	-	-	-	-	0.5	0.3	0.3	-	-	0.8	0.3
S35-SF5	-	-	-	0.3	-	0.3	0.3	0.3	0.3	0.3	0.3
S50-SF5	-	-	-	-	0.3	0.3	0.5	0.5	0.3	0.3	0.8

D.1.2 Photos of Carbonation Samples

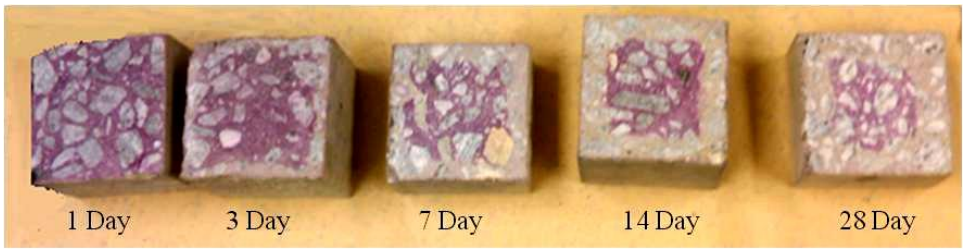

Figure D.1: T2 carbonation samples (76.2 x 76.2 mm (3 x 3 in.))

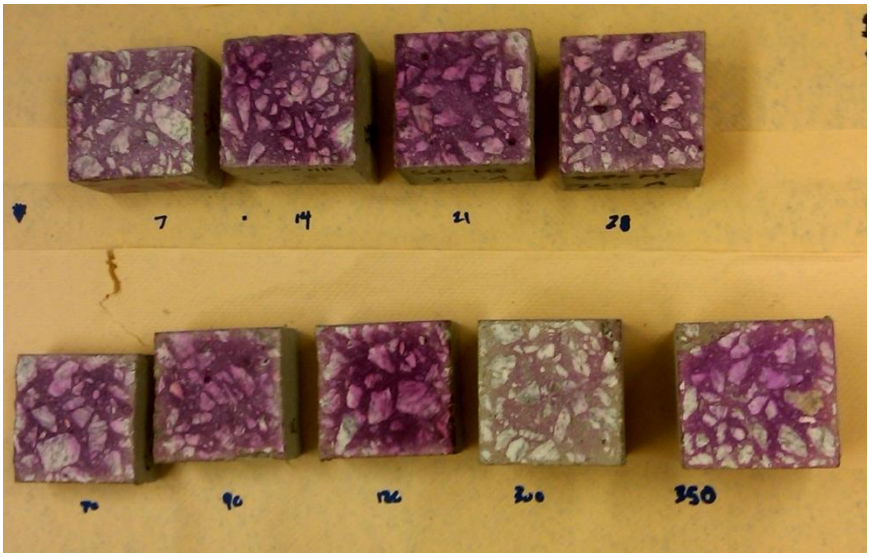

Figure D.2: T3-F15 carbonation samples (76.2 x 76.2 mm (3 x 3 in.))

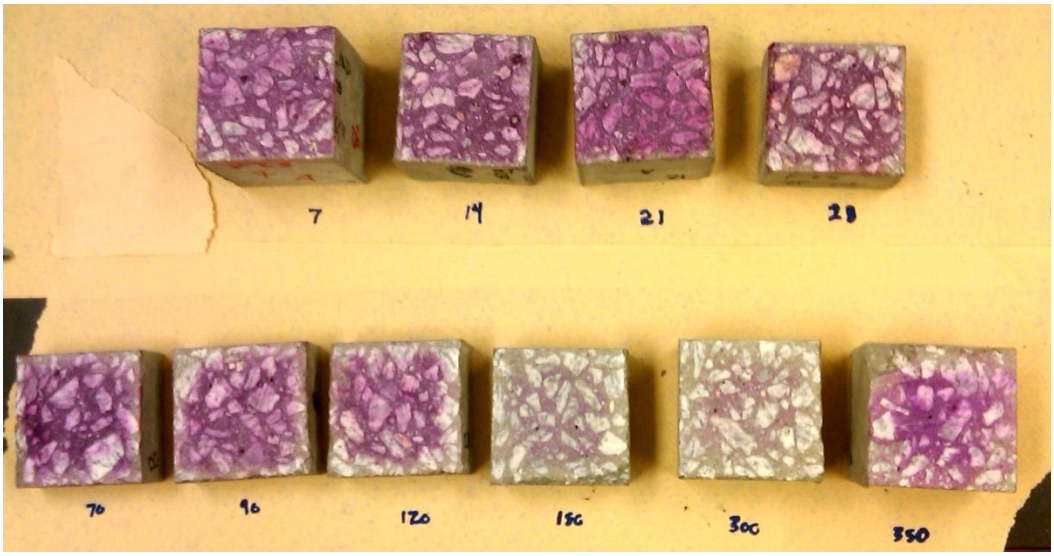

Figure D.3: F25 carbonation samples (76.2 x 76.2 mm (3 x 3 in.))

Figure D.4: F25-MK5 carbonation samples (76.2 x 76.2 mm (3 x 3 in.))

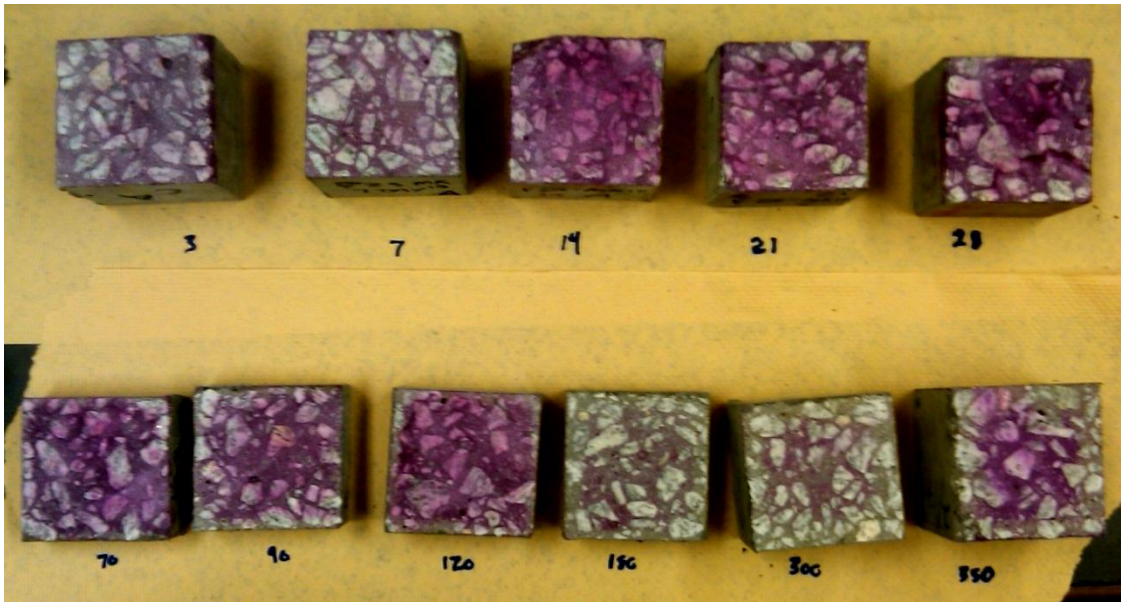

Figure D.5: F25-MK10 carbonation samples (76.2 x 76.2 mm (3 x 3 in.))

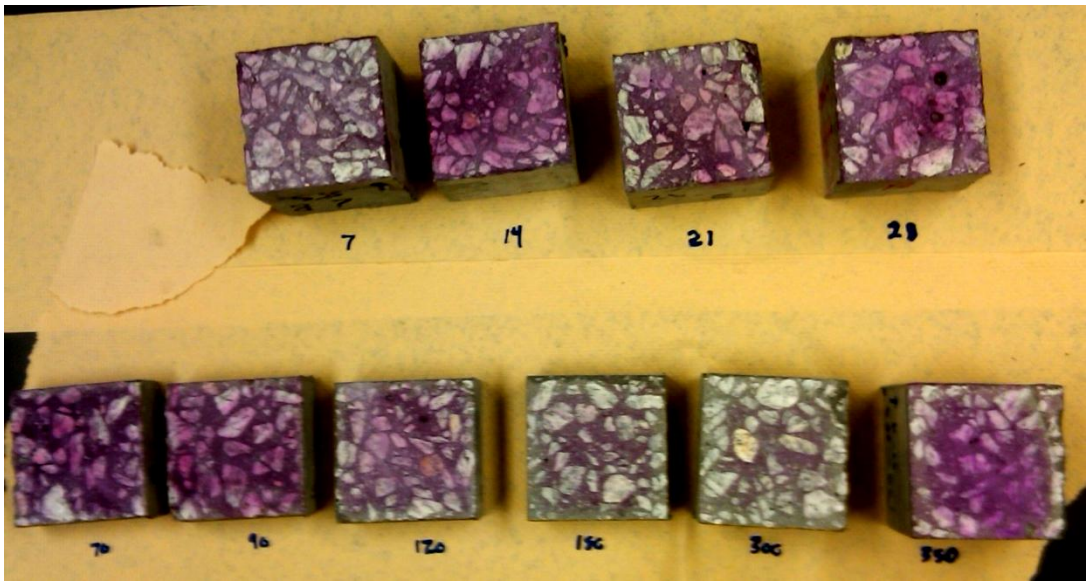

Figure D.6: F25-SF5 carbonation samples (76.2 x 76.2 mm (3 x 3 in.))

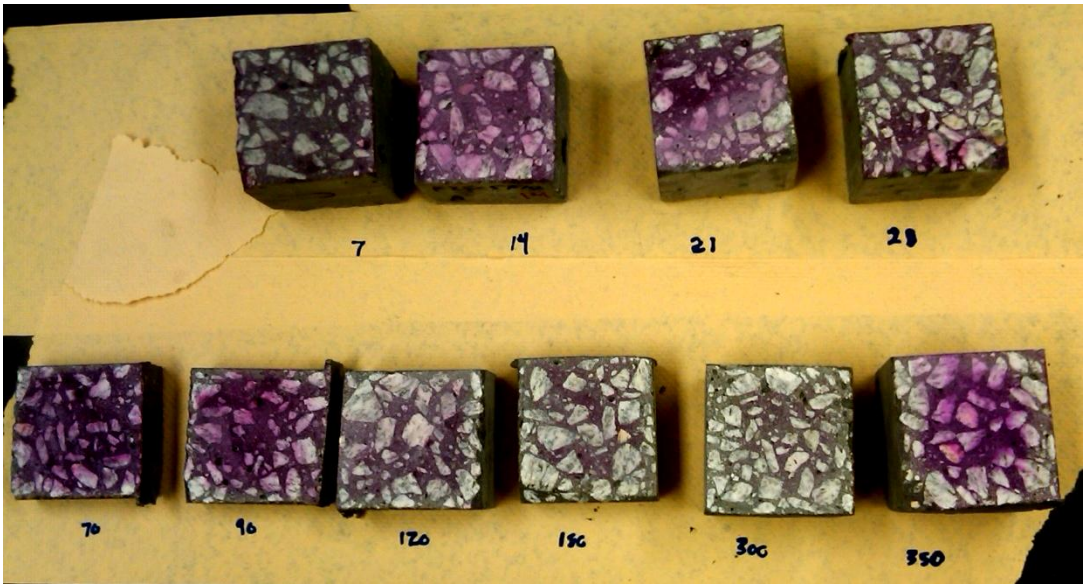

Figure D.7: F25-SF10 carbonation samples (76.2 x 76.2 mm (3 x 3 in.))

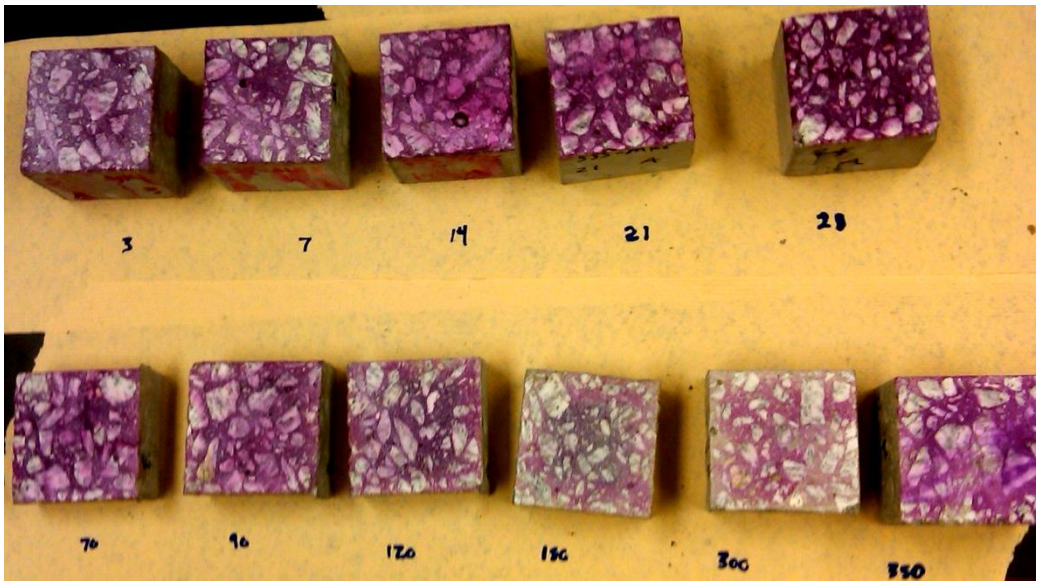

Figure D.8: S35-MK5 carbonation samples (76.2 x 76.2 mm (3 x 3 in.))

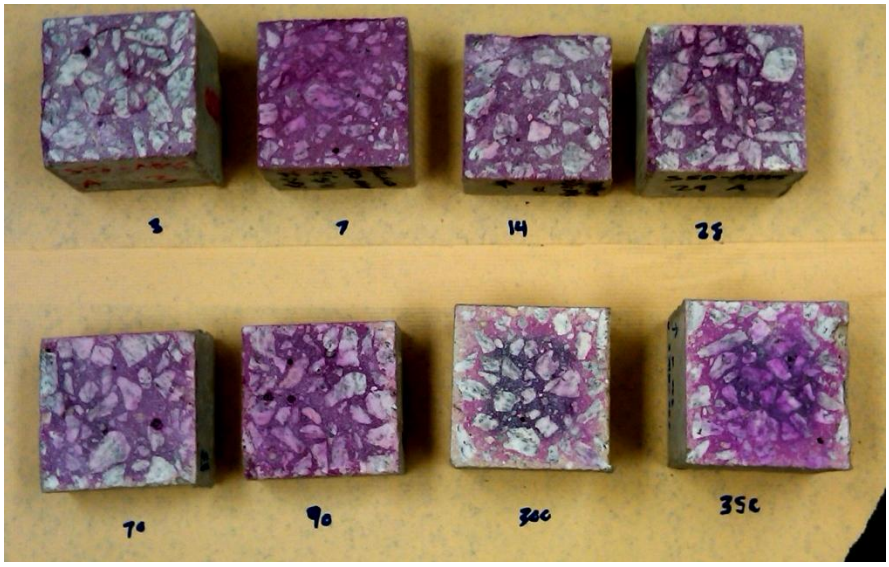

Figure D.9: S50-MK5 carbonation samples (76.2 x 76.2 mm (3 x 3 in.))

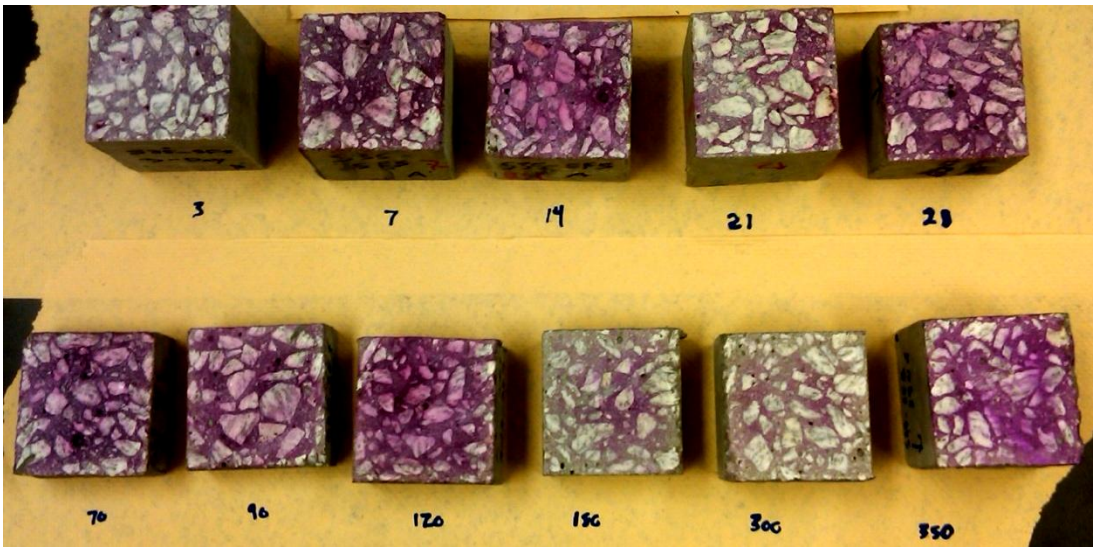

Figure D.10: S35-SF5 carbonation samples (76.2 x 76.2 mm (3 x 3 in.))

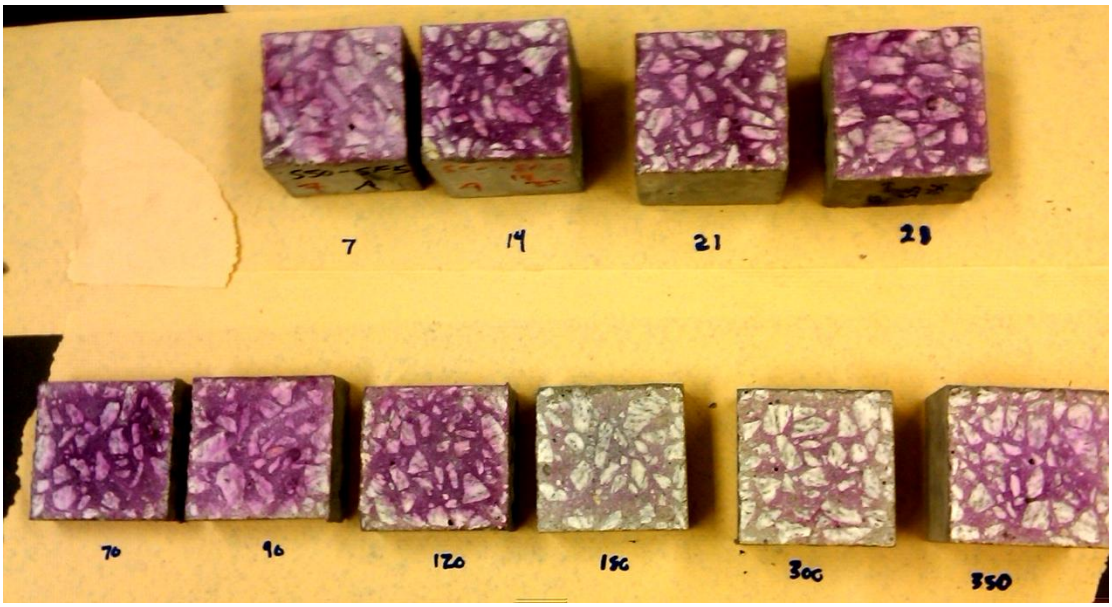

Figure D.11: S50-SF5 carbonation samples (76.2 x 76.2 mm (3 x 3 in.))

D.2 Carbonation Regression Parameters

Table D.3: Experimentally determined carbonation constant and R^2 values (1 in. = 25.4 mm)

Mix Design	Carbonation Constant, K ($mm/yr^{0.5}$)	R^2
T2	3.71	0.981
T3-F15	0.61	0.921
F25	0.75	0.972
F25-MK5	0.67	0.989
F25-MK10	0.50	0.982
F25-SF5	0.47	0.966
F25-SF10	0.54	0.970
S35-MK5	0.76	0.936
S50-MK5	0.54	0.941
S35-SF5	0.63	0.988
S50-SF5	0.58	0.983

APPENDIX E

SULFATE ATTACK RESISTANCE TESTING

E.1 ASTM C 1012 Expansion Testing

E.1.1 Expansion Results

Table E.1: ASTM C 1012 expansion readings from initial to 15 weeks

	Expansion after exposure period (%)						
Mix Design	**1 week**	**2 week**	**3 week**	**4 week**	**8 week**	**13 week**	**15 week**
T2	0.013	0.016	0.016	0.019	0.027	0.028	0.031
T3	0.012	0.013	0.015	0.015	0.014	0.026	0.028
T5	0.007	0.008	0.009	0.012	0.016	0.020	0.020
T3-F15	0.006	0.009	0.011	0.012	0.011	0.019	0.021
F25	0.008	0.012	0.017	0.018	0.018	0.028	0.029
F25-MK5	0.009	0.014	0.017	0.019	0.020	0.032	0.035
F25-MK10	0.018	0.022	0.025	0.027	0.032	0.036	0.036
F25-SF5	0.008	0.019	0.018	0.017	0.020	0.023	0.023
F25-SF10	0.007	0.013	0.013	0.014	0.015	0.018	0.018
S35-MK5	0.006	0.010	0.014	0.014	0.019	0.023	0.024
S50-MK5	0.007	0.013	0.013	0.013	0.013	0.016	0.018
S35-SF5	0.012	0.018	0.018	0.017	0.020	0.025	0.025
S50-SF5	0.017	0.019	0.018	0.018	0.024	0.027	0.027

Table E.2: ASTM C 1012 expansion readings from 4 months to 11 months

	Expansion after exposure period (%)						
Mix Design	**4 month**	**6 month**	**7 month**	**8 month**	**9 month**	**10 month**	**11 month**
T2	0.032	0.038	0.051	0.054	0.061	0.069	0.079
T3	0.029	0.035	0.052	0.063	0.086	0.133	-
T5	0.021	0.020	0.036	0.044	0.056	0.071	-
T3-F15	0.021	0.021	0.030	0.030	0.030	0.032	-
F25	0.032	0.038	0.043	0.043	0.043	0.047	0.048
F25-MK5	0.038	0.047	0.054	0.056	0.060	0.066	0.074
F25-MK10	0.036	0.036	0.041	0.041	0.042	0.042	-
F25-SF5	0.024	0.031	0.032	0.034	0.034	0.035	0.036
F25-SF10	0.022	0.026	0.025	0.026	0.026	0.027	0.026
S35-MK5	0.024	0.031	0.032	0.034	0.036	0.036	-
S50-MK5	0.019	0.020	0.022	0.022	0.022	0.023	0.022
S35-SF5	0.024	0.030	0.036	0.034	0.038	0.038	0.041
S50-SF5	0.028	0.034	0.039	0.038	0.042	0.042	0.045

Table E.3: ASTM C 1012 expansion readings from 12 months to 18 months

	Expansion after exposure period (%)						
Mix Design	**12 month**	**13 month**	**14 month**	**15 month**	**16 month**	**17 month**	**18 month**
T2	0.087	0.100	-	0.125	0.138	0.158	0.177
T3	0.237	-	0.428	0.527	0.637	0.738	0.907
T5	0.099	-	0.128	0.138	0.152	0.175	0.201
T3-F15	0.032	-	0.036	0.038	0.039	0.041	0.041
F25	0.050	-	-	0.062	0.070	0.078	0.090
F25-MK5	0.083	-	0.102	0.136	0.161	0.190	0.218
F25-MK10	0.042	-	0.045	0.044	0.044	0.045	0.045
F25-SF5	0.036	-	0.038	0.039	0.039	0.041	
F25-SF10	0.027	-	0.028	0.029	0.029	0.029	
S35-MK5	0.039	-	0.042	0.044	0.044	0.048	0.047
S50-MK5	0.023	-	-	0.026	0.025	0.025	0.026
S35-SF5	0.041	-	0.044	0.044	0.045	0.046	
S50-SF5	0.046	-	0.049	0.050	0.051	0.053	

E.1.2 Compressive Strength Gain Data

Table E.4: Compressive strength gain of mortar cubes for ASTM C 1012 criterion

	Compressive Strength (MPa)					
Mix Design	**1 Day**	**2 Day**	**3 Day**	**4 Day**	**5 Day**	**6 Day**
T2	27.7	-	-	-	-	-
T3	35.2	-	-	-	-	-
T5	29.4	-	-	-	-	-
T3-F15	28.5	-	-	-	-	-
F25	15.5	18.9	18.5	-	19.0	23.3
F25-MK5	17.4	18.7	-	18.7	27.5	-
F25-MK10	15.6	-	22.7	-	-	-
F25-SF5	19.4	22.4	-	-	-	-
F25-SF10	22.2	-	-	-	-	-
S35-MK5	16.8	-	22.9	-	-	-
S50-MK5	11.6	-	20.7	-	-	-
S35-SF5	8.8	-	-	19.4	24.5	-
S50-SF5	9.7	-	-	16.4	19.0	21.1

E.2 Compressive Strength Degradation

Table E.5: Initial strength of paste cube samples at beginning of exposure (1 ksi = 6.89 MPa)

Mix Design	Initial Compressive Strength (MPa)
T2	40.5
T3	26.4
T5	29.7
T3-F15	29.7
F25	30.4
F25-MK5	24.0
F25-MK10	24.3
F25-SF5	29.3
F25-SF10	23.3
S35-MK5	24.2
S50-MK5	27.1
S35-SF5	20.2
S50-SF5	31.6

Table E.6: 28 day strength of control and sulfate exposure specimens (1 ksi = 6.89 MPa)

	28-Day Compressive Strength (MPa)			
	Average		Std. Dev.	
Mix Design	Exposed	Control	Exposed	Control
T2	39.7	32.9	2.0	3.4
T3	34.2	30.4	3.0	7.5
T5	26.6	22.9	3.6	3.8
T3-F15	33.5	31.9	2.0	1.2
F25	27.1	22.2	4.9	1.1
F25-MK5	24.6	24.6	3.0	2.5
F25-MK10	22.3	23.0	1.3	1.5
F25-SF5	30.5	29.1	1.4	4.0
F25-SF10	24.5	26.8	1.8	2.3
S35-MK5	24.3	26.4	1.5	2.6
S50-MK5	23.5	24.1	1.8	2.5
S35-SF5	26.2	23.4	2.8	1.4
S50-SF5	30.5	27.1	4.9	2.9

Table E.7: 90 day strength of control and sulfate exposure specimens (1 ksi = 6.89 MPa)

	90-Day Compressive Strength (MPa)			
	Average		Std. Dev.	
Mix Design	Exposed	Control	Exposed	Control
T2	54.4	48.8	4.7	1.5
T3	39.7	39.4	4.9	3.1
T5	39.0	36.5	2.9	2.5
T3-F15	33.1	43.7	2.8	2.2
F25	31.5	27.4	2.9	2.0
F25-MK5	22.9	26.8	1.9	1.6
F25-MK10	25.3	28.6	1.7	1.2
F25-SF5	24.8	29.8	3.1	1.2
F25-SF10	32.2	39.4	1.9	2.4
S35-MK5	34.7	35.2	2.2	3.2
S50-MK5	26.9	26.2	2.4	2.5
S35-SF5	27.7	32.4	4.2	4.2
S50-SF5	32.0	39.1	1.8	1.9

Table E.8: 180 day strength of control and sulfate exposure specimens (1 ksi = 6.89 MPa)

	180-Day Compressive Strength (MPa)			
	Average		Std. Dev.	
Mix Design	Exposed	Control	Exposed	Control
T2	55.8	45.0	4.6	3.9
T3	32.7	42.1	3.5	2.6
T5	57.3	46.3	5.6	3.2
T3-F15	24.7	44.7	2.7	4.4
F25	41.1	43.0	4.2	2.4
F25-MK5	25.5	32.7	4.0	1.7
F25-MK10	30.5	34.9	0.8	1.8
F25-SF5	31.5	41.2	4.9	3.2
F25-SF10	29.4	43.0	2.1	3.4
S35-MK5	25.7	32.2	3.5	1.3
S50-MK5	27.0	31.8	2.7	1.6
S35-SF5	31.8	48.4	2.1	1.9
S50-SF5	27.5	42.3	2.0	1.9

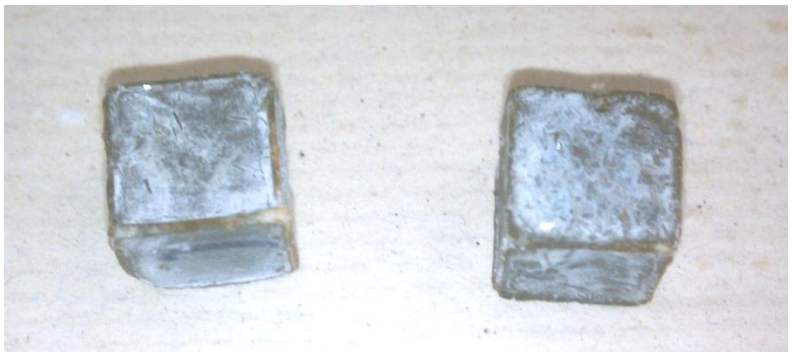

(a)

(b)

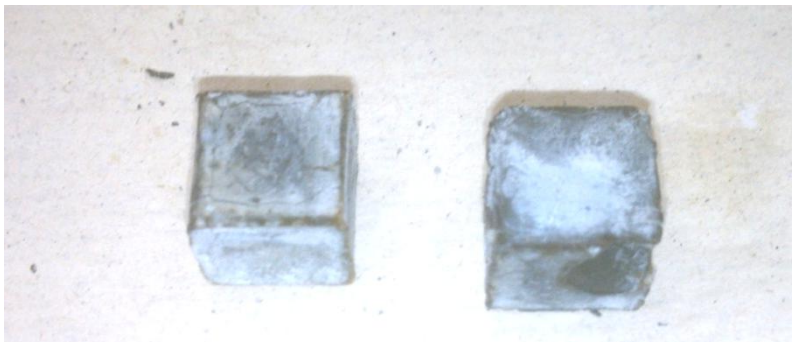

(c)

Figure E.1: Control (left) and 180-day sulfate exposure specimen for (a) T2, (b) T3, and (c) T5 (12.7 mm cubes (0.5 in.))

(a)

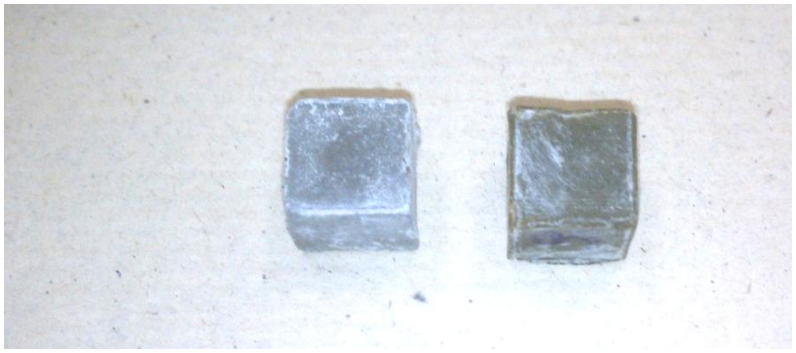

(b)

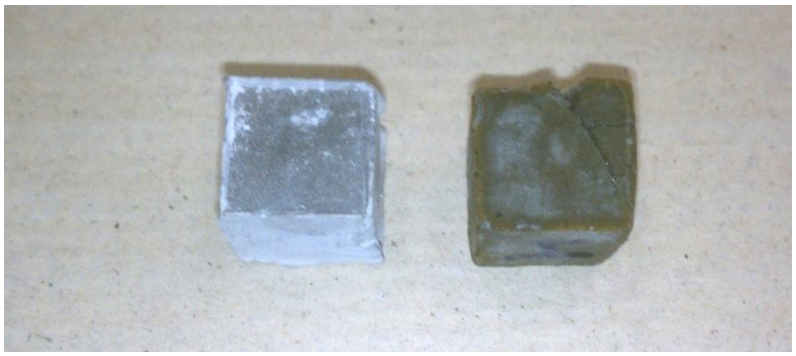

(c)

Figure E.2: Control (left) and 180-day sulfate exposure specimen for (a) T3-F15, (b) F25, and (c) F25-MK5 (12.7 mm cubes (0.5 in.))

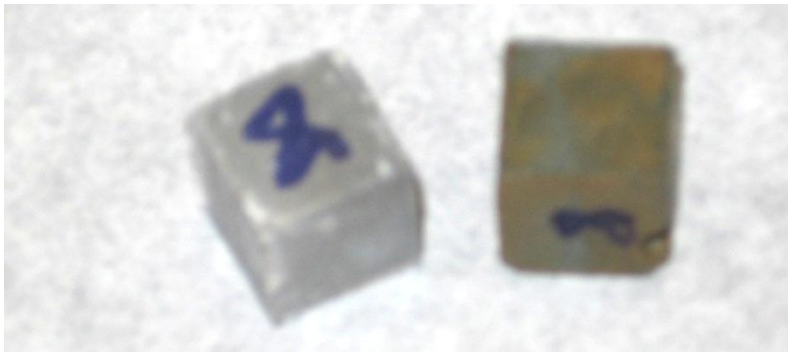

(a)

(b)

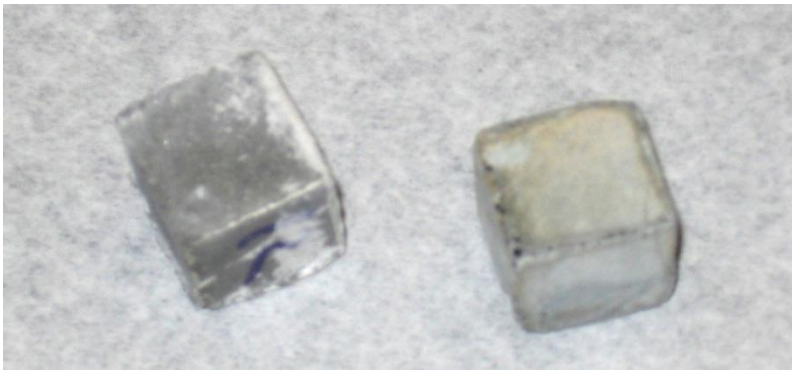

(c)

Figure E.3: Control (left) and 180-day sulfate exposure specimen for (a) F25-MK10, (b) F25-SF5, and (c) F25-SF10 (12.7 mm cubes (0.5 in.))

(a)

(b)

(c)

Figure E.4: Control (left) and 180-day sulfate exposure specimen for (a) S35-MK5, (b) S50-MK5, and (c) S35-SF5 (12.7 mm cubes (0.5 in.))

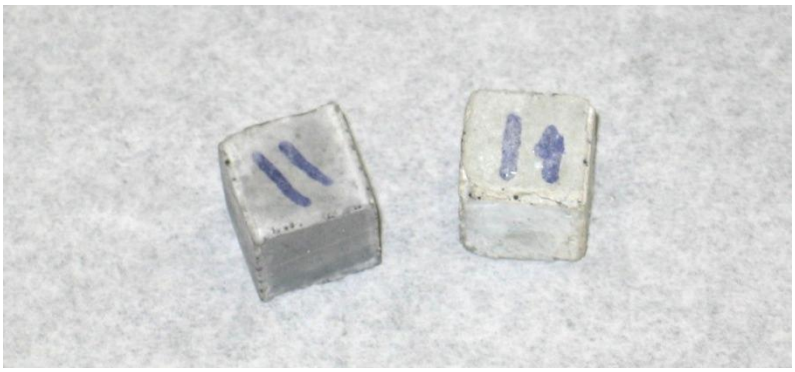

Figure E.5: Control (left) and 180-day sulfate exposure specimen for S50-SF5 (12.7 mm cubes (0.5 in.))

E.3 Quantitative X-Ray Diffraction

E.3.1 Diffraction Patterns

E.3.1.1 180-day Control Specimens

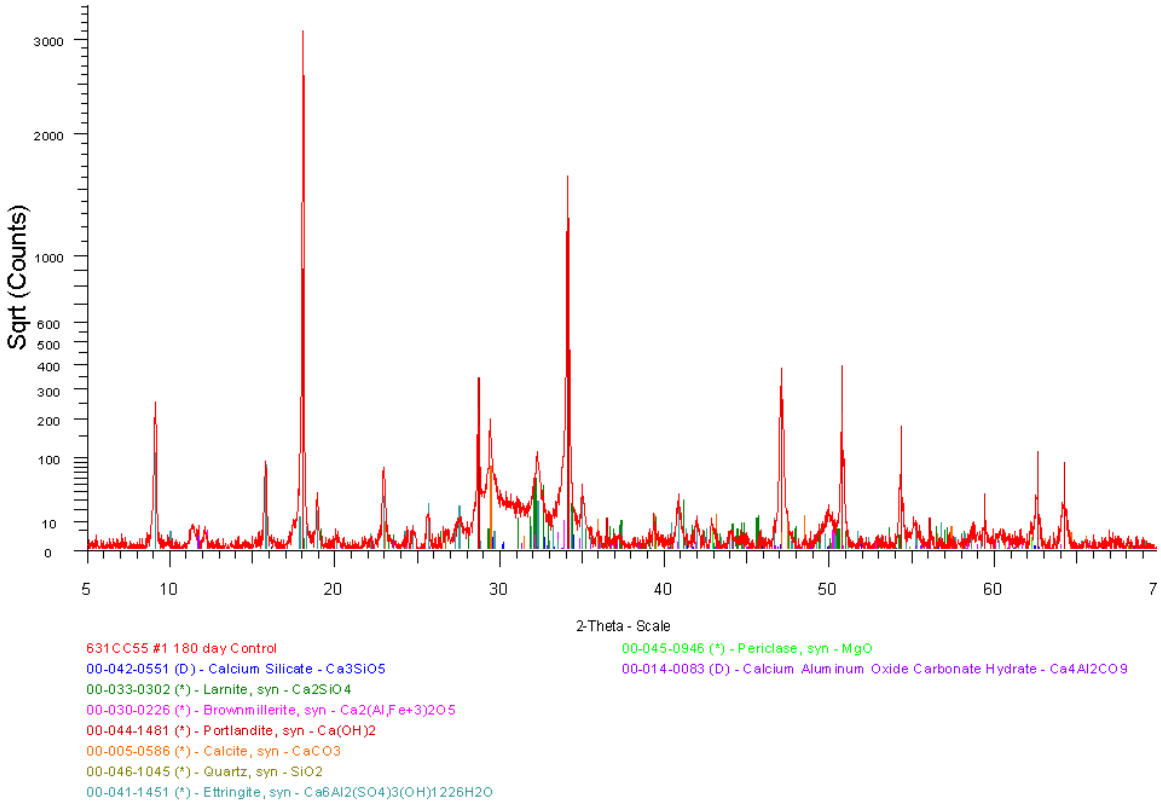

Figure E.6: T2 180-day Control XRD Pattern

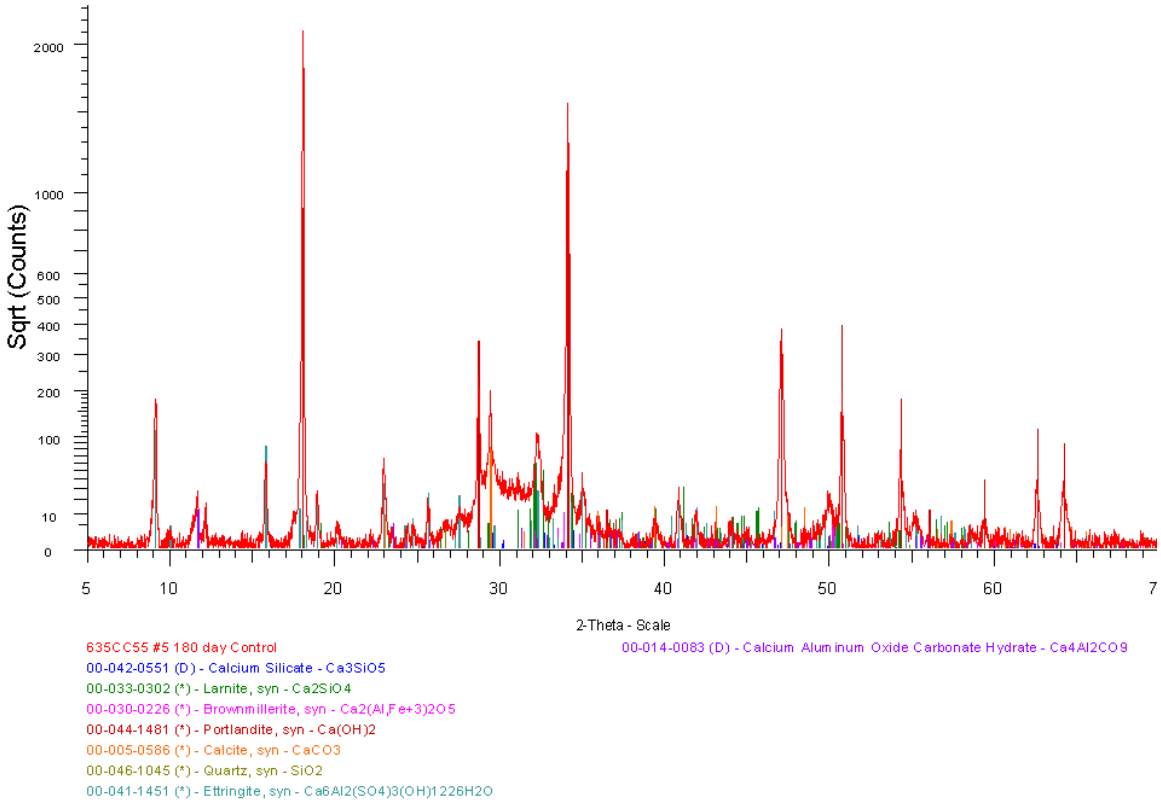

Figure E.7: T3 180-day Control XRD Pattern

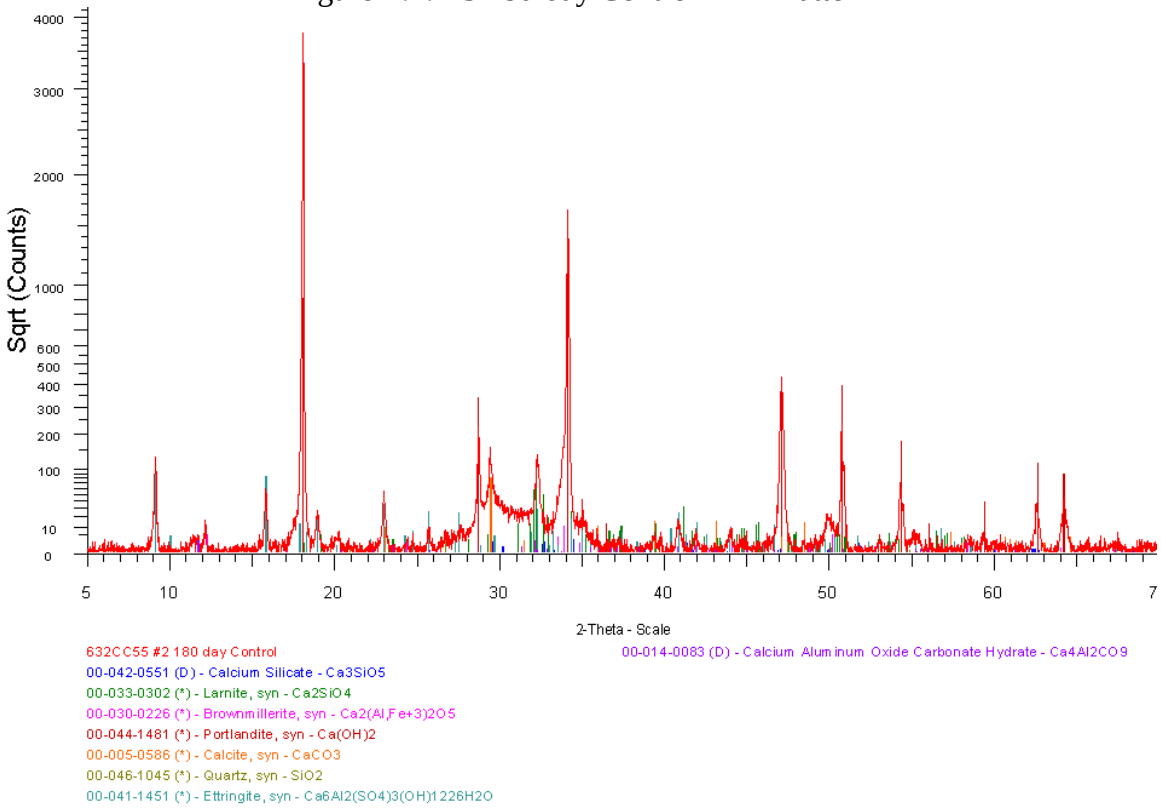

Figure E.8: T5 180-day Control XRD Pattern

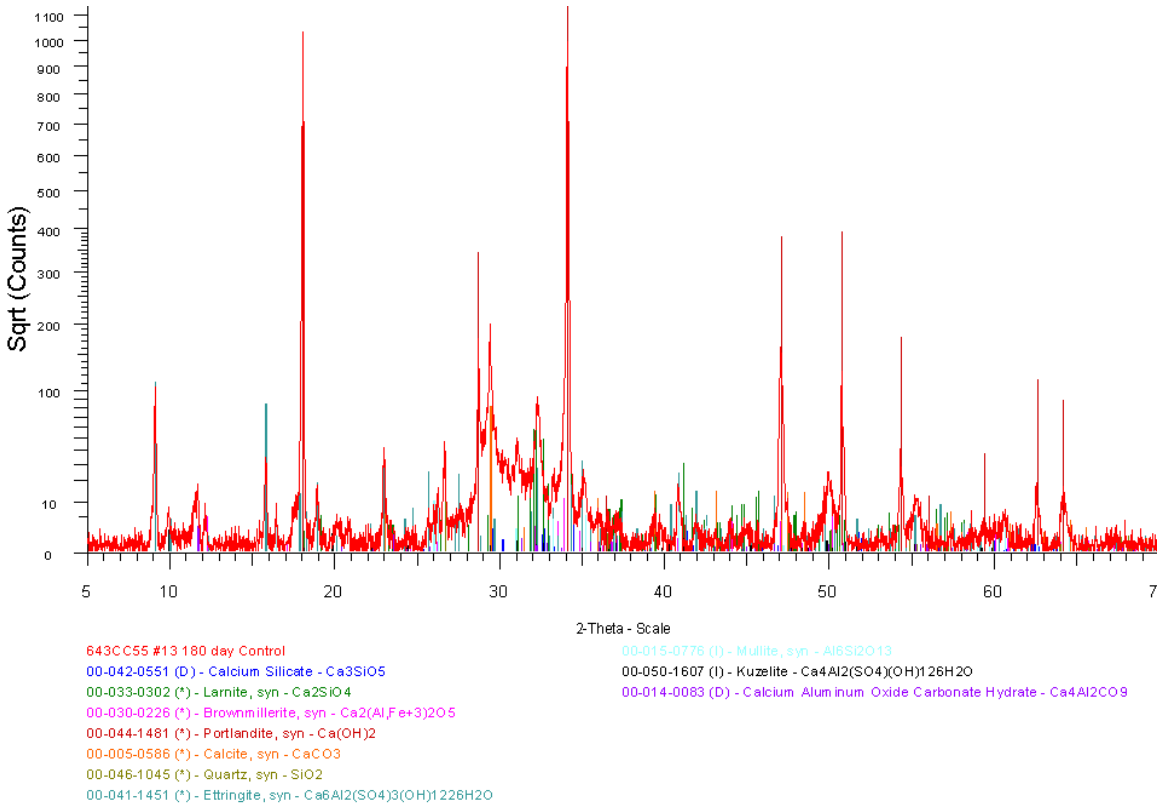

Figure E.9: T3-F15 180-day Control XRD Pattern

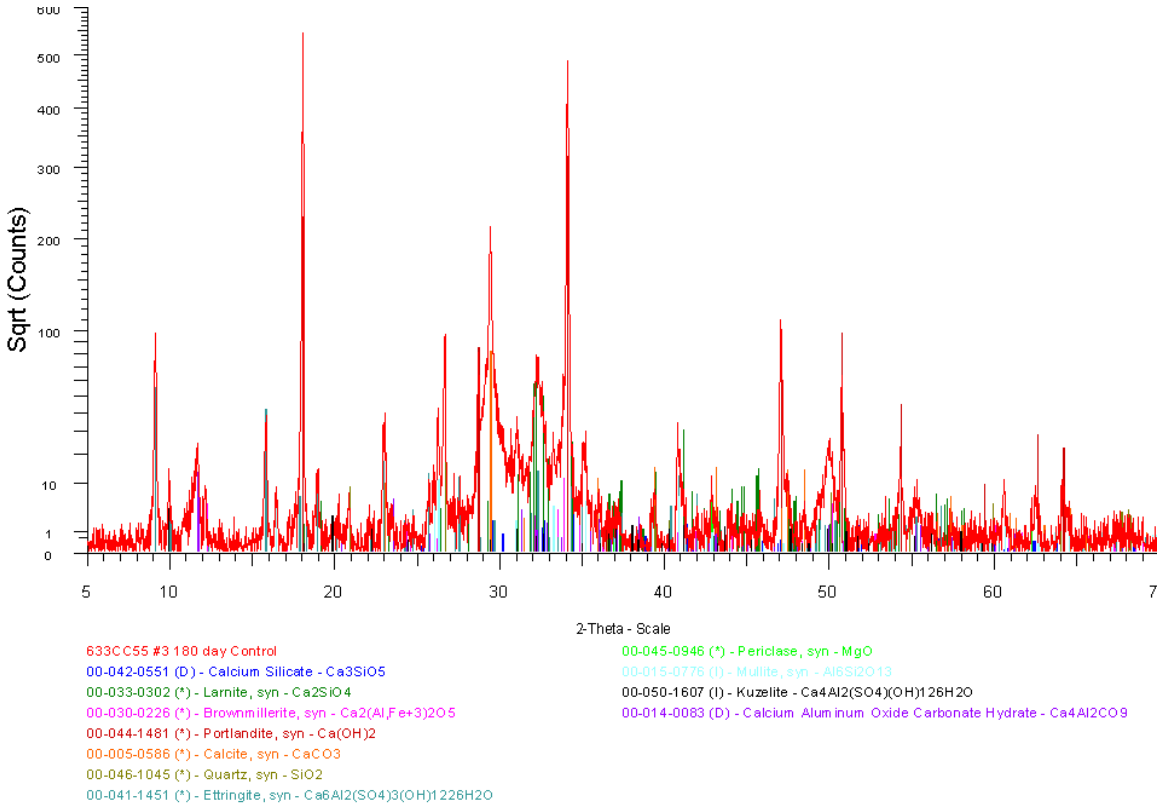

Figure E.10: F25 180-day Control XRD Pattern

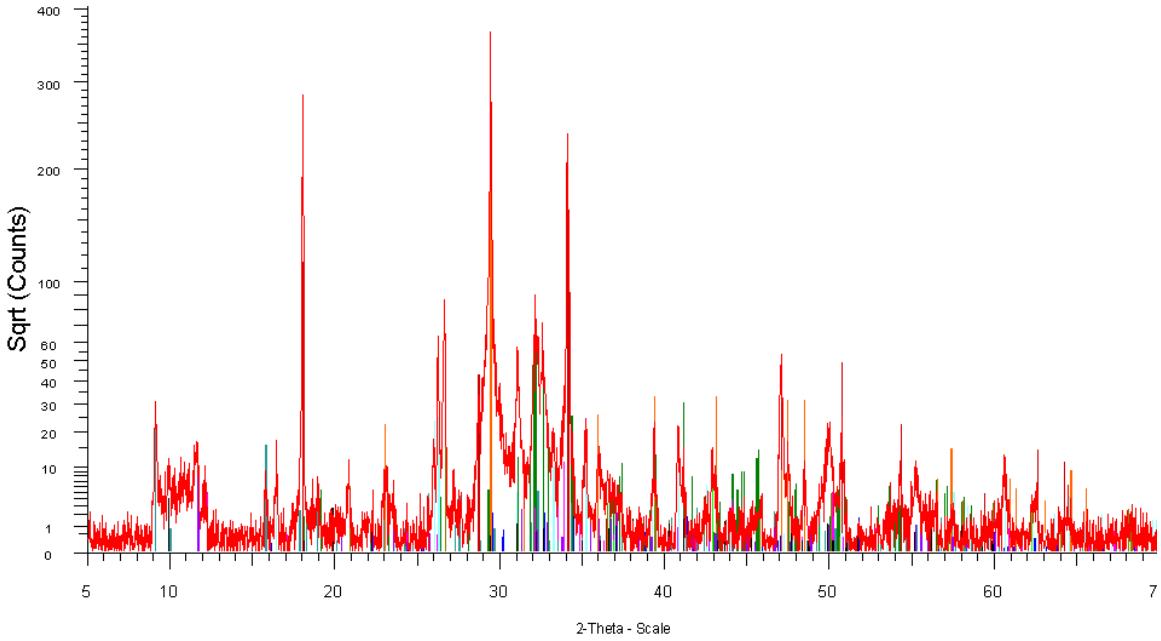

Figure E.11: F25-MK5 180-day Control XRD Pattern

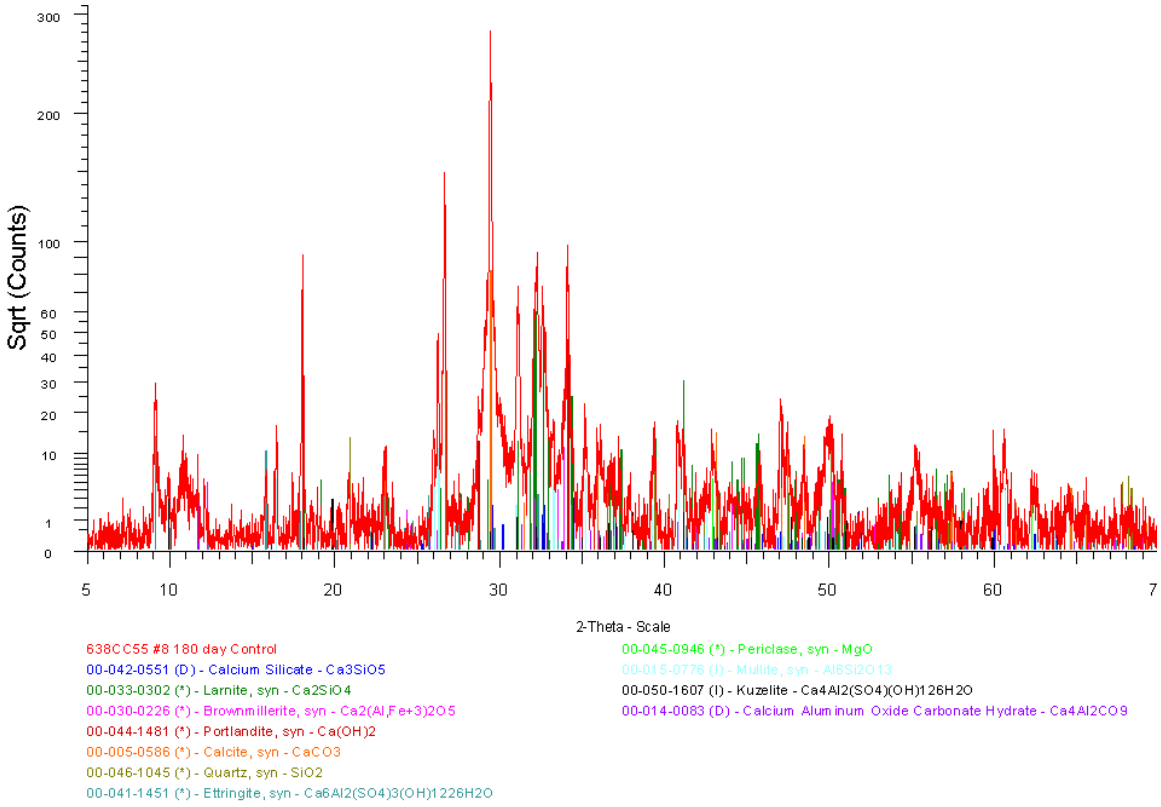

Figure E.12: F25-MK10 180-day Control XRD Pattern

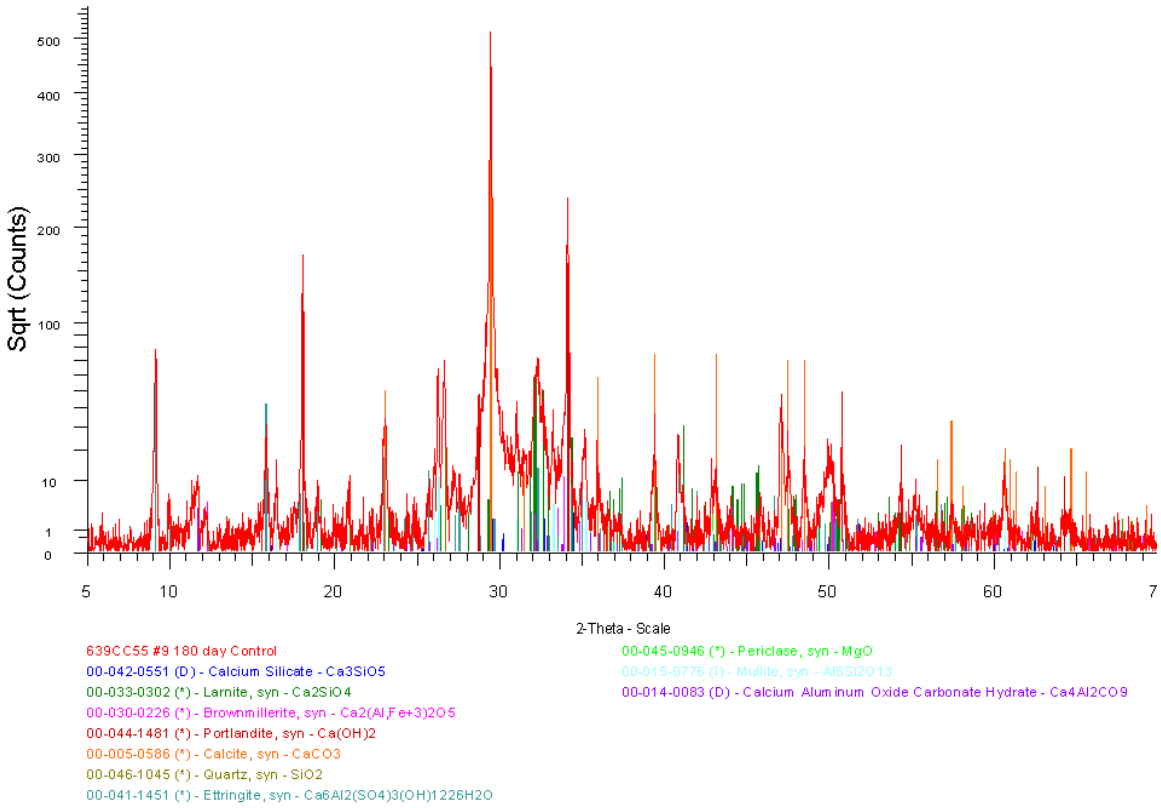

Figure E.13: F25-SF5 180-day Control XRD Pattern

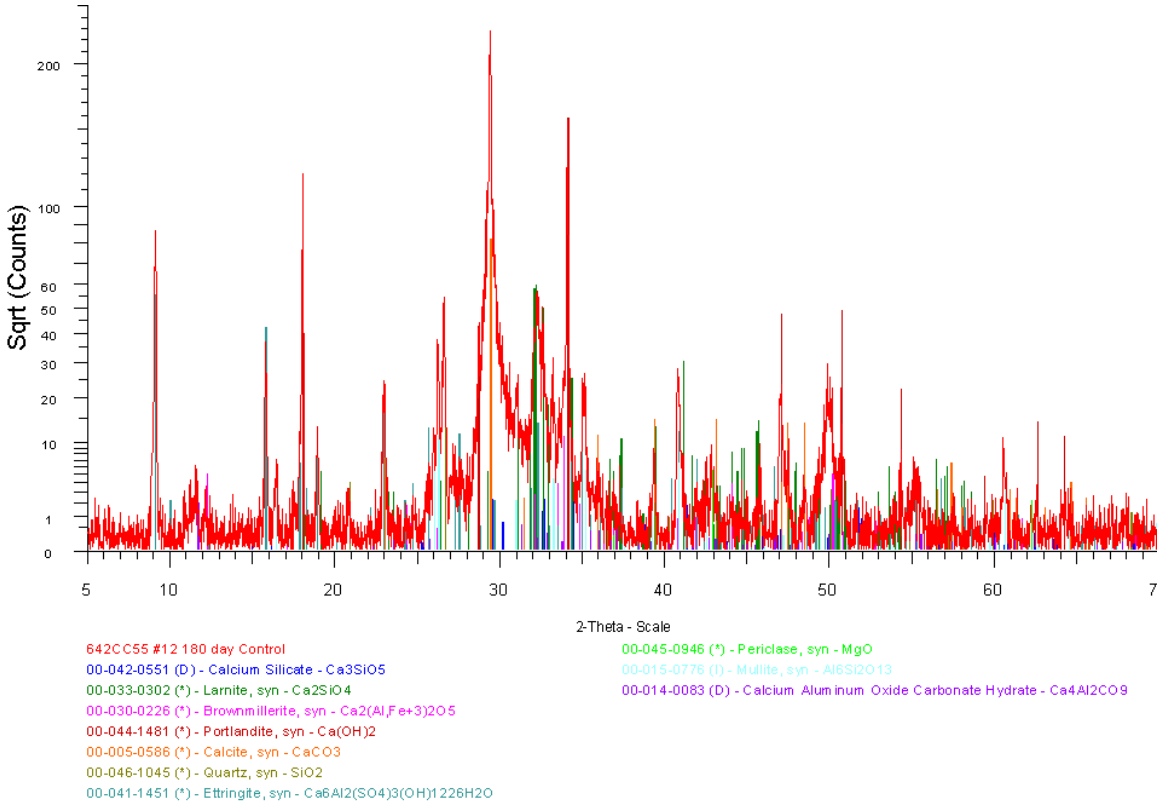

Figure E.14: F25-SF10 180-day Control XRD Pattern

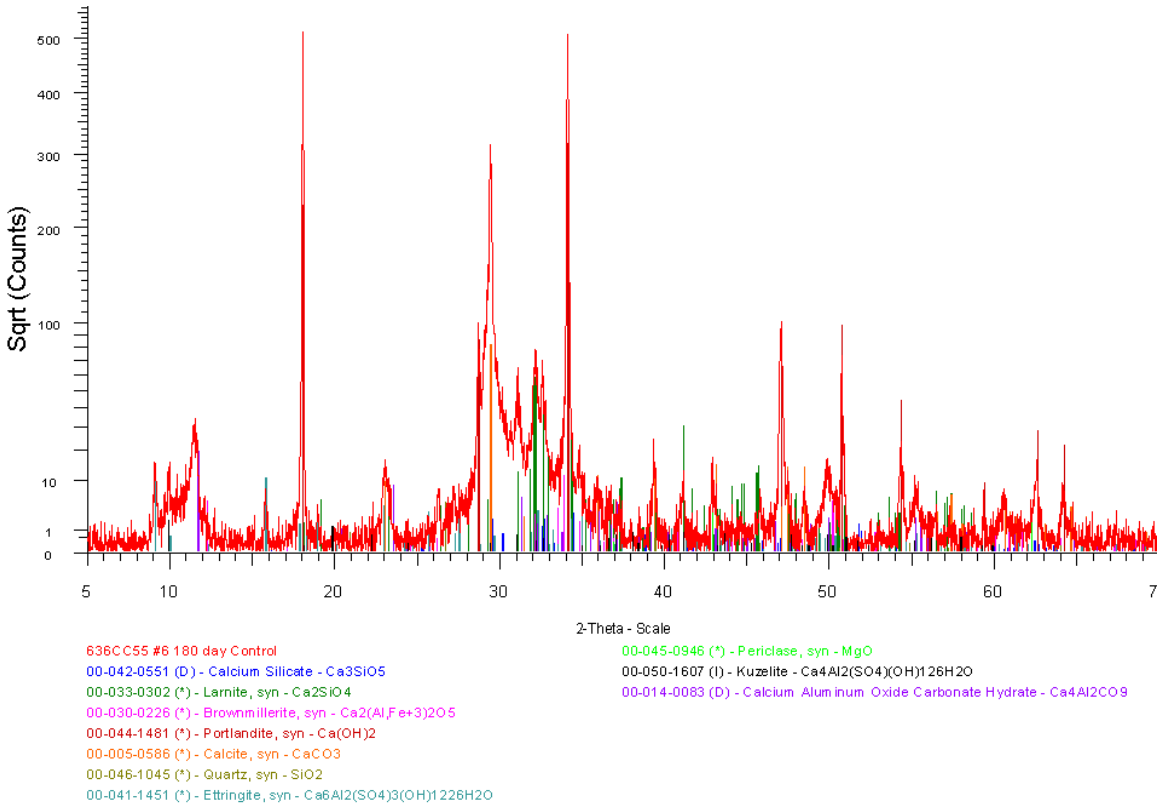

Figure E.15: S35-MK5 180-day Control XRD Pattern

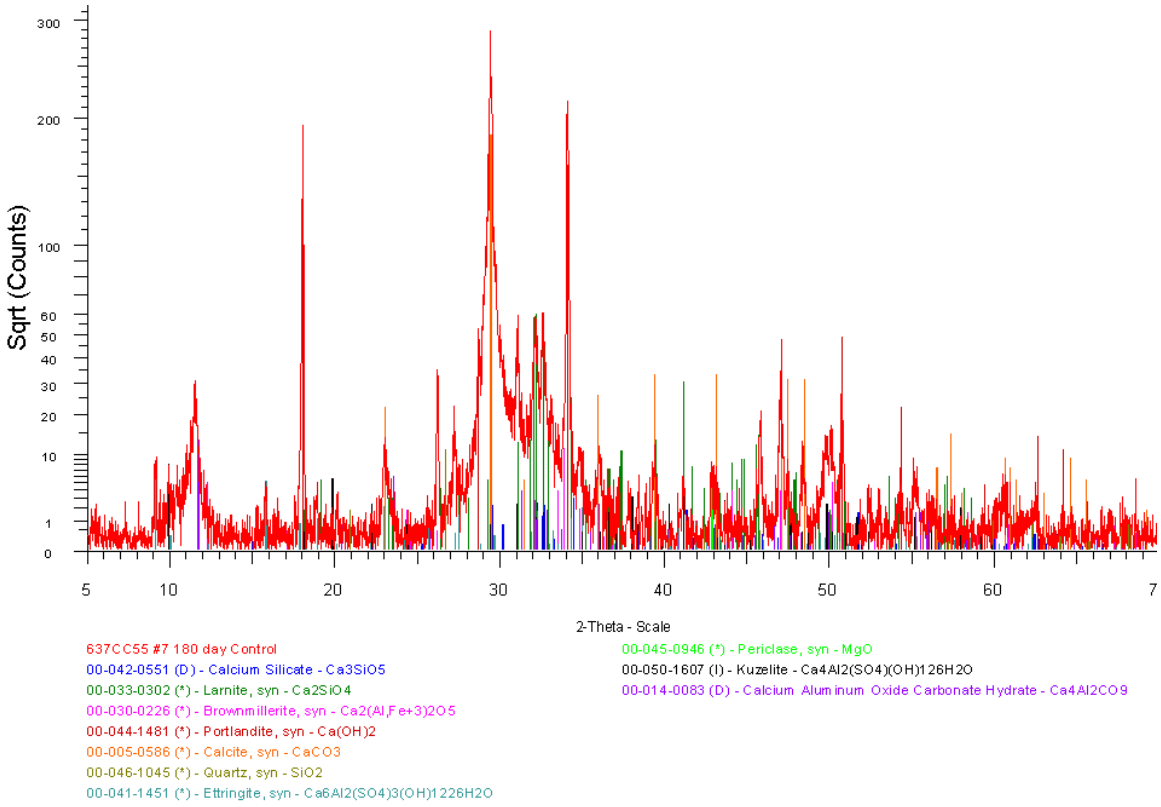

Figure E.16: S50-MK5 180-day Control XRD Pattern

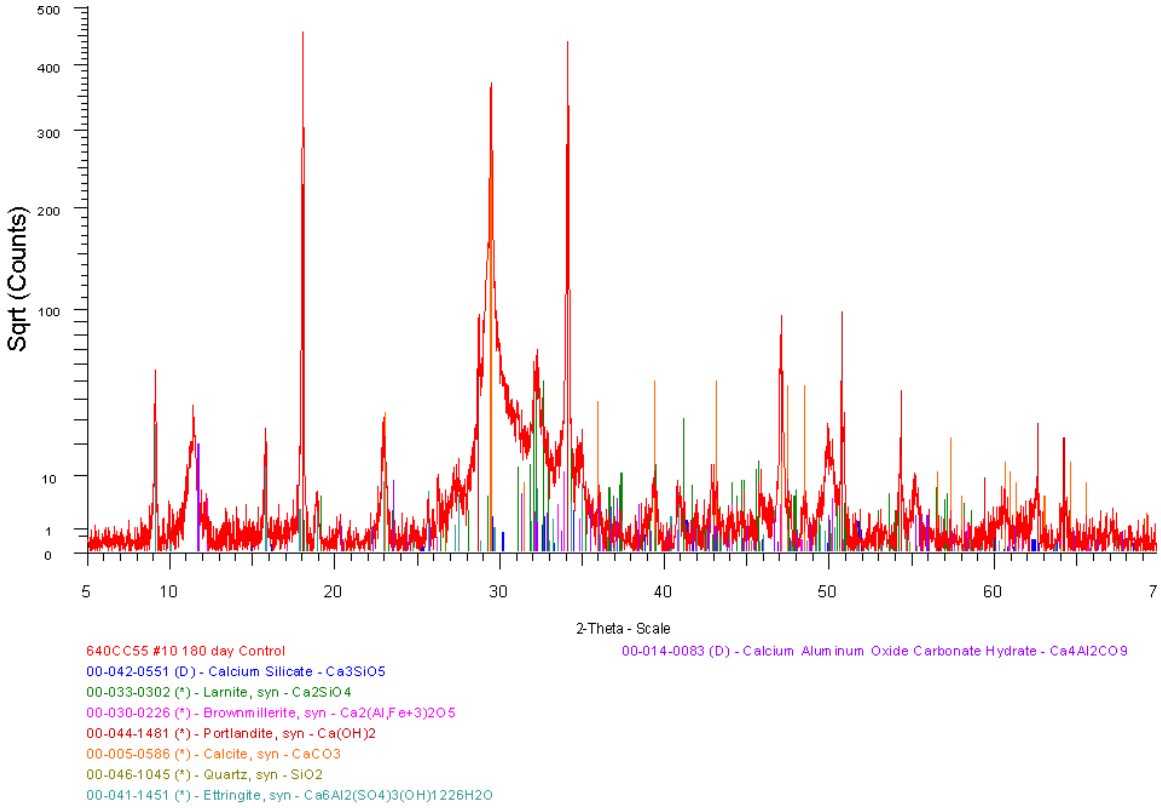

Figure E.17: S35-SF5 180-day Control XRD Pattern

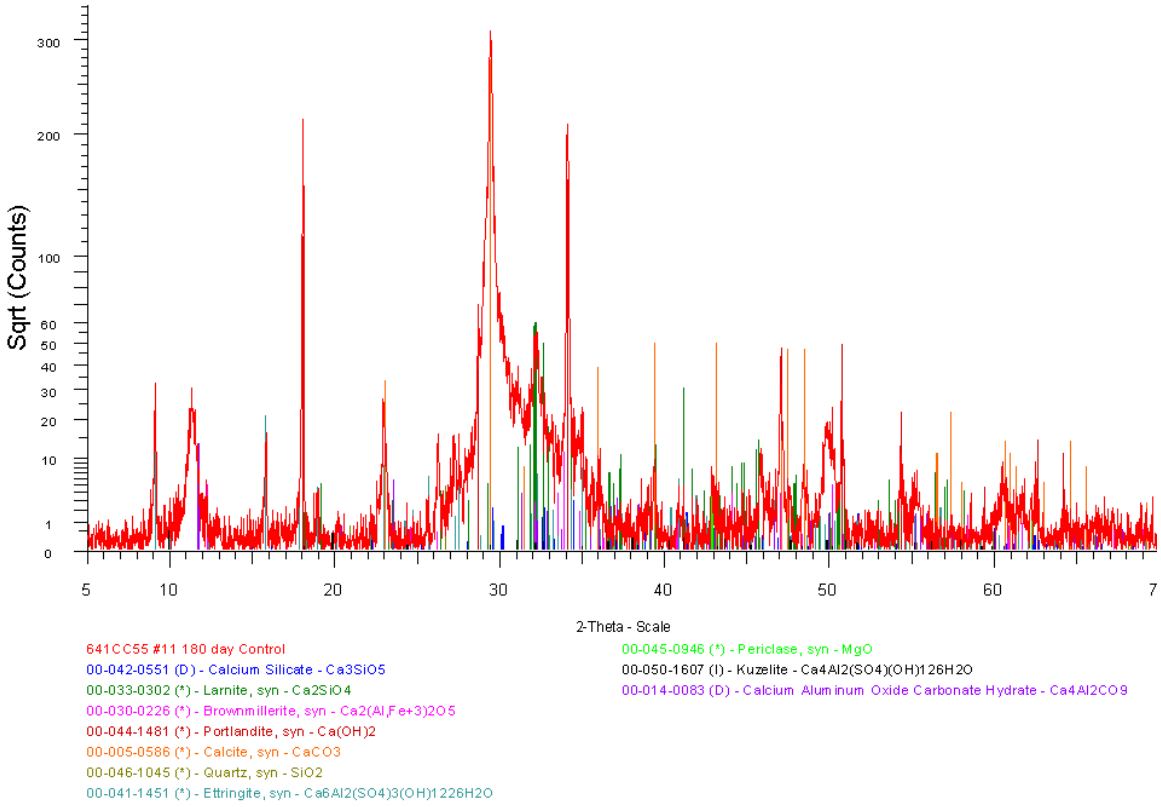

Figure E.18: S50-SF5 180-day Control XRD Pattern

E.3.1.2 90-day Sulfate Exposure Specimens

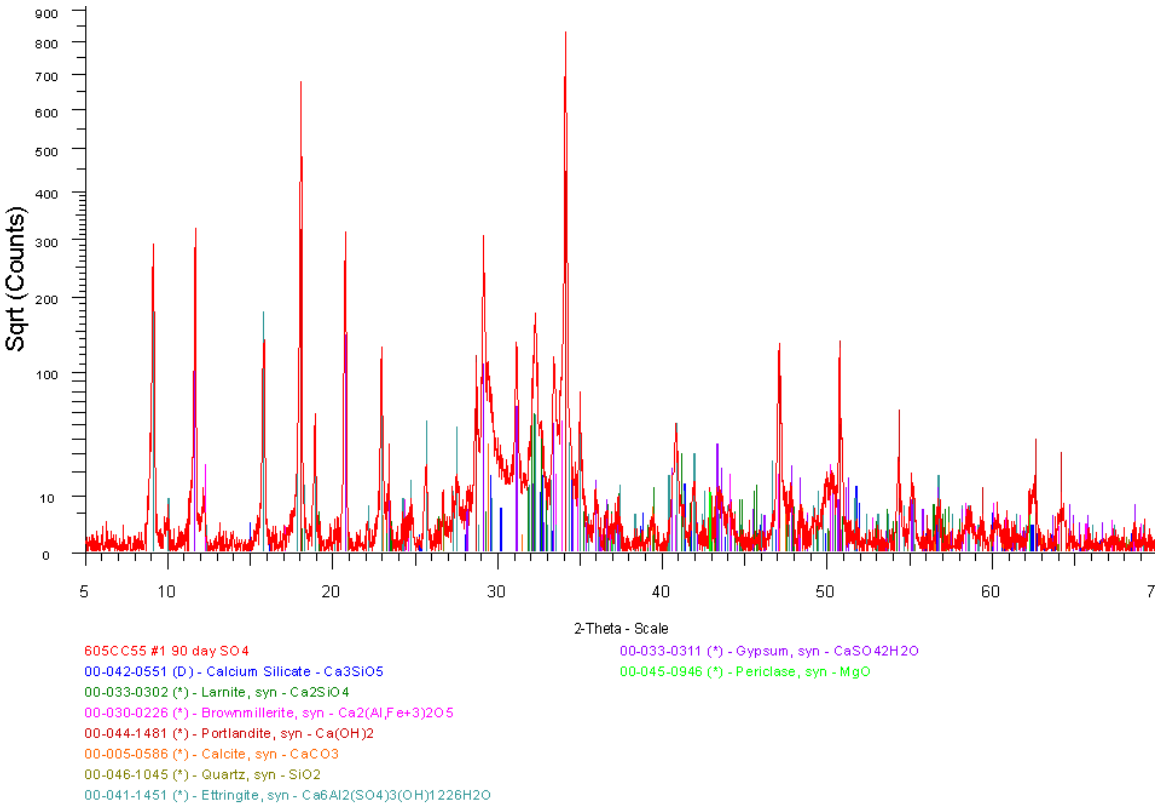

Figure E.19: T2 90-day Sulfate Exposure XRD Pattern

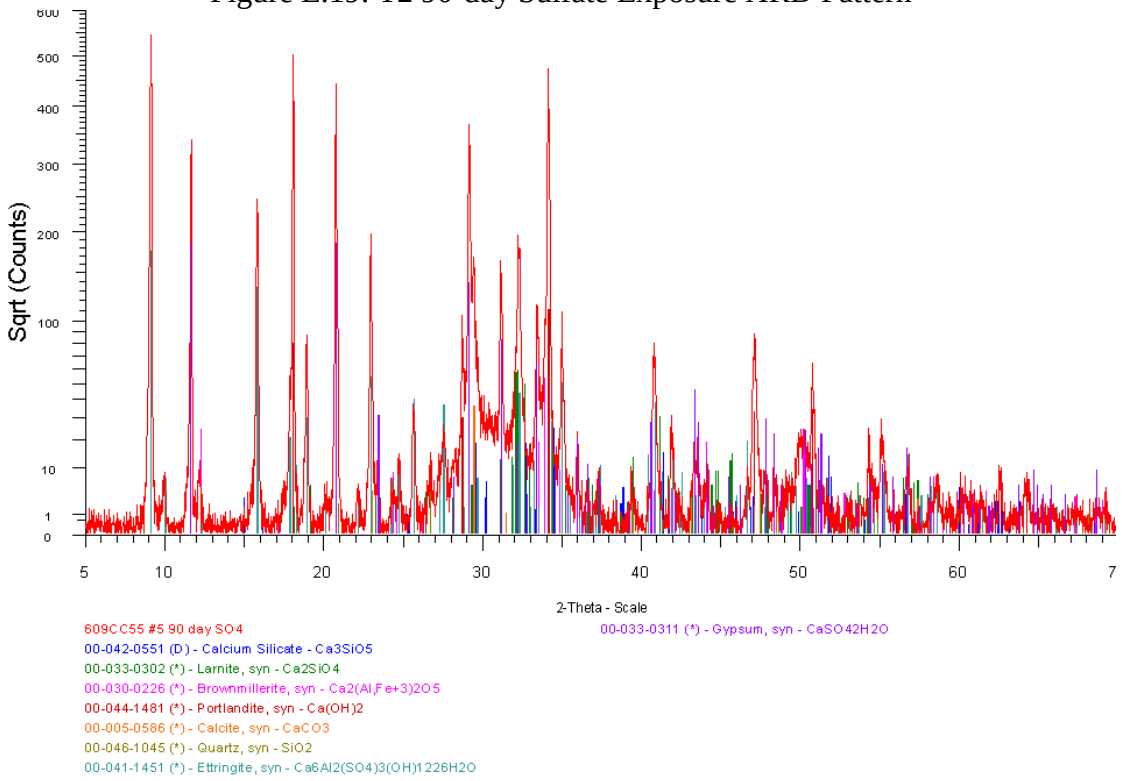

Figure E.20: T3 90-day Sulfate Exposure XRD Pattern

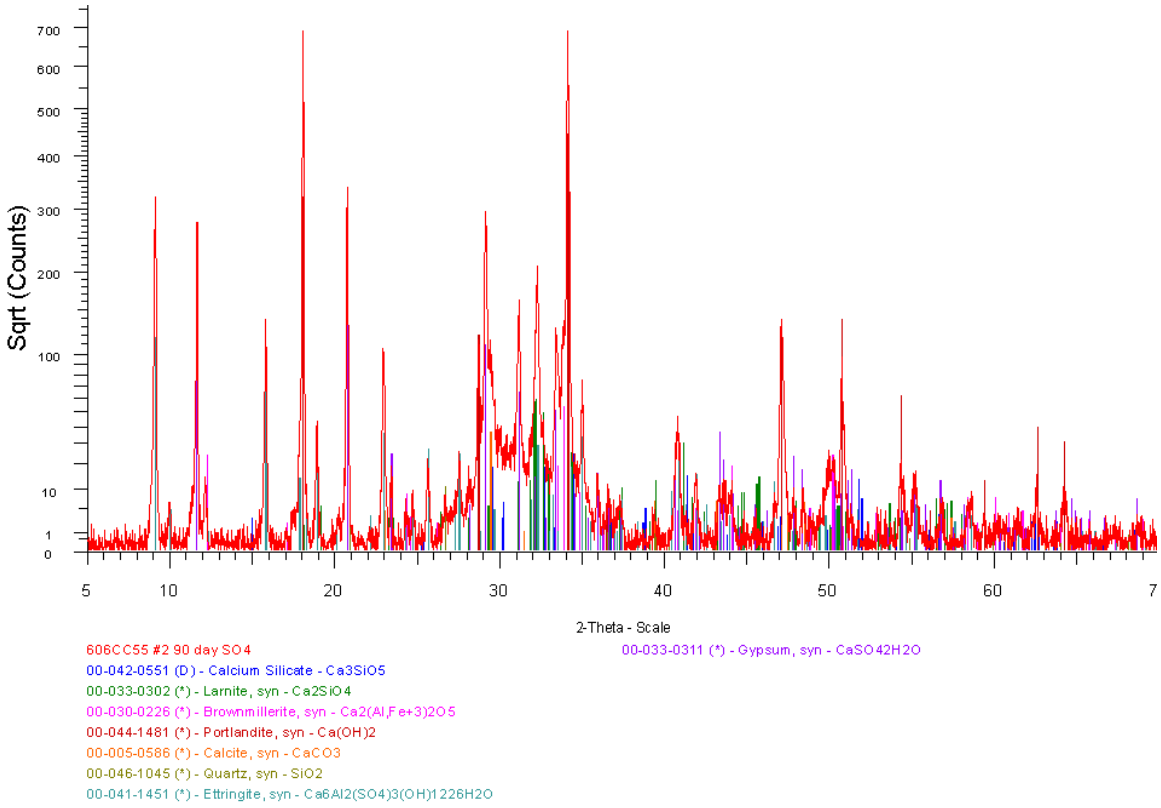

Figure E.21: T5 90-day Sulfate Exposure XRD Pattern

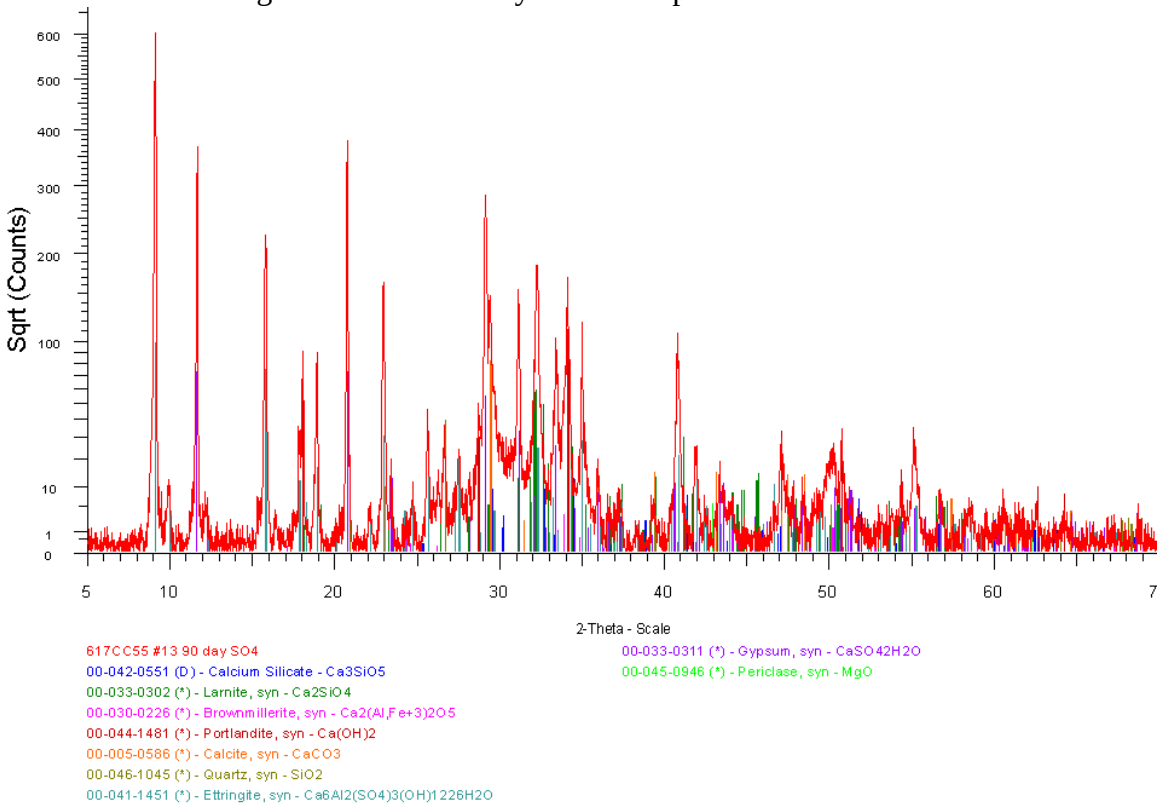

Figure E.22: T3-F15 90-day Sulfate Exposure XRD Pattern

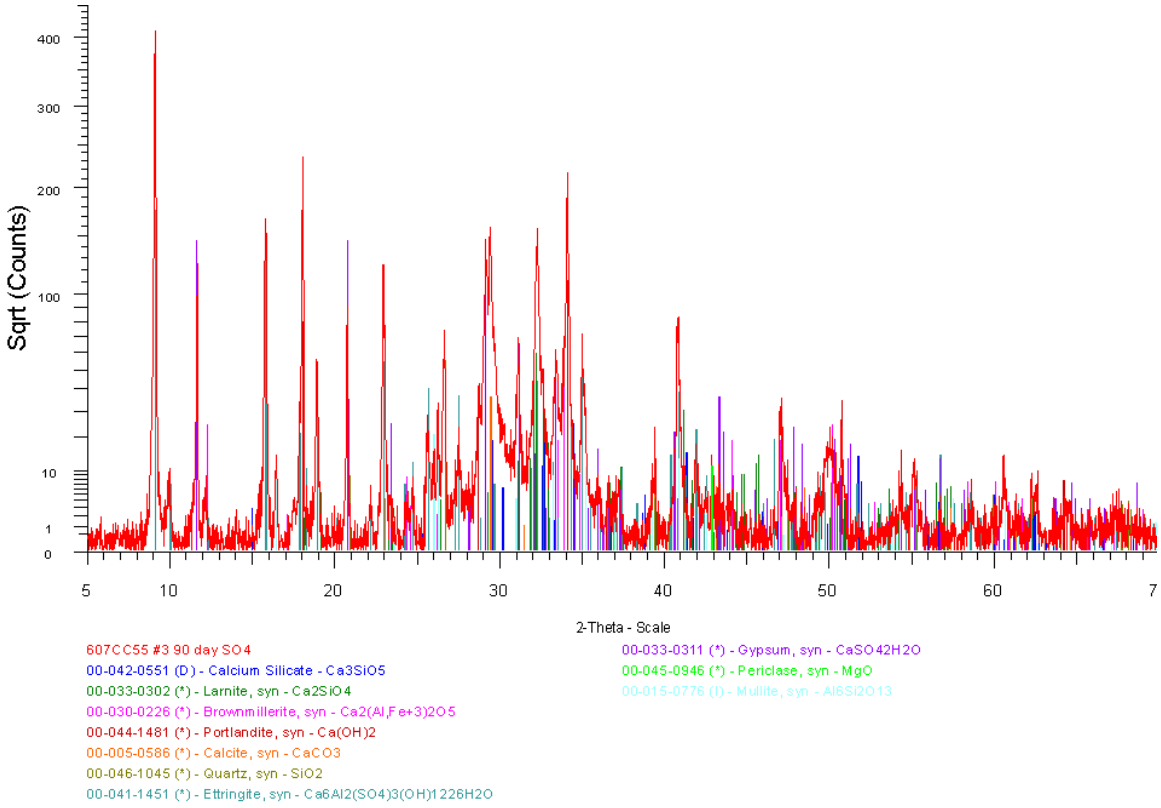

Figure E.23: F25 90-day Sulfate Exposure XRD Pattern

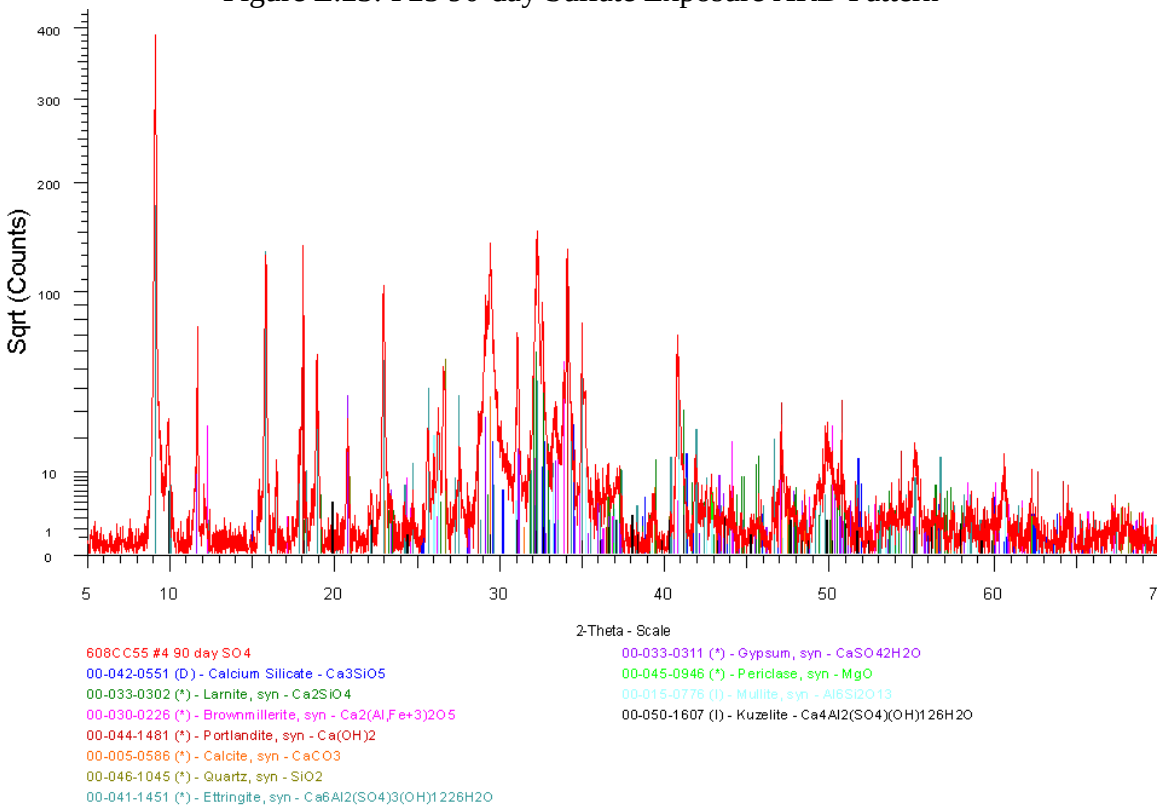

Figure E.24: F25-MK5 90-day Sulfate Exposure XRD Pattern

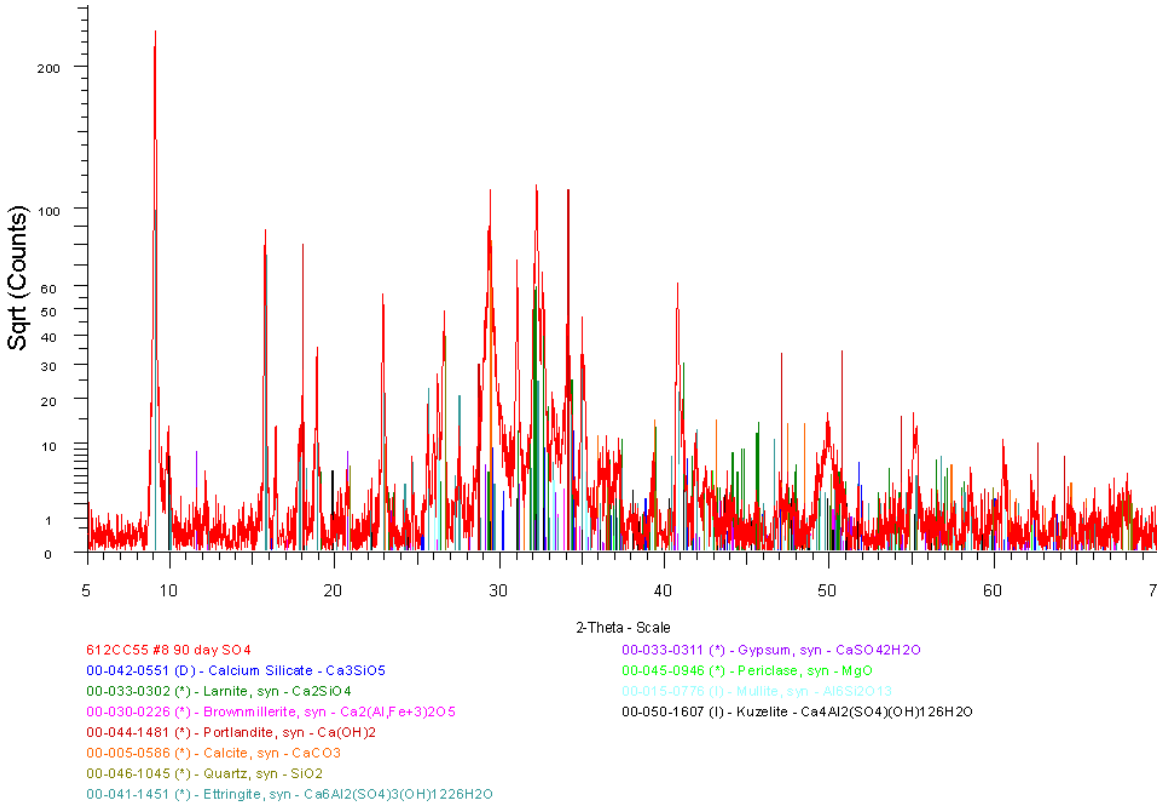

Figure E.25: F25-MK10 90-day Sulfate Exposure XRD Pattern

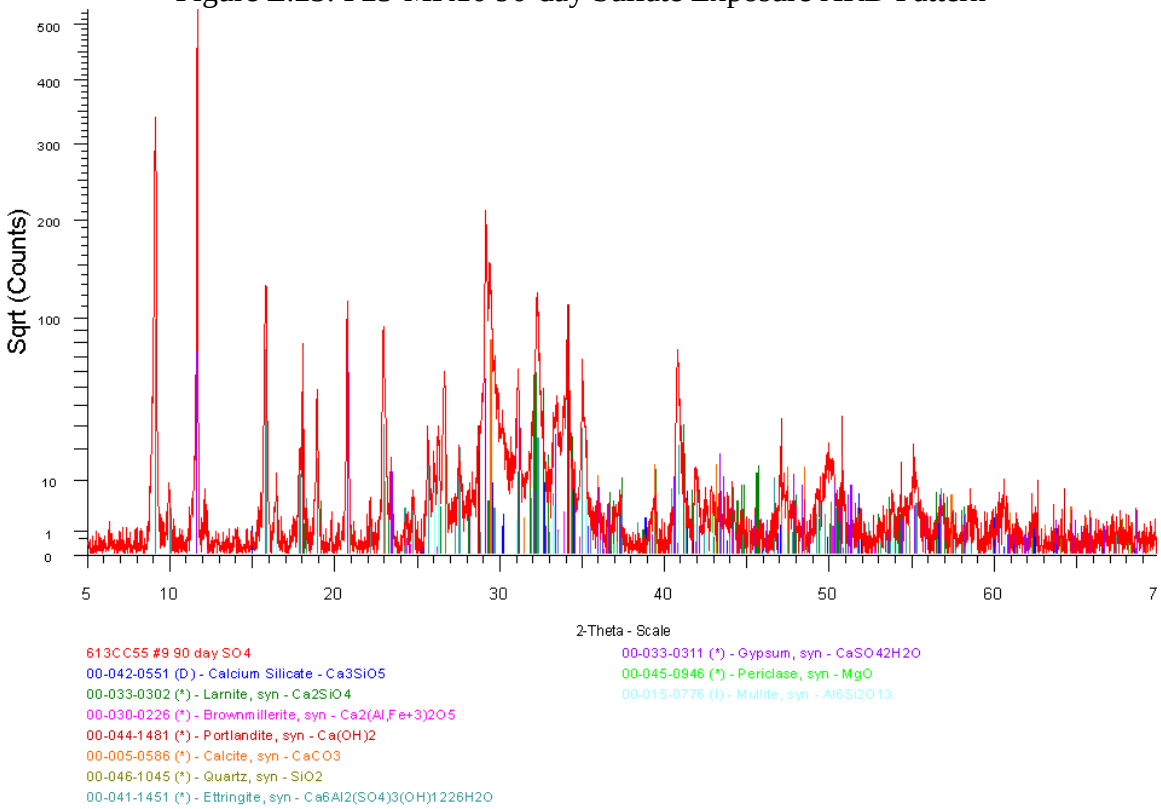

Figure E.26: F25-SF5 90-day Sulfate Exposure XRD Pattern

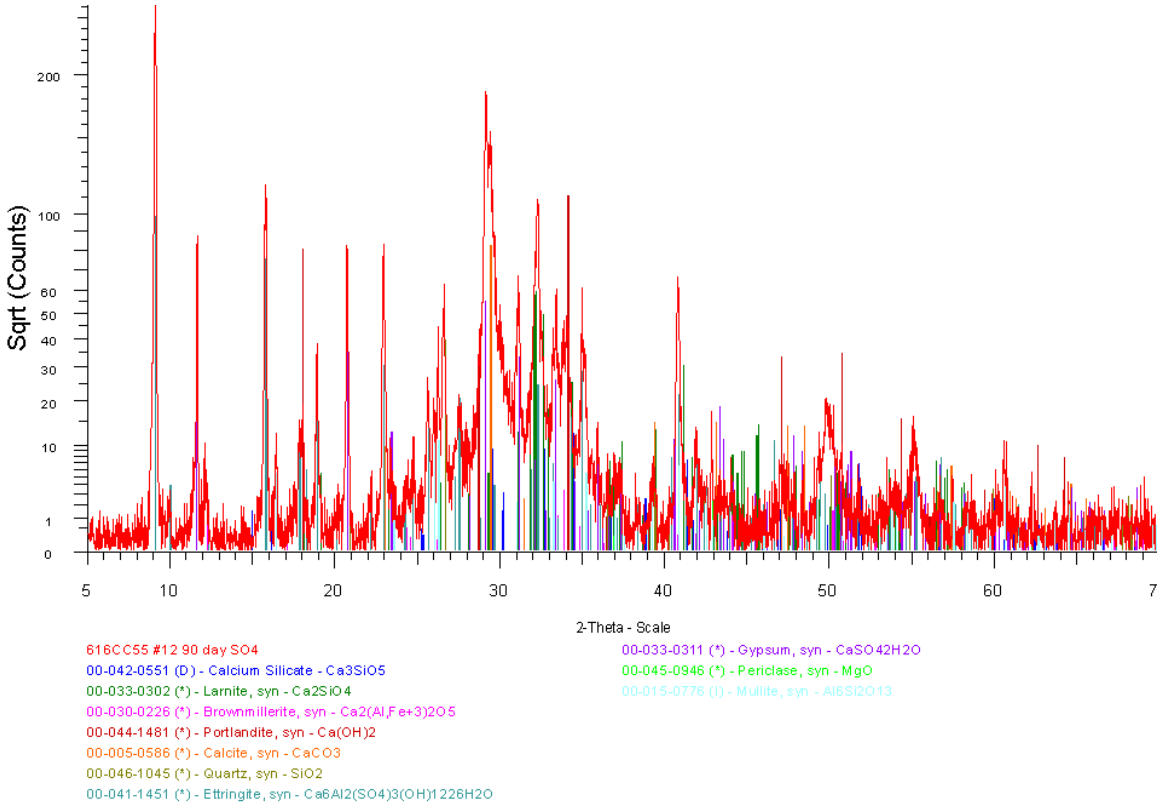

Figure E.27: F25-SF10 90-day Sulfate Exposure XRD Pattern

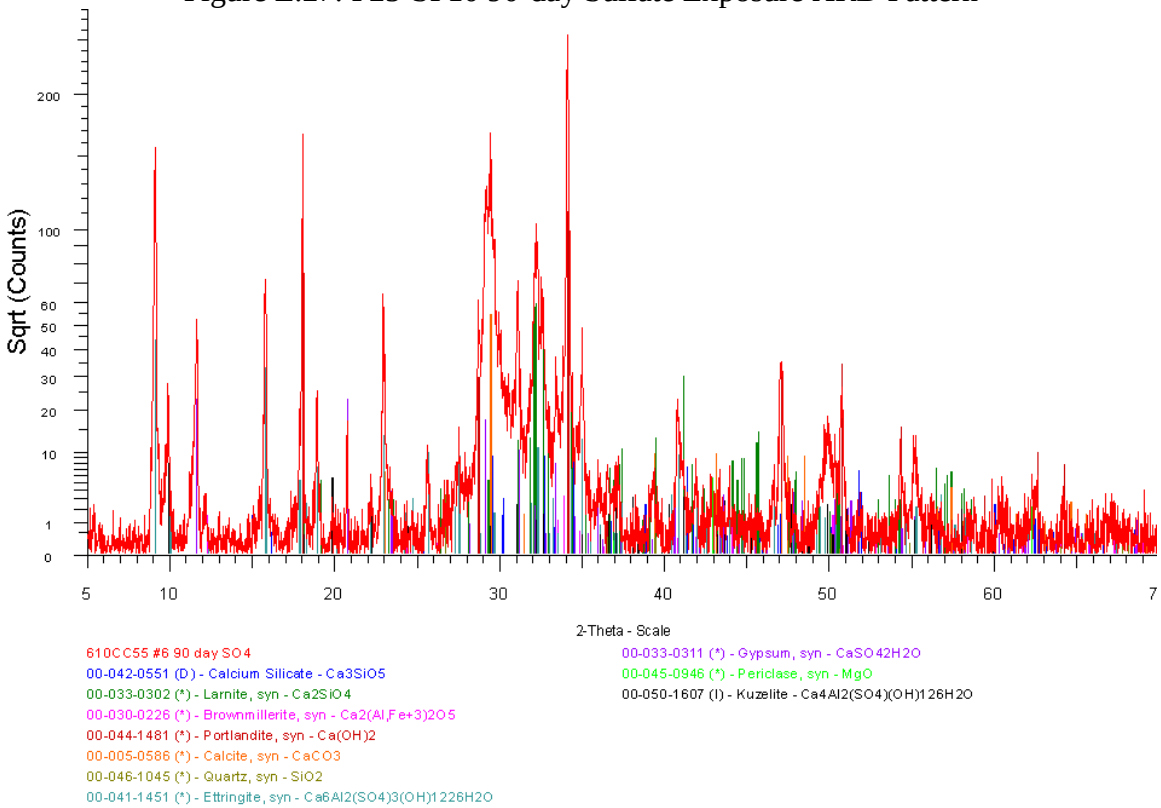

Figure E.28: S35-MK5 90-day Sulfate Exposure XRD Pattern

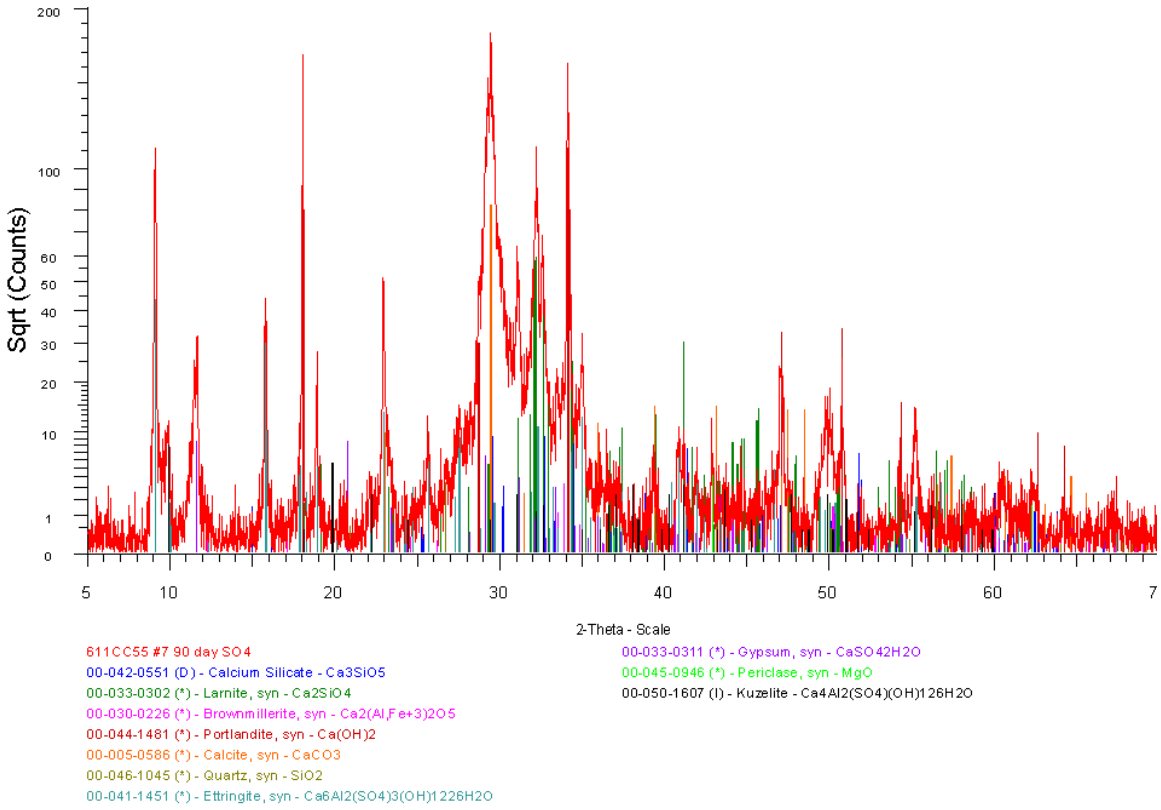

Figure E.29: S50-MK5 90-day Sulfate Exposure XRD Pattern

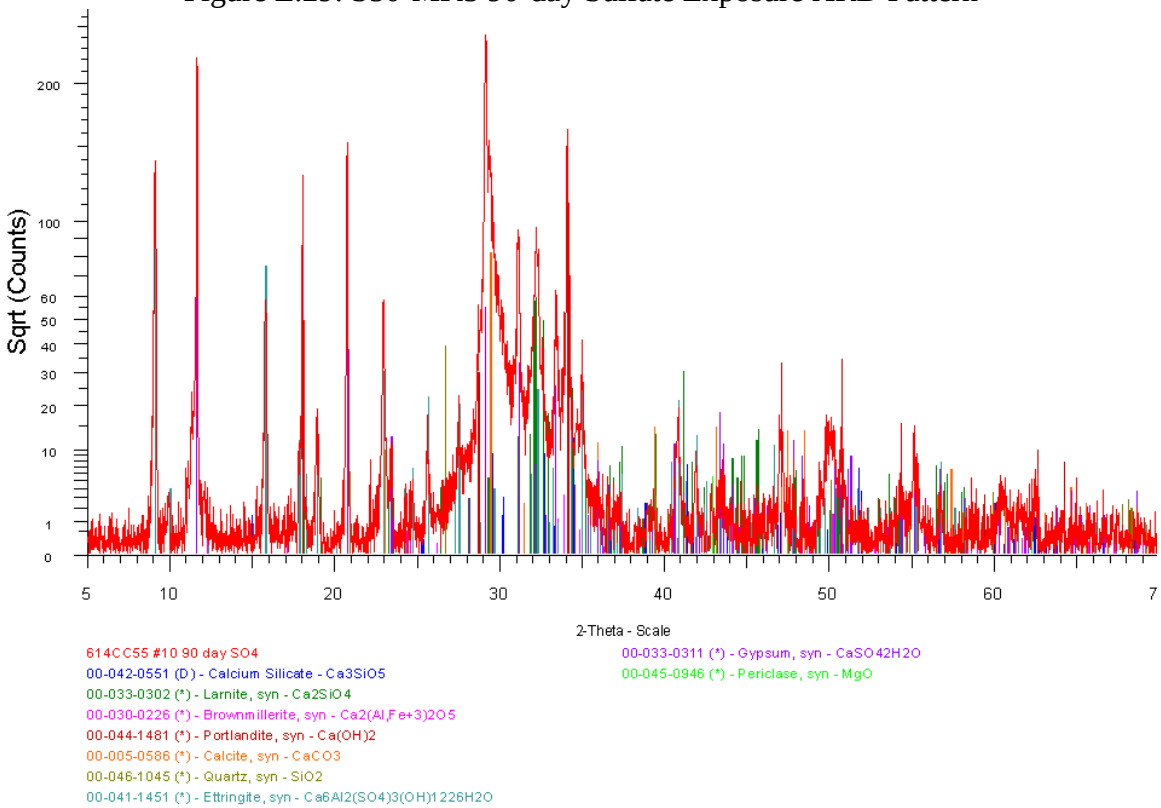

Figure E.30: S35-SF5 90-day Sulfate Exposure XRD Pattern

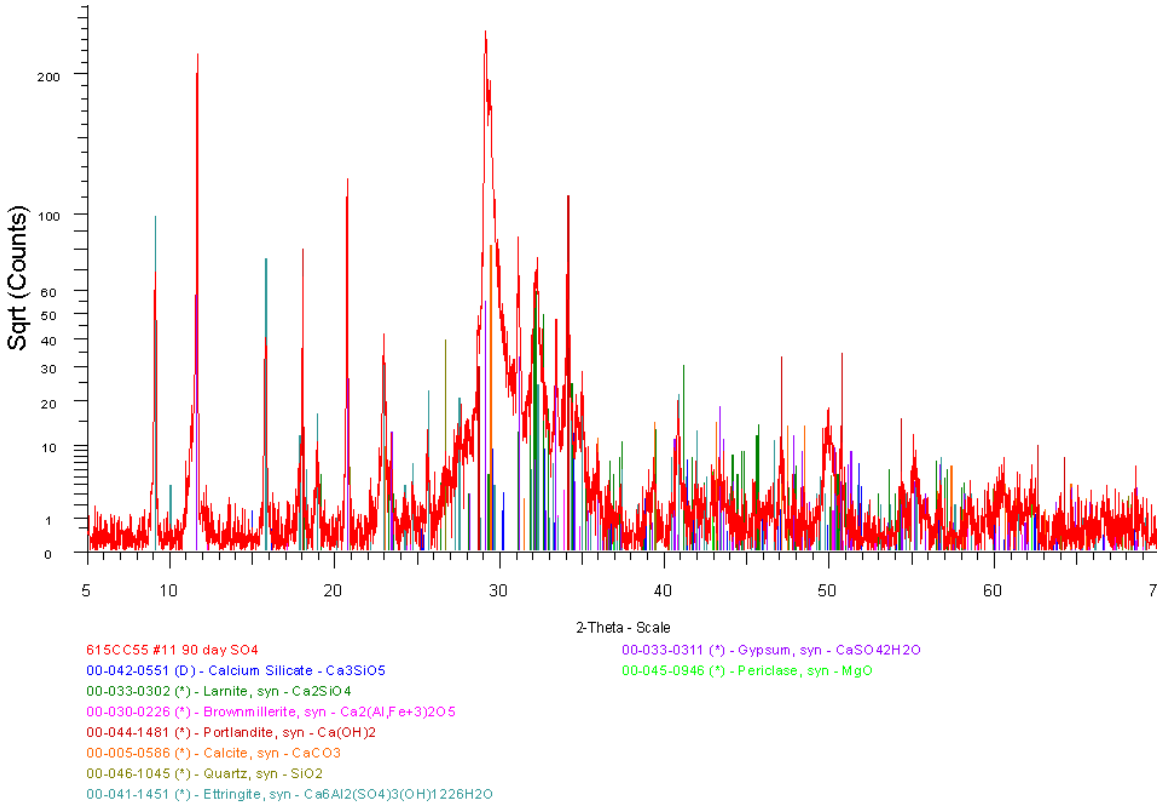

Figure E.31: S50-SF5 90-day Sulfate Exposure XRD Pattern

E.3.1.3 180-day Sulfate Exposure Specimens

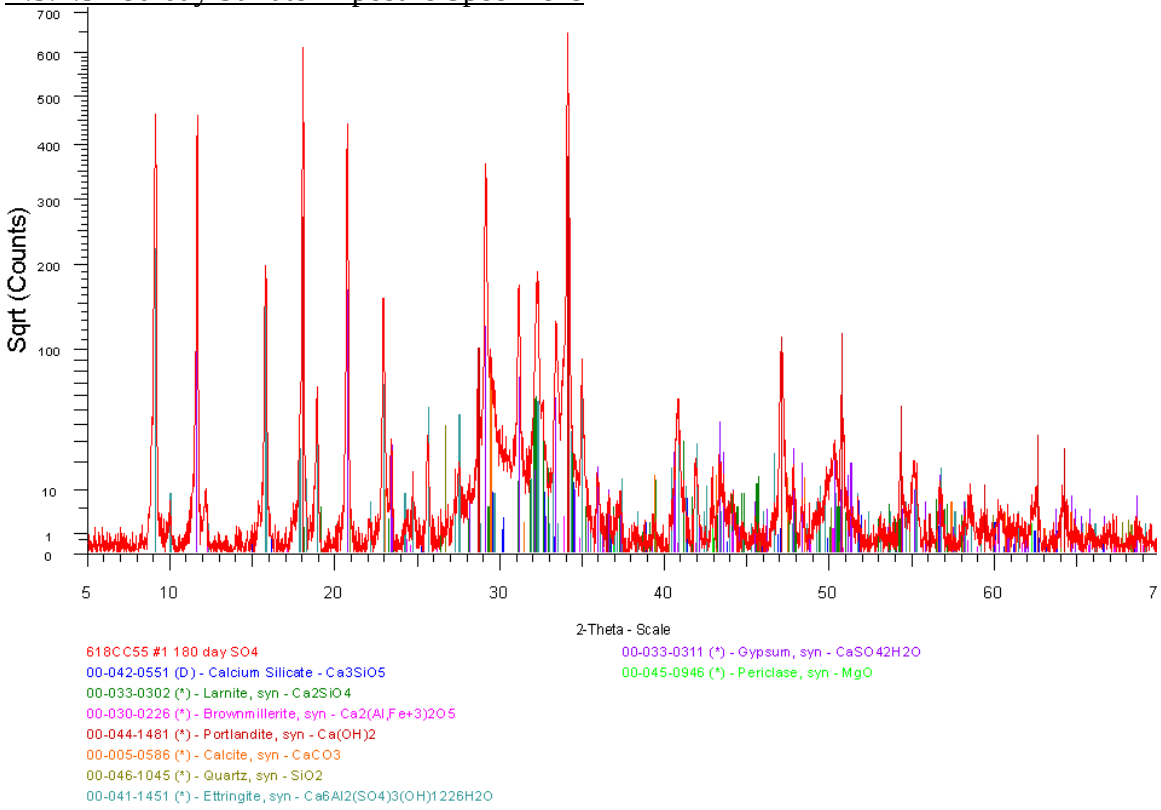

Figure E.32: T2 180-day Sulfate Exposure XRD Pattern

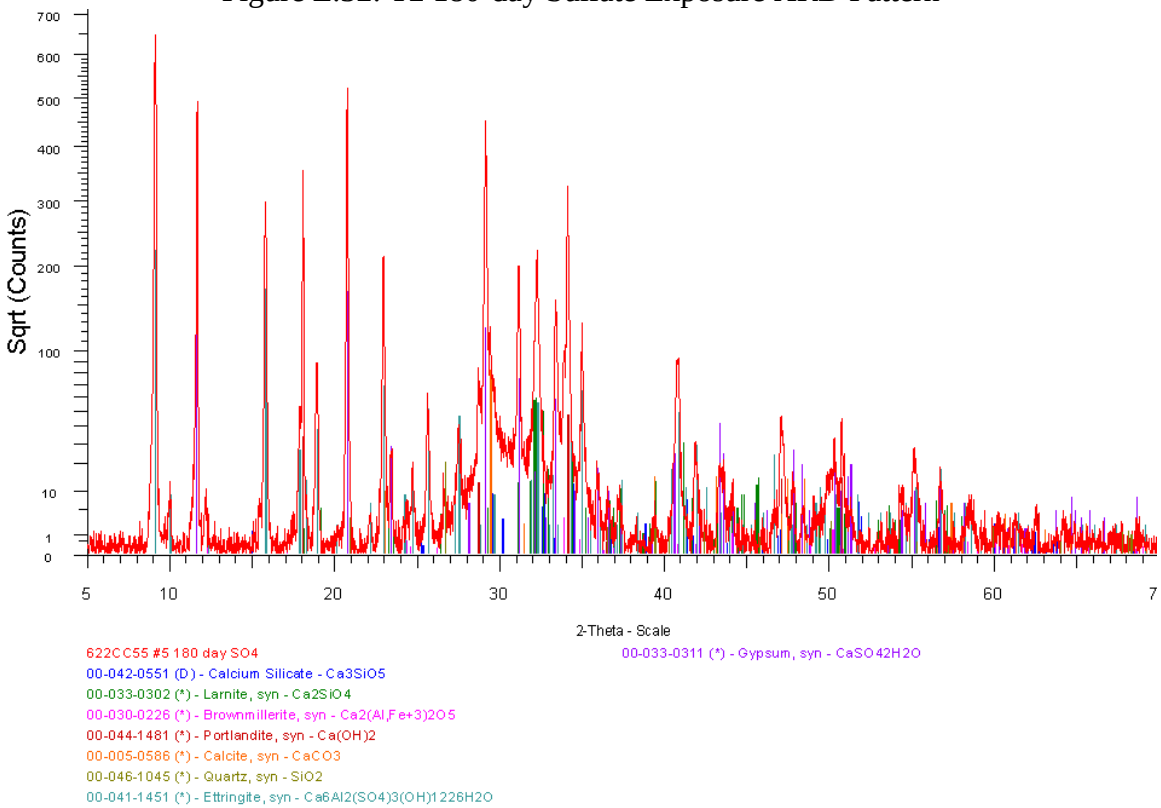

Figure E.33: T3 180-day Sulfate Exposure XRD Pattern

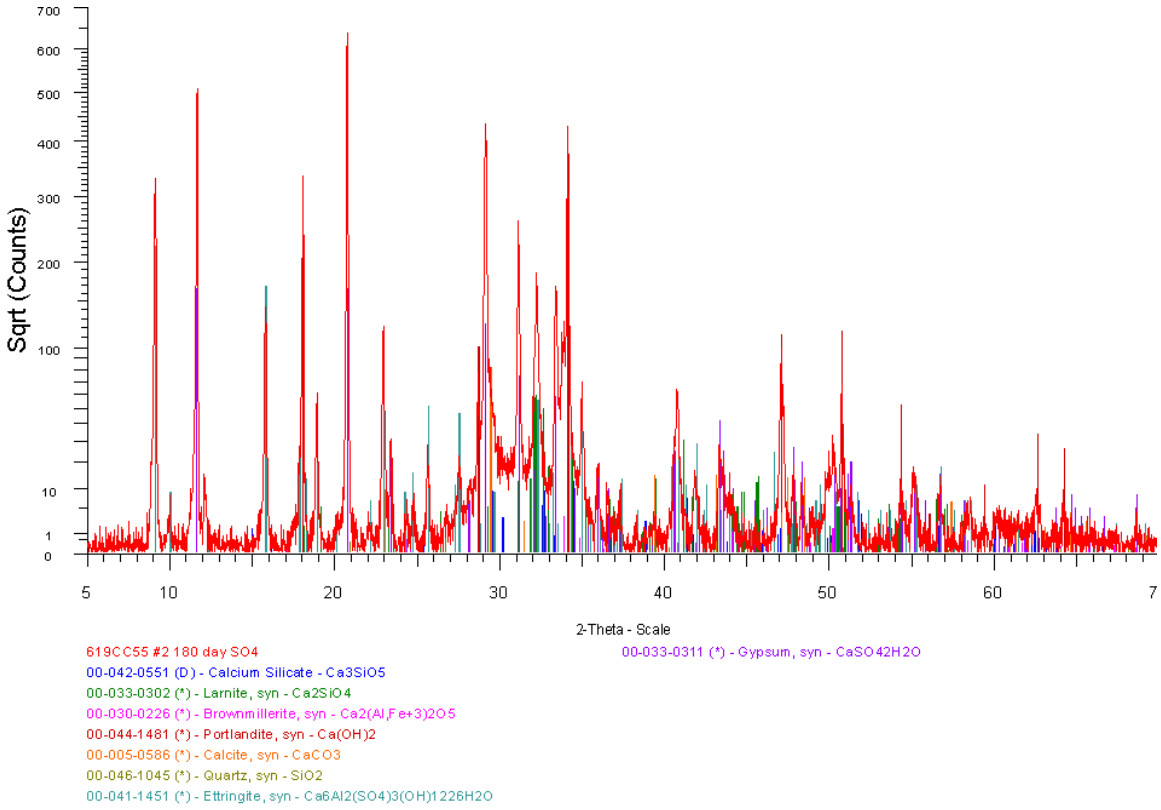

Figure E.34: T5 180-day Sulfate Exposure XRD Pattern

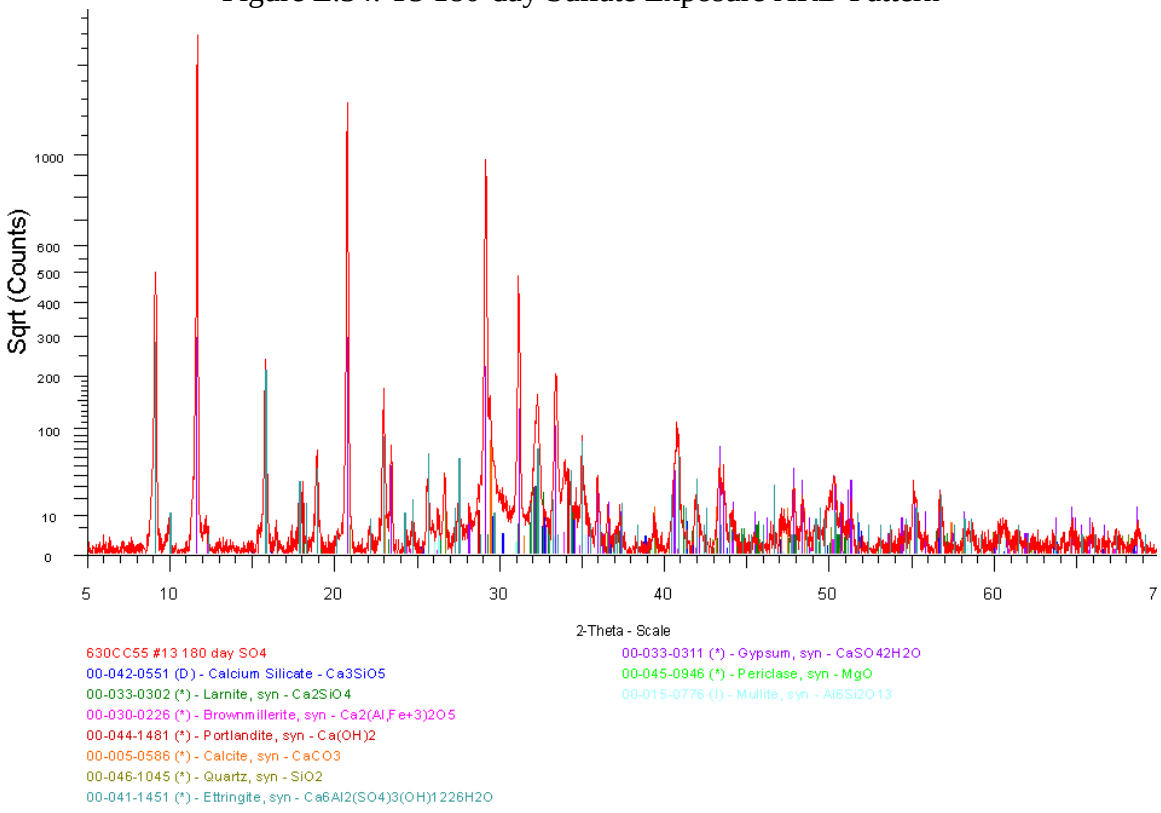

Figure E.35: T3-F15 180-day Sulfate Exposure XRD Pattern

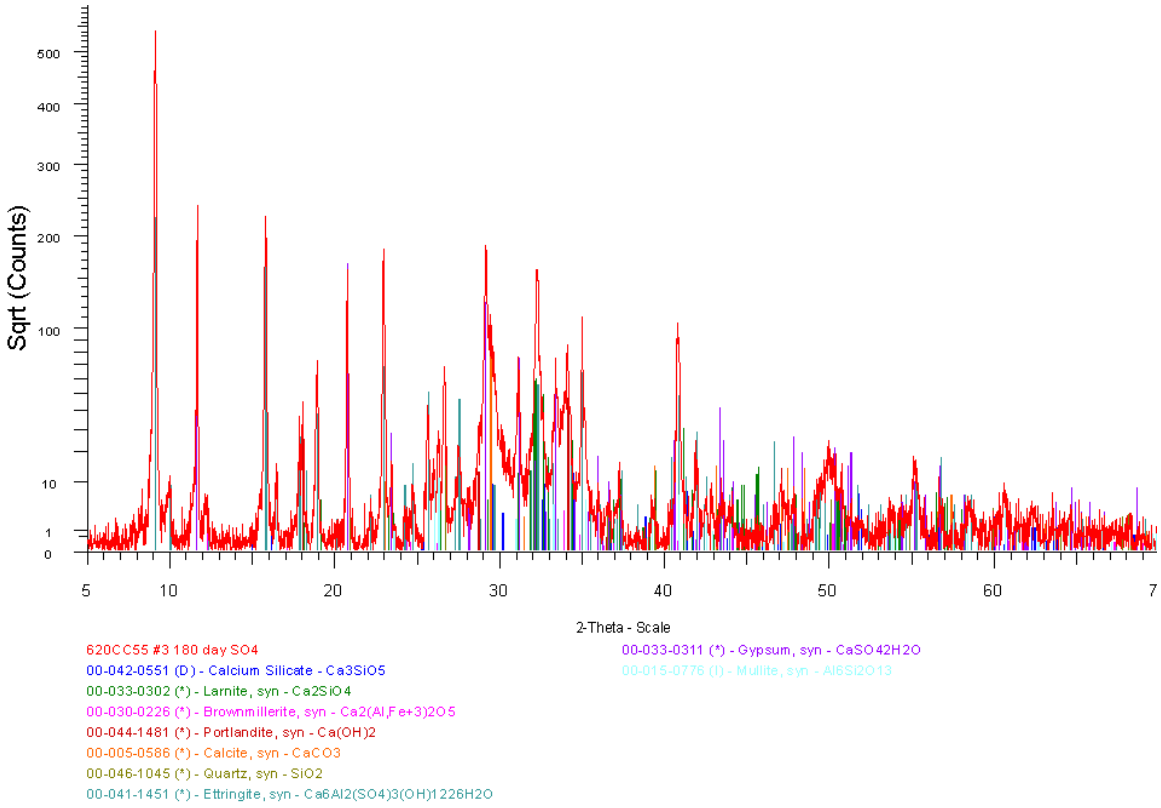

Figure E.36: F25 180-day Sulfate Exposure XRD Pattern

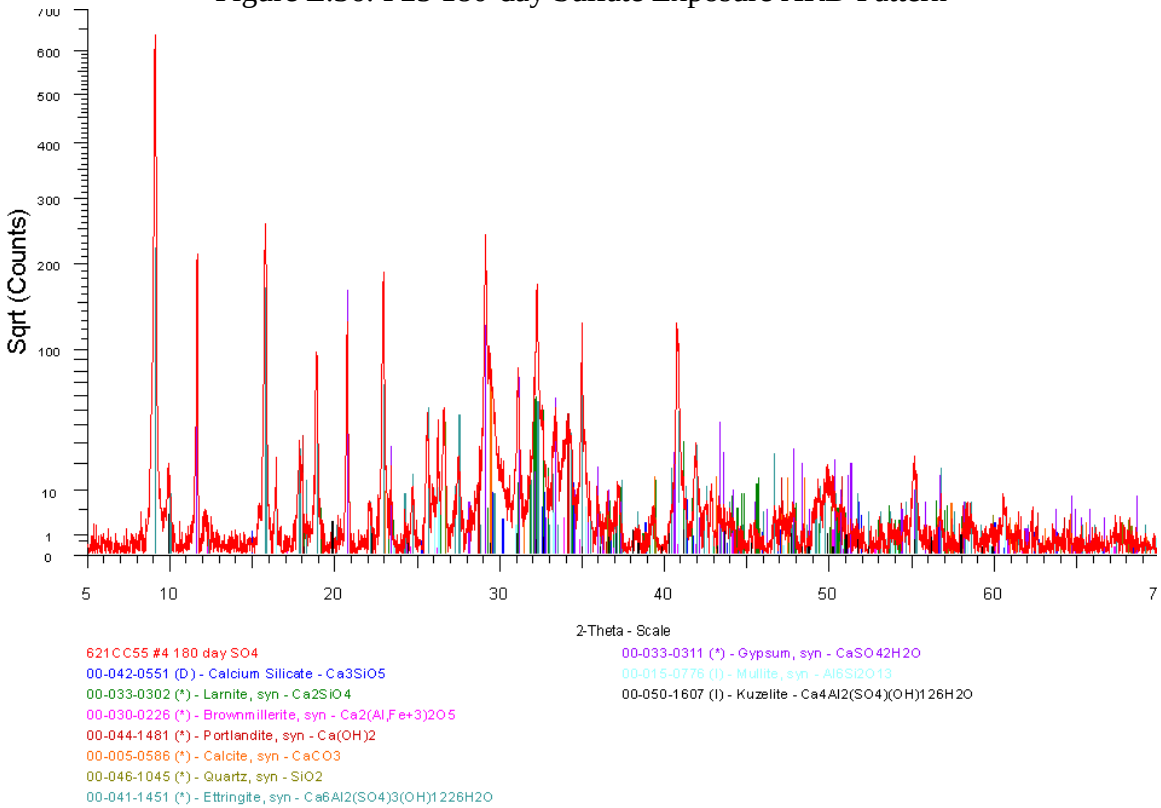

Figure E.37: F25-MK5 180-day Sulfate Exposure XRD Pattern

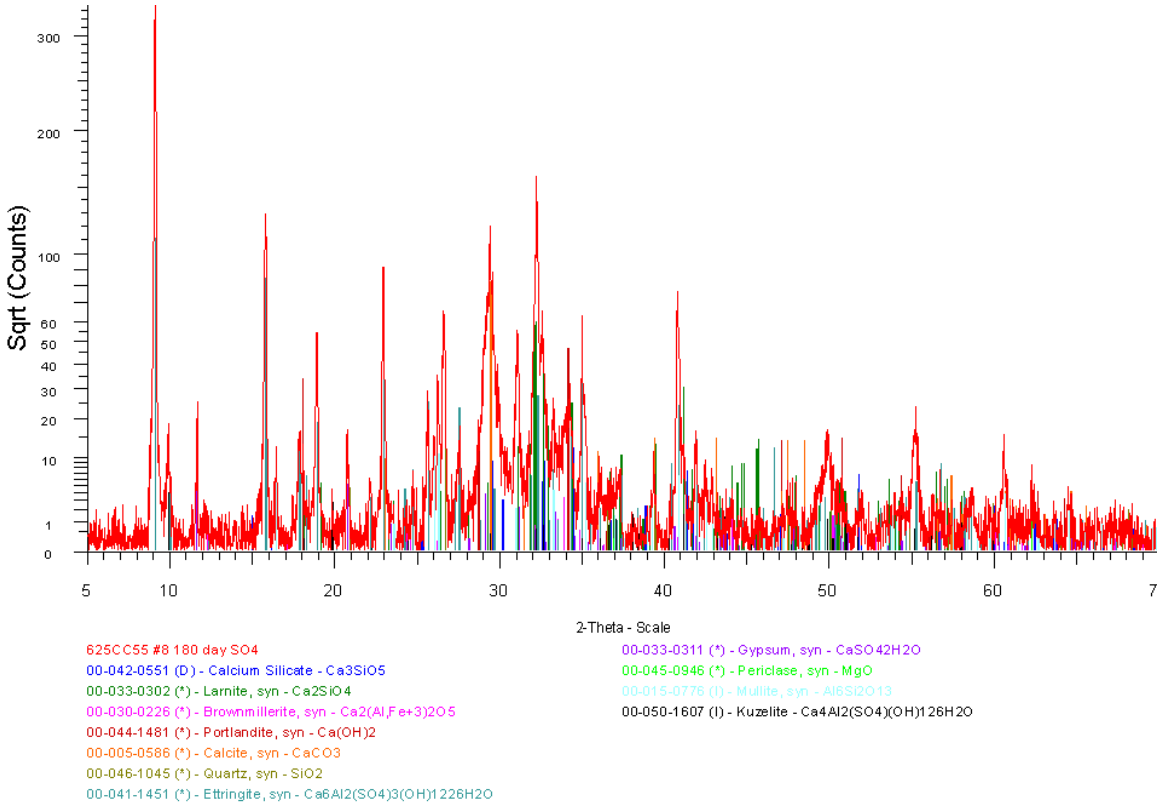

Figure E.38: F25-MK10 180-day Sulfate Exposure XRD Pattern

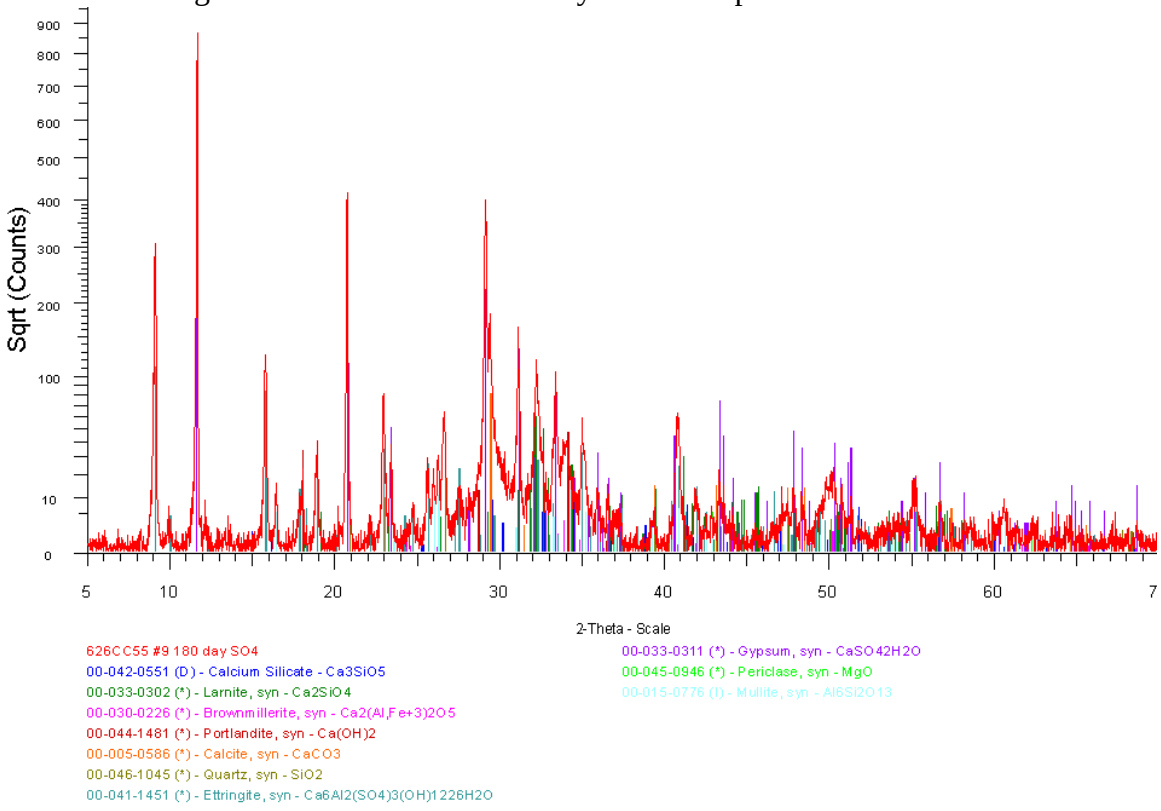

Figure E.39: F25-SF5 180-day Sulfate Exposure XRD Pattern

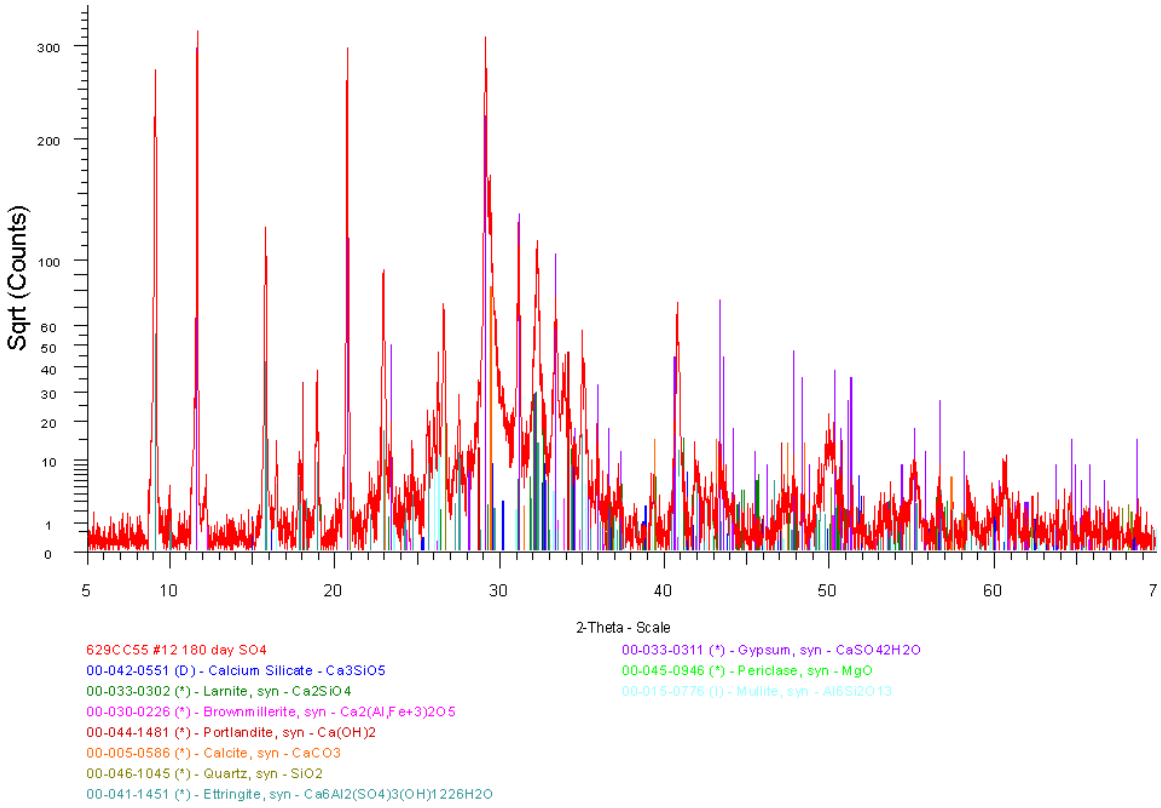

Figure E.40: F25-SF10 180-day Sulfate Exposure XRD Pattern

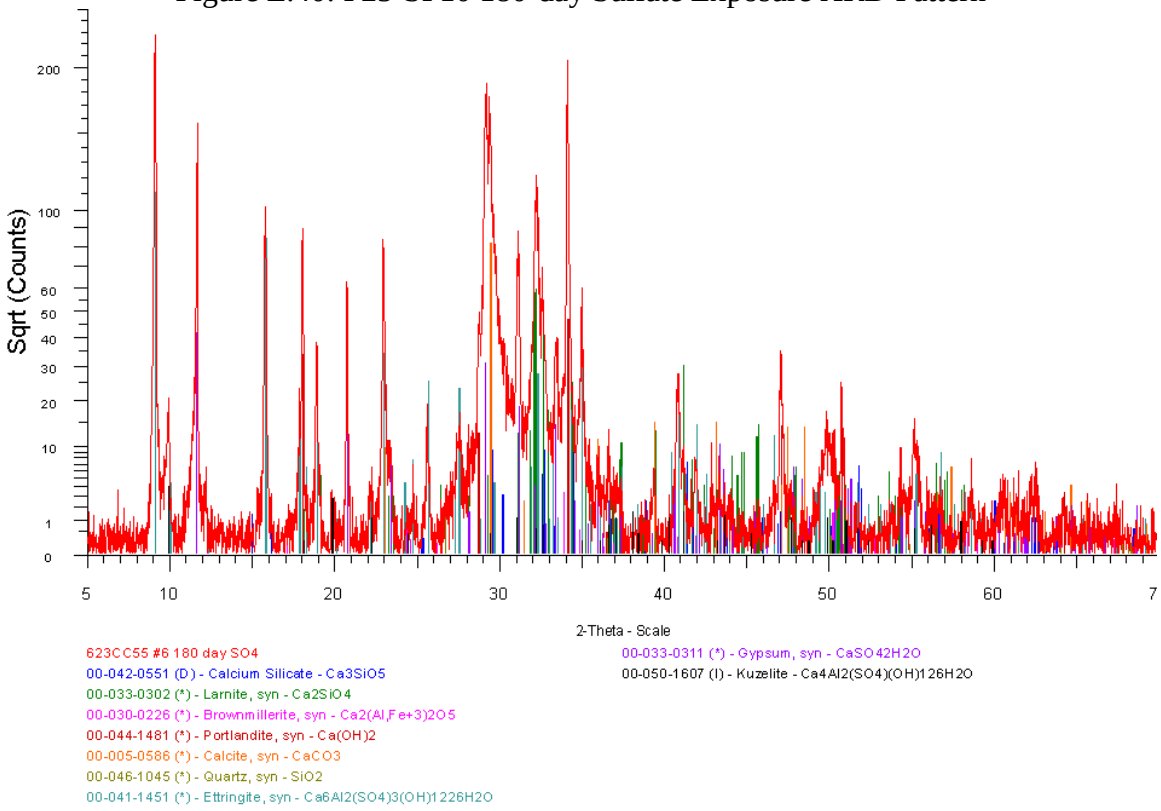

Figure E.41: S35-MK5 180-day Sulfate Exposure XRD Pattern

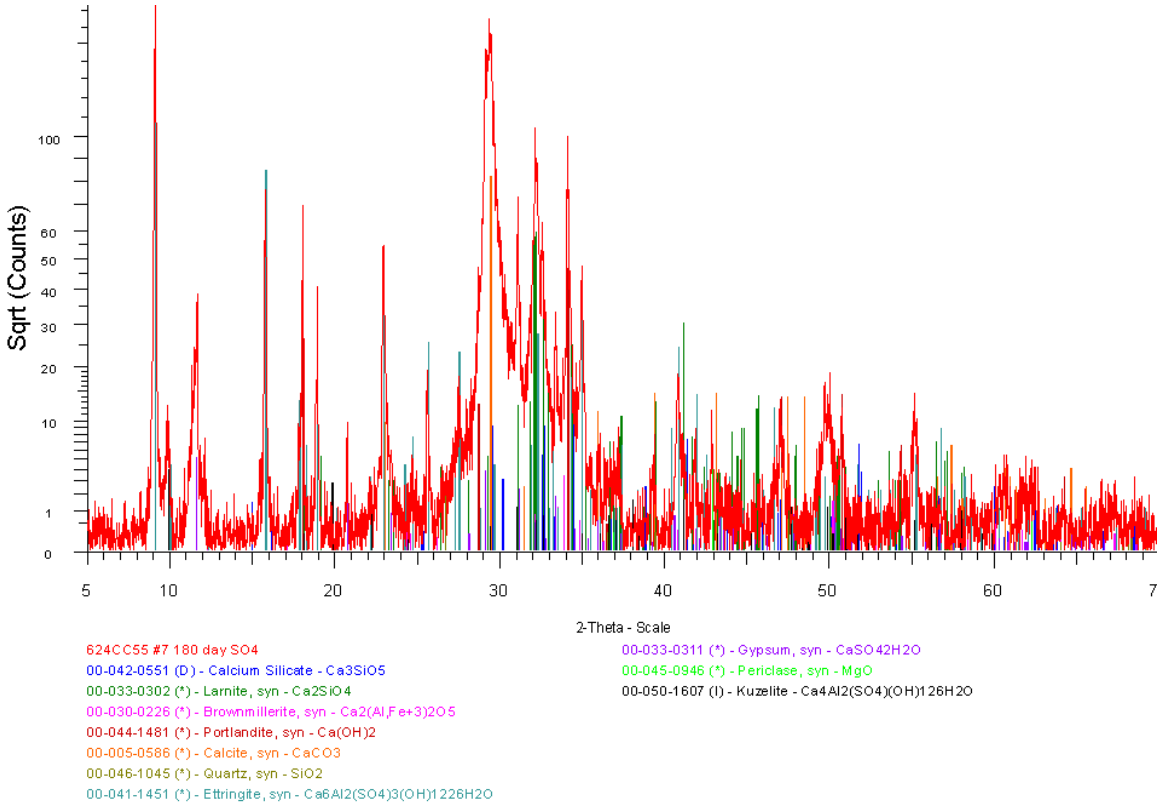

Figure E.42: S50-MK5 180-day Sulfate Exposure XRD Pattern

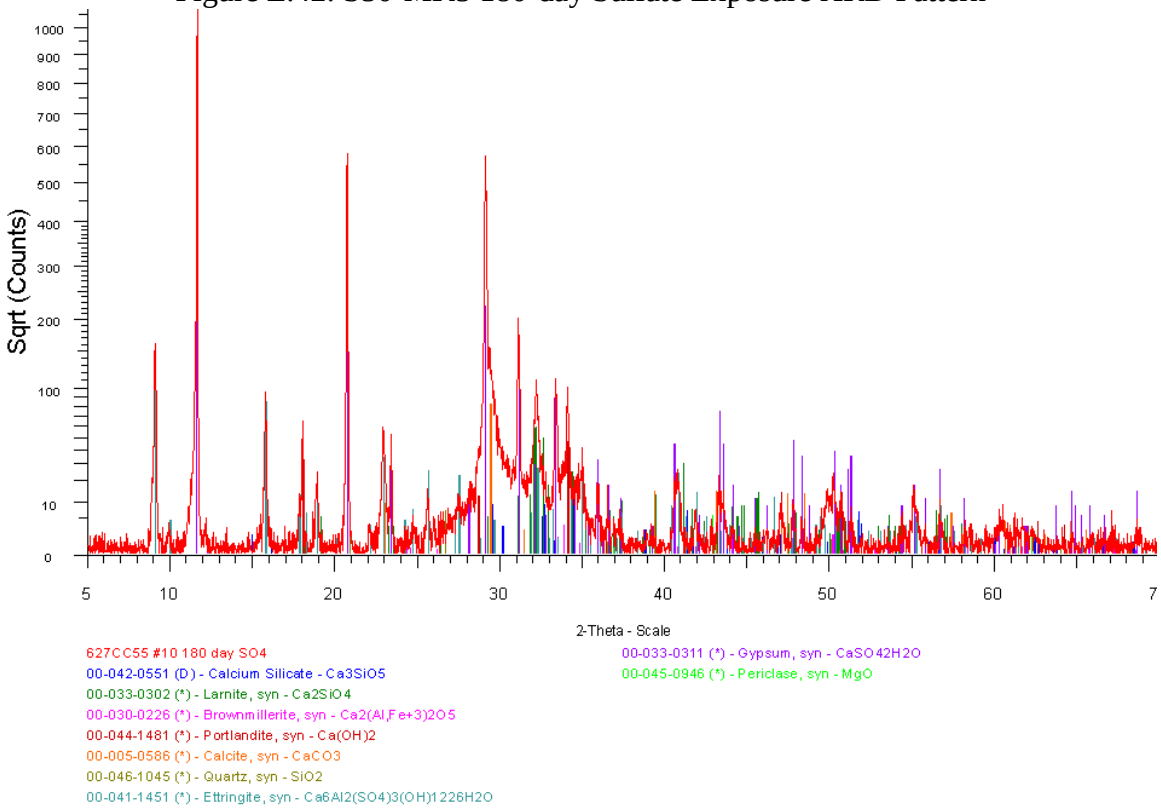

Figure E.43: S35-SF5 180-day Sulfate Exposure XRD Pattern

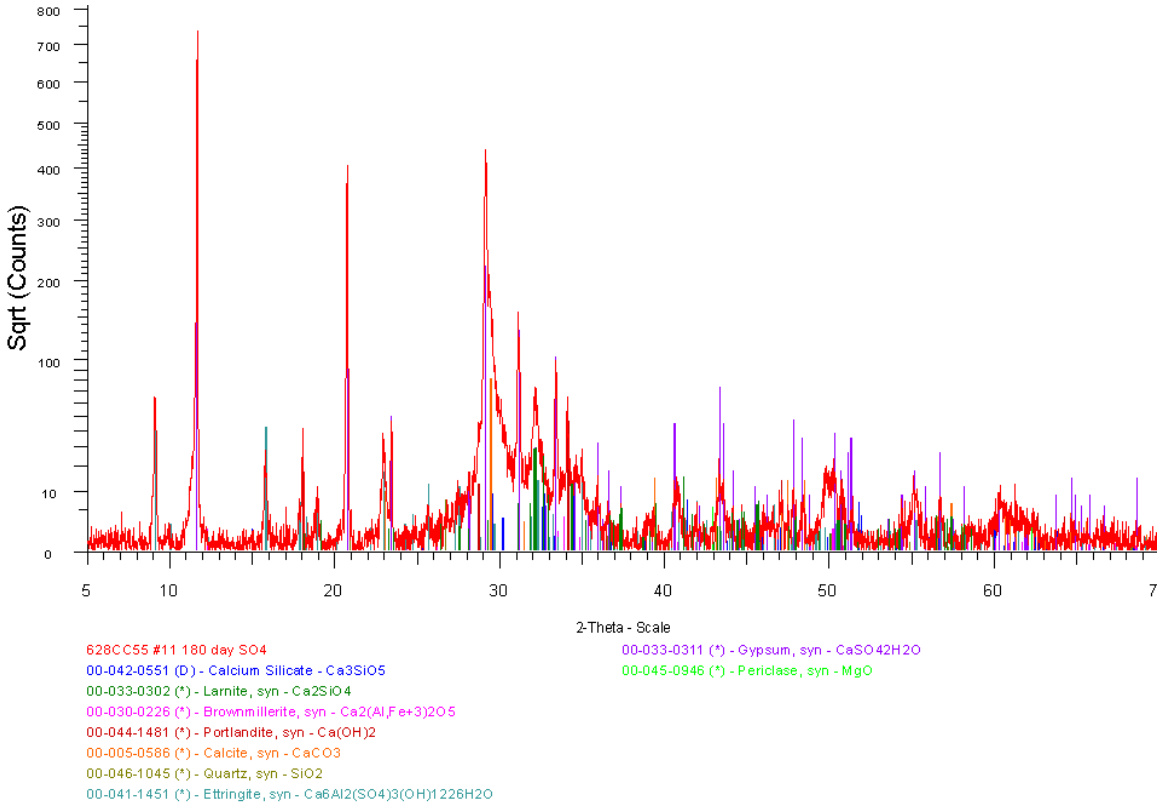

Figure E.44: S50-SF5 180-day Sulfate Exposure XRD Pattern

E.3.2 Quantitative X-Ray Diffraction Analysis Results

Table E.9: C_3S and C_2S contents of mix designs after sulfate exposure

	C_3S			C_2S		
Mix Design	180 days Control	90 days Sulfate	180 days Sulfate	180 days Control	90 days Sulfate	180 days Sulfate
T2	3.64	3.38	2.91	1.34	7.69	5.08
T3	0.86	1.49	2.07	1.16	3.12	4.93
T5	2.43	2.58	2.31	0.35	2.94	1.64
T3-F15	2.849	2.35	1.48	1.449	6.29	4.89
F25	5.39	1.70	3.35	11.55	11.34	9.23
F25-MK5	6.04	2.23	3.17	12.93	13.23	9.93
F25-MK10	4.90	2.06	2.35	17.29	17.00	14.36
F25-SF5	1.89	1.91	2.06	11.80	8.95	5.47
F25-SF10	2.886	2.01	1.99	15.619	10.68	7.93
S35-MK5	9.81	10.48	9.35	9.81	9.19	9.75
S50-MK5	12.75	9.94	11.56	9.63	15.61	12.25
S35-SF5	9.87	9.18	7.42	5.85	8.56	4.75
S50-SF5	10.06	11.75	10.59	9.38	10.24	2.66

Table E.10: C_3A and C_4AF contents of mix designs after sulfate exposure

	C_3A			C_4AF		
Mix Design	180 days Control	90 days Sulfate	180 days Sulfate	180 days Control	90 days Sulfate	180 days Sulfate
T2	0.161	0.09	0.00	16.554	14.78	13.59
T3	0.235	0.10	0.39	9.722	9.56	9.13
T5	0	0.15	0.01	16.068	13.11	12.65
T3-F15	0.425	0.21	0.47	9.036	9.88	6.91
F25	0.579	0.00	0.11	13.179	11.42	11.02
F25-MK5	0.658	0.00	0.01	8.781	8.87	7.60
F25-MK10	1.157	0.00	0.00	7.612	7.17	6.74
F25-SF5	0.687	0.00	0.24	10.398	11.32	11.96
F25-SF10	0.703	0.07	0.09	14.51	11.59	10.50
S35-MK5	0	0.00	0.00	10.777	11.33	9.45
S50-MK5	0.626	0.00	0.00	16.091	13.03	10.88
S35-SF5	0.124	0.00	0.00	18.26	14.85	11.64
S50-SF5	0.331	0.00	0.00	18.703	14.62	12.96

Table E.11: Portlandite and quartz contents of mix designs after sulfate exposure

	Portlandite			Quartz		
Mix Design	180 days Control	90 days Sulfate	180 days Sulfate	180 days Control	90 days Sulfate	180 days Sulfate
T2	34.88	16.61	12.77	0.787	0.73	0.61
T3	43.226	11.68	7.81	1.573	1.44	0.86
T5	44.353	18.57	11.52	1.347	1.31	0.65
T3-F15	30.532	4.85	1.16	4.998	3.18	2.71
F25	14.124	5.62	2.13	6.501	5.18	4.86
F25-MK5	9.834	3.44	0.85	7.119	4.84	4.55
F25-MK10	5.524	1.66	0.46	10.674	6.02	6.40
F25-SF5	8.869	2.72	0.84	7.259	6.06	5.87
F25-SF10	6.309	1.14	0.29	7.66	6.12	6.00
S35-MK5	20.471	9.94	7.51	0.717	0.73	0.68
S50-MK5	12.259	7.02	4.16	0.881	0.89	0.56
S35-SF5	16.522	6.61	3.85	1.216	1.07	1.21
S50-SF5	9.885	3.90	2.75	1.129	1.92	1.52

Table E.12: Calcite and ettringite contents of mix designs after sulfate exposure

	Calcite			Ettringite		
Mix Design	180 days Control	90 days Sulfate	180 days Sulfate	180 days Control	90 days Sulfate	180 days Sulfate
T2	6.01	2.86	2.76	29.347	33.25	38.41
T3	6.015	5.20	2.42	28.424	44.44	47.83
T5	5.373	3.81	2.56	24.912	35.68	37.08
T3-F15	9.15	3.77	3.68	21.288	44.66	36.68
F25	6.598	5.06	1.72	17.926	39.91	44.74
F25-MK5	13.971	4.56	2.01	7.226	41.18	49.64
F25-MK10	14.984	4.58	4.46	13.182	41.10	43.04
F25-SF5	17.336	5.15	5.01	18.358	41.31	35.55
F25-SF10	8.479	3.94	4.32	22.001	40.50	36.77
S35-MK5	15.196	6.99	6.28	8.815	34.26	38.24
S50-MK5	17.028	8.59	7.19	5.252	29.81	37.73
S35-SF5	12.702	4.42	4.38	12.655	32.77	32.79
S50-SF5	14.225	7.65	8.35	10.105	28.63	27.24

Table E.13: Monocarbonate and gypsum contents of mix designs after sulfate exposure

	Mono Carbonate			Gypsum		
Mix Design	180 days Control	90 days Sulfate	180 days Sulfate	180 days Control	90 days Sulfate	180 days Sulfate
T2	6.037	0.00	0.00	0	19.31	22.78
T3	8.782	0.00	0.00	0	22.40	24.33
T5	4.966	0.00	0.00	0	21.86	31.57
T3-F15	12.198	0.00	0.00	0	18.63	36.05
F25	12.414	0.00	0.00	0	9.13	11.89
F25-MK5	16.397	0.00	0.00	0	6.83	10.67
F25-MK10	11.098	0.00	0.00	0	5.03	7.05
F25-SF5	9.216	0.00	0.00	0	10.31	21.53
F25-SF10	7.37	0.00	0.00	0	11.68	19.59
S35-MK5	19.694	0.00	0.00	0	9.77	13.21
S50-MK5	22.495	0.00	0.00	0	8.50	10.79
S35-SF5	20.391	0.00	0.00	0	21.18	32.97
S50-SF5	23.07	0.00	0.00	0	20.47	32.83

Table E.14: Periclase and mullite contents of mix designs after sulfate exposure

	Periclase			Mullite		
Mix Design	180 days Control	90 days Sulfate	180 days Sulfate	180 days Control	90 days Sulfate	180 days Sulfate
T2	1.017	1.24	0.97	0	0.00	0.00
T3	0	0.06	0.00	0	0.00	0.00
T5	0.138	0.00	0.00	0	0.00	0.00
T3-F15	0	0.19	0.07	5.243	5.22	5.39
F25	0.316	0.92	0.75	9.702	8.99	9.77
F25-MK5	1.473	0.89	0.71	13.695	9.44	9.31
F25-MK10	1.294	0.35	0.77	8.304	10.53	10.48
F25-SF5	1.026	1.00	0.66	12.354	10.72	10.22
F25-SF10	1.295	0.89	0.54	13.005	11.01	11.94
S35-MK5	0.973	1.00	0.88	0	0.00	0.00
S50-MK5	1.031	1.07	1.08	0	0.00	0.00
S35-SF5	1.464	0.63	0.53	0	0.00	0.00
S50-SF5	1.215	0.80	0.25	0	0.00	0.00

Table E.15: Kuzelite content of mix designs after sulfate exposure

	Kuzelite		
Mix Design	180 days Control	90 days Sulfate	180 days Sulfate
T2	0.224	0.06	0.13
T3	0.011	0.52	0.23
T5	0.063	0.00	0.00
T3-F15	2.833	0.78	0.52
F25	1.719	0.74	0.45
F25-MK5	1.881	4.51	1.54
F25-MK10	3.979	4.50	3.90
F25-SF5	0.805	0.55	0.60
F25-SF10	0.164	0.37	0.04
S35-MK5	3.739	6.32	4.64
S50-MK5	1.952	5.55	3.80
S35-SF5	0.942	0.72	0.45
S50-SF5	1.895	0.02	0.85

APPENDIX F

SELF-HEALING INVESTIGATION RESULTS

F.1 Photographs of Samples Preparation and Cracking

Figure F.1: Post-tensioning of specimens

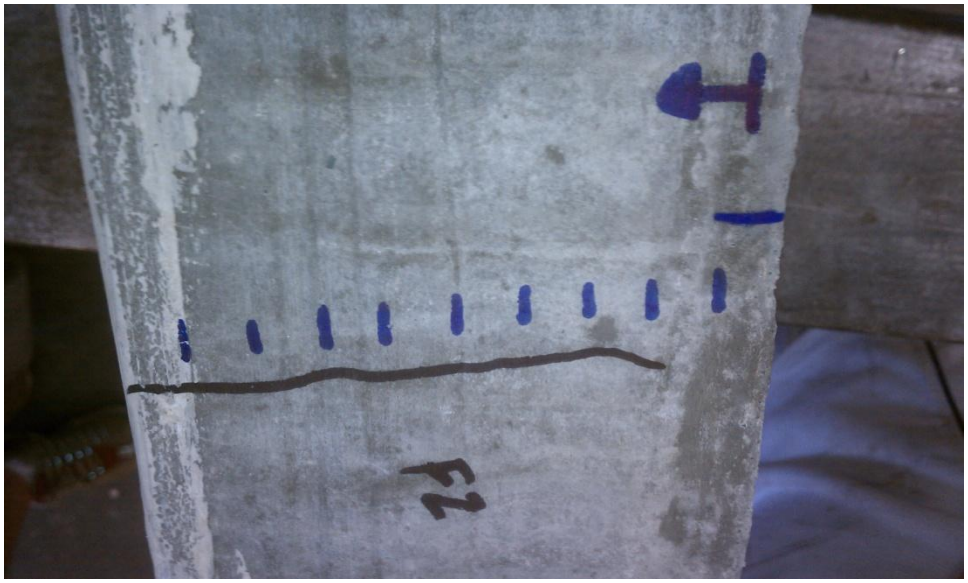

Figure F.2: Crack width measurement marks every ½ in. on flexure specimen

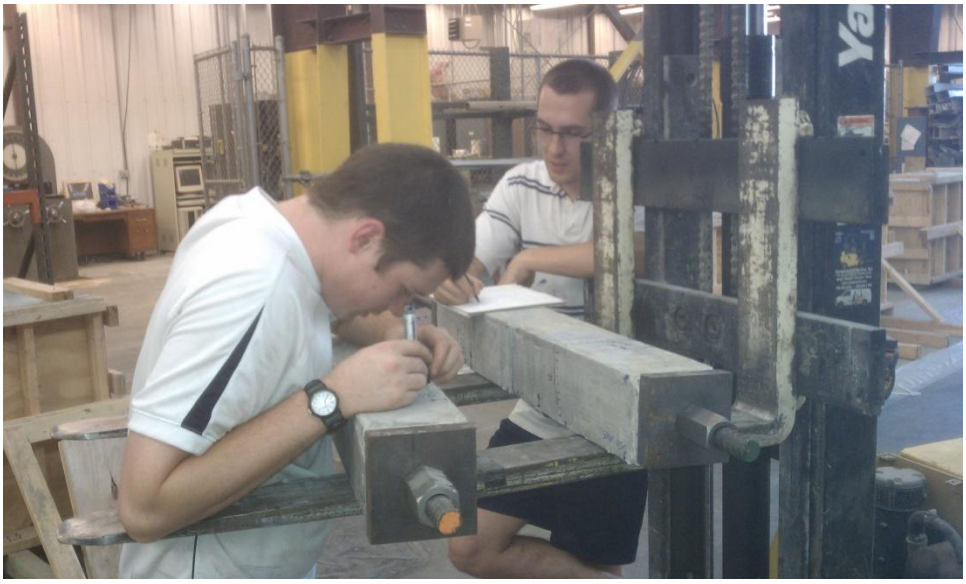

Figure F.3: Graduate students taking crack width measurements before sealing and exposure

Figure F.4: Graduate student sealing the sides of specimens with aluminum tape

Figure F.5: Sealed specimens with aluminum tape and epoxy with exposure container attached

Figure F.6: Exposure surface inside of ponding container with simulated seawater solution

F.2 Self-Healing Crack Images

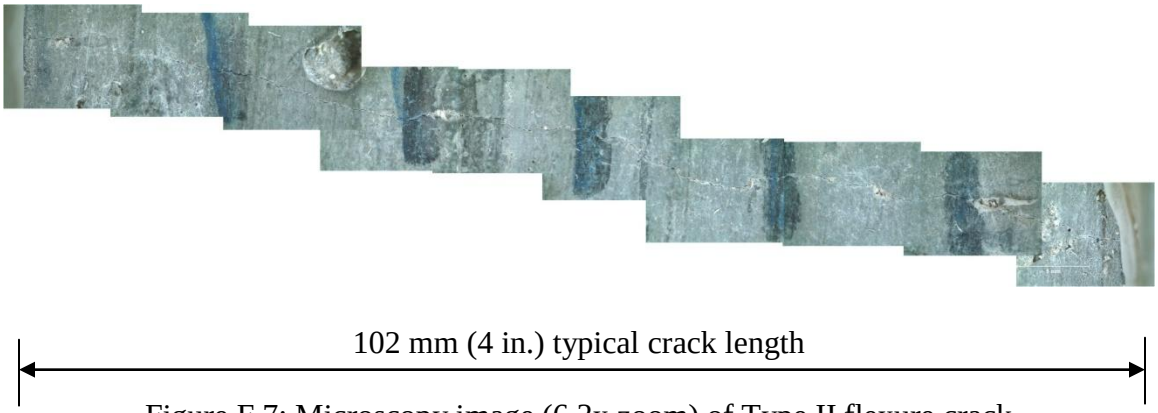

Figure F.7: Microscopy image (6.3x zoom) of Type II flexure crack

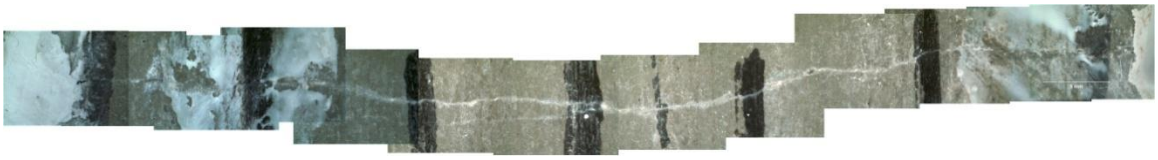

Figure F.8: Microscopy image (6.3x zoom) of Type II tension crack

Figure F.9: Microscopy image (6.3x zoom) of T3-F15 flexure crack

Figure F.10: Microscopy image (6.3x zoom) of T3-F15 tension crack

Figure F.11: Microscopy image (6.3x zoom) of F25 flexure crack

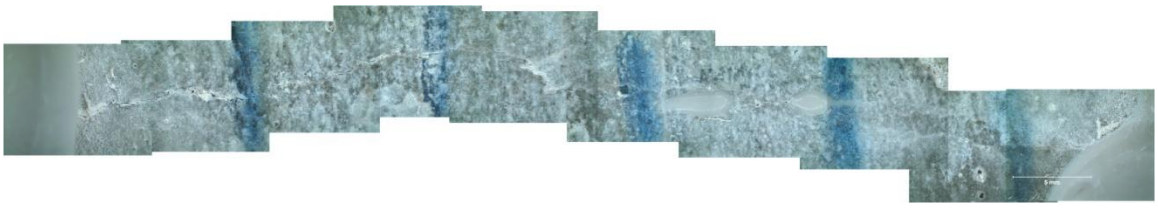

Figure F.12: Microscopy image (6.3x zoom) of F25 tension crack

Figure F.13: Microscopy image (6.3x zoom) of S35-MK5 flexure crack

Figure F.14: Microscopy image (6.3x zoom) of S35-MK5 tension crack

Figure F.15: Microscopy image (6.3x zoom) of S50-MK5 flexure crack

Figure F.16: Microscopy image (6.3x zoom) of S50-MK5 tension crack

F.3 Self-Healing Chloride Ingress Titration Data

Tables F.1 through F.15 provide the titration results for control, tension, and flexure specimens to the center of the grinding increment in mm (1 in. = 25.4 mm).

Table F.1: Type II control sample titration data

	Concentration (% Mass)			
Depth (mm)	**C1**	**C2**	**Average**	**Std. Dev.**
0.5	0.484	0.440	0.462	0.031
1.5	0.263	0.458	0.360	0.138
2.5	0.304	0.508	0.406	0.144
3.5	0.203	0.400	0.302	0.139
4.5	0.170	0.350	0.260	0.128
5.5	0.207	0.290	0.249	0.058
7	0.137	0.248	0.193	0.079
9	0.080	0.143	0.111	0.044
11	0.059	0.059	0.059	0.000
13	0.037	0.036	0.036	0.001

Table F.2: Type II tension sample titration data

	Concentration (% Mass)			
Depth (mm)	**T1**	**T2**	**Average**	**Std. Dev.**
1	0.502	0.544	0.523	0.030
3	0.468	0.402	0.435	0.046
5	0.373	0.276	0.325	0.069
7	0.276	0.204	0.240	0.051
9	0.249	0.142	0.195	0.075
11	0.192	0.073	0.132	0.084
13	0.175	0.133	0.154	0.030
15	0.189	0.079	0.134	0.077
17	0.168	0.044	0.106	0.087
19	0.141	0.044	0.093	0.069
76.2	0.048	0.053	0.051	0.004

Table F.3: Type II flexure sample titration data

	Concentration (% Mass)			
Depth (mm)	**F1**	**F2**	**Average**	**Std. Dev.**
1	0.389	0.332	0.360	0.040
3	0.313	0.280	0.297	0.023
5	0.237	0.244	0.240	0.005
7	0.151	0.196	0.174	0.032
9	0.163	0.139	0.151	0.016
11	0.117	0.090	0.104	0.019
13	0.103	0.060	0.081	0.031
15	0.092	0.042	0.067	0.035
17	0.059	0.050	0.054	0.007
19	0.059	0.047	0.053	0.008
76.2	0.014	0.011	0.012	0.002

Table F.4: T3-F15 control sample titration data

	Concentration (% Mass)			
Depth (mm)	**C1**	**C2**	**Average**	**Std. Dev.**
0.5	0.317	0.441	0.379	0.088
1.5	0.315	0.412	0.364	0.069
2.5	0.216	0.364	0.290	0.105
3.5	0.234	0.359	0.297	0.089
4.5	0.151	0.296	0.224	0.102
5.5	0.129	0.216	0.172	0.062
7	0.061	0.213	0.137	0.107
9	0.060	0.156	0.108	0.068
11	0.000	0.105	0.052	0.074
13	0.000	0.025	0.013	0.018

Table F.5: T3-F15 tension sample titration data

	Concentration (% Mass)			
Depth (mm)	**T1**	**T2**	**Average**	**Std. Dev.**
1	0.530	0.535	0.532	0.003
3	0.494	0.440	0.467	0.038
5	0.406	0.332	0.369	0.053
7	0.322	0.226	0.274	0.068
9	0.244	0.234	0.239	0.007
11	0.208	0.223	0.216	0.010
13	0.186	0.167	0.177	0.013
15	0.143	0.130	0.137	0.010
17	0.128	0.118	0.123	0.007
19	0.127	0.105	0.116	0.015
76.2	0.030	0.085	0.057	0.039

Table F.6: T3-F15 flexure sample titration data

	Concentration (% Mass)			
Depth (mm)	**F1**	**F2**	**Average**	**Std. Dev.**
1	0.520	0.501	0.510	0.013
3	0.454	0.425	0.439	0.020
5	0.368	0.262	0.315	0.074
7	0.332	0.279	0.306	0.037
9	0.249	0.173	0.211	0.054
11	0.195	0.146	0.171	0.034
13	0.166	0.061	0.114	0.074
15	0.139	0.073	0.106	0.047
17	0.100	0.053	0.076	0.033
19	0.077	0.039	0.058	0.027
76.2	0.009	0.014	0.011	0.004

Table F.7: F25 control sample titration data

	Concentration (% Mass)			
Depth (mm)	**C1**	**C2**	**Average**	**Std. Dev.**
0.5	0.578	-	0.578	-
1.5	0.477	0.355	0.416	0.086
2.5	0.332	0.364	0.348	0.023
3.5	0.262	0.348	0.305	0.061
4.5	0.262	0.241	0.251	0.014
5.5	0.221	0.149	0.185	0.051
7	0.154	0.079	0.117	0.053
9	0.087	0.038	0.063	0.035
11	0.047	0.000	0.024	0.033
13	0.018	0.000	0.009	0.013

Table F.8: F25 tension sample titration data

	Concentration (% Mass)			
Depth (mm)	**T1**	**T2**	**Average**	**Std. Dev.**
1	0.494	0.454	0.474	0.028
3	0.405	0.481	0.443	0.054
5	0.376	0.439	0.407	0.045
7	0.292	0.289	0.290	0.002
9	0.235	0.206	0.221	0.020
11	0.220	0.158	0.189	0.044
13	0.200	0.093	0.147	0.076
15	0.154	0.099	0.127	0.039
17	0.132	0.114	0.123	0.012
19	0.132	0.113	0.122	0.013
76.2	0.034	0.038	0.036	0.003

Table F.9: F25 flexure sample titration data

	Concentration (% Mass)			
Depth (mm)	**F1**	**F2**	**Average**	**Std. Dev.**
1	0.404	0.577	0.490	0.122
3	0.344	0.515	0.430	0.121
5	0.281	0.383	0.332	0.072
7	0.253	0.287	0.270	0.024
9	0.146	0.194	0.170	0.034
11	0.100	0.147	0.123	0.033
13	0.076	0.119	0.098	0.030
15	0.056	0.076	0.066	0.014
17	0.034	0.068	0.051	0.024
19	0.035	0.064	0.050	0.021
76.2	0.007	0.007	0.007	0.000

Table F.10: S35-MK5 control sample titration data

	Concentration (% Mass)			
Depth (mm)	**C1**	**C2**	**Average**	**Std. Dev.**
0.5	0.656	0.545	0.601	0.079
1.5	0.630	0.532	0.581	0.069
2.5	0.550	0.465	0.508	0.060
3.5	0.562	0.491	0.527	0.050
4.5	0.445	0.327	0.386	0.083
5.5	0.255	0.206	0.230	0.034
7	0.131	0.148	0.140	0.012
9	0.053	0.029	0.041	0.017
11	0.027	0.000	0.013	0.019
13	0.019	0.000	0.009	0.013

Table F.11: S35-MK5 tension sample titration data

	Concentration (% Mass)			
Depth (mm)	**T1**	**T2**	**Average**	**Std. Dev.**
1	0.493	0.524	0.508	0.022
3	0.472	0.407	0.440	0.046
5	0.333	0.144	0.239	0.133
7	0.207	0.118	0.163	0.063
9	0.107	0.081	0.094	0.018
11	0.097	0.080	0.089	0.012
13	0.098	0.063	0.081	0.025
15	0.093	0.079	0.086	0.010
17	0.064	0.039	0.052	0.017
19	0.057	0.000	0.029	0.041
76.2	0.036	0.024	0.030	0.008

Table F.12: S35-MK5 flexure sample titration data

	Concentration (% Mass)			
Depth (mm)	**F1**	**F2**	**Average**	**Std. Dev.**
1	0.561	0.597	0.579	0.026
3	0.476	0.465	0.470	0.008
5	0.344	0.340	0.342	0.003
7	0.241	0.171	0.206	0.050
9	-	0.139	0.139	-
11	0.144	0.160	0.152	0.012
13	0.110	0.146	0.128	0.025
15	0.101	0.100	0.100	0.001
17	0.040	0.099	0.069	0.041
19	0.000	0.060	0.030	0.042
76.2	0.000	0.000	0.000	0.000

Table F.13: S50-MK5 control sample titration data

	Concentration (% Mass)			
Depth (mm)	**C1**	**C2**	**Average**	**Std. Dev.**
0.5	0.465	0.444	0.455	0.015
1.5	0.547	0.471	0.509	0.053
2.5	0.463	0.403	0.433	0.042
3.5	0.385	0.357	0.371	0.020
4.5	0.284	0.197	0.240	0.061
5.5	0.201	0.115	0.158	0.061
7	0.108	0.038	0.073	0.049
9	0.043	0.000	0.022	0.031
11	0.000	0.000	0.000	0.000
13	0.000	0.000	0.000	0.000

Table F.14: S50-MK5 tension sample titration data

	Concentration (% Mass)			
Depth (mm)	**T1**	**T2**	**Average**	**Std. Dev.**
1	0.591	0.575	0.583	0.012
3	0.440	0.419	0.429	0.015
5	0.330	0.304	0.317	0.018
7	0.221	0.207	0.214	0.010
9	0.220	0.197	0.208	0.016
11	0.176	0.193	0.184	0.012
13	0.153	0.205	0.179	0.037
15	0.138	0.219	0.179	0.057
17	0.144	0.164	0.154	0.014
19	0.167	0.185	0.176	0.013
76.2	0.021	0.107	0.064	0.061

Table F.15: S50-MK5 flexure sample titration data

	Concentration (% Mass)			
Depth (mm)	**F1**	**F2**	**Average**	**Std. Dev.**
1	0.588	0.562	0.575	0.018
3	0.585	0.441	0.513	0.102
5	0.437	0.345	0.391	0.065
7	0.248	0.235	0.242	0.009
9	0.144	0.187	0.166	0.031
11	0.136	0.122	0.129	0.011
13	0.101	0.114	0.107	0.010
15	0.062	0.113	0.087	0.036
17	0.062	0.142	0.102	0.057
19	0.056	-	0.056	-
76.2	0.000	0.014	0.007	0.010

APPENDIX G

HIGH PERFORMANCE MARINE CONCRETE FOR COASTAL GEORGIA: USAGE CONDITIONS

G.1 Introduction

The deterioration of precast prestressed concrete piles in marine environments has become an area of concern based on several structures having shown extensive deterioration after only 30 years of service. Recent research has shown that concrete piling can experience damage due to multiple deterioration mechanisms, including chemical, physical, and biological attack. This deterioration leads to reductions in mechanical properties, serviceability, and aesthetics of the structure.

As part of the ongoing research to develop concrete mix designs capable of providing service lives of 100+ years, a study was performed to identify where high-performance marine concretes (HPMC) are needed to attain the desired service life through the monitoring of the chloride and sulfate concentrations present in surface water.

G.2 Methodology and Results

The chloride and sulfate concentrations in coastal Georgia (Brantley, Bryan, Camden, Charlton, Chatham, Effingham, Glynn, Liberty, Long, McIntosh, and Wayne Counties) were analyzed to determine where high-performance marine concrete (HPMC) is necessary. This was performed by utilizing data available from the United States Geological Survey (USGS) monitoring stations (USGS, 2010). Only sites for surface water with more than 3 data points were considered. A skew normal distribution was fit

to the data for use in statistical analyses of the sites. The skew normal distribution was selected for its ability to fit data with a positive or negative skew that was present in the data collected (Azzalini, 2005). Then for each site, the 75th percentile of the concentration for chloride and sulfates was determined. The results for both chloride and sulfate concentration were compared versus their distance inland from Atlantic Ocean coast and site elevation (mean sea level is reference).

Figure G.1 presents the chloride concentration relative to distance inland, and Figure G.2 shows the chloride concentration compared to the site elevation. Figure G.3 presents the sulfate concentration relative to distance inland, and Figure G.4 shows the sulfate concentration compared to the site elevation.

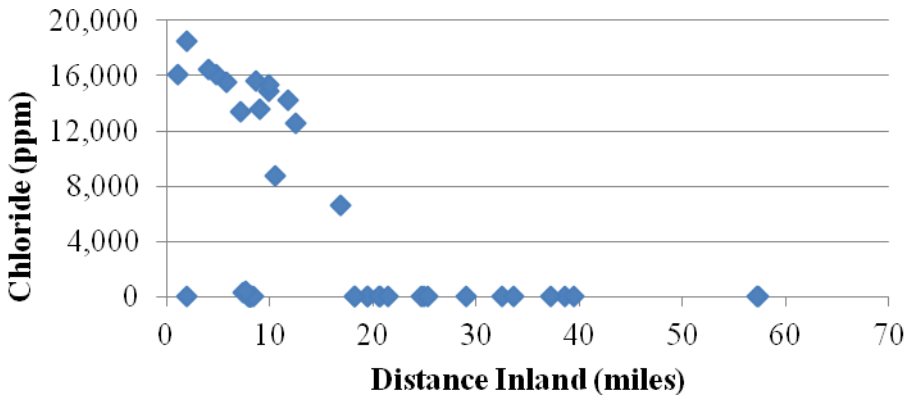

Figure G.1: Chloride concentration versus distance inland (1 mile = 1.6 km)

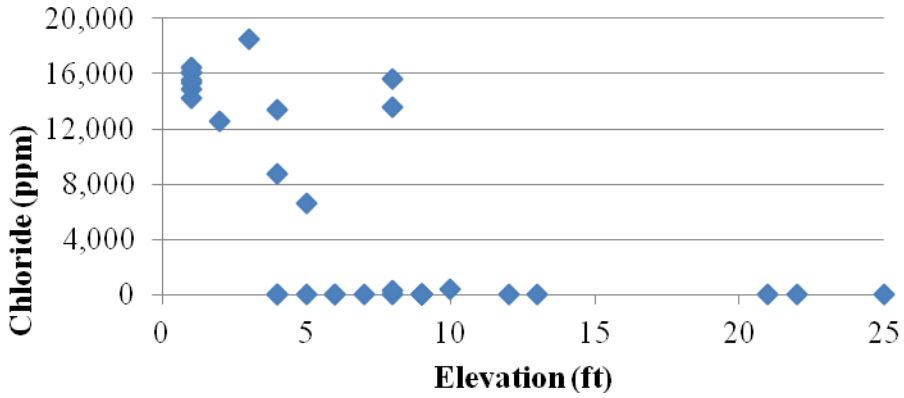

Figure G.2: Chloride concentration versus site elevation (1 ft = 0.3 m)

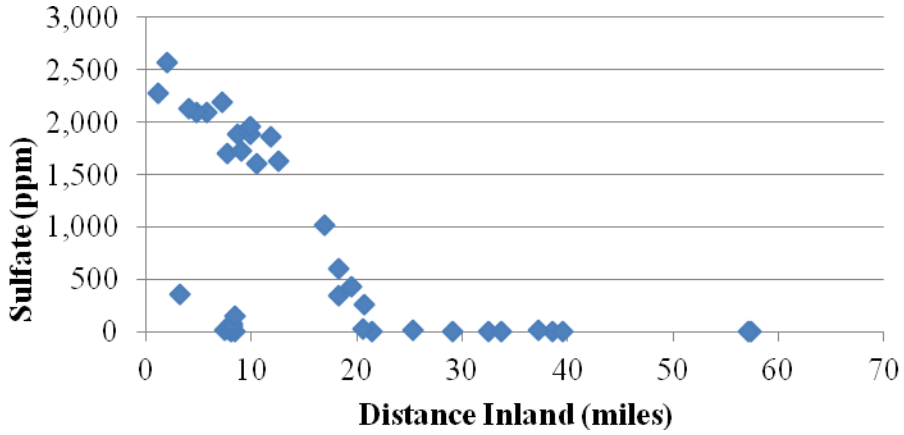

Figure G.3: Sulfate concentration versus distance inland (1 mile = 1.6 km)

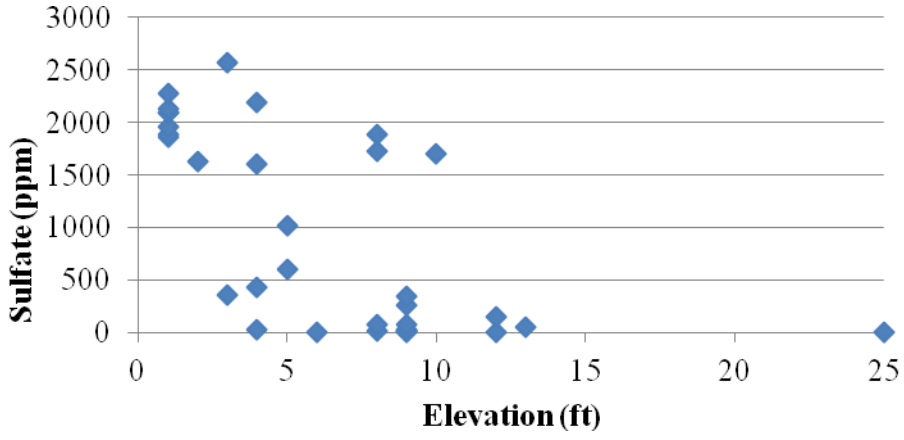

Figure G.4: Sulfate concentration versus site elevation (1 ft = 0.3 m)

Figures G.1 through G.4 demonstrate that both the chloride and sulfate concentration decrease with increasing distance inland, as well as with increases in elevation. Next, the data were compared with exposure limits that would necessitate the use of a HPMC. For sulfate concentration, the limit of 150 ppm given by ACI 201 (2010) was used, and for chlorides a threshold of 500 ppm was chosen to match the value used by the USGS (2010) for differentiating between brackish and fresh water. Table G.1 presents the maximum values of distance inland and elevation for sites with concentrations in excess of the limits chosen.

Table G.1: Maximum inland distance and elevation of sites requiring use of HPMC (1 mile = 1.6 km, 1 ft = 0.3 m)

	Inland Distance (miles)	**Site Elevation (ft)**
Chloride	16.9	8
Sulfate	20.7	12

Figure G.5 presents a map of the sites monitored for chloride concentrations. Red icons represent a concentration above 500 ppm where HPMC is needed, blue icons represent sites where chloride levels are negligible.

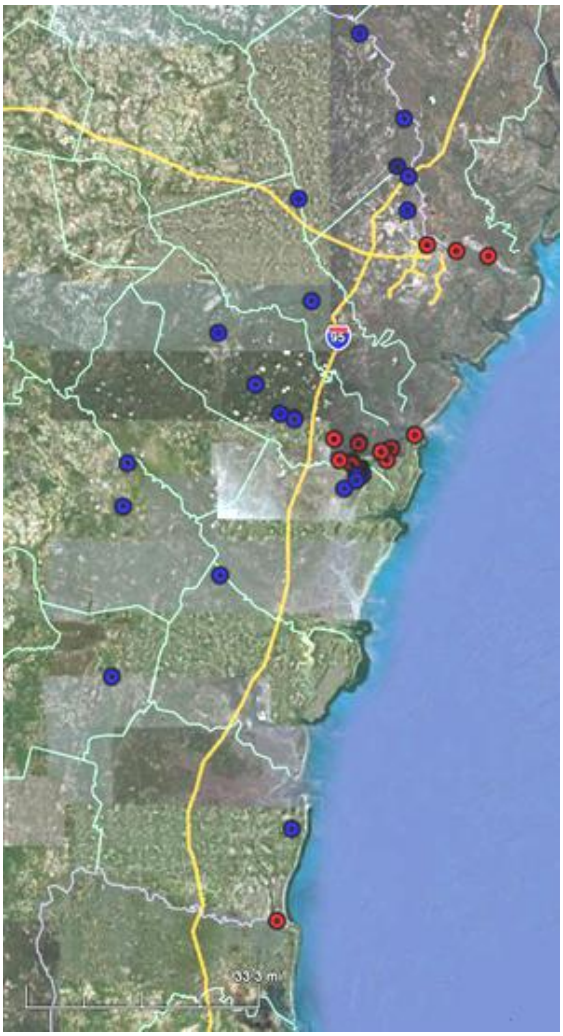

Figure G.5: Map of chloride sampling sites (Google, 2011)

Figure G.6 presents a map of the sites monitored for sulfate concentrations. Red icons represent a sulfate concentration above 1,500 ppm where HPMC with an ASTM C 150 (2009) Type V cement or equivalent is required by ACI 201.2R-10 (2010) is needed, yellow icons represent a concentration between 150 ppm and 1,500 ppm HPMC with an ASTM C 150 (2009) Type II cement or equivalent is required by ACI 201.2R-10 (2010) is needed, and blue dots represent sites where sulfate levels are negligible.

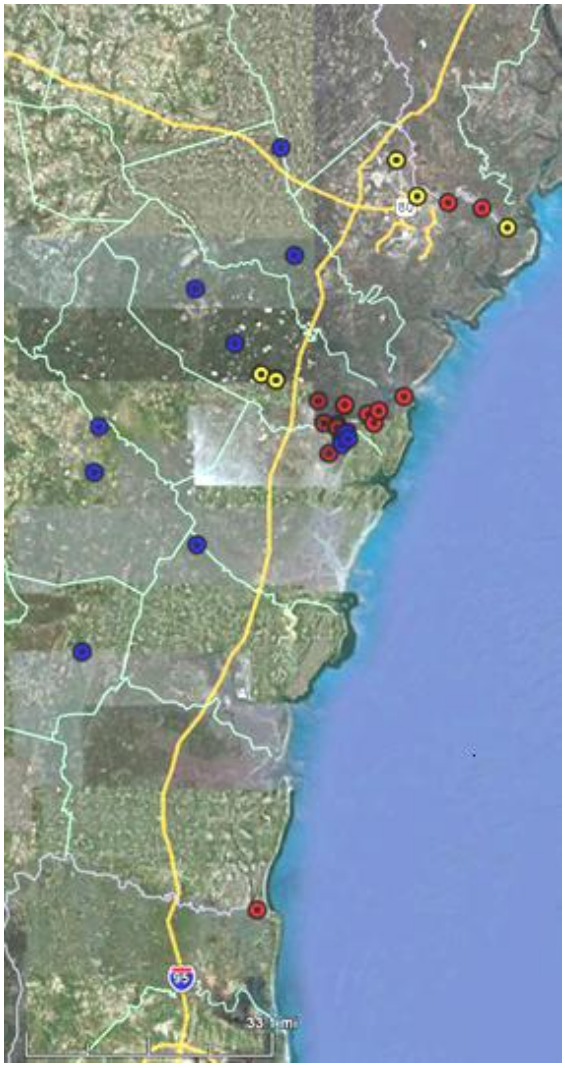

Figure G.6: Map of sulfate sampling sites (Google, 2011)

G.3 Conclusions and Recommendations

The analysis of USGS monitoring sites along the coast of Georgia suggests that HPMC is necessary for service lives of 100+ years. The data suggest that HPMC is not necessary at sites over 33.8 km (21 miles) inland from the coast. Alternatively, site elevation may be used as a criterion for usage, and a recommended value of 3.9 m (13 ft) is suggested. Figure G.7 shows a map of coastal Georgia with the 33.7 km (21 mile) suggested distance present marked with a blue line. Any site to the east of the blue line

requires the use of

HPMC.

Figure G.7: Proposed HPMC use map for submerged piles, original map from GDOT (2011)

REFERENCES

AASHTO LRFD Bridge Design Specifications, 4th ed. (2007), American Association of Highway and Transportation Officials, Washington D.C.

ACI Committee 201 (2010). "ACI 201.2R-10 Guide to Durable Concrete," *ACI Manual of Concrete Practice,* ACI 201.2R-10, American Concrete Institute, Farmington Hills, MI.

ACI Committee 211, (1991). "ACI 211.1R-91 Standard Practice for Selecting Proportions for Normal, Heavyweight, and Mass Concrete," *ACI Manual of Concrete* Practice, ACI 211.1R-91, American Concrete Institute, Farmington Hills, MI, pp. 38.

ACI Committee 211, (2008). "ACI 211.4R-08 Guide for Selecting Proportions for High-Strength Concrete Using Portland Cement and Other Cementitious Materials," *ACI Manual of Concrete* Practice, ACI 211.4R-08, American Concrete Institute, Farmington Hills, MI, pp. 25.

ACI Committee 214 (2010). "Guide for Obtaining Cores and Interpreting Compressive Strength Results," *ACI Manual of Concrete Practice*, ACI 214.4R-10, American Concrete Institute, Farmington Hills, MI, pp. 17.

ACI Committee 222 (2001), "ACI 222R-01 Protection of Metals in Concrete against Corrosion," *ACI Manual of Concrete Practice*, ACI 222R-01, American Concrete Institute, Farmington Hills, MI.

ACI Committee 222 (2001). "Corrosion of Prestressing Steels," *ACI Manual of Concrete Practice,* ACI 222.2R-01, American Concrete Institute, Farmington Hills, MI, pp. 43.

ACI Committee 224R-90 (1998). "ACI 224R-90 Control of Cracking in Concrete Structures," *ACI Manual of Concrete Practice*, ACI 224R-90, American Concrete Institute, Farmington Hills, MI.

ACI Committee 318 (2008). "Building Code Requirements for Structural Concrete (ACI 318-08) and Commentary," American Concrete Institute. Farmington Hills, Michigan.

ACI Committee 363 (1997). "Report on High-Strength Concrete," *ACI Manual of Concrete Practice,* ACI 363R-92, American Concrete Institute. Farmington Hills, Michigan.

Akoz, F.; Koral, S.; Yuzer, N.; Turker, F. (1995). "Effects of Sodium Sulfate Concentration on the Sulfate Resistance of Mortars with and without Silica Fume," *Cement and Concrete Research*, V. 25, pp. 1360-1368.

Al-Amoudi, O.S.B. (2002). "Attack on Plain and Blended Cements Exposed to Aggressive Sulfate Environments," *Cement and Concrete Composites*, V. 24, pp. 305-316.

American Association of State Highway and Transportation Officials (1980) "T259-80: Standard Method of Test for Resistance of Concrete to Chloride Ion Penetration," Washington, D.C., U.S.A.

Andrade, C. (1993). "Calculation of Chloride Diffusion Coefficients in Concrete From Ionic Migration Measurements," *Cement and Concrete Research*, V. 23, pp. 724-742.

Andrade, C. and Sanjuan, M.A. (1994), "Experimental Procedure for the Calculation of Chloride Diffusion Coefficients in Concrete from Migration Tests," *Advances in Cement Research*, V. 6, pp. 127-134.

Angst, U.; Elsener, B.; Larsen, C.; Vennesland, O. (2009). "Critical Chloride Content in Reinforced Concrete – A Review," *Cement and Concrete Research*, V. 39, pp. 1122-1138.

ASTM C 39 (2005). "Standard Test Method for Compressive Strength of Cylindrical Concrete Specimens," American Society for Testing and Materials, West Conshohocken, PA, pp. 7.

ASTM C 150 (2009). "Standard Specification for Portland Cement," American Society for Testing and Materials, West Conshohocken, PA, pp. 10.

ASTM C 469 (2002). "Standard Test Method for Static Modulus of Elasticity and Poisson's Ratio of Concrete in Compression," American Society for Testing and Materials, West Conshohocken, PA, pp. 5.

ASTM C 805 (2008). "Standard Test Method for Rebound Number of Hardened Concrete," American Society for Testing and Materials, West Conshohocken, PA, pp. 3.

ASTM C 876 (2009). "Standard Test Method for Corrosion Potentials of Uncoated Reinforcing Steel in Concrete," American Society for Testing and Materials, West Conshohocken, PA, pp. 7.

ASTM C 1012 (2009). "Standard Test Method for Length Change of Hydraulic-Cement Mortar Bars Exposed to a Sulfate Solution," American Society for Testing and Materials, West Conshohocken, PA, pp. 6.

ASTM C 1152 (2004). “Standard Test Method for Acid-Soluble Chloride in Mortar and Concrete,” American Society for Testing and Materials, West Conshohocken, PA, pp. 4.

ASTM C 1157 (2004). “Standard Performance Specification for Hydraulic Cement,” American Society for Testing and Materials, West Conshohocken, PA, pp. 5.
ASTM C 1202 (2007). “Standard Test Method for Electrical Indication of Concrete’s Ability to Resist Chloride Ion Penetration,” American Society for Testing and Materials, West Conshohocken, PA, pp. 6.

ASTM C 1218 (1999). “Standard Test Method for Water-Soluble Chloride in Mortar and Concrete,” American Society for Testing and Materials, West Conshohocken, PA, pp. 3.

ASTM C 1327 (2008). “Standard Test Method for Vickers Indentation Hardness of Advanced Ceramics,” American Society for Testing and Materials, West Conshohocken, PA, pp. 8.

ASTM C 1556 (2004). “Standard Test Method for Determining the Apparent Chloride Diffusion Coefficient of Cementitious Mixtures by Bulk Diffusion,” American Society for Testing and Materials, West Conshohocken, PA, pp. 7.

ASTM C 1580 (2009). “Standard Test Method for Water-Soluble Sulfate in Soil,” American Society for Testing and Materials, West Conshohocken, PA, pp. 3.

ASTM E 1131 (2008). “Standard Test Method for Compositional Analysis by Thermogravimetry,” American Society for Testing and Materials, West Conshohocken, PA, pp. 5.

Atis, C.D. (2003). “Accelerated Carbonation and Testing of Concrete Made With Fly Ash.” *Construction and Building Materials,* V. 17, pp. 147-152.

Azzalini, A. (2005). “The Skew-normal Distribution and Related Multivariate Families,” *Scandinavian Journal of Statistics,* Vol. 32, No. 2, pp. 159-188.

Bamforth, P. (1993). “Concrete Classification for R.C. Structures Exposed to Marine and Other Salt-Laden Environments,” *Structural Faults and Repair Conference,* Edinburgh, UK.

Bang, S. S.; Galinat, J. K.; Ramakrishnan, V. (2001). “Calcite Precipitation Induced by Polyurethane-immobilized *Bacillus pasteurii*,” *Enzyme and Microbial Technology*, V. 28, pp. 404-409.

Bard, V.; Radlinska, A.; Cohen, M.; Weiss, W.J. (2009). *Relating Material Properties to Exposure Conditions for Predicting Serice Life in Concrete Bridge Decks in Indiana.* Publication FHWA/IN/JTRP-2007/27., Indiana Department of Transportation and Purdue University, West Lafayette, Indiana.

Basheer, L.; Kropp, J.; Cleland, D. (2002). "Assessment of the Durability of Concrete from Its Permeation Properties: A Review." *Construction and Building Materials.* V. 15, pp. 93-103.

Batis, G.; Pantazopoulou, P.; Tsivilis, S.; Badogiannis, E. (2005). "The Effect of Metakaolin on the Corrosion Behavior of Cement Mortars." *Cement and Concrete Composties.* V. 27, pp. 125-130.

Bentur, A; Diamond, S.; Berke, N. (1997). *Steel Corrosion in Concrete*, E&FN, Spon, London.

Bentz, D.P. (2000). "Influence of Silica Fume on Diffusivity in Cement-Based Materials II. Multi-Scale Modeling of Concrete Diffusivity," *Cement and Concrete Research*, V. 30, pp. 1121-1129.

Berke, N. S., and Hicks, M.C. (1992). "Estimating the Life Cycle of Reinforced Concrete Decks and Marine Piles Using Laboratory Diffusion and Corrosion Data," *Corrosion Forms and Control for Infrastructure, ASTM STP 1137*, American Society for Testing and Materials, Philadelphia.

Bertolini, L; Elsener. B.; Pedeferri, P.; Polder, R. (2004). *Corrosion of Steel in Concrete: Prevention Diagnosis, Repair*, Wiley-VCH, pp. 392.

Biswas, M., et al. (2010). "Bioremediase a Unique Protein from a Novel Bacterium BKH1, Ushering a New Hope in Concrete Technology," *Enzyme and Microbial Technology*, V. 46, pp. 581-587.

Bleszynski, R.; Hooten, R.; Thomas, M.; Rogers, C. (2002). "Durability of Ternary Blend Concrete with Silica Fume and Blast-Furnace Slag: Laboratory and Outdoor Exposure Site Studies." *ACI Materials Journal.* V. 99, pp. 499-508.

Böhni, H. (2005), Corrosion in Reinforced Concrete Structures, Woodhead Publishing Ltd., Cambridge, UK.

Bonakdar, A. and Mobasher, B. (2010). "Multi-parameter Study of External Sulfate Attack in Blended Cement Materials," *Construction and Building Materials*, V. 24, pp. 61-70.

Bonen, D. (1993). "A Microstructural Study of the Effect Produced by Magnesium Sulfate on Plain and Silica Fume-bearing Portland Cement Mortars," *Cement and Concrete Research*, V. 23, pp. 541-553.

Borgard, B., Ramirez, C.; Somayaji, S.; Jones, D.; Keeling, D.; Heidersbach, R. (1991). "Failure Analysis in Concrete Structures: A Cornparison of Field Data with Results from Laboratory Exposures," *Corrosion*, V. 47, pp.758-769.

Broomfield, J. P. (2007), *Corrosion of Steel in Concrete*, Taylor and Francis Group, New York, NY.

Brown, P. (1981). "An Evaluation of the Sulfate Resistance of Cements in a Controlled Environment," *Cement and Concrete Research*, V. 11, pp. 719-727.
Chang, C. F., and Chen, J. W. (2006), "The Experimental Investigation of Concrete Carbonation Depth," *Cement and Concrete Research*, V. 36 (9), pp. 1760-1767.

Cobanoglu A.; Lampros T.; Hershberger R.; Norman D.; Murata K.; Kawakami K.; Matsunaga Y.; Yamashita S. (1997), "Determination of Sulfate in Brackish Waters by Laser Raman Spectroscopy," *Analytica Chimica Acta*, 344, pp 153-157.

Cohen, M. D. and Mather, B. (1991). ''Sulfate attack on concrete— Research needs.'' ACI Materials Journal, V. 88, pp. 62– 69.

Collepardi, M.; Marcialis, A.; Turriziani, R. (1972). "Penetration of Chloride Ions into Cement Pastes and Concrete," *Journal of the American Ceramic Society*, V. 55, pp.534-535.

Concrete Durability Center (2005). *Concrete Works Version 2.0 Users Manuel*.

Concrete Durability Center (2007). *Concrete Works* (Version 2.1.3) [Software]. Available from http://www.texasconcreteworks.com

Courard, L.; Darimont, A.; Schouterden, M.; Ferauche, F.; Willem, X.; Degeimbre, R. (2003). "Durability of Mortars Modified with Metakaolin," *Cement and Concrete Research*, V. 33, pp. 1473-1479.

Crossett, K.; Culliton, T.; Wiley, P.; Goodspeed, T. (2004). "Population Trends Along the Coastal United States: 1980 to 2008," *Coastal Trends Report Series*, National Oceanic and Atmospheric Administration. Available from: oceanservice.noaa.gov/programs/mb/pdfs/coastal_pop_trends_complete.pdf.

De Muynck, W.; Debrouwer, D.; Debelie, N.; Verstraete, W. (2008). "Bacterial Carbonate Precipitation Improves the Durability of Cementitious Materials," *Cement and Concrete Research*, V. 38, pp. 1005-1014.

Dhir, R.K.; Jones, M.; Ahmed, H.; Seneviratne, A. (1990). "Rapid Estimation of Chloride Diffusion Coefficient in Concrete," *Magazine of Concrete Research*, V. 42, pp. 177-185.

Diab, H.; Bentur, A.; Heitner-Wirguin, C.; Ben-Dor, L. (1988). "The Diffusion of Cl-Ions through Portland Cement and Portland Cement-Polymer Pastes," *Cement and Concrete Research*, V. 18, pp. 715-722.

Edvardsen, C. (1995). "Chloride Penetration into Cracked Concrete," Proceedings of the RILEM International Workshop on Chloride Penetration into Concrete, St-Remy-les-Chevreuse, France, Oct. l5-l8, pp. 243-249.

Edvardsen, C. (1996). "Water Penetrability and Autogenous Healing of Separation Cracks in Concrete," *Betonwerk and Fertigteil Technik-Concrete Precasting Plant and Technology*, V. 62, pp. 77-85.

Edvardsen, C. (1999). "Water Permeability and Autogenous Healing of Cracks in Concrete." *ACI Materials Journal.* V. 96, pp. 448-454.

Ehlen, M.A. (2009). *Life 365* (Version 2.1) [Software]. Available from http://www.life-365.org

Ehlen, M.A.; Thomas, M.; Bentz, E. (2009). "Life 365 Service Life Prediction Model Version 2.0," *Concrete International*, V. 31.

Francois, R. and Arliguie, G. (1999). "Effect of Microcracking and Cracking on The Development of Corrosion in Reinforced Concrete Mernbers," *Magazine of Concrete Research*, V. 51, pp. 143- 150.

Francois, R. and Maso, J. (1988). "Effect of Damage in Reinforced Concrete on Carbonation or Chloride Penetration," *Cement and Concrete Research*, V. 18, pp. 961-970.

Geiker, M.; Thaulow, N.; Anderson, P. (1990). "Assessment of Rapid Chloride Ion Permeability Test of Concrete With and Without Mineral Admixtures", *Durability of Building Materials*, (ed. J.M Baker, P.J. Nixon, A.J. Majumdar, H. Davis) E&FN Spon, London, pp. 493-502.

Georgia Department of Transportation (2004). "Section 500- Concrete Structures," *Georgia Department of Transportation Standard Specifications*, Available from www.dot.ga.gov/doingbusiness/theSource/Pages/specifications.aspx.

Google Earth (2011). *Map of Coastal Georgia*, created December 5th, 2011.

Gowripalan, N.; Sirivivatnanon, V.; Lim, C. (2000). "Chloride Diffusivity of Concrete Cracked in Flexure," *Cement and Concrete Research*, V. 30, pp. 725-730.

Gruber, K.A.; Ramlochan, T.; Boddy, A.; Hooton, R.; Thomas, M. (2001). "Increasing Concrete Durability with High-reactivity Metakaolin." *Cement and Concrete Composites.* V. 23, pp. 479-484.

Guneyisi, E.; Gesoglu, E.; Mermerdas, K. (2010). "Strength Deterioration of Plain and Metakaolin Concretes in Aggressive Sulfate Environments," *Journal of Materials in Civil Engineering*, V. 22, pp. 403-407.

Heide, N. (2005). *Crack Healing in Hydrating Concrete.* Masters thesis. Delft University of Technology. pp.128.

Hooton, R. and Emery, J. (1990). "Sulfate Resistance of a Canadian Slag Cement," *ACI Materials Journal*, V. 87, pp. 547-555.

Hopkins, S.E. (1962). "Distribution of the Species of *Cliona* (boring sponge) on the Eastern Shore of Virginia in Relation to Salinity," *Chesapeake Science*, V. 3, pp. 121-125.

Ismail, M.; Toumi, A.; Francois, R.; Gagne, R. (2008). "Effect of Crack Opening on the Local Diffusion of Chloride in Cracked Mortar Samples," *Cement and Concrete Research*, V. 38, pp. 1106-1111.

Jacobsen, S.; Marchand, J.; Boisvert, L. (1996). "Effect of Cracking and Healing on Chloride Transport in OPC Concrete." *Cement and Concrete Research.* V. 26, pp. 869-881.

Jacobsen, S.; Marchand, J.; Gerard, B. (1998). "Concrete Cracks 1: Durability and Self Healing – A Review," Proceedings of the Second International Conférence on Concrete under Severe Conditions, Tromso, Norway, Jun. 21-24, pp.217-231.

Jia, Y.; Aruhan, B.; Yan, P. (2012). "Natural and Accelerated Carbonation of Concrete Containing Fly Ash and GGBS after Different Initial Curing Period," *Magazine of Concrete Research*, V. 64, pp. 143-150.

Johnson, D.; Miltenberger, M.; Almy, S. (1996). "Determining Chloride Diffusion Coefficients for Concrete using Accelerated Test Methods," *Proceedings on Performance of Concrete in a Marine Environment*, New Brunswick, Canada, pp. 95-114.

Jonkers, H. M.; Thijssen, A.; Muyzer, G.; Copuroglu, O.; Schlangen, E. (2008). "Application of Bacteria as Self-healing Agent for the Development of Sustainable Concrete," *Ecological Engineering*, V. 36, pp. 230-235.

Kanaya, M.; Masuda, Y.; Abe, M.; Nishiyama, N. (1998). "Diffusion of Chloride Ions in Concrete Exposed in the Coastal Area," *Concrete Under Severe Conditions 2: Environment and Loading*, E & FN Spon, pp. 242-249.

Khatib, J. M. and Wild, S. (1998). "Sulphate Resistance of Metakaolin Mortar." *Cement and Concrete Research*, V. 28, pp. 83-92.

Koch, G. H.; Brongers, M.; Thompson, N.; Virmani, Y.; Payer, J. (2008), "Corrosion Costs and Preventive Strategies in the United States," National Association of Corrosion Engineers, Houston, TX.

Konin, A.; Francois, R.; Arliguie, G. (1998). "Penetration of Chlorides in Relation to the Microcracking State into Reinforced Ordinary and High Strength Concrete," *Materials and Structures*, V. 31, pp. 310-316.

Kurth, J.C. (2008). *Mitigating Biofilm Growth through the Modification of Concrete Design and Practice*. Master's Thesis. Georgia Institute of Technology. pp. 234.

Kurtis, K.E.; Monteiro, P.; Madanat, S. (2000). "Empirical Models to Predict Concrete Expansion Caused by Sulfate Attack," *ACI Materials Journal,* V. 97, pp. 156-162.

Kurtis, K.E.; Shomglin, K.; Monteiro, P.; Harvey, J.; Roesler, J. (2001). "Accelerated Test for Measuring Sulfate Resistance of Calcium Sulfoaluminate, Calcium Aluminate, and Portland Cements," *Journal of Materials in Civil Engineering,* V. 13, pp. 216-221.

Lauer, K. and Slate, F.O. (1955). "Autogenous Healing of Cement Paste." *Journal of the American Concrete Institute.* V. 41, June, pp. 1083-1097.

Lea, F.M. (1971). *The Chemistry of Cement and Concrete,* 3rd Edition, Chemical Publishing Co., New York, pp. 627.

Lee, S.; Moon, H.; Swamy, R. (2005). *"*Sulfate Attack and Role of Silica Fume in Resisting Strength Loss," *Cement and Concrete Composites,* V. 27, pp. 65-76.

Li, X., and Zhang, D. (2011) " Effect of Binary Admixture of Fly Ash and Slag on the Carbonation of Concrete for Hydraulic Structure," *Advanced Materials Research,* V. 150, pp. 1673-1676.

Luo, R.; Cai, Y.; Wang, C.; Huang, X. (2003). "Study of Chloride Binding and Diffusion in GGBS Concrete." *Cement and Concrete Research.* V. 33, pp. 1-7.

Luping, T. (1995). "On Chloride Diffusion Coefficients Obtained by Using the Electrically Accelerated Methods," *RILEM International Conference*, Paris, France.

Luping, T., and Nilsson, L.O. (1992). "Chloride Diffusivity in High Strength Concrete at Different Ages," *Nordic Concrete Research,* V. 11, pp. 162-171.

Mangat, P.S. and Gunisamy**,** K. (1987). "Chloride Diffision in Steel Fibre Reinforced Marine Concrete," *Cement and Concrete Research,* V. 17, pp. 385-396.

Mangat, P.S. and Khatib, J. M. (1995). "Influence of Fly Ash, Silica Fume, and Slag on Sulfate Resistance of Concrete," ACI Materials Journal, V. 92, pp. 542-552.

Mangat, P.S., and Molloy, B.T. (1994). "Prediction of Long Term Chloride Concentration in Concrete," *Materials and Structures,* V. 27, pp. 338-346.

Maslehuddin, M.; Page, C.; Rasheeduzzafar (1996). "Effect of Temperature and Salt Contamination on Carbonation of Cements." *Journal of Materials in Civil Engineering,* V. 63, pp. 63-69.

McGrath., P. and Hooton, R.D. (1996). "Influence of Voltage on Chloride Diffusion Coefficients From Chloride Migration Tests," *Cement and Concrete Research*, V. 26, pp. 1239-1244.

Mehta, P.K. (1975). ''Evaluation of Sulfate-resisting Cements by a New Test Method,'' *Journal of ACI,* V. 72, pp. 573–575.

Mehta, P.K. (1991). *Concrete in the Marine Environment*, Elsevier Science Pulishers, New York, NY, pp. 214.

Mehta, P. K., and Gjorv, O. E. (1974). ''A New Test for Sulfate Resistance of Cements,*''Journal of Testing and Evaluation*, V. 2, pp. 510–515.

Miller, A.N.; Strychar, K.; Shirley, T.; Rutzler, K. (2010). "Effects of Heat and Salinity Stress on the Sponge *Cliona celata*," *International Journal of Biology*, V. 2, pp. 3-16.

Mindess, S.; Young, J.; Darwin, D. (2003). *Concrete*, 2nd Edition, Prentice Hall Publishers, Upper Saddle River, NJ.

Mobasher, B. and Mitchell, T.M. (1988). "Laboratory Experience with the Rapid Chloride Permeability Test," *ACI SP-108: Permeability of Concrete*, (ed. D. Whiting, A. Walitt), American Concrete Institute.

Mohammed, T.U. and Hamada, H. (2003). "Corrosion of Steel Bars in Concrete at Joints under Tidal Environment." *ACI Materials Journal.* V. 100, pp. 265-273.

Mohammed, T.U., and Hamada, H. (2003). "Relationship Between Free Chloride and Total Chloride Contents in Concrete," *Cement and Concrete Research*, V. 33, pp. 1487-1490.

Monteiro, P. and Kurtis, K. (2003). "Time to Failure for Concrete Exposed to Severe Sulfate Attack," *Cement and Concrete Research*, V. 33, pp. 987-993.

Murata, K.; Cobanoglu, A.; Lampros, T.; Hershberger, R.; Norman, D.; Kawakami, K.; Matsunaga, Y.; Yamashita, S. (1997). "Determination of Sulfate in Brackish Waters by Laser Raman Spectroscopy," *Analytica Chimica Acta*, V. 344, pp 153-157.

National Cooperative Highway Research Program (2007), *Report 595: Application of the LRFD Bridge Design Specifications to High-Strength Structural Concrete: Flexure and Compression Provisions*, Transportation Research Board, Washington D.C.

Neumann, A.C. (1966). "Observations on Coastal Erosion in Bermuda and Measurements of the Boring Rate of the Sponge, *Cliona lampa*," *Limnology and Oceanography*, V. 11, pp. 92-108.

Neville, A.M. (1997). *Properties of Concrete*, 4 ed., John Wiley and Sons, New York, NY, pp. 844.

Nicol, W.L. and Reisman, H.M. (1976). "Ecology of the Boring Sponge (*Cliona celata*) at Gardiner's Island, New York," *Chesapeake Science*, V. 17, pp. 1-7.
Odler, I. (1997). "Expansive Reactions in Concrete," Materials Science of Concrete II, John Wiley & Sons Inc., New Jersey, pp. 221-247.

Otsuki, N.; Miyazato, S.; Diola, N.; Suzuki, H. (2000). "Influences of Bending Crack and Water-Cement Ratio on Chloride-Induced Corrosion of Main Reinforcing Bars and Stirrups," *AC1 Materials Journal*, V. 97, pp. 454-464.

Papadakis, V.G. (2000). "Effect of Supplementary Cementing Materials on Concrete Resistance against Carbonation and Chloride Ingress." *Cement and Concrete Research*, V. 30, pp. 291-299.

Papadakis, V.G.; Vayenas, C.; Fardis, M. (1991). "Fundamental Modeling and Experimental Investigation of Concrete Carbonation." *ACI Materials Journal*, V. 88, pp. 363-373.

Parks, J.; Edwards, M.; Vikesland, P.; Dudi, A. (2010). "Effects of Bulk Water Chemistry on Autogenous Healing of Concrete," *Journal of Materials in Civil Engineering*, V. 22, pp. 515-524.

Patil, H. S.; Raijiwala, D.; Prashant, H.; Vijay, B. (2008). "Bacterial Concrete – A Self Healing Concrete," *International Journal of Applied Engineering Research*, V. 3, pp. 1719-1725.

Pease, B., Couch, J., Geiker, M., Stang, H., and Weiss, J. (2009). "Assessing the Portion of the Crack Length Contributing to Water Sorption in Concrete Using X-Ray Absorption," *Proceedings of ConcreteLife'09: Second International RILEM Workshop on Concrete Durability and Service Life Planning*, Haifa, Israel.

Pedersen, V. and Arntsen, B. (1998). "Effect of Early-Age Curing on Penetration of Chloride Ions into Concrete in the Tidal Zone," *Concrete Under Severe Conditions 2: Environment and Loading*, E & FN Spon, pp. 468-477.

Polder, R.B. (1995) "Chloride Diffusion and Resistivity Testing of Five Concrete Mixes for Marine Environment," *RILEM International Conference*, Paris, France.

Raharinaivo, A.; Brevet, P.; Grimaldi, G.; Pannier, G. (1986). "Relationship between Concrete Deterioration and Reinforcing-Steel Corrosion," *Durability of Building Materials*, V. 4, pp. 97-112.

Rodriguez, O.G. (2001). *Influence of Cracks on Chloride Ingress into Concrete.* Masters thesis. University of Toronto. pp.273.

Roy, D.M. (1989). "Hydration, Microstructure and Chloride Diffusion of Chloride Ions in Hardened Cement Pastes," *ACI SP-114,* V. 2, American Concrete Institute, Detroit, pp. 1265-1281.

Roziere, E.; Loukili, A.; El Hachem, R.; Grondin, F. (2009). "Durability of Concrete Exposed to Leaching and External Sulfate Attacks," *Cement and Concrete Research*, V. 39, pp. 1188-1198.

Sahmaran, M. (2007). "Effect of Flexure Induced Transverse Crack and Self-healing on Chloride Diffusivity of Reinforced Mortar," *Journal of Material Science,* V. 42, pp. 9131-9136.

Sahmaran, M.; Keskin, S.; Ozerkan, G.; Yaman, I. (2008). "Self-healing of Mechanically-loaded Self Consolidating Concretes with High Volumes of Fly Ash," *Cement and Concrete Composites,* V. 30, pp. 872-879.

Saleem, H., et al. (2010). "Durability and Strength Evaluation of High-performance Concrete in Marine Structures," *Construction and Building Materials,* V. 24, pp. 878-884.

Scott, P.J.B.; Moser, K.; Risk, M. (1988). "Bioerosion of Concrete and Limestone by Marine Organisms," *Marine Pollution Bulletin*, V. 19, pp. 219-222.

Sideris, K.K.; Savva, A.; Papayianni, J. (2006). "Sulfate Resistance and Carbonation of Plain and Blended Cements," *Cement and Concrete Composites*, V. 28, pp. 47-56.

Skalny, J.; Marchand, J.; Odler, I. (2002). *Sulfate Attack on Concrete*, Spon Press, New York, NY, pp. 217.

Smith, B.G. (2001). "Durability of Silica Fume Concrete Exposed to Chloride in Hot Climates." *Journal of Materials in Civil Engineering.* V. 13, pp. 41-48.

Stanish, K.D. and Thomas, M. (2003). "The Use of Bulk Diffusion Tests to Establish Time-dependent Concrete Chloride Diffusion Coefficients." *Cement and Concrete Research.* V. 33, pp. 55-62.

Stanish, K.D.; Hooton, R.; Thomas, M. (1997). *Testing the Chloride Penetration Resistance of Concrete: A Literature Review*, FHWA contract report, pp. 33.

Streicher, P.E. and Alexander, M.G. (1995). "A Chloride Conduction Test for Concrete," *Cement and Concrete Research*, V. 25, pp. 1284-1294.

Sulapha, P.; Wong, S.; Wee, T.; Swaddiwudhipong, S. (2003). "Carbonation of Concrete Containing Mineral Admixtures." *Journal of Materials in Civil Engineering.*V. 15, pp. 134-143.

Suryavanshi, A.; Swamy, R.; Cardew, G. (2002). "Estimation of Diffusion Coefficients for Chloride Ion Penetration into Structural Concrete," *ACI Materials Journal,* V. 99, pp. 441-449.

Suzuki, K.; Ohno, Y.; Praparntanatorn, S.; Ninomiya, H.; Tamura, H. (1989)**. "**Influence of Flexural Crack on Corrosion of Steel in Concrete," *Technology Reports of the Osaka University,* V.39, pp. 49-57.

Suzuki, K.; Ohno, Y.; Praparntanatorn, S.; Tamura, H. (1990)**. "**Mechanism of Steel Corrosion in Cracked Concrete," Corrosion of Reinforcement in Concrete Construction, Third International Symposium, Wishaw, UK**;** Elsevier Applied Science, pp. 19-28.

Termkhajornkit, P.; Nawa, T., Yamashiro, Y.; Saito, T. (2009). "Self-healing Ability of Fly Ash - Cement Systems," *Cement and Concrete Composites,* V. 31, pp. 195-203.

Thomas, M. and Bamforth, P. (1999). "Modelling Chloride Diffusion in Concrete: Effect of Fly Ash and Slag." *Cement and Concrete Research.* V. 29, pp. 487-495.

Thomas, M.D.A. and Matthews, J.D. (2004). "Performance of PFA Concrete in a Marine Environment – 10 Year Results." *Cement and Concrete Composites.* V. 26, pp. 5-20.

Thomas, M.D.A., and Jones, M.R. (1996). "A Critical Review of Service Life Modeling of Concretes Exposed to Chlorides," *Concrete in the Service of Mankind: Radical Concrete Technology,* (eds. R.K. Dhir and P.C. Hewlett), E.&F.N. Spon, London, pp. 723-736.

Thomas, M.D.A.; Shehata, M.; Shashiprakash, S.; Hopkins, D.; Cail, K. (1999). "Use of Ternary Cementitious Systems Containing Silica Fume and Fly Ash in Concrete." *Cement and Concrete Research.* V. 29, pp. 1207-1214.

Thomas, M.D.A.; Scott, A.; Bremner, T.; Bilodeau, A.; Day, D. (2008). "Performance of Slag Concrete in Marine Environment." *ACI Materials Journal.* V. 105, pp. 628-634.

Thuresson, T.; Hansson, C.; Seabrook, P.; Tullmin, M. (1997). "Effect of Cracking and Accelerated Curing on the Corrosion of Steel Embedded in High Performance Concretes Exposed to an Industrial Effluent," Fourth international Conference, Sydney, Australia, CANMET/ACI SP-170, Farmington Hills, Michigan, pp. 965-986.

Tikalsky, P. and Carrasquillo, R. (1992). "Influence of Fly Ash on the Sulfate Resistance of Concrete," *ACI Materials Journal,* V. 89, pp. 69-75.

Torii, K. and Kawamura, M. (1994). "Effects of Fly Ash and Silica Fume on the Resistance of Mortar to Sulfuric Acid and Sulfate Attack." *Cement and Concrete Research*, V. 24, pp. 361-370.

UNEP/GRID-Arendal (2005). "Trends in Natural Disasters," UNEP/GRID-Arendal Maps and Graphics Library, Available at:http://maps.grida.no/go/graphic/trends-in-natural-disasters.

USGS Surface Water Information Pages, United States Geological Survey, June 3rd, 2010, from http://water.usgs.gov/osw/.

Van Tittelboom, K.; Belie, N.; Mynck, W.; Verstraete, W. (2010). "Use of Bacteria to Repair Cracks in Concrete," *Cement and Concrete Research*, V. 40, pp. 157-166.

Winitzki, S. (2006). "A Handy Approximation for the Error Function and Its Inverse," Lecture note, Ludwig-Maximilians University, Munich, Germany.

Yang, Y.; Lepech, M.; Yang, E.; Li, V. (2009). "Autogenous Healing of Engineered Cementitious Composites under Wet–Dry Cycles." *Cement and Concrete Research.* V. 39, pp. 382-390.

Zea, S. and Weil, E. (2003). "Taxonomy of the Caribbean Excavating Sponge Species Complex *Cliona carribaea – C. Aprica – C. langae* (Porifera, Hadromerida, Clionaidae)," *Caribbean Journal of Science*, V. 39, pp. 348-370.

Zhang, M.H., and Gjorv, O.E. (1991). "Permeability of High Strength Lightweight Concrete," *ACI Materials Journal*, V. 88, pp. 463-469.